Wind Energy in the Built Environment: An Experimental and Numerical Investigation of a Building Integrated Ducted Wind Turbine Module

A Thesis submitted for the Award of the Degree
Doctor of Philosophy (Ph.D.)

by

Robert K. W. Dannecker
Diplom-Physiker

Energy Systems Research Unit ESRU
Department of Mechanical Engineering
Faculty of Engineering
University of Strathclyde
Glasgow, Scotland
United Kingdom

September 2001

Viva

28th August 2001, Department of Mechanical Engineering, University of Strathclyde in Glasgow

Chairman: Prof. Dr. D. Gorman, Division of System Dynamics and Control, Department of Mechanical Engineering, University of Strathclyde

Supervisor: Dr. A. D. Grant, Senior Lecturer, Depute Director of the Energy Systems Research Unit, Department of Mechanical Engineering, University of Strathclyde

Internal Examiner: Dr. T. J. Scanlon, Lecturer, Division of Thermofluids, Department of Mechanical Engineering, University of Strathclyde

External Examiner: Prof. Dr. R. McD. Galbraith, Shoda Chair, Head of the Department of Aerospace Engineering, University of Glasgow

Copyright

Esta tesis está dedicada a nuestra pequeña, felizmente esperada

Marianna Sophia Dannecker Tamayo

quien llegó al mundo junto con el término de este trabajo

" Es gibt überhaupt keine Möglichkeit, in logischer Strenge aus vergangener Erfahrung auf die Zukunft zu schließen. Und doch ist der Schluß auf die Zukunft die ganze Pointe der Physik. Die Physik prophezeit. Sie verändert die Welt. Die Technik ist im Stadium des Entwurfs immer zukünftige Technik. Das heißt der Empirismus vermag einen Grundzug der empirischen Wissenschaften nicht wirklich aufzuhellen. Er sagt zwar, als Beschreibung, richtige Dinge darüber, aber er scheint nicht zu wissen, was er sagt."

Carl Friedrich Freiherr von Weizsäcker
Die Einheit der Natur, Studien
Carl Hanser Verlag, München, 1971
Deutscher Taschenbuch Verlag, Reihe Wissenschaft, München, 1995

Abstract

Wind is now established in Europe as a major 'renewable energy' resource, but its large scale exploitation is increasingly limited by environmental issues. Hence, on the way to a more sustainable development, it is desirable to seek ways to incorporate it into small scale embedded generation. As a first step, a prototype of a small scale Ducted Wind Turbine has been developed and tested, which seems to be feasible for integration into a conventional building. The wind flow around the building generates differential pressures which may cause an enhanced massflow through the turbine.

This thesis is concerned with the investigation of the flow through building integrated duct configurations. Hence, pressure and wind speed measurements have been carried out on a wind tunnel model at different angles of incident wind. Different duct geometries with attached spoilers have been tested, and it was confirmed that wind speeds up to 30 % higher than in the approaching free stream are induced in the duct, in some cases tolerating an angle of incident wind up to ± 60°.

The experimental work proceeded in parallel with Computational Fluid Dynamics modelling. Adaptive gridding of the complex full model geometry required a two dimensional approach, which was used to compare the predicted flow behaviour qualitatively. Three dimensional simulation of the flow field in the building integrated duct could be compared with experimental results. A new flow field mapping approach was initialised to form a two stage process in which conditions in the large-scale flow domain, modelled in a coarse three dimensional simulation, are used as boundary conditions for a localised simulation of the duct flow.

Based on performance measurements of a free standing prototype in field trials and the experimentally determined wind speed in the duct, a power prediction model was developed. For the Scottish climate, the proposed device compares favorably with conventional small wind turbines and photovoltaics.

The presented work evaluates the concept of harvesting wind energy in the built environment and provides outlines for the future design of a building integrated Ducted Wind Turbine module.

Table of Contents

1. Introduction

1.1. Wind Energy in Europe: towards Embedded Generation in the Built Environment

Early cultures in Europe had already sailing boats, and wind energy conversion through windmills goes in many regions in Europe back to the early 13th century. Since this time, it has fascinated and inspired scientists and artists, and wind energy has become part of the cultural scene. Ancient sailors understood lift and influenced the development of windmill sails, and 500 years later windmill sails had major features of modern wind turbine blades (Dodge 2000). The introduction of fossil fuels, the development of the steam engine with external condenser through James Watt in Scotland, and more recently electrification closed down step by step all the windmills. They remained either as ruins or were refurbished as museums and tourist attractions. But it is remarkable, that the last historical tower windmills (for example behind Greenock near Glasgow) stopped their operation only in the second half of the 20th century, working as hybrid systems in tandem with electric and diesel motors.

There was a period without any significant new development. Without the economic need and the necessary awareness of environmental issues, only a few machines were built mainly as research and demonstration projects rather than for power production. Significant contributions came especially from Denmark from the end of the 19th century (Poul la Cour) and from Germany since the 1930s, and the basic design of modern wind energy plants was laid down (Hütter 1942).

The oil crises in the early 1970s sparked political awareness of Europe's dependency upon the world energy market, and among other considerations the feasibility to harvest wind energy arose. The development started slowly, supported by both national and European agencies, and failures of several early prototypes in the 1980s (for example the GROWIAN project in Germany) jeopardised the concept of wind power generation in larger scale. Meanwhile, the sudden emergence of a market in California created a proving-ground, which manufacturers (principally Danish) used to advance the technology and to improve reliability. With increasing environmental awareness manifested in the 1990s in the World Climate Conferences in Rio and Kyoto, 'renewable energy' became a major topic on the European agenda (European Commission 1997, 2000), and many countries opened their electricity market to private electricity providers under certain trade regulations. This measures among others provided the framework for the expansion of European wind technology, which has in the space of less than 20 years evolved from an insignificant industry making small and simple machines into a technology which can compete with the well established forms of power generation (European Commission 1998).

Scotland has the largest wind energy resource in Europe. The exploitation of this resource is regulated by planning authorities, and the contribution of wind energy to the overall supply is still minor.

In general, wind energy has many positive environmental and economical facets, but critical voices arise against the visual impact of large scale power devices and their profitability, and discussion about wind energy pervades all parts of the society with expert opinions for and against (Alt et alt. 1998; Wolfrum 1997). Irritating effects of flickering sunlight and shadow-play are reported, and complaints about noise pollution generally confine wind energy devices to sparsely populated areas. Emitted low frequencies out of the audible range, the infrasound, are claimed by some critics; these are difficult to shield and affect the well-being. Wind energy plants in remote areas still need local infrastructure like access roads and foundations, grid connection, and their impact on wildlife and local microclimate is controversial.

These critical issues do not affect the wind energy device which is under consideration here. The submitted investigation (Dannecker and Grant 1999) concerns the development of an approach for wind energy exploitation in an urban environment, using Ducted Wind Turbines which are integrated within the building structure as modular units. These devices make use of pressure differences and local accelerated flow which arise in wind flow around buildings. Both effects may increase the mass flow through the turbine and therefore enhance power output. Integration and ducting minimises visual impact, power is created close to the demand site in the building, and their small size keeps possible noise emission out of the infrasound range. Perhaps this fundamental investigation presented here opens the way for a sound method to harvest wind energy as a new source of embedded 'renewable energy' in the built environment.

1.2. Objective and Content of this Thesis

The objective of the present work is to prove a new concept of a building integrated Ducted Wind Turbine module.

In order to understand this concept, Chapter 2 will combine a literature review with the outline of the basic wind flow pattern around building structures.

Currently, the development of the Ducted Wind Turbine deals with two basically different design options:

1. fee standing but integrable into a cladding structure
2. complete integration through a inserted duct at the wall roof corner of a building

As the development of the first device type has already proceeded towards a testing prototype, results from its field trials are reported.

But the focal point of the present work is the investigation of the complete integration of a possible turbine in an inserted duct at the wall / roof edge of a building. This idea is born out of a combination of thoughts concerning the wind flow around the leading wall / roof edge and the use of pressure differentials for power augmented wind turbines, which is reviewed in Chapter 3.

This aim is achieved by means of experimental and numerical methods. Therefore, investigations of the aerodynamical behaviour of a small scale model building with different integrated duct modifications have been carried out in the department's open section wind tunnel, which will be subject of Chapter 4.

Chapter 5 covers the theoretical background of Computational Fluid Dynamics (CFD). The outline of the two- and three dimensional set up of the numerical model has been analysed in Chapter 6, which concerns the modelling of complex flow fields in particular in the duct region (Chapter 7). In the context of this work, the author has attempted to trace out a method for a coupled three dimensional / two dimensional flow field simulation approach.

Finally in Chapter 8, a power prediction model is proposed on the base of the achieved results, to estimate the performance of the building integrated Ducted Wind Turbine Module in comparison with established renewable energy technologies in the built environment.

The conclusion in Chapter 9 evaluates the whole concept based on the results of the present work and will outline a programme of necessary future investigations.

References

Hütter U., Ingenieurschule Weimar, Germany 1942; Beitrag zur Schaffung von Gestaltungsgrundlagen für Windkraftwerke; Dissertation an der Technischen Hochschule Wien, Austria, 22th December 1942

Dodge D.M.; Illustrated History of Wind Power Development; TelosNet Bookstore, Centenial, Colorado, USA, 2000

Communication Document from the Commission of the European Communities, DG XVII, Directorate-General for Energy and Transport; Energy for the Future: Renewable Sources of Energy; White Paper for a Community Strategy and Action Plan; COM (97) 599 final, 26th November 1997

Discussion Document from the Commission of the European Communities, DG XVII, Directorate-General for Energy and Transport; Towards a European Strategy for Energy Supply; Green Paper; COM (2000) 769, 29th November 2000

Commission of the European Communities, DG XVII, Directorate-General for Energy and Transport; Wind Energy – The Facts; Catalogue No CS-16-98-392-EN-C, 1998

Alt F., Claus J. und Scheer H. (Herausgeber); Windiger Protest. Konflikte um das Zukunftspotential der Windkraft; Ponte Press, Bochum, Germany, 1998

Wolfrum O. (Herausgeber); Windkraft: eine Alternative, die keine ist; Verlag Zweitausendeins, Frankfurt a.M., Germany, 1997

Dannecker R. and Grant A.; Wind Energy in the Built Environment, Final Scientific Report, Project No. JOR3-CT97-5008 (DG12-DEMA); Commission of the European Communities, DG XII, Directorate-General for Science, Research and Development, JOULE-Non Nuclear Energy Research, December 1999

2. Wind Energy in the Built Environment

2.1. The Structure of the Wind in Urban Areas

Wind appears through pressure differentials between regions in the atmosphere. Due to surface characteristics the friction generates a certain boundary layer, the shear flow. It determines the vertical profile of flow parameters, like velocity and turbulent intensity. Atmospheric boundary layer models anticipate surface related parameters (roughness height, friction velocity, displacement height) which adjust the model to the specific wind site. The equations of motion are all based on the conservation of momentum, but they differ because of the forces which are taken into account (Singer et al. 1967, Harris and Deaves 1980, Bergmann 1995). Therefore, predicted wind velocity profiles differ significantly.

The characteristics of the wind depend among others on the vertical exchange in the atmosphere.

Temperature differences, as they arise from heated surfaces, cause a buoyant flow. The different wind situations may be classified in three main sections, according to the turbulent exchange (Singer et al.1967).

An unstable boundary layer occurs, when the temperature is higher at the ground and rapidly decreases with height. In this thermal stratified (Monin and Obuchov 1954) boundary layer, at low average wind velocities (less then 3 m/s horizontally), vertical buoyant flow dominates and thermal turbulence exceeds frictional turbulence. The air may rise up many hundreds of meters and may create a dome effect over cities. Especially at night, cooled air drops down and there is wind flow into the city from its outskirts. Pollution and moisture play an important role in heat storage in the atmosphere over the city and may disturb the turbulent exchange significantly (Dargent 1996). At higher wind velocities, the buoyant flow becomes less important and the frictional turbulence dominates.

Neutral atmosphere is approached with negligible heat flux. The height of the boundary layer can rise to hundreds of meters. The turbulence is due to friction. A wind approaching a city will create a highly turbulent zone from the ground to approximately twice the average building height (Dargent 1996). Above, the wind will generate a mean profile according to the vertical gradient of the wind due to the shear force. The displacement height may be interpreted as the vertical shift of the effective ground level for the wind velocity profile over the city. In this case the vertical velocity gradient is much larger than in thermal stratification.

A stable boundary layer occurs when the air is cooled at the ground. In this case the vertical velocity gradient is also large and the height of the boundary layer may drop down to 100 m over a smooth terrain. Approaching the city, the wind will behave in similar manner to the case of the neutral atmosphere.

In all cases, over the rougher urban terrain the wind is more turbulent, or gusty, than over smooth terrain. The average longitudinal turbulence length scale is in the range of 100 to 1000 m. The turbulent intensity declines from around 50 % and reaches a level of approximately 10 % in the upper part of the atmospheric boundary layer over the city. The wind velocity may increase by 50 % in a height of two times the average building height above the city. Data series have been taken on tall buildings over the years, in Europe probably starting with Gustave Eiffel at his tower (305 m) in Paris at the end of the 19th century (Eiffel 1900). Since the sixties it became a common practice to record the wind climate data on extended high rise buildings in cities, for example on broadcasting towers (Helliwell 1971). Based on theoretical considerations and measured data series, Davenport was one of the first to describe the properties of gustiness in terms of the spectra and the scales. Reliable estimates of these quantities could be made from the mean wind velocity and the ground roughness (Davenport 1963, Davenport 1967). Today, various standard functions including tables with appropriate adapting parameters have been developed for wind engineering and civil engineering purposes (ESDU 1993, ASHRAE 1993, European Wind Atlas 1989, BRE 1989). In order to predict the wind speed above a town, the average wind speed of the region (at standard 10 m height) may be requested at the nearest airport or taken from the standard wind speed map (BRE 1989, Meteorological Office 1976). This wind speed value may be extrapolated to city conditions by means of one of the standard functions. The resulting standard wind profile often is extended to levels below the average building height down to the ground level. In reality this process might not be very reliable. If this method fails for the specific case, a detailed investigation may have to take place.

Generally it can be stated, that in the turbulent zone below the displacement height, the wind will be determined by local effects in interaction with the building. At an open site, the wind speed at pedestrian height may be about three-quarters of the speed measured at the standard 10 m height, but in the city it may be only about one-quarter to one-third. If the wind meets a building which is considerably taller than its neighbours, this general shelter effect may not occur and the local flow situation may be completely reversed. Much of the approaching wind is deflected downwards, carrying high speed winds towards ground level. Some of this wind forms horizontal vortices in the space between the buildings in the neighbourhood. At the building corners the flow accelerates and may form high speed jets which stretch downwind for a considerable distance. Therefore the grouping of the buildings may have a significant influence on the local flow situation. Also, the interaction of the wind with local small scale obstructions like balconies and plant rooms might shorten the turbulence length locally. As the wind creates a suction area on any leeward faces, communication between windward and leeward areas will cause a strong wind which penetrates into the wake region behind the building. The extension of the recirculation zone leeward of the building depends on the aspect ratio of the building itself, but the influence of the building wake may persist for a distance downstream which corresponds to several building heights. Hence the flow situation for a grouping of several high rise buildings may differ very much from the pattern around any single one.

In order to give guidance to city planners, some practical standard functions have been created which determine the different areas of the flow field according to the aspect ratio of a single rectangular building (BRE 1994, ASHRAE 1993). But buildings of an even moderately complex shape can generate flow patterns which are too complex to model with a scaled function. The effect of nearby buildings is also very difficult to generalise. Accurate representation of the local wind flow can usually take place only by means of experimental or computational modelling of the whole flow domain.

References

Singer L.A., Busch N.E. and Frizzola J.A.; The Micrometeorology of the Turbulent Flow Field in the Atmospheric Surface Boundary Layer; Proc. of the International Research Seminar 'Wind Effects on Buildings and Structures', Ottawa, Canada, 11th -15th September 1967, Vol. 1 pp. 557-594.

Harris R.I. and Deaves D.M.; The Structure of Strong Winds; Proc. of the London Construction Industry and Information Association (CIRIA) Conference 'Wind Engineering in the Eighties', London, England, 12th - 13th November 1980, Paper 4, pp. 4-1 to 4-93.

Bergmann J.C.; Zur Quantifizierung des vertikalen Austausches in einer idealisierten neutralen oder stabilen planetarischen Grenzschicht – Ein Konzept zur Herleitung des vertikalen Austauschkoeffizienten; Dissertation, Fakultät für Geowissenschaften, Universität Hamburg, Germany, Januar 1995.

Monin A.S. and Obuchov A.M.; Fundamentale Gesetzmäßigkeiten der turbulenten Vermischung in der bodennahen Schicht der Atmosphäre; Berichte (Trudy) des Geophysikalischen Instituts der Akademie der Wissenschaften der SSSR No. 24 (151), page 163, 1954.

Dargent C.; Contribution à la modélisation de la dispersion de pollutants – Etude de sillages autour d'obstacles de forme parallélépipédique; Thèse de Docteur, Physique et Chimie de l'Environnement, Institut Nationale de Polytechnique (INP) de Toulouse, France, Septembre 1996.

Eiffel G.; Travaux Scientifiques exécutés â la tour de trois cent metres; L. Maretheux, Paris, France 1900

Helliwell N.C.; Wind over London; Proc. of the 3rd International Conference on Wind Effects on Buildings and Structures, Tokyo, Japan, 1971, pp. 23-32

Davenport A.G.; The Relationship of Wind Structure to Wind Loading; Proc. of the 16th Symposium on Wind Effects on Buildings and Structures, National Physical Laboratory, Teddington, Middlesex, England, 26th - 28th June 1963

Davenport A.G.; The Dependence of Wind Loads on Meteorological Parameters; Proc. of the International Research Seminar 'Wind Effects on Buildings and Structures', Ottawa, Canada, 11th -15th September 1967, Vol. 1, pp. 19-82

Engineering Science Data Unit ESDU, Wind Engineering , Wind Speed and Turbulence, Vol.1a: Characteristics of Atmospheric Turbulence near the Ground. Item No 85020, April 1993. ESDU International, London. ISBN 0 85679 526-7

ASHRAE Handbook 1993, Fundamentals, Chapter 14: Airflow around Buildings; American Society of Heating, Refrigerating and Air-Conditioning Engineers (ASHRAE), Atlanta, USA; ISBN 0-910110-97-2

European Wind Atlas; published for the Commission of the European Communities, DGXII, Directorate-General for Science, Research and Development; by I. Troen and E.L. Petersen at Riso National Laboratory Denmark. ISBN 87-550-1482-8

BRE Digest 346; The Assessment of Wind Loads; Building Research Establishment, Department of the Environment, United Kingdom
Part 1: Background and Method, July 1989
Part 3: Wind Climate in the United Kingdom, August 1989
Part 4: Terrain and Building Factors and Gust Peak Factors, August 1989
Part 5: Assessment of Wind Speed over Topography, November 1989
Part 7: Wind Speeds for Serviceability and Fatique Assessments, November 1989

Maps of Hourly Mean Wind Speed over the United Kingdom 1965-1973; Climatological Memorandum No.79, The Meteorological Office, United Kingdom 1976

BRE Digest 390; Wind around Tall Buildings; Building Research Establishment, Department of the Environment, United Kingdom July 1994

2.2. The Interaction of the Wind with the Building in Urban Areas

With the appearance of modern high rise buildings, it became urgent to provide a sound basis for structural design. Hence, series of data have been recorded at selected buildings worldwide. Values of pressures and its fluctuations on the building faces have been related to the wind speed and the characteristics of turbulence and gustiness, at different heights over built up areas.

One of the early field trials was carried out at the Empire State Building in New York 1932-1936 (Rathbun 1940). The obtained results showed irregularity to a very high degree. Even negative pressures were recorded on the windward face, and high wind speeds at the top of the building did not correspond with low readings at half of the building height. The investigation indicated that there was no consistency between wind tunnel results for the Empire State Building model and its real load patterns in New York. But the frequency response of the manometer system in use was too low to indicate gusty patterns, and the readings from different parts of the building were not made simultaneously. Hence changes in the incident wind may have caused misleading observations.

In Europe, investigations started in the sixties in Great Britain. The Building Research Establishment (BRE) developed a pressure transducer and conducted a series of tests at different buildings in London, up to 130 m height (Newberry 1963). Successive records for the same wind direction show a general similarity to wind tunnel results. However, the experiments were not able to deliver non-dimensionalised pressure coefficients because of insecurity in the reference pressure of the gauges used. But very interesting observations were made of the dynamic changes in pressure distribution. Positive pressure built up fast and simultaneously over a wide surface, but the suction peaks are of very short duration and act only over small areas at any one instant. It was stated that this pressure pattern fluctuation is linked to gusty changes in wind direction rather than by changes in the incident wind speed. Therefore, gust factors should be taken into account for any design predictions, as the steady condition in wind tunnel testing may not represent the natural wind flow.

For the case that the wind traverses several tall buildings in its approach towards the building under investigation, a large reduction of the wind load was found. Generally, the suction load on the leeward side was remarkably low (Newberry et al. 1968). The stagnation point seems to occur on the windward face at approximately 80 % of the building height, and above this the pressure coefficient drops by only 10 %, which contradicts wind tunnel observations.

Pressure recordings on a 40 m high building in an Australian university campus area support the latter observation (Melbourne 1971). The pressure coefficient agrees with the wind tunnel measurements only at the stagnation point at approximately 80 % building height. On the upper half, the wind pressure on the building exceeds the model data, whereas on the leeward side the suction in the wake of the real building is 20 to 30 % less than in the wind tunnel. The characteristic of the turbulence in the approaching flow affects the wake behind the obstacle.

In a similar comparison at a ca. 200 m high building in Montreal, it is stated that only in the lower levels is a reasonable agreement between wind tunnel data and full scale data achievable (Standen et al.1971). In particular the pressure fluctuations on the model due to simulated turbulence do not correspond to measured values on the building.

In order to include the effect of gustiness, the approach of the design wind pressure has been developed. It is the product of the reference mean velocity pressure at full scale building roof height, the pressure coefficient obtained by wind tunnel tests with simulated boundary layer shear flow, and at least one correction factor which allows for gusts (Davenport et al. 1971). Values for the correction factor for short gusts are obtained by recording the power spectra of the wind pressures. At a 147 m high building in Tokyo, gust periods over a range from 10^{-3} Hz to the shortest at 10 Hz have been measured at an average wind velocity of 25 m/s, which increased the short term pressure on exposed cladding by a gust factor of up to 3.5 (Miyoshi et al. 1971). But the relationship of wind structure to wind loading as first stated by Davenport (Davenport 1963) seems to be more complex, according to an investigation in the 1980s. At a 59 m high building in Tokyo, the turbulence intensity has been measured in the range of 19 to 33 % at a longitudinal scale of turbulence of 38 to 287 m (Matsui et al. 1982). As the wind was nearly normal to the windward face, wind pressure fluctuations originate from upstream velocity fluctuations. The wave number of the recorded power spectral density of the wind pressures exceeds the range of the turbulence scale. Also, maximum instantaneous static pressures did not occur necessarily simultaneously with maximum instantaneous dynamic pressure. In particular wind pressure fluctuations on the leeward face are very moderate and they hardly follow the wind speed fluctuations. The turbulence intensity of the wind pressure has a minimum in the area of the stagnation point, which is extended from 75 to 90 % building height. Above, the pressure coefficient exceeds 0.9, below the pressure coefficient takes on values over 0.8. On the leeward side, the pressure coefficient is nearly constant at zero or even slightly positive. On the one hand, this could be caused by the internal pressure situation which balances arising suction, but the case of zero suction at the leeward side was also confirmed at another building with proven minimal permeability (no windows or other openings) at the leeward side.

It seems to be that the interaction of the building with turbulent and gusty flow is not completely understood. Davenport therefore includes a safety factor, based on statistical uncertainty, in the National Building Code of Canada (Davenport 1983), which lays down the basis for the civil engineering standards in many other countries.

References

Rathbun J.C.: Wind Forces on Tall Buildings; Transactions of the American Society of Civil Engineers (ASCE), paper 2056, Vol. 105 (1940), pp. 1-41

Newberry C.W.: The Measurement of Wind Pressures on Tall Buildings; Proc. of the 16th Symposium 'Wind Effects on Buildings and Structures', Vol.1, pp. 114-149; National Physical Laboratory, Teddington, Middlesex, England, 26th -28th June 1963

Newberry C.W., Eaton K.J. and Mayne J.R.: Wind Loading of a Tall Building in an Urban Environment - A Comparison of Full Scale and Wind Tunnel Tests; Proc. of a Symposium on 'Wind Effects on Buildings and Structures', Loughborough University of Technology, England, 2nd -4th April 1968, Vol 1

Melbourne W.H.: Comparison of Pressure Measurements Made on a Large Isolated Building in Full and Model Scale; Proc. of the 3rd International Conference on 'Wind Effects on Buildings and Structures', Tokyo, Japan, 1971, pp. 253-262

Standen N.M., Dalgliesh W.A. and Templin R.J.; A Wind Tunnel and Full Scale Study of Turbulent Wind Pressures on a Tall Building; Proc. of the 3rd International Conference on 'Wind Effects on Buildings and Structures', Tokyo, Japan, 1971, pp. 199-209

Davenport A.G. and Dalgliesh W.A.; A Preliminary Appraisal of Wind Loading Concepts of the 1970 Canadian National Building Code; Proc. of the 3rd International Conference on 'Wind Effects on Buildings and Structures', Tokyo, Japan, 1971, pp. 441-450

Miyoshi S., Ida M. and Miura T.; Wind Pressure Coefficients on Exterior Wall Elements of Tall Building; Proc. of the 3rd International Conference on 'Wind Effects on Buildings and Structures', Tokyo, Japan, 1971, pp. 273-264

Matsui G, Suda K. and Higuchi K.; Full-Scale Measurement of Wind Pressures acting on a High-Rise Building of Rectangular Plan; Journal of Wind Engineering and Industrial Aerodynamics, Vol. 10, 1982, pp. 267-286

Davenport A.G.; On the Assessment of the Reliability of Wind Loading on Low Buildings; Journal of Wind Engineering and Industrial Aerodynamics, Vol. 11, 1983, pp. 21-37

2.3. Wind Tunnel Experiments of Wind Flow around Buildings

Parallel to full scale measurements at buildings in the city as described above, series of wind tunnel tests on model houses have been conducted in order to investigate the aerodynamical loads for civil engineering purposes. Aerodynamic loads on a fixed solid object correspond to the loss of momentum in its wake. Hence important work has been carried out to extend the original theory of wake flow (Schlichting 1965). Based on detailed measurements of mean and turbulent wake flow parameters behind a cube and behind a rectangular block, empirical equations could be derived which describe the wake flow parameterised in terms of the obstacle dimension. Drag and overturning moment is related to the spatial integral of the momentum loss in the wake flow, and theoretical prediction of the wake flow may result in the prediction of forces on the object (Counihan and Hunt 1969-1971).

Today, standards are available for very simple geometry like rectangular blocks, measured in a smooth uniform flow at Reynolds number 10^4 -10^6 (ESDU 1993). The given standards for blocks of different aspect ratios may be applied to estimate wind loads on buildings under certain constraints. When the building is smaller then the length scale of turbulence in the wind (according to ESDU 1993 this is 60 m high and 50 m wide), it may be enveloped by whole gusts. Therefore the static loading can be estimated using the ESDU standards, modified with the wind speed profile. If the dynamic component of loading is significant, the standard coefficient may be scaled with the design gust factor and the exposure factor as developed from Davenport (Davenport and Dalgliesh 1971, Davenport 1983). For the design purpose, drag- and force coefficients as integrative values acting on the object as a whole or on its surfaces are often sufficient. Under different flow conditions, an additional allowance of ± 20 % should be made for uncertainties. In the case of pressure coefficients, small variations in the flow caused by turbulence and gusts may alter the overall magnitude of pressure and its distribution over the surface, because of flow separation, possible reattachment and vortex generation. Increased turbulence has little effect on front face pressures, but turbulence tends to promote reattachment of the flow at the wall of the object due to increased mixing and a thicker shear layer (Roberson and Rutherford 1969). Hence, not only do the pressures on the object change in the extreme case from suction (separated flow) to overpressure (reattached flow), also the suction in the wake behind the house declines by up to 40 % and alters its extension. With increasing turbulence in the approaching flow, the near wake at the object may be affected by a surrounding turbulence field which carries small scale vorticity and increases momentum and mass transfer into the thicker layer (Laneville et al. 1975). Therefore, for pressure coefficients the standards refer to the datum conditions which have not much in common with the real wind flow around buildings. But these standards have the advantage, that for simple geometry the measured distribution may be parametrically analysed and the influence of different aspect ratios, wind directions and incident velocity profiles can be predicted.

In the 1960s, substantial work was done to make the flow in a wind tunnel more similar to real conditions and to find scaling laws which allow the prediction of pressure coefficients at real buildings from those observed on small scale models. Those investigations show certain trends, but generalisation towards standardised pressure coefficients even for single rectangular blocks with certain aspect ratios is not yet possible. In particular work has to be done to investigate the combination of all effects caused by the wind velocity profile over the city, the turbulence intensity and length scale, gusts at various angles of incidence and the influence of shelter and wake flow through neighbouring buildings.

First investigations to achieve more realistic wind tunnel model conditions result in a linear model-law (Jensen 1958). The product of the wind velocity and the size of the object should be alike in the model test and in nature (Reynolds number similarity). In fact, wind tunnel tests are often carried out at values of Reynolds number which are in magnitude 100 times too small. The general flow pattern around objects with sharp edges is not greatly affected by changes in the Reynolds number, in particular if the flow is either normal or tangential to the object surfaces. The flow always separates at the sharp edges. In the case of rounded shapes, the separation point migrates with changes in Reynolds number, hence a wind tunnel experiment with a rounded tower model is much more delicate. Jensen even argues that in case of rectangular blocks, the natural wind flow is fully turbulent and therefore the Reynolds number is of no significance. This underlines the requirement for a simulated turbulent boundary layer flow in the wind tunnel. The roughness height of the natural flow should be linearly downscaled according to the model scale. A rough surface upstream of the working section of the tunnel creates the required turbulent boundary layer wind velocity profile. For small models of one storey houses, the values of suction depend significantly on the correct scaling of the roughness parameter. A smoother wind flow creates much less suction above the roof and on the leeward face.

Jensen's approach of linear scaling can be extended to the longitudinal length scale of turbulence which is a measure of the dominant eddy size (Cook 1977). The turbulent length scale is a function of height above the ground. The linear scale of any building model should be matched to the boundary layer scale factor, otherwise the building model generated turbulence will not match the simulated atmospheric turbulence. The result of this mismatch has been investigated by Baines.

For taller building models, the influence of the wind speed distribution on the pressure coefficients differed from Jensen's observation. In a simulated boundary layer produced by a grid at the entrance of the working section, the effect of the wind speed gradient on a skyscraper model was to reduce the suction on the roof by as much as half (Baines 1963). Generally, taller buildings have a higher suction on the roof. On a lower building of four to five storeys, the velocity distribution of the incident flow is stated to have no significant effect on roof suctions. According to Baines, the areas of flow reattachment will be very different for the model building and the real structure. In a conventional wind tunnel the eddies are an order of magnitude or more smaller than the size of the model, whereas in the field the eddies are mostly an order of magnitude larger than the structure. The Reynolds number of the flow over the building was 500 times that over the model. Therefore the turbulent structure is completely different from the real wind situation.

Simulation of turbulence characteristics of the flow should include the intensities, probability distributions and spectra (both shape and scale) of the individual components and their higher order correlations (Reynold stresses) (Davenport and Isyumov 1967). Therefore the experimental set up should be a combination of roughness element surface and a low grill at the entrance of the wind tunnel working section. Due to the resulting velocity gradient with height, a general reduction of all positive pressures is observed. Along the roof and on the leeward face, the suction is reduced significantly. When the extended building is surrounded by a lower built up area, Davenport observed also effects due to the grouping. Fluctuating pressures are much lower where the extended building is sheltered by lower buildings upstream, whereas the wind induced pressures on the lower buildings showed a much higher peak suction. Pressure fluctuations along the edge of the building are seen to contain a strong component at the vortex shedding frequency.

The dependence of the Strouhal number, a measure of the vortex shedding frequency, on the mean drag coefficient of the obstacle shows that the occurrence of vortex shedding is very likely in the built environment (Maccabee 1968). Investigations of vortex shedding from two different plates normal to the airflow, the plates set up a certain distance behind each other, showed a strong dependence of the distance between the plates. These early experiments support the idea of turbulence 'resonance', due to spacing.

The transition in the vortex pattern from the horse shoe type to the von Kármán type seems to depend on the aspect ratio (height / width) (Sakamoto 1985). Namely when the width of the obstacle is relatively large, the flow from the top joins with the flow from the side and forms the horse shoe type vortex. With the decrease of the width of the object, the flows separating from each side become stronger then the flow from the top, hence the wake is rather controlled by the side flow which form the von Kármán type vortex. The strength of circulation of the horseshoe vortex surrounding the base of the prism decreases with increase in aspect ratio.

As soon as the model is not isolated, prediction of the flow and pressure field in its vicinity becomes complex. In an early work, for a pair of cuboids a theoretical model has been proposed, based on fundamental fluid mechanics (Brittner and Hunt 1979). It is assumed that the flow between the paired arrangement is driven by the pressures on each single building as measured in a model test. In physics, this kind of superposition normally takes an interaction term or a perturbation term into account. Solutions to this new system are found by optimisation. Although this is missed out in the presented model, the authors claim it could predict to some extend measured wind speeds above the ground in vicinity of the models. Length scales for vorticity are determined through the geometrical arrangement of the pair (for example from the gap width between models).

For groups of buildings, the flow field has to be reassessed as a whole. The findings for a single obstacle in the flow can not be extrapolated to describe the situation of different obstacles interacting in one flow field. Investigations for single rectangular blocks of different aspect ratios show the limitations of a general law of spacing. Even with constant flow and two simple rectangular models, the geometry of the single models and their local arrangement lead to a huge variety in flow patterns (Latiff 1989). For a pair of identical models, the upstream model experiences a higher suction over the roof than a single isolated model. The expansion and the intensity of flow separation seems to be increased by a second sheltered model. If the second shielded model does not extend beyond the upstream model, positive pressure coefficients appear over a wide area of the roof. The vorticity in the gap in between causes suction at the windward face of the sheltered model and reduces the suction at the leeward wall of the upstream model. Corner vortices from the upstream model entrain the vortex in front of the downstream model. The width of the upstream model affects the pressure on the roof of the sheltered model, even if both models have similar height. If the wind turns through 90° and the models lay side by side, the effect of proximity is to reduce the suction over the roof of both models equally. A change of wind direction causes quite complex flow situations, and combination with variations of the geometrical parameters like spacing and the model size for two, three and more models creates a vast amount of data which will not follow parametric laws.

A way out of the dilemma of interaction between separate models, is to model the general effect of a built up area in the surrounding of the building under investigation. The number of models is now so large that the single interaction can be replaced by observing the impact on the building under investigation in the matrix of the surrounding lower sheltering buildings, varying the plane area density (= built up plane area / whole plane area) (Hussain and Lee 1980). Wake interference starts at a plane area density larger than 12 %, which causes a reduction of pressure at the windward face with negative pressure coefficients possible. Suction above the roof decreases up to 20 to 40 % of its value on a single model. At higher plane area densities, the values of the measured pressure coefficients stabilise. With increasing the height of the building under investigation above the surrounding models, positive values of pressure coefficient establish on the windward side but with shifting stagnation area. The suction above the roof is generally lower than for an isolated model, but rises with relative building height quite sharply.

Based on parametrical analysis of wind tunnel test results on models of simple geometry, an empirical numerical model has been developed which takes the geometrical parameters of the obstacle and its surrounding as well as wind parameters into account (Grosso 1992). Here, the distribution of the pressure coefficient over the surfaces was fitted to polynomial functions. This model tries to combine the various results to an entirety.

References

Schlichting H.; Grenzschicht Theorie; Braun'sche Verlagsbuchhandlung Karlsruhe, Germany,1965 or in translation: Boundary-Layer Theory; McGraw-Hill Book Company, London, England, 1979

Counihan J.: Further Measurements in a Simulated Atmospheric Boundary Layer; Laboratory Note No. RD/L/N 68/69 1969
Hunt J.C.R. and Smith G.P.: A Theory of Wakes behind Buildings and some Provisional Experimental Results; Laboratory Note No. RD/L/N 31/69 1969
Hunt J.C.R.: Further Aspects of the Theory of Wakes behind Buildings and a Comparison of the Theory with Experimental Results; Laboratory Report No. RD/L/R 1665 1970
Counihan J.: An Experimental Investigation of the Wake behind a Two-Dimensional Block and behind a Cube in a Simulated Boundary Layer Flow; Laboratory Note No. RD/L/N 115/7 1971
Former Central Electricity Research Laboratories CERL, Leatherhead, United Kingdom, nowadays with National Power, Swindon, United Kingdom.

Engineering Science Data Unit ESDU, Wind Engineering – Mean Loads on Structures, Volume 2b– Fluid forces, pressures and moments on rectangular blocks, Item No 71016, 1993, ESDU International, London.

Davenport A.G. and Dalgliesh W.A.; A Preliminary Appraisal of Wind Loading Concepts of the 1970 Canadian National Building Code; Proc. of the 3rd International Conference 'Wind Effects on Buildings and Structures', Tokyo, Japan, 1971, pp. 441-450

Davenport A.G.: On the Assessment of the Reliability of Wind Loading on Low Buildings; Journal of Wind Engineering and Industrial Aerodynamics, Vol.11, 1983 pp. 21-37

Roberson J.A. and Scott Rutherford G.: Turbulence Effects and Drag of Angular Blunt Bodies; Proc. of the American Society of Civil Engineers, Journal of the Hydraulics Division, Vol. 95 No. HY2 1969, pp. 781-785
Laneville A., Gartshore I.S. and Parkinson G.V.: An Explanation of some Effects on Bluff Bodies; Proc. of the 4th International Conference on 'Wind Effects on Buildings and Structures', Heathrow, England, 1975, pp.333-341

Jensen M.; The Model-Law for Phenomena in Natural Wind; Ingeniøren-International Edition Vol. 2, No. 4, 1958, pp. 121-128

Cook N.J.: Determination of the Model Scale Factor in Wind Tunnel Simulations of the Adiabatic Atmospheric Boundary Layer: Journal of Industrial Aerodynamics, Vol. 2, 1977/78, pp.311-321

Baines W.D.: Effects of Velocity Distribution on Wind Loads and Flow Patterns on Buildings: Proc. of the 16th Symposium on 'Wind Effects on Buildings and Structures', National Physical Laboratory, Teddington, Middlesex, England, 26th-28th June 1963, Vol.I

Davenport A.G. and Isyumov N.: The Application of the Boundary Layer Wind Tunnel to the Prediction of Wind Loading; Proc. of the International Research Seminar 'Wind Effects on Buildings and Structures', Ottawa, Canada, 11th-15th September 1967, Vol.I

Maccabee F.G.: The Present State of Knowledge of Flow round Buildings; Proc. of a Symposium on 'Wind Effects on Buildings and Structures', Loughborough University of Technology, England, 2nd–4th April 1968

Sakamoto H.: Aerodynamic Forces Acting on Rectangular Prism Placed Vertically in a Turbulent Boundary Layer; Journal of Wind Engineering and Industrial Aerodynamics, Vol. 18, 1985, pp.131-151

Brittner R.E. and Hunt J.C.R.: Velocity Measurements and Order of Magnitude Estimates of the Flow between two Buildings in a Simulated Atmospheric Boundary Layer; Journal of Wind Engineering and Industrial Aerodynamics, Vol. 4, 1979, pp.165-182

Latiff Z.A.: Wind Loads on Structures and the Effect of Shielding; PhD thesis, Division of Thermo-Fluid and Environmental Engineering, Department of Mechanical Engineering, University of Strathclyde, Glasgow, Scotland, February 1989

Hussain M. and Lee B.E.: An Investigation of Wind Forces on Three Dimensional Roughness Elements in a Simulated Atmospheric Boundary Layer; Scientific Report BS56, Part II;
Flow over Large Arrays of Identical Roughness Elements and the Effect of Frontal and Side Aspect Ratio Variations; Scientific Report BS57, Part III;

The Effect of Central Model Height Variations Relative to the Surrounding Roughness Arrays; Department of Building Science, University of Sheffield, England, July 1980

Grosso M.; CPCALC*, Fundamentals and Users Manual; Department of Environmental Science and Technology, Polytechnic University of Turin;
Part of the PASCOOL-Project under coordination of M. Santamouris and A. Argiriou, Group Building Environmental Studies, Laboratory of Meteorology, Department of Applied Physics, University of Athens;
Commission of the European Communities, DG XII, Directorate-General for Science, Research and Development, JOULE II - Energy Conservation and Utilisation; Contract No. JOU2-CT92-0013

2.4. Numerical Modelling of Wind Flow around Buildings

Since the 1980s, with progress in computer technology and the development of Computational Fluid Dynamic codes, a lot of work has been carried out to explore Computational Fluid Dynamics as a prediction tool for the purpose of wind engineering. Simulation of wind flow in the built environment incorporates a large flow domain, whereas the turbulent flow requires a fine mesh for good resolution. The number of cells is limited through the required memory space of the computer, and the computational time rises significantly. Therefore, experience had to be gained in grid refinement and choice of optimum grid size. Nodes must be closely spaced near the obstacle where steep gradients of flow properties occur, but can be distributed more widely towards the domain boundaries. The flow boundary should be so far away, that the impact of the obstacle on the flow field at the boundary is negligibly small. A flow domain may be vertically 5 times obstacle height, and to capture the wake extension it may be necessary to expand the domain to 15 times obstacle height downstream (Moustafa 1988).

The standard approach is to apply boundary conditions for the solved variables to the cells at the boundary, either as Dirichlet or Neumann type. A further model of a homogenous turbulent flow field supplies the open boundary on top of the flow domain with a constant shear stress through an inter-fluid friction velocity, similar to the retarding shear stress at the ground (Richards and Hoxey 1993). Initialisation in steady state simulation is less important. The approach of initial approximation combines boundary layer inflow with axis-symmetric potential flow generated by a fluid source and a fluid sink (Paterson and Apelt 1989). The purpose of this potential flow is to minimise the effect of the building on the far field flow so that the boundaries can be brought in close to the building without distorting the flow. The values at the open boundaries are fixed to the initialised values.

For a typical Reynolds number of 10^6 the surface boundary layer at the building walls is of magnitude 10^{-2} m, the atmospheric boundary layer and the outer wake region is of magnitude 10^2 m. One approach has been to use a variable grid with spacing ranging from one to five meters in the vicinity of buildings and from ten to twenty meters in the free stream and in the wake region. For grid points adjacent to solid surfaces appropriate frictional source terms are included in the momentum equation. Turbulence modelling was not applied. The solution of the flow field was purely based on momentum conservation (steady Navier-Stokes) and mass conservation. The general wake structure was found to be in good agreement (± 20 %) with measured data, and as far as the reverse vortex flow for a paired arrangement of blocks is concerned, turbulence seems to be of secondary influence (Hannson et al. 1986).

A more detailed view of the wake structure and quantitative comparison of predicted and measured values of force and pressure coefficients show significant discrepancies between measurements and simulation. For the paired arrangement, the general structure of separated flow is well predicted, but the steady state solution incorporating the standard k-e model fails to predict longitudinal horseshoe vortices interacting with the recirculation zone in between the two buildings. In particular for the case of two equally tall buildings, the predicted suction on the leeward side of the first building is too low and also the suction on the windward side of the sheltered building is much higher than predicted. On the windward side facing the approaching flow directly, the prediction of the pressure coefficient distribution is fairly accurate. In regions of flow separation, the distribution of pressure at the walls seems to depend highly upon the turbulence structure (Latiff 1989).

The latter can be directly compared with results of a single low rise building, modelled in the same manner using the same version of the same software package (PHOENICS) (Richards 1989). Comparison of the scale measurements and three dimensional simulation results show excellent agreement on the windward roof slope, but the predicted suction in the wake at the leeward slope is too high. But generally the agreement of three dimensional simulation with observed flow patterns and pressure coefficients is good. The three dimensional simulation shows significant lower suction over the roof than a two dimensional simulation.

A transient solution with the k-ε model predicted successfully the vortex flow around a rectangular block (Baetke et al. 1987). A first investigation dealt with the influence of the domain size on the pressure values. In particular a flow domain which is too close to the top of the cube (1.5 heights above the cube) causes an increase in suction of $\Delta C_P = -0.2$. The shape of the distribution is undisturbed, but the values suffer an 'offset'. This reinforces the need to model a flow domain which is significantly larger than the flow region of interest. In order to investigate the influence of turbulence on the flow pattern around the building, two cases were simulated: nearly uniform flow with low turbulence intensity, and a simulated atmospheric boundary layer with high turbulence intensity. The numerical approach made use of a special averaging procedure for the eddy viscosity which allows physically consistent treatment of the boundary conditions at sharp edges. Smooth uniform flow did separate at the upper windward edge, but did not reattach on the roof and created a separation bubble expanding over the whole top of the cube. A small horseshoe vortex on the ground develops towards the leading edge and is carried downstream. In the case of high turbulence level in the simulated shear inflow, just a small separation bubble is found over the front part of the roof, after which the flow reattaches and the values of suction fall close to zero. Two strong counter rotating vortices are generated at swept-back leading edges, they influence the flow field above the top surface and interact with the wake of the cube. Diagonal inflow generates a vertical vortex behind the trailing edge, and on the windward side the stagnation point may switch intermittently from one side to the other of the vertical leading edge. This work shows that probably only a transient simulation is able to generate flow pattern and pressure distributions, which actually correspond with the measured mean values in all respects. Correct prediction of transient phenomena like vortex shedding is a demanding task and may need the implementation of a different scheme to reduce numerical false diffusion (Scanlon 1992). For general wind engineering applications, the steady state solution is rather more feasible.

To distinguish the effects of turbulence intensity and modelled velocity distribution in steady state, the flow around a group of small houses has been simulated according to a wind tunnel experiment (Häggkvist et al. 1989). The standard k-ε model allows one upstream to implement inflow profiles for momentum and the turbulent parameters independently. The pressure field was not sensitive to alterations of turbulence level. Changes of velocity distribution led to different pressure distributions on the windward face, but the leeward face remained pretty much unchanged. Variation of turbulence level does mainly affect the wake and hence the pressure field at the leeward face.

High turbulence intensity in a sheared boundary layer results in a reduced size of recirculation wake directly behind a building (Zhang et al. 1992). A low level of turbulence intensity upstream generates an inner wake of 1.7 obstacle heights, whereas a high level of turbulence leads to a reduced wake of just 1.5 obstacle heights downstream. A high level of turbulence at the inflow boundary seems to increase the turbulent kinetic energy in the whole flow field, which raises the mean velocity deficit in the inner wake. The outer wake shows even after a distance of ten obstacle heights a significant loss of momentum compared with the upstream approaching profile.

A similar k-ε approach shows that the simulated values of suction on the roof tend to be over predicted due to inadequate modelling of turbulence generated by smaller eddies at the separation point and in the reattachment zone (Baskaran and Stathopoulos 1989).

Improvements were achieved with the streamline curvature correction and a preferential dissipation correction.

The modelling of turbulence in the near wall region was the main topic of a study which was based on precise measurements of the turbulent kinetic energy k in vicinity of the wind tunnel model (Murakami and Mochida 1989). The most important factor for small numerical errors in predicted pressure distribution is a high mesh resolution at the windward corner. In a flow domain of 15.7 obstacle heights in total length, 5.2 and 9.7 obstacle heights as domain height and lateral width respectively, an adequate near wall mesh size was determined as the 24th part of the total obstacle height. With this fine mesh it was possible to predict separation, recirculation and reattachment of the flow very well, but the standard k-ε turbulence model did not deliver the measured values of the turbulent kinetic energy. In the wake, it predicted lower levels of turbulent kinetic energy, hence the mean flow velocity in the wake and its extension was larger than measured. At the windward corner, the calculated zone of high turbulent kinetic energy k exceeded the measured region greatly, hence the overall magnitude of turbulence at the windward corner is over predicted. This is where high values of suction arise. The values of kinetic energy dissipation ε as assigned to the cell by means of the appropriate wall function (log. law) have a significant influence on the local flow behaviour. If the near wall cell size is too large, the value of the kinetic energy dissipation will be very small and the turbulent kinetic energy will be increased. Therefore increased turbulent viscosity will make the flow too diffusive, and large turbulent flow mixing hinders the occurrence of reverse flow at windward corners.

The previous work was extended in particular with regard to the flow behaviour in the wake (Murakami et al. 1992). The recirculation zone in the wake is seen as an area where turbulent energy production and turbulent energy dissipation are not in local equilibrium. As the turbulent energy dissipation is too large, the turbulent mixing due to the turbulent eddy viscosity is too weak to cause the velocity deficit which would diminish the large reverse velocity. The k-ε model poorly reproduces anisotropic properties of normal stress which cause the anisotropy of turbulence. This anisotropy is especially large in the von Kármán vortex street. In comparison, steady large eddy simulation (LES) showed the best agreement with experimental wind tunnel data. Hence the study continued with unsteady LES, two dimensional and three dimensional. In the three dimensional case the distribution of the mean surface pressure coefficient corresponded well to the experimental data. Two dimensional simulation predicted too large suction on the side faces caused by highly accelerated flow and the separation at the edges. In the transient simulation, the spectrum of velocity fluctuation is for the two dimensional case a narrow band with a sharp peak frequency, while in the three dimensional simulation the turbulent energy transfer takes place throughout a wide spectrum range. Energy cascade happens through the mechanism of vortex stretching which is essentially three dimensional even though the mean flow field may be two dimensional. Therefore, a two dimensional transient simulation may not reproduce unsteady flow phenomena and related turbulence structures.

Even though turbulent flow in the built environment may be highly determined by transient phenomena, the transient turbulent simulation exceeds the constraints for common wind engineering applications. Therefore, a hybrid steady/transient model is suggested (Richards and Wanigaratne 1993). While using the steady k-ε turbulence model, the solution embodies information on the turbulent state of the flow. This information may be used to predict rms (root mean square) pressure fluctuations of the mean pressure coefficient at the wall, taking the mean turbulent kinetic energy at the relevant height and the local turbulent kinetic energy at the zone of interest into account. Serious difficulties arise in this model when directional fluctuations cause strong fluctuations of the pressure coefficient.

Steady state simulation of turbulent cross flow through a building with communication from the windward to the leeward face was undertaken with the standard k-ε model and a new k-ε model for low Reynolds numbers (Yaghoubi 1998). The simulation is conducted purely two-dimensionally, which results in the typical extreme expanded wake structure. Interesting is the observed Reynolds number dependency of the wake structure, which is somehow in contradiction to the experience of similar flow patterns for rectangular bodies at different Reynolds numbers. Obviously, with higher Reynolds numbers the turbulent kinetic energy concentrates significantly close to the solid boundary, in particular at the roof corners and above the flat roof. The reattachment point of the separated flow above the roof moves towards the leading edge with increasing Reynolds number from 2×10^5 to 5×10^6. The variation of the reattachment point of the wake is in the range of 10 % but without clear tendency.

The basic limitation of Computational Fluid Dynamic models for wind flow in the built environment is the size of the structure and the whole flow domain. The influence of the cell sizing and the distribution of cells is very significant, but the limited number of cells and the required runtime is a serious constraint. Only in rare cases for very simple structures it is possible to model the three dimensional wind flow around buildings accurately corresponding to measured pressure and velocity fields.

References

Moustafa A.A.: Numerical Analysis of Turbulent Flow over Offshore Structures; PhD thesis, Division of Thermo-Fluids and Environmental Engineering, Department of Mechanical Engineering, University of Strathclyde, Glasgow, Scotland, 1988

Richards P.J. and Hoxey R.P.: Appropriate Boundary Conditions for Computational Wind Engineering Models using the k-ε Turbulence Model; Journal of Wind Engineering and Industrial Aerodynamics, Vol. 46-47, 1993, pp. 145-153

Paterson D.A. and Apelt C.J.: Simulation of Wind Flow around Three Dimensional Buildings; Building and Environment, Vol. 24, No. 1, 1989, pp. 39-50

Hannson T., Summers D.M. and Wilson C.B.: A Three-Dimensional simulation of Wind Flow around Buildings; International Journal of Numerical Methods in Fluids, Vol. 6, 1986, pp. 113-127

Latiff Z.A.: Wind Loads on Structures and the Effect of Shielding; PhD thesis, Division of Thermo-Fluid and Environmental Engineering, Department of Mechanical Engineering, University of Strathclyde, Glasgow, Scotland, 1989

Richards P.J.: Computational Modelling of Wind Flow around Low-Rise Buildings using PHOENICS; Divisional Note DN 1508, March 1989, Building and Livestock Division, AFRC Institute of Engineering Research, Silsoe, Bedford, United Kingdom.

Baetke F., Werner H. and Wengle H.: Computation of Turbulent Flow around a Cube on a Vector Computer; Proceedings of the 6th Symposium on Turbulent Shear Flows, Vol. 9, 1987, pp. 20-2-1 to 20-2-6

Scanlon T.J.: Vortex Shedding Flowmeter - Pulsating Flow CFD Studies; PhD thesis, Division of Thermo-Fluid and Environmental Engineering, Department of Mechanical Engineering, University of Strathclyde, Glasgow, Scotland, 1992

Häggkvist K., Svensson U. and Taesler R.; Numerical Simulations of Pressure Fields around Buildings; Building and Environment, Vol. 24, No. 1, 1989, pp. 65-72

Zhang Y.Q., Arya S.P.S., Huber A.H. and Snyder W.H.; Simulating the Effects of Upstream Turbulence on Dispersion around a Building; Report No. EPA 600/A-92/228 (1992), Atmospheric Research and Exposure Assessment Laboratory, Office of Research and Development, U.S. Environmental Protection Agency, USA, 1992

Baskaran A. and Stathopoulos T.; Computational Evaluation of Wind Effects on Buildings; Building and Environment, Vol. 24, No. 4, 1989, pp. 325-333

Murakami S. and Mochida A.; Three Dimensional Numerical Simulation of Turbulent Flow around Buildings using the k-ε turbulence model; Building and Environment, Vol. 24, No. 1, 1989, pp. 51-64

Murakami S., Mochida A., Hayashi Y. and Sakamoto S.; Numerical Study on Velocity-Pressure Field and Wind Forces for bluff Bodies by k-ε, ASM and LES; Journal of Wind Engineering and Industrial Aerodynamics, Vol. 41-44, 1992, pp. 2841-2852

Richards P.J. and Wanigaratne B.S.;A Comparison of Computer and Wind-Tunnel Models of Turbulence around the Silsoe Structures Building; Journal of Wind Engineering and Industrial Aerodynamics, Vol. 46-47, 1993, pp. 439-447

Yaghoubi M., Zamankhan P. and Sabzevari A.; Numerical Analysis of Two-Dimensional Wind Flow in and around Rectangular Buildings, Part I: Modelling and Simulation, Part II: Flow field and Ventilation; Wind Engineering, Vol. 22, No. 2, 1998, pp. 81-112

2.5. The Standard Wind Pressure Coefficient for Buildings

Compatible with the British Standard BS 6399: Part 2, data for pressure coefficients for the walls and roofs of bluff-shaped buildings are provided for civil engineering purposes (BRE 1989). They form the basis to derive loads, in combination with gust and wind direction related factors. The distribution of pressure coefficients is approximated in different regions or zones on the surface of the building. For the wall they are vertical stripes. For the flat roof, these are rectangular zones. The extent of the zones is determined by the slenderness ratio (height / width) and depends also on the direction of the incident wind. For a cube, the mean stagnation pressure coefficient for a stripe in the middle of the windward wall for a frontal wind is $C_P = 0.88$. The lowest suction of $C_P = -1.21$ appears on the sidewalls in the separated region. The highest pressure on the roof is generally on the downstream part and could reach $C_P = 0.2$ in the case of reattachment. The lowest suction is indicated at an angle of incidence of 30° stating $C_P = -2.0$ on the roof near the windward edge. Standards are also given for monopitch and duopitch, hipped and intersecting duopitch roofs.

References

BRE Digest 346; The Assessment of Wind Loads, Part 6: Loading Coefficients for Typical Buildings, November 1989; Building Research Establishment, Department of the Environment, United Kingdom, ISBN 0851254225

See also 'The Designer's guide to Wind Loading of Building Structures Part2', BRE

2.6. The Assessment of Wind Energy in the Built Environment

The nature of wind flow interacting with buildings offers many possibilities to harvest wind energy, but investigations to assess the wind energy potential in the built environment are rare. Jenkins and Graham obtained experimental data on the capturable flux of wind energy passing through predetermined cross sections (the 'turbine areas') adjacent to representative building models in the wind tunnel (WEB, Jenkins and Graham 1995, 1997). As the effective resistance of an operating turbine may affect the flow, the wind turbines itself were modelled by pre-characterised woven wire mesh. The wind flow through the mesh was measured by means of hot wire anemometry. In this way a building wind energy response factor was created, for different heights and different wall faces dependent on the adjacent wind. In combination with local climate data and the characteristics of a proposed vertical axis wind conversion system, it is then possible to estimate mean annual wind energy yield. For a typical multi-storey building in an urban area, the annual prediction is in the range of 2/3 of its usual lighting load (around 24 kWh/m^2 floor area). Energy capture is enhanced by siting in a gap between building blocks (twin towers in close vicinity) given a suitable prevailing wind direction. The wind energy generation there is about twice that of a stand alone turbine of the same area in an open site. Of course, the turbine area of building integrated turbines is limited.

Without modelling the turbine itself, estimation of wind energy potential might sometimes be based on the wind surface pressure, local mean wind velocities and turbulent velocities.

Given the adjacent regions of large pressure differentials likewise at sharp edges of rectangular shaped buildings (for example the upper wall roof edge), an integrated turbine should be able to make use of an induced accelerated flow, where the intake is located in the high stagnation pressure region, and the flow expands in the low under pressure region at the outlet. It is the same principle as the concentrator / diffuser augmented turbine (see Chapter 3), and the same basic fluid mechanics can be applied. Therefore, the increase in momentum is directly proportional the square root of the difference between the pressure coefficients at inlet and outlet. As the power rises with the cube of wind speed, a difference of $\Delta C_p = 1.5$, caused by $C_p = +0.8$ on the windward side and $C_p = -0.7$ at the roof, may increase the wind power by 83 %. The same suggestion was made to determine the local flow velocity induced by vortices on the roof while recording the pressure ($V = V_{free} \cdot (1 - C_p)^{1/2}$) (Kind 1975). Of course, this fluid mechanical consideration does not take many features into account which significantly affect the energy available in the wind. On the device side, it misses out the characteristic of the turbine / generator. Further, this simple approach disregards any kinetic energy losses in the mean flow due to turbulence and recirculation, and it does not take any vortex development into account. The latter may play an important role in the power augmention of an integrated turbine. Another problem is that the impact of the turbine outflow, expanding in the low pressure region, on the pressure values in the outlet region itself is difficult to predict. It depends very much on the character of the flow, which varies with Reynolds number and angle of incidence. Therefore, a generalized model of this interaction is perhaps not very reasonable.

The main part of the work presented in this thesis deals with measurement and Computational Fluid Dynamics simulation of the wind flow in these regions. It can be stated that local effects of turbulence, recirculation and vortex development have the most significant impact on the local flow field through any building-integrated turbine, which affects the energy generation directly.

Concerning local wind acceleration, the most promising regions for wind turbine installation appear to be at the edges of the windward façade. Further, for sloped roofs it seems to be promising to use the wind acceleration above the ridge line. The behaviour of the flow at the corners of the building depends very much on the angle of incidence. At sharp edges the flow separates and local wind speed can exceed the mean flow velocity by a factor of 2 or more. In the wake of flow separation, vortex formation might occur. To assess the wind energy potential, areas of local flow augmentation must be determined.

References

Graham J.M.R. and Jenkins N.H.A.; Wind Energy Associated with Buildings; BEPAC and EPSRC Web-Conference, February 5th-6th 1997, England,
http://www.iesd.dmu.ac.uk/bepac/

Jenkins N.H.A. and Graham J.M.R.; Measurement and Prediction of Wind Energy in Association with Buildings; Proc. of the 17th Annual Conference of the British Wind Engineering Association BWEA 17, 1995, Warwick, England.

Commission of the European Communities, DG XII, Directorate General for Science, Research and Development; 4th framework, JOULE Programme; WEB – Wind Energy for the Built Environment; Research Contract No. JOR3-CT98-0270
Final scientific report exspected to be published 2001.

Campbell N. and Stankovic S., Graham M. and Parkin P., van Duijvendijk M. and de Gruiter T.: Wind Energy for the Built Environment (Project WEB); to be published in the Proceedings of the 2001 European Wind Energy Conference, Copenhagen, Denmark, 2nd-6th July 2001

Kind R.J.: Tests to Determine Wind Speeds for Scouring and Blowoff of Roof Top Gravel: Proc. of the 4th International Conference on Wind Effects on Buildings and Structures, edited by the Building Research Establishment BRE, hold at Heathrow, England, 1975, pp.591-604

2.7. Wind Energy Conversion associated with Conventional Buildings

Given the potential of wind energy in the built environment, it is logical to consider the application of wind energy conversion systems for conventional buildings. It is not generally practical that the building should be adapted and converted into an aerodynamic structure which serves the turbine as a flow augmenter (see Chapter 3) and works as a huge wind power plant. Simple wind power devices should rather be developed to be integrated into the usual structure of a conventional building, without impairing the building's common functionality. Ideally it should be achievable to integrate wind energy conversion systems into buildings which were built many years before without any purpose to harvest wind energy. This approach could result in an enhancement of the use of embedded renewable energy, complementary to solar energy applications in the building sector.

In early times a building was either built as a windmill, or did not harvest any wind energy. However, according to historical sources of the author's home region, in the second half of the 16th century, there were serious planning and negotiations on the way in order to integrate ducted drag windmill devices, similar to the 7th century Persian drag windmill (Sivasegaram 1986). In order to supply Strasbourg with grain milling in difficult times of low water level, the fortifications architect Daniel Specklin (1536-1589) worked out plans to integrate such vertical axis drag windmills into the upper two floors of the medieval citadel towers of the town (Fischer 1996). Conventional windmills inside the town were not feasible because of the area density of the buildings. Also, it was important to secure that grain milling could take place inside the citadel. Translated into today's terminology, the project was based on sound considerations towards supply and demand matching in times of entangled internal and external political tension. According to Specklin's historical correspondence, there must have been quite a few drag devices with vertical axis in a ducting, distributed throughout Europe. Unfortunately, because of failures in planning and management, Specklin's plans were never realised.

Up to now, wind energy in the built environment has consisted mainly of the installation of a conventional wind turbine next to a house, with the generated power (electricity or even heat) directly fed into the local energy system of the house (Twidell et al. 1988). There, the integration just takes place on the energy supply side.

A recent project, the 'Dutch Pavilion' of the Netherlands at the World Exhibition Expo 2000 in Hanover in Germany, involved the installation of conventional horizontal axis wind turbines with shortened masts (Lagerwey 'design-turbines') on the roof of the building (Renewable Energy World 2000, Roos 1998). It is supposed that the generated power is significant due to the high exposure of the turbines. For obvious reasons, the size of such turbines must be quite limited. Still, in the United States a type of horizontal axis turbine with three twisted blades can be purchased in a set with a roof mounted kit, and is supposed to deliver up to 600 W in strong winds (Southwest Windpower, Arizona, USA).

Basically, the development of feasible wind energy conversion systems to be integrated in the built environment is still at the stage of early beginning. The concept of using vertical axis turbines with the axis running vertically parallel to the edges of tall buildings (3 m diameter and half building height in overall length) and horizontally along the whole roof ridge is envisaged in a research work to assess wind energy available for a building, as described above (WEB). The most promising area to yield wind energy seems to be the space in between two large twin towers in close vicinity, but the question of a suitable wind energy conversion system to harvest this energy remains open. Recently, the Rutherford Appleton Laboratory in England gained some experience with small new designed vertical axis wind turbines (DIC GLOBULAN and SOLAVENT W500) to be mounted on the roof of the buildings. In Europe, the focus is on improvement and modification of existing wind turbine types suitable for deployment in the built environment (Timmers 2001). Independent from the European effort, a Japanese group seems currently working on the development of a vertical axis wind turbine suitable for buildings (Maruyama et al. 2001).

Taylor introduces the concept of planar wind concentrators for particular application on roof ridges (Taylor 1998). The design consists of vertical axis turbine modules, which are installed in series in similar manner to the research project (WEB). Taylor's idea may look promising, but detailed prototype development with a larger scale model seems to be still outstanding. Concepts to integrate large power augmented vertical axis wind turbines in the structure of special aerodynamical shaped buildings are still appearing and exist mainly as designers idea in draft form (Future Systems 1998). Until now, very little expertise concerning the implementation of vertical axis turbines in the built environment has been gained.

Apart from the conventional horizontal axis and the common vertical axis turbine, other types of turbines are currently under investigation. One ongoing research project looks at a wind generator system invented by the late Count Alain deBriey, which is described as 'combining the advantages of both horizontal and vertical axis type wind generator' and claims to be particularly suited for integration into the built environment (ENK), once it is designed, developed and tested. Another design seems to be based on the augmented vortex in a cylinder (tornado type). Therefore, it is planned to place the turbines in small tubes and to distribute them over the flat roof like ventilation stacks (Hong Nam Lam 2000). The efficiency of those turbines might be affected when the flow over the roof separates at the leading edge and covers the turbines in the bubble of recirculating flow.

References

Sivasegaram S.: Power Augmentation in Wind Rotors: A Review; Wind Engineering, Vol. 10, No. 3, 1986, pp.163-179

Fischer A.: Daniel Specklin aus Straβburg (1536-1589): Festungsbaumeister, Ingenieur und Kartograph; Veröffentlichungen der Kommission für geschichtliche Landeskunde in Baden-Württemberg; Jan Thorbecke Verlag, Sigmaringen, Germany, 1996.

Twidell J.W., Woodbridge K., Barbour D., Stepek A. and Robertson I.; A Solar / Wind Heated House and a Small Island Community, Orkney, Scotland; Proc. of the International Conference on 'Energy for Rural and Island Communities V', held at the University of Tasmania, Hobart, May 1988; published as 'Energy for Rural and Island Communities V', Pergamon Press, Oxford (England) 1988, Editor J. Twidell

Renewable Energy World, Vol. 3, No. 5, September-October 2000, pp. 24 - 25; Small Turbines for Urban Environments

Roos R; Zes landschappen vormen samen één gebouw; Kunst, The Netherlands, 18th June 1998

Southwest Windpower, Arizona, USA; Air 403 Wind Generator + roof mounted kit

WEB – Wind Energy for the Built Environment; Research Contract No. JOR3-CT98-0270, Commission of the European Communities, DG XII, Directorate-General for Science, Research and Development; 4th framework, JOULE Programme;
Final scientific report expected to be published 2001.

Timmers G., Ecofys in Utrecht (The Netherlands): Wind Energy comes to Town – Small Wind Turbines in the Urban Environment: Renewable Energy World, Vol. 4, No. 3, May – June 2001, pp. 112-119

Maruyama Y., Shimura M., Yoshie R. and Seki K.; Development of a Vertical Axis Wind Turbine with Straight Blades Suitable for Buildings: to be published in the Proceedings of the 2001 European Wind Energy Conference, Copenhagen, Denmark, 2nd-6th July 2001

Taylor D.; Using Buildings to Harvest Wind Energy: Building Research and Information, Vol. 26, No.3, 1998, pp. 199-202

Architekten Duo 'Future Systems', London: Neue Bau-Ideen für sanfte Energien: Das Haus, Ausgabe Baden M3172E Juli / August, page 34, Germany, 1998

Project Reference: ENK5-2000-35001: Wind Generator System with Significant Technical Advantages over Existing Technology and particularly suited for Integration into the Built Environment: Commission of the European Communities, DG XII, Directorate-General for Science, Research and Development; 5th framework, EESD (Energy, Environment and Sustainable Development) Programme:
Final scientific report expected to be published 2001/2002.

Hong Nam Lam: Building-Integrated Photovoltaic System Combined with Ducted Wind Turbines; Proc. of the 16th European Photovoltaic Solar Energy Conference and Exhibition; May 1st-5th 2000, Glasgow, Scotland.

2.8. Development of the Ducted Wind Turbine Module and its Embedding in Conventional Building Structure

The Ducted Wind Turbine module is based on the principle of using the turbine casing to guide horizontal inflow vertically through a turbine with vertical shaft. Different patents show the application of this idea in the history of technical development (Scovel and Ross, 1897; Cooper 1910; Buri 1934).

In 1979 a ducted wind energy conversion device was patented by an Glaswegian Engineer (Webster 1979). It was intended for construction in modular form, either free-standing or as part of a larger structure. It uses ducting to direct air through an axial-flow turbine with a vertical shaft (Figure 2.8.1). Development proceeded slowly for a variety of reasons, and the model never reached the production stage. The ducting was very rudimentary and served mainly as a container for the moving parts, and certain features of the original design were questionable, for example the louvres at the inlet as a flow regulator and the internal guide vanes (Figure 2.8.1).

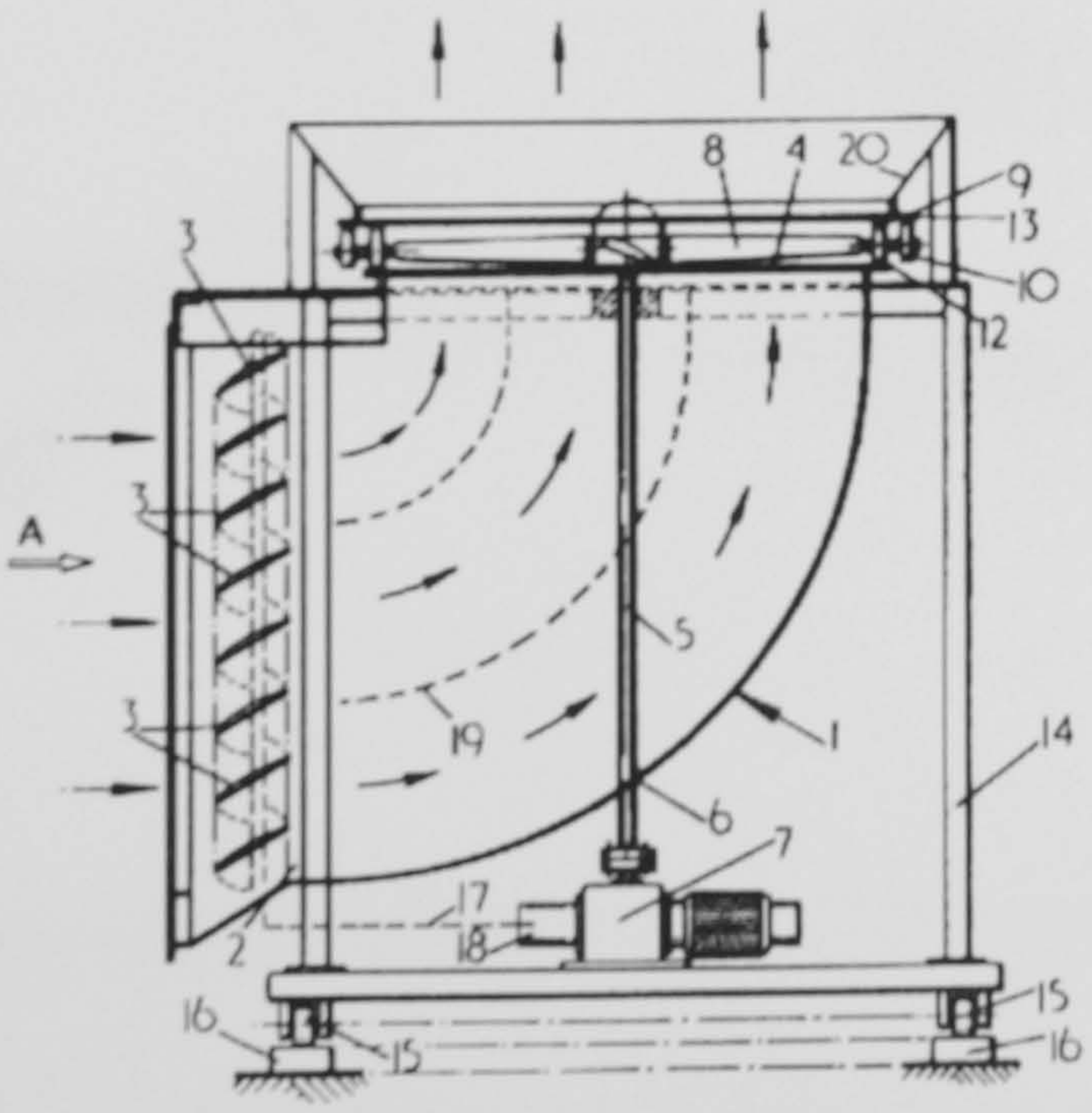

Figure 2.8.1: Original drawing of the Webster Patent (Webster 1979)

After the inventor's death, the family approached the Department of Mechanical Engineering at the University of Strathclyde in Glasgow. Here evaluation and further development of the Webster patented concept has been initialised (Nasr el-Din et al. 1992). A high solidity rotor gave the best performance, and power coefficients (based on the torque as measured at the shaft) of C_p = 0.2 were obtained. The peak power coefficient was increased to C_p = 0.26 by the addition of a spoiler at the outlet. Wind tunnel tests using different wind directions showed that the machine is still effective for misalignments in excess of 30°.

These results were encouraging enough to construct a first prototype: A 90° duct from an air-conditioning system was fitted with a 6-bladed rotor cut down from a Marlec 50 W wind turbine. The solidity of this rotor was 0.5 and its blade angles were not adjustable. This prototype was tested at a field trial at the National Wind Turbine Test Center in Myres Hill, which was part of the former National Engineering Laboratory NEL, some 15 miles from Glasgow. Its performance during the trial period was compared with a standard 50 W horizontal axis wind turbine (Rutland Windcharger WG 910) (Grant et al. 1994).

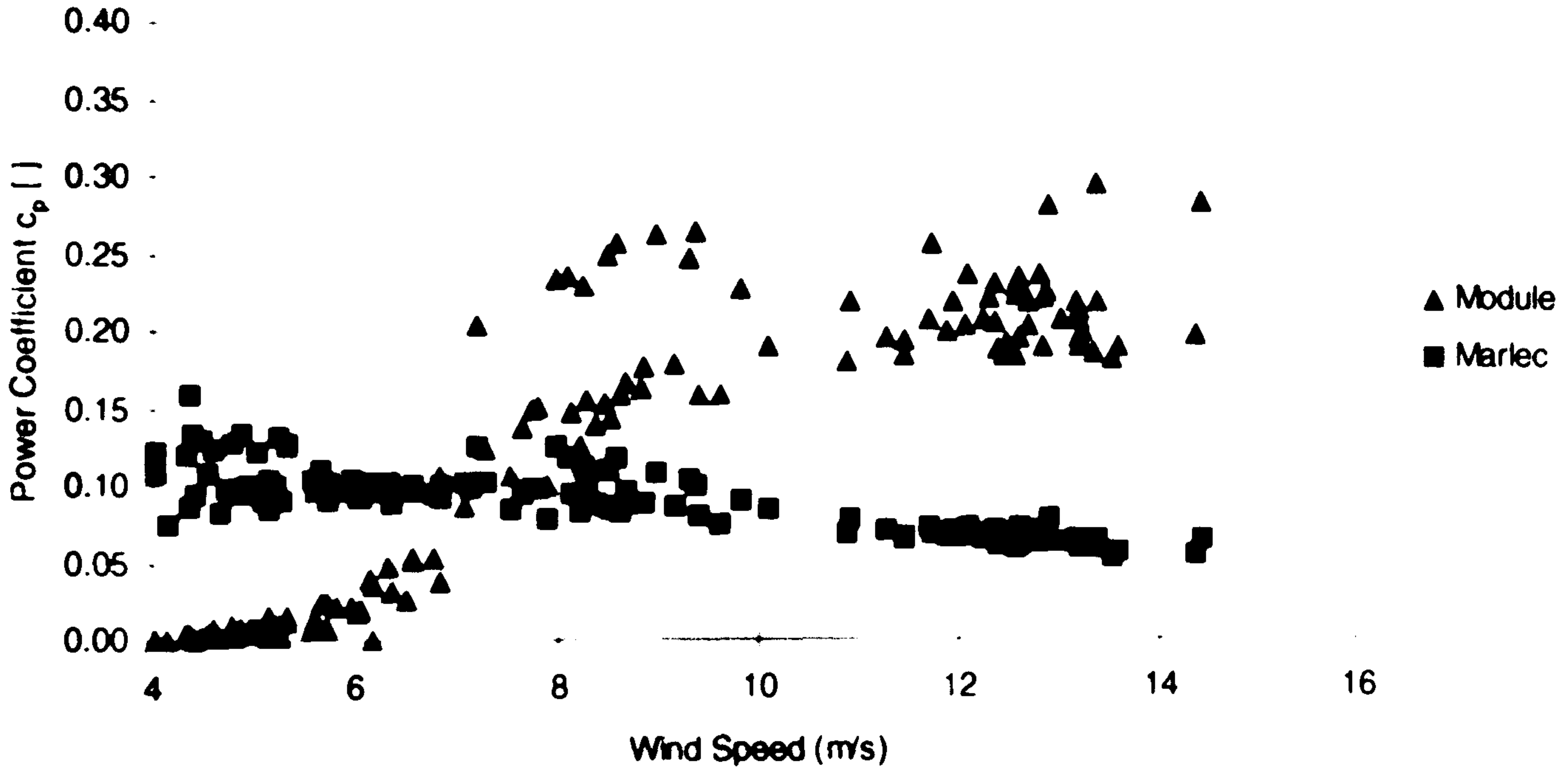

Figure 2.8.2: Performance of the first prototype during its field trial (Grant et al. 1994)

The module's performance was clearly deficient at low wind speeds, but this could have been largely caused by a mismatch between the characteristics of the rotor and the generator. But in particular at higher wind speeds, when aligned with the wind, it compared favourably with the conventional turbine with power coefficients exceeding 0.2 (Figure 2.8.2), which is a respectable value for such a small rotor. Further, it tolerated up to 30° misalignment without serious loss of performance. As reported, the field testing came to an abrupt end during a period of extremely strong winds, where 10-minute averages of over 90 km/h wind speed were recorded. The standard wind turbine failed with blade breakage, the module continued to operate and survived intact.

Up to 1996, the development of the Ducted Wind Turbine focused on the free standing device, and a number of student projects included performance tests of the model in the wind tunnel (Figure 2.8.3).

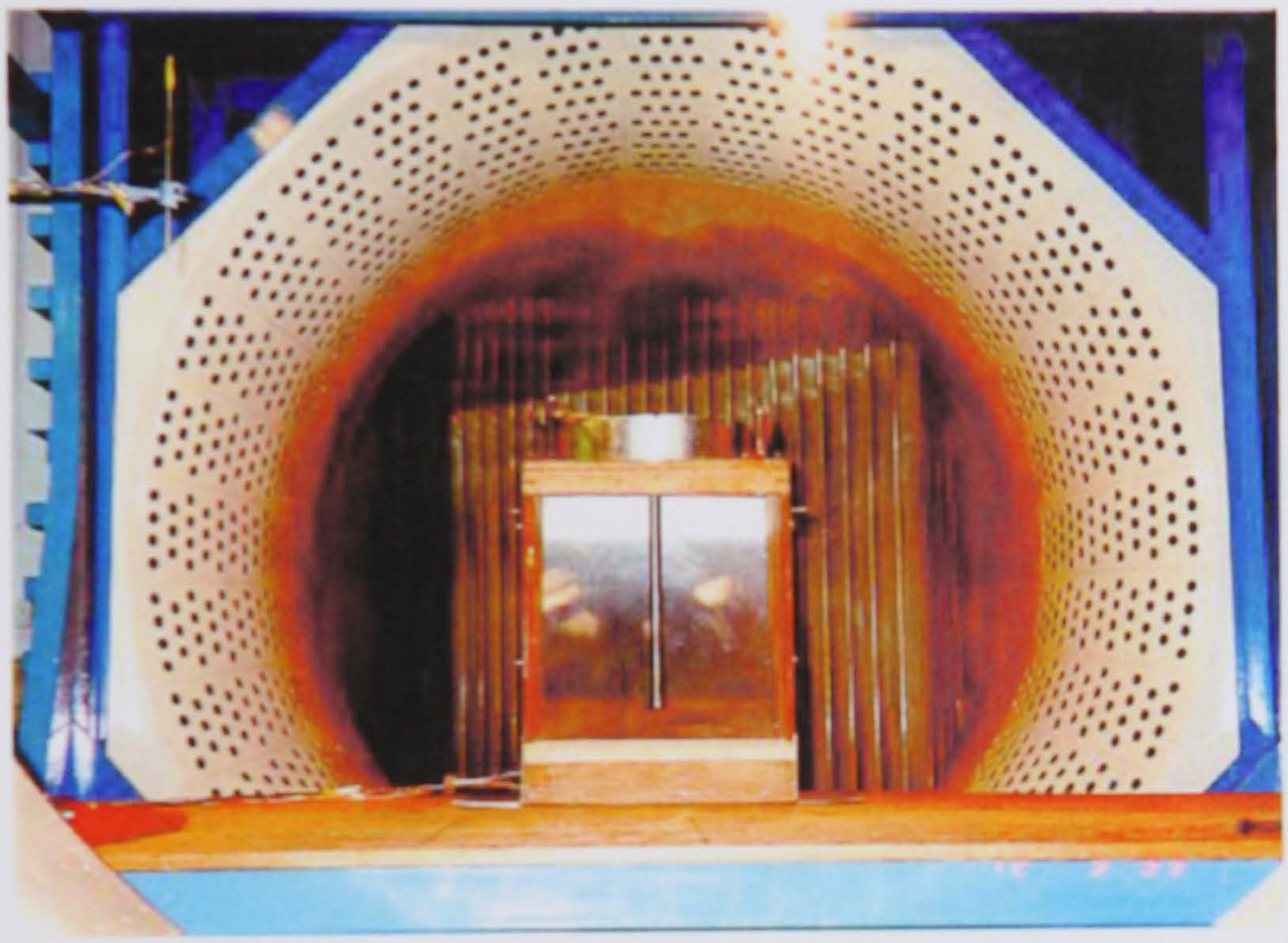

Figure 2.8.3: Test module in the Departments open section wind tunnel, jet diameter 1.50 m

The small scale wind tunnel test module (Figure 2.8.3) is a simplification of the original Webster patent (Figure 2.8.1): the inlet and outlet slats, the yawing system and the guide vanes in the duct are removed. The rotor is a fan rotor of 300 mm diameter, 7 blades at a pitch angle of 20 degrees and the hub diameter is 136 mm (solidity $\sigma = 0.72$). The cowling is a circular metal ring. Basic performance tests were carried out by recording shaft speed and torque.

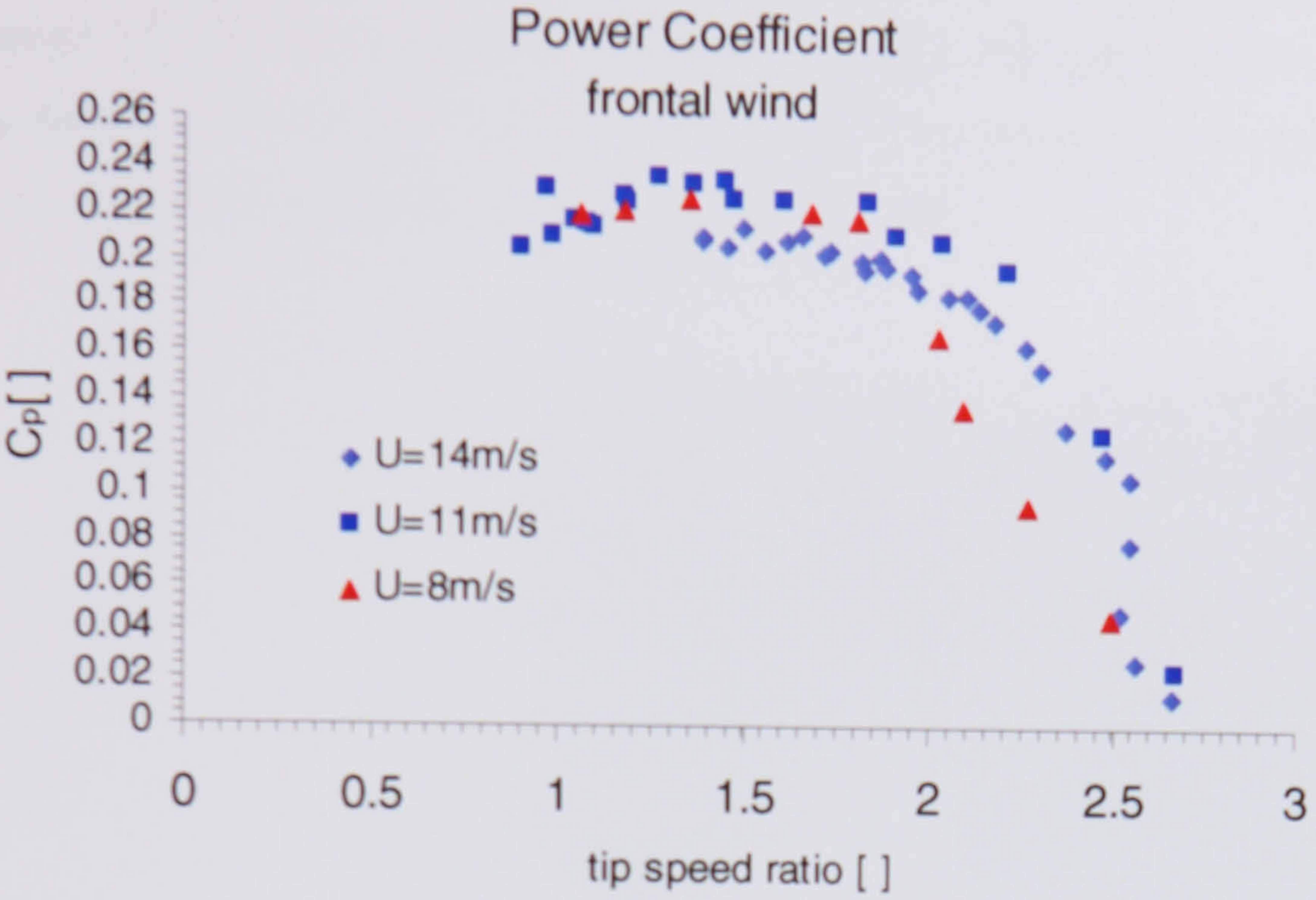

Figure 2.8.4: Performance of the test module (Figure 2.8.3) with roof spoiler (Andina Pendas 1999)

In particular a vast variety of additional spoilers at inlet and outlet, flaps, shrouds and hub cabs under different angles of incidence and different wind speeds were tested and their performance was compared with the field trial (Cook 1992, Kilpatrick 1993, Andina Pendas 1999). Overall, a power coefficient larger than 0.2 for a high solidity rotor at a tip speed ratio not exceeding two is the common feature of performance for all tests, either in laboratory scale or during field trial. The tolerance for misalignment lay in the range of 20 to 30 degrees. Surprisingly, the turbine shows the best performance when not perfectly aligned with the wind, under a small incident angle of around 10 to 15 degrees (see Figure 2.8.6). It is suggested that swirl created in the housing might enhance the turbine's performance.

The research project towards integration of a ducted wind energy module into the built environment started 1996 and concentrated on a number of different aspects (Dannecker and Grant 1999, Dannecker et al. 1999). The first was, based on the experience gained with the free standing model, to develop a prototype to be integrated into the cladding system at the leading edge of a roof. In order to gain experience with the performance of the Ducted Wind Turbine in the built environment, the former prototype from Myres Hill was refurbished. The outlet was fitted with a smooth shroud enclosing a high solidity fan rotor ($\sigma = 0.73$) of 10 blades, diameter 480 mm. The shaft was directly connected to a Rutland 910 series generator (12 V single phase), which generates 90 W at full load. The power output was measured against selected load resistors (100 Ω / 30 Ω). In 1998 the device was mounted on the roof top (Figure 2.8.5) next to the Department's weather station.

Figure 2.8.5: Free standing prototype device on top of the James Weir Building, University of Strathclyde in Glasgow

This allowed correlation of the turbines performance with climate data (Aris 1998). Monitoring was performed with the data logging system LABVIEW and displayed to a Personal Computer in the Departments reference library. It took samples at a frequency of 1 kHz and averaged over 5 minutes.

Figure 2.8.6 shows a set of analysed data gathered during the second half of the year 1998. For this range of wind speeds between 5 and 6 m/s, a power coefficient of 0.2 and above was reached when aligned with the wind (in Figure 2.8.6 the building faces 196° from due North), the peak power coefficient occurring under misalignment of around 15°

(corresponding in Figure 2.8.6 to 180°), as described above. Taking this shift into account, it seems to tolerate ± 20° misalignment without significant loss of performance.

In contrast to the tests in the wind tunnel, the presented power coefficient is based on the electrical output of the attached generator. Therefore improvements in performance for all wind speeds should be attainable with optimised resistor load matching to the generator's characteristics. Given the fact that the turbine works best at a tip speed ratio of around 1.5, the range of rotational speed for the generator is relatively low. The determination of the characteristics of a motor or generator becomes more and more difficult at low speeds, but work in the Department's laboratory gave evidence that the generator will work most efficiently under a lower load resistance of around 10 Ω. Lower resistance requires a larger shaft torque on the generator, which has to be provided from the turbine rotor, and the aerodynamical design of the rotor plays an important role here. But it is suggested that a power coefficient of 0.3 could be a realistic target.

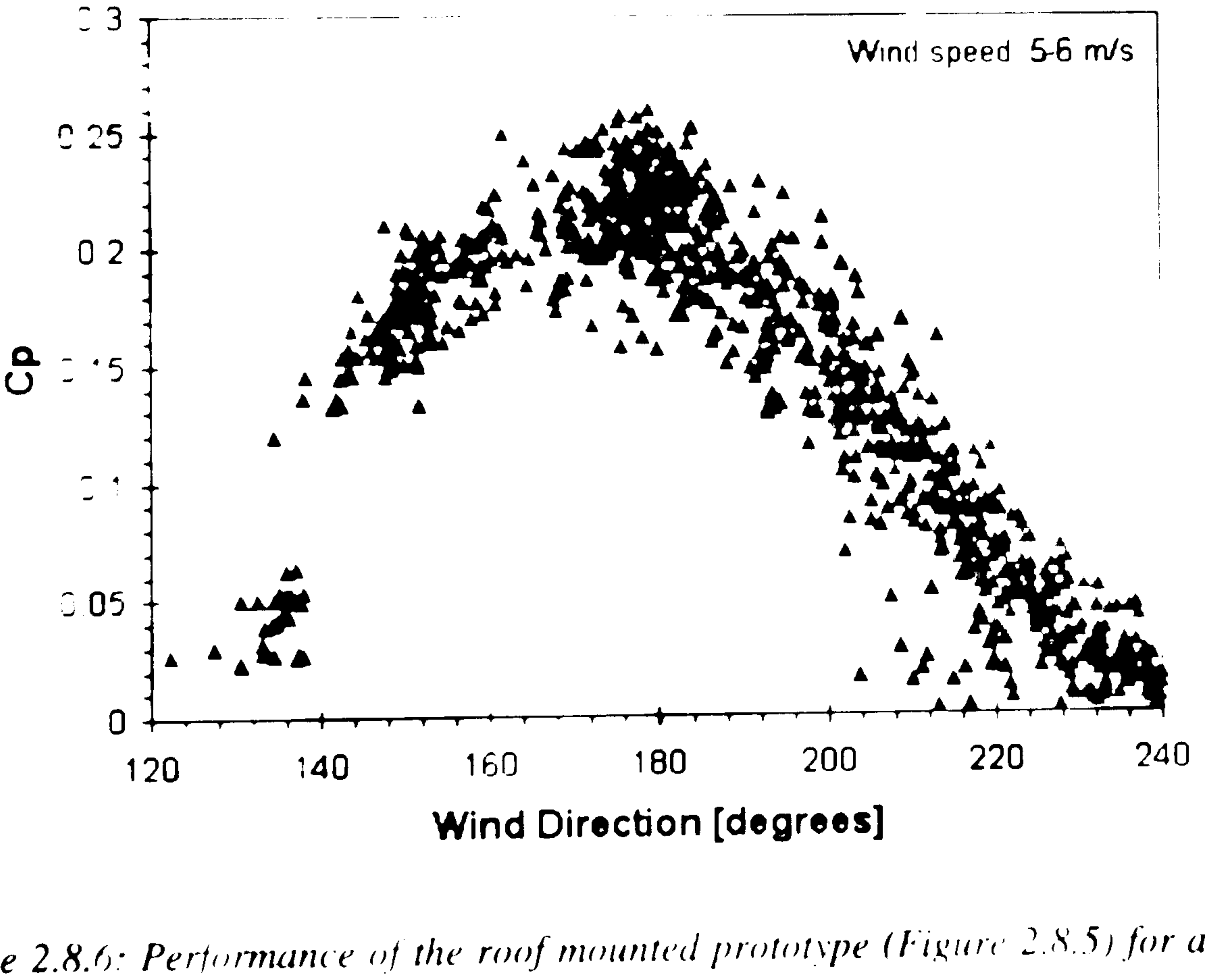

Figure 2.8.6: Performance of the roof mounted prototype (Figure 2.8.5) for a range of low wind speeds (Dannecker et al. 1999).

Based on this encouraging experience, a free standing new prototype was designed at the Energy Systems Research Unit of the University (Figure 2.8.7). Here, as the first results of

Computational Fluid Dynamics suggested better performance from a relatively straight duct (Dannecker 1998), an aerodynamic casing was conceptually realised with a straight back wall and a smoothly curved inlet to avoid flow separation, in contrast to the previous prototype (Figure 2.8.5). Also, the spoiler above the outlet had a much wider opening than with the previous prototype in Figure 2.8.5. Both aspects are seen to be important to avoid unnecessary loss of momentum of the air stream passing through. Unfortunately, because of architectural constraints at the intended deployment site (the Lighthouse, center of Glasgows '1999 City of Architecture' celebration), the size of the turbine was limited to a rotor diameter of 450 mm. It consists of a 150 mm hub and six cambered airfoil blades (MARLEC) (solidity $\sigma = 0.53$). Again, the Rutland 910 generator was used. However, as a new feature, the spoiler carries a solar photovoltaic panel under a pitch angle of 42°, which is cooled by the flowing air to improve the panel's efficiency. Hence, a hybrid system was created where the spoiler links and improves the performance of both systems (Grant and Dannecker 2000). It is suggested that the new prototypes are integrated in the structure of the cladding façade which typically forms a parapet around the roof. This might provide power enhancement because of locally induced higher wind speeds. Other roof mounted designs integrated in the façade cladding may also work successfully and have been proposed (Grant and Dannecker 2000).

In 1999 several of these prototypes were manufactured in the departmental workshop of the University and have been deployed on the top of the 'Lighthouse' building, the focus of the celebration of Glasgow 1999 European City of Architecture and Design. The Energy Systems Research Unit of the University carried out the design and construction as part of the RE-Start project which aimed to demonstrate the potential benefits of deploying renewable energy technologies in the urban environment (RE-Start 1996). At the time of writing this thesis, the installation to monitor the performance of the deployed devices is not completed yet, hence performance data will be reported at a later stage. It is intended to record the climate data, to monitor the wind turbine performance and to measure temperature and massflow rates of the vented air cavity under the installed solar panels. Each Ducted Wind Turbine is rated at 90 W, with the integral photovoltaic spoiler at 85 W. Based on a generalised Glasgow climate data file which is used in building energy simulation (see Chapter 8), it was possible to predict that the Ducted Wind Turbines are a sound complement to photovoltaic systems (Grant and Dannecker 2000). A simulation of the integration aspects of the embedded generation system and the predicted matching of supply and demand has been recently presented (Clarke et al. 2000).

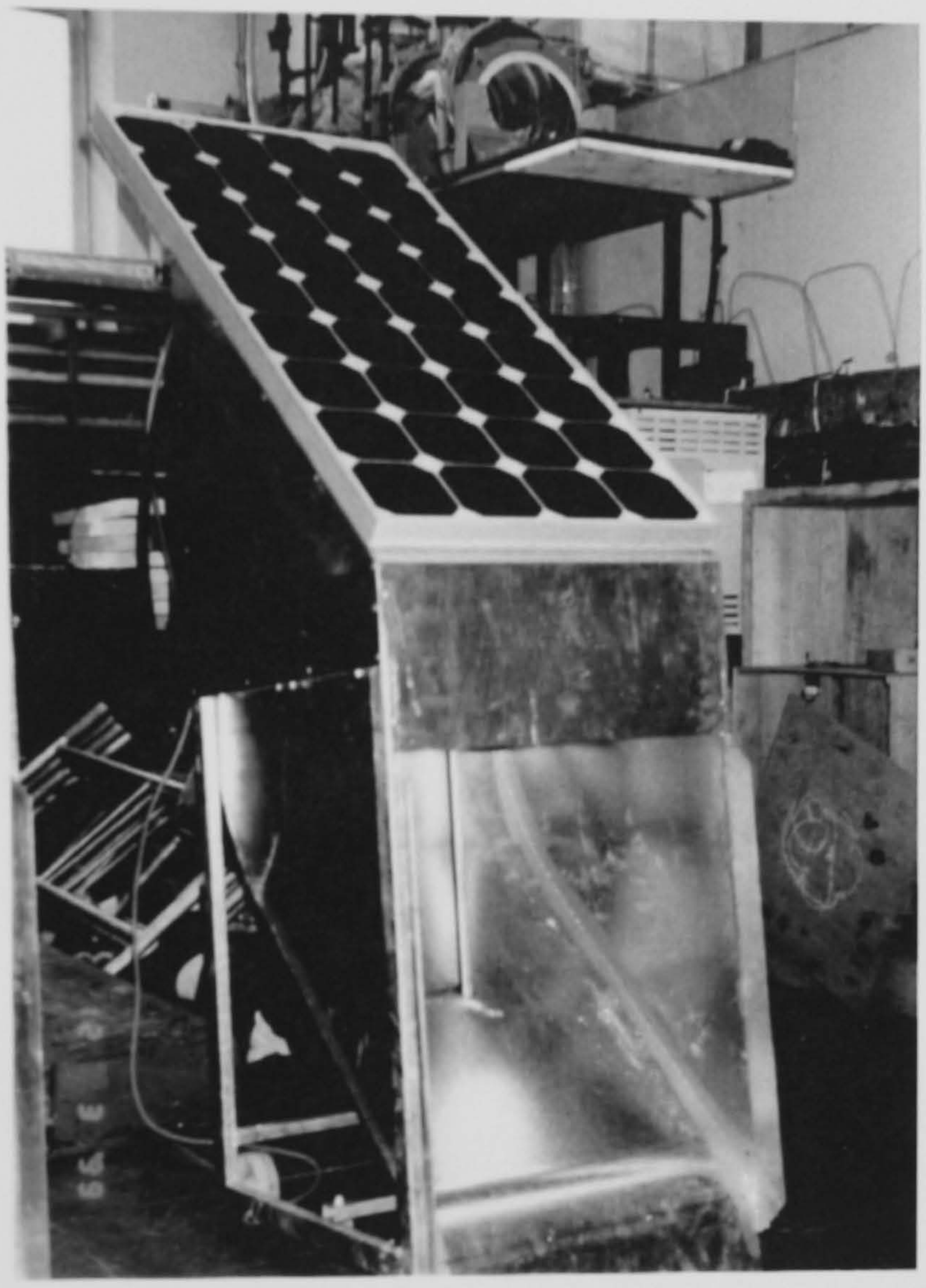

Figure 2.8.7: Free standing hybrid PV / Wind Energy Module prototype, in the Departments workshop, James Weir Building, University of Strathclyde in Glasgow

The bulk of the work presented in this thesis focuses on the aerodynamical aspects of the complete integration of the turbine casing in the leading edge of a flat roof. Up to now, the complete integration of the Ducted Wind Turbine is only an idea (Dannecker 1999) and has not been demonstrated in practice.

Roof mounted devices gain directly from the accelerated flow field around the leading edge, whereas completely integrated devices are supposed to gain rather from induced high wind speeds in the duct due to the pressure differential between the duct inlet at the front façade and the outlet at the flat roof. Here, different aspects like the shape of the inlet and the duct or the installation of spoiler at inlet and outlet may play an important role.

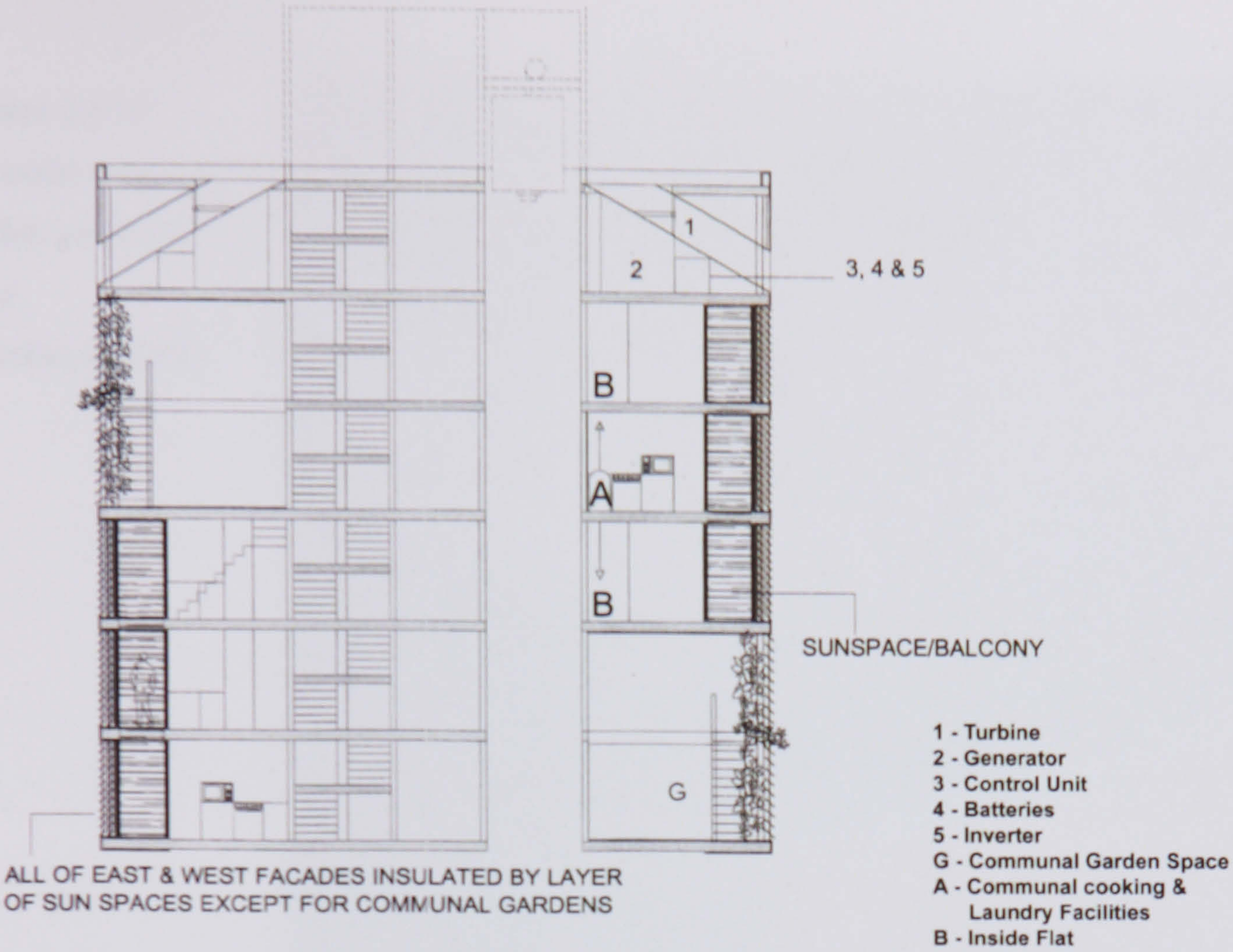

Figure 2.8.8: Cross-sectional view of the complete integration of the Ducted Wind Turbine integrated in a conventional building with flat roof (Parkinson 2001)

Figure 2.8.9:
An artist's view, duct inlets at the upper part of the front façade
(Parkinson 2001)

Figure 2.8.10:
An artist's view, duct outlets on the flat roof
(Parkinson 2001)

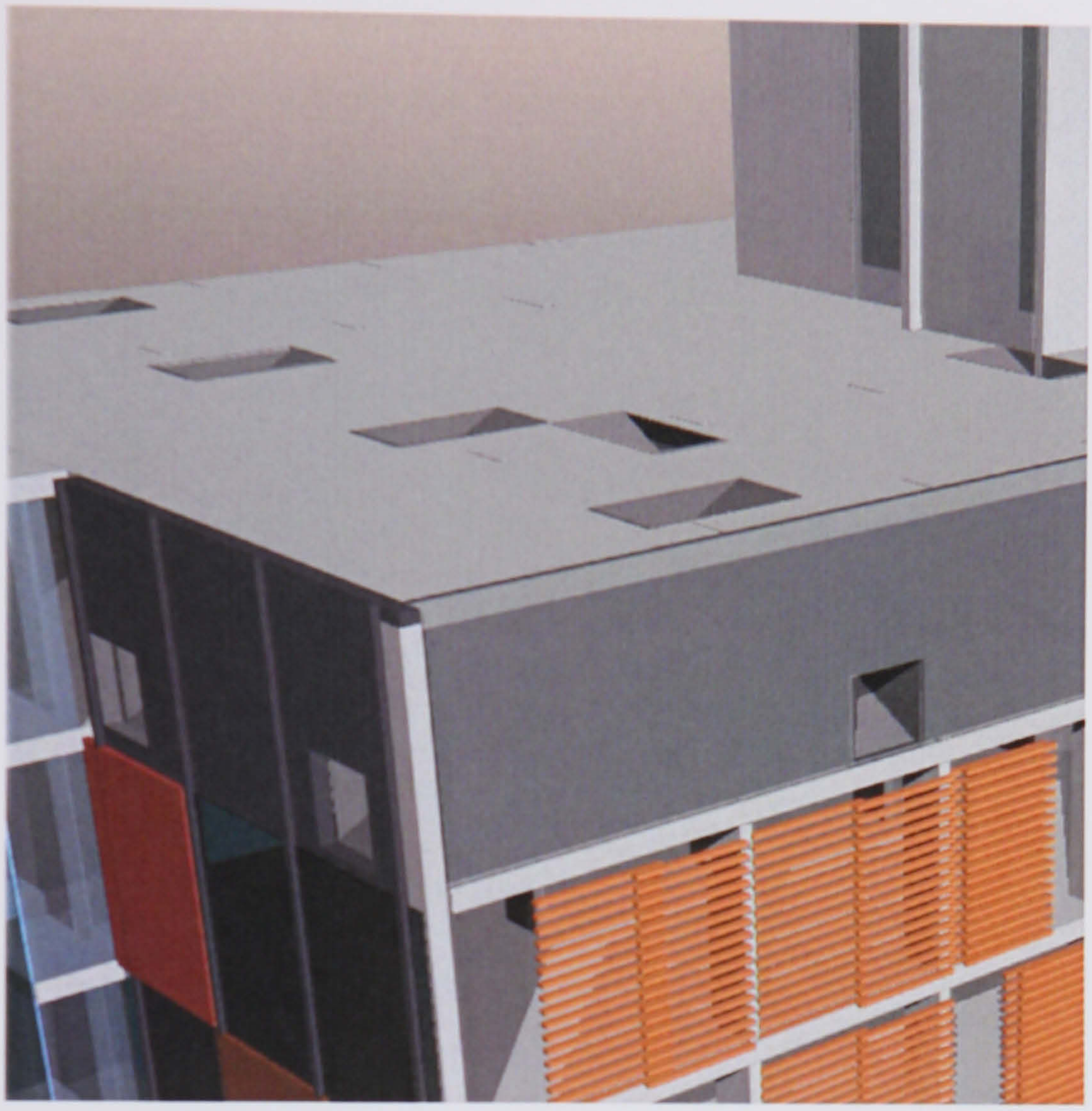

From the beginning it was assumed, that the proposed duct should be either straight or of concentrator or diffuser type. Because of the rectangular bending, it was not possible to make use of a casing design of previous models (see Chapter 3.2). Also, the idea of integrating a compact machine with short canal could not be realised with a logarithmic spiral as inlet curve. Therefore, the duct types are based on parameters which can be found for air conditioning systems (Miller). However, the air conditioning duct system is optimised for a closed circuit flow, and its application to the presented open flow problem might not be optimal.

It is very difficult to predict the flow behaviour under different angles of incidence. Also, the situation of flow entrainment at the duct outlet into a region where there is likely to be a generated edge vortex is very complex, in particular under angles of incidence.

The presented work attempts to explore this complex flow problem by means of experimental and computational modelling. This might be a basic contribution to future prototype development and the complete integration of the Ducted Wind Turbine in the built environment.

References

Scovel E.J. and Ross C.F., Illinois, USA; Windmill, USA Patent No. 581311, 1897

Thomas Brown Cooper, W.R.M. Thomson & Co., Glasgow, Scotland; Improvements in and relating to Wind Driven Motors, United Kingdom Patent No. 12069, 1910

Buri A., Sulzer & Frères Société, Winterthur, Kanton Thurgau, Switzerland; Cooling Fan for Vehicles Driven by Internal Combustion Engines, USA Patent No. 1966787, 1934

Webster G.W., Glasgow, Scotland; Devices for Utilizing the Power of the Wind, USA Patent No. 4154556, 1979

Nasr el-Din S., Grant A.D. and Lee C.K.: A Wind Energy Module for Low Power Applications; Energy for Rural and Island Communities VI (Proceedings of the International Conference, Editor John Twidell), Pergamon Press, Oxford, England, 1992

Grant A.D., Nasr el-Din S.A. and Kilpatrick J.; Development of a Ducted Wind Energy Converter; Wind Engineering, Vol. 18, No. 6, 1994

Cook I.; The Performance Evaluation of a Ducted, Vertical Axis Wind Turbine; MSc Thesis, Department of Mechanical Engineering, Energy Systems Division, University of Strathclyde in Glasgow, Scotland, 1992

Kilpatrick J.; Analysis of a Vertical Axis Wind Turbine; MSc Thesis, Department of Mechanical Engineering, Energy Systems Division, University of Strathclyde in Glasgow, Scotland, 1993

Dannecker R.K. and Grant A.D.; Wind Energy in the Built Environment; Final Scientific Report, Project No. JOR3-CT97-5008 (DG12-DEMA); Commission of the European Communities, DGXII, Directorate-General for Science, Research and Development, JOULE-Non Nuclear Energy Research, December 1999

Dannecker R., Quinonez Varela G. and Grant A.: Development of the Building Integrated Ducted Wind Turbine Module; Proc. of the 21st Annual British Wind Energy Association Conference (BWEA21), Cambridge, England, 1st-3rd September 1999

Andina Pendas I.: Investigation of a Wind Energy Module; external Proyecto Fin de Carrera, Escuela Téchnica Superior de Ingenieros Industriales e Ingenieros Informaticos, Universidad de Oviedo, Gijón, Spain / Energy Systems Division, Department of Mechanical Engineering, University of Strathclyde in Glasgow, Scotland, 1999

Aris M.S.: Ducted Wind Turbines for the Urban Environment; MSc Thesis, Department of Mechanical Engineering, Energy Systems Division, University of Strathclyde in Glasgow, Scotland, 1998

Dannecker R.: The Ducted Wind Turbine Module and its Integration in a Conventional Building; Proc. of the 2nd European 'Marie Curie' Workshop Conference; Commission of the European Communities, DG XII, Directorate-General for Science, Research and Development, JOULE-Non Nuclear Energy Research; hold at the Hydraulics and Maritime Research Center HMRC, The Munster Institute, University College Cork, Ireland, April 1998

Grant A.D. and Dannecker R.: A Hybrid PV / Wind Energy Module for Integration in Buildings; Proc. of the 16th European Photovoltaic Solar Energy Conference and Exhibition; May 1st-5th 2000, Glasgow, Scotland.

RE-Start (Renewable Energy Strategies and Technologies for Regenerating Towns), targeted project under the RUE (Rational Use of Energy) in the building sector; THERMIE, 4th framework 1996; Commission of the European Communities, DG XVII, Directorate-General for Energy and Transport.

Clarke J.A., Hensen J.L.M., Johnstone C.M. and Macdonald I.: On the Use of Simulation in the Design of Embedded Energy Systems; Proc. of the 6th International Building Performance Simulation Association IBPSA Conference 'Building Simulation '99 ', Vol.1, pp.113-119, Kyoto, Japan, 1999

Clarke J.A., Johnstone C.M., Macdonald I.A., French P., Gillan S., Glover C., Patton D., Devlin J. and Mann R.: The Deployment of Photovoltaic Components within the Lighthouse Building in Glasgow; Proc. of the 16th European Photovoltaic Solar Energy Conference and Exhibition, May 1st-5th 2000, Glasgow, Scotland

Dannecker R.: Building Integrated Ducted Wind Turbine Module: Current State and Prospects of Future Development; Proc. of the 5th European 'Marie Curie' Workshop Conference; Commission of the European Communities, DG XII, Directorate-General for Science, Research and Development, JOULE - Non Nuclear Energy Research; hold at CIEMAT-DLR, Plataforma Solar de Almeria PSA, Almeria, Spain, September 1999

Parkinson A.: Housing Project: Rehabilitation of High-Rise Block 2 & 4 Fountainwell Terrace, Sighthill, Glasgow; 4th Year Project in Architectural Studies, Department of Architecture, Community Design Unit, University of Strathclyde in Glasgow, Scotland, June 2001

Miller D.S.: Internal Flow Systems; Vol. 5, BHRA Fluid Engineering Series

3. Power Augmented Wind Turbines

3.1. The Concept of the Pressure Differential

The theoretical upper limit to the amount of energy that can be extracted from the wind energy flux by a wind turbine of given dimensions is around 59 % (Betz 1926). The Betz limit is derived from three conservation laws, conservation of energy, axial (longitudinal) momentum and mass, applied to a one-dimensional flow, the stream-tube. The turbine is replaced by an actuator disk of area A_t. The velocity u_t is continuous through the rotor (mass conservation) and is the arithmetic mean of the velocity u_i far in front and u_e far behind the actuator disk, but the static pressure shows a sudden drop $\Delta p = p_1 - p_2$ across the disk due to energy absorption by the turbine. It is assumed that the Bernoulli equation is appropriate to use in the wake. When energy is absorbed by the turbine, the exit wind velocity u_e in the wake is smaller then the entering wind speed u_i, therefore the massflow through the turbine is smaller than the massflow through the same area in the free stream far in front of the turbine. As the absorption of energy in the turbine limits the massflow through the turbine, it limits the maximum amount of energy which can be transferred into power by the turbine. The power coefficient C_P

$$C_P = \frac{\frac{1}{2}\rho u_t A_t (u_i^2 - u_e^2)}{\frac{1}{2}\rho u_i^3 A_t} = \frac{u_t A_t \cdot \Delta p}{\frac{1}{2}\rho u_i^3 A_t}$$

reaches its maximum $C_P = 16 / 27$ when $u_t / u_i = 2 / 3$ and $u_e / u_i = 1 / 3$.

The power output of a wind turbine may exceed this limit, if it is possible to increase the mass flow through the turbine in some way (see Chapter 8.5).

References

Betz A.: Windenergie und ihre Ausnutzung durch Windmühlen; Verlag Vandenhoeck und Ruprecht, Göttingen, Germany, 1926
(reprint in ökobuch Verlag Staufen, Germany 1982, 1994)
also in Prandtl L.; Schraubenpropeller mit geringstem Energieverlust: nach der Königlichen Gesellschaft der Wissenschaften zu Göttingen, Mathematisch-Physikalische Klasse, pp. 193-217, Germany, 1926
or in L.Prandtl: Gesammelte Abhandlunngen; Julius Springer Verlag, Berlin, Germany, 1961
reprinted in
Betz A. and Prandtl L.: Vier Abhandlungen zur Hydrodynamik und Aerodynamik, Göttingen, Germany 1927

3.2. Realising the Concept: Power Augmentation in Ducted Wind Turbines

Sivasegaram reviews different design approaches to achieve wind power augmentation, from the early centuries up to the eighties (Sivasegaram 1986).

A bell mouth intake in front of the turbine facilitates capture of a wider spectrum of wind directions. Further, it acts as a flow concentrator. It was shown that the concentrator systems contribute to the performance characteristics of the rotor. Rotors with concentrators start with lower air velocities in the free stream. In the main range of wind speeds, about 5 m/s to 15 m/s, they run at significantly higher tip speed ratios producing up to twice as much mechanical power at the rotor as an unducted rotor (Berkoune 1990).

More efficient are devices where an increased massflow is realised by a reduction of the pressure in front of the turbine (which means higher turbine inflow velocity as the free stream wind speed) and a consequently increased pressure recovery towards the free-stream pressure behind the turbine. The application of a diffuser behind the turbine has the desired result. Dependent on the diffuser efficiency and the diffuser area ratio, the power coefficient may exceed the Betz limit by a factor of 2 (de Vries 1979). Especially short streamline formed diffusers with annular wing flaps at the rear, designed to reduce the static pressure at the diffuser exit, may lead to a 2.5 times increase in power coefficient compared to the Betz limit. In the late seventies, when aeroplane manufactures occupied the wind turbine market in the United States, the diffuser augmented wind turbine was investigated by Foreman and Gilbert (Foreman and Gilbert 1977, 1978, 1979, 1983). It was stated that a diffuser augmented wind turbine can provide around three to four times more power then a conventional turbine. This enormous increase in massflow is mainly due to swirling flow in the diffuser, which is created through boundary layer control slots at the housing in interaction with the turbine wake. The peripheral accelerated flow controls the development of the boundary layer and avoids flow separation from the diffuser wall. Otherwise flow separation would occur because of the very strong adverse pressure gradients inside the diffuser, and this would hinder the massflow. Concepts using short diffusers with a large opening angle and a big aspect ratio could create an exit plane pressure coefficient of $c_P = -1.4$, and a power augmentation factor of 6 to 8 is predicted. Similar beneficial effects of inflow swirl and radial distortion on diffuser performance were measured as part of the investigation of a large scale wind tunnel, for airflow in the same pressure range (Eckert et al.1980). It was found that a long contraction duct produces better inflow to the fan than does a short one. To avoid the long duct, a gentle (cubic wall contour) contraction is much more favourable than an abrupt contraction.

When the aspect of short streamline formed diffusers is elaborated further, an annular wing or shroud operates equally well. In addition to the increase in mass flow, the small tip clearance avoids tip losses. The sectional lift on the annular wing has to be directed inwards towards the turbine axis, and the corresponding circulatory flow around the section of the annular wing induces an increased velocity through the area enclosed. A pilot plant based on a NACA 4412 cross-section annular wing housing a simple axial flow turbine yields a power augmentation of at least a factor of two compared with a conventional wind turbine of the same size (Igra 1980,1981); further improvements on turbine and shroud may result in power augmentation of a factor 4.

The circulatory flow around the shroud acts as vortex ring. Likewise, a vortex ring may be created by a tip vane attached to the tip of the turbine blade, which results in the same effect of increased mass flow and performs well with similar efficiency (Van Holten 1974, 1981). This power augmentation concept is feasible on operating wind turbines, as it bars any larger additional structure.

Some proposed kinetic wind energy concentrators are based upon the concept of extracting the kinetic energy concentrated in the small area of trailing-edge vortices of wings (straight and delta shaped). The very complex oncoming swirling flow to the turbine and the large load fluctuation in changing flow conditions seems to limit the feasibility of this approach (Greff 1983).

The synthesis of the concepts of the kinetic wind energy concentrator and the concentrator duct was created as the Helical Vortex Wind Concentrator. This is an annular disk of stationary, radial, aerofoil sectioned stator blades which entrain the wind, through the orifice formed by the surrounding blades, onto the wind turbine downstream. It is suggested that this device will induce wind velocities two times higher than in the free stream (Olivieri 1990).

The large structure of the duct limits the size of any of the proposed ducted wind turbines. Igra reports about the heavy structure and material requirements to stand the loads involved. Further more the alignment of the turbine with changing wind direction is impaired, but Igra reports that about 30^0 misalignment was tolerated by the pilot plant. Therefore the idea arises to include a power augmented wind turbine in the structure of a building. The tower like buildings which result serve mainly as housing for turbine and duct. The pressure drop of an intense artificial vortex is used to increase the massflow through an axial turbine. The vortex is generated inside a suitable tower that can interact omnidirectionally with the incoming wind. As the tower is open at the top, interaction with the wind at the outlet creates an additional low pressure region. First concepts were formulated in the middle of the 1970s by various groups, probably originated by Yen (Yen 1976) and Loth (Loth 1976). Since then different model configurations have been tested in order to achieve further enhancement from better aerodynamics at the inflow side and to investigate geometrical proportions (Windrich and Fricke 1984). A further synthesis has been proposed, where a huge vertical diffuser acts as vortex tower and uses the pressure drop above the outlet due to the interaction of the wind with the building (Rom and Bowen 1988). Prediction of wind energy enhancement goes up to a factor of 4 compared with a conventional wind turbine, but it is difficult to draw quantitative conclusions from wind tunnel models, because scaling effects might influence vortex development and vortex breakdown significantly. Also, the behaviour in gusty winds as they appear in nature remains unknown. A pilot plant of this type does not exist, and at this time there is no project which might prove the tornado wind concept in real scale.

References

Sivasegaram S.: Power Augmentation in Wind Rotors: A Review; Wind Engineering, Vol. 10, No. 3, 1986, pp. 163-179

Berkoune A.: Testing of Rotors with Concentrators; Proc. of the 12th Annual British Wind Energy Association Conference (BWEA12), Norwich, England, 27th - 30th March 1990

de Vries O.: Fluid Dynamic Aspects of Wind Energy Conversion; NATO, Advisory Group for Aerospace Research and Development AGARD, AGARDograph No. 243, July 1979, ISBN 92-835-1326-6.

Foreman K.M. and Gilbert B.L., Grumman Aerospace Corporation, New York, USA; US Department of Energy Contract No EY-76-C-2-2616; Technical Development of the Diffuser Augmented Wind Turbine (DAWT) Concept; Wind Engineering, Vol.3, No.3, 1979

Gilbert B.L., Oman R.A. and Foreman K.M.: Fluid Dynamics of Diffuser Augmented Wind Turbines; Proc. of the 12th Intersociety Energy Conversion Engineering Conference, Washington D.C., USA, 1977, pp. 1651-1659

Gilbert B.L. and Foreman K.M.: Experimental Demonstration of the Diffuser Augmented Wind Turbine Concept; Proc. of the 13th Intersociety Energy Conversion Engineering Conference, San Diego, California, USA, 1978, pp. 2082-2098

Gilbert B.L. and Foreman K.M.: Experiments with a Diffuser-Augmented Model Wind Turbine; Transactions of the American Society of Mechanical Engineers (ASME), Journal of Energy Resources Technology, Vol. 105, March 1983, pp. 46-53

Eckert W.T., Johnston J.P., Simons T.D., Mort K.W. and Page V.R.: An Experimental Investigation of two large Annular Diffusers with Swirling and Distorted Inflow; NASA Technical Paper 1628, NASA, February 1980; Ames Research Center, NASA, Moffet Field, California 94035, USA, 20th August 1979

Igra O.: Research and Development for Shrouded Wind Turbines; Energy Conversion and Management, Vol. 21, 1981, pp. 13-48

Igra O.: Shrouded Wind Turbine Research in Israel; The International Journal of Ambient Energy, Vol. 2, No. 2, April 1981, pp. 85-96

Igra O.: Preliminary Results from the Shrouded Wind-Turbine Pilot Plant; Journal of Energy, Vol. 4, No. 4, Jul-Aug 1980, pp. 190-192

Van Holten Th.: Performance Analysis of a Windmill with Increased Power Output due to Tipvane Induced Diffusion of the Air Stream; Memorandum M-2245, Delft University of Technology, Delft, The Netherlands, 1974

Van Holten Th.; Concentrator Systems for Wind Energy, with emphasis on Tip-vanes; Wind Engineering, Vol. 5, No. 1, 1981, pp. 29-45

Greff E.: Windenergiekonzentratoren: Theoretische und experimentelle Studie zur Erhöhung der Leistungsdichte von Windturbinen in Wirbeln; Dissertation, Rheinisch-Westfälische Technische Hochschule (RWTH) Aachen, Germany, 1983, published as
Fortschritt-Berichte, Verein Deutscher Ingenieure VDI, Reihe 7 (Strömungstechnik) Nr. 73, VDI Verlag Düsseldorf, Germany, 1983, ISSN 0341-1753

Olivieri D.A., Sharpe D., Boyle G.A. and Taylor D.A.; Design and Testing of a Concentrator Wind Turbine; Proc. of the 12th Annual British Wind Energy Association Conference (BWEA12), Norwich, England, 27th -30th March 1990

Yen J.T., Grumman Aerospace Corporation, New York, USA; Tornado-Type Wind Energy System: Basic Consideration; Proc. of the International Symposium on Wind Energy Systems (organised by BHRA Fluid Engineering), 7th-9th September 1976, Cambridge, England.

Loth J.L.; W.V.U. Wind Energy Concentrators; Proc. of the International Symposium on Wind Energy Systems (organised by BHRA Fluid Engineering), 7th-9th September 1976, Cambridge, England.

Windrich J. and Fricke J.; Systematic Study of TWS Performance; Solar Energy, Vol. 33, No. 3-4, 1984, pp. 289-303

Rom H.T. and Bowen A.J.; The use of a Ducted Wind Turbine Within a Tall Building; Wind Engineering, Vol. 12, No. 4, 1988, pp. 226-235

3.3. Theoretical Modelling of Ducted Wind Turbines

The simple axial momentum theory of Betz (Betz 1926), which originated from Rankine and Froude (Rankine 1865, Froude W. 1878 and Froude R.E. 1889) illustrates the importance of increased massflow rate and pressure differential across the turbine in order to achieve power augmentation, but it can not cope with the complex flow behaviour in particular in close vicinity downstream of the turbine. Therefore, any theoretical prediction of the power coefficient for augmentation concepts based on one dimensional axial momentum theory (the stream tube) is limited.

Glauert (Glauert 1935) includes in his discussion the rotation left behind in the wake. According to the conservation of angular momentum for the system of the airstream and impeller, the two move counter rotationally. Further, the torque transferred to the flow field and the entraining trailing vorticity contributes to the complete kinetic energy left in the wake and decreases the maximum attainable power coefficient.

Further information may be obtained from this model using blade element theory to optimise the rotor. Hütter (Hütter 1977) states that the theoretical optimum of the power coefficient may be increased by wake divergence and turbulent mixing by up to 13 %. Prandtl and Goldstein (Prandtl and Tietjens 1957, Goldstein 1929) have analysed the helical vortex sheet wake. The induced velocities fluctuate between blade passages, which reduce the net momentum change and therefore the net power extracted by means of a tip loss factor. This calculation includes the blade element analysis, which substitutes for the actuator disk theory. Simple blade element theory predicts an increased power output for high tip speed ratios, because the tip losses and the wake rotation loss decrease. This tendency is opposed by increasing profile drag for high tip speed ratios.

Even today it remains difficult to predict the complex flow structure in the near wake region, which may extend over about 2-4 rotor diameters downstream. In this near wake region, axial and radial pressure gradients, caused by the kinetic energy extraction at the rotor, relax. This causes the centerline velocity to drop to a minimum at between 1 and 2 rotor diameters downstream, and the wake width increases. The velocity drop recovers by turbulent fluid mixing and the rotor tip vortices and the introduced bulk swirl decay within 2 to 3 diameters. Further downstream large scale turbulence generated in the annular shear layer spreads into the wake core, the wake takes on a Gaussian profile and the centerline deficit decays monotonically. As soon as the pressure gradients no longer dominate the flow, the turbulent mixing of the wake can be modelled solving the turbulent transport equations, or in an simplified approach with an eddy viscosity model using a Biot-Savart law for the radial component of momentum (Ainslie 1988). The eddy viscosity has to be fitted with an empirical filter function, because of inequilibrum between the mean velocity field and the turbulence field up to 5 diameters downstream the rotor.

Regarding the flow field close to the rotor, a finite difference procedure has been developed for the prediction of three dimensinonal rotor blade-vortex interactions, applied to helicopter blades. The rotor flow field was computed using the unsteady 3-d Euler equations, and the embedded vortex wake flow field was computed with the Biot-Savart law (Hassan et al. 1992). The theoretical work was accompanied by experiments to measure the blade vortex interaction (Kokkalis and Galbraith 1987).

Calculation of the flow field for ducted wind turbines to predict power coefficients or to evaluate a design option is not so elaborate. At the fluid mechanics level of analysis, all performance characteristics are determined by the assumption of the exit flow condition for the duct. For exit pressure lower than free stream static pressure, wake expansion downstream of the duct creates a higher massflow and therefore a higher power coefficient for the turbine. Still, the experimental findings for streamline formed diffuser wind turbines (all 'venturi' types) are supported by a basic fluid mechanical stream tube model which allows design optimisation by simple means (Kentfield 1978). It can not provide any further information regarding the complex flow behaviour of the system duct / rotor.

Hence, details of duct geometry must enter into the wake analysis, and a proper performance prediction depends on modelling of the entire flow. Zapletal and Flechter (Zapletal and Flechter 1983) used a numerical boundary element method to analyse the design of diffuser augmented wind turbines. The flowfield is modelled by potential flow, the boundary conditions are specified as either Dirichlet or Neumann type. Green's theorem then gives an integral equation formulation where the surfaces are introduced as a perturbance potential by a surface distribution of sources. This procedure is basically the lifting line / lifting surface approach for aerodynamic design studies. The integrals are solved numerically as a set of linear equations. Simplified models of the turbine wake and the developed boundary layer are represented by sources and can therefore be combined with the potential flow theory. The turbine effect can then be seen in terms of reduced momentum in the streamline pattern.

Systematic wind energy calculations related to the annular duct system have been undertaken by Koras, using lifting line theory for the rotor whilst the duct is treated as a superposition of vortex rings (Koras and Georgalas 1988) assuming a high value of tip-clearance. Later, this group presents a simple empirical formula which reproduces the first accurate results. Dependent on tip speed ratio and geometrical design parameters, a power coefficient in the range of 0.7 to 0.8 is stated (Georgalas, Koras et al. 1991). For ducted wind turbines with small tip-clearance, a sophisticated calculation is based on lifting line theory for the rotor and lifting surface theory representing the action of the duct (Politis and Koras 1995). The flow field was obtained using vorticity continuity formulation in the rotor coordinate system. In particular for the determination of the position of the rotor trailing vortex they use the Helmholtz Second Law of vorticity dynamics according to which the vortex lines coincide with the streamlines in a steady free vortex sheet. So the rotor wake surface becomes a general helicoidal surface. For high tip speed ratios and wing section shrouds, a power coefficient of 0.8 and larger is predicted.

Lifting line and lifting surface theory is well established to calculate potential flow fields, especially in the field of aeronautics where it is a sophisticated tool to evaluate design options. Rotational flow can be introduced by means of continuity, and different sources can be imposed on the field in advance to model expected effects of kinetic energy losses or gains. The prediction of turbulence accompanied by wind energy losses in the rotor duct system will be not feasible with the quoted theoretical work.

References

Betz A.; Windenergie und ihre Ausnutzung durch Windmühlen; Vandenhoeck und Ruprecht Verlag, Göttingen, Germany 1926; reprint in ökobuch Verlag Staufen, Germany 1982, 1994; also in Prandtl L.; Schraubenpropeller mit geringstem Energieverlust: nach der Königlichen Gesellschaft der Wissenschaften zu Göttingen, Mathematisch-Physikalische Klasse, pp. 193-217, Germany, 1926 (or in L.Prandtl; Gesammelte Abhandlunngen, Springer Verlag, Berlin, Germany 1961)

reprinted in Betz A. and Prandtl L: Vier Abhandlungen zur Hydrodynamik und Aerodynamik, Göttingen, Germany 1927

Glauert H.: Aerodynamische Theorie; Verlag von Julius Springer, Berlin, Germany 1935

Hütter U.: Optimum Wind Energy Conversion Systems; Ann. Rev. Fluid Mech., Vol. 9, 1977, pp 399–419

Rankine W.J.: Transactions, Institute of Naval Architects, Vol. 6, 1856, pp.13

Froude W.: Transactions, Institute of Naval Architects, Vol. 19, 1878, pp.47

Froude R.E.; Transactions, Institute of Naval Architects, Vol. 30, 1889, pp.390

Prandtl L and Tietjens O.G.: Applied Hydro- and Aerodynamics; Dover Publications Inc., England 1957

Goldstein S.; On the Vortex Theory of Screw Propellers; Proc. of the Royal Society, A123, 1929, pp. 440–465

Ainslie J.F.; Calculating the Flow Field in the Wake of Wind Turbines; Journal of Wind Engineering and Industrial Aerodynamics, Vol. 27, No. 113, January 1988, pp. 213-224

Hassan A.A., Tung C. and Sankar L. N.; Euler Solutions for Self-Generated Rotor Blade-Vortex Interactions; International Journal for Numerical Methods in Fluids, Vol. 15, 1992, pp. 427–451

Kokkalis A. and Galbraith R.A.McD.; Description of, and Preliminary Results from, a new Blade-Vortex Interaction Test Facility; Proc. 12th European Rotorcraft Forum, hold in Garmisch-Partenkirchen, Germany, September 1985
and also: Results from the Glasgow University Blade-Vortex Interaction (B.V.I.) Facility; Proc. 13th European Rotorcraft Forum, hold in Arles, France, September 1987

Kentfield J.A.; The Prediction of the Optimum Performance of Venturi-Type Wind Energy Concentrators; Proc. of the 5th annual UMR-DNR Conference on Energy, University of Missouri-Rolla, Vol.5, pp. 57-61, USA, 1978

Zapletal E. and Flechter C.A.J.: A Boundary Element Formulation for Diffuser Augmented Wind Turbines; Proc. of Computational Techniques and Applications: CTAC-83, Sydney, Australia, 1983, pp. 327-334

Koras A.D. and Georgalas C.G.: Calculation of the Influence of Annular Augmentors on the Performance of a Wind Rotor; Wind Engineering, Vol. 12, No. 4, 1988, pp. 257-267

Georgalas C.G., Koras A.D. and Raptis S.N.: Parametrization of the Power Enhancement Caculated for Ducted Rotors with Large Tip Clearance; Wind Engineering, Vol. 15, No. 3, 1991, pp. 128-136

Politis G.K. and Koras A.D.: A Performance Prediction Method for Ducted Medium Loaded Horizontal Axis Wind Turbines; Wind Engineering, Vol. 19, No. 5, 1995, pp. 273-288

4. Experimental Investigation

4.1. The Windtunnel

The aerodynamic laboratory of the University contains a open jet closed return wind tunnel (Figure 4.1.1) of overall length of 12.40 m. The open jet working section measures 2.60 m in length. Width and height of the working section are given by the geometry of the inflow nozzle, which has a contraction ratio of 1:1.5 . The diameter of the circular nozzle opening is 1.50 m. The wind flow leaves the working section through a wide bell mouth funnel which feeds the return circuit.

The effective working height and working width is significantly smaller than the nozzle opening. As a rule of thumb, the obstacle in the wind flow should certainly not exceed half the jet diameter in height, but detailed investigations have to assure the maximal size of the model in order to obtain experimental results free from blockage effects. Similar considerations apply to the model width. In this sense, the effective working section has to be determined before the actual experimental starts.

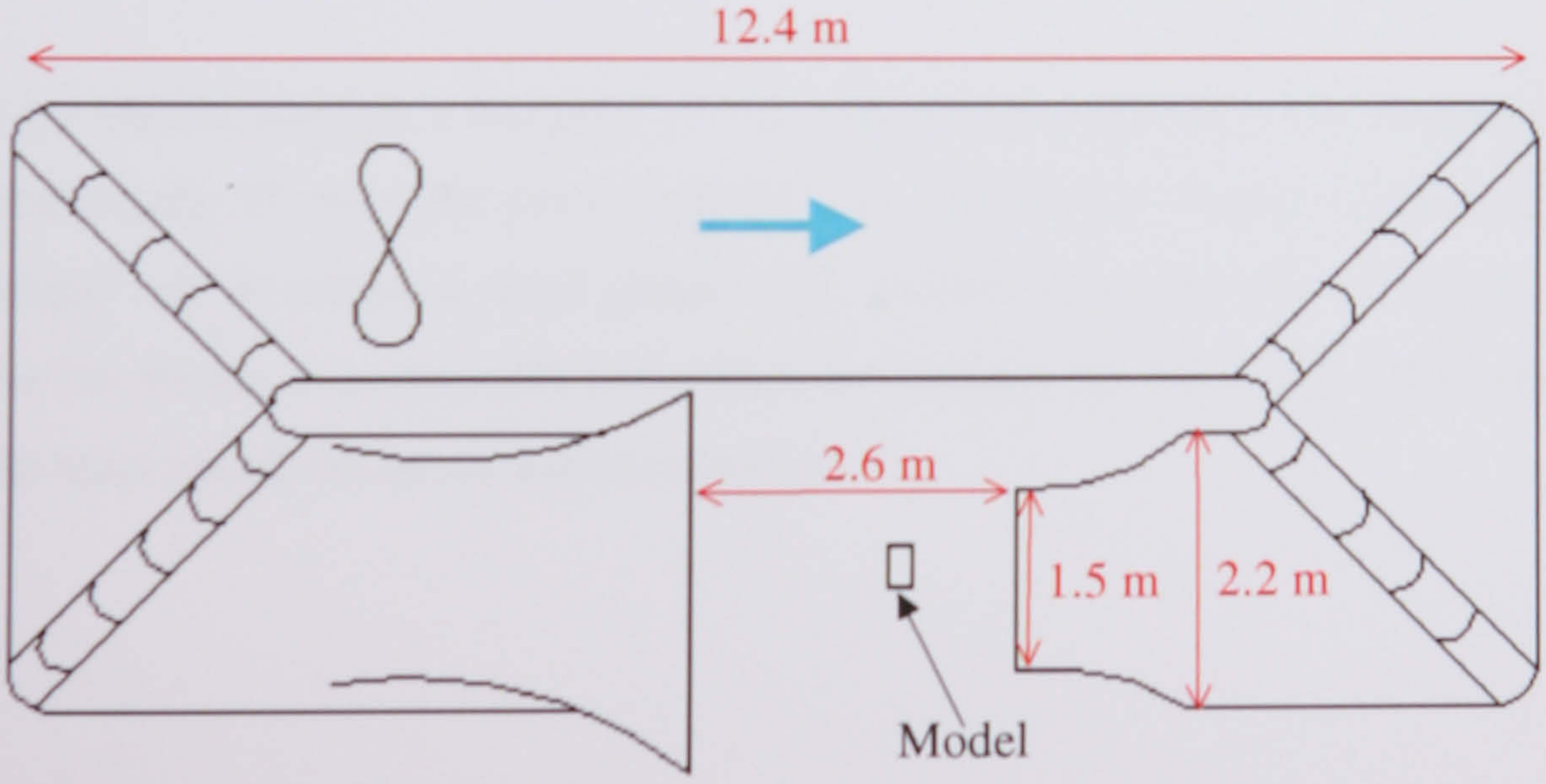

Figure 4.1.1: Schematic drawing, plan view of wind tunnel

In the working section, it is possible to lower or raise the ground plane, which includes a turntable. The wind speed in the tunnel is monitored by means of a Pitot-Static tube, at a location shown in Figure 4.1.2. The pressure reading is usually taken from an inclined manometer.

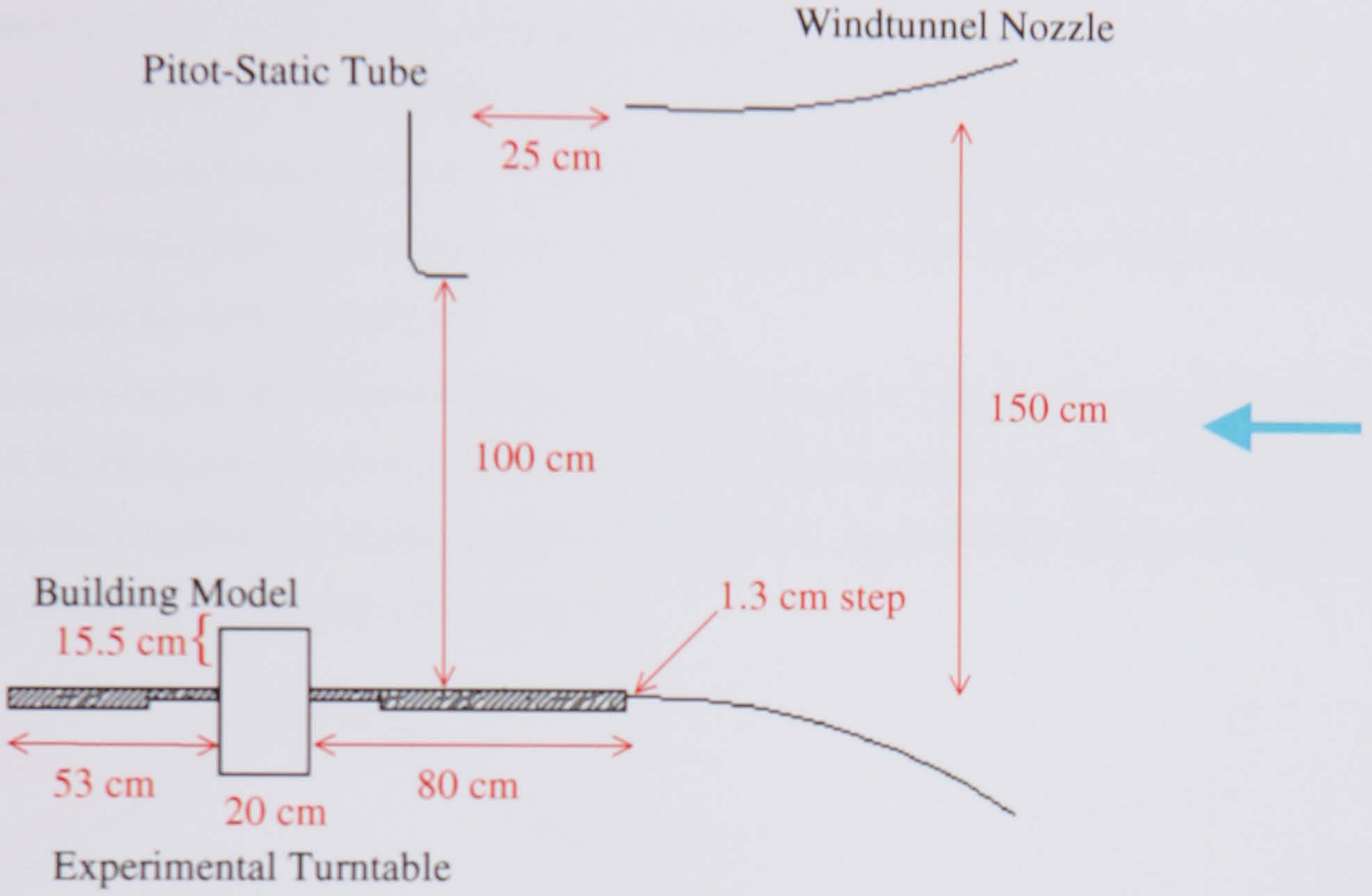

Figure 4.1.2: Schematic drawing, side view of the open working section of the windtunnel with recessed building model (see Chapter 4.5)

The fan is six bladed and has a diameter of 2 m, providing airspeeds in the working section up to approximately 35 m/s. The fan is coupled to a 40 kW D.C. motor, which is part of a 'Ward-Leonard' set in which a three phase A.C. motor drives the D.C. generator which supplies the fan motor. A coarse and a fine rheostat controls the D.C. stator field supply. In this way the wind speed can be set and maintained.

4.2. The Wind Tunnel Model

The wind tunnel model house (scale 1:100) was built by Leyk, who also performed the first measurements (Leyk 1997). It is a rectangular block constructed from Perspex and plywood. The overall height of the model is 600 mm, the width is 350 mm and the depth is 200 mm. A manual 2-dimensional traverse device is fitted into the model and allows a hot wire probe to be moved in longitudinal and transverse directions over the flat roof. A scale on the probe holder indicates the vertical position.

As the model consists of different sections, its height can be reduced. As explained later (in Chapter 4.5), the model was lowered to 370 mm and recessed into the turn table of the wind tunnel, so that its effective height became 155 mm. The simple block (Figure 4.2.1) can be modified by incorporating ducts and spoilers.

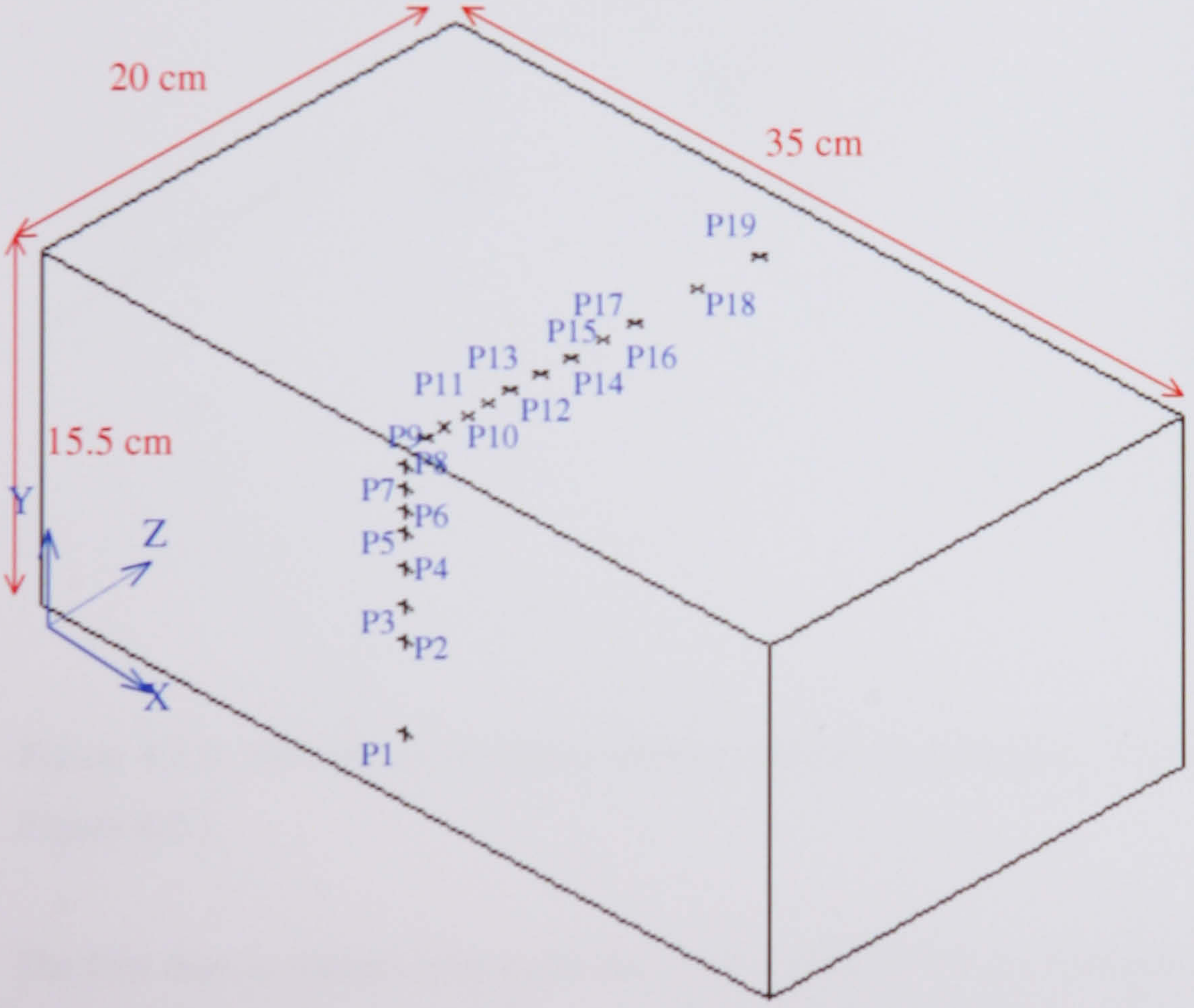

tapping	coordinates [cm]
P1	17.5 ; 3; 0
P2	17.5 ; 7; 0
P3	17.5 ; 8.5; 0
P4	17.5 ; 10.25; 0
P5	17.5 ; 11.75; 0
P6	17.5 ; 12.75; 0
P7	17.5 ; 13.75; 0
P8	17.5 ; 14.75; 0
P9	17.5 ; 15.5; 1
P10	17.5 ; 15.5; 2
P11	17.5 ; 15.5; 3
P12	17.5 ; 15.5; 4
P13	17.5 ; 15.5; 5
P14	17.5 ; 15.5; 6.5
P15	17.5 ; 15.5; 8
P16	17.5 ; 15.5; 9.5
P17	17.5 ; 15.5; 11
P18	17.5 ; 15.5; 14
P19	17.5 ; 15.5; 17

Figure 4.2.1: Simple block, experiment 1

Pressure tappings are located along the centerline of the front wall, on the roof and inside each duct. Two different duct geometries were tested, in combination with three different designs of front spoiler above the inlet. Figures 4.2.1 to 4.2.13 show the different experimental configurations of the model, details of duct and spoiler and the location of pressure tappings.

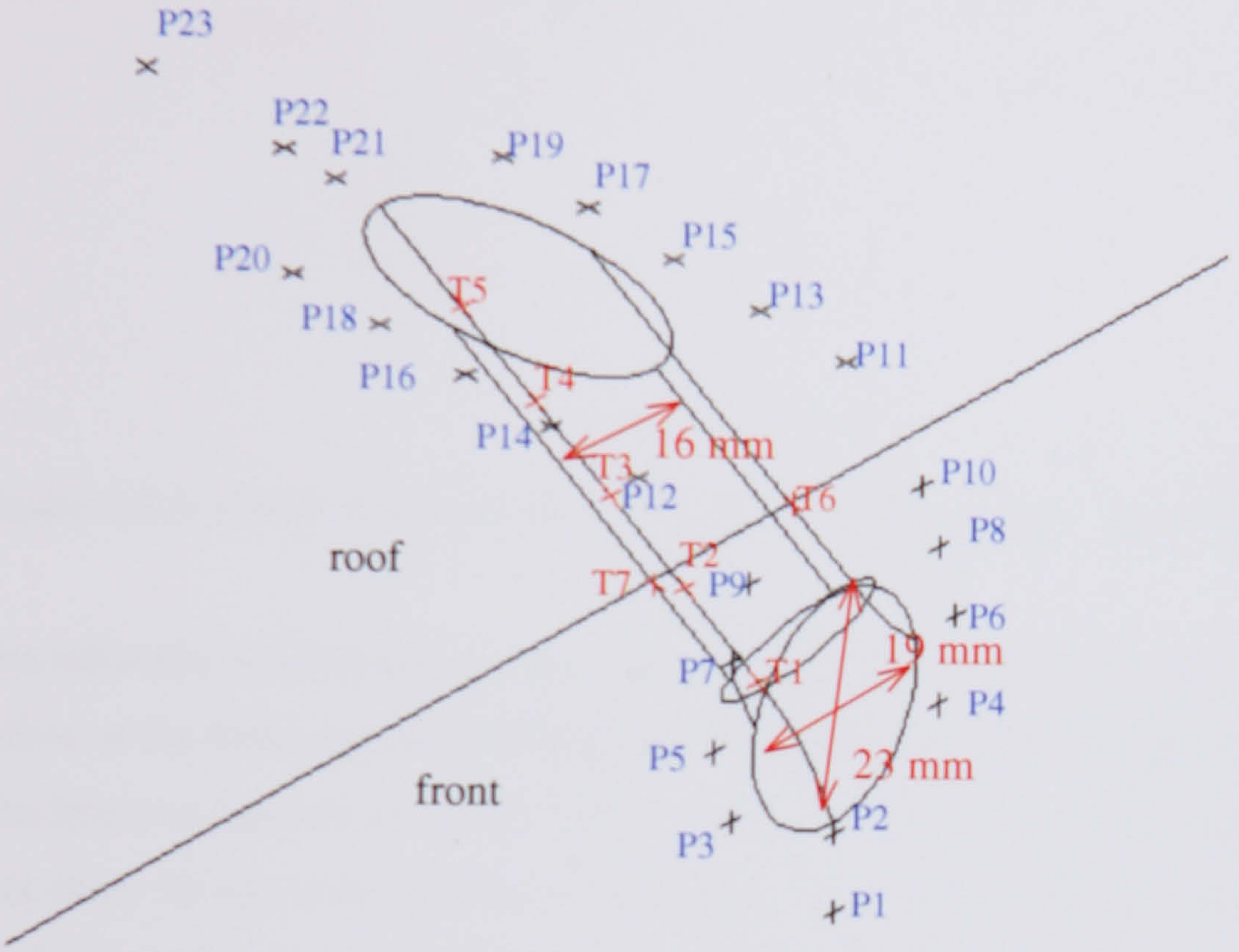

tapping	coordinates [cm]
P1	17.5; 11.1; 0
P2	17.5; 11.9; 0
P3	16.3; 12.6; 0
P4	18.7; 12.6; 0
P5	16.1; 13.4; 0
P6	18.9; 13.4; 0
P7	16.3; 14.2; 0
P8	18.7; 14.2; 0
P9	16.5; 14.9; 0
P10	18.5; 14.9; 0
P11	18.7; 15.5; 1.1
P12	16.3; 15.5; 1.1
P13	18.7; 15.5; 2.1
P14	16.3; 15.5; 2.1
P15	18.7; 15.5; 3.1
P16	16.3; 15.5; 3.1
P17	18.7; 15.5; 4.1
P18	16.3; 15.5; 4.1
P19	18.7; 15.5; 5.1
P20	16.3; 15.5; 5.1
P21	17.5; 15.5; 5.8
P22	17.5; 15.5; 6.4
P23	17.5; 15.5; 8.0
T1	17.5; 13; 0.9
T2	17.5; 13.5; 1.7
T3	17.5; 14; 2.55
T4	17.5; 14.6; 3.4
T5	17.5; 15.1; 4.3
T6	18.3; 14.3; 1.2
T7	16.7: 14.3: 1.2

Figure 4.2.2: 3D-view of 30 ° duct without spoiler, experiment 2. Coordinate system like in Figure 4.2.1

The first duct is straight with a circular cross section of 16 mm diameter, which is fitted at an angle of 30° to the horizontal into the upper part of the front panel (Figures 4.2.2 and 4.2.3). The corners at the inlet are smoothly curved. Pressure tapping are located inside the duct along the base line (T1 to T5) and right and left at the side wall of the duct (T6 and T7).

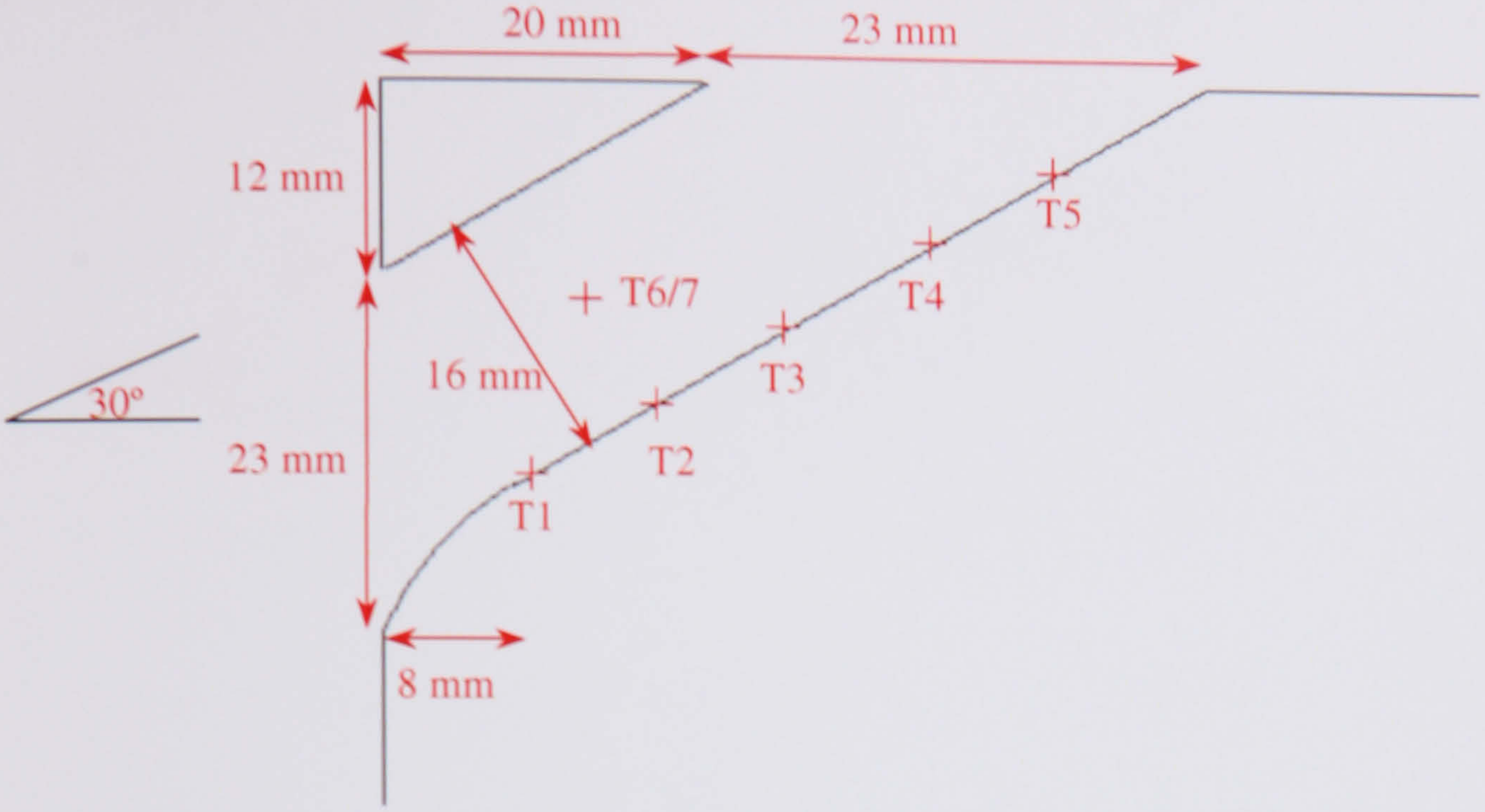

Figure 4.2.3: Cross-sectional view of 30 ° duct without spoiler, experiment 2.

The influence of different spoiler, either as wind shields at the outlet or to capture a higher inflow at the front, may be investigated. Here, three different spoilers at the inlet were tested. The first two spoilers are made from cut Perspex tubes. The smaller one is 3.5 mm thick, 16 mm deep, 28 mm wide and has a inner radius of 12 mm (spoiler I) (Figures 4.2.4 and 4.2.5), the larger is 6 mm thick, 21 mm deep, 86 mm wide and 33 mm high with an inner radius of 95 mm (spoiler II) (Figures 4.2.6, 4.2.7, 4.2.10 and 4.2.11). The third spoiler is a straight plate with rounded edges, 17 mm deep, 42 mm wide and 5 mm thick (spoiler III) (Figures 4.2.12 and 4.2.13).

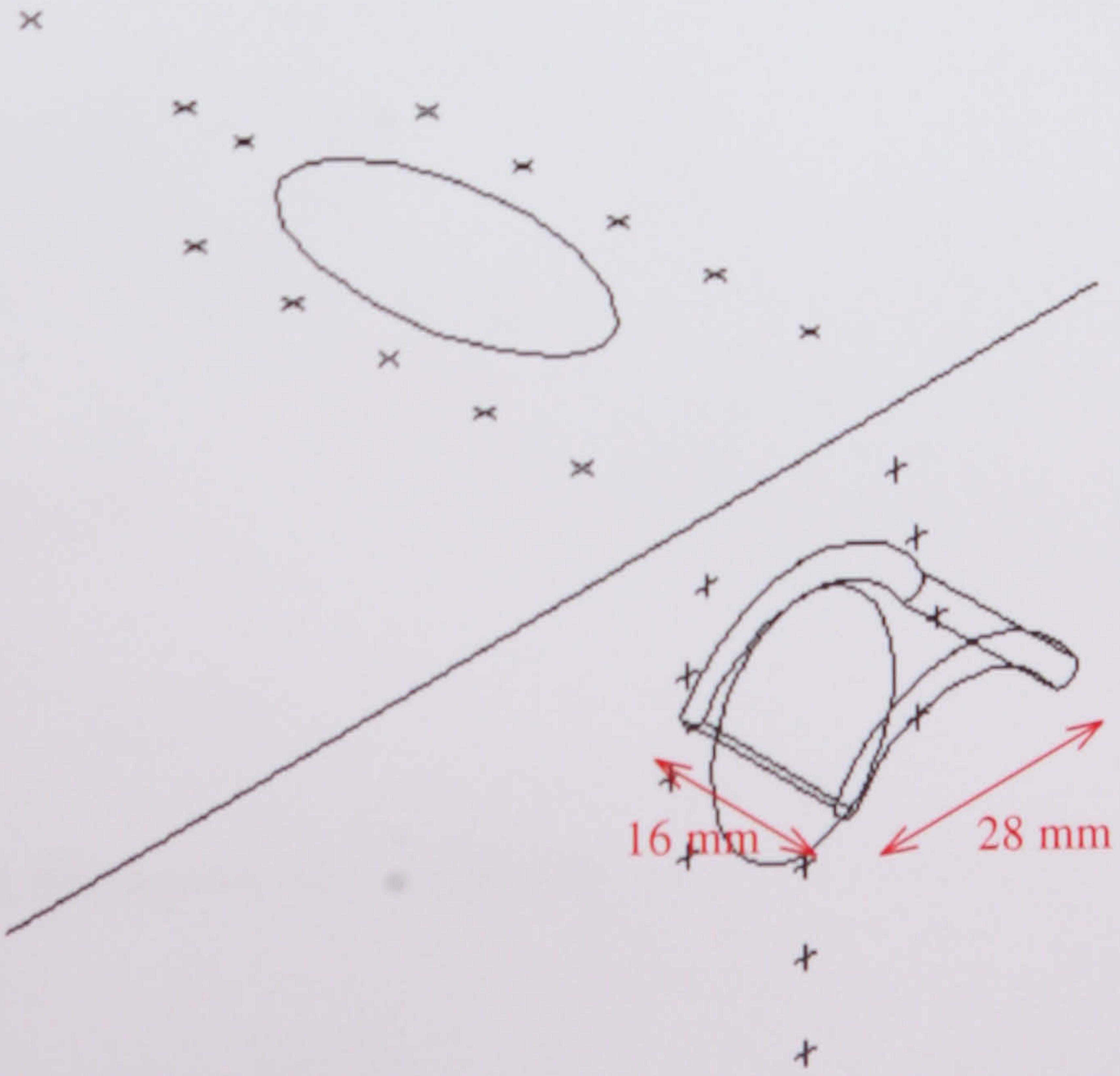

Figure 4.2.4: 3D-view of 30 ° duct, front spoiler I, experiment 3

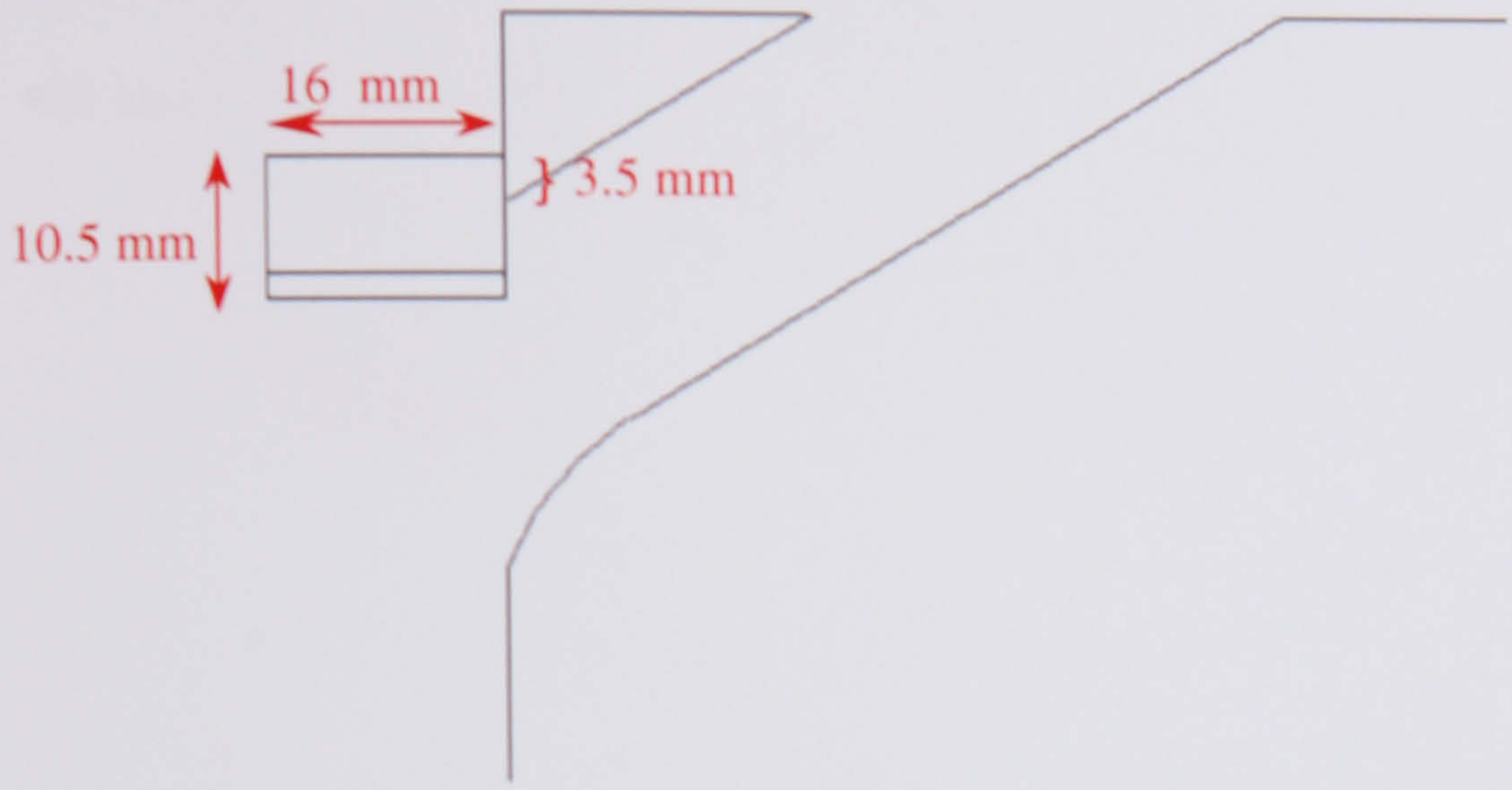

Figure 4.2.5: Cross-sectional view, 30 ° duct, front spoiler I, experiment 3

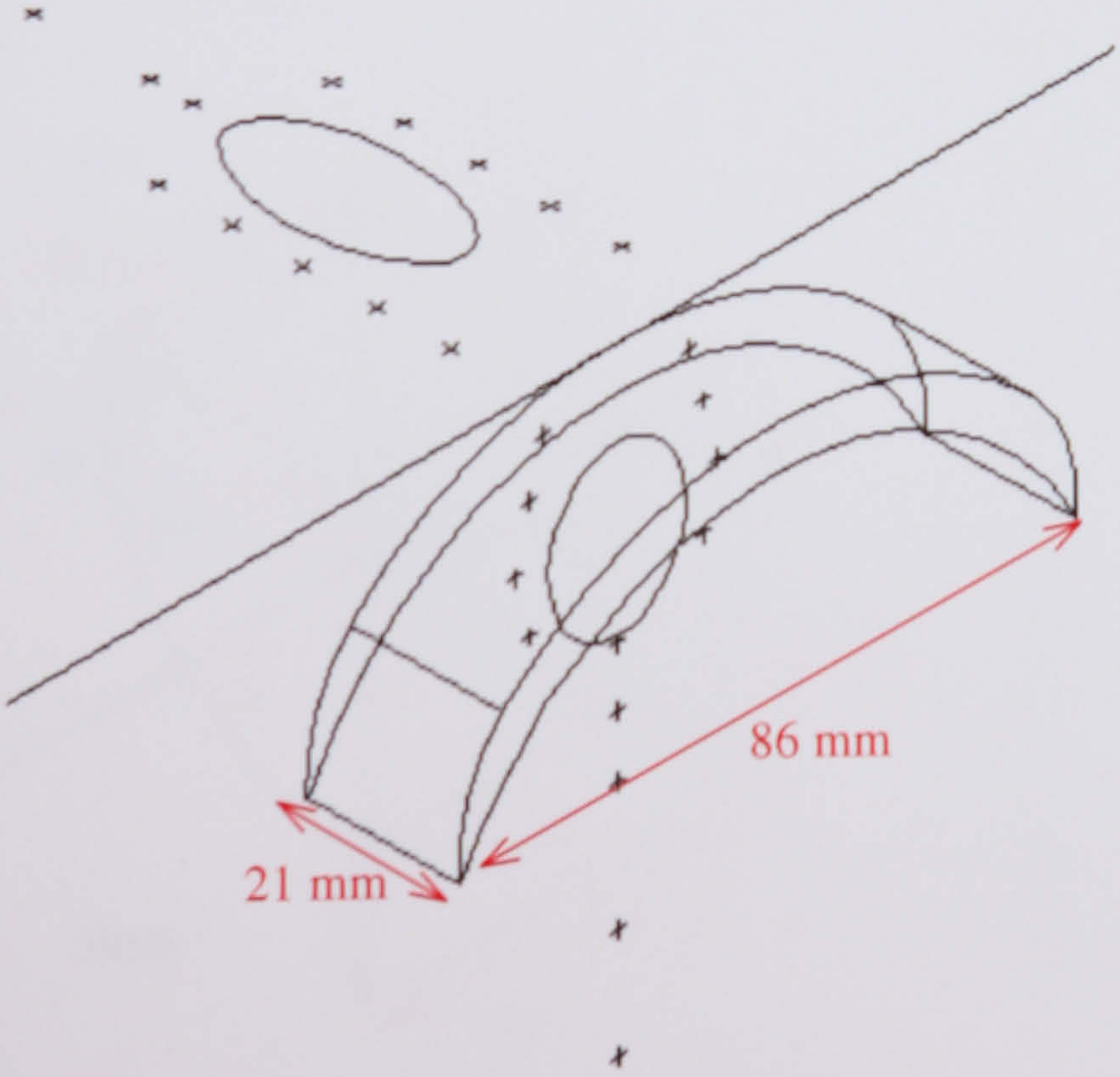

Figure 4.2.6: 3D-view of 30 ° duct, front spoiler II, experiment 4

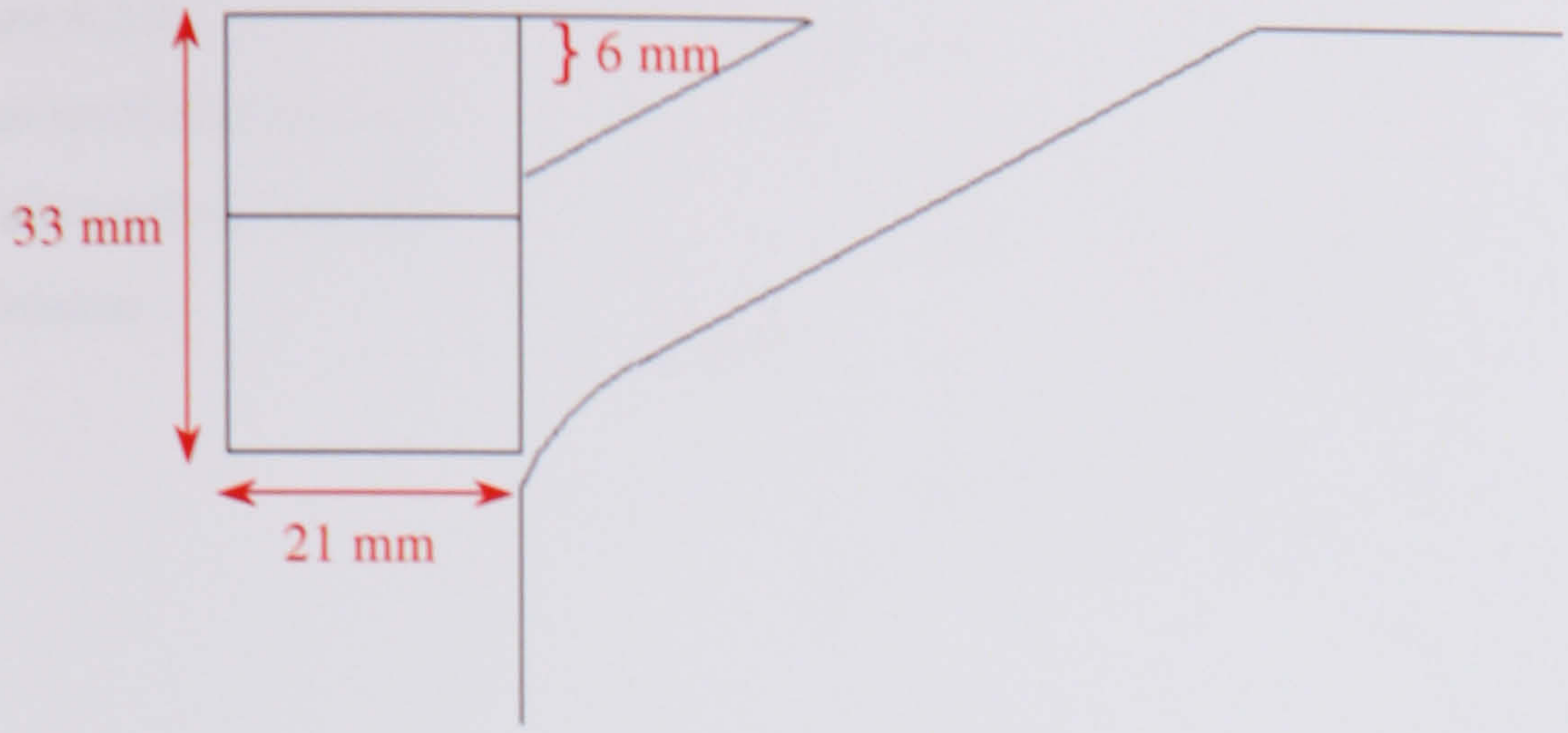

Figure 4.2.7: Cross-sectional view of 30 ° duct, front spoiler II, experiment 4

The second duct consists of a square opening (27 mm high, 25 mm wide) with rounded corners in the front panel followed by a 90° bend with the same sectional area as the front opening. The thickness of the Perspex of the front panel is 6 mm (Figures 4.2.8 and 4.2.9). Pressure tapping inside the duct are situated along the base line (T1 to T6) and right and left at the side wall of the duct (T7 and T8).

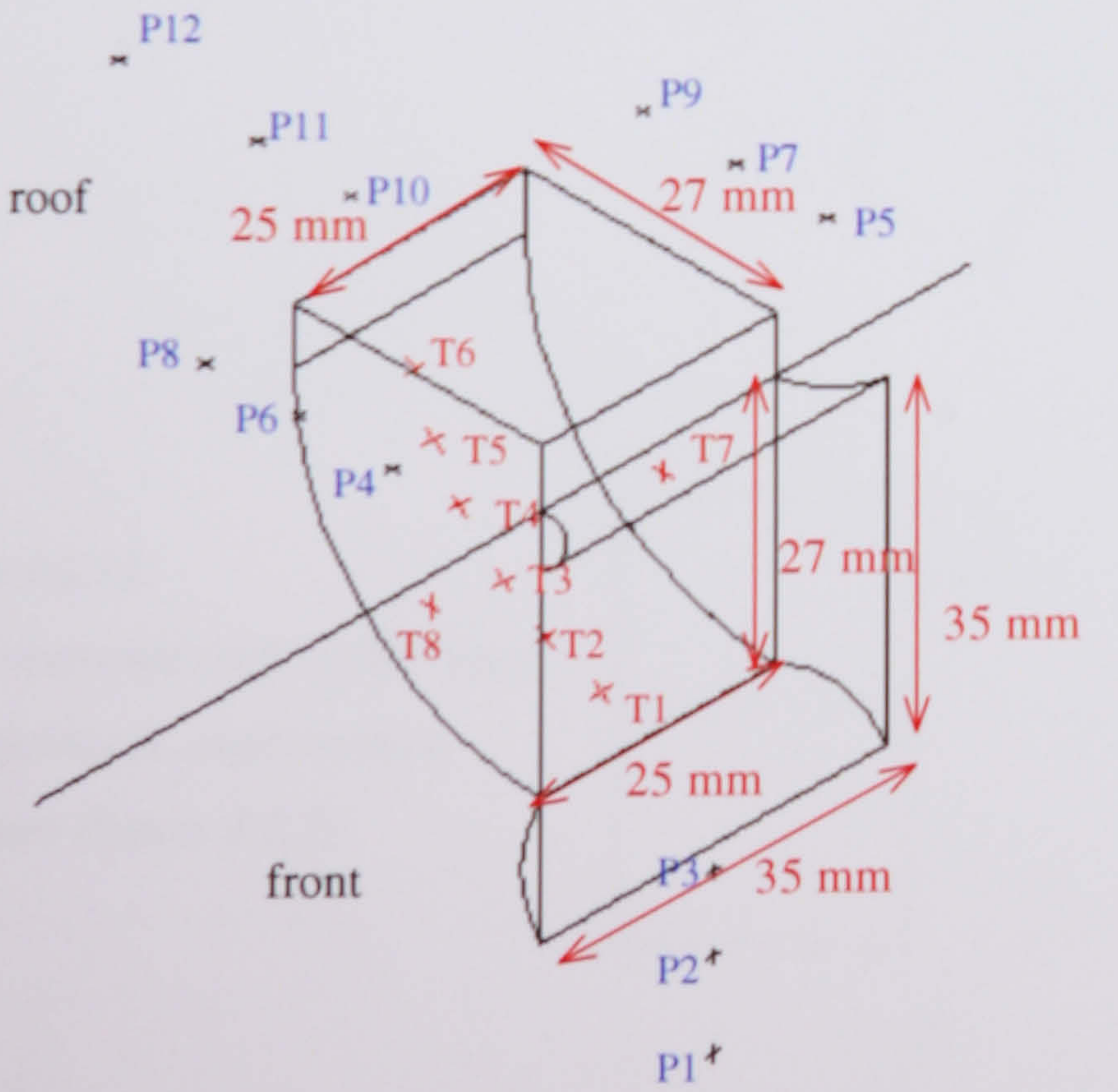

tapping	coordinates [cm]
P1	17.5; 9.5; 0
P2	17.5; 10.3; 0
P3	17.5; 11; 0
P4	15.05; 15.5; 1.1
P5	19.95; 15.5; 1.1
P6	15.05; 15.5; 2.1
P7	19.95; 15.5; 2.1
P8	15.05; 15.5; 3.1
P9	19.95; 15.5; 3.1
P10	17.5; 15.5; 3.9
P11	17.5; 15.5; 4.9
P12	17.5; 15.5; 6.4
T1	17.5; 12.3; 1.1
T2	17.5; 12.55; 1.7
T3	17.5; 12.9; 2.2
T4	17.5; 13.4; 2.7
T5	17.5; 13.8; 3.0
T6	17.5; 14.4; 3.2
T7	18.75; 13.7; 1.8
T8	16.25; 13.7; 1.8

Figure 4.2.8: 3D-view of 90 ° duct without spoiler, experiment 5. Coordinate system like in Figure 4.2.1

Figure 4.2.9:
Cross-sectional view of 90 ° duct without spoiler, experiment 5.

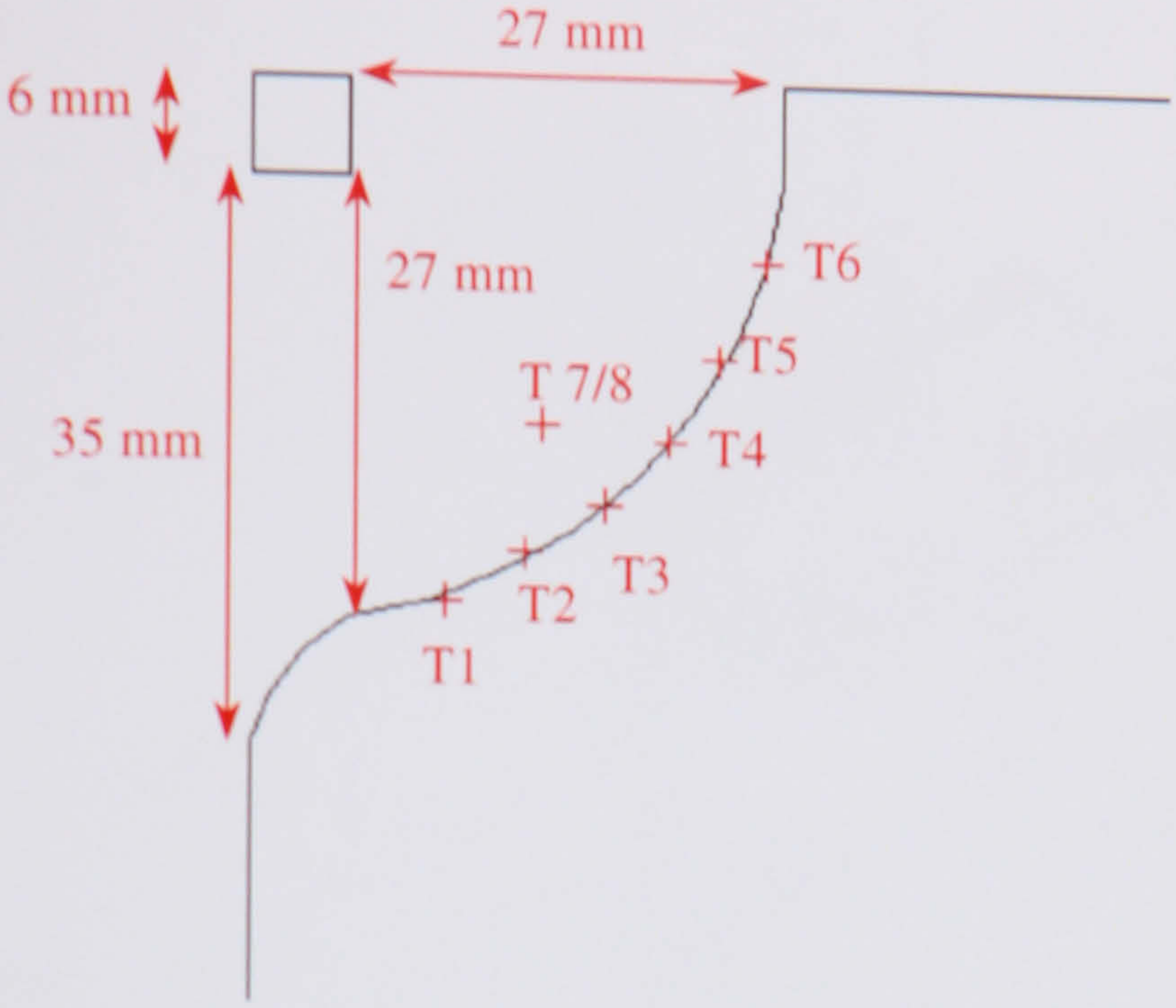

Figure 4.2.10:
3D-view of 90 ° duct, front spoiler II, experiment 6 (compare Figure 4.2.6)

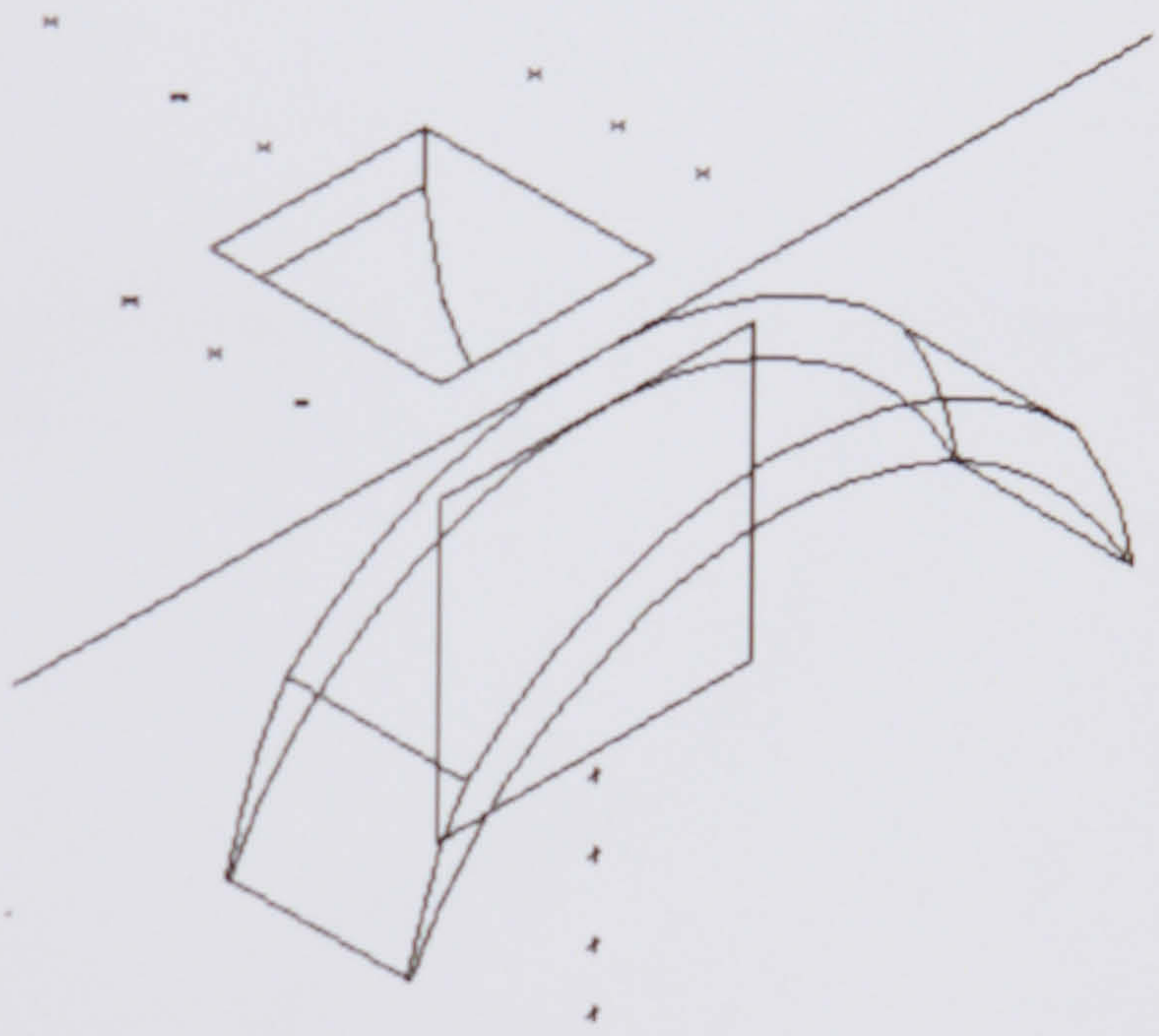

Figure 4.2.11:
Cross-sectional view of 90 ° duct, front spoiler II, experiment 6 (compare Figure 4.2.7)

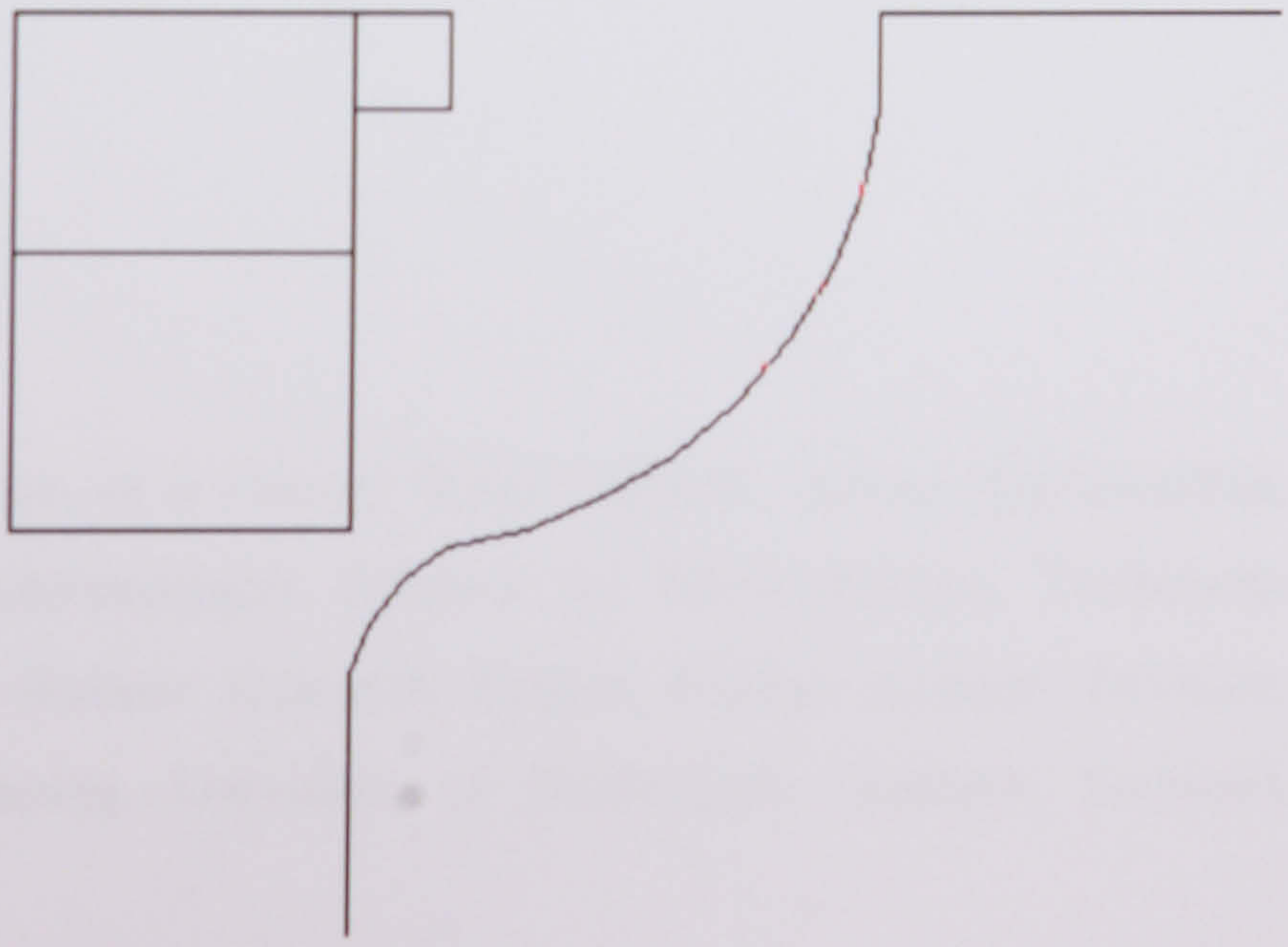

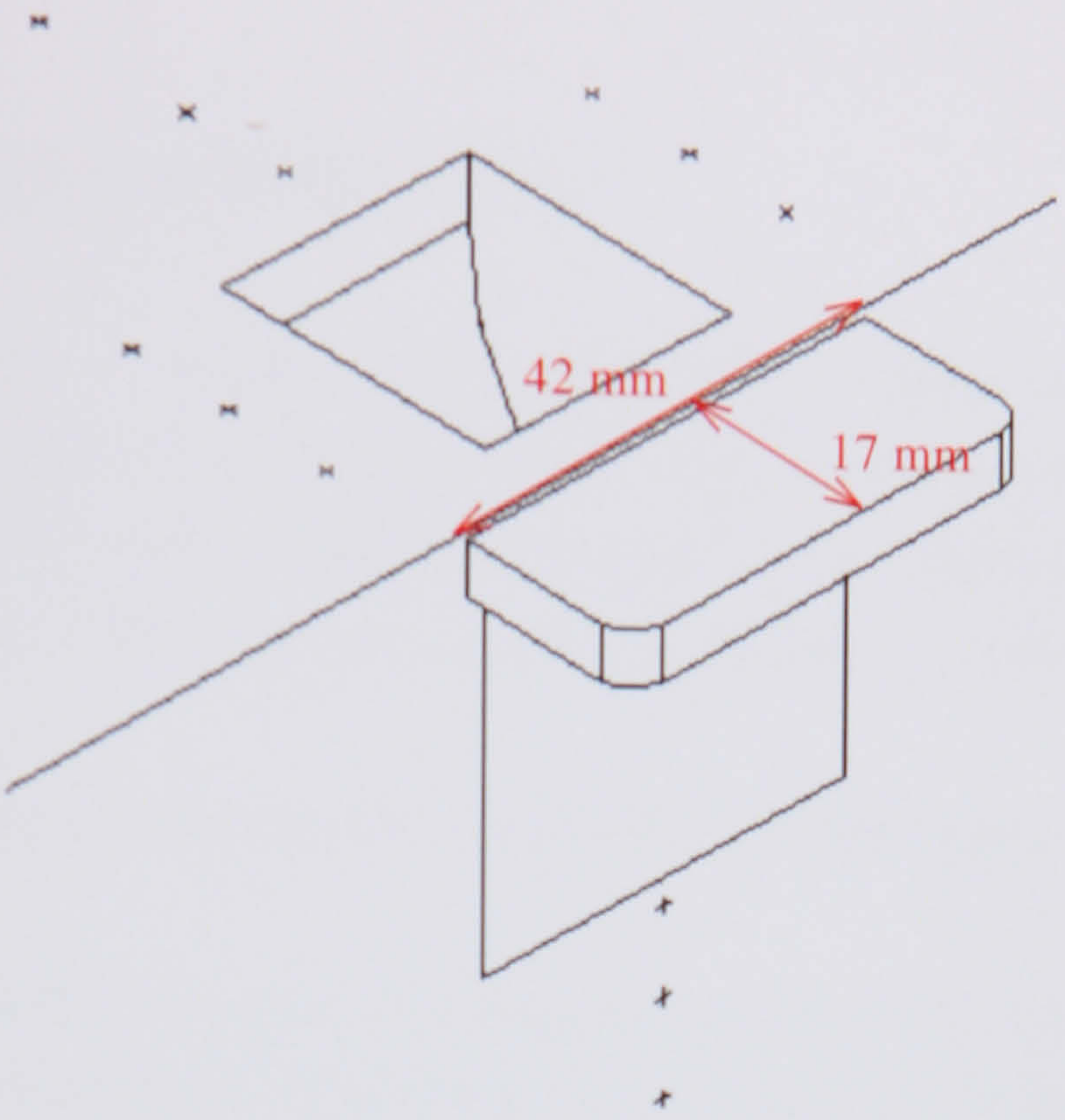

Figure 4.2.12:
3D-view of 90 ° duct, front spoiler III, experiment 7

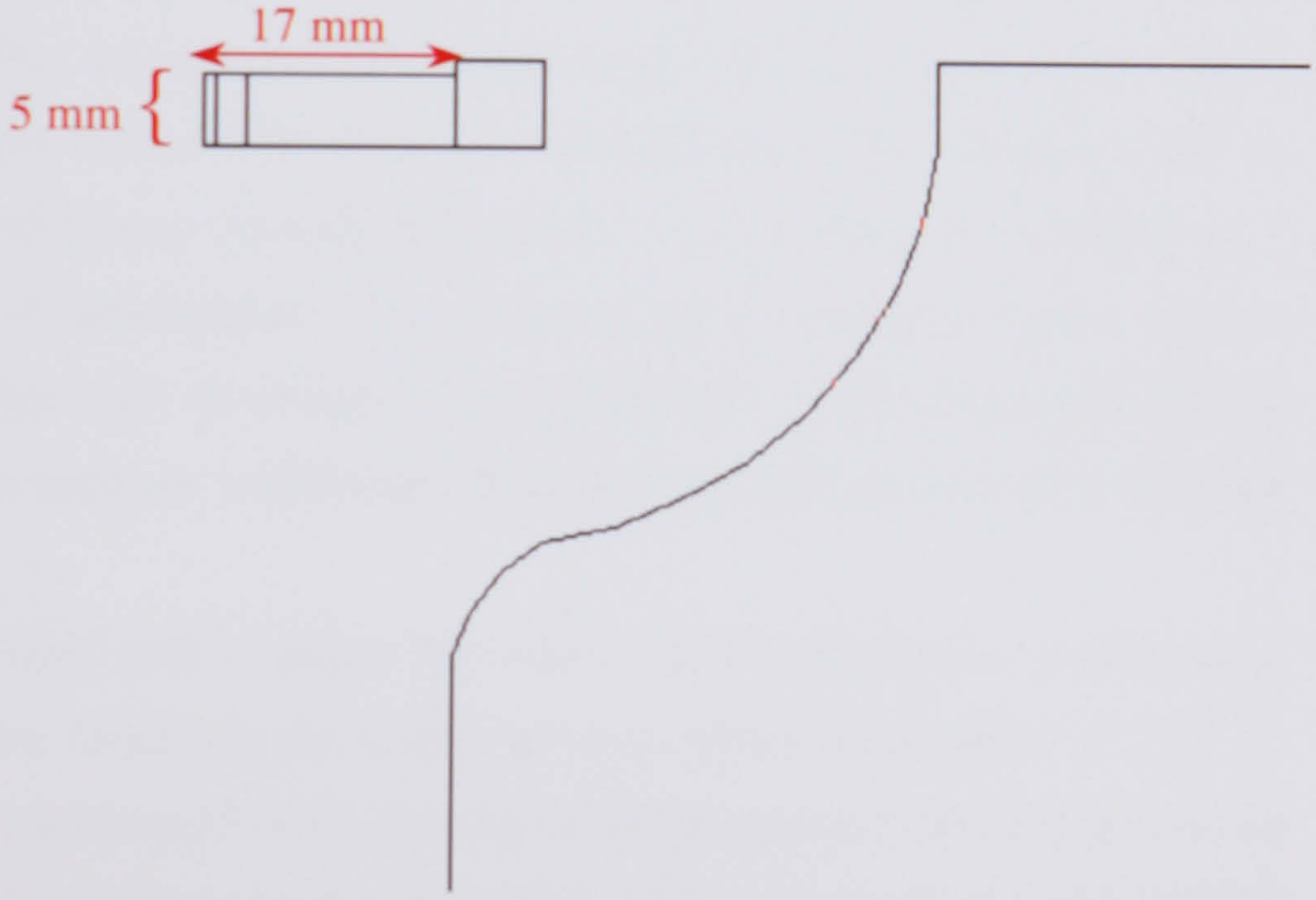

Figure 4.2.13:
Cross-sectional view of 90 ° duct, front spoiler III, experiment 7

Reference

Leyk M.; Aerodynamical Investigation of a Ducted Wind Turbine; externe Studienarbeit, Fachgebiet Energietechnik und Reaktoranlagen, Fakultät für Maschinenbau, Technische Universität Darmstadt, Germany / Student Research Project, Energy Systems Division, Department of Mechanical Engineering, University of Strathclyde, Glasgow, Scotland, October 1997

4.3. Measurements: Instrumentation, Readings, Errors

As already stated, a Pitot-Static tube is mounted in the wind tunnel working section approximately 1 m above the experimental table (see Figure 4.1.2). As it is an open working section, no flow reflections from nearby walls could disturb the measurement, and the tube was aligned with the mean air stream. Differential pressure readings are taken by means of an inclined manometer.

To calculate the density of air, readings are taken from the thermometer and the barometer in the laboratory.

As in previous experimental (Leyk 1997) estimates, a reading error of half a scale unit on thermometer, barometer and inclined manometer could lead to an error less than 1 % for the chosen range of wind speeds.

Pressures obtained from the model's pressure tappings have been measured with an inclined manometer in parallel with a low range (±100 Pa or ±10 mm H_2O) electromanometer (Greer Electromanometer M12). The accuracy of the electromanometer was tested with a digital pneumatic pressure calibrator (Druck DPI 602) and both displays were compared with an inclined manometer. Both electronic displays differed by no more than 0.3 mm H_2O (or 3 Pa) over the whole range of measurement. The values of the inclined manometer were in between. Therefore, a display error of around 0.15 mm H_2O (or 1.5 Pa) may occur. During the experiments, calculated pressure coefficients from the two sources showed a maximal deviation of 0.01.

Local velocities were obtained with a single hot wire constant temperature anemometer (Dantec 56C 17 CTA). After balancing the bridge for an overheat temperature of 150° C, calibration of the probe was performed on the test rig of the laboratory in the free jet issuing from an orifice plate. The pressure across the orifice was measured with an inclined manometer. The data acquisition system was set to a sampling frequency of 1 kHz. Each recorded value was the average of 4096 samples. During calibration, variation of the mean voltage value may be caused by the bias of the probe, which is at most 0.002 V. The calibration chart for the probe was fitted with a fourth order polynomial with the deviation $R^2 = 0.9996$ (see Appendix III). The bias of the probe may cause a maximum error in the higher range of recorded velocities (15 m/s) of 0.15 m/s, which is 1 %. This error is much smaller than errors which may occur through voltage drift during the performance of the experiment. Voltage drift is often caused by inaccurate bridge balance. To avoid such errors, it is important to observe the zero velocity voltage before and after the measurement.

It is difficult to take mean values in regions of high turbulence. Manometers integrate over a low level of turbulence, but for strong turbulence the readings fluctuated, and the reading was taken as average. For very turbulent flow, each recorded value (which is an average of 4096 samples) from the hot wire system differed significantly. Hence, in regions of very turbulent flow, many values were taken in order to calculate the average mean value. During the data analysis, insecure values were either canceled or included with reservation.

The hot wire anemometer indicates the normal component of velocity across the single wire. Hence a horizontal wire is not sensitive to a directional change of the flow in the vertical plane. A horizontal deviation of the flow like a swirl component reduces the normal component. It is difficult to decide whether a low reading is due to a reduced flow velocity or a change in flow direction or both. For measurements in the duct, reference to local pressure readings may help to overcome these difficulties.

References

Leyk M.: Aerodynamical Investigation of a Ducted Wind Turbine; externe Studienarbeit, Fachgebiet Energietechnik und Reaktoranlagen, Fakultät für Maschinenbau, Technische Universität Darmstadt, Germany / Student Research Project, Energy Systems Division, Department of Mechanical Engineering, University of Strathclyde, Glasgow, Scotland, October 1997

Instruction Manual, Greer Electromanometer M12, Mercury Electronics (Scotland) LTD, Pollok Castle Estate, Newton Mearns, Glasgow

Druck DPI 602 Portable Multi-Channel Pressure Indicator/Calibrator, User Manual 1994, Druck Ltd, Fir Tree Lane, Groby, Leicestershire, LE6 0FH

Dantec 56C 17 CTA (Constant Temperature Anemometer) System Manual, DISA Electronik, Denmark; see also:

Perry A.E.; Hot-Wire Anemometry; Oxford Science Publications, Oxford Clarendon 1982

4.4. Flow Conditions in the Working Section

The vertical flow profile at different positions downstream from the nozzle in the centerline of the jet proved to be similar for different wind velocities. Up to approximately 1.0 m height, the velocity profile was fairly uniform, with slightly (< 1 %) higher velocity in the lower part. Above, the velocity drops by up to 5 % (Figure 4.4.1). The profile shown was measured over the turntable in the working section of the wind tunnel (Leyk 1997) and was confirmed by the author. The height of the turntable itself was 0.19 m above the lower edge of the nozzle opening. Therefore, the flow divides at the leading edge, and develops a boundary layer, but it was so thin that it could not be detected with the Pitot-static tube. A possible explanation for the slightly increased speed over the turntable might be the flow acceleration due to the nozzle opening (compare Figure 4.1.2).

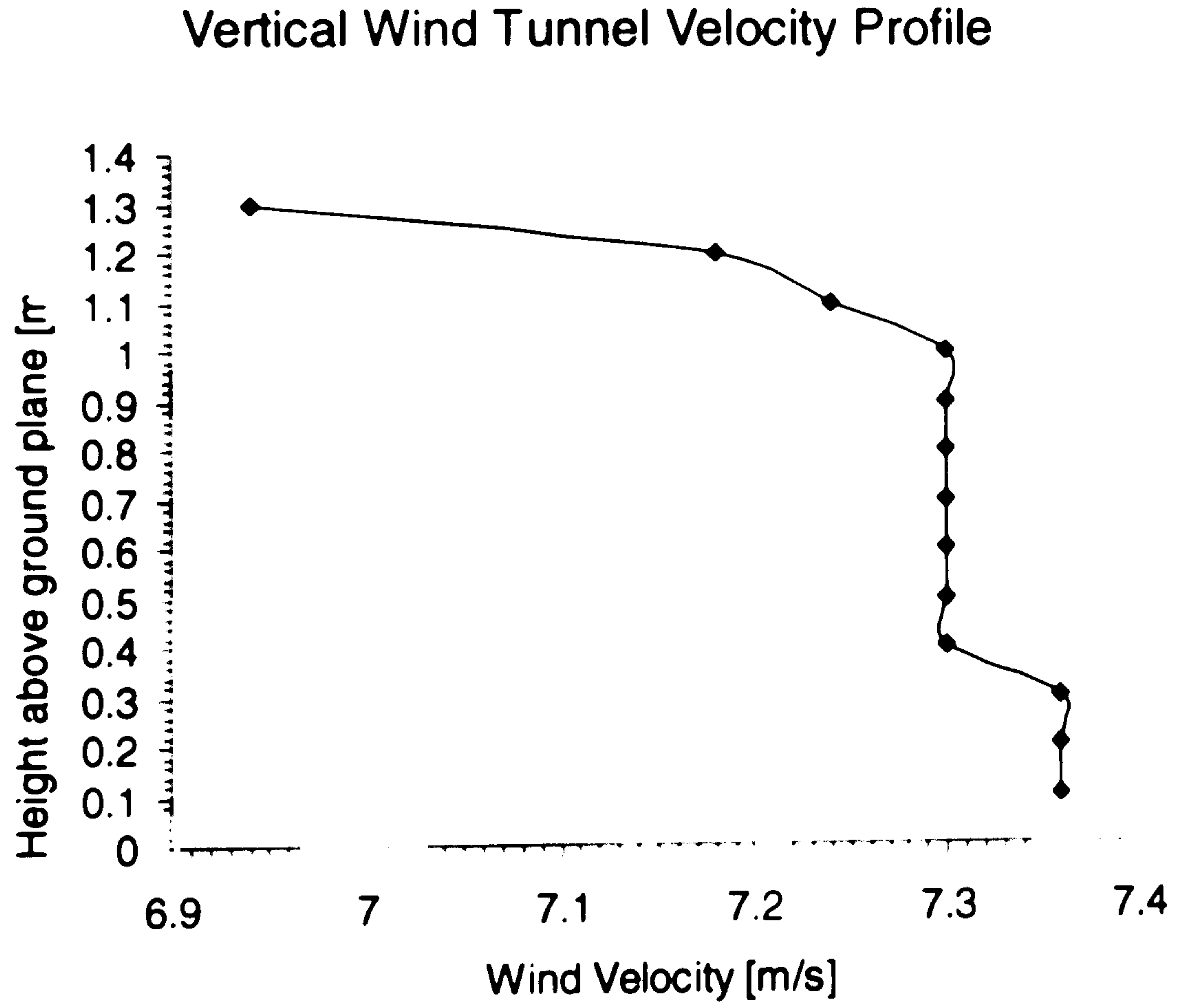

Figure 4.4.1: Vertical velocity profile over ground plane (Leyk 1997)

The transverse velocity profile (Figure 4.2.2) was measured for different wind velocities at approximately 0.25 m height above the ground plane (Docherty 2000). The measurement was conducted with a single hot wire filament along a traverse line in 0.8 m downstream from the nozzle in the designated model position. The investigated width was only about 0.6 m in the center of the 1.5 m wide working section.

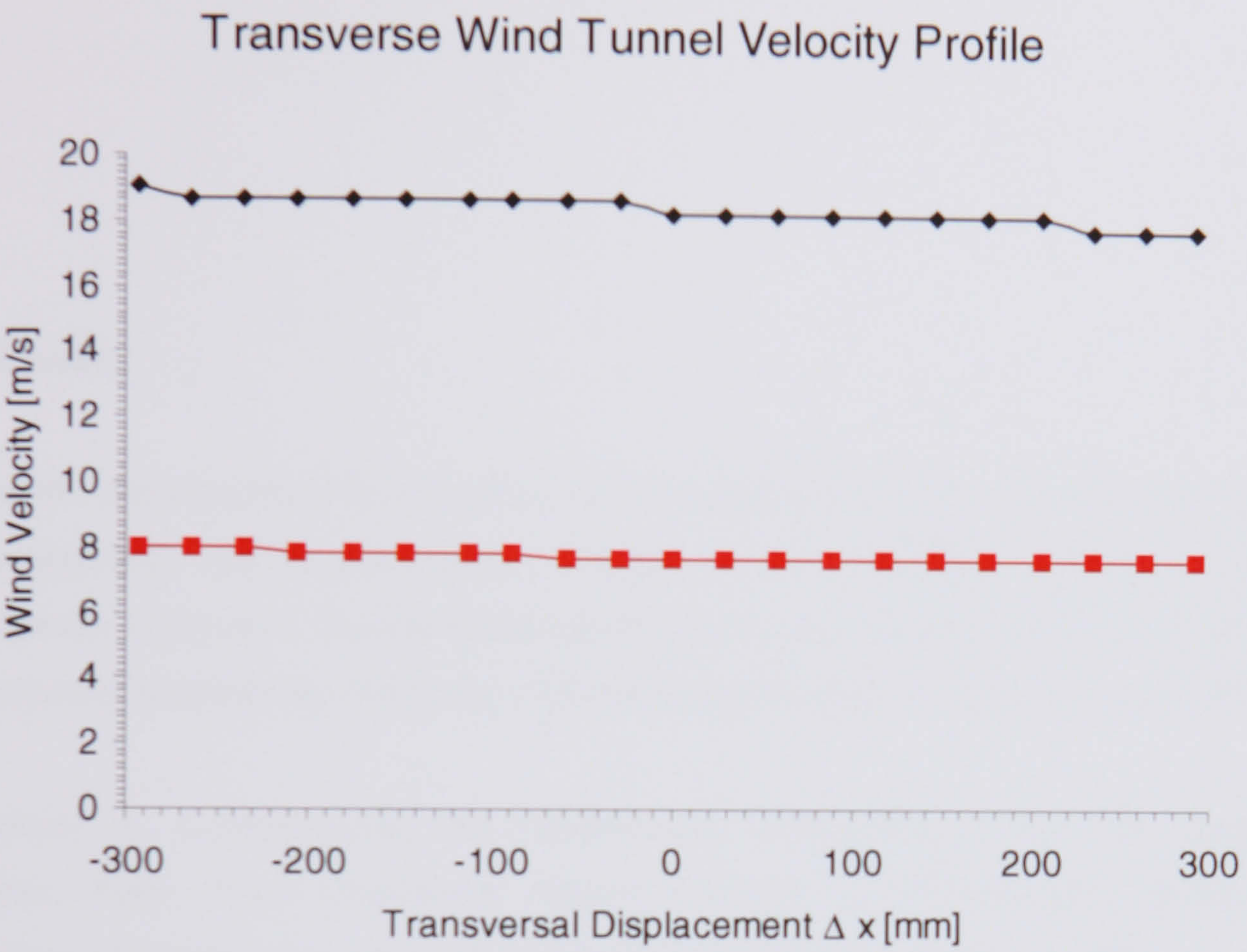

Figure 4.4.2: Transversal velocity profile (Docherty 2000). Δ x is the transversal displacement from the wind tunnel jet axis.

For different wind speeds, the velocity profile was never completely symmetrical. In the upper range of applied wind velocities, the measured velocity values rise towards the inner side of the wind tunnel circuit gradually. To right and left of the symmetry line the velocity values differ by about 2 %. For very low wind speeds, this could be measured only at the far end of the investigated area. Whereas for wind speeds higher then 15 m/s, a distinct change in velocity occurred very close to the symmetry line. As this measurement was conducted with a single hot wire, it is difficult to decide whether this change is due to a change in the magnitude of the wind velocity or rather due to a change in its direction of around 10° to 15°. A combination of both is possible. Interpretation of measured pressures at the surface tappings of a rectangular model (stagnation pressure at the front and suction at the sides) (Docherty 2000) showed that it is more likely to be a directional effect. Latiff interpreted deviations from 'symmetrical' results, measured in the same wind tunnel, as being due to an asymmetric horizontal velocity profile (Latiff 1989).

References

Leyk M.: Aerodynamical Investigation of a Ducted Wind Turbine, Studienarbeit, Fachgebiet Energietechnik und Reaktoranlagen, Fakultät für Maschinenbau, Technische Universität Darmstadt, Germany / Student Research Project, Energy Systems Division, Department of Mechanical Engineering, University of Strathclyde, Glasgow, Scotland, October 1997

Docherty A., Computational and Experimental Calculations of the Flow around Bluff Bodies: Final Years Conference Report, Division of Thermofluids, Department of Mechanical Engineering, University of Strathclyde, Glasgow, Scotland, 2000

Latiff Z.A.; Wind Loads on Structures and the Effect of Shielding; PhD thesis, Division of Thermo-Fluid and Environmental Engineering, Department of Mechanical Engineering, University of Strathclyde, Glasgow, Scotland, 1989

4.5. Blockage Effects

The overall pressure coefficient distribution on the front façade of the model building was found to be in good agreement with accepted values and is insensitive to changes in wind velocity, as might be expected. Also changes in the model height have no significant influence on these values. It is very different for the pressure coefficients on the flat roof. During the first investigations (Leyk 1997), it became obvious that the tall model of 0.6 m height and 0.35 m width generates much smaller suction on the roof when compared with standard values (C_p = -0.5 to -0.6 in ESDU 1993) for the appropriate range of Reynolds number. Also, this tall model disturbed the flow in the region of the Pitot-Static tube, in particular at higher wind speeds (> 15 m/s). This hampered the determination of the freestream wind speed. For closed working sections it is recommended that the ratio of the wind facing model area and the tunnel cross-sectional area should not exceed 5 % (Whitbread 1963; Rae and Pope 1984). For this open working section it was experienced that suction on the roof increased sharply while turning the model through 90°, in which configuration the model is under the 5 % threshold of blockage. It is noticeable that for civil engineering purposes (BRE 1989), the quoted values of suction at the front part of the flat roof are much greater, in the range of C_p = -1.1 or more, without distinguishing between the different depth to width ratios of the buildings. But for flow over smooth surface mounted small scale blocks as reported by ESDU (ESDU 1993), this high value of suction at the upwind part of the roof is seen solely for blocks which are much deeper than wide. Turning the present test model through 90° would fulfil this requirement, however those values of very high suction on the upwind area of the roof could not be confirmed experimentally.

The experimental programme was designed to investigate integrated ducts on the wide side of the building, to minimize three-dimensional edge effects on the duct flow. Therefore it was necessary to turn the wide side to the wind. Hence the model had to be recessed into the experimental table, to reduce its height to 155 mm. The blockage ratio was then around 3.0 %, and the suction above the model roof then showed a sound correspondence with the standard values for small scale cuboids (ESDU 1993).

References

Leyk M.: Aerodynamical Investigation of a Ducted Wind Turbine, Studienarbeit, Fachgebiet Energietechnik und Reaktoranlagen, Fakultät für Maschinenbau, Technische Universität Darmstadt, Germany / Student Research Project, Energy Systems Division, Department of Mechanical Engineering, University of Strathclyde, Glasgow, Scotland, October 1997

Engineering Science Data Unit ESDU, Wind Engineering – Mean Loads on Structures, Volume 2b – Fluid Forces, Pressures and Moments on Rectangular Blocks, Item No 71016, 1993; ESDU International, London.

Whitbread R.E.: Model Simulation of Wind Effects on Structures; Proc. of the 16th Symposium on 'Wind Effects on Buildings and Structures', National Physical Laboratory, Teddington, Middlesex, England, 26th -28th June 1963, Vol. I

Rae W.H. and Pope A.: Low Speed Wind Tunnel Testing; John Wiley & Sons, New York, 1984

BRE Digest 346: The Assessment of Wind Loads, Part 6: Loading Coefficients for typical Buildings, November 1989; British Department of the Environment, Building Research Establishment, Garston, Watford WD27JR.

4.6. Experiments Performed

Initially measurements were performed at two different wind speeds (around 7 m/s and 16 m/s). Data analysis of non-dimensional values showed no significant variation between sets of data obtained at these different wind speeds. It was seen to be advantageous to operate in the fairly linear part of the hot wire calibration chart, corresponding to higher wind speed. Rotation of the model relative to the wind was in 5° steps (Figure 4.6.1).

Experiment No.	Configuration	Angles of incidence
I	plain box, without duct, without spoiler	$+45^\circ \geq \alpha \geq -45^\circ$
II	30° duct, without spoiler	$+45^\circ \geq \alpha \geq 0^\circ$
III	30° duct, spoiler I	$+45^\circ \geq \alpha \geq 0^\circ$
IV	30° duct, spoiler II	$+60^\circ \geq \alpha \geq 0^\circ$
V	90° duct, without spoiler	$+65^\circ \geq \alpha \geq 0^\circ$
VI	90° duct, spoiler II	$+75^\circ \geq \alpha \geq 0^\circ$
VII	90° duct, spoiler III	$+75^\circ \geq \alpha \geq 0^\circ$

In order to gain insight into the flow conditions in the duct, the velocity inside the duct along the centerline of the model was measured with the hot wire probe (see Figures 4.6.2 and 4.6.3) and pressures were recorded at tappings on the duct wall (see Figures 4.2.3 and 4.2.9). Therefore the probe was inserted 2 mm deep into the duct outlet on the flat roof, and the profile was scanned in steps of 5 mm (Figure 4.6.2). For the 90 duct, the probe could be inserted from above into the duct in order to measure the inlet profile, again in 5 mm vertical steps. Here, the outlet profile was scanned in 4 mm steps (Figure 4.6.3).

The single wire was always aligned perpendicular to the centerline of the model. Therefore it indicated the component of velocity which is projected in the vertical plane of symmetry of the model. If internal flow is aligned with the duct, the reading could be used to give a mass flow across the duct area. If the flow swirls, the measurement on the plane of symmetry neglects the lateral component. An accurate measurement of each component is only possible with a multi hot wire system. But the single hot wire system with its 3 mm tip and a filament of approximately 1mm length is well suited to the small model duct. The main task was in any case to demonstrate that the duct would induce high internal wind speeds due to its location and geometry.

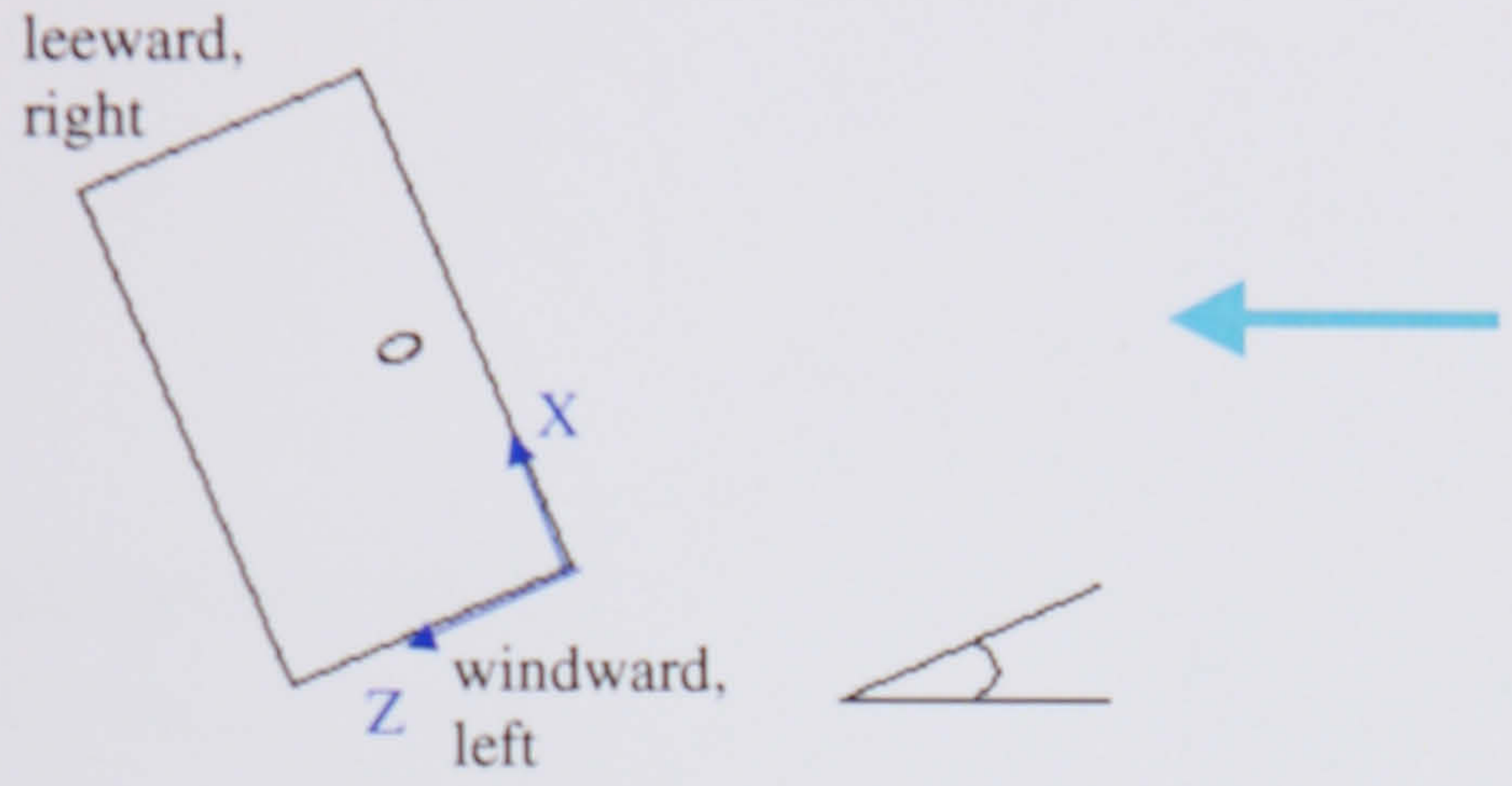

Figure 4.6.1: Convention of angles (anticlockwise, positive) and sides, schematic drawing; wind tunnel model, view from the top

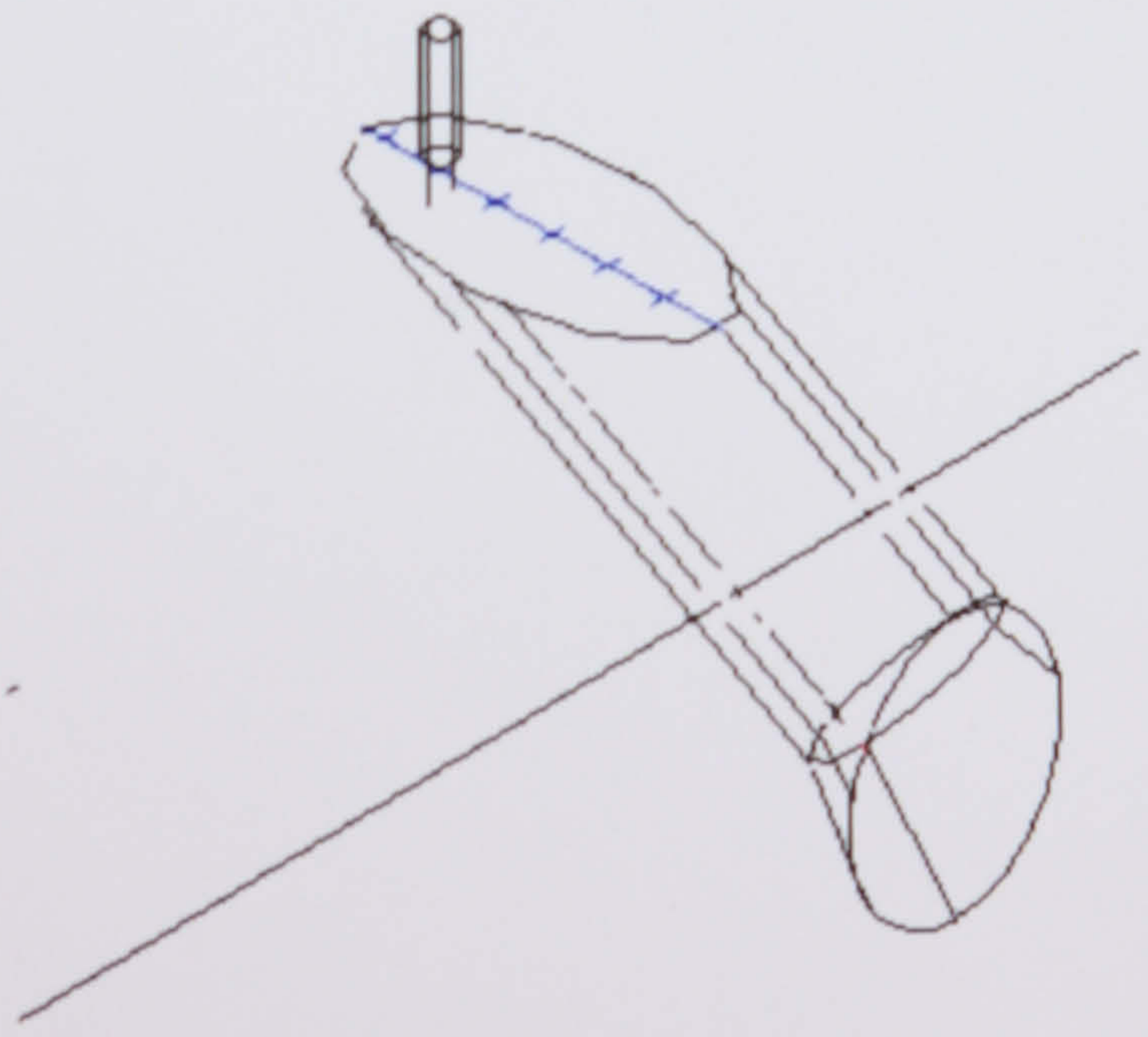

Figure 4.6.2: 30° duct: Hot wire scans in the outlet in 5 mm steps, 2 mm deep inserted

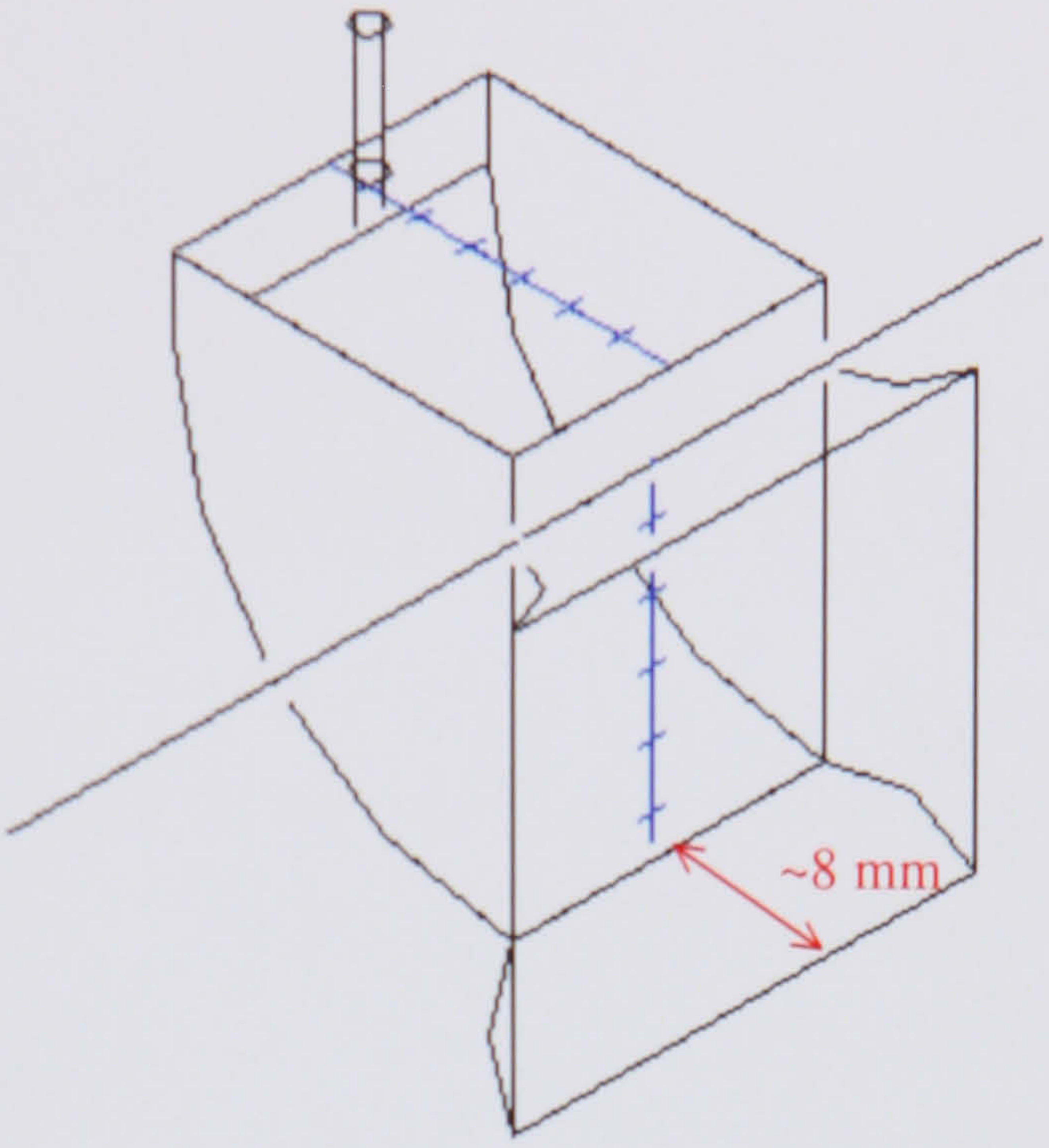

Figure 4.6.3: 90° duct: Hot wire scans in outlet in 4 mm steps, 2 mm deep inserted. Vertical scan in inlet (around 8 mm deep) in 5 mm steps.

4.7. Simple Rectangular Block

4.7.1. Pressure Distribution for the Simple Block

To determine the areas of high pressure and suction, the model was first tested without a duct and the pressure values were recorded along the centerline of the front façade and the roof for different angles of oncoming wind.

At the front façade, as the wind is brought to the rest by the obstruction, the kinetic wind energy is converted into static pressure. A pressure gradient occurs at the front façade, with low pressures near the ground, which leads to a downward flow. The steep decline of the pressure on the lower part of the building must be due to a boundary layer created at the table surface (Figure 4.7.1.1). The influence of the boundary layer diminishes with larger angles.

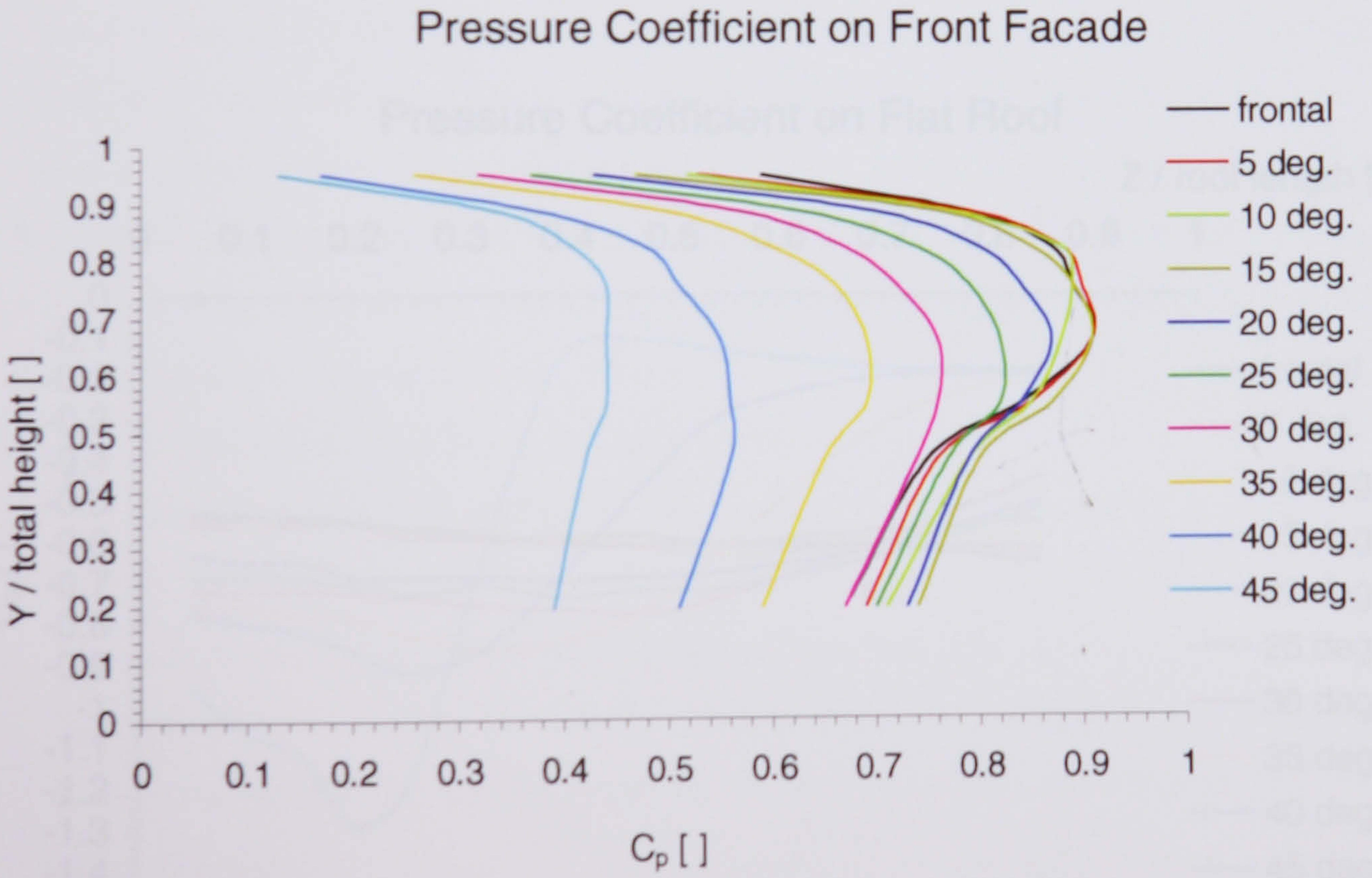

Figure 4.7.1.1: Pressure distribution along the centerline at the front façade for various angles of incidence. Positive angles are anti-clockwise (see Figure 4.6.1)

The highest positive pressure is at approximately 70 % of the model height, with air above that point flowing upwards and that below flowing downwards. This stagnation point is lower than those reported for real buildings (see Chapter 2.2), but the high pressure zone extends to over 80 % building height. Hence the pressure field differs only slightly from those experienced on real buildings. At model scale, the stagnation point varies with the modelled boundary layer, but stagnation points between 70 % and 90 % building height are reported (see Chapter 2.3). The pressure coefficient does never reach the value 1.0 . A possible explanation might be that some kinetic energy dissipates due to turbulence. The ESDU standard (see Figure 4.7.2.1) for stagnation is also lower than $C_p=1.0$. Another explanation might be that the flow at the front wall has a vertical component, as the flow travels over the region of the roll-up vortex at the base of the building and moves over the leading roof edge (see Figure 6.3.1.1). Only the component of momentum normal to the wall generates the stagnation pressure.

It is obvious in Figure 4.7.1.1, that the frontal incidence does not create the highest pressure on the front facade. This is very likely due to the transverse freestream profile in the wind tunnel (see Chapter 4.4) and will be considered later.

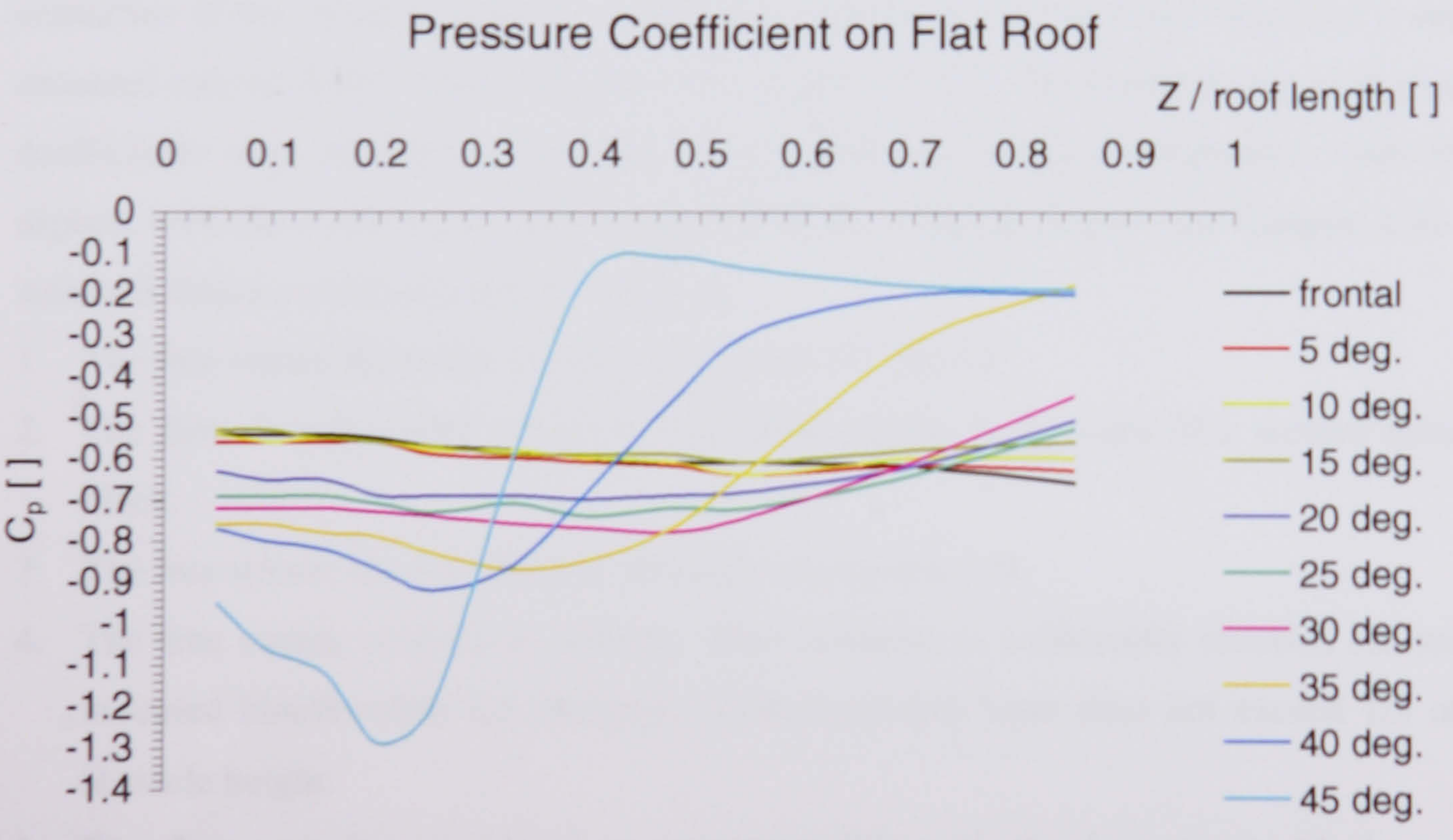

Figure 4.7.1.2: Pressure distribution along the centerline at the flat roof for various angles of incidence. Positive angles are anti-clockwise (see Figure 4.6.1)

At the sharp edge between front façade and flat roof, suction occurs through flow separation. At this sharp edge, fast recirculating flow could be visualised in the wind tunnel using woollen thread. The uniform suction over the whole roof indicates that the whole roof is in the zone of separated flow. Larger angles of incidence cause higher suction at the upwind edge, and finally the separating shear layer rolls up into the helix of horseshoe vortex streets along both eaves, as reported by Kind (Kind 1986). The pressure differential between the upper part of the front façade and the roof edge is thus maintained for angles of incidence of 45° or more (see Figure 4.7.1.2). Over the downwind part of the roof, the inner wake smoothes out and creates a much lower suction ($C_P = -0.2$) which is reported downwind of long roofs, either in real scale (see Chapter 2.5) or in model scale (ESDU 1993). This drop in suction indicates reattachment of the separated flow at the rear part of the roof.

4.7.2. Comparison with Standard Values

In order to check the reliability of the measured values, the pressure coefficients along the centerline of the rectangular block model were compared with standard values for a surface mounted cuboid (ESDU 1993) (Figures 4.7.2.1 and 4.7.2.2). The standard values of pressure coefficients were obtained at standard datum conditions, which correspond in most of the aspects with the wind tunnel flow conditions in the working section (see Chapter 4.4). The standard datum conditions (ESDU 1993) are

1. The free stream Reynolds number is between 10^4 and 10^6.
2. The flow is unbounded except by the surface-plane in the case of a surface mounted block.
3. The free stream has a turbulence intensity of less then 1 %.
4. The free stream velocity is uniform. This condition is sufficiently satisfied for surface mounted blocks when the thickness of the boundary layer does not exceed 1/5 of the obstacle height.
5. The flow may be considered as incompressible with the free stream Mach number smaller than 0.2.

It is very likely, that the thickness of the boundary layer over the wind tunnel turntable exceeded 1/5 of the obstacle height. This can be seen over the lower part of the front facade, where the boundary layer over the turntable in the wind tunnel (see Figure 4.1.2) causes a drop in pressure (Figure 4.7.2.1).

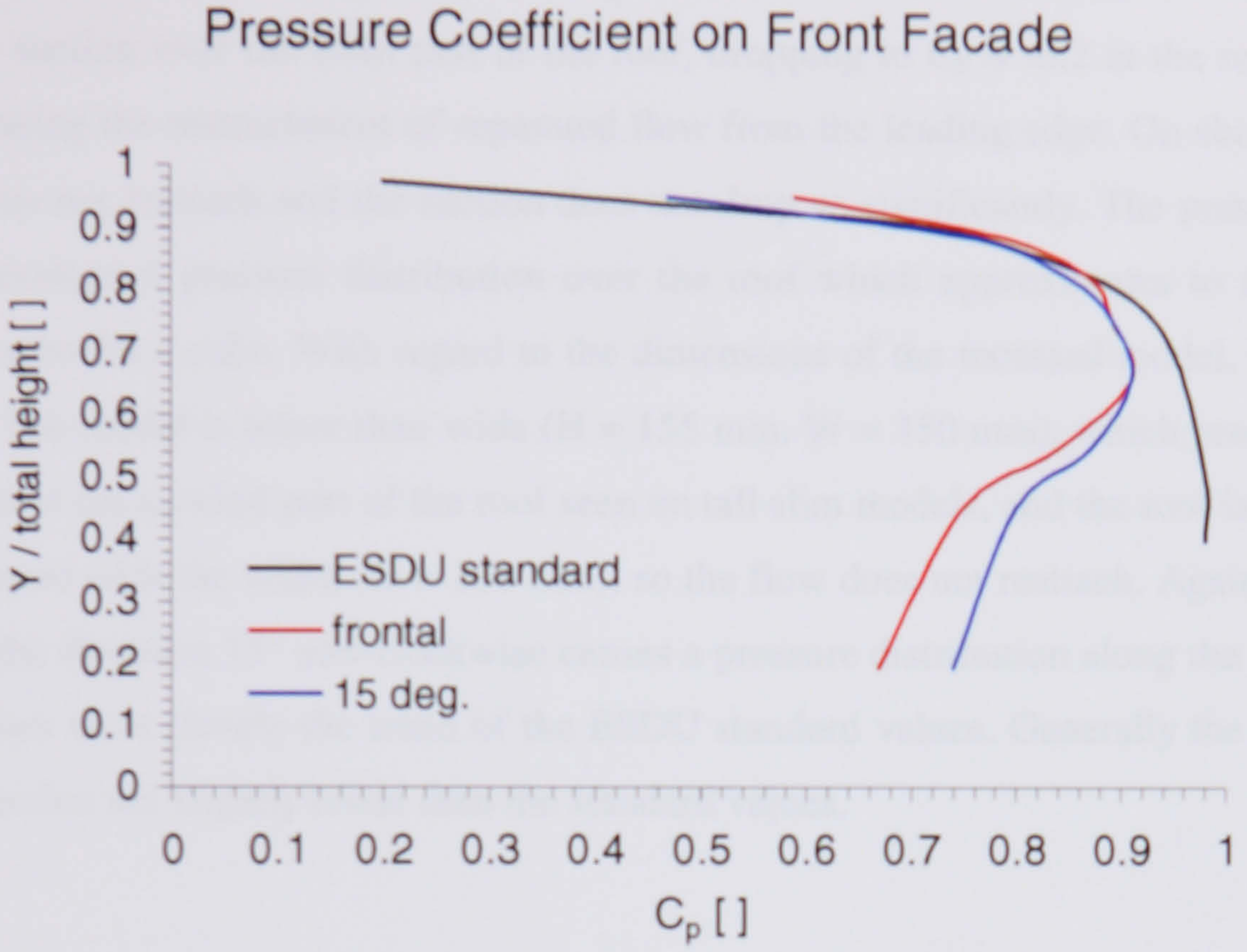

Figure 4.7.2.1: Comparison of experimental values with standard values of the pressure coefficient distribution at the front façade of a cuboid

In comparison, the ESDU data were recorded for a flow with a thin boundary layer causing a higher stagnation pressure in particular over the lower half of the obstacle. Also, the experimental pressure coefficient at the stagnation point is lower then one. This indicates that the 155 mm high model was at least partly immersed in a shear layer. The pressure distributions correspond only in the upper region, where the turbine duct is intended to be placed. It is encouraging, that the pressure distribution in this region seems to be rather independent of the nature of the incoming flow.

The highest stagnation pressure occurs when the model is turned around 15° anti-clockwise from the geometrical centerline of the working section of the wind tunnel. This finding corresponds with the measured freestream velocity profile and points to a deviation of the flow from the geometrical centerline in the working section of the wind tunnel. As later measurements confirm these findings, the direction 15° anti-clockwise is seen to approximate to the 'normal' direction.

According to ESDU, on the front façade the pressure distribution along the centerline for a wide rectangular obstacle with the model's aspect ratio does not differ from that for a cube, differences arising only right and left of the centerline. However, pressure coefficients along the centerline of the flat roof depend on the aspect ratio of the obstacle. Slim and tall cuboids create high suction over the front part of the roof, dropping to $C_P = -0.2$ at the rear of long roofs, indicating the reattachment of separated flow from the leading edge. On shorter roofs, the flow does not reattach and the suction does not drop so significantly. The present model however develops a pressure distribution over the roof which approximates to the ESDU standard results for a cube. With regard to the dimensions of the recessed model, this is not surprising. The model is lower then wide (H = 155 mm, W = 350 mm), which precludes the high suction at the upwind part of the roof seen on tall slim models, and the roof is relatively short compared with the width (D = 200 mm), so the flow does not reattach. Again it can be stated that the direction 15° anti-clockwise causes a pressure distribution along the centerline which follows most closely the trend of the ESDU standard values. Generally the measured values of suction are slightly lower then the standard values.

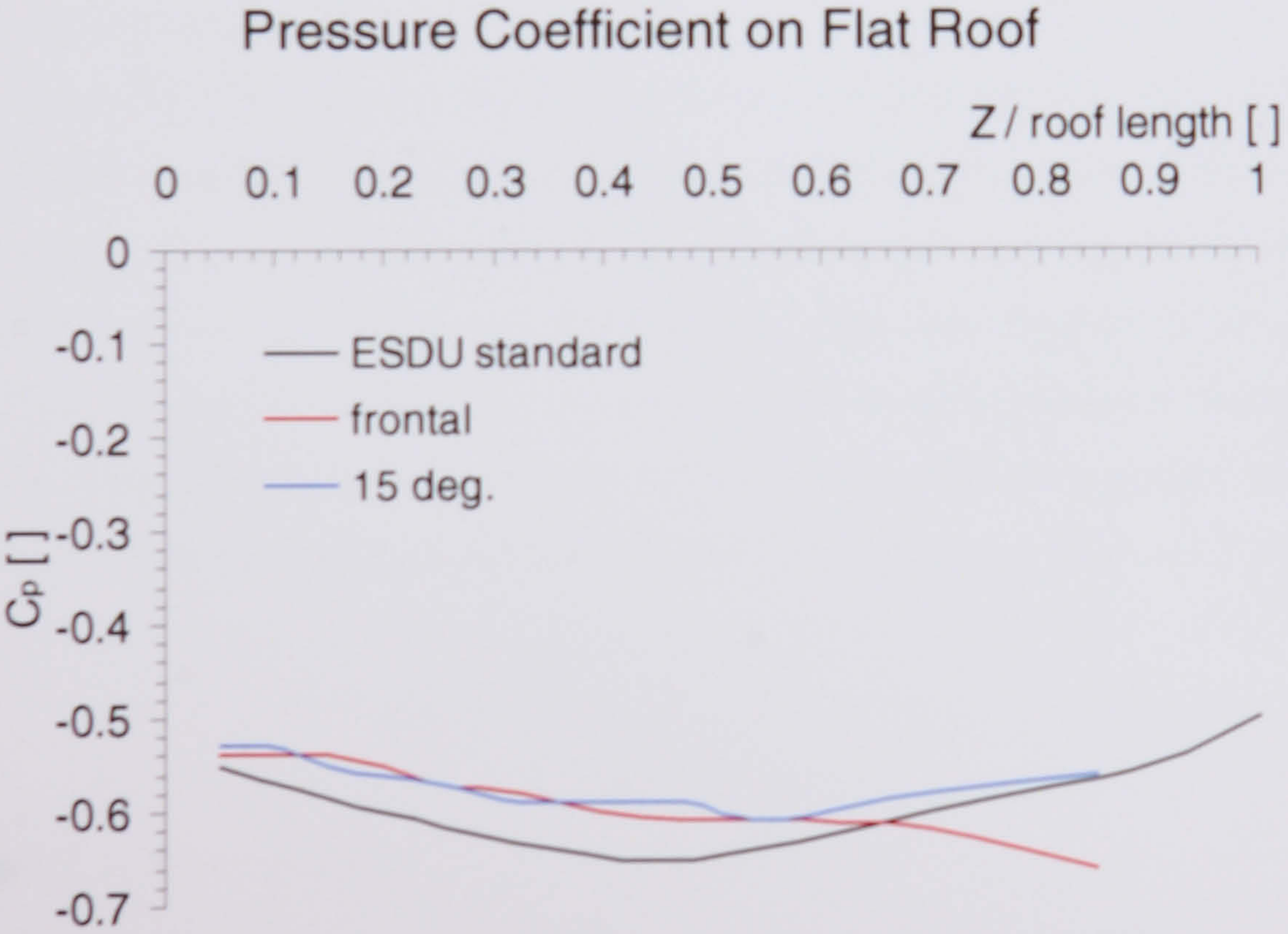

Figure 4.7.2.2: Comparison of experimental values with standard values of the pressure coefficient distribution on the front façade of a cube

As the standard values are not for exactly the same aspect ratio as the model, this comparison should not be overstressed. Apart from this, the uniform flow condition as described in the

ESDU data sheet is lacking the boundary layer present in the experiment. But the comparison shows that the generated pressures at the model faces correspond well with standard values for small scale models in the same range of Reynolds number. It is worth noting that the high values of suction reported for real scale buildings at the front edge of the roof (see Chapter 2), are not found at small scale models with windflow normal to the façade.

In the following chapter, the deviation of the mean wind velocity in the working section of the tunnel is taken into account when comparing the results for different angles of incidence.

References

Kind R.J.; Worst Suctions near Edges of Flat Rooftops on Low-Rise Buildings; Journal of Wind Engineering and Industrial Aerodynamics, Vol. 25, 1986, pp.31-47

Engineering Science Data Unit ESDU, Wind Engineering - Mean Loads on Structures, Volume 2b - Fluid Forces, Pressures and Moments on Rectangular Blocks, Item No 71016, 1993; ESDU International, London.

4.8. The 30° Duct Configurations

At the upper part of the front façade, the wind accelerates to reach its maximum speed in the region of the wall-roof edge. The straight 30 duct connects the high pressure area at the front façade with the suction area above the flat roof, as the center of the inlet is located slightly above the stagnation zone at 85 % building height. It was hoped that this pressure differential would induce high velocities in the duct flow. Geometrical changes at the duct inlet were tested in an attempt to improve the performance in terms of induced high velocities and to increase the range of tolerated angles of incidence.

With regard to the freestream velocity profile in the wind tunnel (see Chapter 4.4) and the conclusions drawn from pressure measurements on the block surface in the previous section, one should bear in mind that the direction 15° anti-clockwise from the geometrical centerline of the working section is seen to approximate to the wind direction 'normal' to the front façade. However, for the sake of clarity, the angle will always be measured with reference to the geometrical centerline.

As the hot wire probe is highly sensitive to damage when touching the walls of the duct, a clearance from the wall had to be maintained. Hence data could be acquired over about 75 % of the duct diameter along the main axis of the elliptical outlet opening. At the rear part of the opening, it was not possible to insert the probe 2 mm deep because of the duct's flat angle of 30° to the horizontal. Therefore it was impossible to resolve the near wall flow.

The hot wire probe will measure the velocity perpendicular to the wire, in this case probably in direction parallel to the duct axis, at least to a good approximation (Figure 4.6.2).

4.8.1. 30° Duct without Spoiler

With no modifications to the duct, the flow velocity in the middle of the duct was, for incident wind 15° normal to the façade, up to 20 % higher than the free stream velocity. The velocity distribution is fairly symmetrical as would be expected for a straight duct. The maximum increase in speed is achieved with a wind approaching under 35° normal to the façade (Figure 4.8.1.1). At this angle, the pressure distribution indicates the establishment of an edge vortex along the roof corner (see Figure 4.7.1.2.). Further rotation had no positive impact on the induced wind speed, in spite the increased pressure difference between the zones where inlet and outlet are located. The velocity distribution of the flow field becomes very unsymmetrical. In particular in the upwind part of the duct, the speed diminishes.

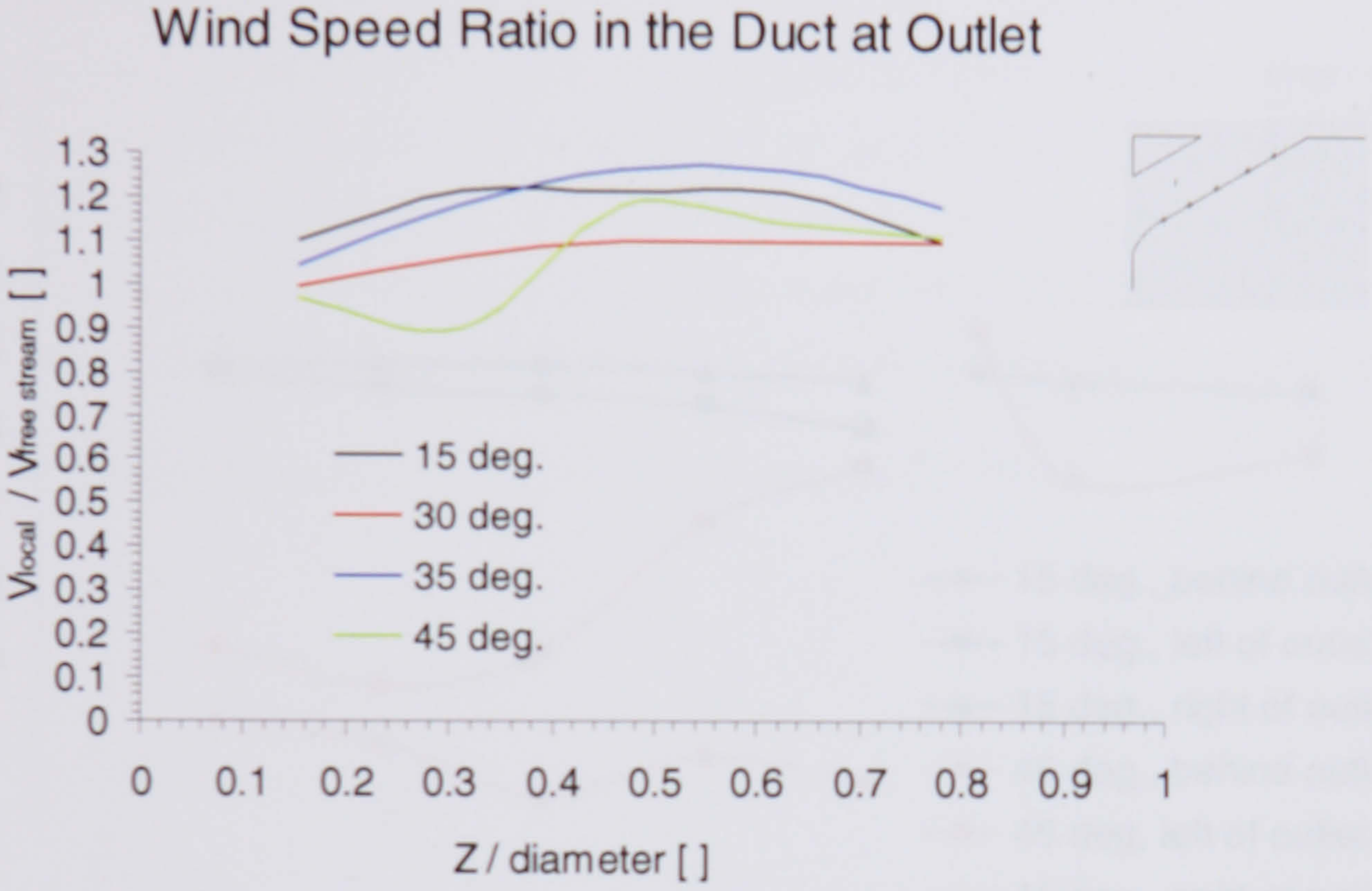

Figure 4.8.1.1:Experiment 2, 30° duct without spoiler

As the jet leaving the duct enters the flow separation zone over the front part of the roof, the pressure distribution to the left and right of the outlet (pressure tappings P11 to P20 in Figure 4.2.2) indicates changes to the local flow pattern. A wind direction normal to the façade does not cause any significant loss of suction in the neighborhood of the duct outlet, and the distribution of pressure all around the outlet seems to remain uniform. But for wind approaching at 45° normal to the front façade, the suction on the downwind side of the duct exit (pressure tappings P11, P13, P15, P17, P19 in Figure 4.2.2) is higher than at the leading edge (pressure tappings P12, P14, P16, P18, P20 in Figure 4.2.2) and is also larger than the suction for the model without a duct (compare Figures 4.8.1.2 and 4.7.1.2). For wind at an angle of incidence, the jet entrainment has also some impact on the pressure distribution further downstream the outlet which may indicate a change in the separated flow region.

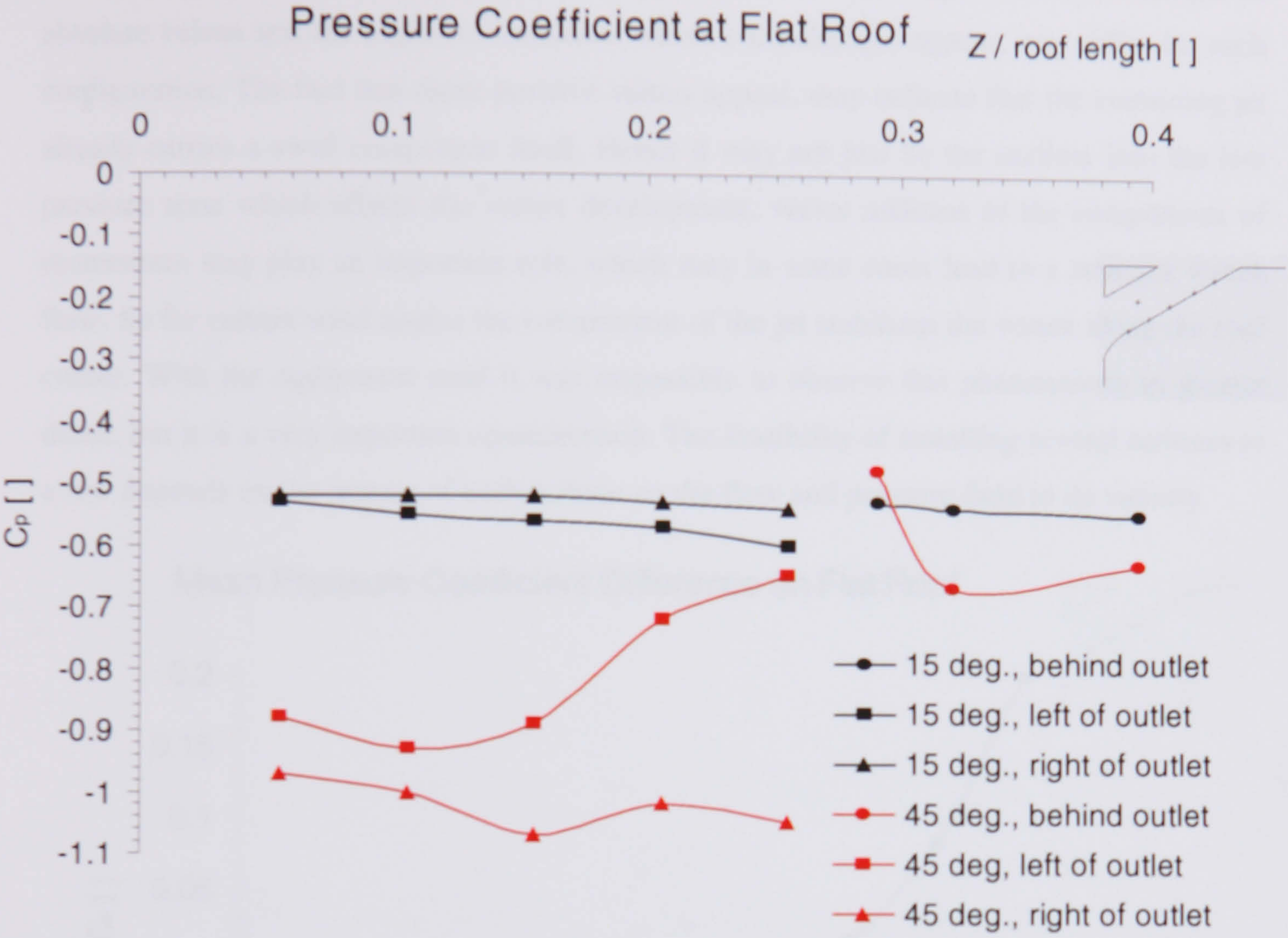

Figure 4.8.1.2: Experiment 2, 30° duct without spoiler. Pressure distribution around the outlet for various angles of incidence.

The average difference between the pressure coefficients right and left of the outlet opening (Figure 4.8.1.3) may indicate the impact of the jet entrainment. This value is calculated as the difference between the plane areas under the C_P distributions (windward left side – leeward right side), divided by the baseline. The highest reading of wind speed in the duct is achieved at the angle (35°) (see Figure 4.8.1.1) which it will be seen generates the lowest absolute difference in average pressure coefficients to right and left of the duct outlet (Figure 4.8.1.3).

High negative values indicate the breakdown of the vortex along the roof edge. The entrained jet expands into the low pressure area and reduces the suction when carried downstream, which disturbs the stable vortex. Positive values indicate that the entrainment of the jet into the flow separation zone causes even a higher value of suction when carried downstream in the vortex along the roof edge. In general the change from negative to positive values is consistent throughout all experiments, but the magnitude of the change, its absolute values and the angles of incidence where such changes appear, may differ for each configuration. The fact that those positive values appear, may indicate that the entraining jet already carries a swirl component itself. Hence it may not just be the outflow into the low pressure zone which affects the vortex development, vector addition of the components of momentum may play an important role, which may in some cases lead to a stronger vortex flow. So for certain wind angles the entrainment of the jet stabilizes the vortex along the roof corner. With the equipment used it was impossible to observe this phenomenon in greater detail, but it is a very important consideration. The feasibility of installing several turbines in a row depends on the impact of each turbine on the flow and pressure field in its vicinity.

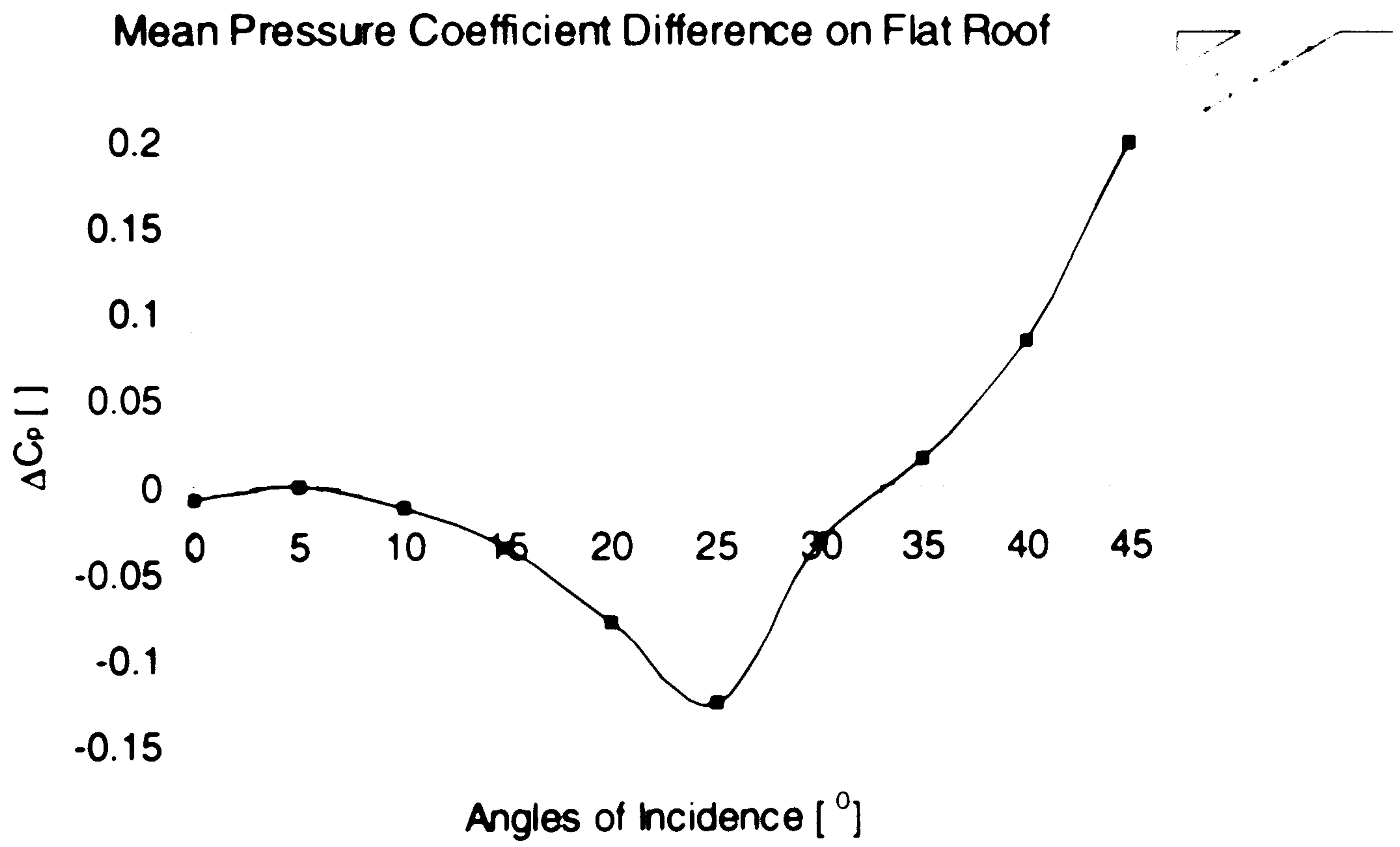

Figure 4.8.1.3: Experiment 2. 30° duct without spoiler. Differential pressure between windward and leeward tappings near the duct outlet (see Figure 4.2.2) at various angles of incidence.

On the front façade, the situation is much more simple (Figure 4.8.1.4). With larger angles of incidence, the pressure decreases. Next to the duct inlet, the pressure on the trailing (leeward) side is always higher than on the leading (windward) side. For a group of ducts mounted in a row, there seems unlikely to be any adverse interaction between adjacent duct entrances, for all wind approach angles. But it may well be that the front wall will suffer a general drop in pressure when there are several ducts installed.

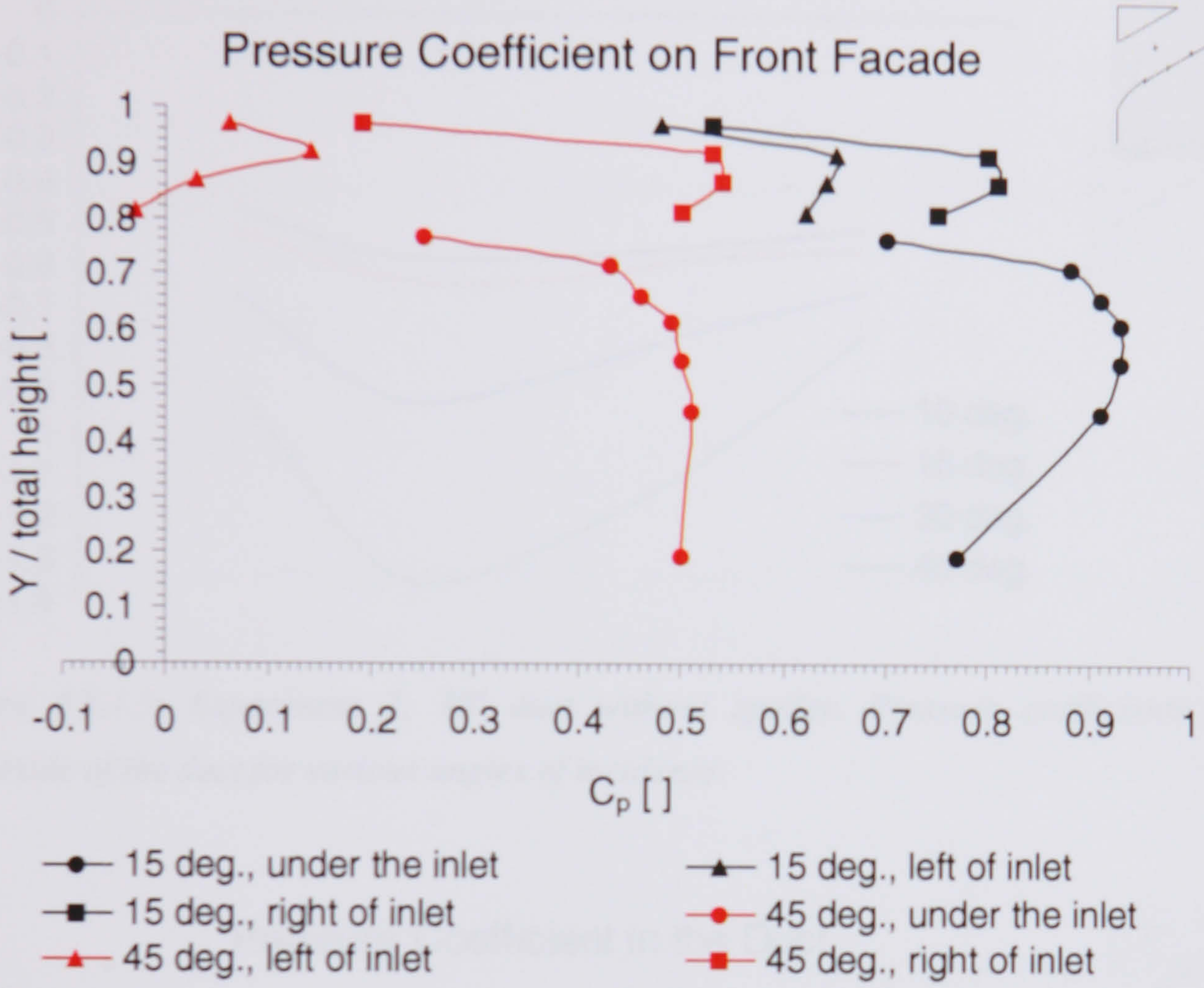

Figure 4.8.1.4: Experiment 2, 30° duct without spoiler. Pressure coefficients to windward and leeward of the duct inlet at various angles of incidence.

The presence of a swirl flow through the duct can be suggested by analysing the pressure readings in the duct (Figure 4.8.1.5). With increasing angles of incidence, the tappings along the centerline on the underside in the duct (see tappings T1 to T5 in Figure 4.2.3) indicate flow separation at the windward side, and the generated separation bubble over the floor of the duct covers only the second pressure tapping (T2 in Figure 4.2.3). Hence, the entering flow from the windward side passes over the separation bubble, deviates at the opposite leeward wall and leaves the duct at the rear part, where accelerated flow has been measured (see Figure 4.8.1.1). So, a swirling motion of the flow passes through the duct after less than one revolution.

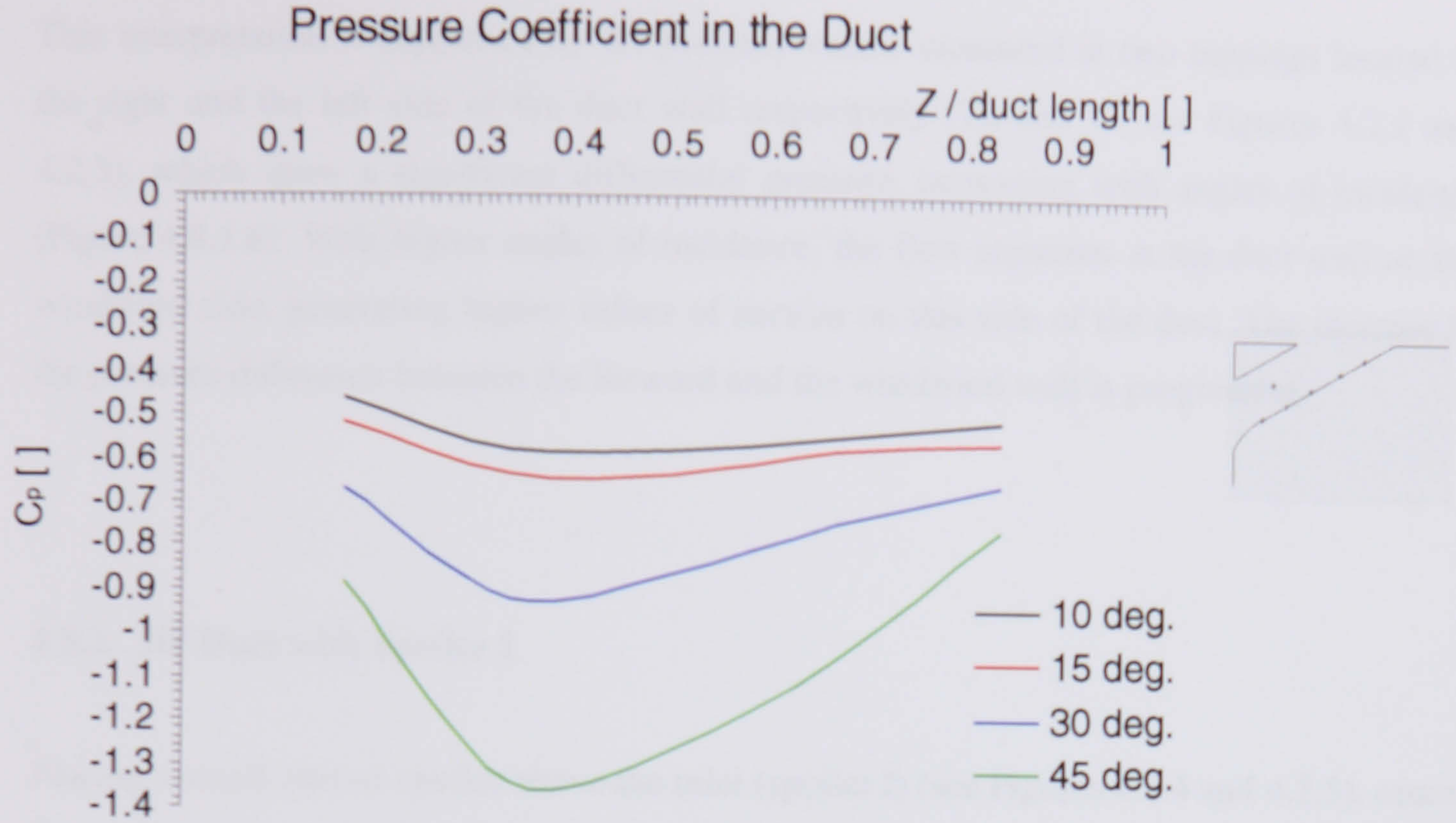

Figure 4.8.1.5: Experiment 2, 30° duct without spoiler. Pressure coefficients on the underside of the duct for various angles of incidence.

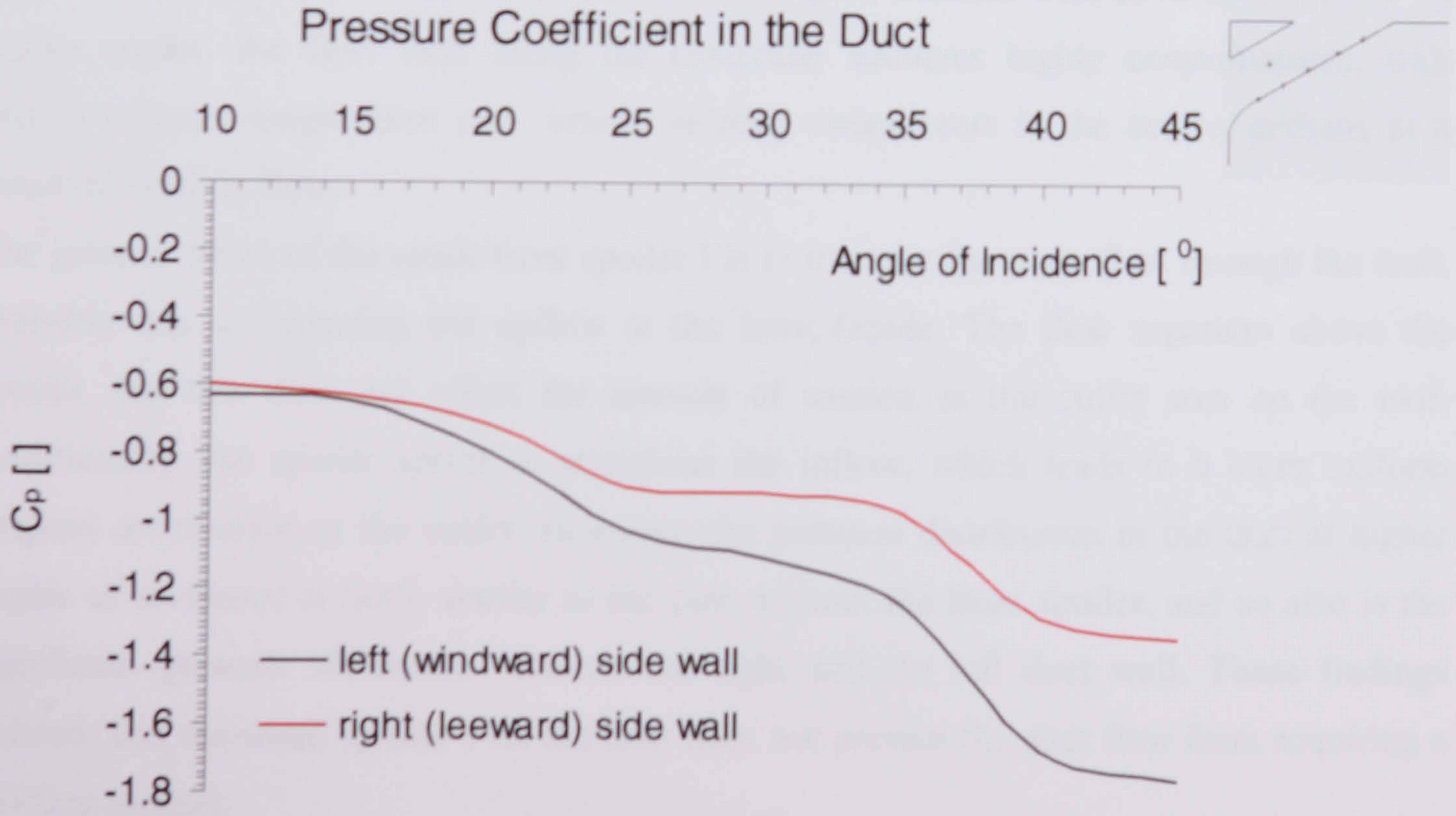

Figure 4.8.1.6: Experiment 2, 30° duct without spoiler. Pressure at the side walls to windward and leeward in the duct at various angles of incidence.

This interpretation is supported by the pressure values measured at two tappings located at the right and the left side of the duct wall respectively (T6 and T7 see Figures 4.2.2 and 4.2.3), which show a significant differential pressure, increasing with angles of incidence (Figure 4.8.1.6). With higher angles of incidence, the flow separates at the duct wall on the windward side, generating higher values of suction on this side of the duct. The increase in the pressure difference between the leeward and the windward wall is progressive.

4.8.2. 30° Duct with Spoiler I

Placing a small curved spoiler above the inlet (spoiler I) (see Figures 4.2.4 and 4.2.5), causes a significant and fairly uniform increase in flow velocity at the duct outlet (Figure 4.8.2.1). Wind flow at 15° normal to the front facade is accelerated by at least 20 % in the intended turbine plane. Maximum induced wind speeds occur at an angle of inclination of 25°. Here, the measured velocity distribution exceeds the free stream speed by about a third. At an angle of inclination of 35°, the distribution is still quite uniform with 25 % acceleration. At higher angles, the flow field along the centerline becomes highly unsymmetrical, with greatly reduced longitudinal and vertical velocity components in the centre, perhaps as a result of swirling flow.

The general effect of the small front spoiler I is to increase the mass flow through the duct, probably due to capturing the upflow at the front façade. The flow separates above the spoiler, but this does not affect the amount of suction in the outlet area on the roof. Additionally, the spoiler seems to straighten the inflow, which leads to a more uniform velocity distribution at the outlet. However, the pressure distribution in the duct at higher angles of incidence is fairly similar to the case without the front spoiler, and so also is the significant pressure difference between the right and the left duct wall. These findings indicate that the small spoiler over the inlet does not prevent the duct flow from acquiring a swirling motion.

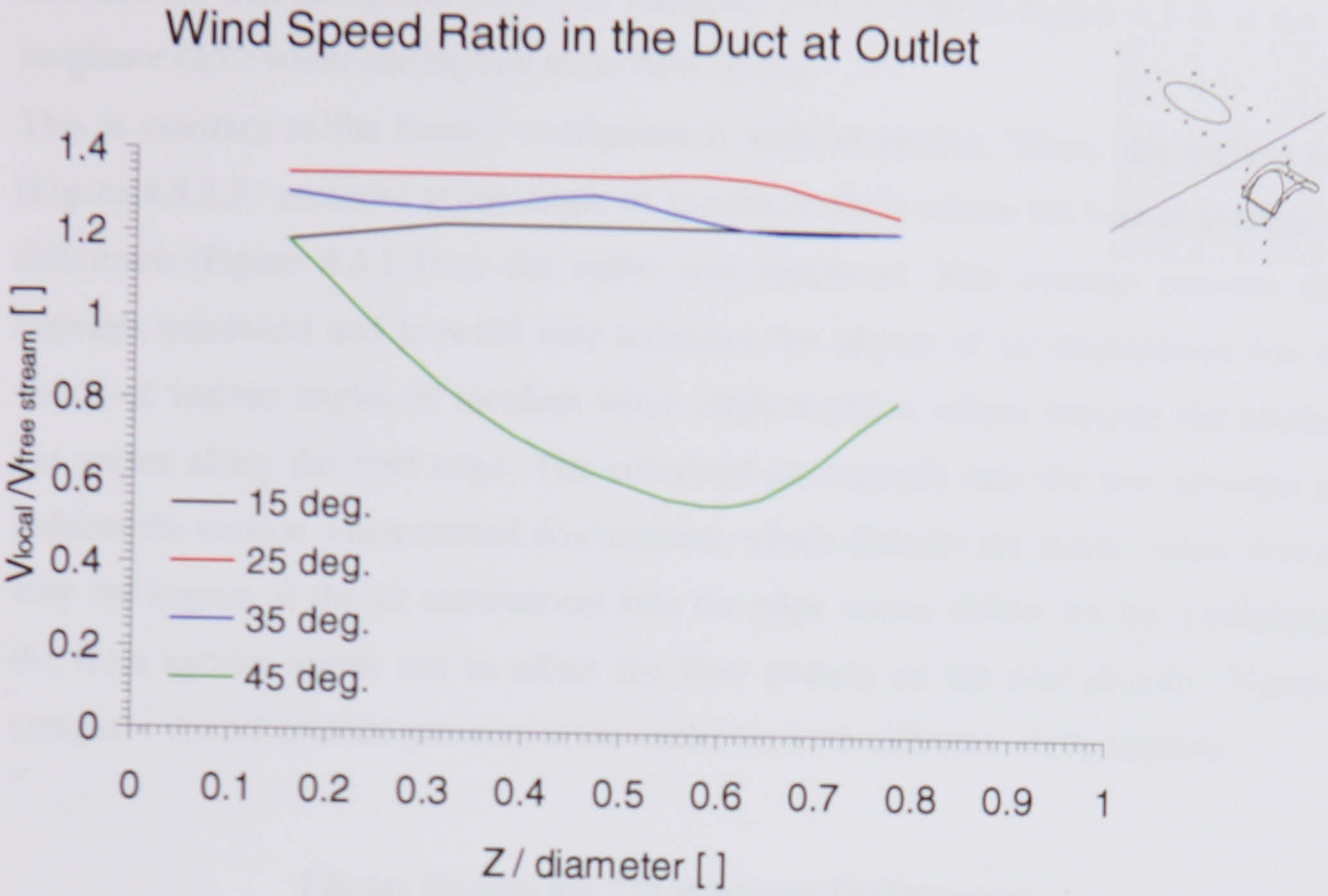

Figure 4.8.2.1: Experiment 3, 30° duct with front spoiler I.

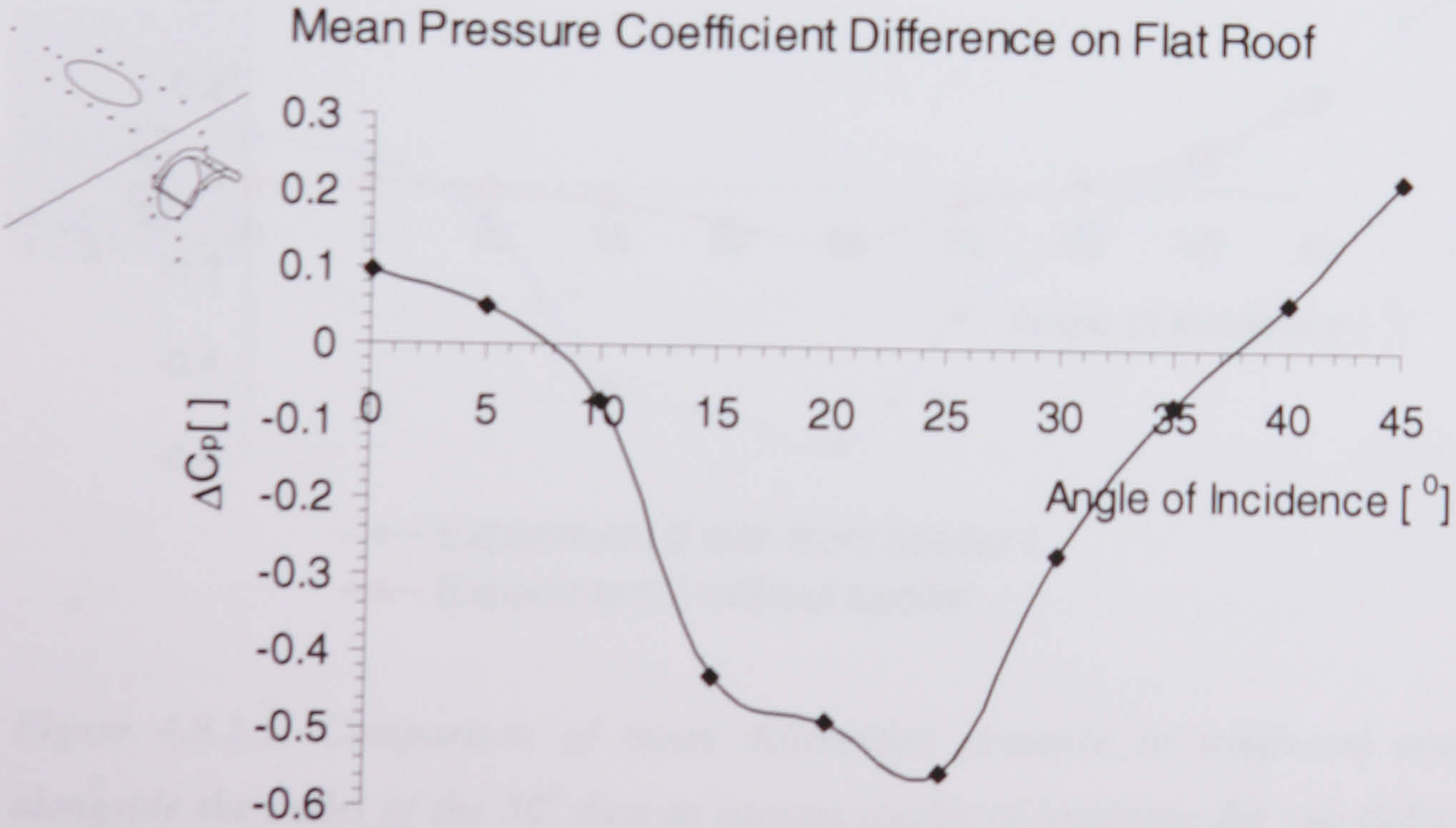

Figure 4.8.2.2: Experiment 3, 30° duct with front spoiler I. Differential pressure between windward and leeward tappings near the duct outlet at various angles of incidence.

Figure 4.8.2.2 shows the highest negative average pressure difference between windward and leeward side alongside the outlet (tappings P11 to P20 in Figure 4.2.2) at the angle of incidence (25°) where the highest mass flow occurs

This is contrary to the former configuration without spoiler. There, the highest massflow (Figure 4.8.1.1) occurred at the angle of incidence (35^0) where the lowest average pressure difference (Figure 4.8.1.3) at the outlet was measured. This average pressure difference between windward and leeward side indicates the impact of jet entrainment into the edge vortex at various angles of incident wind. High negative values indicate the breakdown of the vortex along the roof edge. The entrained jet expands into the low pressure area and reduces the suction when carried downstream, which disturbs the stable vortex. It is not clear why the impact of the jet entrainment into the edge vortex differs for the configurations, as the front spoiler seems not to affect the flow pattern on the roof directly. Figure 4.8.2.3 compares the differential pressure at the outlet for both different configurations.

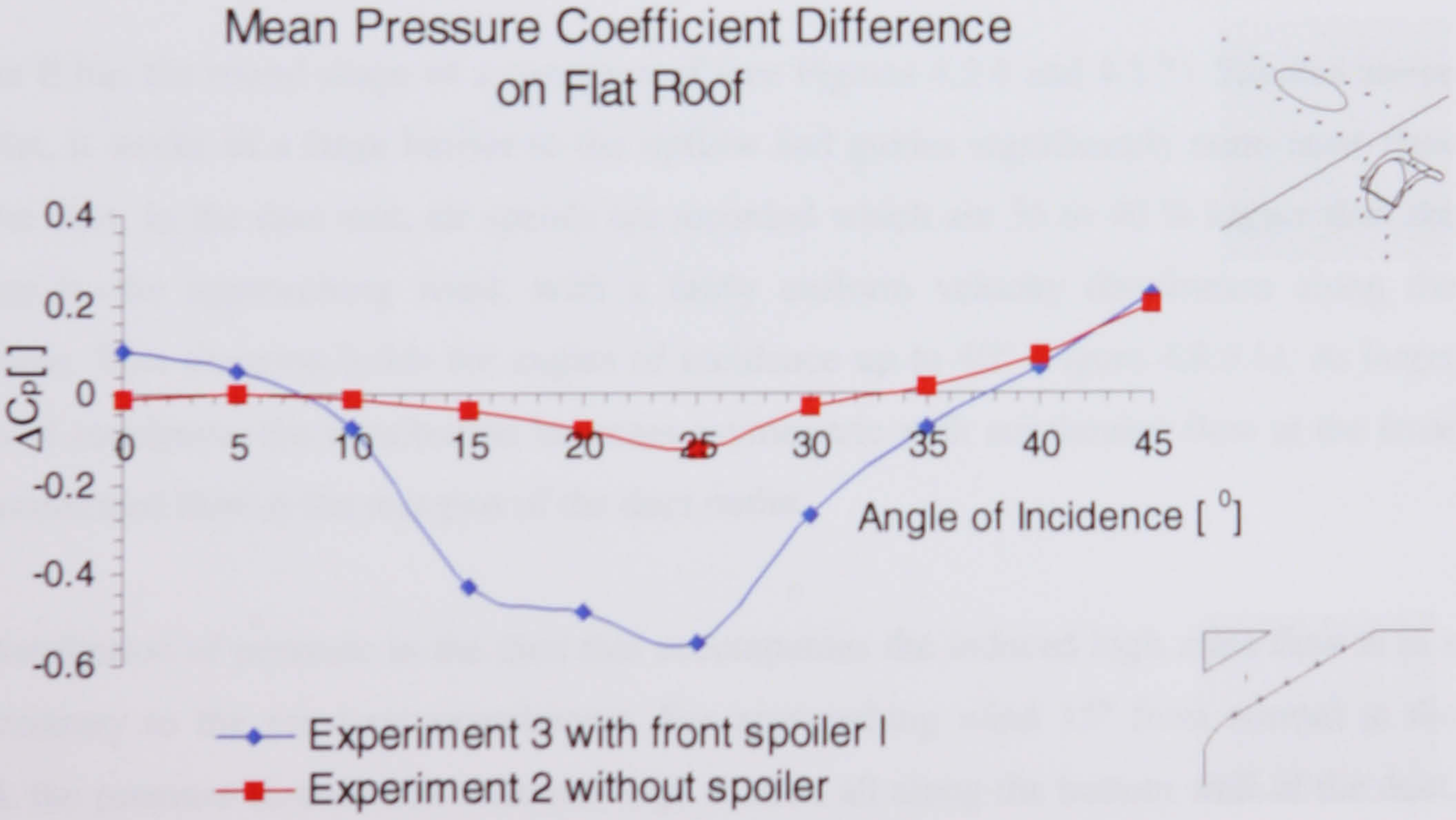

Figure 4.8.2.3: Comparison of mean differential pressure to windward and leeward alongside the outlet of the 30^0 duct at various angles of incidence for two different model configurations.

The jet stream of higher speed through the duct with spoiler I causes a more negative pressure differential over a wider range of angles. Negative pressure differential means that there is less suction on the leeward side than on the windward side. This might indicate that the jet entrainment at higher speeds into the edge vortex perturbs the vortex. Therefore, neighbouring turbines downstream would see less suction. Extrapolating this finding, one could suggest that the higher the massflow through the single duct, the less beneficial is its jet entrainment for adjacent turbines. However, the absolute values of suction on the leeward side for each angle of incidence are still similar to what is measured at the roof edge without any integrated duct for windflow normal to the façade (C_p ~ -0.5 to -0.6), which might indicate that for each angle of incidence a row of turbines could still work well enough. But the topic is complex, and it is difficult to predict. Hence, further experiments with multiple ducts at the roof edge are necessary.

4.8.3. 30° Duct with Spoiler II

Spoiler II has the round shape of a canopy roof (see Figures 4.2.6 and 4.2.7). Situated above the inlet, it works as a large barrier to the upflow and guides significantly more mass flow into the duct. In the duct exit, air speeds are recorded which are 35 to 40 % higher than the velocity in the approaching wind, with a fairly uniform velocity distribution along the centerline. This situation holds for angles of incidence up to 40° (Figure 4.8.3.1). At larger angles of incidence, the distribution becomes asymmetric with accelerated flow at the front and decelerated flow at the rear part of the duct outlet.

The distribution of pressure in the duct that accompanies the induced high mass flow is in a way contrary to the previous experiments. For approaching wind 15° from normal to the model, the pressure distribution indicates high suction all along the bottom wall of the duct. With increasing angles of incidence, the suction at the tappings in the duct reduces. The pressure distribution for 60° incidence in Figure 4.8.3.2 is very similar for 45° incidence in Figure 4.8.1.5. Hence, it is very likely that similar swirling flow conditions are generated in the duct with spoiler II for higher angles of incidence. However, in the previous experiment (Figure 4.8.1.5) the generation of a swirl with increasing angles of incidence went along with an increased suction at the underside of the duct. Here, a reduction of speed (see Figure 4.8.3.1) arises with the generation of swirl at higher angles of incidence.

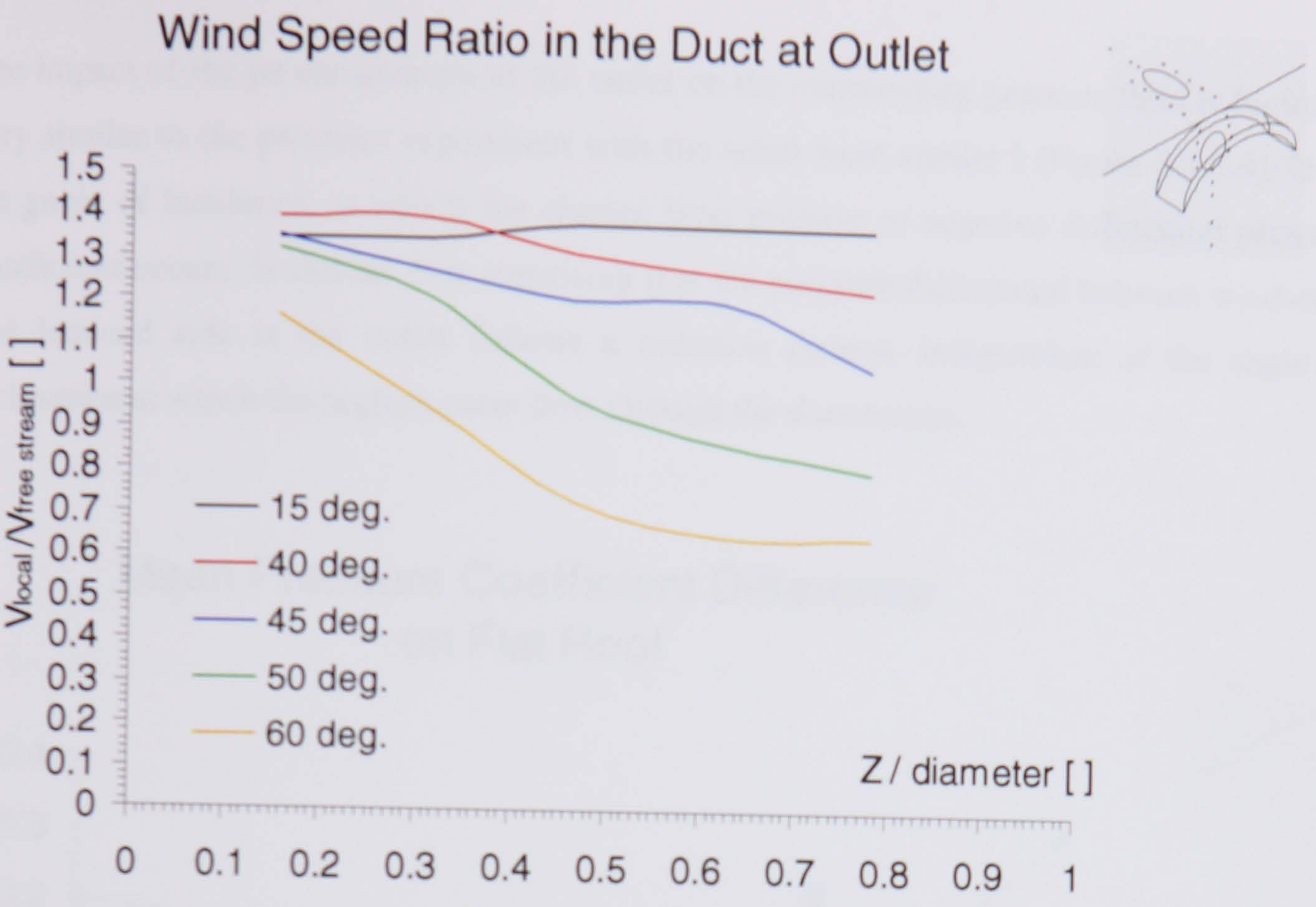

Figure 4.8.3.1: Experiment 4, 30° duct with front spoiler II

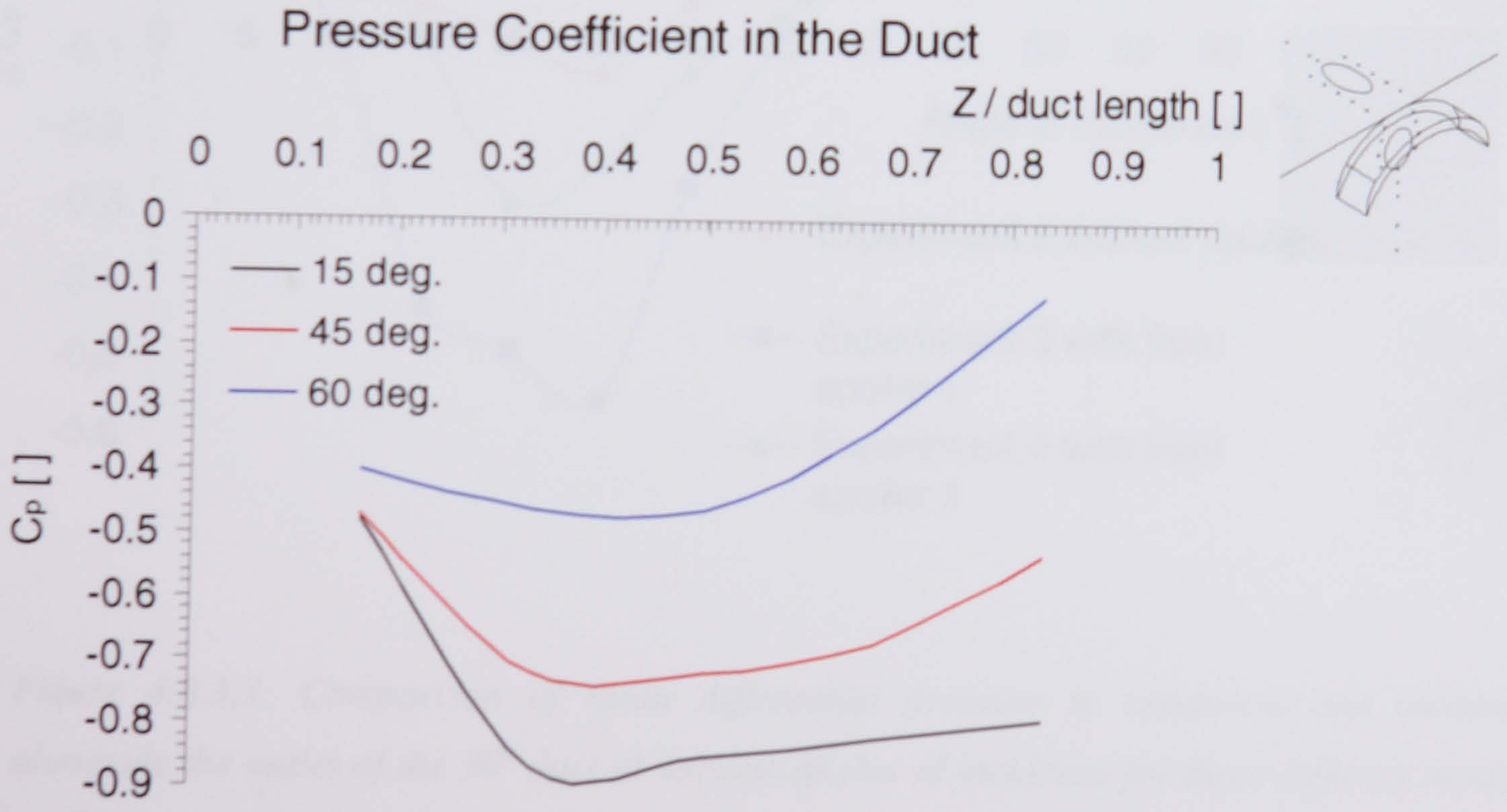

Figure 4.8.3.2: Experiment 4, 30° duct with front spoiler II. Pressure coefficient on the underside in the duct for various angles of incidence.

The impact of the jet entrainment at the outlet on the surrounding pressure field is basically very similar to the previous experiment with the small front spoiler I (Figure 4.8.3.4). Only the angle of incidence, at which the change from positive to negative differential pressure coefficient occurs, is shifted. It is surprising that the pressure differential between windward and leeward side at the outlet follows a common pattern, independent of the angle of inclination at which the highest mass flow through the duct occurs.

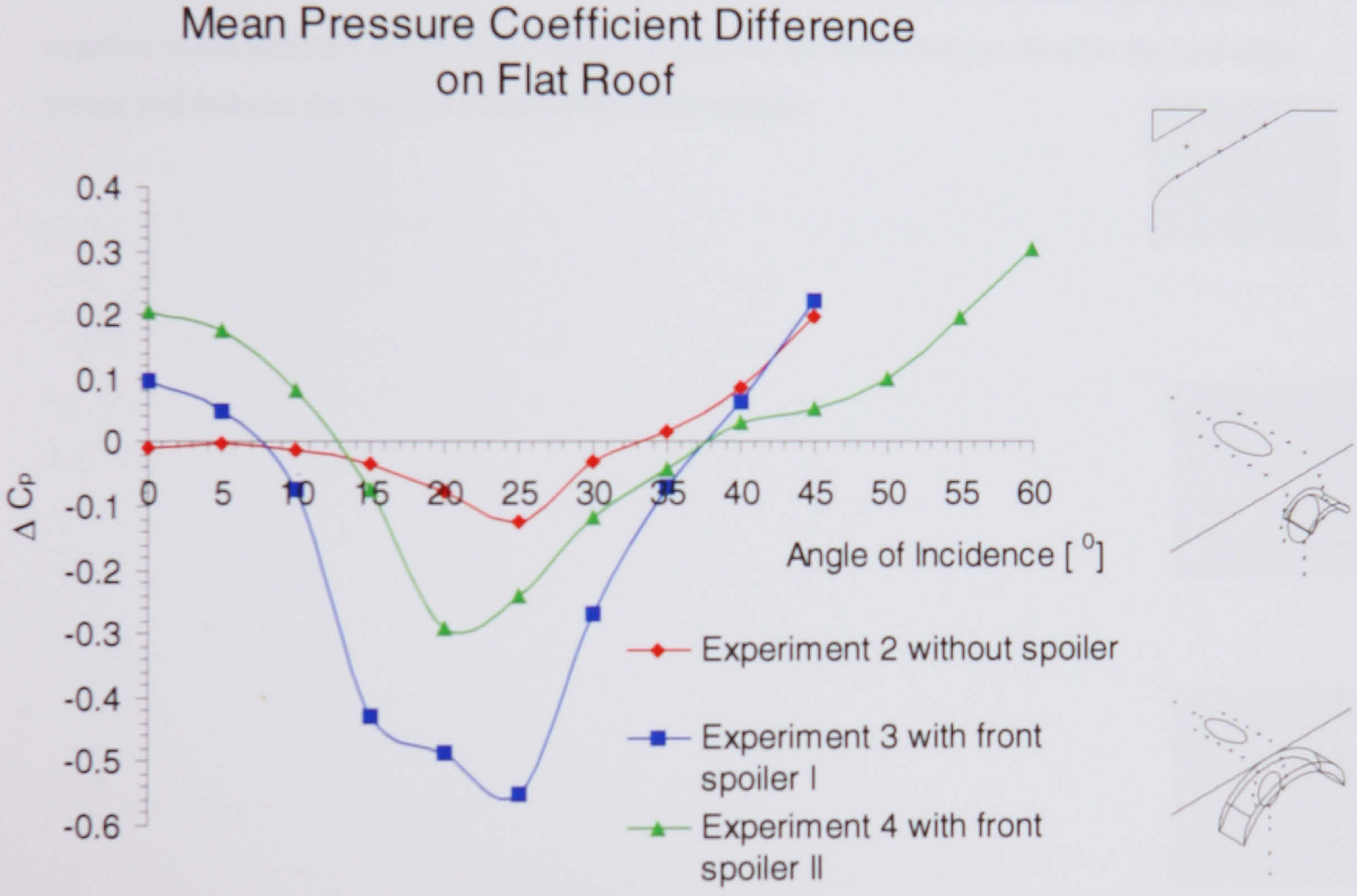

Figure 4.8.3.3: Comparison of mean differential pressure to windward and leeward alongside the outlet of the 30⁰ duct at various angles of incidence for three different model configurations.

However, in all experiments, the wind speed ratio in the outlet falls rapidly and the flow becomes non-uniform as soon as Δ C_p becomes positive. Any further rise of Δ C_p goes along with the breakdown of wind acceleration in the duct. For experiment 3, the highest induced wind speed at the outlet (see Figure 4.8.2.1) goes along with the maximum negative mean pressure coefficient difference alongside the outlet (see Figure 4.8.2.3 or 4.8.3.3). This does not hold for experiment 2 and experiment 4. For the duct without spoiler, the highest induced wind speeds occur at minimum negative mean pressure coefficient difference. But all experiments with the 30° duct show, that high induced wind speeds in the duct go along with negative mean pressure coefficient. Hence, in general the entrained jet disturbs the roof edge vortex and reduces the suction when carried downstream.

4.9. The 90° Duct Configurations

In this measurement series, the center of the inlet of the duct is located at 87 % of building height, but the curved inlet starts at 74 % of building height (see Figures 4.2.8 and 4.2.9). Hence the inlet is situated close to the stagnation zone to connect the high pressure region at the front part with the low pressure zone above the roof. As with the previous configuration it was hoped that the pressure differential would induce high velocities in the duct flow.

The curved geometry of the duct causes a non uniform velocity distribution inside the duct. Findings in the previous experiments showed that a front spoiler induces higher speeds and supports a more uniform speed profile at the outlet. Hence, the impact of two different spoilers was of particular interest.

Again, one should be reminded that due to the horizontal velocity profile of the wind tunnel flow, the direction 10 to 15° anti-clockwise is seen to approximate to the wind direction 'normal' to the front façade of the model.

As described in Chapter 4.6, hot wire measurements were taken at inlet and outlet of the duct (see Figure 4.6.3).

4.9.1. 90° Duct without Spoiler

Wind approaching normal to the façade enters the lower part of the duct (see Figure 4.2.8 and 4.2.9) with significantly lower momentum than the free flow, while at the upper part inside the duct inlet the flow accelerates (Figure 4.9.1.1). Comparison with CFD simulations (see Chapter 7) shows that this velocity profile may indicate the presence of a flow separation bubble in the lower part of the inlet. With increasing angles of incidence, the inflow velocity exceeds the free wind speed and the vertical profile flattens out. Finally, for steep angles of incidence, the higher values of inflow momentum are recorded in the lower part of the duct. It may be that the flow separation bubble starts to migrate at an angle of incidence larger then 50°, and flow separation at the leading duct sidewall becomes predominant.

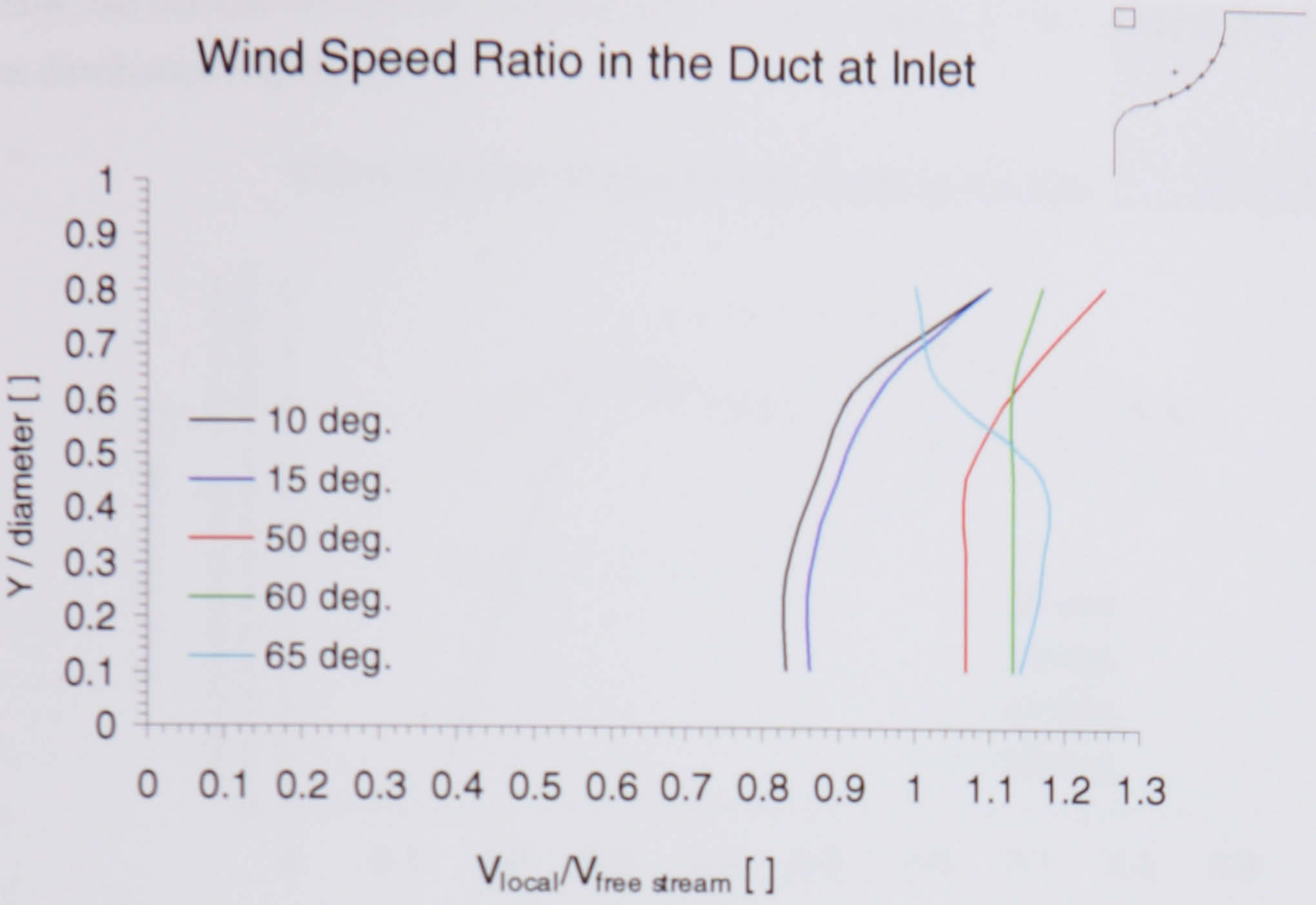

Figure 4.9.1.1:Experiment 5, 90° duct without front spoiler

This inflow profile develops in a certain way through the duct. Certainly the sharp rectangular upper edge in the duct (see Figure 4.2.9) creates flow separation and will be the first issue for aerodynamical improvements (see Chapter 7). It may well cause the large drop in flow velocity at the front part of the outlet which is measured regularly for lower angles of incidence (Figure 4.9.1.2). But generally, the air speed declines towards the rear part of the outlet, as expected for a flowfield following the 90° curve. From 15 to 40° incidence the measured velocity at the outlet increases. Highest mass flow at the outlet occurs at 50° incidence (Figure 4.9.1.2), which also gives the highest local velocity measured at the inlet (see Figure 4.9.1.1).

The reduced inflow in the lower part of the inlet (Figure 4.9.1.1) corresponds with the downward sloping profile at the rear part of the duct (Figure 4.9.1.2). The straight inflow profile of high velocity at 60° incidence goes along with an outlet profile which shows slightly higher massflow at the rear part than in the front part. Here it is likely that already flow separation has occurred in the upper part of the inlet, but more strongly at the windward side wall. Such a separation zone could not be explored with the measurements along the centerline in the middle of the duct. Larger angles of incidence than 60° are not beneficial to the flow, but one can see that basically the inflow profile (Figure 4.9.1.1) corresponds to the outlet distribution (Figure 4.9.1.2).

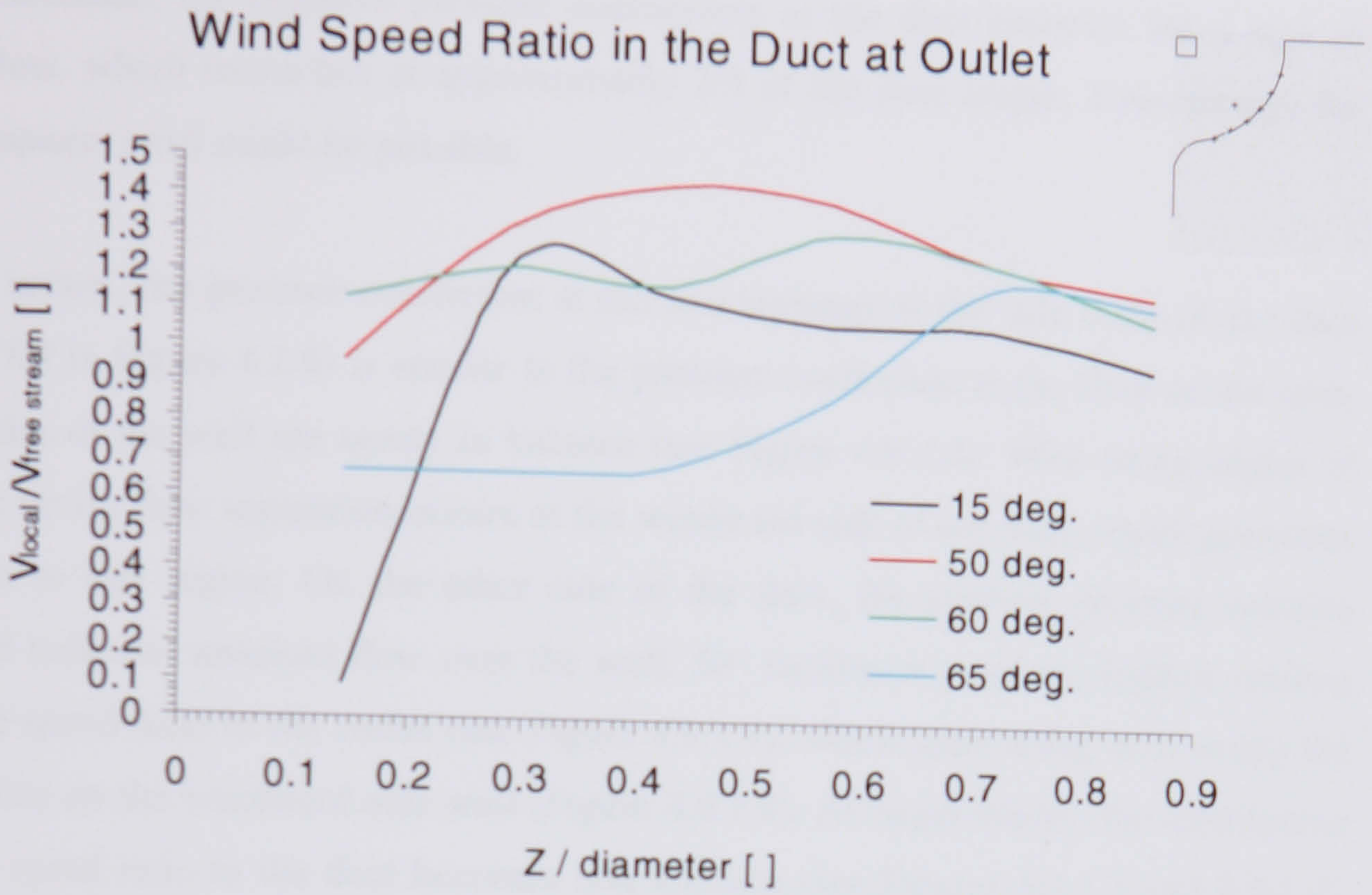

Figure 4.9.1.2: Experiment 5, 90° duct without front spoiler

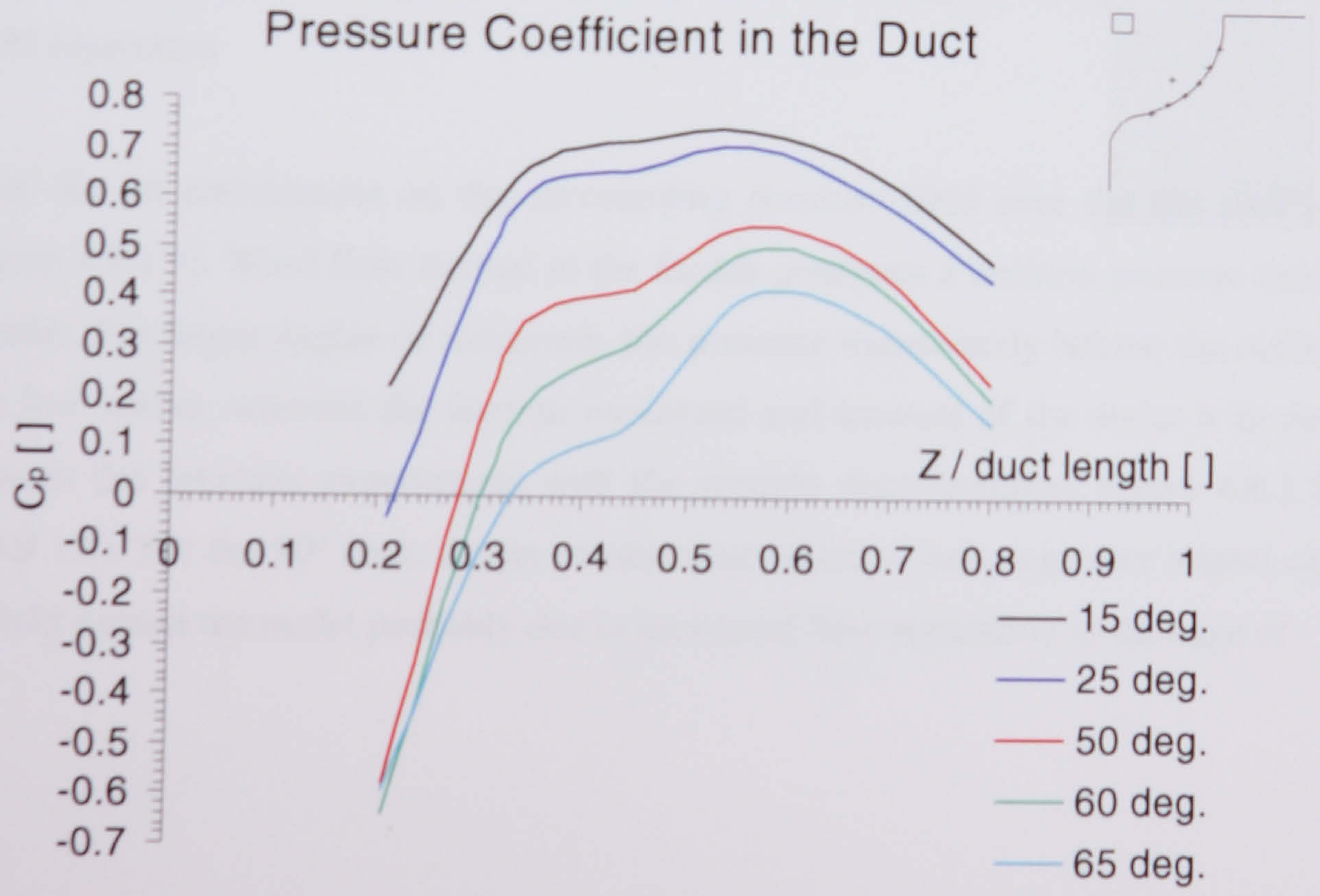

Figure 4.9.1.3: Experiment 5, 90° duct without front spoiler. Pressure coefficient at the underside in the duct for various angles of incidence.

The pressure distribution on the outer wall of the duct (see tappings T1 to T6 in Figures 4.2.8 and 4.2.9) indicates (Figure 4.9.1.3) that the inflow at 15° seems to be smooth, but at higher angles of incidence, the negative pressure coefficients at the duct entrance are a sign of separated flow, which reattaches at approximately 2/3 of the duct length. Even though the housing is square, swirl might be possible.

For normal inflow, the pressure coefficient at the two tappings at the side walls of the duct (tappings T7/8 in Figure 4.2.9) is similar to the pressure coefficient at the floor of the inlet, and both sides of the wall are nearly in balance (see Figure 4.9.1.4). With rising angles of incidence, a strong flow separation occurs at the windward side of the wall, which generates high suction in this region. On the other side of the duct, the positive pressure remains constant and indicates attached flow over the wall. 50° incidence gives the highest reading for the wind speed ratio in the outlet (see Figure 4.9.1.1), which goes along with nearly the highest suction on the windward side wall (Figure 4.9.1.4). At larger angles, the distribution of the wind speed ratio in the duct becomes non uniform (see Figures 4.9.1.1 and 4.9.1.2), while the suction reaches its lowest point and starts to rise again (Figure 4.9.1.4). It should be mentioned that at large angles, the suction values on the windward side walls were recorded as fluctuating in the range of $\Delta C_P = \pm 0.1$. This indicates a high amount of turbulence and separation

The impact of the jet entrainment on the surrounding pressure field over the flat roof is complex (Figure 4.9.1.5). Wind flow normal to the façade generates a uniform pressure field around the outlet. For larger angles of incidence, the pressure immediately behind the outlet drops to very low values, whereas the suction windward and leeward of the outlet is in the same range as in the previous experiments with the straight duct (compare Figure 4.8.1.2 with Figure 4.9.1.5). For the 90° duct, the jet entrainment seems to have a greater impact on the pressure field behind the outlet probably due to increased flow separation at the edge of the outlet.

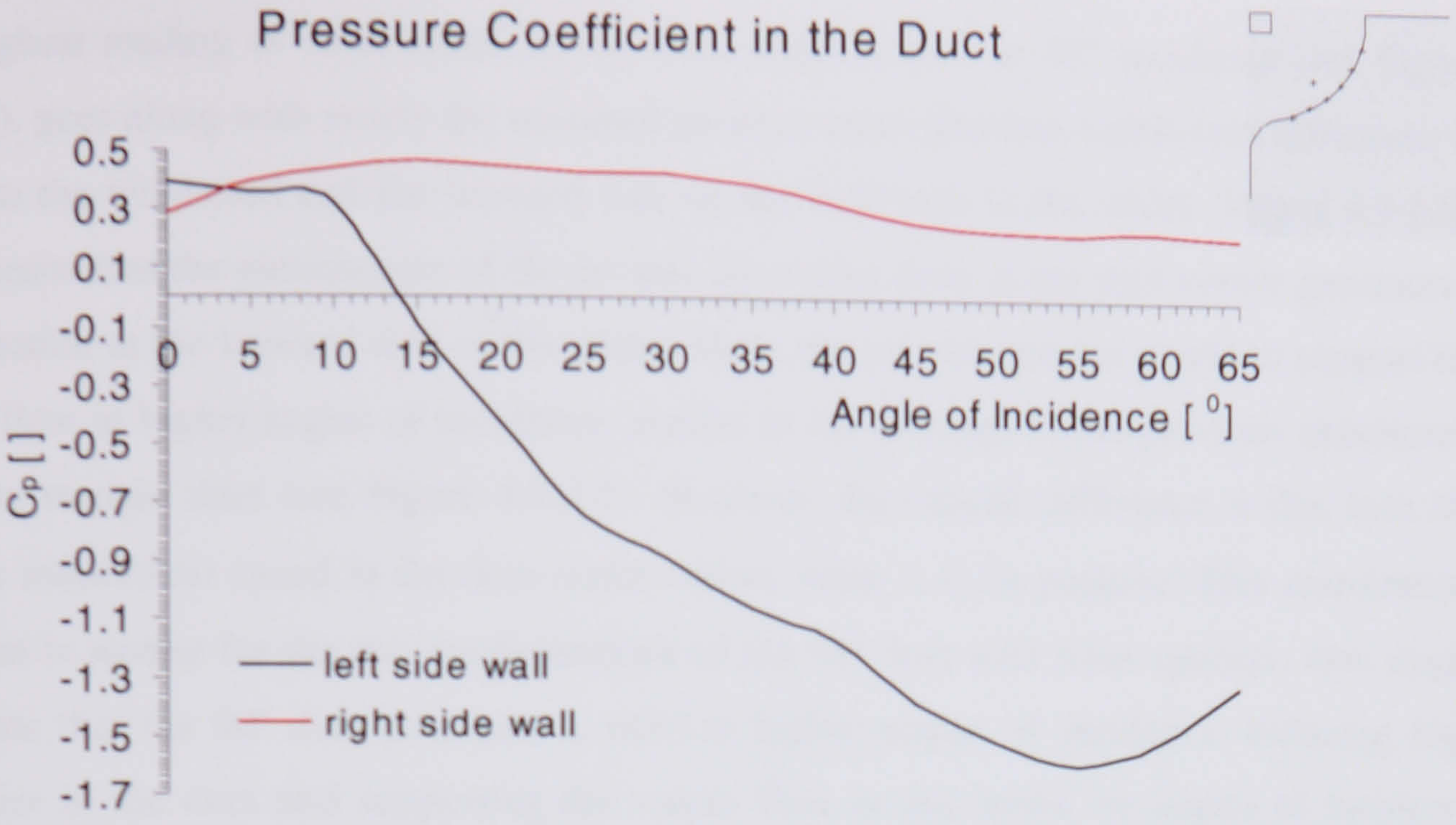

Figure 4.9.1.4: Experiment 5, 90° duct without front spoiler. Pressure at the side walls windward (left) and leeward (right) in the duct at various angles of incidence.

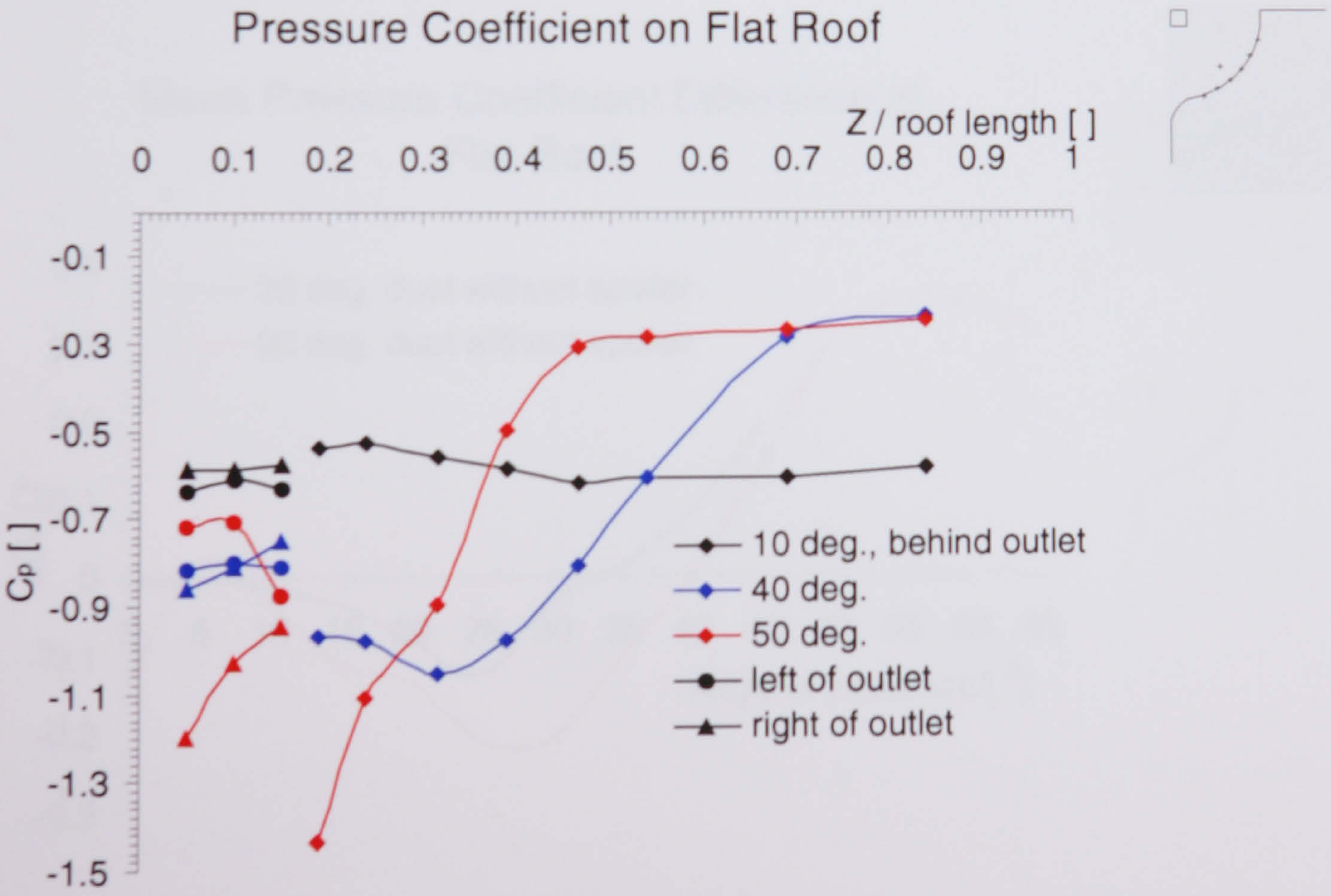

Figure 4.9.1.5: Experiment 5, 90° duct without front spoiler. Pressure distribution around the outlet for various angles of incidence

The highest reading of wind speed in the duct, which occurs at 50° incidence (see Figure 4.9.1.2), goes along with nearly the maximal positive mean pressure coefficient difference in between the windward and the leeward side on the roof next to the outlet (Figure 4.9.1.6). This means that the entrainment of the jet into the vortex flow at the roof corner generates a high suction at the leeward side of the outlet. Here, the jet entrainment seems to support the vortex flow at higher angles of incidence, similar to the findings in the previous experiment with the straight duct (see Figure 4.8.2.3). However, the crucial difference is that here the highest induced air speed in the duct outlet occurs when ΔC_p is positive. This entrainment situation is similar for the two configurations of the 90° duct with front spoilers. One might speculate that the 90° duct generates a swirl at higher angles of incidence, inducing high velocities in the duct and supporting the vortex flow at the outlet. At angles of incidence lower than 40°, the mean differential pressure is negative, but reaches its minimum with $\Delta C_p \sim -0.2$. This is however a relatively low pressure differential, and in general one might argue that these findings indicate a beneficial interaction with any adjacent 90° ducts along the roof edge.

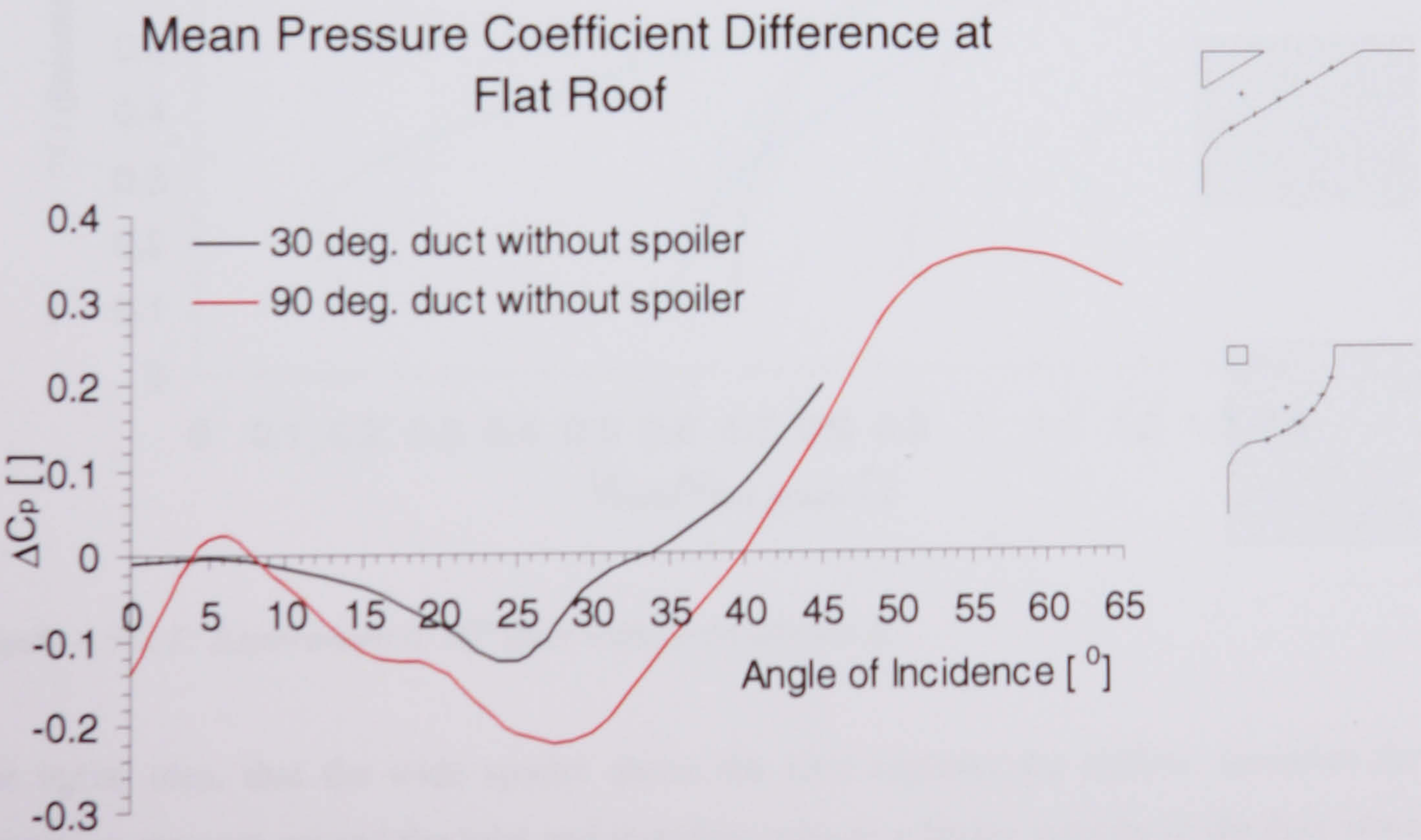

Figure 4.9.1.6: Comparison of mean differential pressure between windward and leeward tappings alongside the duct exit at various angles of incidence for two different duct configurations without spoiler.

4.9.2. 90° Duct with Spoiler II

Attaching spoiler II, the wide canopy hood, at the inlet of the 90° duct (see Figures 4.2.10 and 4.2.11), does not increase the inflow velocity, as was hoped. Capturing some upflow with the wide front spoiler seems to promote flow separation in the lower part of the inlet, at least for larger angles of incidence (Figure 4.9.2.1). Maximum inflow occurs at 45°, and further rotation causes a decelerated flowfield in the lower half of the duct inlet. Compared with the inflow profiles of the previous configuration without spoiler (see Figure 4.9.1.1), the canopy front spoiler seems not to be beneficial.

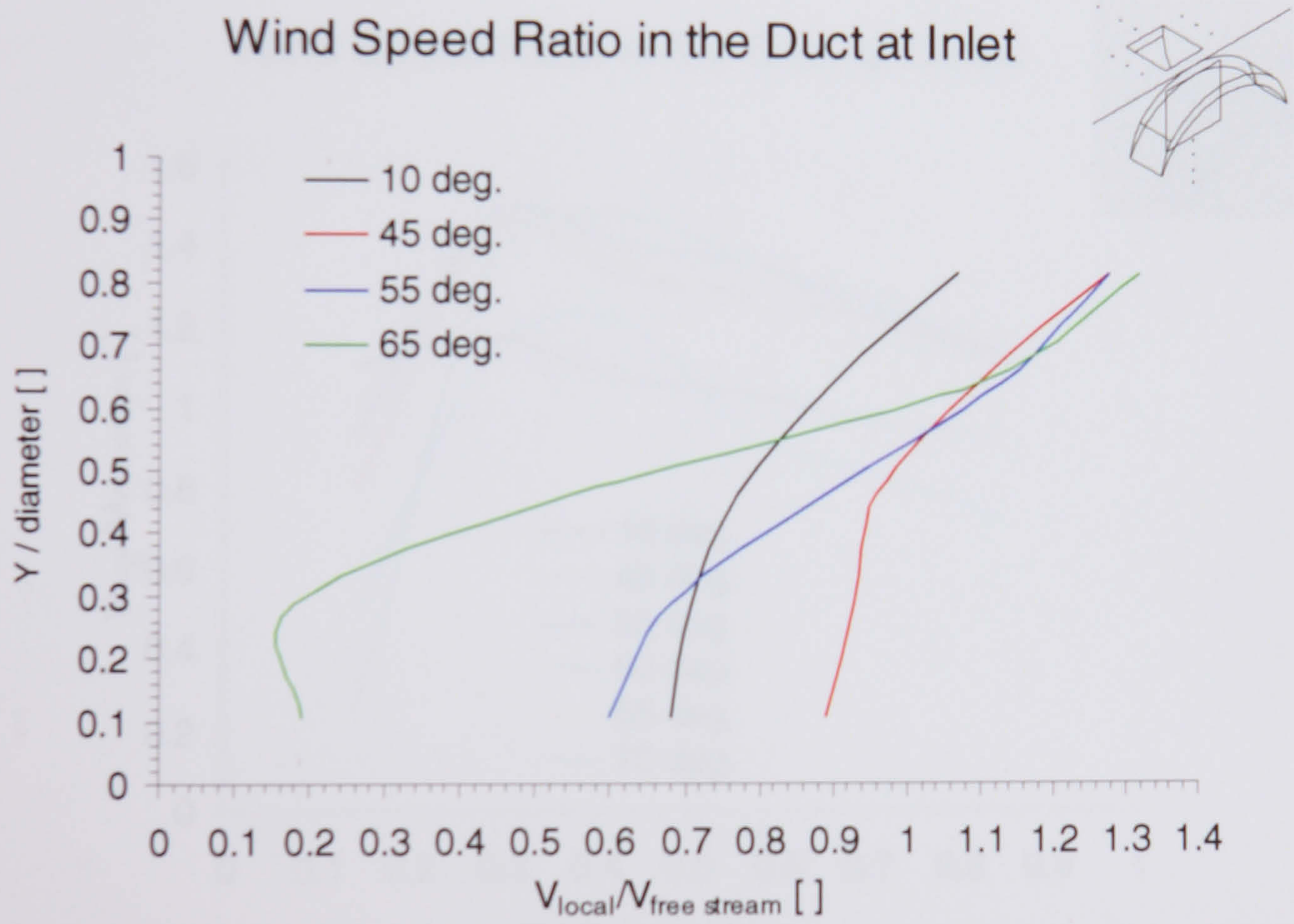

Figure 4.9.2.1: Experiment 6, 90° duct with front spoiler II.

The initial idea, that the wide spoiler above the inlet captures the upflow, increases the stagnation pressure around the inlet and therefore induces a higher velocity in the duct when measured downstream at the outlet in the intended turbine plane, does not hold true in such simple terms. As the inflow velocity is lower than in the previous case, one might expect deceleration in the intended turbine plane at the outlet. However, the wind velocity at the outlet (Figure 4.9.2.2) has a peak value of over 40 % above free stream velocity at 45 to 65°

incidence, and the distribution drops smoothly towards the rear part of the outlet corresponding with the lower velocity at the inflow in the lower part of the duct. For wind normal to the façade, the performance is very close to the previous case without any spoiler at the inlet. For the large angle of 65° incidence, the current spoiler configuration has a significant advantage: the inflow profile (see Figure 4.9.2.1) does not reverse its shape (see Figure 4.9.1.1), and the profile at the outlet indicates still an average velocity which is higher than the free stream (Figure 4.9.2.2). For each angle of incidence, the outlet profile shows a significant drop in the upwind region. Better aerodynamical design of the upper edge of the duct could improve this flow situation (see Chapter 7).

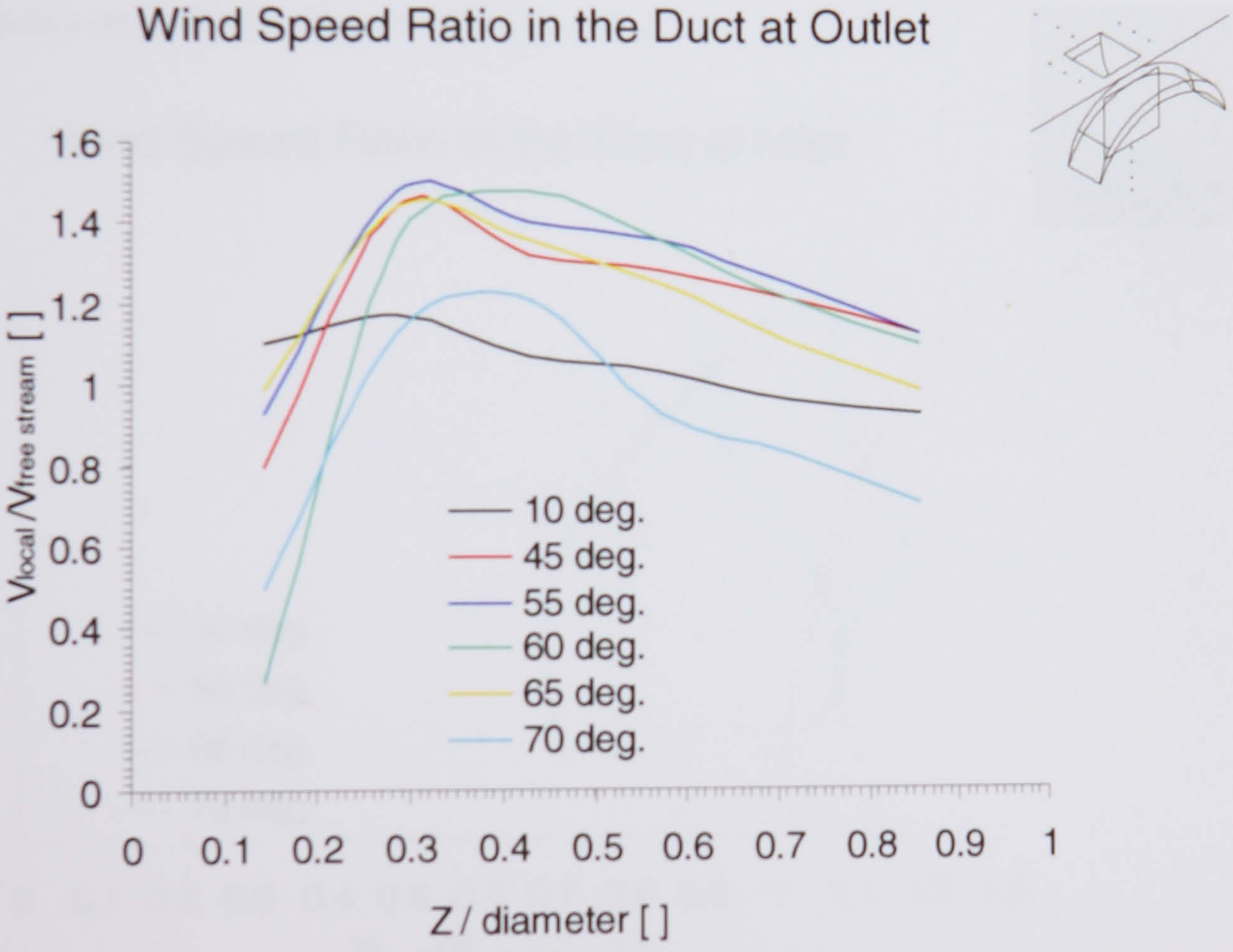

Figure 4.9.2.2: Experiment 6, 90° duct with front spoiler II.

It is surprising that the rather poor results at the inlet go along with an encouraging increase in wind speed at the outlet. More clarity could be achieved with two and three dimensional hot wire measurements. This results show, that measured velocities in the duct do not automatically indicate the massflow.

4.9.3. 90° Duct with Spoiler III

The last test (Experiment 7) was carried out with a straight flat, rectangular piece of Perspex as spoiler III. It was placed directly above the inlet and is slightly wider then the opening (see Figures 4.2.12 and 4.2.13). This configuration shows a much more uniform inflow profile (Figure 4.9.3.1) than the previous spoiler configuration (see Figure 4.9.2.1), rather similar to that what has been measured at the 90° duct without any spoiler (see Figure 4.9.1.1), but shifted towards lower speed. Up to 55° incidence, the inflow profile has the typical gradient caused by separation in the lower part of the inlet and acceleration at the upper wall. At around 65° incidence, the inflow profile straightens, and higher angles of rotation cause a rapid decline (Figure 4.9.3.1).

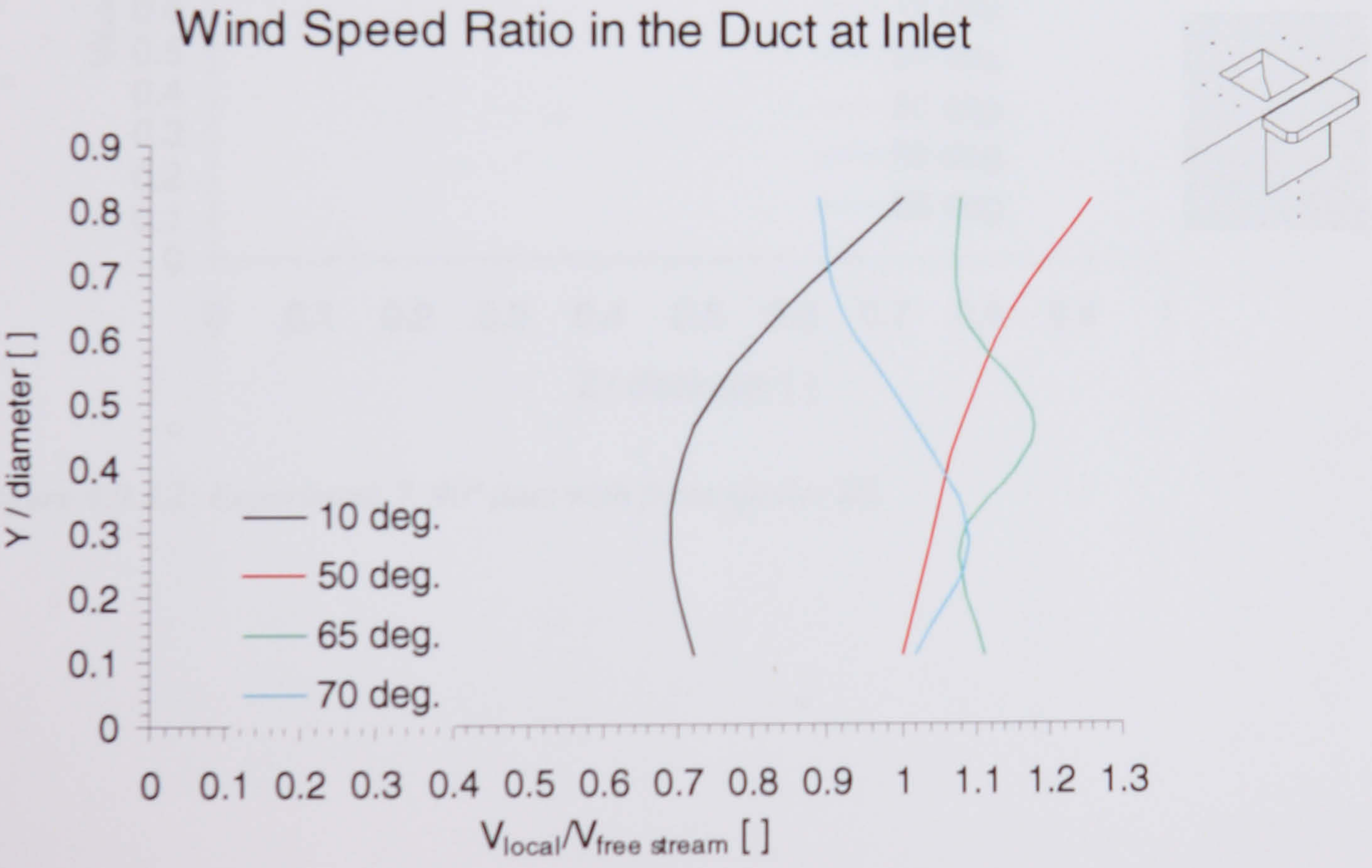

Figure 4.9.3.1:Experiment 7, 90° duct with front spoiler III

The speed at the outlet reaches peak values of nearly 50 % above the free stream wind speed at 50° incidence (Figure 4.9.3.2). However, as in the previous experiments with the 90° duct, for inflow normal to the façade, the speed acceleration is not impressive. With rising angles of incidence, the induced wind speed increases and the velocity distribution becomes less uniform. The tendency towards a higher speed in the upwind part of the outlet remains, up to the maximum massflow at 50° incidence. With further rotation, the speed in the downwind part of the outlet exceeds the speed in the upwind part. At 65° incidence, the speed in the upwind part falls below the free stream velocity.

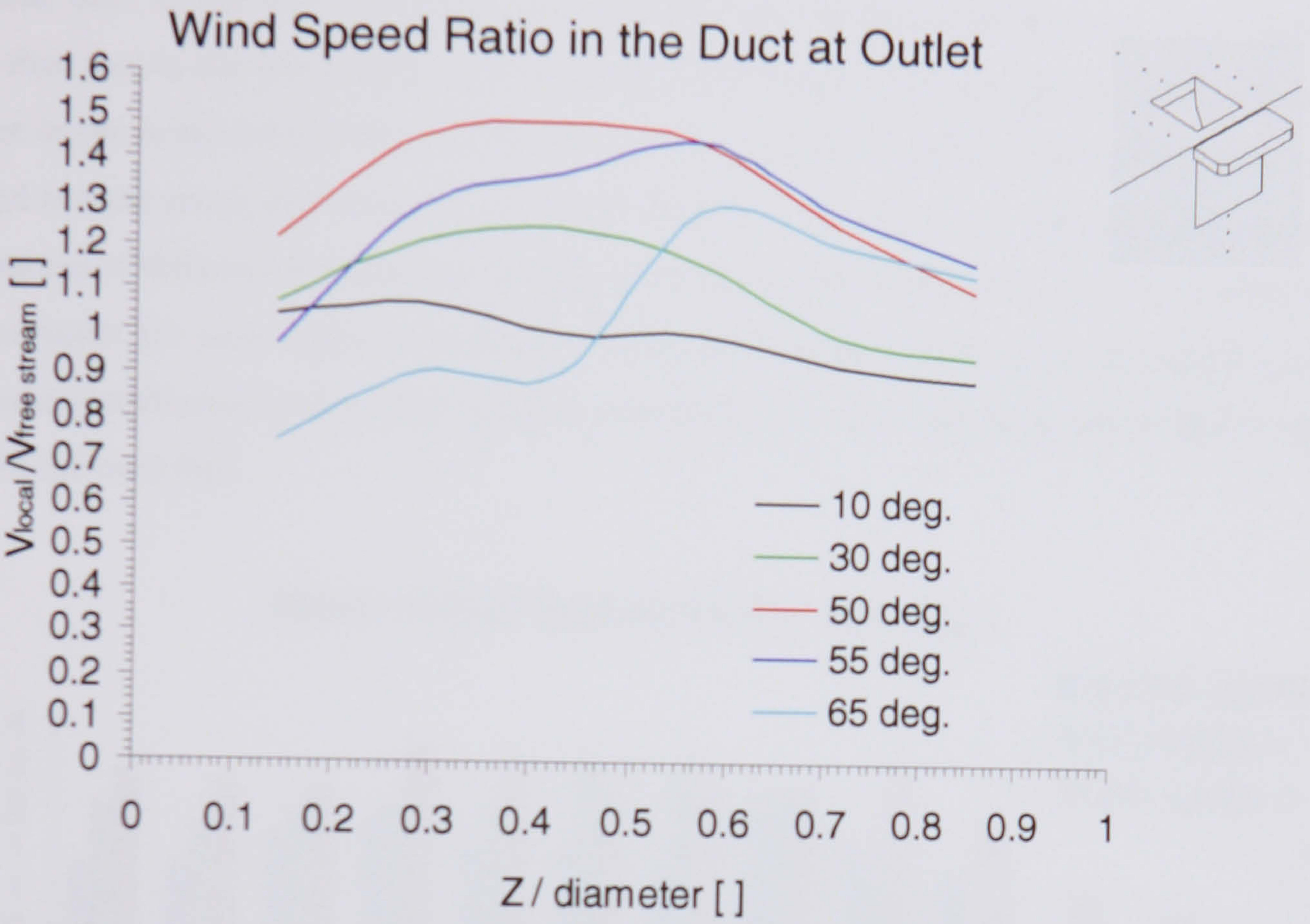

Figure 4.9.3.2: Experiment 7, 90° duct with front spoiler III.

4.10. Summary of the Experimental Results and Conclusions

As the wind approaches the building model, it generates a high pressure zone at the front façade and suction above the flat roof. These pressure zones communicate through an integrated duct at the wall roof edge. Both tested duct designs can induce a wind speed higher than that in the free stream, in the intended turbine plane at the outlet. Spoilers above the inlet improve the performance of the configuration, with a higher wind speeds across the intended turbine plane and toleration of larger angles of incidence. In order to compare the performance of different devices, the average wind speed ratio (Figures 4.10.1 and 4.10.2) in the duct outlet for each angle of incidence has been calculated. Hence, the measured wind speed ratio distribution in the outlet along its centerline has been integrated and related to the length of the base line.

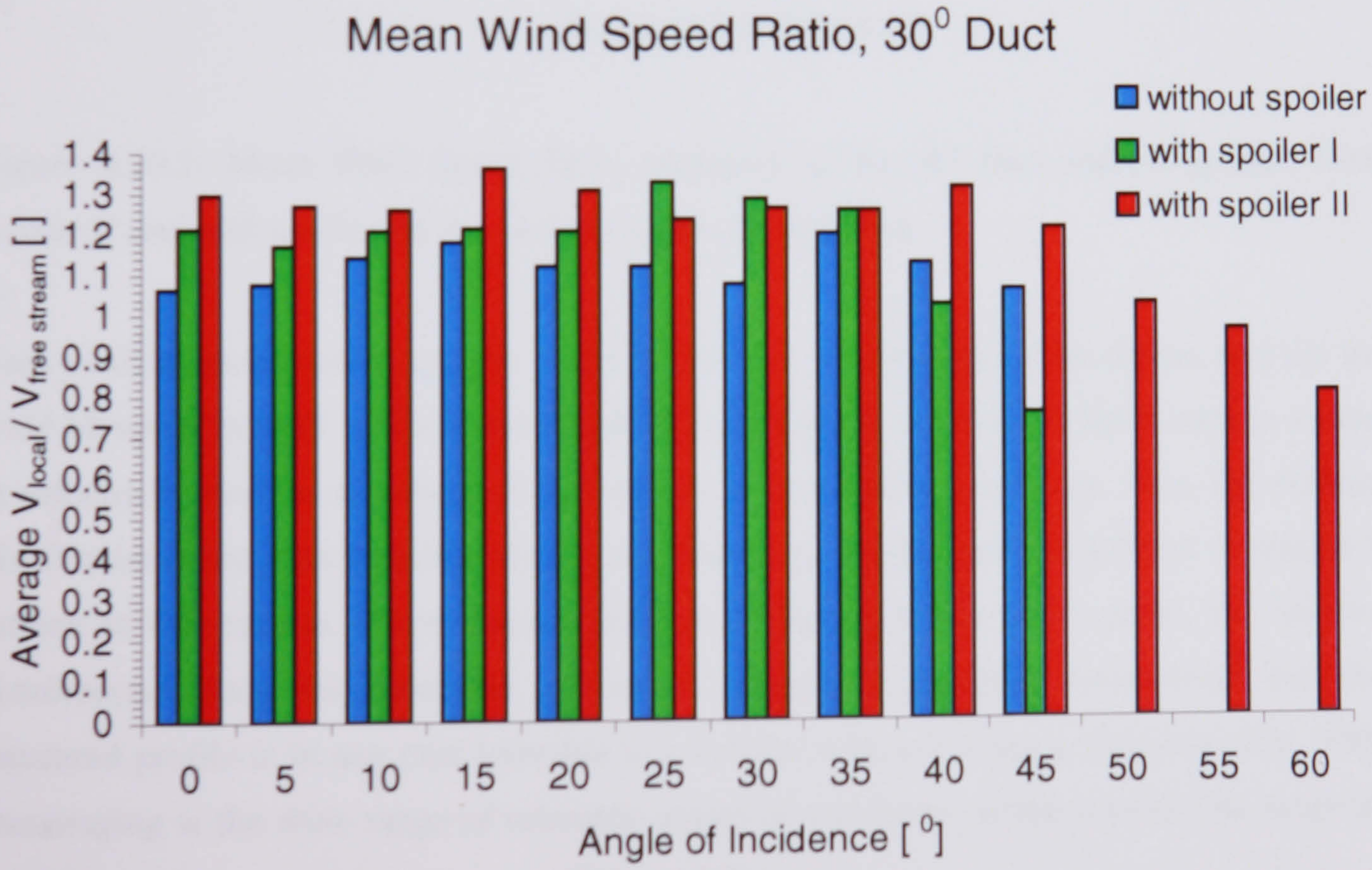

Figure 4.10.1: Mean Wind Speed Ratio measured in the 30° duct without spoiler, with spoiler I and with spoiler II, for various angles of incidence.

According to the convention of angles of incidence, one should bear in mind that 10 to 15° anti-clockwise seems to approximate to the wind direction 'normal' to the façade.

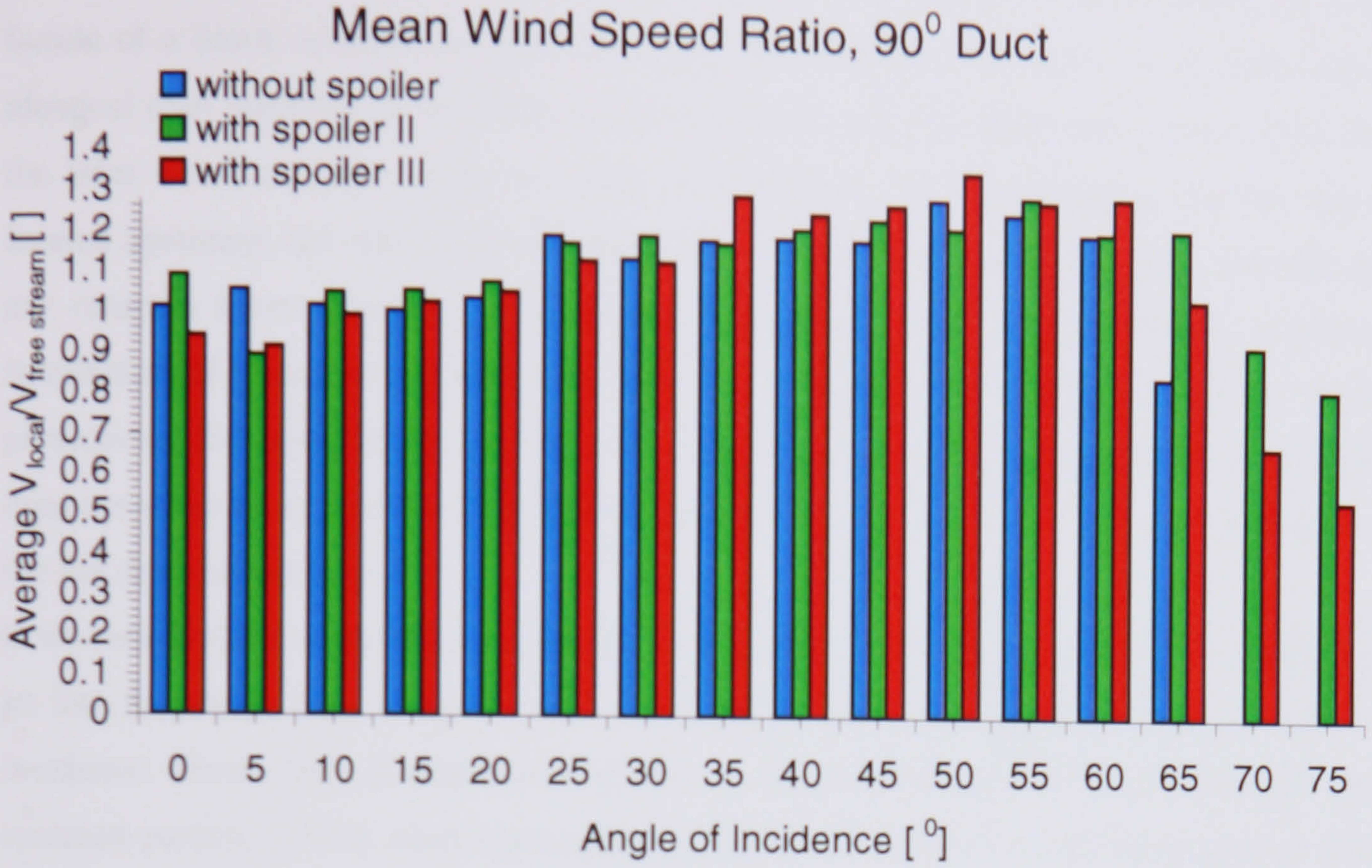

Figure 4.10.2: Mean Wind Speed Ratio measured in the 90° duct without spoiler, with spoiler II and with spoiler III, for various angles of incidence.

Each configuration reaches its best performance at a certain angle of incidence, and not for wind blowing 'normal' towards the facade. Exceeding this angle leads fairly soon to a drop in velocity beyond the threshold of the velocity in free stream conditions. Also, the velocity distribution in the duct becomes highly unsymmetrical, which makes it difficult to operate a turbine in this regime. When there is increased velocity in the outlet plane, the velocity distributions along the centerline are never uniform or complete symmetrical, but the measured profile is in any case tolerable to a turbine with soft stalling characteristics. Very encouraging is the wide range of tolerable angles of incidence, which exceeds the range of ± 30° for the free standing device (see Chapter 2.8).

In certain conditions, the 30° duct seems to induce a swirl which passes through the duct after less than one revolution. In the 90° duct, flow separation takes place, but the overall picture is not as clear. A flow formation develops in both ducts which remains stable up to a critical angle of incidence, with induced high velocities in the outlet plane.

Wind approaching the façade at an angle of incidence creates on the windward side next to the inlet a low pressure zone, whereas the pressure on the leeward side either exceeds or at least keeps the value of pressure, which is measured along the vertical centerline at the facade of a block without duct for this angle of incidence. This seems to indicate that an identical duct installed in the close neighborhood would not experience a lower pressure at the inlet. For the model under an angle of incidence, we can categorize the one duct as located upstream, the other as downstream along the wall roof edge. The one upstream does not create a lower pressure on its downstream side, which would therefore enable the installation of a number of ducts with turbines in a row. There might be a overall drop in pressure on the front facade, but this will be an effect of the ensemble. But this conclusion does not allow us to examine flow rates through the ducts, as it does not take the situation on the flat roof into account.

If we look at the corresponding situation at the outlet on the flat roof, the entrainment of the jet into the vortex flow along the wall roof edge has different impact for different angles of incidence. Here, each configuration shows a specific characteristic, but there are some common patterns. If the wind approaches normal to the façade, no configuration any shows significant loss of suction at the flat roof edge and the negative pressure remains uniform around the outlet. With rising angles of incidence, the ducts induce a drop in suction downstream on the leeward side and a rise in suction on the windward side of the outlet. But the minimum downstream suction is still of similar magnitude to what is created by wind normal to the façade.

Towards larger angles of incidence, the situation reverses and the suction downstream exceeds the suction windward. The angle of incidence where this transition takes place depends perhaps on the size of the duct or the strength of the jet entrainment. Taking both together, it seems to be that it depends on the absolute mass flow entrainment. However, we did not perform measurements to determine the mass flow.

There is no clear relation between the angle of incidence where maximal wind speed is induced, and the differential pressure to windward and leeward of the duct outlet. Maximal induced wind speed was observed at maximal negative differential pressure, maximal positive differential pressure or nearly zero differential pressure. This may be caused by the different swirl characteristics of the entraining inflows. It could be better observed with more sophisticated experimental facilities, such as three channel hot wire anemometry or laser doppler anemometry.

The effect of the flow entrainment at the outlet on the surrounding flow and pressure field has an essential influence on the performance of an identical duct in the neighborhood. In some cases for the 90° duct, the second duct would even benefit from the first. In the worst case for the 30° duct, the second duct does not experience increased suction at larger angles of incidence.

The relation between the pressure difference at inlet and outlet and the actual flow through the duct is in particular at large angles of incidence fairly complex. Induced high velocities have been measured in the outlet plane, whereas the inflow velocities were below the free stream velocity.

In order to get a clear picture of the flow situation at several ducts, it is necessary to test combinations of ducts at various spacing.

Also, flow and pressure fields may change significantly if a real turbine is operating in a larger scale prototype. This will affect the swirl component and the momentum of duct outflow and subsequent entrainment.

The measured wind speed ratio along the centerline at the duct outlet is taken into account, in order to present a power prediction model (in Chapter 8) using one dimensional streamline theory for the wind turbine. The interpretation of the measured speeds as massflows is not accurate, in particular as the integrated profiles at the inlet and the outlet do not coincide. However it is possible to estimate flow rates and to get a rough estimation of the likely performance.

5. Theoretical Background of Computational Fluid Dynamics

5.1. The Governing Equation of Transport

The governing equations of fluid flow are based on the conservation laws of physics. This involves the conservation of mass, momentum and energy, Newton's second law of motion and thermodynamic equations of state. Mass balance for a certain fluid element in the flow field means, that the rate of increase of mass of the fluid element equals the net rate of massflow into the fluid element. With the density ρ as mass per unit volume, it is written as

$$\frac{\partial \rho}{\partial t} = -div(\rho\vec{u}) \tag{5.1.1}$$

The partial time derivative is a rate of change in time. The divergence expresses the net massflow out of the fluid element and describes the convection, a scalar value. It is zero for the steady case (trivial case), and for an incompressible fluid. For an incompressible fluid, convection can be described by the rate of change of other free variables, for example the temperature. Here, an equation of state applies. In general, divergence free fields contain no sources or sinks.

The rate of change for a general scalar flow field property ϕ per unit volume following a fluid particle in the flow of homogeneous density ρ and mean velocity **u** is given by its substantive derivative.

$$\rho\frac{D\phi}{Dt} = \rho\left(\frac{\partial \phi}{\partial t} + \vec{u}grad\phi\right) \tag{5.1.2}$$

The gradient of ϕ is the vector which describes the change of the value of the scalar property of the fluid particle moving in the flow, concerning the three coordinates in space. Examples of this scalar property are energy or each single component of the vector of momentum.

If we consider again the fluid element in the flow field, which is penetrated by the flow and does not move within the field like the fluid particle, the generalisation of the rate of change for a conserved flow property is

$$\frac{\partial(\rho\phi)}{\partial t} + div(\rho\phi\vec{u}) = \rho\frac{D\phi}{Dt} \tag{5.1.3}$$

$$\Rightarrow \qquad \phi\left(\frac{\partial \rho}{\partial t} + div\rho\vec{u}\right) + \rho\left(\frac{\partial \phi}{\partial t} + \vec{u}grad\phi\right) = \rho\frac{D\phi}{Dt}$$

For a small fluid element, the flow density ρ in this control volume is assumed as constant.

$$\Rightarrow \qquad \phi\frac{\partial\rho}{\partial t}+\rho\frac{\partial\phi}{\partial t}+\rho\phi\, div\, u+\rho \vec{u}\, grad\phi+\phi\vec{u}\, grad\rho=\rho\frac{D\phi}{Dt} \tag{5.1.4}$$

As the first term equals zero by virtue of mass conservation, the rate of increase of a fluid property ϕ of a fluid particle following the flow, is determined through the balance of the rate of increase of the fluid property ϕ of this certain fluid element and the net rate of flow of ϕ out of the element. In detail, this states for the three components of momentum and for the energy

$$\rho\frac{Du}{Dt}=\frac{\partial(\rho u)}{\partial t}+div(\rho u\vec{u}) \tag{5.1.5}$$

$$\rho\frac{Dv}{Dt}=\frac{\partial(\rho v)}{\partial t}+div(\rho v\vec{u}) \tag{5.1.6}$$

$$\rho\frac{Dw}{Dt}=\frac{\partial(\rho w)}{\partial t}+div(\rho w\vec{u}) \tag{5.1.7}$$

$$\rho\frac{DE}{Dt}=\frac{\partial(\rho E)}{\partial t}+div(\rho E\vec{u}) \tag{5.1.8}$$

According to Newton's second law of motion, we consider the rate of change of momentum in the flow by highlighting the sum of all contributing forces. We distinguish between two types of forces, body forces and surface forces. Body forces interact in between volumes, and the intensity of the forces are measured as force/volume. Examples are the forces with the potential ∝ 1/r like the Lorentz forces or the Gravity, and the related forces caused by inertia like centrifugal, centripetal, buoyancy and the virtual Coriolis force. The force itself is modelled as a vector interacting between points (for example 'centers of gravity') to enable analytical understanding. Surface forces interact with surfaces, and they are measured as force / plane area. Examples are pressure forces, viscous forces (stresses), capillary forces and surface tension. Each force on each surface has itself three spatial components as the vector of force may have many orientations relative to the surface. In this way, surface forces are represented by a tensor τ of second order with 3 x 3 components.

$$\hat{\tau} = \begin{pmatrix} \tau_{xx} & \tau_{xy} & \tau_{xz} \\ \tau_{yx} & \tau_{yy} & \tau_{yz} \\ \tau_{zx} & \tau_{zy} & \tau_{zz} \end{pmatrix} \qquad (5.1.9)$$

The usual suffix notation τ_{ij} indicates the stress force per unit plane area in the i-direction towards a plane normal to the j-direction (Figure 5.1.1).

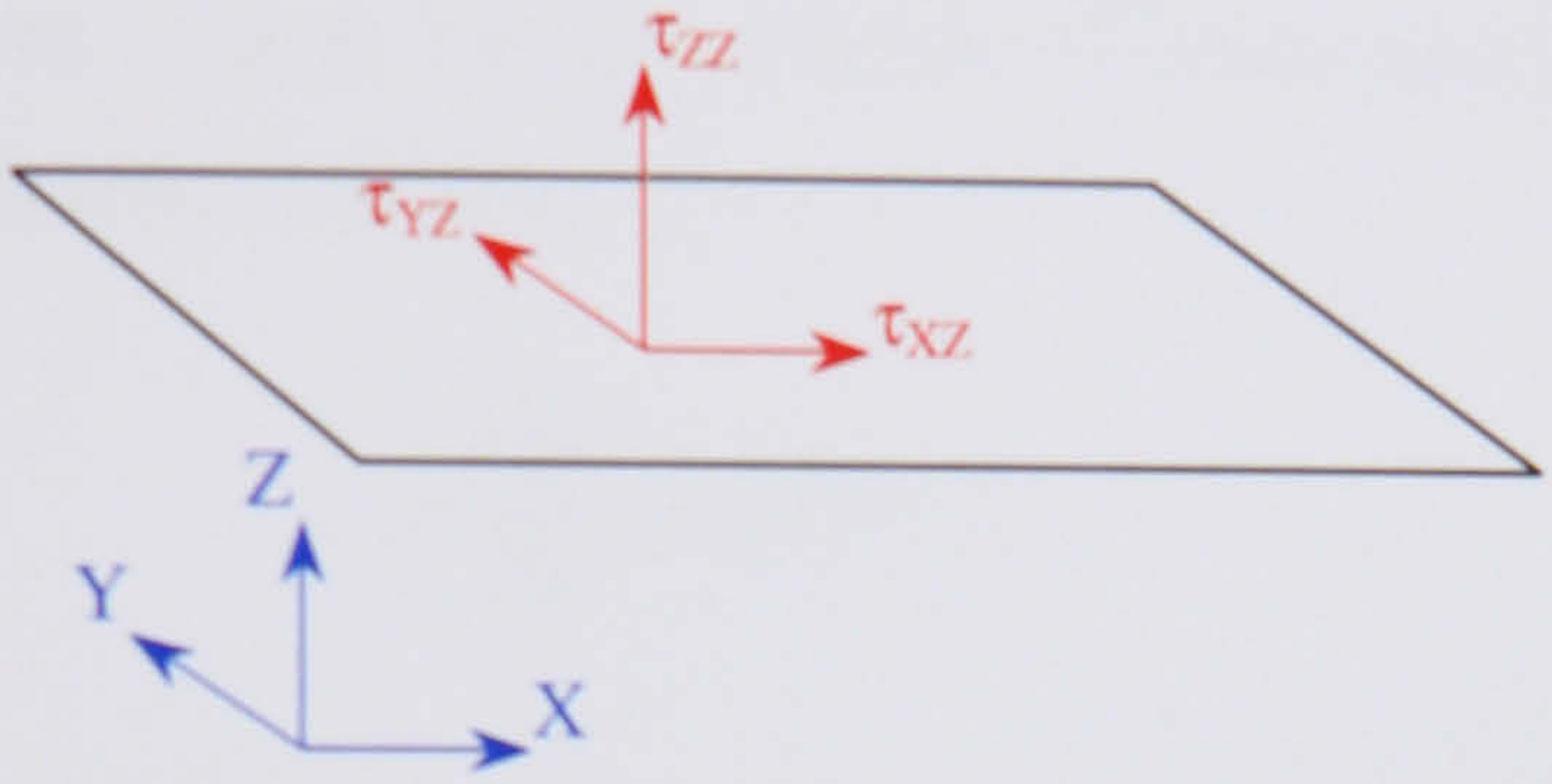

Figure 5.1.1: Stress components on surface

This tensor is symmetrical ($\tau_{ij} = \tau_{ji}$), so 6 components are independent. The non-diagonal components are acting tangentially to the surface and are viscous stress components. The diagonal stress components are normal to the surface and can be interpreted as internal pressure components of the fluid element. If we take the external pressure, the pressure in the flow field around the fluid element, into account, which acts towards each surface, the diagonal components of the stress tensor modify, therefore

$$\hat{\tau} = \begin{pmatrix} \tau_{xx} - p & \tau_{xy} & \tau_{xz} \\ \tau_{yx} & \tau_{yy} - p & \tau_{yz} \\ \tau_{zx} & \tau_{zy} & \tau_{zz} - p \end{pmatrix} \qquad (5.1.10)$$

In case there is also a certain body force **S** interacting with the volume of the fluid element, the sum of forces seen by the fluid element becomes with respect to Gauss rule:

$$\vec{F} = \oiint_{\vec{s}} \hat{\tau} d^2\vec{s} + \iiint \vec{S} d^3\vec{r} = \iiint div\, \hat{\tau} d^3\vec{r} + \iiint \vec{S} d^3\vec{r} = \iiint (div\, \hat{\tau} + \vec{S}) d^3\vec{r} \qquad (5.1.11)$$

The divergence of the tensor is simply a vector with three components, and each one consists of the sum of the partial derivatives of the rows or columns of the tensor accordingly.

$$(div\,\hat{\tau})_i = \sum_j \frac{\partial \tau_{ij}}{\partial x_j} = \sum_j \frac{\partial \tau_{ji}}{\partial x_j} \qquad (5.1.12)$$

In the limit of small volumes,

$$div\,\hat{\tau} = \frac{\dot{F}_{surface}}{V} \qquad (5.1.13)$$

which is the force acting on a fluid element caused by stress and pressure differences. Therefore, the momentum equation becomes

$$\rho \frac{D\vec{u}}{Dt} = div\,\hat{\tau} + \vec{S} \qquad (5.1.14)$$

The contributing force S is regarded as 'Source' term, since the related field is not source / sink free (divergence free). For example, the gravity field includes the 'masspoint', the Lorentz field includes the charge, here the flow field includes a source of mass flow. In equilibrium conditions, the left hand side of the momentum equation equals zero.

Fields of stress add up with normal force fields simply component by component, therefore

$$\rho \frac{Du}{Dt} = \frac{\partial(-p+\tau_{xx})}{\partial x} + \frac{\partial \tau_{yx}}{\partial y} + \frac{\partial \tau_{zx}}{\partial z} + S_x \qquad (5.1.15)$$

$$\rho \frac{Dv}{Dt} = \frac{\partial \tau_{xy}}{\partial x} + \frac{\partial(-p+\tau_{yy})}{\partial y} + \frac{\partial \tau_{zy}}{\partial z} + S_y \qquad (5.1.16)$$

$$\rho \frac{Dw}{Dt} = \frac{\partial \tau_{xz}}{\partial x} + \frac{\partial \tau_{yz}}{\partial y} + \frac{\partial(-p+\tau_{zz})}{\partial z} + S_z \qquad (5.1.17)$$

The rate of change of momentum is equal to the total force in each direction due to surface stresses, plus the rate of increase of momentum due to sources.

In a Newtonian fluid the viscous stresses are proportional to the rates of deformation. The dynamic viscosity μ relates stresses to linear deformation, the second viscosity λ relates stresses to volumetric deformation. For the diagonal components we have

$$\tau_{xx} = 2\mu\frac{\partial u}{\partial x} + \lambda div\bar{u} \tag{5.1.18}$$

$$\tau_{yy} = 2\mu\frac{\partial v}{\partial y} + \lambda div\bar{u} \tag{5.1.19}$$

$$\tau_{zz} = 2\mu\frac{\partial w}{\partial z} + \lambda div\bar{u} \tag{5.1.20}$$

and for the nondiagonal components the shearing linear deformations are

$$\tau_{xy} = \tau_{yx} = \mu\left(\frac{\partial u}{\partial y} + \frac{\partial v}{\partial x}\right) \tag{5.1.21}$$

$$\tau_{xz} = \tau_{zx} = \mu\left(\frac{\partial u}{\partial z} + \frac{\partial w}{\partial x}\right) \tag{5.1.22}$$

$$\tau_{yz} = \tau_{zy} = \mu\left(\frac{\partial v}{\partial z} + \frac{\partial w}{\partial y}\right) \tag{5.1.23}$$

For incompressible liquids, div **u** = 0 and the volumetric deformation does not play any role. For gases, a good approximation is $\lambda=2/3\ \mu$ (Schlichting 1965). Substitution of the above shear stresses into the momentum equations (5.1.15 to 5.1.17) yields to the Navier-Stokes equations (5.1.24 to 5.1.26)

$$\rho\frac{Du}{Dt} = -\frac{\partial p}{\partial x} + \frac{\partial}{\partial x}\left(2\mu\frac{\partial u}{\partial x} + \lambda div\bar{u}\right) + \frac{\partial}{\partial y}\left(\mu\left(\frac{\partial u}{\partial y} + \frac{\partial v}{\partial x}\right)\right) + \frac{\partial}{\partial z}\left(\mu\left(\frac{\partial u}{\partial z} + \frac{\partial w}{\partial x}\right)\right) + S_x$$

$$\rho\frac{Dv}{Dt} = -\frac{\partial p}{\partial y} + \frac{\partial}{\partial x}\left(\mu\left(\frac{\partial u}{\partial y} + \frac{\partial v}{\partial x}\right)\right) + \frac{\partial}{\partial y}\left(2\mu\frac{\partial v}{\partial y} + \lambda div\bar{u}\right) + \frac{\partial}{\partial z}\left(\mu\left(\frac{\partial v}{\partial z} + \frac{\partial w}{\partial y}\right)\right) + S_y$$

$$\rho\frac{Dw}{Dt} = -\frac{\partial p}{\partial z} + \frac{\partial}{\partial x}\left(\mu\left(\frac{\partial u}{\partial z} + \frac{\partial w}{\partial x}\right)\right) + \frac{\partial}{\partial y}\left(\mu\left(\frac{\partial v}{\partial z} + \frac{\partial w}{\partial y}\right)\right) + \frac{\partial}{\partial z}\left(2\mu\frac{\partial w}{\partial z} + \lambda div\bar{u}\right) + S_z$$

After rearrangement of the terms and including small contributions to the viscous stress terms in the source term, the Navier-Stokes equations simplify as follows:

$$\rho\frac{Du}{Dt} = -\frac{\partial p}{\partial x} + div(\mu gradu\ ) + S_x \tag{5.1.27}$$

$$\rho\frac{Dv}{Dt} = -\frac{\partial p}{\partial y} + div(\mu gradv\ ) + S_y \tag{5.1.28}$$

$$\rho\frac{Dw}{Dt} = -\frac{\partial p}{\partial z} + div(\mu gradw\ ) + S_z \tag{5.1.29}$$

Combining the conservation equation for a fluid element (5.1.3) with the Navier-Stokes equations (5.1.27 to 5.1.29), a general transport equation for a transported flow property φ is found as

$$\rho \frac{D\phi}{Dt} = \frac{\partial(\rho\phi)}{\partial t} + div(\rho\phi u) = div(\Gamma grad\phi) + S_{\phi} \tag{5.1.30}$$

It states that the rate of increase of φ for the fluid element plus the net rate of flow of φ out of the fluid element due to convection is equal to the rate of increase of φ due to diffusion and sources. The coefficient of diffusion is Γ.

5.2. The Turbulence Model

The influence of turbulent fluctuations is taken into account by introduction of a time-varying fluctuating component $\varphi'(t)$. This fluctuating component perturbates the mean flow property ϕ, and the general variable is $\varphi(t) = \phi + \varphi'(t)$.

Similar, the velocity decomposes as $u(t) = U + u'(t)$. The turbulent kinetic energy per unit mass is defined as

$$k' = \frac{1}{2}\left(< u'^2 >_t + < v'^2 >_t + < w'^2 >_t\right) \qquad (5.2.1)$$

with the time averaged values

$$< \varphi' >_t = \frac{1}{\Delta t}\int^{\Delta t} \varphi'(t)dt \equiv 0 \qquad \text{and} \qquad < \varphi'^2 >_t = \frac{1}{\Delta t}\int_0^{\Delta t} \varphi'(t)^2 dt \geq 0 \qquad (5.2.2)$$

The turbulence intensity T referring to a mean flow velocity U_{ref} is

$$T = \frac{\sqrt{2/3 \cdot k}}{U_{ref}} \qquad (5.2.3)$$

Note that turbulent fluctuations are always three dimensional. If we insert the decomposed flow properties in the Navier-Stokes equations (5.1.27 to 5.1.29), we find the Reynolds equations (5.2.4 to 5.2.6)

$$\frac{\partial(\rho U)}{\partial t} + div(\rho U\vec{U}) = -\frac{\partial P}{\partial x} + div(\mu grad U) + \left[-\frac{\partial(\rho < u'^2 >_t}{\partial x} - \frac{\partial(\rho < u'v' >_t}{\partial y} - \frac{\partial(\rho < u'w' >_t}{\partial z}\right] + S_x$$

$$\frac{\partial(\rho V)}{\partial t} + div(\rho V\vec{U}) = -\frac{\partial P}{\partial x} + div(\mu grad V) + \left[-\frac{\partial(\rho < u'v' >_t}{\partial y} - \frac{\partial(\rho < v'^2 >_t}{\partial x} - \frac{\partial(\rho < v'w' >_t}{\partial z}\right] + S_y$$

$$\frac{\partial(\rho W)}{\partial t} + div(\rho W\vec{U}) = -\frac{\partial P}{\partial x} + div(\mu grad W) + \left[-\frac{\partial(\rho < u'w' >_t}{\partial y} - \frac{\partial(\rho < v'w' >_t}{\partial z} - \frac{\partial(\rho < w'^2 >_t}{\partial x}\right] + S_z$$

The scalar transport equation becomes (5.2.7)

$$\frac{\partial(\rho\phi)}{\partial t} + div(\rho\phi\vec{U}) = div(\Gamma_\phi grad\phi) + \left[-\frac{\partial(\rho < u'\varphi' >_t)}{\partial x} - \frac{\partial(\rho < v'\varphi' >_t)}{\partial y} - \frac{\partial(\rho < w'\varphi' >_t)}{\partial z} + S_\phi\right]$$

Comparing (5.2.7) with the transport equation of a general fluid property (5.1.30) we may identify the additional Reynolds stress tensor. It consist of three normal stresses and six shear stresses:

$$\tau_{xx} = -\rho < u'^2 >_t \qquad (5.2.8)$$

$$\tau_{yy} = -\rho < v'^2 >_t \qquad (5.2.9)$$

$$\tau_{zz} = -\rho < w'^2 >_t \qquad (5.2.10)$$

$$\tau_{xy} = \tau_{yx} = -\rho < u'v' >_t \qquad (5.2.11)$$

$$\tau_{xz} = \tau_{zx} = -\rho < u'w' >_t \qquad (5.2.12)$$

$$\tau_{yz} = \tau_{zy} = -\rho < v'w' >_t \qquad (5.2.13)$$

In turbulent flow these turbulent shear stresses are large compared to viscous shear stresses. Including all stress terms, the number of variables exceeds the number of equations. This is known as the closure problem and states the need for turbulence modelling. The main task of turbulence modelling is to develop computational procedures to predict the Reynolds stress terms and the transport terms.

The Boussinesq approximation links the Reynolds stresses linearly to the mean rates of deformation analogous to (5.1.21) to (5.1.23), including the turbulent viscosity (or sometimes eddy viscosity) μ_t or the kinematic turbulent viscosity $\nu_t=\mu_t/\rho$:

$$\tau_{ij} = -\rho < u'_i u'_j >= \mu_t \left(\frac{\partial U_i}{\partial x_j} + \frac{\partial U_j}{\partial x_i} \right) \qquad (5.2.14)$$

The turbulent transport of a general scalar property is modelled as turbulent diffusion

$$-\rho < u_i'\varphi' >= \Gamma_t \frac{\partial \phi}{\partial x_i} \qquad (5.2.15)$$

where Γ_t is the turbulent diffusivity. The turbulent Schmidt number is defined as $\sigma_t=\mu_t/\Gamma_t$, characterizing the mixing process in a turbulent flow field. This ratio is often nearly constant and equal to 1, but in some cases (for example the atmospheric boundary layer in the urban area) the mixing process might be anisotropic and the turbulent Schmidt number then depends on the spatial direction.

Turbulence levels and turbulent stresses vary from point to point in the flow. Assuming that the turbulent viscosity μ_t is isotropic, the k-ε model defines two further transport equations, one for the turbulent kinetic energy k (5.2.1) and a second for ε, the rate of dissipation of the turbulent kinetic energy. The turbulent kinetic energy represents the sum over the diagonal elements (5.2.8) to (5.2.10) in the Reynolds stress tensor, which are according to Boussinesq (5.2.14) linked to the rate of deformation caused by the turbulent fluctuating component of momentum. The kinetic energy decomposes into the mean kinetic energy K and the turbulent kinetic energy k'

$$<k(t)>_t = K + k' = \frac{1}{2}\left(U'^2 + V'^2 + W'^2\right) + \frac{1}{2}\left(<u'^2>_t + <v'^2>_t + <w'^2>_t\right) \qquad (5.2.16)$$

Consistent with this model, the rate of deformation of a fluid element in a turbulent flow field decomposes into a mean and a fluctuating component,

$$\hat{e}_{ij}(t) = \hat{E}_{ij} + \hat{e}'_{ij} \qquad (5.2.17)$$

as a symmetrical tensor according to the three spatial directions of the deformation at each surface of the fluid element. Analogous to a vector, two tensors add component by component.

$$\hat{e}_{ij}(t) = \begin{pmatrix} e_{xx} & e_{xy} & e_{xz} \\ e_{yx} & e_{yy} & e_{yz} \\ e_{zx} & e_{zy} & e_{zz} \end{pmatrix} = \begin{pmatrix} \frac{\partial U}{\partial x} & \frac{1}{2}\left(\frac{\partial U}{\partial y} + \frac{\partial V}{\partial x}\right) & \frac{1}{2}\left(\frac{\partial U}{\partial z} + \frac{\partial W}{\partial x}\right) \\ \frac{1}{2}\left(\frac{\partial U}{\partial y} + \frac{\partial V}{\partial x}\right) & \frac{\partial V}{\partial y} & \frac{1}{2}\left(\frac{\partial V}{\partial z} + \frac{\partial W}{\partial y}\right) \\ \frac{1}{2}\left(\frac{\partial U}{\partial z} + \frac{\partial W}{\partial x}\right) & \frac{1}{2}\left(\frac{\partial V}{\partial z} + \frac{\partial W}{\partial y}\right) & \frac{\partial W}{\partial z} \end{pmatrix} +$$

$$\begin{pmatrix} \frac{\partial u'(t)}{\partial x} & \frac{1}{2}\left(\frac{\partial u'(t)}{\partial y} + \frac{\partial v'(t)}{\partial x}\right) & \frac{1}{2}\left(\frac{\partial u'(t)}{\partial z} + \frac{\partial w'(t)}{\partial x}\right) \\ \frac{1}{2}\left(\frac{\partial u'(t)}{\partial y} + \frac{\partial v'(t)}{\partial x}\right) & \frac{\partial v'(t)}{\partial y} & \frac{1}{2}\left(\frac{\partial v'(t)}{\partial z} + \frac{\partial w'(t)}{\partial y}\right) \\ \frac{1}{2}\left(\frac{\partial u'(t)}{\partial z} + \frac{\partial w'(t)}{\partial x}\right) & \frac{1}{2}\left(\frac{\partial v'(t)}{\partial z} + \frac{\partial w'(t)}{\partial y}\right) & \frac{\partial w'(t)}{\partial z} \end{pmatrix}$$

$$= \begin{pmatrix} \frac{\partial U}{\partial x}+\frac{\partial u(t)}{\partial x} & \frac{1}{2}\left(\frac{\partial U}{\partial y}+\frac{\partial V}{\partial x}\right)+\frac{1}{2}\left(\frac{\partial u(t)}{\partial y}+\frac{\partial v(t)}{\partial x}\right) & \frac{1}{2}\left(\frac{\partial U}{\partial z}+\frac{\partial W}{\partial x}\right)+\frac{1}{2}\left(\frac{\partial u(t)}{\partial z}+\frac{\partial w(t)}{\partial x}\right) \\ \frac{1}{2}\left(\frac{\partial U}{\partial y}+\frac{\partial V}{\partial x}\right)+\frac{1}{2}\left(\frac{\partial u(t)}{\partial y}+\frac{\partial v(t)}{\partial x}\right) & \frac{\partial V}{\partial y}+\frac{\partial v(t)}{\partial y} & \frac{1}{2}\left(\frac{\partial V}{\partial z}+\frac{\partial W}{\partial y}\right)+\frac{1}{2}\left(\frac{\partial v(t)}{\partial z}+\frac{\partial w(t)}{\partial y}\right) \\ \frac{1}{2}\left(\frac{\partial U}{\partial z}+\frac{\partial W}{\partial x}\right)+\frac{1}{2}\left(\frac{\partial u(t)}{\partial z}+\frac{\partial w(t)}{\partial x}\right) & \frac{1}{2}\left(\frac{\partial V}{\partial z}+\frac{\partial W}{\partial y}\right)+\frac{1}{2}\left(\frac{\partial v(t)}{\partial z}+\frac{\partial w(t)}{\partial y}\right) & \frac{\partial W}{\partial z}+\frac{\partial w(t)}{\partial z} \end{pmatrix} \tag{5.2.18}$$

A governing equation for the kinetic energy is obtained by multiplying the Reynolds equations (5.2.4 to 5.2.6) with the three components of momentum.

For the mean kinetic energy it states

$$\frac{\partial(\rho K)}{\partial t}+div(\rho K\vec{U}) = div(-P\vec{U}+2\mu\vec{U}\hat{E}_{ij}-\rho\vec{U}<u_i'u_j'>_t)-2\mu\hat{E}_{ij}\hat{E}_{ij}-\rho<u_i'u_j'>_t\hat{E}_{ij} \tag{5.2.19}$$

and in the same way for the turbulent kinetic energy

$$\frac{\partial(\rho k)}{\partial t}+div(\rho k\vec{U}) =$$

$$div(-<p'\vec{u}'>_t+2\mu<\vec{u}'\hat{e}_{ij}'>_t-\rho<\vec{u}'(u_i'u_j')>_t)-2\mu<\hat{e}_{ij}'\hat{e}_{ij}'>_t-\rho<u_i'u_j'>_t\hat{E}_{ij} \tag{5.2.20}$$

The individual terms in the transport equation for the kinetic energy (5.2.19 and 5.2.20) have the physical meaning as follows:

I : rate of change of transported property (here kinetic energy)

II: transport by convection

III: transport by pressure

IV: transport by viscous stresses

V: transport by Reynolds stresses

VI: rate of dissipation

VII: turbulence production

Note, that the scalar product of two tensors is a scalar, in complete analogy to vectors

$$\hat{E}_{ij}\hat{E}_{ij} = \sum_{i=1}^{3}\sum_{j=1}^{3} e_{ij}e_{ij}$$

The linear vector function UE$_{ij}$ remains a line-vector by rules of matrix algebra:

$$\hat{U}\hat{E}_{ij} = \begin{pmatrix} ue_{xx} + ve_{yx} + we_{zx} \\ ue_{xy} + ve_{yy} + we_{zy} \\ ue_{xz} + ve_{yz} + we_{zz} \end{pmatrix}^{t}$$

The term (VI) determines the dissipation of kinetic energy caused by work of the turbulent eddies against the viscous stress. The rate of dissipation per unit mass is defined by

$$\varepsilon = 2\nu < \hat{e}_{ij}'\hat{e}_{ij}' >_{t} \qquad [\mathrm{m^2/s^3}] \qquad (5.2.21)$$

The standard k-ε model (Launder and Spalding 1974) simplifies the transport equations. The length scale for large scale turbulence is defined as

$$l = \frac{\sqrt[3]{k}}{\varepsilon} \quad (5.2.22)$$ with the turbulent eddy viscosity $$\mu_t = \rho C_\mu \frac{k^2}{\varepsilon} \qquad (5.2.23)$$

The turbulent kinetic energy k as well as the turbulent kinetic energy dissipation ε are treated as transported flow properties according to the transport equations

$$\frac{\partial(\rho k)}{\partial t} + div(\rho k\bar{U}) = div\left[\frac{\mu_t}{\sigma_k} grad k\right] + 2\mu_t E_{ij} - \rho\varepsilon \qquad (5.2.24)$$

$$\frac{\partial(\rho\varepsilon)}{\partial t} + div(\rho\varepsilon\bar{U}) = div\left[\frac{\mu_t}{\sigma_\varepsilon} grad\varepsilon\right] + C_{1\varepsilon}\frac{\varepsilon}{k}2\mu_t\hat{E}_{ij}\hat{E}_{ij} - C_{2\varepsilon}\rho\frac{\varepsilon^2}{k} \qquad (5.2.25)$$

The constants σ and C are adjustable.

The single terms in the transport equations have the physical meaning as follows:

I : rate of change of transported property (k or ε)

II: transport by convection

III: transport by diffusion

IV: rate of production of fluid property (k or ε)

V : rate of destruction of fluid property (k or ε)

The production and destruction of turbulent kinetic energy k is proportional to the production and destruction of the turbulent kinetic energy dissipation ε.

5.3. The Finite Volume Method

All numerical discretisation is based on the concept of finite differences. Numerical discretisation of a three dimensional field leads to finite volumes. The governing partial differential equations in Chapter 5.1 have been derived from the 'control volume' (or fluid element) model, and the flow properties which are measured for the control volume (values inside the control volume and rates of change across the control volume boundaries) determine the transport of a single fluid particle. In analytical language, the control volume decreases to infinitesimally small size, and the flow properties are functions of the spatial coordinate. In the language of numerical methods, the control volume reaches small but finite size, and the flow properties are homogeneous inside the finite control volume, so that the flow field changes only from the one finite control volume to the other. In this way, the whole flow domain disintegrates into finite volumes. Formal integration of the partial differential equation over the finite volume (and for the transient case over a finite time step as well) discretizes the differential equation into a set of linear scalar equations with coefficients and variables, which have to be determined through interpolation methods. As the calculation of the flow field is iterative, during each single iteration all the variables are populated with interpolated values.

The changing properties of the flow field follow the general transport equation (see Eq. 5.1.30). In order to discretize the equation, we integrate over a finite time step Δt and a finite control volume $\Delta V = dx\, dy\, dz$ (see Eq. 5.3.1). For turbulent flows, the equations are time averaged by means of the gradient transport hypothesis (see Eq. 5.2.15)

$$<\rho u \Phi>_t = -\sigma_t \operatorname{grad} \Phi$$

with the turbulent exchange coefficient σ_t.

It is presumed that the time over which the averaging is made is long compared to the time scale of the turbulent motion but small compared with the time scale of the transient mean flow.

$$\begin{aligned}
&\int_{\Delta t}\frac{\partial}{\partial t}\int_{\Delta V}\rho\phi dV dt+\int_{\Delta t}\oiint_{A}\rho\phi\vec{u}d\vec{A}dt=\int_{\Delta t}\oiint_{A}\Gamma grad\phi d\vec{A}dt+\int_{\Delta t}\int_{\Delta V}S_{\Phi}dVdt\\
&\Rightarrow\int_{\Delta V}\left|\rho\phi dV\right|_{t}^{t+\Delta t}+\Delta t\oiint_{A}\left|\rho\phi\vec{u}d\vec{A}\right|_{t}^{t+\Delta t}=\Delta t\oiint_{A}\left|\Gamma grad\phi d\vec{A}\right|_{t}^{t+\Delta t}+\Delta t\int_{\Delta V}\left|S_{\phi}dV\right|_{t}^{t+\Delta t}\\
&\Rightarrow\frac{1}{\Delta t}\int_{\Delta V}\left|\rho\phi dV\right|_{t}^{t+\Delta t}+\oiint_{A}\left|\rho\phi\vec{u}d\vec{A}\right|_{t}^{t+\Delta t}=\oiint_{A}\left|\Gamma grad\phi d\vec{A}\right|_{t}^{t+\Delta t}+\int_{\Delta V}\left|S_{\phi}dV\right|_{t}^{t+\Delta t}\\
&\Rightarrow\frac{\left|\rho\phi\Delta V\right|_{t+\Delta t}-\left|\rho\phi\Delta V\right|_{t}}{\Delta t}+\oiint_{A}\left|\rho\phi\vec{u}d\vec{A}\right|_{t+\Delta t}=\oiint_{A}\left|\Gamma grad\phi dA\right|_{t+\Delta t}+\left|S_{\phi}\Delta V\right|_{t+\Delta t}
\end{aligned}\tag{5.3.1}$$

The transient term has to be evaluated at the start t = t_0 and at the end t = t_0 + Δt of the time interval. In the terms of convection, diffusion and source, the new values (at t = t_0 + Δt , the end of the time interval) are supposed to prevail throughout the whole time interval. This time discretisation scheme is called 'fully implicit upwinding', a forward marching approach which is the default scheme in PHOENICS.

To evaluate the closed surface integration for non-orthogonal grids and cells with curved faces is a complex approach. The projection of the normal vector for each cell face has to be taken into account in order to capture all contributions to the flow in a certain direction. Curved surfaces are therefore disintegrated into small plane areas. This yields to a huge amount of terms and variables in the discretized equations. For the cube (Figures 5.3.1 and 5.3.2) it states (Eq. 5.3.2-5.3.4)

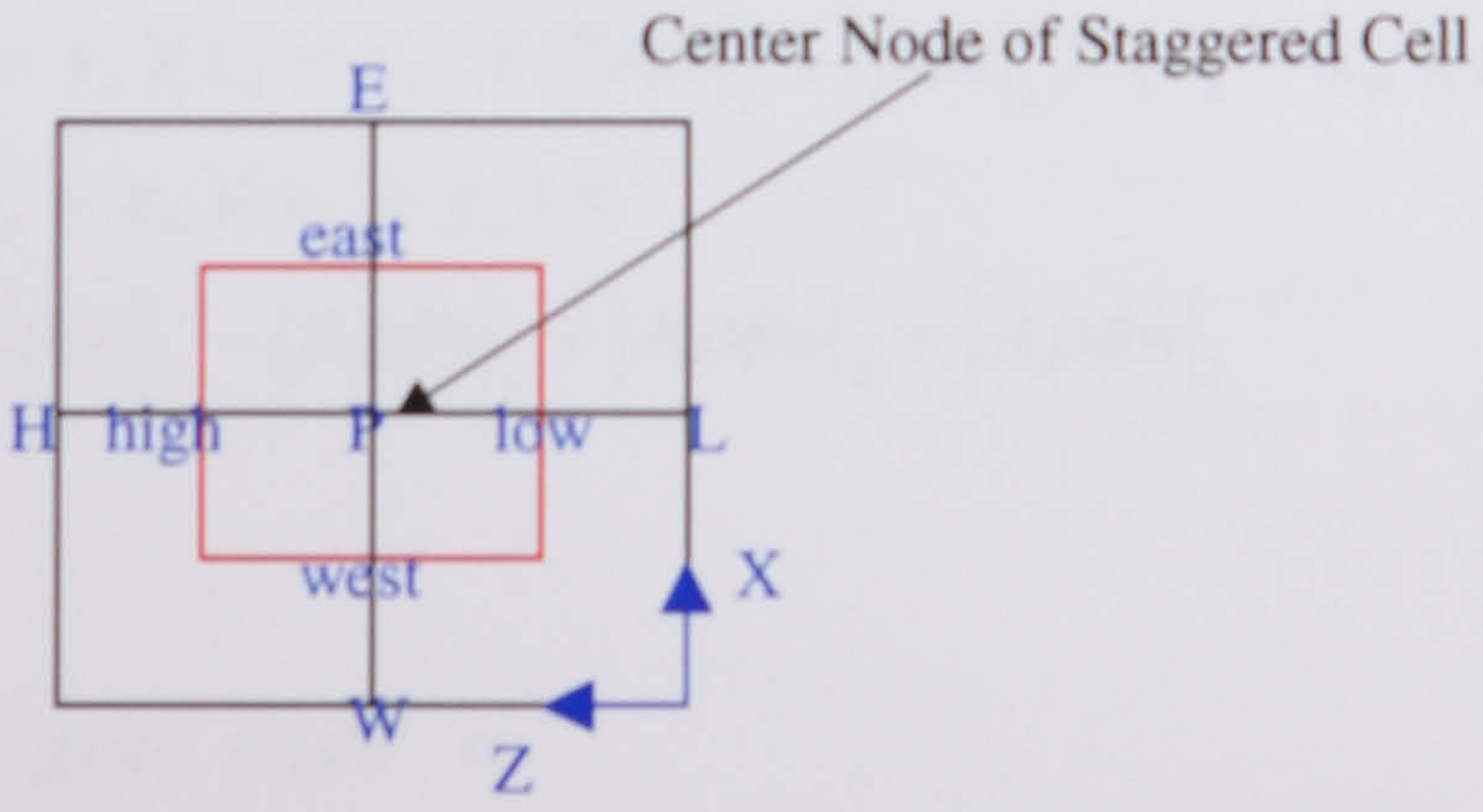

Figure 5.3.1: View from the top of Figure 5.3.2

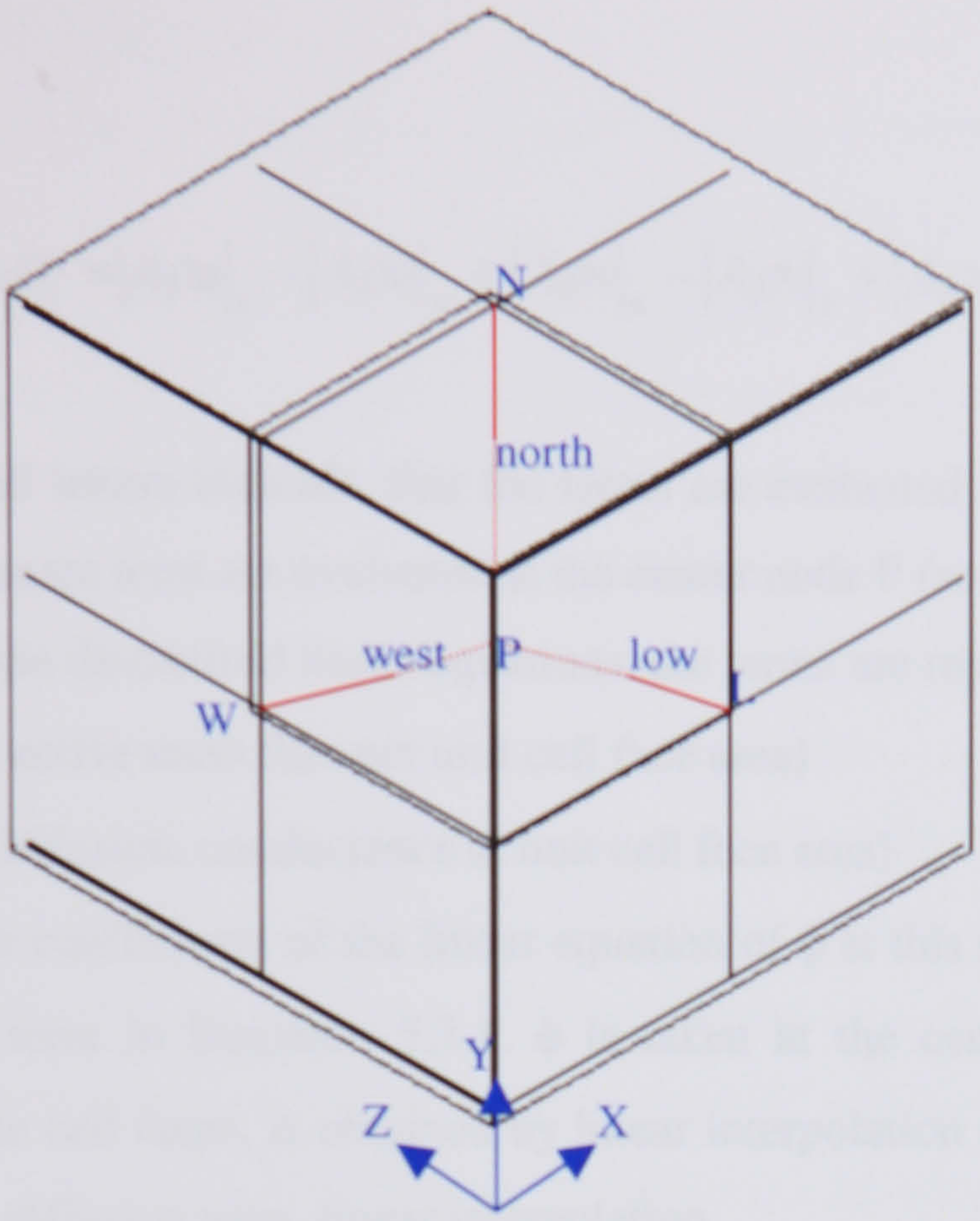

Figure 5.3.2: Convention of walls, nodes and coordinate directions for the cuboid cell, staggered grid

Convection:

$$\oiint_{\Delta A} \rho\phi\vec{u}d\vec{A} = \int_{\Delta V} div(\rho\phi\vec{u})dV = \int_{x_w}^{x_e}\int_{y_s}^{y_n}\int_{z_l}^{z_h}\left[\frac{\partial(\rho\phi u)}{\partial x} + \frac{\partial(\rho\phi v)}{\partial y} + \frac{\partial(\rho\phi w)}{\partial z}\right]dxdydz =$$

$$\int_{y_s}^{y_n}\int_{z_l}^{z_h}\left|\partial(\rho\phi u)\right|_w^e dydz + \int_{x_w}^{x_e}\int_{z_l}^{z_h}\left|\partial(\rho\phi v)\right|_s^n dxdz + \int_{x_w}^{x_e}\int_{y_s}^{y_n}\left|\partial(\rho\phi w)\right|_l^h dydy =$$

$$(\left|\rho\phi u\right|_e - \left|\rho\phi u\right|_w)\cdot(y_n - y_s)(z_h - z_l) + (\left|\rho\phi v\right|_n - \left|\rho\phi v\right|_s)\cdot(x_e - x_w)(z_h - z_l)$$

$$+ (\left|\rho\phi w\right|_h - \left|\rho\phi w\right|_l)\cdot(x_e - x_w)(y_n - y_s) =$$

$$\left|A\rho\phi u\right|_e - \left|A\rho\phi u\right|_w + \left|A\rho\phi v\right|_n - \left|A\rho\phi v\right|_s + \left|A\rho\phi w\right|_h - \left|A\rho\phi w\right|_l \tag{5.3.2}$$

Diffusion:

$$\oiint_{\Delta A} \Gamma grad\ \phi d\vec{A} = \int_{\Delta V} div\,(\Gamma grad\ \phi)dV =$$

$$\left|A\Gamma\frac{\partial}{\partial x}\phi\right|_e - \left|A\Gamma\frac{\partial}{\partial x}\phi\right|_w - \left|A\Gamma\frac{\partial}{\partial y}\phi\right|_n - \left|A\Gamma\frac{\partial}{\partial y}\phi\right|_s - \left|A\Gamma\frac{\partial}{\partial z}\phi\right|_h - \left|A\Gamma\frac{\partial}{\partial z}\phi\right|_l \tag{5.3.3}$$

Continuity:

$$\int_{\Delta V} div(\rho \vec{u})dV = \left|A\rho u\right|_e - \left|A\rho u\right|_w + \left|A\rho v\right|_n - \left|A\rho v\right|_s + \left|A\rho w\right|_h - \left|A\rho w\right|_l = 0 \qquad (5.3.4)$$

Indices of small letters indicate, that the terms are evaluated at the cell faces. The transient term and the source term are evaluated at the center node P (see Figures 5.3.1 and 5.3.2). In order to obtain discretised linear equations, the terms are represented by the variables

$F = \rho uA$ (convective mass flux per unit cell face area)

$D = A\Gamma / \delta x$ (diffusion, conductance at unit cell face area)

which form the coefficients of the linear equation of ϕ at this node. In the transient term and in the source term in Equation 5.3.1, ϕ is taken at the central node P. The variable D, evaluated at the cell faces, is obtained by linear interpolation of the values of ρ and Γ at the nodes. For the diffusion term, linear interpolation

$$\phi_a = \frac{1}{2}(\phi_P + \phi_E)$$

leads to the cell face value for the next cell in the staggered grid. For the convective term (see Eq. 5.3.2), different interpolation methods (discretisation schemes) are established depending on the nature of the flow (for example 'upwinding').

Inhomogeneous spatial distribution of scalar flow field properties like pressure, density, concentration of a certain species and temperature act as driving forces and change momentum. Applying a discretisation scheme, the transported scalar properties and the sources are calculated at the cell center nodes. The components of momentum are calculated at the faces. But the gradient of the scalar property over the cell is also calculated from its values at the faces, in the way that the scalar values at the faces are interpolated between the values of the cell center node and the neighbouring center node. Therefore, a regular scalar field pattern can cause significant error. The way out is to use a staggered grid superimposed to the original grid. The cell faces of the staggered grid fall together with the nodes of the original grid (see Figure 5.3.1). The momentum components are evaluated at the original grid cell faces and are inscribed at the staggered grid nodes. The scalar variables are evaluated at the nodes of the original grid, which therefore coincide with the cell faces of the staggered grid. So in the case of a regular scalar flow field pattern, the gradient of the scalar flow property, representing a source term, is very different from the result of a non staggered single mesh approach.

The alternative to the staggered-grid approach is the co-located velocity formulation. For non staggered calculations the momentum conservation equations are the same as for staggered grid arrangements, but the pressure gradients and the cell face velocities are calculated differently. Additional to the cell face velocity components U1, V1 and W1 there are the node velocity components UC1, VC1 and WC1. In general, cell face pressures for each direction and appropriate source terms are added in the discretised equations. An additional interpolation scheme defines all velocity components and the pressure in terms of nodal values. The co-located velocity algorithm is specially enhanced to treat interdomain links as they occur in multi-block grids and fine-grid embedding. In this sub-domain decomposition method, separate grids are linked together through common boundaries. Separate grids can be either the grids created for parts of the computational domain with complex geometry, or fine grids embedded into the coarse ones to increase resolution in certain areas as required. With the use of body fitted coordinate systems for each single sub-domain, a whole flow domain of high geometrical complexity can be composed including different grid densities.

5.4. The Discretisation Schemes

Any discretisation scheme obeys fundamental properties; conservativeness, boundedness, transportiveness.

- Conservativeness requires the conservation of mass flow at adjacent control volumes; the flux through a common face of adjacent control volumes must be represented by the same expression for each node.
- Boundedness: the set of of linear algebraic equations for each node is solved iteratively, starting from a initial distribution of ϕ. A sufficient condition for a convergent iterative method can be expressed in terms of the values of the coefficients of the discretised equations.
- Transportiveness: the nondimensional cell Peclet number Pe = F/D is a measure of relative strength of convection and diffusion. General, in a homogeneous flow domain, pure diffusion flow (Pe=0) is isotropic and stagnant, whereas convection is coupled with a main direction. Therefore, the influence of the central node on the neighbourhood nodes is borne out in the discretisation scheme.

The central differencing scheme interpolates linearly between the central node and an adjacent node. It is suitable for highly diffusive flows in a fine grid. The upwind differencing scheme also interpolates linearly between the central node and a neighbourhood node, but takes the flow direction into account. In the direction of the flow, the face values are set equal to the nodal values accordingly. This scheme is specially designed for highly convective flows. The hybrid differencing scheme is a combination of central and upwind differencing schemes, using a local Pe number for each face to weigh locally the contribution of convection and diffusion to the mean flow. It uses the upwind differencing scheme which omits physical diffusion when the cell Peclet number is larger than two, but otherwise reverts to the central differencing scheme and retains physical diffusion. The discretised equation for the pure convection-diffusion problem for the node P is given by

$$a_P\phi_P = a_W\phi_W + a_E\phi_E + a_S\phi_S + a_N\phi_N + a_L\phi_L + a_H\phi_H + a_P^0\phi_P^0 + S_u$$

with (5.4.1)

$$a_P = a_W + a_E + a_S + a_N + a_L + a_H + a_P^0 + \Delta F - S_P$$

and

$$\Delta F = F_e - F_w + F_n - F_s + F_h - F_l$$

$$a_P^0 = \frac{|\rho \Delta V|_{t-\delta t}}{\Delta t}$$

The coefficients are as follows:

$$\begin{aligned}
a_W &= \max\left[F_w, \left(D_w + \frac{F_w}{2}\right), 0\right] \\
a_E &= \max\left[-F_e, \left(D_e - \frac{F_e}{2}\right), 0\right] \\
a_S &= \max\left[F_s, \left(D_s + \frac{F_s}{2}\right), 0\right] \\
a_N &= \max\left[-F_n, \left(D_n - \frac{F_n}{2}\right), 0\right] \\
a_L &= \max\left[F_l, \left(D_l + \frac{F_l}{2}\right), 0\right] \\
a_H &= \max\left[-F_h, \left(D_h - \frac{F_h}{2}\right), 0\right]
\end{aligned} \qquad (5.4.2)$$

Both sides of the discretised equation (Eq. 5.4.1) contain Φ at the new time step; the time marching procedure starts with an initial field Φ . The system of algebraic equations must be solved at each time level.

The boundary conditions enter the discretised equations via source terms, which replace the terms for the corresponding cell face accordingly (see Chapter 5.6).

The default scheme used in PHOENICS 2.2.1 (CHAM) for all variables is the hybrid differencing scheme, although the option exists to use the upwind-differencing scheme.

Upwind and hybrid differencing schemes are bounded and stable, but suffer from numerical (false) diffusion if the velocity vector is not parallel to one of the coordinate directions. The hybrid differencing scheme is only marginally more accurate than the upwind differencing scheme, as the central differencing scheme will be restricted to regions of low Peclet number.

The accuracy of hybrid and upwind schemes is only first-order in terms of Taylor series truncation error. Generally, any interpolation method improves its accuracy with the refinement of discretisation. Therefore, mesh refinement is one method to remedy the problem of numerical diffusion. However, the round-off error accumulates with large numbers of cells, which may cause finite continuity errors in connection with the setting of the coefficient CO to a large number (see Chapter 5.7). Above all, the necessary degree of refinement is often impractical for engineering purposes and its required memory size may easily exceed available capacity. Schemes with higher orders of accuracy in terms of truncation errors have been proposed in an attempt to improve resolution.

Linear higher order interpolation methods involve more neighbouring points and reduce the discretisation errors. For example, the QUICK (quadratic upstream interpolation for convective kinetics) scheme uses a three node upstream weighted quadratic interpolation. At the boundary, the third node is not available. Therefore, an artificial mirror node is extrapolated across the boundary by symmetry. The QUICK scheme may increase the accuracy of the solution, but may suffer from the boundedness problem. In flow fields with large gradients of ϕ, the QUICK scheme can produce non-physical solutions and numerical instability. To eliminate the boundedness problem, flux blending methods or flux limiter methods have been proposed. The latter modify linear higher order schemes by using a 'flux limiter' which enforces a boundedness criterion based on the local solution behaviour. The 'flux-limiter' is either a linear function of the gradient of the variable F evaluated at the cell center and at one face with a constant coefficient K (therefore called kappa-formulations), or, it is a function of the gradient ratio of the variables F evaluated at center and faces. The latter scheme is therefore non-linear.

The co-located velocity formulation requires different interpolation schemes for pressure and momentum. In case of the linear pressure gradient interpolation, the cell face pressures are written as linearly interpolated values from the cell nodal values (the cell in question and the adjacent cell). Consequently, in the balance equations for the nodal velocities, the nodal pressure in the cell is replaced by this interpolated value. This results in the pressure – velocity decoupling because the difference equations for nodal velocities do not contain the pressure of the node in question any more. To evaluate the velocity components at the cell face, the momentum interpolation algorithm from Rhie and Chow (CHAM) uses the discretised momentum equations for the two neighbouring nodes as the interpolation formulae, but replaces the terms representing the pressure gradient across the cell face by one which is centred about it. The cell face velocities are then used to calculate the fluxes for the finite difference coefficients, while the pressure force differences are calculated by linear interpolation. In this implementation of the non staggered algorithm, U1, V1 and W1 are still solved, but the values of these quantities will be overwritten in each iteration with values which have been obtained from the cell-face velocity interpolation formulae (UC1, VC1, WC1).

PHOENICS 2.2.1 (CHAM) provides for 5 alternative linear schemes and 12 alternative non linear schemes. The selection of a suitable scheme involves a compromise between accuracy and numerical stability. Generally, non linear (bounded) schemes can be applied if severe convergence difficulties are encountered or to avoid non-physical solutions (for example negative values for k and ε).

5.5. The Iterative Solution

As each finite volume holds a set of linear equations dependent on the number of variables which have to be solved, the whole flow field is represented by a set of matrices, for each transported fluid property one matrix. The order of the matrix is determined from the number of cells in the flow domain in each direction. The form of those matrices is controlled by the discretisation scheme. Dependent on the number of grid nodes, this system of linear equations is often very large. There are two types of solution techniques, the direct method and the iterative method. Computational methods to solve a matrix directly use a standardized Gaussian elimination or the Cramers rule, but the storage requirement of this methods is too large to be efficient. Iterative methods are based on the repeated application of a simple algorithm, which may lead to convergence when the system of equations satisfies exacting criteria. The number of necessary iterations is not predictable and a simulation may take long, but the required storage is relatively little and enables the computation. Typical methods are the Jacobi or the Gaus-Seidel method, both are point-by-point methods. Such a method can be useful when the non-linearities are severe, because the rate of change of variable from sweep to sweep is low and therefore introduces additional stability. Widely used in CFD programs is the Thomas tri-diagonal matrix algorithm, which is actually a direct non-iterative method for one-dimensional situations using stepward forward elimination and stepward back substituting. For two and three dimensional problems, this method is applied in sweeps line by line in each selected plane. Further extension of the Thomas algorithm leads to the whole field solver, which can be specified for all scalar variables. It is always recommended for the pressure correction equation and is preferable when non-linearities are slight.

However, higher order discretisation schemes which link in each discretisation equation the central node of the finite volume to other than its immediate neighbour, require also that the sweep process incorporates a larger number of neighbouring contributions. In the use of a body fitted coordinate system, the discretised equations normally contain a large number of contributions from surrounding nodes. Here, other methods like the 'strongly implicit procedure' (SIP) or the conjugate gradient method (CGM) are in use.

The transport equations for each momentum component are coupled, because the coefficients depend on the convective mass flux variable F, which is itself a linear function of all three components of momentum, evaluated at the cell faces. As described above, the values at the cell faces are determined by means of discretisation schemes from nodal values. The coupling is twofold: an internal coupling in each momentum transport equation between variable and coefficient, and secondly, the solution of each momentum component influences the coefficients in the transport equations of the other momentum components. Therefore, the iterative procedure has to update the coefficients accordingly. Further, the pressure gradient term in the Navier-Stokes equations (Eq. 5.1.24 to 5.1.26) acts as an important driving force for the transport of all fluid properties, but the pressure field is unknown as well. Obviously, pressure is not a transported fluid property, therefore there is no transport equation for pressure. To overcome this under-determination, the continuity equation is solved for the transport of density and the transport equation for energy is solved to determine the temperature field. The pressure finally can be calculated with an equation of state. However, in many cases the flow is treated as incompressible, there is no information about temperature distribution and the flow field has open boundaries. But any correct pressure field which is applied to the momentum equations should result in a velocity field which satisfies the continuity equation for a constant density. This correct pressure field is, starting from an initial setting, achieved by successive iterative adjustments on a staggered grid. The iterative calculation of the staggered grid arrangement is essentially a perturbation approach, only that the perturbation acts basically as an approximate correction term which refines the solution in each iteration. To initiate the SIMPLE (Semi-Implicit Method for pressure-Linked Equations) calculation process, the initial pressure field condition is used to calculate velocity field components from the discretised momentum equation. Calculation of the continuity errors for each cell (inflow-outflow) yields a field of velocity component corrections. But as the velocity field is also subject to the constraint that it should satisfy the continuity equation, the discretised continuity equation arises as an equation for the correction pressure field, including a source term of imbalance. The pressure correction equation diverges during the iteration unless some underrelaxation factor is used in order to obtain a closer pressure correction. The obtained velocity components are therefore also corrected with the underrelaxation approach. Underrelaxation is perturbation of the field in terms of a linear function of the variable in question. The following iteration step solves the discretised momentum equation and the continuity equation based on the under-relaxed values which determine the coefficients. For a converging solution, the imbalance decreases. An overestimated underrelaxation factor may lead to oscillatory or even divergent behaviour, and a value which is too small causes extremely slow convergence.

Refinements to the SIMPLE procedure have produced more economical and stable iteration methods. The algorithm SIMPLER (SIMPLE Revised) uses the pressure corrections to obtain velocity corrections only. The discretised continuity equation is used to derive a discretised equation for pressure, instead of a pressure correction equation as in SIMPLE. This yields to an intermediate pressure field corresponding to the velocity field without the pressure correction, which causes a fast convergence of the iteration.

A further derivation of SIMPLE is the PHOENICS default algorithm SIMPLEST (SIMPLE Shortened). SIMPLE takes both diffusion and convection effects of velocity changes simultaneously into account, whereas SIMPLEST disregards the convection effect of changing velocity. The coefficients in the momentum equations contain only diffusion contribution, convection terms are added to the source term. As the convection terms arise from the continuity equation, an erroneous flux takes away from one cell what it adds to another. Therefore, treatment of the convection terms as source in the discretised momentum equation has greatly increased robustness and convergent behaviour of the solution algorithm.

5.6. Convergence

5.6.1. Residuals

A converged solution of the whole flow field is achieved, when each part of the field obeys conservation principles. In numerical terms, the residuals are defined as imbalances in the finite volume equation (compare Equation 5.4.1)

$$E_P = a_P \Phi_P - \sum_i a_i \Phi_i + b \qquad (5.6.1.1)$$

The term b stands here for remaining sources. Summation takes place over all sides of the cell and, in the transient case, over the time step (i = S, N, W, E, H, L, T).
The sum over the residuals are extended to the current slab (in case of slab-wise solution) or to the whole field (in case of whole field solution) and normalized with the residual reference factor RESREF(Φ).

$$\sum |E_P| \, / \, \mathrm{RESREF}(\Phi) \qquad (5.6.1.2)$$

When this ratio falls below 1.0 (default value), solution for that variable Φ stops. When this happens for all variables, sweeping stops. Here, an additional factor RESFAC can be applied to act as a tolerance, and the critical value of the ratio above can be set lower than 1.0.
In the case of convergence, the residuals reduce during the iteration process by several orders of magnitude, and the sums of the sources at the boundaries balance.
Typical setting for the RESREF(Φ) are a small fraction of the incoming flow times the value of the variable brought in. Hence, given the inflow velocity **U** = (u, 0, 0) and the constant flow density ρ it is recommended to set for the solved variables P, U, V, W, k and ε

RESREF (P) = 0.001 ρ u
RESREF (U) = 0.001 ρu^2 , RESREF (V) = 0.001 ρu^2 , RESREF (W) = 0.001 ρu^2
RESREF (k) = 0.001 ρ u k
RESREF (ε) = 0.001 ρ u ε

5.6.2. Relaxation

Relaxation influences the rate at which a converged solution is achieved. Excessive relaxation will slow down unnecessarily the rate of convergence, too little relaxation may not avoid divergence. Relaxation factors have to be applied for each variable solved.

Linear relaxation means, that the new value for the variable at each cell is taken as

$$\Phi_{p,new} = \Phi_{p,previous} + \alpha\,(\Phi_{p,current} - \Phi_{p,previous}) \qquad (5.6.2.1)$$

with the linear relaxation factor α ($0 \le \alpha \le 1.0$). A value of 0.3 to 0.7 normally suffices. Linear under-relaxation (α=0.4) is often required for the pressure variable in non-orthogonal grids. For the applied body-fitted coordinate system (see Chapter 6.1.2.1 and Chapter 7), linear relaxation for the variables P, k and ε with $\alpha = 0.5$ is recommended (CHAM).

False-Time-Step Relaxation results from adding an extra source term to the finite volume equation (compare Equation 5.4.1).

$$(\Phi_{p,current} - \Phi_{p,new})\,\rho\, V_{cell} / \Delta t_{false} \qquad (5.6.2.2)$$

This kind of relaxation is called False-Time-Step, because the term which is here added to the steady finite volume equation has the same form as the transient term if the calculation is transient. The false time step may be set proportional to a characteristic time scale of the problem. It can be evaluated as a characteristic length scale (based on the cell size in the region of particular interest), divided by a characteristic velocity (which is expected in this region). It has the effect of making the new value of the variable close to the current value when the false time step is large, and changes occur only after many repetitions of the adjustment process. For the applied body-fitted coordinate system (see Chapter 6.1.2.1 and Chapter 7), False-Time-Step relaxation for the collocated velocity components is recommended (CHAM).

5.7. The Sources and Boundaries

Solution of field equations requires spatial boundary conditions, which are either of Dirichlet or Neumann type. In transient problems, the initial field at $t = t_0$ of all variables needs to be specified as well. Field initialisation involves no special measures other than setting the variables to appropriate values at the beginning of the simulation. Spatial boundary conditions enter the discretised equations by suppression of the link to the boundary side and modification of the source terms. The source term S of the flow property Φ in the general transport equation (Eq. 5.1.30) evaluated at the node P has the general form

$$S_\Phi = f \cdot CO \cdot (VAL - \Phi_P) \tag{5.6.1}$$

where f is a multiplying factor, CO is the source coefficient and VAL states the in-cell value of the variable Φ. Specific setting of CO and VAL for the cells at the boundary characterises the boundary. The multiplying factor f determines the source type (volume or surface). The unit of the source term for a specific flow property Φ is the unit of the flow property times the unit of the rate of change of mass ([Φ]·[kg]/[s]). For example, the velocity has the unit of specific momentum ([kg·m/s]/[kg]), therefore the source of momentum has the unit of force [N]. The coefficient CO has the unit ([kg/s]/[f]), with [f] stating the unit of the multiplying factor which determines the source type. The unit of the value VAL is obviously the same as the unit of the desired flow property Φ. There may be many sources for a single cell, each representing a different physical effect or boundary condition. If there are several contributors to one source, the total contribution adds up to

$$S_\Phi = CO_1(VAL_1 - \Phi_P) + CO_2(VAL_2 - \Phi_P) + CO_3(VAL_3 - \Phi_P)\ldots. \tag{5.6.2}$$

CO_1 and VAL_1 might represent a 'true' source, for example an inflow of momentum, the other terms might represent interactions between the cell and a region outside the integration domain beyond the cell walls. For the flow property ϕ at the node P the discretised linear equation states

$$\Phi_P = \frac{(a_E\Phi_E + a_W\Phi_W + \ldots + S + CO_1 \cdot VAL_1 + CO_2 \cdot VAL_2 + \ldots)}{(a_E + a_W + \ldots + a_\Phi + CO_1 + CO_2 + \ldots)} \tag{5.6.3}$$

When the boundary condition fixes the value of ϕ at the node P in the cell, then CO is set to a very large number and VAL is set to the desired value of ϕ_P. Equation (5.6.3) reduces then approximately to ϕ_P = VAL. When the boundary condition fixes the flux of ϕ across the boundary cell into the flow domain, CO must be given a negligibly small value. This sets the source equal to $f \cdot CO \cdot VAL$ independently of the value of ϕ_P. Therefore, VAL must be chosen so that the source equals the desired flux (VAL = ϕ/CO).

The setting of CO provides the boundary condition with a certain degree of stiffness. For example, a very large CO fixes the value of Φ in the cell, but the magnitude or even the sign of the flow rate of this specific fluid property will be hard to determine in advance.

The simulation specifies solely the flow variables of pressure, momentum and the scalar turbulent transport variables k and ε. In terms of physics, the spatial boundary conditions are determined as follows:

Inflow condition: Mass-flow conditions are supplied by way of pressure boundary conditions. The physical notation is that fluid is forced into the domain because some external pressure (the prescribed VAL) exceeds the pressure which obtains in the cell. Typically, the inflow is modelled as a diffusive flux assuming a pressure gradient across the inflow boundary. Therefore, the mass-flow, by means of a in-cell source term, is fixed, irrespective of the internal pressure which is allowed to float. The inflow of momentum is modelled as a convective flux of momentum across the boundary, stating a momentum source in the boundary cells. The inflow of scalar properties (k,ε) is also modelled as flux across the boundary, by means of an appropriate in-cell source. Hence, the inflow condition is determined by gradients normal to the boundary causing a flux across the boundary, not by fixed values of the flow property itself. The inflow condition can be modelled as non-uniform, for example the atmospheric boundary layer can be modelled as a function of momentum and turbulent intensity over the height.

Outflow condition: if the open outlet boundary is selected in regions of undisturbed flow where the flow is fully developed, no change occurs in the flow direction. Therefore, the gradients of the scalar variables in flow direction are zero. Further, the gradient of the components of momentum which are tangential to the boundary face are zero as well. The value of pressure is set to a uniform mean pressure value, and the value of the component of momentum normal to the boundary face (the convective flux) is fixed at zero, which enables the diffusive flux to be flexible in order to obey conservation principles. Flexible diffusive flux across the boundary goes along with a pressure gradient across the boundary – here, the stiffness of the boundary plays a important role.

A specified outflow, for example the extraction by means of a fan, is modelled in the same way as an inflow.

Wall surface boundary conditions: The wall-function approach bridges the viscous sublayer at the wall to provide near wall boundary conditions for the transported flow properties. The wall conditions are derived from the values of the dependent variables at the near wall grid node, and appropriate sources or sinks apply to this grid node. The momentum component normal to the wall is set to zero in the near wall grid node. For the tangential components, wall friction causes a wall shear stress τ_w in the near wall grid node. Directly at the wall, the no-slip condition for viscous fluids is assumed. Low-Reynolds number models need a very fine grid towards the wall boundary layer in order to achieve the necessary resolution to apply this laminar boundary condition directly. Standard models calculate the wall shear stress at the near wall grid node in order to determine the source terms for momentum, turbulent kinetic energy and its dissipation.

The implementation of wall boundary conditions in turbulent flows starts with the evaluation of the dimensionless wall distance y^+ as function of the boundary layer friction velocity u_τ tangential to the wall and the kinematic viscosity ν of the fluid of density ρ (Schlichting 1965).

$$y^+ = \frac{\Delta y_P}{\nu}\sqrt{\frac{\tau_W}{\rho}} = \frac{\Delta y_P}{\nu}\cdot u_\tau \tag{5.6.4}$$

A near wall flow is taken to be laminar if $y^+ \leq 11.63$. Otherwise the near wall grid node is considered to be in the logarithmic law region of a turbulent boundary layer. In case of a near wall layer in local equilibrium the logarithmic law of the wall

$$\frac{u_P}{u_\tau} = \frac{1}{\kappa}\ln E\cdot y^+ \tag{5.6.5}$$

applies, strictly to near wall nodes whose y^+ values are in the range of $30 < y^+ < 130$ (CHAM). Versteeg and Malalasekera state a wider range of tolerance, $30 < y^+ < 500$ (Versteeg and Malalasekera 1995). Equation 5.6.5 is evaluated with the von Karman constant κ and the roughness parameter E. These constants are empirical constants, and both may vary from case to case. Assuming the laminar sublayer, the wall stress value can be approximately obtained from the Newton's equation of viscosity (absolute viscosity μ)

$$\tau_w = \mu \frac{u_P}{\Delta y_P} = \rho v \frac{u_P}{\Delta y_P} \tag{5.6.6}$$

Δy_P is the distance from the near wall grid node normal to the adjacent wall boundary, u_P is the calculated value of the velocity tangential to the wall boundary in the near wall grid node. This very simplified model can be used to check the range of the non-dimensionalised wall distance y^+ and to modify the appropriate near wall grid in order to insure the applicability of the chosen wall function.

For equilibrium turbulent boundary layers the near-wall values for k and ε may be fixed at the nodes as

$$k = \frac{u_\tau^2}{\sqrt{C_\mu}} \quad (5.6.7) \qquad \text{and} \qquad \varepsilon = \frac{u_\tau^3}{\kappa \cdot \Delta y_P} \quad (5.6.8)$$

with the dimensionless constant C_μ.

The logarithmic law of the wall has been applied in many different ways, including near wall temperature distribution which changes the physical properties of the fluid. Additionally, the wall function for heat transfer activates the sink of enthalpy owing the presence of the wall.

A generalisation of the logarithmic law of the wall to non-equilibrium conditions (CHAM, Launder and Spalding 1974) employs $k^{1/2}$ as the characteristic velocity scale rather than the friction velocity u_τ. For local equilibrium the model reduces to the equilibrium wall function approach. Non equilibrium conditions are for example stated for near wall turbulent transport of heat. Generally, the logarithmic law of the wall can take different roughness wall functions into account, according to empirical functions describing the roughness parameter E (CHAM, Schlichting 1965).

Symmetry boundary condition: Often, a flow field can be regarded as mirror symmetrical. Therefore, it is possible to reduce the simulation to one half of the field. The symmetry boundary condition states, that no flow and no scalar flux across the mirror plane takes place. The velocity normal to the plane is set to zero, and the values of all other scalar properties of the near boundary cells are mirrored across the boundary so that no gradient occurs. In the discretised equations for the pressure correction field the link with the symmetry boundary side is cut by setting the appropriate coefficient a to zero.

References and Bibliography

Schlichting H.; Grenzschicht Theorie; Braun'sche Verlagsbuchhandlung Karlsruhe, Germany, 1965
Boundary-Layer Theory; McGraw-Hill Book Company, London, England, 1979

Launder B.E. and Spalding D.B.; The Numerical Computation of Turbulent Flows; Computer Methods in Applied Mechanics and Engineering, Vol. 3, 1974, pp. 269-289

Versteeg H.K. and Malalasekera W.; An Introduction to Computational Fluid Dynamics, The Finite Volume Method; Addison Wesley Longman Ltd., Harlow, England, 1995

CHAM; Concentration, Heat and Momentum Ltd., London SW19 5AU
PHOENICS, version 2.2.1., online help encyclopaedia
Launder B.E., Spalding D.B. et al., Imperial College London

Scanlon T.J.; Vortex Shedding Flowmeter - Pulsating Flow CFD Studies; PhD thesis, Division of Thermo-Fluid and Environmental Engineering, Department of Mechanical Engineering, University of Strathclyde, Glasgow, Scotland, 1992

Patankar S.V.; Numerical Heat Transfer and Fluid Flow; Series in Computational Methods in Mechanics and Thermal Sciences, Hemisphere Publishing Corporation, USA, 1980

Özisik M.N.; Finite Difference Methods in Heat Transfer; CRC Press, Florida, USA, 1994

Abbott M.B. and Basco D.R.; Computational Fluid Dynamics, An Introduction for Engineers Longman Scientific and Technical, Harlow, England, and also John Wiley and Sons, New York 1989

Warsi Z.U.A.; Fluid Dynamics, Theoretical and Computational Approaches; CRC Press, Florida, USA, 1993

Rodi W.: A New Algebraic Relation for Calculating the Reynolds Stresses; ZAMM, Mechanics of Fluid, Vol. 56, 1976, pp. 219-221

Pope S.B.: A more general Effective-Viscosity Hypothesis; Journal of Fluid Mechanics, Vol. 72, Part 2, 1975, pp. 331-340

Rotta J.C.: A Family of Turbulence Models for Three-Dimensional Boundary Layers; Proc. of the 1st International Symposium on Turbulent Shear Flows, hold at the Pennsylvania State University, USA, 18th-20th April, 1977, Springer Verlag, 1979, pp. 267-278

Rotta J.: Statistische Theorie nichthomogener Turbulenz; Zeitschrift für Physik, Band 129, 1951, pp. 547-572

Launder B.E.: Turbulence Modelling for the Nineties: Second Moment Closure....and Beyond?; Lecture Notes in Physics, No. 371, pp. 1-18
Editor K.W. Morton, Springer Verlag, 1990

Bradshaw P.: Turbulence: the Chief Outstanding Difficulty of our Subject; Experiments in Fluids, Vol. 16, 1994, pp. 203-216

6. Initial Simulations with Computational Fluid Dynamics

With the software package PHOENICS, version 2.2.1 (CHAM) a two and a three dimensional analysis for the wind flow over a building block has been carried out. Preliminary investigations were focused on the flow behaviour as modelled in two and three dimensions in a cartesian grid without any integrated duct. In all simulations, of main interest was the pressure at the upper part of the wall and the front part of the building. In particular, these initial investigations explored the influence of the grid distribution, cell size and the number of cells, inflow and boundary conditions, and in particular the systematic difference of the flow field modelled in two or three dimensions.

The initial investigation was necessary to provide a basis for modelling the building with an integrated duct, as the grid requirements to model such a building are demanding. In order to achieve good resolution in the region of the duct, a special grid technique had to be applied, which allows one to link domains of different cell sizes and different cell numbers together. The first three dimensional attempt failed because the required disk space exceeded the capacity of the server of the networked UNIX workstation cluster. Also, the network traffic slowed down the calculation significantly. Hence, the first complete simulations were made in two dimensions. Initially it was hoped that the two dimensional simulation might represent qualitatively the flow in the symmetry plane of the building. However, the investigation showed a systematic mismatch between two dimensional simulated flow and results in the symmetry plane of three dimensional flow. The three dimensional simulation of the building in a simple cartesian grid provided a quantitatively sound result and formed the basis of an approach to couple a detailed two dimensional simulation of the flow through the building integrated duct with the general external flow field as calculated in the three dimensional simulation (see Chapter 7). A three dimensional simulation of the building with integrated duct has been carried out (see Chapter 7) since a sufficiently powerful processor became available in early summer 2000.

6.1.1. General Modelling Approach

All simulations are steady state. Transient simulation would show interesting effects like vortex shedding, or the impact of gusts which may perhaps play a not insignificant role regarding the lifetime of the Ducted Wind Turbine. But the transient approach to modelling the building with integrated duct in three dimensions would require an amount of disk space which exceeds the capacity of the most processors.

All simulations show only wind flow normal to the front façade. In the two dimensional simulation, no lateral incidence is possible. The three dimensional simulation makes use of the symmetry plane as mirror plane. Hence inflow with an angle of incidence would be inverted at the symmetry plane. Three dimensional simulation of the whole building with integrated duct requires an amount of cells which exceeds the capacity of most processors.

The flow is modelled as incompressible. Therefore, the flow disturbance caused by the obstacle can be recognised even in far distance. As the impact of the obstacle on the flow domain is very different if the case is modelled two or three dimensionally, a flow domain was chosen which meets the criteria of 'undisturbed boundaries' for both cases. Also the size of the flow domain depends on the applied boundary conditions and the implementation of sources and sinks in the flow domain (see Chapter 2.4).

In the real scale simulation, the building is 30 m high, 20 m deep and 35 m wide. The flow field around reaches 160 m upstream, 500 m downstream and 320 m above the building, and in the three dimensional case as well 160 m to each side (Figure 6.1.1.1). Non dimensionalized with the obstacle height, it would be around 17 H downstream, 5 H upstream, 11 H above and also 5 H to each side. As the flow field depends on all dimension sizes and on the initial inflow conditions, a general strict scaling rule can not be given.

The small wind tunnel model in three dimensions is of course on a different scale. The model was 15.5 cm high, 20 cm deep and around 35 cm wide. The whole flow domain was limited to 1.20 m in height, 2.0 m downstream and 1.0 m upstream, and 60 cm to each side. This size of the flow domain corresponds to the real conditions in the working section of the wind tunnel. Non dimensionalised, the flow domain is smaller by a factor 2. As the incompressible flow can expand in three dimensions around the obstacle, these relatively close boundaries are assumed to be in the undisturbed flow domain. In the simulation, the computer model was 1:100 upscaled. A test simulation had shown no difference in the surrounding flow and pressure field around two blocks, one at model scale, one at full scale.

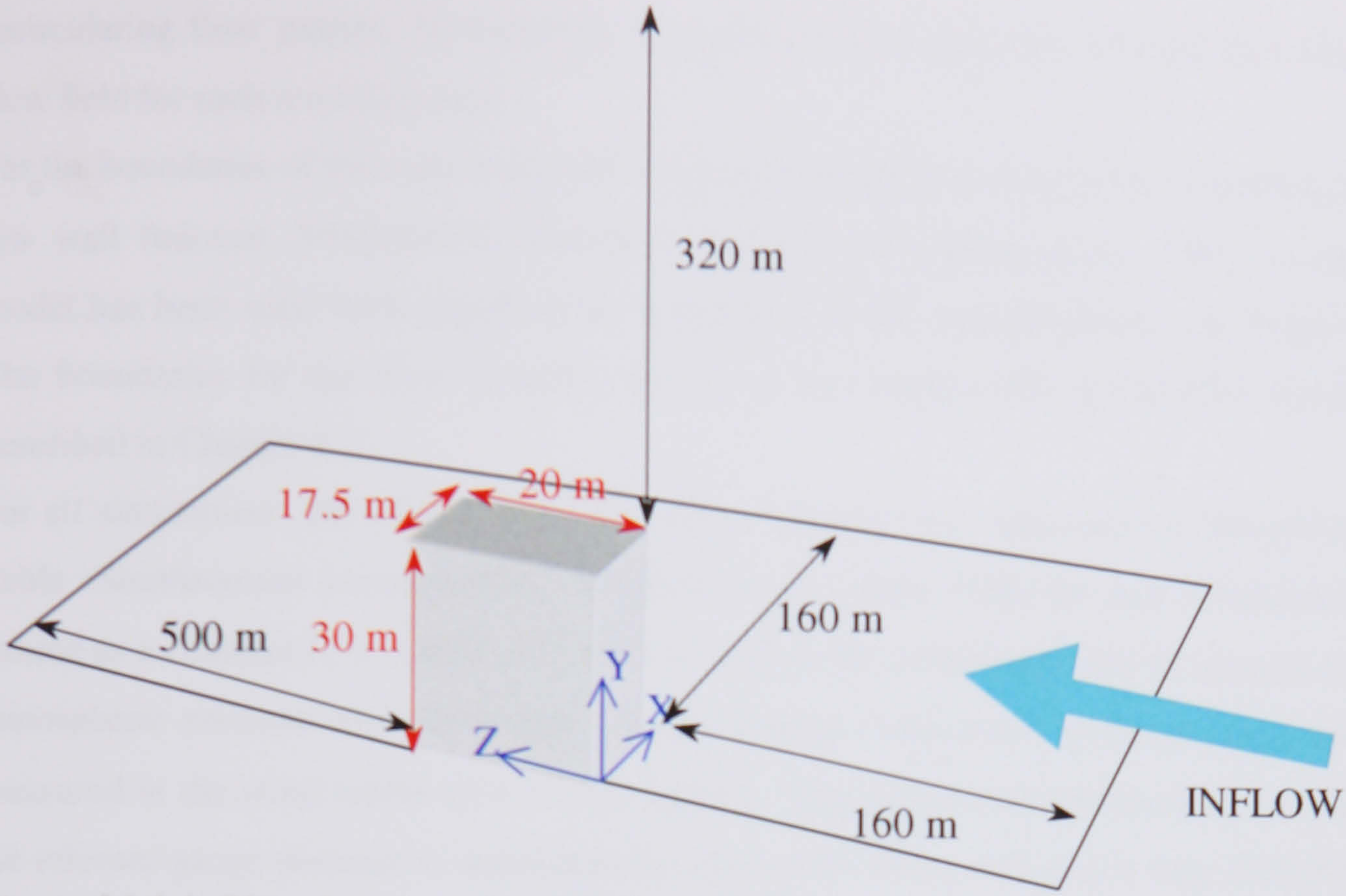

Figure 6.1.1.1: Flow domain, schematic drawing

The two simulations generated quantitatively and qualitatively identical flow- and pressure fields around the obstacle. As each simulation was carried out with the identical inflow boundary (16.5 m/s), it seems to be the case that the simulated results are independent of the Reynolds number. A significant difference occurs only for the Y^+ values, which depend directly on the cell size (see Chapter 5.7). In order to compare with all other simulations (Chapters 6 and 7) and the experimental investigation (Chapter 4), the three dimensional simulation of the building with integrated duct is carried out with the upscaled copy of the wind tunnel model.

Different turbulent models have been considered in advance. The potential flow field calculation (Laplace equation) fails to predict recirculation and vorticity, the laminar model prove in the same sense unsatisfactory. The low Reynolds number model (Lam and Bremhorst 1981, as quoted in PHOENICS (CHAM)) overestimated the tickness of the laminar sublayer at the wall and produced a nearly uniform, but far too low suction over the roof (Dannecker 1998). The standard k-ε model as provided in PHOENICS has a wide range of applicability (Launder and Spalding 1973, Versteeg and Malalasekera 1995), and different variations are widely used to model wind flow in the built environment (see Chapter 2.4). The implementation of the standard k-ε model makes it possible to predict recirculating flow pattern. Nevertheless it is necessary to interpret critically the simulated flow field for each modelled case.

For the boundaries of the solid walls and the ground of the flow domain, the equilibrium log-law wall function (PHOENICS (CHAM), Versteeg and Malalasekera 1995) for the k-ε model has been used with regard to the evaluation of the dimensionless wall distance Y^+. The boundaries for the flow variables are set at the border cells of the flow domain as described in Chapter 5.7 .

For all simulations, the value for the kinematic viscosity was taken from a Meteorological Table (Smithsonian) corresponding to standard air values (Franzini and Finnemore) and treated as a constant ($\nu = 1.4553 \cdot 10^{-5}$ m^2/s) as well as the temperature, the air density and the atmospheric pressure over the height. The air density corresponds to the average value as measured in the wind tunnel ($\rho = 1.1623$ kg/m^3). This follows the simulation procedure as the relevant gauge pressure is automatically set to zero. Those parameters vary certainly in a natural flow field of more than 600 m length and 350 m height, and the shape and stability of the natural boundary layer depends in reality on this conditions (see Chapter 2.1). The assumptions can be seen as the common wind engineering approach: as the buoyancy flow does not change the calculated flow significantly, it is neglected in order to reduce the number of variables to solve.

As described above (see Chapter 2.1), proposed profiles of the wind in urban areas vary. In order to investigate the influence of possible wind gradients, all encountered approaches were compared. Consistent in most of the reported work was a logarithmic law for the vertical velocity profile. The component of the turbulence intensity normal to the vertical boundary layer declines hyperbolically with height (ESDU 1993), and the profile of the turbulent kinetic energy k was determined as proportional to the square of the vertical velocity weighted with the turbulence intensity. The profile for the turbulent kinetic energy dissipation ε was derived as proportional to the product of the k-profile and the first derivative of the vertical velocity profile with height.

Implementation of such an inflow profile had no significant effect on the pressure distribution above the flat roof when modelled in two dimensions. In three dimensions, it leads to a general decrease in suction. In both cases, the pressure on the lower part of the front façade declined as expected in boundary layer shear flow. Generally it can be assumed that in the two dimensional simulation, no reasonable boundary layer inflow function with steady positive slope factor will alter the flow field in the vicinity of the building in such a way that the computed pressure coefficients on the front façade and the roof will give a close match to those seen in experiment or three dimensional simulation (Dannecker and Grant 1998). Aware of the difficulty in defining a boundary layer profile in urban areas and given the systematic error connected with the two dimensional approach, all simulations were carried out with a uniform inflow profile in order to have a sound basis for comparison. The inflow velocity corresponds to the average wind speed at which the wind tunnel tests were conducted (v = 16.5m/s).

The uniform scalar inflow condition of the turbulent kinetic energy k assumes 40 % of the mean velocity as turbulence, following the standard recommendation for the first 10 m above ground level in urban conditions (ESDU 1993). Earlier tests showed that different levels of turbulence do not significantly alter the pressure coefficient distribution on the front façade (Dannecker and Grant 1998). But it is assumed that the wind carries this high turbulent intensity into any integrated duct. Therefore, the uniform inflow condition of the turbulent kinetic energy dissipation ε was obtained from the given turbulent kinetic energy k and a characteristic length (duct inlet diameter) (Versteeg and Malalasekera 1995). The length scale applied here may not be appropriate compared with the length scale in the atmospheric boundary layer, which may be in building roof height around 60 m. However, as mentioned above, changes in the turbulent inflow conditions had little effect on the overall flow field. In the simulation of the wind tunnel geometry (see Chapter 7), the average wind tunnel turbulence of only 1 % (ESDU 1993) was assumed, in order to have the same flow conditions as in the tunnel. The aim of simulating the wind tunnel geometry was to compare experimental with numerical values.

First ideas to overcome the systematic error in two dimensional simulation (Dannecker 1999) resulted in an approach to couple a two dimensional simulation to a three dimensional calculated flow field.

Finally, a summary of the applied initial and boundary conditions is presented:

Inflow:

1. mean inflow velocity, convective flux of momentum across boundary with its normal component W = 16.5 m/s, its tangential components U,V = 0.0
2. scalar variables as convective flux across the boundary

   $k = 1.5 \cdot (U_{ref} \cdot T_i)^2$ with $U_{ref} = W$ and $T_i = 0.4$ turbulence intensity

$\varepsilon = C_\mu^{0.75} \cdot k^{1.5} / l$ with $C_\mu = 0.09$ and $l = 0.07 \cdot$ duct diameter (hydraulic diameter)

C_μ is a dimensionless adjustable constant to specify the eddy viscosity

Von Karman constant $\kappa = 0.41$ (CHAM)

The wall roughness parameter E has a value between 8 and 10 for smooth walls (CHAM)

3. Mass flow = $\rho \cdot W$ with $\rho = 1.1623$ kg/m^3 fixed as in cell source term, diffusive flux, assumes pressure gradient across the boundary
4. Gauge pressure $p = 0.0$ in the flow field. $\nu = 1.4553 \cdot 10^{-5}$ m^2/s constant kinematic viscosity

Outflow, open boundary condition:

1. $\text{grad}_N\, k = \text{grad}_N\, \varepsilon = 0.0$, the gradient of the scalars normal to the boundary are zero
2. $\text{grad}_N\, U_T = 0.0$, the normal gradient across the boundary of this component of momentum which is tangential to the boundary is set to zero.
3. $U_N = 0.0$, the convective flux of the component of momentum normal to the boundary is fixed to zero
4. The value of pressure is fixed with a certain stiffness to gauge pressure, which enables the diffusive flux to be flexible in order to obey conservation principles.

Wall, solid boundary condition:

1. $U_N = 0.0$, the component of momentum normal to the boundary is fixed to zero
2. directly at the wall, the no-slip condition applies to the tangential components of momentum: $U_T = 0.0$
3. Bridge of laminar sublayer with equilibrium logarithmic wall function, which calculates k and ε as function of the wall shear stress. The rate of turbulence production equals the rate of dissipation (see Chapter 4.5).
4. There is no need for pressure boundary conditions, the boundary conditions fall on momentum nodes in the case of a staggered grid. Alternatively in the body fitted coordinate system, the wall boundaries apply to co-located velocities.

Accuracy:

In all simulations the hybrid differencing scheme was used (see Chapter 5.4). The residual reference factor RESREF was calculated as a function of the inflow boundary conditions (compare Chapter 5.6.1). In order to simplify, the density of air was set to 1 kg/m^3. Hence,

RESREF (P) = 0.001 W [kg/m^{2}s]

RESREF (U) = RESREF (V) = RESREF (W) = 0.001 W^2 [kg/ms^2]

or for the collocated velocity components UC, VC, WC accordingly

RESREF (k) = 0.001 W k [kg/s^3]

RESREF (ε) = 0.001 W ε [kg/s^4]

In all simulations, relaxation (compare Chapter 5.6.2) for the scalar variables P, k and ε took place with the linear relaxation factor $\alpha = 0.5$. The False-Time-Step relaxation factors for the velocity components U, V, W (or UC, VC, WC accordingly) were based on the cell size in duct region and the estimated velocities in each direction (domain residence time of the transported flow property). In our case, the false time step reached values from around 0.2 s to 0.05 s. The false time step may be 10 or 100 times the domain residence time (CHAM).

In general, the converged solution obeys global mass flow conservation and the residuals dropped for several orders of magnitude. The first criteria has to be verified in the result file at the inflow and outflow boundaries, the second one is displayed during the iteration process.

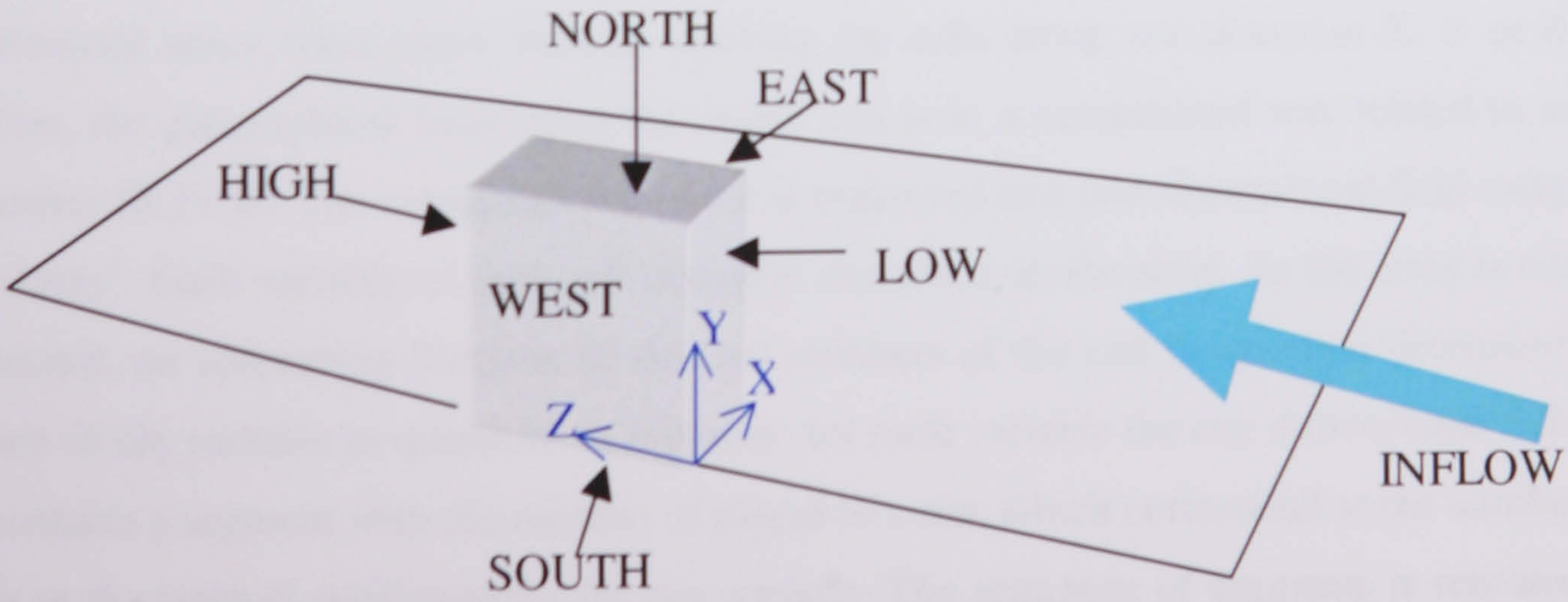

Figure 6.1.1.2: Convention of coordinate directions in the simulations, schematic drawing.

6.1.2. Organisation of Geographical and Computational Space: Grid and F-Array

6.1.2.1. The Body-Fitted Grid

Accurate representation of the duct with inlet and spoiler required a body fitted coordinate system. Further, it was very important to have a good resolution with many cells in the critical region in and around the duct. On the other hand, a vast number of cells makes excessive demands on disk space. Therefore, the whole flow domain was assembled with many different subdomains, which were specially tailored. Each single subdomain can be created using a power law factor in all three coordinate directions. This makes it possible to supply a selected region of the subdomain with a finer grid than the rest. If the grid structure of one subdomain is compatible with the neighbouring subdomain, both can be linked together. The linkage feature permitted the linkage of one single cell of the first subdomain to two or more cells of the second subdomain, as long as the cells were geometrically attached in close proximity. Hence it was possible to increase the cell size gradually domain by domain towards the far flow field. Independent from this linkage method, it is possible to insert a fine grid into the initial coarse one. Transition in between the different grids takes place with regard to conservation of mass and momentum locally in between the linked cells. The alteration in the body fitted coordinate direction at the subdomain connection at the duct outlet at the roof, which occurs naturally because of the duct bending (see Figures 7.1.1, 7.1.2, 7.1.5, 7.1.6, 7.2.1.3 and 7.2.1.4), has been overcome by using a non natural linkage method. This method provides a link in between two subdomains, which have geometrically a common boundary, but their coordinate systems are not aligned to each other (PHOENICS (CHAM)).

Obstacles are not part of the flow domain. Assembling the various subdomains in the computational space takes place through stacking the cells along one direction X, Y or Z. Therefore, the geographical location of the single cell is in a complicated way related to its cell number IX,IY,IZ. The computational space is organised as a one dimensional field array, the 'F-Array'. Each variable of each cell occupies one place on the array. As the array is one dimensional, an addressing function of the cell numbers of the cell in question determines the place of the variable in question. In this way, for each variable the one dimensional field array contains a segment with the number of places in a row which correspond to the number of cells in the stacked configuration for one z-plane. The sequence of segments is repeated for the following z-plane and so on. For example, for the three variables with storage p, v, w the one dimensional field array is populated

```
←=============================== F-Array =========……==========→
←===========1. Z-slab==================→←===========2.Z-slab==...
   P--------------------V-----------------W----------------   P--------------------V--------...
     NX*NY places      NX*NY places   NX*NY places      NX*NY places
```

The addressing function is:

$$LF=L0F(VARIABLE)+IY+NY*(IX-1)+NX*NY*(IZ-1)*NV \tag{6.1.2.1.1}$$

with NV= number of variables with storage
and L0F(VARIABLE)= first array place of variable

In this method of assembling highly non orthogonal subdomains and linkage via common boundaries, the decoupling of pressure and momentum does not take place with a common staggered grid. The alternative method is the collocated velocity method (see Chapter 5.4).

6.1.2.2. The Cartesian Grid

The cartesian grid limits the flow field to rectangular shapes. The obstacle is part of the flow field but its cells are provided with a porosity factor to block the cells completely. There is one single cartesian coordinate system for the whole flow domain, which is modelled in one block and not decomposed into many subdomains as in the previous approach. However, the spacing along each axis can be defined as non uniform, hence segments of fine grid can alterate with a coarse grid. Power law grid spacing is a common feature for each single segment. This grid refinement is not localised, it is a refinement of the spacing of the whole set of associated planes. In some cases, the need for certain grid refinements could therefore cause a huge increase of the number of cells in the domain.

Each cell number IX, IY, IZ corresponds directly to its geographical location, as there is no need to generate a stacked configuration. Each variable of each cell is placed on the one dimensional field array, the F-array.

Population of the field array for a single z-slab with NX*NY cells takes place as shown

IY increasing

⇑

NY	2*NY	3*NY	(NX-1)*NY	NX*NY
NY-1	2*NY-1	....	......	NX*NY-1
.....	....	....	......	......
....	.....	....	...	.....
2	NY+2	....	......	.....
1	NY+1	2*NY+1	....	(NX-1)*NY+1

⇒ IX increasing

The addressing function is:

$$LF=LOF(VARIABLE)+IY+NY*(IX-1)+NX*NY*(IZ-1) \qquad (6.1.2.2.1)$$

The following investigations for flow around the block have been carried out with the cartesian grid approach, which requires significantly less storage and runtime than the simulations in a multi domain grid with body fitted coordinate system.

References

CHAM; Concentration, Heat and Momentum Ltd., London SW19 5AU
PHOENICS, version 2.2.1., online help encyclopaedia
Launder B.E., Spalding D.B. et al., Imperial College London

Lam C.K.G. and Bremhorst K.: A Modified Form of the k-ε Model for Predicting Wall Turbulence; ASME Journal of Fluids Engineering, Vol. 103, p. 456 , 1981

Dannecker R.; The Ducted Wind Turbine Module and its Integration in a Conventional Building; Proc. 2nd European 'Marie Curie' Workshop Conference; Commission of the European Communities, DG XII, Directorate-General for Science, Research and Development, JOULE- Non Nuclear Energy Research; hold at the Hydraulics and Maritime Research Center HMRC, The Munster Institute, University College Cork, Ireland, April 1998

Launder B.E. and Spalding D.B.; The Numerical Computation of Turbulent Flows; Computer Methods in Applied Mechanics and Engineering, Vol. 3, pp. 269-289, 1974

Versteeg H.K. and Malalasekera W.; An Introduction to Computational Fluid Dynamics – The Finite Volume Method; published by Longman Group Ltd. 1995, ISBN 0-582-21884-5

Smithsonian Meteorological Tables, 6th revised edition, Robert J. List, U.S. Weather Bureau, Smithsonian Miscellaneous Collections Volume 114, Smithsonian Institution Press, City of Washington, USA

European Wind Atlas; published for the Commission of the European Communities, DG XII, Directorate-General for Science, Research and Development, by I. Troen and E.L. Petersen at Risø National Laboratory Denmark, ISBN 87-550-1482-8

Franzini J.B. and Finnemore E.J.; Fluid Mechanics with Engineering Applications; 9th Edition 1997, The McGraw-Hill Companies, Inc., ISBN 0-07-0219141

ESDU Engineering Science Data Unit, Wind Engineering, Wind Speed and Turbulence 1a, Characteristics of Atmospheric Turbulence near the Ground, Part II: Single Point Data for Strong Winds (Neutral Atmosphere); Item No 85020, Issued October 1985, with amendments A to F April 1993, ESDU International London, ISBN 0 85679 526 – 7, ISSN 0143 – 2702

Dannecker R. and Grant A.: Wind Energy in the Built Environment; Intermediate Scientific Report to the Commission of the European Communities, DG XII, Directorate-General for Science, Research and Development, JOULE -Non Nuclear Energy Research, Project No JOR3-CT97-5008 (DG12-DEMA), September 1998

Dannecker R.; Computational Fluid Dynamics of the Wind Flow around a Building and its Influence on Design and Performance of the Integrated Ducted Wind Turbine Module; Proc. 4th European 'Marie Curie' Workshop Conference, Commission of the European Communities, DG XII, Directorate-General for Science, Research and Development, JOULE-Non Nuclear Energy Research; hold at the Department of Mechanical Engineering, University of Leeds, England, April 1999

6.2. Modelling of the Building without Integrated Duct

Initially various grids were tested in order to assess the sensitivity of the flow field solution to different grids. In two dimensional simulation, the coarse grid needed around 3000 sweeps and the fine grid around 4000 sweeps to converge. The values for the three dimensional case were around 7000 or 8000 sweeps accordingly. In all cases, convergence was confirmed when the residuals for each of the variables reached values lower than 20. Hence, the average drop for the residuals was 5 to 6 orders of magnitude. Global mass flow conservation was confirmed in the result files at the inflow and outflow boundaries.

6.2.1. Two Dimensional Simulation with Cartesian Grid

Under investigation was in particular the number of cells and their distribution in the vicinity of the obstacle, which were found to be crucial to the achieved solution. The grid was refined until no significant change in the flow patterns and stable values of the range of pressure coefficients on the surfaces was observed. It was found that special caution is needed not to 'over-refine' the grid solely in one dimension, for example by applying a power-law grid distribution. This happens easily for vertical grid refinement over the roof, when the number of cells in the z-direction along the roof is kept constant. It causes a prediction of a false sudden drop in pressure at the leading edge (Dannecker and Grant 1998).

The geometry of the two test cases are summarised as follows:

2D test case	Number of cells	$\Delta y_{P\,front}$	$\Delta y_{P\,roof}$
2D refined	1 x 85 x 106	0.062 m	0.069 m
2D coarse	1 x 37 x 62	0.388 m	0.769 m

Δy_P is the distance from the near wall grid node normal to the adjacent wall boundary (see Chapter 5.7).

Both cases differ mainly in the resolution close to the obstacle:

	refined	coarse
Number of cells along roof length:	26, power law 1.3	10, uniformly distributed
Number of cells above roof (up to 0.5 H):	9, power law 1.5	3, power law 1.5
Number of cells at façade:	35, power law 1.5	15, power law 1.5

The Y^+ values for the refined grid are in the range of application of the wall boundary (see Chapter 5.7). At the façade upper edge $Y^+ = 322$, on the front roof edge 238 and at the rear part of the roof 82. For the coarser grid, wall boundary functions do not apply.

The resulting vector flow patterns both show flow separation at the wall roof edge which extends far above building height into a long wake behind the obstacle. It is seen that the grid refinement encourages the extension of the recirculation zone above the roof and behind the obstacle. If we define the wake length behind the building as the distance to where the flow patterns show the first flow attachment, the coarse grid case (Figure 6.2.1.1) shows a wake length of 9.4 H, H being the building height, whereas grid refinement (Figure 6.2.1.2) increases the wake length to 12.8 H. The recirculation above the roof extended to one fifth or one quarter of building height respectively.

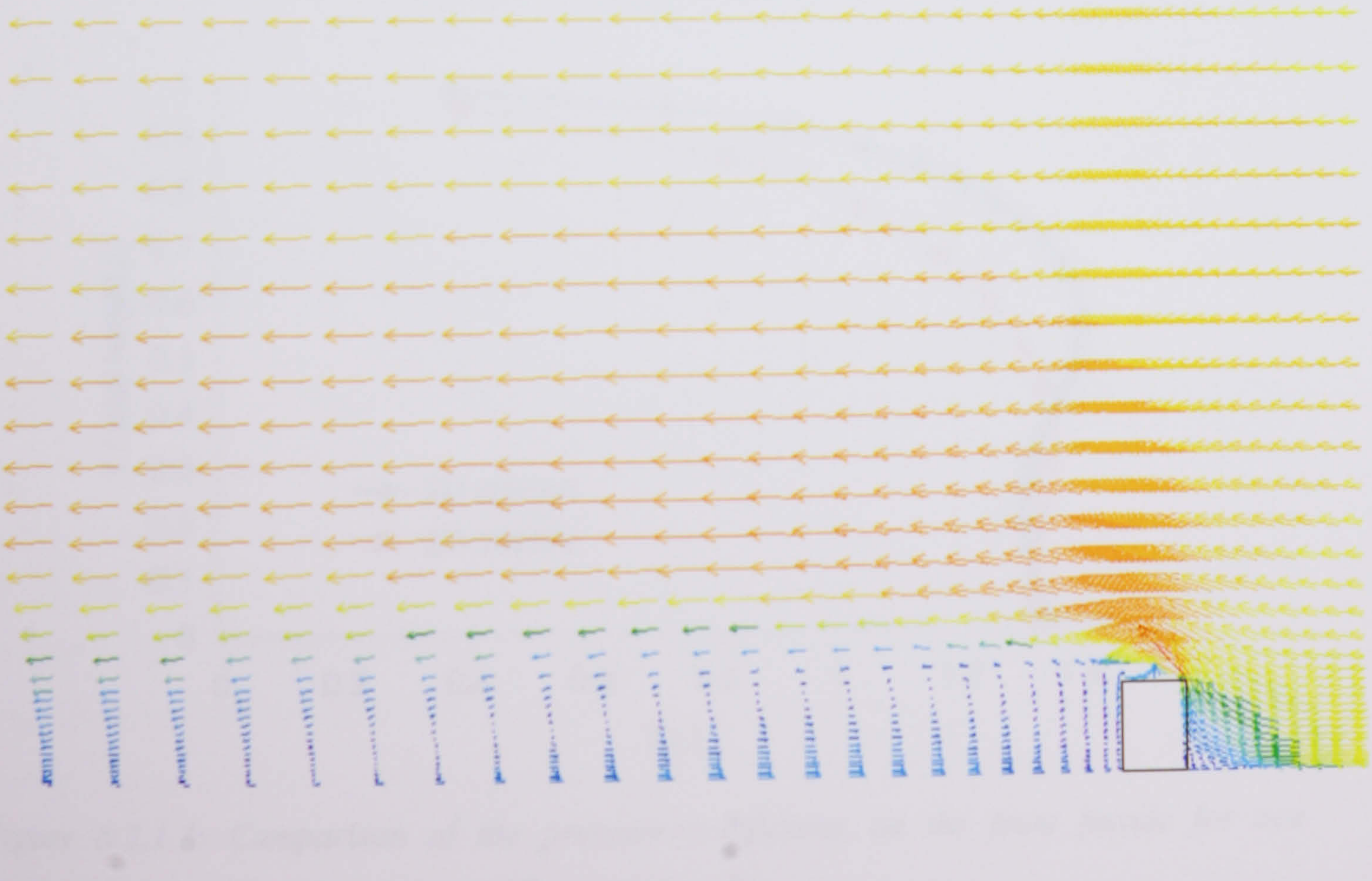

Figure 6.2.1.1: Vector flow pattern in the cross-sectional plane of symmetry, coarse grid

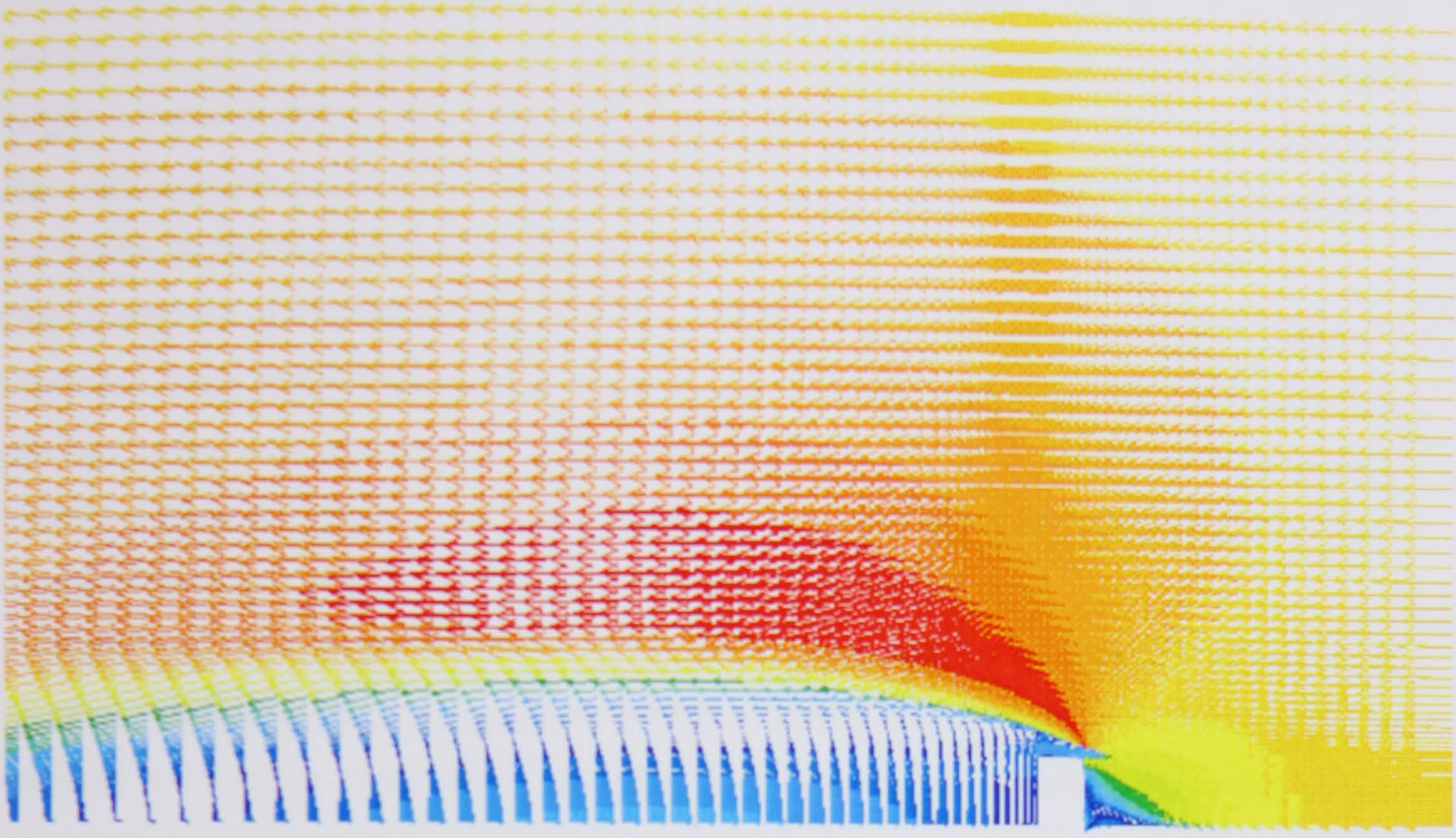

Figure 6.2.1.2: Vector flow pattern in the cross-sectional plane of symmetry, refined grid

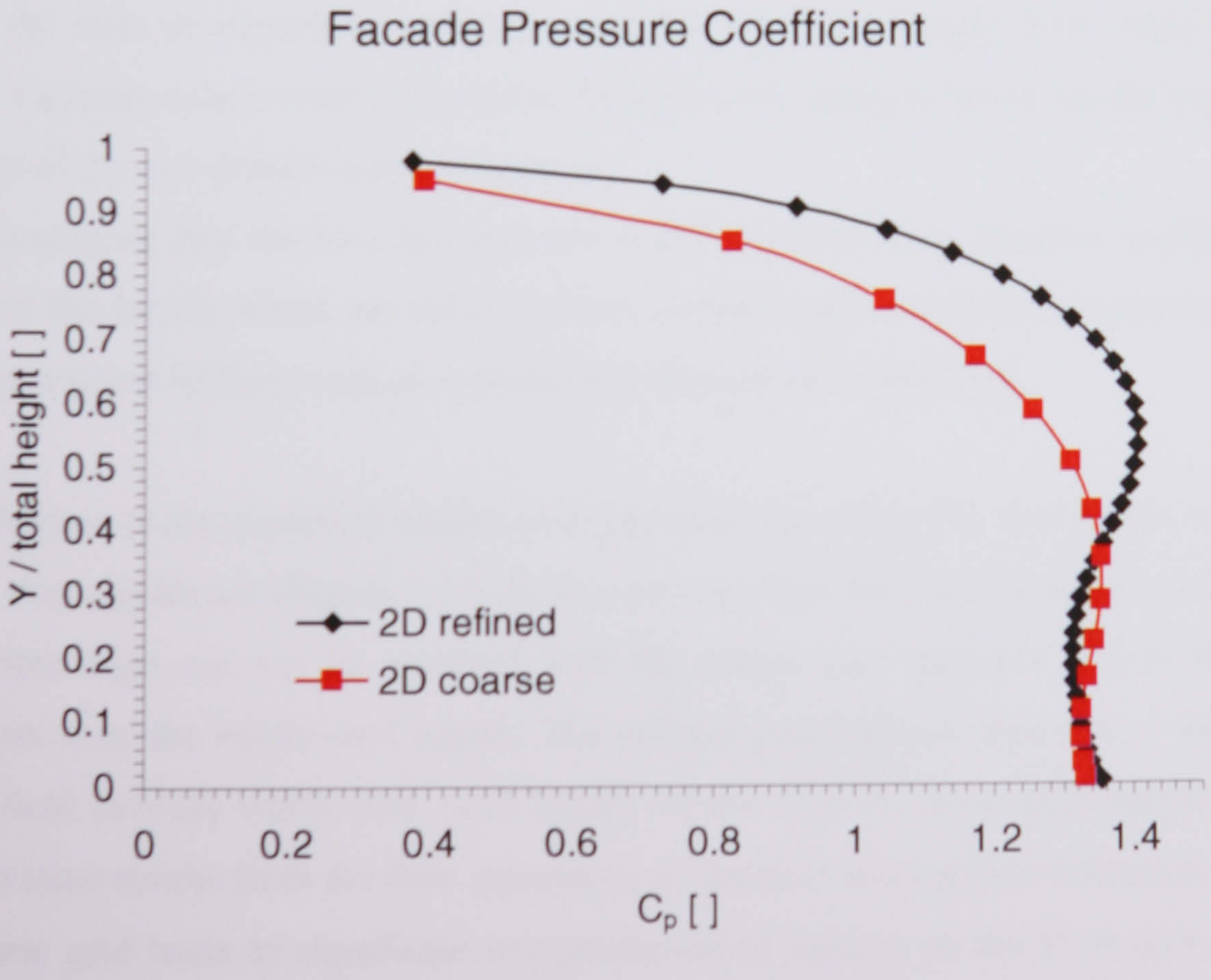

Figure 6.2.1.3: Comparison of the pressure coefficients on the front façade for two dimensional modelled flow for two different test grids.

Figure 6.2.1.3 shows the pressure coefficient on the front façade for the coarse and the refined grid. In the coarse grid, the lesser number of cells towards the upper edge of the façade smoothens the sudden pressure drop of the flow passing onto the roof. It is significant that with both grid distributions, the pressure converges to similar values at the upper edge of the façade, where the duct inlet is intended to be.

Over nearly the whole façade, the pressure coefficient is larger than one! This is seen as a systematic error caused by the two dimensional simulation approach. In reality, the flow deviates in three dimensions, and is turbulent. The third dimension carries momentum away which is not transferred into stagnation pressure. Therefore, any quantitative adoption of two dimensional results even for the plane of symmetry is questionable.

Previous work has shown (Dannecker and Grant 1998), that it is possible to diminish the pressure coefficient on the front façade under the margin of $C_p = 1$ at stagnation height, by applying a boundary layer inflow profile. The thickness of this boundary layer profile exceeded the building height significantly. In this way, it is possible to diminish the impact of the systematic error.

Pressure coefficients larger than one may be experienced where local accelerated flow is brought to rest. As the pressure coefficient is based on the mean flow velocity in the free stream, the ratio of stagnation pressure caused by local accelerated flow could exceed one without violating conservation principles. This does not apply however for the simple cuboid geometry of the two dimensional simulation.

It is encouraging that the two dimensional model could produce pressure coefficients near the top of the façade which are close to three dimensional models and experimental values. This may support further evaluation of the two dimensional modelling.

The difference in the modelled suction over the front part of the flat roof for the two different grids is very significant (Figure 6.2.1.4). It is obvious that the steep pressure gradient arising at the front edge can not be resolved with the coarse grid approach. There, the gradient propagates over the whole roof length. The refined grid solution generates a more uniform suction field over the whole roof, with higher suction near the front edge and at the far rear end. The latter results from the flow separation of the recirculating flow behind the building.

The coarse grid leads to significant overprediction of suction on the front part of the roof, however the fine grid solution shows values of suction at the roof edge which are in the range of reported values, and which are reasonably close to three dimensional modelled values. But regarding the whole roof, even the refined grid can not prevent the systematic error of the two dimensional simulation, which results in an overprediction of suction above the roof. In the two dimensional simulation, the whole massflow passes only over the roof. At the sharp edge the flow accelerates and separates, causing increasingly recirculating flow.

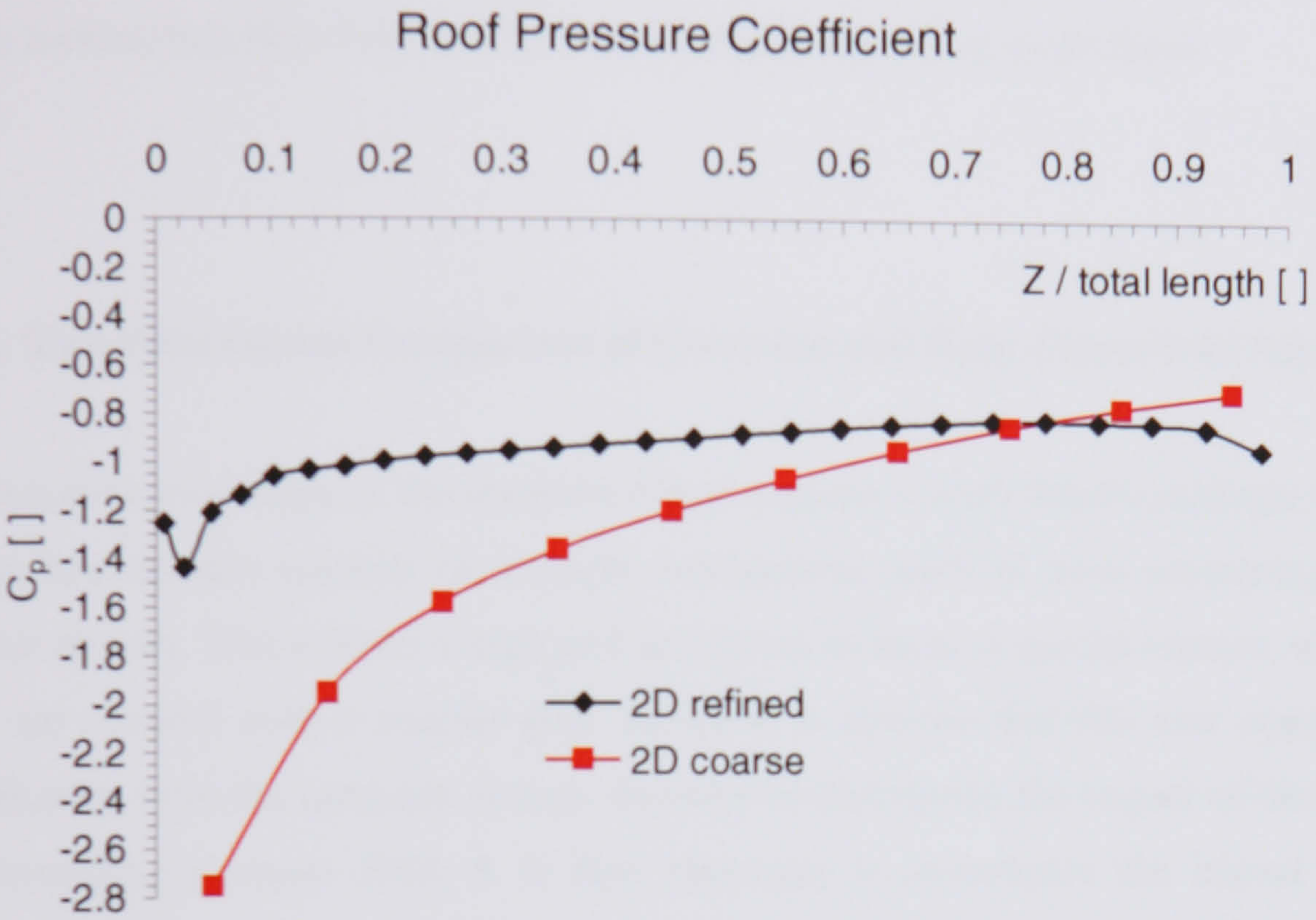

Figure 6.2.1.4: Comparison of the pressure coefficient on the flat roof for two dimensional modelled flow for two different test grids.

6.2.1.1. Conclusions and Recommendations

Near solid surfaces, Δy_p influences the value of the simulated pressure coefficient on this surface. This is very significant for the grid nodes at the sharp edge of the roof. Therefore it was important to investigate the nondimensional wall parameter Y^+. Finer grid resolution makes it possible to resolve steep pressure gradients. Refinement in both directions is important. One dimensional vertical grid refinement above the roof leads to overprediction of the suction at the wall roof edge, therefore the power-law grid distribution has to be applied carefully. Power-law factors were kept below 2. Limitations on grid refinement are imposed by an increase in computational time and in the required disk space. While grid refinement assists in resolving steep pressure gradients, it extends the recirculating zones above the roof and behind the obstacle.

Two dimensional modelling produces a systematic error, which causes overprediction of stagnation pressure on the façade and increased suction above the flat roof. However, in the area of interest around the façade-roof edge, the two dimensional predicted values are close to three dimensional predicted values, experimental values and published standards (see Chapter 6.3.2). Therefore, two dimensional modelled flow through the ducts and its impact on the surrounding flow field will be evaluated qualitatively in more detail.

6.2.2. Two Dimensional Comparison of Cartesian and Body-Fitted Grid Solutions

The non-cartesian shape of the integrated duct requires a body fitted coordinate system. The whole flow domain consists of multiple subdomains, each of them containing a different number of cells. This enables a high grid resolution in areas of special interest, whereas other areas are covered with a coarser grid. Hence it is obvious that this new approach differs significantly from the cartesian system. In order to distinguish the impact of the ductflow on its surounding pressure field, it is first necessary to investigate the impact of the new gridding approach. As we have seen in the previous Chapter 6.2.1, cell size and cell distribution may have a major influence on the calculated pressure coefficients of the building envelope. Hence, the two dimensional simulation of one of the modelled duct configurations (see Chapter 7, configuration VI) was altered. The duct was closed with the wall boundary. The results were compared with the previous two dimensional cartesian approach with a refined grid. Both grids use the same number of cells along the building envelope, but with a slightly different distribution. The body fitted approach uses twice as many cells in the upper half of the front façade, while on the roof the cells are slightly more densely distributed towards the front edge in order to model the duct outlet.

The geometry of the test cases is summarised as follows:

2D test case	Number of cells	$\Delta y_{p\ \mathrm{front}}$	$\Delta y_{p\ \mathrm{roof}}$	$Y^{+}_{\mathrm{façade}}$	Y^{+}_{roof}
2D cartesian refined	1 x 85 x 106	0.062	0.069	238	322
2D body fitted multi domain	1 x 238 x 42	0.134	0.062	443	103

At the edge of interest, the Y^+ values take on their largest values due to the accelerated flow. The lowest values appear somewhere near the rear of the roof where the recirculating velocity is low, and in the stagnation area on the front façade. All Y^+ values are in the required range (see Chapter 5.7).

Comparison of the calculated pressure on the front façade shows (Figure 6.2.2.1), how much the extent of a generated boundary layer over the ground depends on the grid distribution. The body fitted approach has only 50 % of the cells applied on the lower half of the façade, compared with the refined cartesian case. The refined grid can resolve the steep velocity gradient close to the ground, and the height of the shear layer is below the obstacle height. The coarser the grid resolution towards the ground, the larger the growth of the thickness of the shear layer. For the coarse grid resolution, the obstacle may be completely immersed in the shear flow.

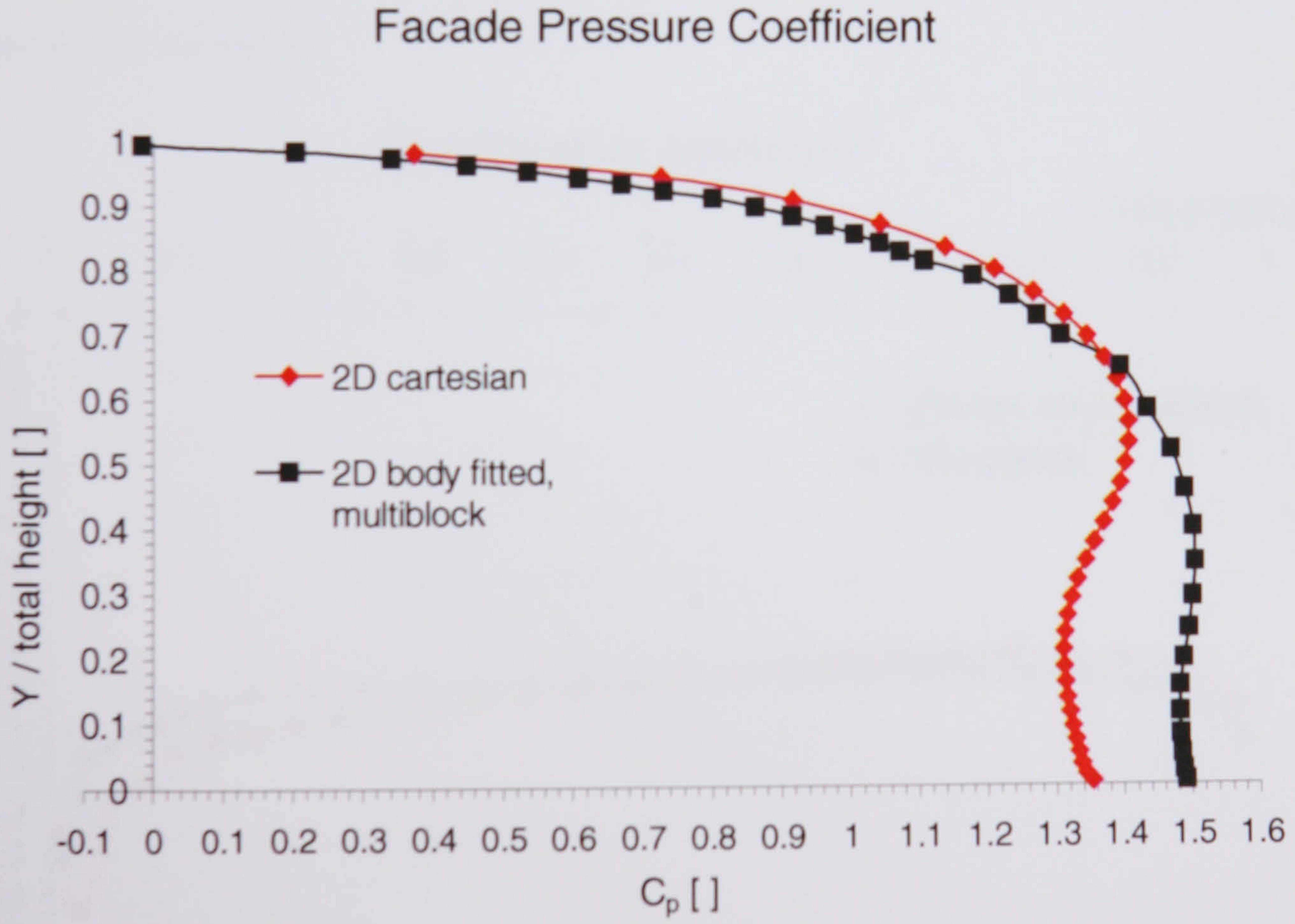

Figure 6.2.2.1: Comparison of the pressure coefficient on the front façade for two dimensional modelled flow for a refined cartesian grid and a multi-domain grid with body fitted coordinates (see Chapter 7, configuration VI)

Compared with the cartesian coarse grid approach from the previous chapter (see Figure 6.2.1.3), the high uniform stagnation pressure distribution at the lower part of the façade indicates that not only the local grid distribution influences the generation of the boundary layer. The vertical grid distribution towards the ground over the whole flowfield upstream from the obstacle determines the generation of the boundary layer. Local grid refinement of the domain in front of the obstacle can not resolve a boundary layer of incoming flow, which has already failed to resolve the steep pressure and velocity gradients further upstream due to a very coarse grid approach. The strength of the multi domain gridding lays in particular in the option gradually to increase the grid size due to the linking of one big cell to a few small cells. This allows localised grid refinement without an overall enormous increase of the amount of cells. Nevertheless, it is important to note, that in the upper part of the façade, the calculated pressures are nearly identical. Due to the finer resolution of the body fitted case, the uppermost value is nearly zero, as expected for the flow passing over the edge. This indicates that modelling an inflow boundary layer does not significantly change the values at the upper part of the façade.

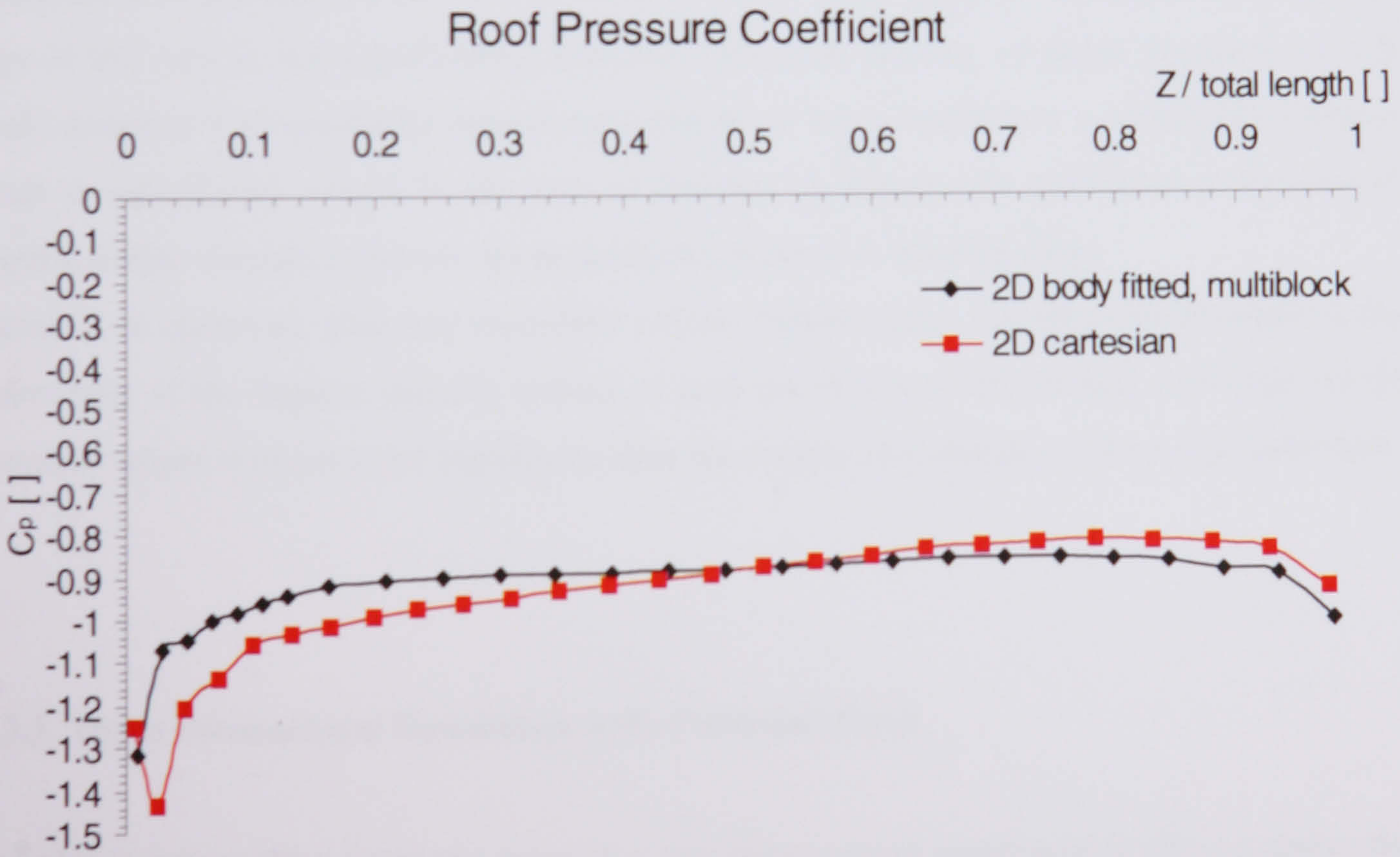

Figure 6.2.2.2: Comparison of the pressure coefficient on the roof for two dimensional modelled flow for a refined cartesian grid and a multi-domain grid with body fitted coordinates (see Chapter 7, configuration VI)

The pressure coefficient along the roof length (Figure 6.2.2.2) is quite similar in magnitude for both cases. However it seems to be the case that the slightly finer grid resolution at the front part of the roof in the body fitted grid results in a steeper pressure gradient. Behind this gradient, the pressure remains uniform. It appears that the finer the resolution is at the front part of the roof, the more uniform is the pressure distribution over the rest of the roof. Because of the need to model a duct, any grid will have a fine resolution at the front part of the roof. Hence it will be expected that the region behind the outlet will normally have a fairly uniform pressure distribution. Any deviation will be due to the impact of the intruding jet stream in the flow field above the roof. The increase in suction at the rear part is caused by flow separation of the recirculating flow behind the building. It does not influence the pressure situation at the front part of the roof.

6.2.2.1. Conclusions and Recommendations

In spite of the fact that the far field gridding upstream influences the incoming flow, the distribution of pressure in the area of interest on the upper part of the façade and the front part of the roof is not significantly affected. The multi-domain gridding approach, to link multi domains with gradually increasing numbers of cells together to a whole flow domain, leads to satisfactory results in the area of interest, as long as the resolution in the area of interest is fine enough to resolve steep gradients around the leading edge.

Hence it is observed, that any modelled inflow domain does not alter the pressure at the upper part of the façade, and the impact of grid resolution at the leading roof edge on the pressure values is much more significant than the impact of a change in incoming shear flow.

6.2.3. Three Dimensional Simulation with Cartesian Grid

In order to assess the systematic error of a two dimensional simulation in the y-z plane, the same grid was extended in the x-direction to simulate the wind flow around the building in three dimensions (see Figure 6.1.1.1). The symmetry plane lays in the y-z plane. To reduce the computational time and required disk space, the domain consisted of just one symmetrical half of the flow domain. The symmetry plane is a boundary which mirrors the variables in the discretised domain. The geometry and the grid in the y-z plane is identical to the previous two dimensional case (see Chapter 6.2.1).

The following figures show the cell distribution; the factor behind the cell number is the power law factor, power law spacing takes place in positive coordinate direction.

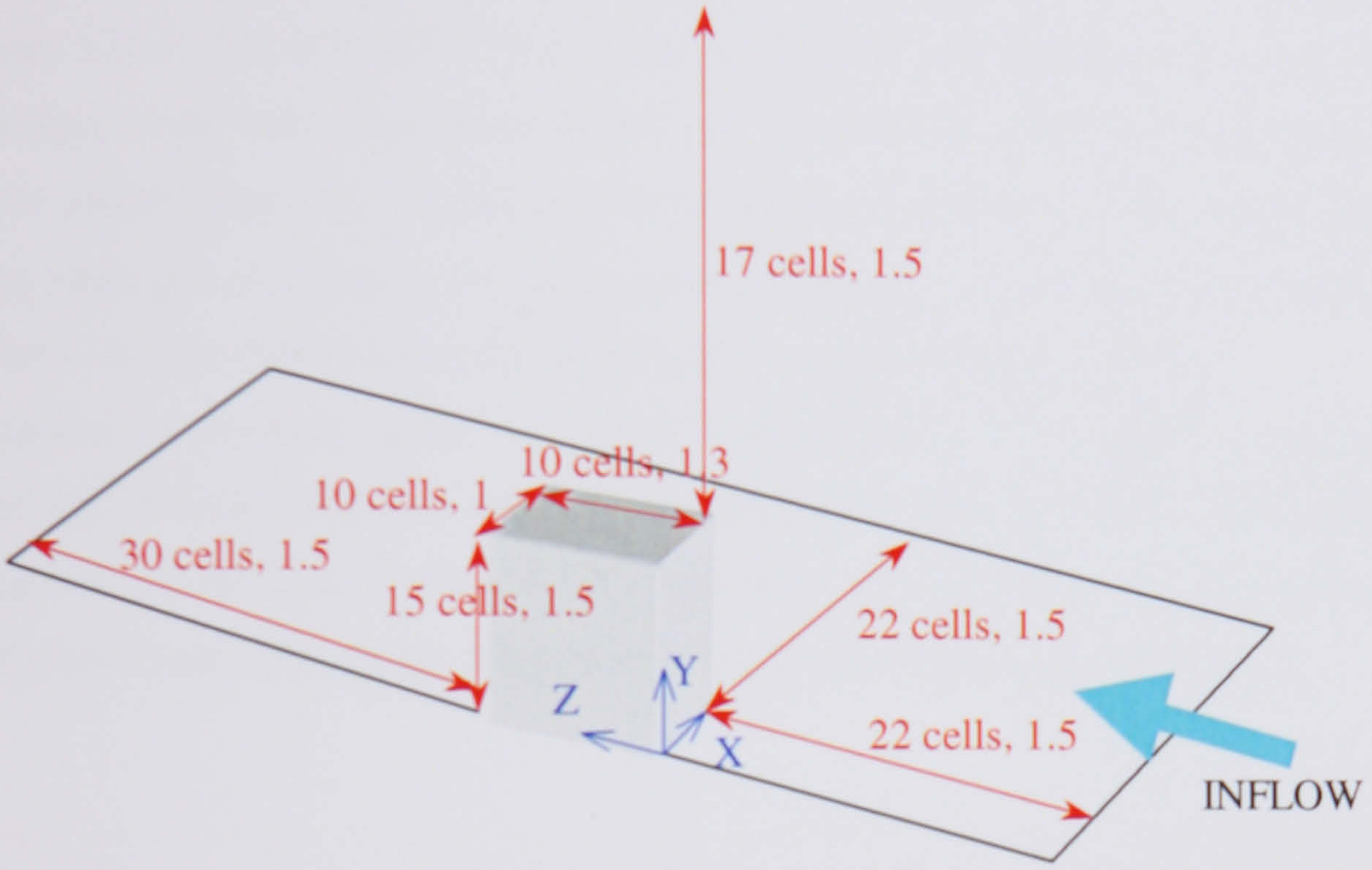

Figure 6.2.3.1: Cell distribution of flow domain, schematic drawing, coarse case.

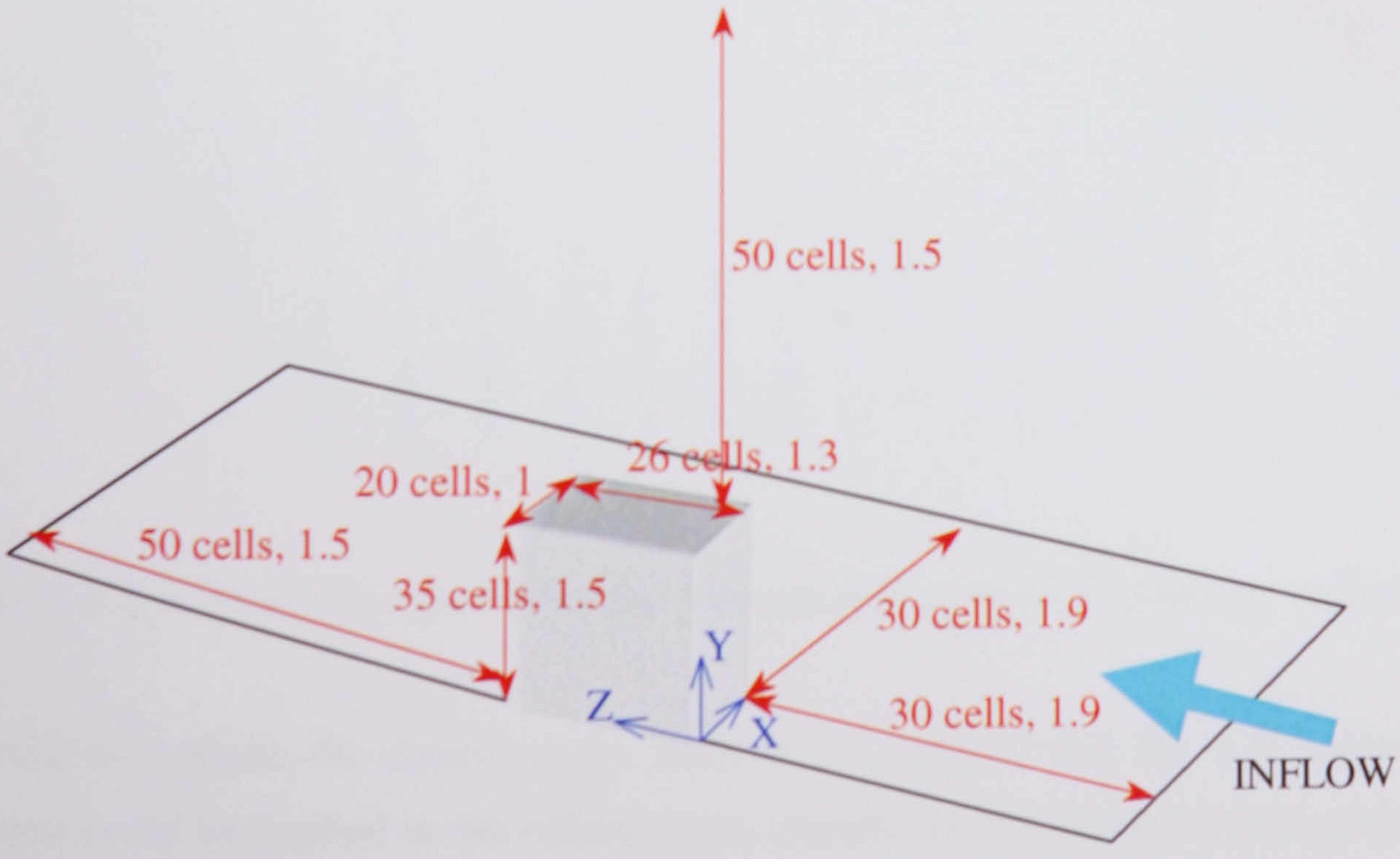

Figure 6.2.3.2: Cell distribution of flow domain, schematic drawing, refined case

The solution of the three dimensional simulated case in the plane of symmetry comprises a very different vector flow pattern to the previous two dimensional solutions. Generally, the wake behind the building is very much shorter then in the two dimensional case.

In the three dimensional simulations, the resolution of the grid has an enormous impact on the size of the recirculating flow zone, similar to the previous two dimensional case (see Chapter 6.2.1). The solution in the refined grid shows a significant flow separation at the front edge of the roof. The recirculation zone above the flat roof rises at the far end of the roof to approximately 0.3 H and progresses in the recirculating wake behind the building, which reattaches at around 3.6 H downstream (Figure 6.2.3.3). The vector flow pattern looks similar to the two dimensional simulated cases, only the wake is shortened.

In contrast, the solution of the coarse grid does not show flow separation and recirculation above the flat roof. The flow seems to be attached to the roof, apart from a small vertical component of the flow vectors in the first layer of boundary cells above the roof. The recirculation wake behind the building reduces to 2 H in length (Figure 6.2.3.4).

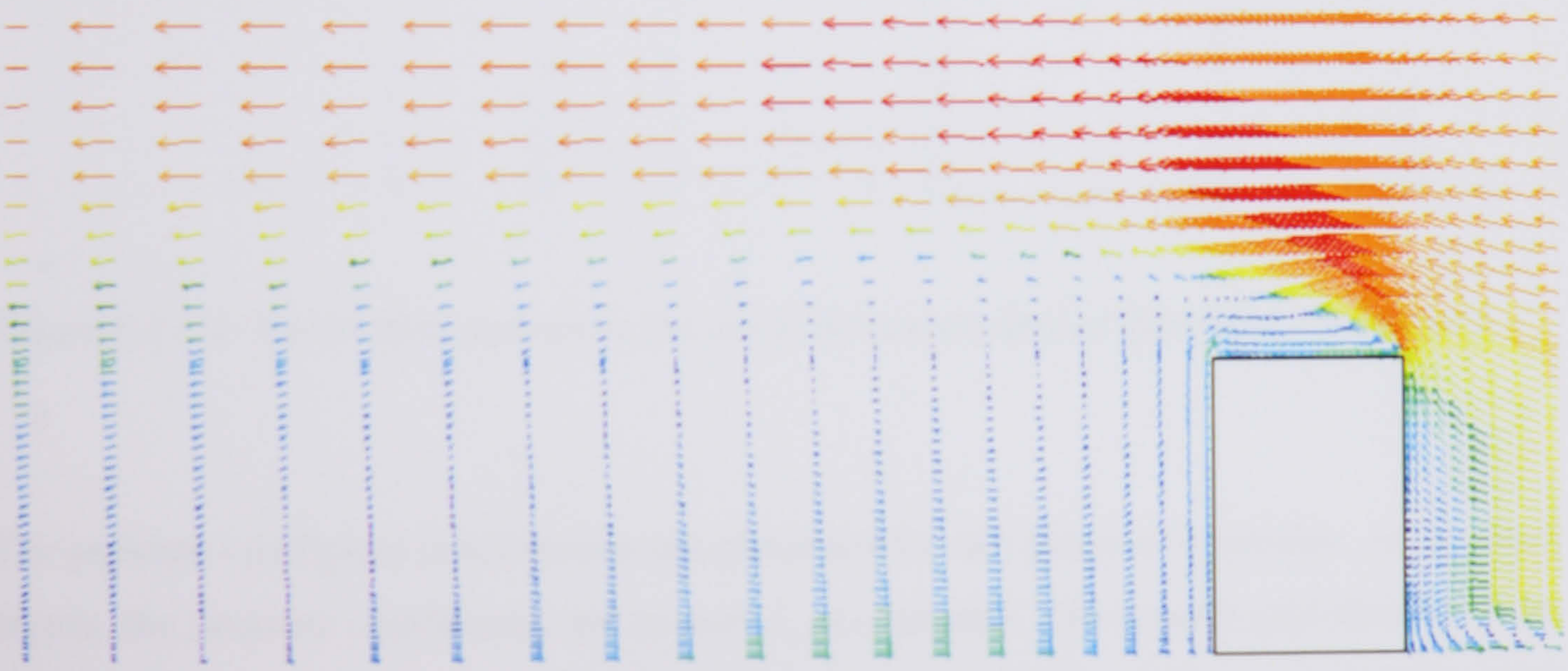

Figure 6.2.3.3: Vector flow pattern in the cross-sectional plane of symmetry, refined grid

In order to evaluate the details at the wall, it was verified that the wall boundary layer function could be applied in the refined case. (Again, for the coarse case the wall function does not apply.)

The Y^+ values are for the plane of symmetry as follows:

top of façade: $Y^+ = 290$ for vertical velocity component v

$Y^+ = 47$ for tangential velocity component u

front of roof: $Y^+ = 231$ for longitudinal velocity component w

$Y^+ = 35$ for tangential velocity component u

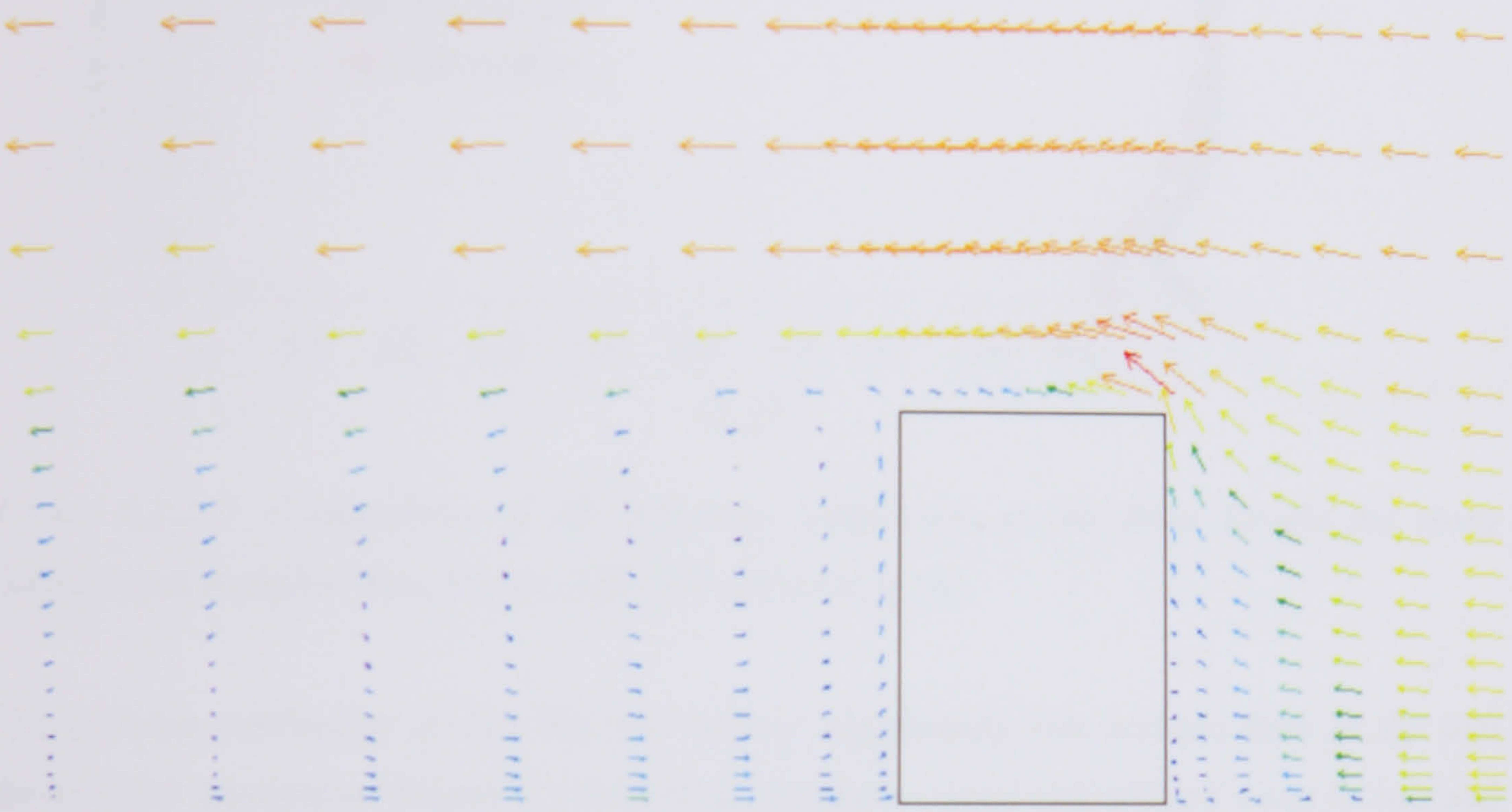

Figure 6.2.3.4: Vector flow pattern in the cross-sectional plane of symmetry, coarse grid

The pressure coefficient distributions are presented for the plane of symmetry. At the front façade, the pressure coefficients are around 1, as expected. The coarser grid deviates from the refined distribution towards the ground, as the coarser grid could not resolve the steep velocity gradient generating the shear flow. The refined grid shows at the base of the façade increased pressure, which might be caused by vorticity which could not be resolved in the coarse grid to that extent. At the top of the façade, the three dimensional simulated pressure coefficient in the refined grid reaches values similar to those calculated in the previous two dimensional approach (compare Figure 6.2.1.3 with Figure 6.2.3.5). Also, the coarse grid pressure coefficient converges with the fine grid pressure coefficient towards the upper edge (Figure 6.2.3.5).

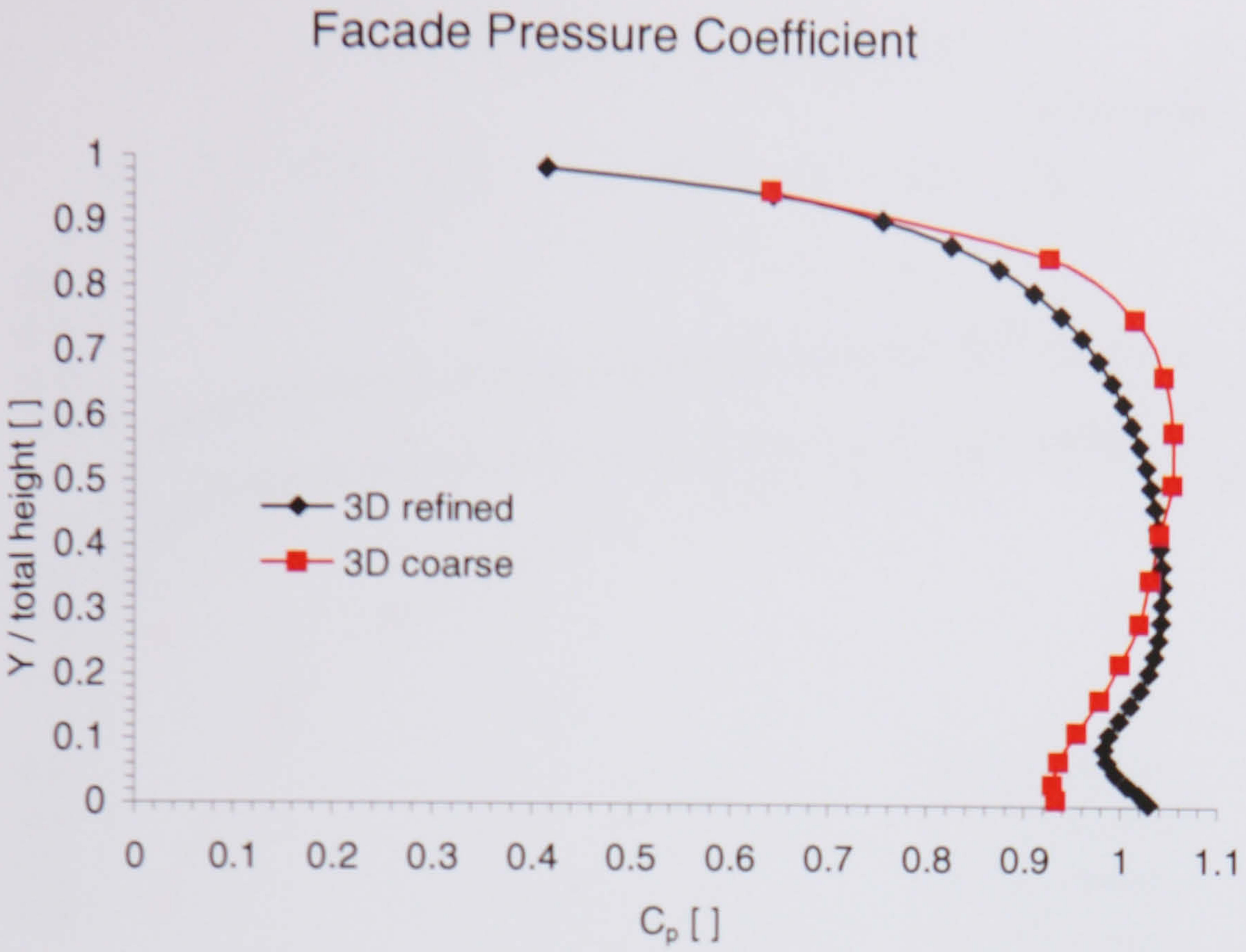

Figure 6.2.3.5: Comparison of the pressure coefficients at the front façade for three dimensional modelled flow for two different cartesian grids.

The pressure coefficient on the flat roof shows significantly less suction then in the two dimensional simulation (Figure 6.2.3.6). If we compare coarse and refined cases in two and three-dimensional simulation, the similarities become obvious. The two dimensional simulated pressure coefficient seems to follow the three dimensional solution more or less, with an offset. This is surprising for the coarse grid, as the three dimensional simulated flow over the roof seems to remain attached, in contrast to the two dimensional case. Higher resolution of the grid again causes a more uniform pressure distribution over the flat roof. As the refined grid allows the flow to separate completely, a more uniform suction occurs inside the flow separation zone along the flat roof until the far end. Further, the refined grid resolves the steep pressure gradient at the front part of the roof.

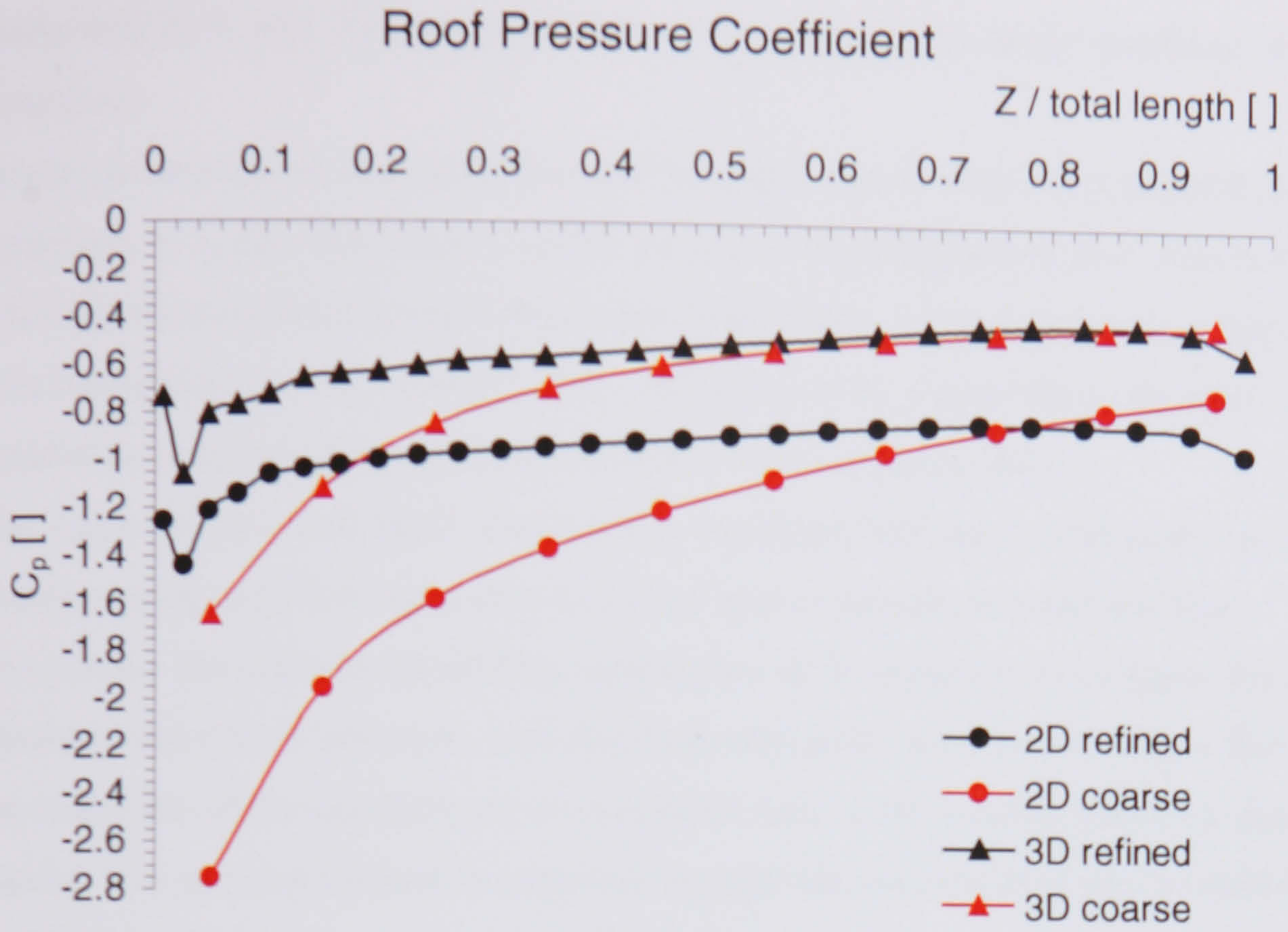

Figure 6.2.3.6: Comparison of the pressure coefficients on the flat roof for two and three dimensional modelled flow for two different grids.

Earlier tests of only vertical grid refinement (Dannecker and Grant 1998) showed, that without further longitudinal refinement, the simulated suction at the front part of the roof became greatly overpredicted (C_p ~ -2.2). Flow separation did not occur with vertical grid refinement, only taking place if an increased number of cells in both vertical and longitudinal directions have been implemented.

6.2.3.1. Conclusions and Recommendations

The pressure coefficient distribution for flow around a cubic obstacle differs significantly between two and three dimensional simulation. Basically, only three dimensional simulation can generate results which are in an acceptable range. Nevertheless, local values in particular in the area where the flow passes the sharp wall roof edge, are similar in both approaches. This may justify the use of two dimensional simulation for a qualitative evaluation of the flow situation in the intended duct area around the wall roof corner.

In three dimensional simulation the separation of flow at the sharp edge occurs only with a significantly refined resolution. Two dimensional simulated results, if used, should be interpreted in a way that takes account of an intrinsically larger predicted zone of flow separation.

Single grid refinement normal to the solid boundary is not adequate to simulate possible flow separation. It is also important to refine the grid in the longitudinal flow direction. Generally, it has to be assured that in each dimension, where flow recirculation is expected, are enough cells implemented in the domain. This will prove to be significant in the three dimensional simulation of the wind flow around a building with integrated duct.

The slopes of two and three dimensional simulated pressure coefficients on the building envelope seem to follow each other to a good approximation, but with an offset.

To evaluate the different modelling approaches, it is important to compare the results with reported values from literature, with standards and with experimental values. But technically, the modelling of the geometry of an integrated duct is not feasible without a significant grid density. The jet stream which is expected through the duct requires also a relatively fine grid resolution. Therefore, the coarse grid approach could never be taken as a basis to model the integrated duct with the body fitted coordinate system.

Reference

Dannecker R. and Grant A.: Wind Energy in the Built Environment: Intermediate Scientific Report to the Commission of the European Communities, DG XII, Directorate-General for Science, Research and Development, JOULE -Non Nuclear Energy Research, Project No. JOR3-CT97-5008 (DG12-DEMA), September 1998

6.3. Comparison of Simulated Results with Reported Values

The present work focuses on the flow situation in the area of the wall roof edge. The main parameters are the pressure coefficients on both faces in that area. However, the local flow situation at this location is also very important, in particular to which extent the flow separates at the sharp edge, and how strongly it recirculates above the roof. Both factors are likely to have some impact on the performance of any ducted wind turbine integrated in that area. If the flow separates at the leading edge, it may reattach at the rear part of the roof or it may not, depending on many parameters. But every part of the flow over the building envelope will in some way be involved in the generated wake behind the building. The loss of momentum in the wake and its depression compared to the free stream is according to the conservation principle (Schlichting 1965) directly related to the drag force, which the obstacle has to withstand. In general terms, by comparing the pressure and the momentum in two identical planes in an incompressible flow normal to its direction, one upstream and one downstream, we explore the longitudinal component of force which the flow experienced or exerted accordingly on the way between the two planes. As the flow around the obstacle is highly three dimensional, the drag force which the obstacle experiences will appear as a loss of momentum in three dimensions in the planes of a virtual cube around the obstacle (Hunt and Smith 1996, Hunt 1970). In a similar manner, the drag force is directly proportional to the pressure coefficient integrated over the whole obstacle envelope. Therefore, properties of the wake and the pressure field on the surface of the obstacle are related, and it is necessary to look at both in order to evaluate the simulated results.

6.3.1. The Wake behind the Block and the Recirculation above the Roof

The flow passing around a tall obstacle separates in many ways. The following simplified schematic sketch (Figure 6.3.1.1) shows separating streamlines in a vertical cross-sectional plane in the mean flow direction, dividing the mean flow field into different zones around the obstacle. At the front, the flow divides at stagnation height, where the flow is deflected downwards and around the building. The flow around the obstacle separates at each sharp edge and generates recirculation.

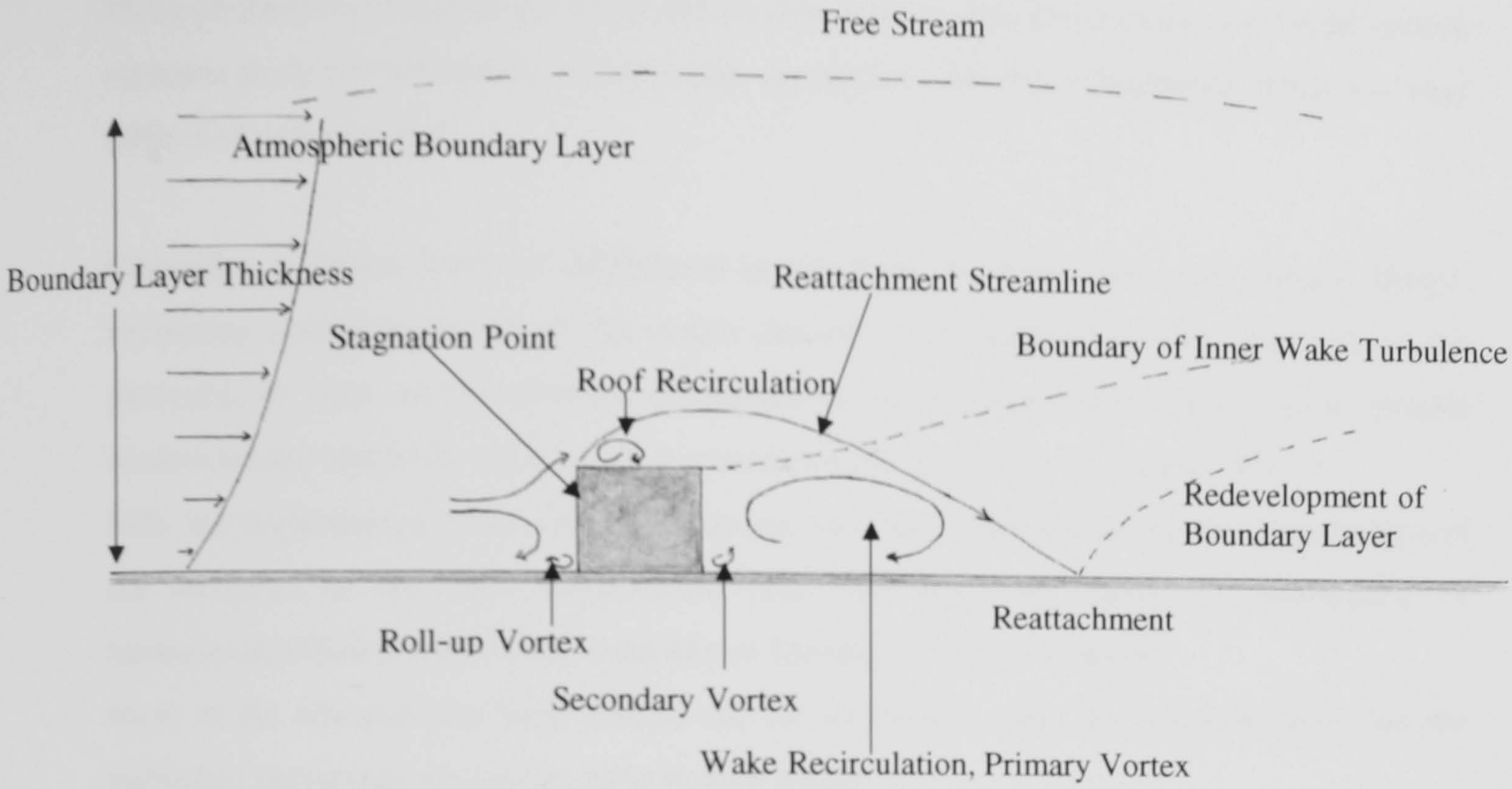

Figure 6.3.1.1: Mean flow streamline pattern for the flow around an obstacle, schematic sketch (Hunt and Smith 1969, Dargent 1996)

The downward flow generates a system of horizontal vortices at the obstacle's base, and the secondary vortex carries opposing circular momentum to the primary vortex. Behind the obstacle, a large recirculation wake is generated.

The presented streamlines do not represent the boundary of the wake, because turbulent intensities and Reynolds stresses will not be regarded in this investigation. Wake boundaries extend beyond the recirculation zones (Schlichting 1965, Hunt and Smith 1969, Hunt 1970, Counihan 1971, Dargent 1996). For example, the roof wake boundary includes a high turbulent region above the roof which gives rise to the pressure drop over the whole roof compared with free flow conditions. Therefore, the low pressure area is not solely restricted to the recirculation zone, it extends to the zone of reattached flow at the rear part of the roof, if this occurs. Here, no attempt is made to compare turbulent intensities and Reynolds stresses with reported values. The main features of comparison are the mean flow recirculation patterns above the roof and behind the obstacle. In particular the recirculation pattern above the roof is seen to be of major importance for the implementation of the ducted wind turbine.

Many parameters influence the recirculation flow pattern, size and momentum. Under certain circumstances, the secondary vortices may not appear, and the reattachment behaviour may differ from case to case.

Generally, a higher level of turbulence in the flow decreases the wake length. Hence, increasing roughness height of the terrain induces a less significant wake and reduces the recirculation zone, as the obstacle submerges in the boundary layer shear. These general tendencies are said to be valid for all geometries with sharp edges (Dargent 1996).
Still, the recirculation zones and the wake are very much determined by the aspect ratios of the obstacle. In the three dimensional case, the width influences the distribution of momentum which is transferred vertically or laterally at the front façade.
Most of the research has been carried out for the simple cube, and even for this case the published investigations lead to quite diverse results.
The wake of a rectangular multistorey building in an urban environment will be influenced by the buildings in its vicinity, and also by longitudinal and vertical pressure gradients in the local atmosphere in the vicinity of the building. Also buoyancy will play a role. But published data on field measurements of wakes and recirculation are very rare (Colmer 1970 as quoted in Counihan 1971), and the author did not come across any publication referring to a similar case under investigation.

All quoted published research in Computational Fluid Dynamics is based on the k-ε model. The wake length behind the building is presented as the distance between the leeward side of the obstacle and the reattachment point at the end of the recirculation zone. This reattachment point may be defined in three different ways. Some cite the stagnation point on the ground behind the obstacle, which might be the most accurate way to determine the wake length. Other ways are to display the vector field pattern or the streamline pattern in a cross-sectional vertical plane in mean flow direction. However, there is sometimes discrepancy between the cited stagnation point and the displayed vector flow patterns (for example with Zhang 1992 or Baetke 1987). For the sake of clarity, in the presented work reattachment will be defined from the vector flow patterns as displayed in the vertical cross-sectional plane, in the first cell above the ground downstream from the obstacle where the flow vector does not show reverse flow any more. In the published literature, where the streamline patterns are

given, a tangent to the streamline was estimated in the section above the ground and the crossover point with the ground line was taken as the estimated reattachment point.
Unfortunately, the simulated flow conditions and the geometry of the obstacle do not precisely correspond to investigations found in literature, hence the comparison is inexact. In order to allow comparison, the dimensions of the recirculation zones are non-dimensionalised with the obstacle height. The inflow profile was simulated as uniform, for the sake of clarity as described in Chapter 6.1.1. However the uniform inflow generates a boundary layer profile, as the ground region in front of the obstacle is represented with wall functions. But the boundary layer thickness will remain below one third of the obstacle height. Here, the inflow carries a turbulence intensity of 40 %, and the dimensions of the obstacle are 30 m height, 20 m depth and 35 m width.

6.3.1.1. Comparison for Two Dimensional Flow

For both different grids, the flow separates at the leading roof edge and does not reattach at the roof. Using the coarser grid (see Figure 6.2.1.1), the length of the recirculation region in the wake of the obstacle is around 9.4 H, and the reciculation zone exceeds the roof height for about 0.2 H, which occurs already over the rear part of the roof. In case the fine grid is applied (see Figure 6.2.1.2.), the recirculation over and behind the obstacle expands significantly. The flow separates at the leading edge, and includes a recirculation zone, which reaches at the rear part of the roof approximately 1/4 H over the roof. The maximum height of the recirculation zone (ca 1.6 H) is reached at approximately half of the distance in between obstacle and reattachment point (ca 12.8 H).

A detailed comparison of numerical and experimental results shows the range of diversity. Dargent (Dargent 1996) simulated the flow around a two dimensional flat rectangular block (D/H = 2/1, depth in flow direction) for two different inflow conditions: A boundary layer profile with a high amount of turbulence and a uniform profile with low turbulence. In the first case, the recirculating flow reattached at 5.5 H behind the obstacle, in the second case at 7.3 H. A corresponding wind tunnel experiment (Moss and Baker 1980 as quoted in Dargent 1996) showed reattachment at 10 H.
Counihan (Counihan 1971) simulated the atmospheric boundary layer in the inner city in a wind tunnel, so that the boundary layer thickness exceeded the obstacle height. This reduced

the reattachment length behind the obstacle to 6 H. Flow visualisation showed reverse flow only up to 4 H downstream, but negative perturbation stresses were measured as far as 6 H. The maximum stress, that is to say the maximum rate of change of perturbation velocity, was measured at 1.5 H vertically and 4 H downstream from the obstacle. This might be interpreted as a zone boundary for the wake. In a previous reported experiment from the same group (Hunt 1970), it is stated that the flow separates from the front edge of the roof, and does not reattach. The greatest longitudinal and vertical turbulent intensities are located at a height of 0.4 H above the rear of the roof. The greatest lateral turbulence intensity occurs higher above the roof (0.7 H).

A reattachment length of 6 H is also quoted for a square two dimensional prism in a shear layer which is around 3/4 H thick (Brittner and Hunt 1979).

For uniform inflow and low roughness height, reattachment length values of 9 H for a two dimensional cuboid up to 12 H for a vertical flat plate are reported (Castro and Fackrell 1976 as reported in Brittner and Hunt 1979). These correspond very well with the presented ones, which are also based on uniform inflow conditions.

For the tall slim rectangular model (D/H = 1/3) Dargent (Dargent 1996) reports reattachment at 9.2 H, or in the case of a square cross-section reattachment 7.5 H. In the later case, the displayed streamline shows flow separation at the front edge of the roof. The flow remains separated over the whole roof length, and the height of the recirculation zone over the rear part of the roof is approximately 1/4 H.

Flow separation and wake behaviour as reported by Dargent supports the results of the presented work and corresponds to experimental work (Bergeles and Athanassiadis 1983). Here, a shear flow with a boundary layer thickness of nearly half the obstacle height, but of only 0.5 % turbulent intensity, generated a long wake of around 11.2 H. This wake is reported to exceed the obstacle height, reaching 1.45 H. For a flat rectangular block (D/H = 2/1), the flow is reported to reattach at approximately 8.5 H downstream.

In a very similar experiment with a block of the same aspect ratio (D/H = 2/1) a reattachment length of 7 H is stated (Arie et al. 1975). Here, no appreciable difference in the velocity profiles around the obstacle can be observed for the two investigated boundary thickness' of 0.55 H and 1.13 H. In both cases, the flow separates at the leading edge and does not reattach on the roof. The maximum height of the dividing streamline of the wake behind the obstacle is quoted as 1.4 H, which corresponds to Bergeles et al. and supports the pattern found in the presented simulation. Arie explains this high wake as due to the Coanda effect, by which the separated shear layer is deflected upwards at the upper surface (Arie et al. 1975).

The two dimensional simulation for the flow over a cube using two different k-ε models shows streamline patterns, which correspond quite well with the presented results (Yaghoubi et al. 1998). Applying the standard k-ε model, the flow separates at the front edge and does not reattach on the roof. At the rear part of the roof, the height of the separated flow zone is approximately 1/4 H above the roof, and behind the obstacle the recirculation zone rises up to 1.5 H. The streamline reattaches at 12.5 H downstream behind the obstacle. A low Reynolds number k-ε model resulted in a more compact wake, but in principle the flow separation remained the same. The recirculation zone was raised further height to approximately 2/3 H above the roof, whereas the reattachment length behind the obstacle shortened to 10 H.

6.3.1.2. Comparison for Three Dimensional Flow

Under the same inflow conditions, a three dimensional simulation for the flow around the cuboid generated a different flow field than that experienced in the two dimensional simulation, even for the plane of symmetry. For the coarse grid resolution (see Figure 6.2.3.4), the flow in the first cell layer over the roof carries a small vertical velocity component, but separation and recirculation can not be resolved. Behind the obstacle it generates a recirculation zone of around 2 H length. The recirculation zone does not exceed the building height.

In the fine grid approach (see Figure 6.2.3.3), the flow separates at the front edge and generates a recirculation bubble which rises to approximately 0.3 H above the rear part of the roof and reattaches at 3.6 H downstream from the obstacle. The recirculation zone behind the obstacle reaches its maximum height of 1.35 H halfway downstream between obstacle and reattachment.

In order to evaluate those results, they are compared with experimental and numerical work and with published standards. Unfortunately, detailed investigations have been mostly carried out for a cube. However, for civil engineering purposes, a standardized approach may be based on a scaling length R, which combines the two dimensions facing the incoming flow (height and width) (ASHRAE 1993). The handbook presents

$$R = B_S^{0.67} \cdot B_L^{0.33}$$

where B_S is the smaller and B_L is the larger of either height or width. The maximum height H_C of the recirculation above the roof is located at a distance X_C from the leading edge. Flow reattachment lengths are L_C for the roof recirculation and L_R for the recirculating wake behind the building. They are related to the scaling length R via

$$H_C = 0.22 \cdot R \qquad X_C = 0.5 \cdot R \qquad L_C = 0.9 \cdot R \qquad L_R = 1.0 \cdot R$$

It is significant that, according to the ASHRAE standard, the wake behind the obstacle does not exceed roof height. The boundary of the recirculation zone in the wake is generally assumed to fall linearly to the ground. This might be an oversimplification, but it corresponds with the three dimensional simulation in the coarse grid approach. Further, it is stated that high turbulence in the incoming flow may decrease the coefficients by up to a factor of 2 and may cause the reattachment locations to fluctuate.

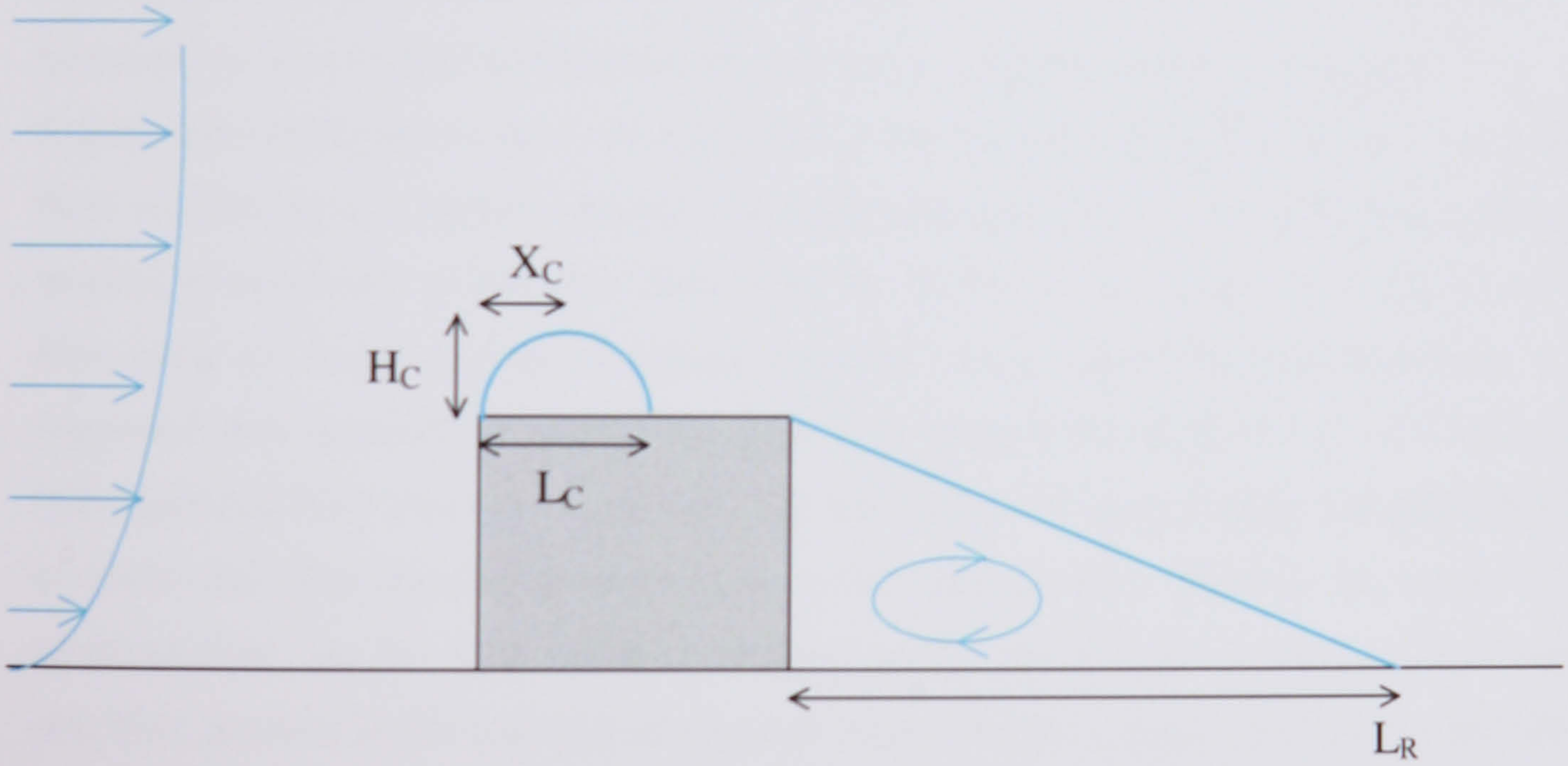

Figure 6.3.1.2.1: Definition of ASHRAE standard measures (ASHRAE 1993)

For the investigated case of 30 m height and 35 m width, the reattachment length of the recirculation over the roof L_C exceeds the obstacles' depth of 20 m. This may be interpreted, that the roof recirculation does not reattach. The maximum height of the roof recirculation zone (0.23 H above the flat roof) occurs at the rear 20 % of the roof length. The flow reattaches behind the building at 1.1 H downstream. Compared with the three dimensional fine grid solution, the recirculation above the roof is well described, the wake length is not, being closer to the coarse grid result. Overall, the picture is not consistent. As the standard is recommended for building plant engineers, it is possible that real scale experience may be very different from Computational Fluid Dynamics simulations and wind tunnel experiments, where in particular an extended recirculation over the roof always goes along with an extended wake behind the obstacle.

Comparison with investigations of flow around cubes shows a vast variety of generated wake patterns. In a comparable CFD-simulation, Latif presents reverse flow only in the first layer of cells above the roof (Latif 1989). Further above, the flow passes as smoothly as in the presented coarse grid result. Hence, the grid resolution seems to play an important role in modelling recirculation. Latif implemented 5 cells to resolve a height of 0.5 H above the roof, compared with three or nine for the presented coarse and fine grid approaches. In the case of Latif, the height of the boundary cell was 0.05 H, compared with the presented fine grid value of 0.02 H. The length of the recirculation zone turned out to be 3.7 H, which corresponds with the presented result for the fine grid. But in contrast to the latter, the recirculation zone behind the building did not exceed the roof height significantly.

Experiments attempted to show the influence of the boundary thickness on the recirculating flow over the top of a surface mounted cube (Robins and Castro 1977), but unfortunately no detailed measurement of the flow field over the roof is given. Suggestions concerning the flow field are based on the measured pressure values along the roof centerline. It is suggested, that approaching shear flow with a boundary layer thickness of 1.4 H generates fully separated flow over the whole roof, but with thinner layers reattachment takes place. It is stated, that flow separation must occur at the leading edge, whatever the nature of the upstream flow. As the high negative pressure coefficient declines sharply to reach nearly zero base pressure at the rear half of the roof, reattachment is suggested. For normal inflow, the wake behind the cube reattaches at around 1.5 H. For 45° inflow, the reattachment length increases to 2 H, and it is suggested that no recirculation occurs over the roof along the diagonal centerline (but an edge vortex may occur).

Other experimental work leads to different conclusions. Flow visualisation showed reverse flow in the wake behind a cube up to 1 H downstream, with flow separation occurring only from the rear trailing edge (Counihan 1971). Here, flow separation from the front edge is only reported for the flow over an infinite beam of square cross-section on a ground plane. For the cube, the maximum perturbation stress is measured at roof level, which gives a hint that there is no significant wake above the roof. This result contradicts the previous measurements from the same laboratory (Hunt 1970, Hunt and Smith 1969), which stated that the flow over the cube separates from the leading edge and reattaches half way along the roof. Even as the flow reattaches, the maxima of all three main axis components of the turbulent intensity are measured 1/6 to 1/7 above the top of the cube. Reverse flow behind the cube is measured up to 1.5 H. Here, the experiments show less recirculation than the presented simulation.

Roof recirculation is also not observed in a simulation (Dargent 1996), which is comparable with the presented one. The flow directly over the roof turned out to be very slow, but not reversing. Reattachment behind the obstacle occurs at 2.5 H (referring to the displayed streamline pattern, 2 H as cited in the text). In the same work, an experiment is quoted, which states for normal inflow towards the cube an extended recirculation zone with reattaching flow at 3 H behind the obstacle and rising to 1.5 H above the obstacle's top (Huber and Snyder 1982 (as quoted in Dargent 1996)). This experiment supports rather the presented fine grid approach.

Also, no roof recirculation is observed simulating different turbulent levels for boundary layer shear flow (Zhang et al. 1992). Vectorplot patterns display the reattachment behind the obstacle at around 2.4 H for a low level of turbulence, 2 H for a high level of turbulence (in the text the cited values are 1.7 H and 2 H respectively).

Murakami and Mochida report experimental work in the wind tunnel, which showed for a cube reverse flow approximately 1 to 1.5 H downstream (Murakami and Muchida 1989). The wake height did not exceed the cube's top. The flow separates at the front edge and reattaches in the middle of the roof, and the height of the recirculation zone over the front part of the roof is about 0.1 H. These experimental results were compared with numerical investigations using the standard k-ε model and three different cartesian meshes. All three different mesh types are still coarser than the fine grid approach in the presented investigation. Murakami and Mochida found in all cases that the flow behind the cube reattaches further downstream than 2 H. It is stated that a fine grid with small mesh interval leads to a higher production of turbulent kinetic energy and increased turbulent energy dissipation. This causes the zone of recirculating flow behind the obstacle to decrease, in particular the reattachment length shortens. Although the wake is overpredicted in the simulation, the pressure coefficients and the recirculation above the roof are consistent with the experimental results.

A succeeding investigation by the same group focused on the performance of different turbulence models (Murakami, Mochida and Hayashi 1992). The k-ε model overestimated reverse flow velocity in the wake, and the reattachment length behind the building was 2 H, confirming the coarse grid result in the presented simulation. Recirculation over the roof was not observed, and the suction at the front of the roof was greatly overestimated. This experience is shared as well with the presented investigation, where the simulated flow generates a higher suction at the front of the roof in the coarse grid approach, without generating a separation bubble of reverse flow. The lack of recirculation over the roof is explained in a paper by the same author (Murakami 1993). The k-ε model seems to overestimate the values of turbulent kinetic energy at roof height. Hence, overestimated turbulent viscosity and diffusion hinders the generation of a recirculating flow pattern.

Streamline curvature treatment of the eddy viscosity in the k-ε model predicted the flow around the cube (Baetke et al. 1987). For uniform inflow with low turbulent intensity, flow separation occurs at the leading edge and the flow does not reattach on the roof. Reattachment occurs according to the vector flow display at around 4 H downstream from the obstacle (whereas the text cites the reattachment zone as 2 to 3 H downstream). The recirculation zone over the roof reaches at the rear part a height of about 0.25 H, and behind the obstacle rises further to 1.3 H. These recirculation patterns correspond very well with the presented simulation using the fine grid. Baetke quotes a nearly uniform pressure coefficient distribution along the roof centerline, with $C_p \sim -0.6$. He compared his simulated pressure coefficients with experimental values (Castro and Robins 1977 as quoted in Baetke 1987) and found excellent consistency. As quoted earlier, Robins and Castro did not link the uniform pressure coefficient distribution over the roof to completely separated flow. Beatke achieved overall consistency by simulating a boundary layer which is used in wind tunnel modelling. The shear layer reattached on the roof at around 0.5 roof length, and the recirculation behind the obstacle reattached at around 3 H and rose to 1.1 H. The pressure coefficient over the roof declined sharply and then recovered to values close to zero towards the rear half of the roof, corresponding to the experimental values of Robins and Castro. The flow patterns suggested by Robins and Castro based on pressure coefficient measurements were verified by this simulation.

For a different geometry (H:D:L = 2:1:1) the streamline curvature correction seems to affect only the reattachment length of the recirculation behind the cuboid (Baskaran and Stathopoulos 1989). Without this correction, the flow separated at the leading edge and did not reattach. The recirculation rose to around 0.25 H above the rear part of the roof, and this height was the maximum attained. Reattachment behind the obstacle occurred at around 2.25 H, or with streamline correction 2.65 H.

A very direct approach to generate the recirculation zone at the front part of the roof has been tested by Paterson and Apelt (Paterson and Apelt 1989). They simulated the flow around the cube in a very coarse grid, and no flow separation occurred above the roof. Fixing the longitudinal velocity at the leading edge of the roof to zero, recirculation and reattachment appeared comparable to Baetke, but the suction turned out to be overpredicted at the leading edge. Reattachment of the recirculation behind the obstacle occurred at 2.5 H downstream. Further on the article displays the streamline pattern over tall rectangular cuboids. All of them show flow separation at the leading edge of the roof, no reattachment downstream along the roof and a recirculation behind the obstacle which exceeds the roof height and reattaches further down than 2 H behind the obstacle. It appears to be a general pattern.

6.3.1.3. Conclusions

The reported results are divers and point out, how strongly the flowfield in the vicinity of the obstacle depends on the experimental conditions or the set up of the numerical model. Nevertheless, a qualitative comparison verifies the presented results for both gridding approaches in general. The fine grid approach might overestimate the size of the recirculation zone and the momentum of the recirculating flow, but not to a large extent. In contrast, the coarse grid approach in three dimensions does not resolve recirculation over the leading front roof edge. Hence it is obvious that grid refinement is the key to modelling recirculation. However, two contrary mechanisms seem to be present. A refined grid is able to resolve pressure and momentum gradients which are the basis of the recirculation pattern. On the other hand, as reported in the literature (Murakami et al.), when using the k-ε model the finer mesh, which is still coarser than the refined grid in the presented simulation, supports dissipation and therefore may shorten or even hinder the recirculation pattern. However, experience in the presented investigation is, that the refined grid leads to rather overestimated recirculation pattern. Hence, the way of grid optimisation will be somewhere in the middle. It seems to be crucial to generate a grid in the wake region that k and ε meet the equilibrium condition. The theoretical equilibrium condition states, that the rate of production and destruction of turbulent kinetic energy k is proportional to the rate of production and destruction of turbulent kinetic energy dissipation ε.

In the presented work, the geometry and the size of the integrated turbine duct requires a distinctive grid refinement in the area in question. The refined grid is in particular necessary to resolve the jet stream through the duct at the area of inflow and its entrainment into the outer wake. Therefore, a completely optimised grid for the flow around the building would perhaps not be compatible with the grid requirements of the duct flow. The presented work attempted to solve this dilemma in the best possible way, and the generated pattern of recirculation seems to correspond quite well with many reported investigations.

Also, it appears that the relation between the pressure coefficient distribution over the roof and the local flow pattern is not unique. In particular the extent of recirculation can not be solely predicted on the basis of pressure coefficients on the roof. For example, in the simulation, a uniform negative pressure coefficient distribution goes along with a large recirculation pattern above the roof. Such an observation is not reported for wind tunnel experiments, and it can not be confirmed in the author's experimental work. On the other hand, a non-uniform pressure distribution over the flat roof, which is reported as indication of flow separation and reattachment, is in the presented investigation generated by the coarse grid approach: a grid, which is not able to resolve the recirculation pattern.

Finally, the lack of real scale field trials is a severe limitation to the evaluation of experimental and numerical modelling.

References

Schlichting H.: Grenzschicht Theorie; Braun'sche Verlagsbuchhandlung Karlsruhe, Germany, 1965

Boundary-Layer Theory; McGraw-Hill Book Company, England, 1979

Hunt J.C.R. and Smith G.P.: A Theory of Wakes behind Buildings and some provisional Experimental Results; Laboratory Note No. RD/L/N 31/69, 1969, Central Electricity Research Laboratories CERL, Leatherhead, today with National Power, Swindon, England.

Hunt J.C.R.: Further Aspects of the Theory of Wakes behind Buildings and a Comparison of the Theory with Experimental Results; Laboratory Report No. RD/L/R 1665, 1970, Central Electricity Research Laboratories CERL, Leatherhead, today with National Power, Swindon, England.

Counihan J.: An Experimental Investigation of the Wake behind a Two-Dimensional Block and behind a Cube in a simulated Boundary Layer Flow; Laboratory Note No. RD/L/N 115/71, 1971, Central Electricity Research Laboratories CERL, Leatherhead, today with National Power, Swindon, England.

Dargent C.: Contribution à la modélisation de la dispersion de pollutants - Etude de sillage autour d'obstacles de forme parallélépipédique; Thèse de Docteur, Physique et Chimie de l'Environnement, Institut Nationale de Polytechnique (INP) de Toulouse, France, Septembre 1996.

Colmer M.J.: Some Full Scale Measurements of the Flow in the Wake of a Hangar; RAE, Bedford, England, T.R. 70202, 1970 (as quoted in Counihan 1971)

Zhang Y.Q., Arya S.P.S., Huber A.H. and Snyder W.H.: Simulating the Effects of Upstream Turbulence on Dispersion around a Building; Report No. EPA 600/A-92/228 (1992), Atmospheric Research and Exposure Assessment Laboratory, Office of Research and Development, U.S. Environmental Protection Agency, USA, 1992

Baetke F., Werner H. and Wengle H.: Computation of Turbulent Flow around a Cube on a Vector Computer; Proceedings of the 6th Symposium on Turbulent Shear Flows, 1987, Vol. 9, pp. 20-2-1 to 20-2-6

Latiff Z.A.; Wind Loads on Structures and the Effect of Shielding; PhD thesis, Division of Thermo-Fluid and Environmental Engineering, Department of Mechanical Engineering, University of Strathclyde, Glasgow, Scotland, February 1989

Moss W.D. and Baker S.; Re-Circulating Flows associated with Two-Dimensional Steps; Aeronautical Quarterly, pp. 151-172, August 1980 (as quoted in Dargent 1996)

Counihan J., Hunt J.C.R. and Jackson P.S.; Wakes behind Two-Dimensional Surface Obstacles in Turbulent Boundary Layers; Journal of Fluid Mechanics, Vol. 64, Part 3, pp. 529-563, 1974 (as quoted in Dargent 1996)

Brittner R.E. and Hunt J.C.R.; Velocity Measurements and Order of Magnitude Estimates of the Flow between two Buildings in a Simulated Atmospheric Boundary Layer; Journal of (Wind Engineering and) Industrial Aerodynamics, Vol. 4, pp. 165-182, 1979

Castro I.P. and Fackrell J.E.; An Investigation of two-dimension Fence Flow with emphasis on Wind Tunnel Blockage Effects; C.E.G.B. Marchwood Rep. R/M/N 901, 1976 (as quoted in Brittner R.E. and Hunt J.C.R. 1979)

Bergeles G. and Athanassiadis N.; The Flow past a Surface Mounted Obstacle; Transactions of the ASME, Journal of Fluids Engineering, Vol. 105, pp. 461-463, 1983

Robins A.G. and Castro I.P.; A Wind Tunnel Investigation of Plume Dispersion in the Vicinity of a Surface Mounted Cube - I. The Flow Field; Atmospheric Environment, Vol.11, pp. 291-297, 1977

Robins A.G. and Castro I.P.; A Wind Tunnel Investigation of Plume Dispersion in the Vicinity of a Surface Mounted Cube - II. The Concentration Field; Atmospheric Environment, Vol. 11, pp. 299-311, 1977

Huber A.H. and Snyder W.H.; Wind Tunnel Investigation of the Effects of a Rectangular shaped Building on Dispersion of Effluents from short adjacent Stacks; Atmospheric Environment, Vol. 16, No. 12, pp. 2837-2848, 1982 (as quoted in Dargent 1996)

ASHRAE Handbook 1993, Fundamentals; Chapter 14: Airflow around Buildings; American Society of Heating, Refrigerating and Air-Conditioning Engineers ASHRAE, Atlanta, USA ISBN 0-910110-97-2

Murakami S. and Mochida A.: Three-Dimensional Numerical Simulation of Turbulent Flow around Buildings using the k-ε Turbulence Model; Building and Environment, Vol. 24, No. 1, pp. 51-64, 1989

Murakami S., Mochida A., Hayashi Y. and Sakamoto S.; Numerical Study on Velocity-Pressure Field and Wind Forces for Bluff Bodies by k-ε, ASM and LES; Journal of Wind Engineering and Industrial Aerodynamics, Vol. 41-44, pp. 2841-2852, 1992

Murakami S.: Comparison of Various Turbulence Models applied to a Bluff Body; Journal of Wind Engineering and Industrial Aerodynamics, Vol. 46&47, pp. 21-36, 1993 (as quoted in Dargent 1996)

Castro I.P. and Robins A.G.: The Flow around a Surface Mounted Cube in Uniform and Turbulent Streams; Journal of Fluid Mechanics, Vol. 79, pp. 307-335, 1977 (as quoted in Baetke 1987)

Paterson D.A. and Apelt C.J.; Simulation of Wind Flow around Three-Dimensional Buildings; Building and Environment, Vol. 24, No. 1, pp. 39-50, 1989

Yaghoubi M., Zamankhan P. and Sabzevari A.: Numerical Analysis of Two-Dimensional Wind Flow in and around Rectangular Buildings - Part I: Modelling and Simulation; Wind Engineering, Vol. 22, No. 2, pp. 81-97, 1998

Baskaran A. and Stathopoulos T.: Computational Evaluation of Wind Effects on Buildings; Building and Environment, Vol. 24, No. 4, pp. 325-333, 1989

Arie M., Kiya M., Tamura H., Kosugi M. and Takaoka K.; Flow over Rectangular Cylinders Immersed in a Turbulent Boundary Layer (Part 2, Flow Patterns and Pressure Distributions); Bulletin of the JSME, Vol. 18, No. 125, pp. 1269-1276, 1975

6.3.2. The Pressure Distribution on the Façade and Roof

In order to investigate the massflow through the duct, it is important to evaluate the simulated pressure coefficient distribution on the front façade and flat roof. However, in particular for the flat roof, the standard values recommended for architects and civil engineers (BRE 1989) differ very much from the standard values valid for small scale models (ESDU 1993). It is obvious that the conditions of the wind flow around buildings is in reality more complex than for small models. This seems to lead to reattachment of separated flow along the roof, and also to much worse suction at the roof edges. This can not be seen simply as an effect of scale, a Reynolds number effect. A simulation of the wind flow around a block with a certain fixed uniform inflow wind speed gave identical results for the real scale block (30 m x 35 m x 20 m) as for the model downsized 1:100. The reason for this difference is rather that small variations in flow conditions can change a local pressure by altering both the overall magnitude of pressure and also its distribution, in particular on the flat roof. The standard model values are not useless for a real scale approach, but in order to calculate loads for real scale applications, additional factors have to be taken into account, such as the design gust velocity, the mean wind speed profile and the amount of turbulence in the flow. Also real scale measurements, observations and experience of wind flow over buildings influenced the set of standard values from BRE. Further, there is a security margin included.

For accurate validation of the numerical model, the ESDU standard data are more practical, as the flow conditions are fixed to datum conditions. The datum conditions are given as follows:

- the free stream Reynolds number is between 10^4 and 10^6, but the length on which the calculated Reynolds number is based is not stated;
- the inflow profile is uniform, and the thickness of the boundary shear layer does not exceed 20 % of the obstacle's height
- the flow is smooth, the turbulence intensity does not exceed 1 %
- the flow is unbounded
- the flow is incompressible

The numerical model with the fine grid meets nearly all of those flow conditions, only the turbulence intensity of the inflow is set to 40 %. Increased turbulence intensity may generally support reattachment of the flow. But because of its aspect ratio, this obstacle does not show reattachment at the roof under the given uniform inflow condition, even for very large turbulence. A detailed analytical correction method for turbulence is worked out in the ESDU data tables for the integrated force coefficient acting on one side of the obstacle, but for the pressure coefficient distribution nothing like this was found. Data for a combination of conditions which depart from datum conditions are almost non-existent.

6.3.2.1. Comparison for Two Dimensional Flow

In the literature, two dimensional flow around an obstacle is most of the time defined as flow between end plates (ESDU 1993). Therefore, the 'infinite' long obstacle (see Figure 6.3.2.1.2) is limited at its very ends, but is not surface mounted. The application is for example a bridge in a valley, or a skyscraper (Rahnema et al. 1996, Sam et al. 1979). In the latter case, the influence of the surface and the roof of the skyscraper on the pressure distribution on the walls is only locally significant.

Standard data are available for two dimensional backward or forward facing steps, which can not be applied to the geometry under investigation, which represents more a infinitely long and thick wall. For the flow over the infinitely long rectangular cuboid, horizontal surface mounted, some difficulties arise, as the pressure coefficient distribution on the flat roof seems to depend strongly on the aspect ratio of height/depth, which is in our case 3/2. The pressure distribution on the front façade is much less sensitive to changes in geometry, but rather sensitive to the inflow conditions. One set of experimental values for an infinitely long rectangular section with D/H = 2/1 has been recorded for different boundary layer thickness (Arie et al. 1975). Arie also stated an empirical law which describes the pressure distribution at the front and back of the object. Very similar in profile to the two dimensional simulated results for the front façade are experimental results, in which the thickness of the boundary layer exceeded the obstacle height for around 37 % (see Figure 6.3.2.1.1). The other distribution in the diagram is measured for a boundary layer thickness of around one third building height (Baines 1963). A thick boundary layer seems to lower the pressure on the upper part of the front façade. It shows as well the extent to which the simulated flow creates a shear upstream of the obstacle.

Overall it is obvious that the simulated values have a shortcoming. The two dimensional simulation seems to lead to an offset, and shifts the values of the pressure coefficient well over the margain of C_p = 1.0 (Figure 6.3.2.1.1).

It would not be possible to predict the massflow through the duct with any accuracy in two dimensional simulation as overestimation of the front pressure will force an unrealistic speed through the duct. The flow through the duct will be compared for different geometries only qualitatively (in Chapter 7).

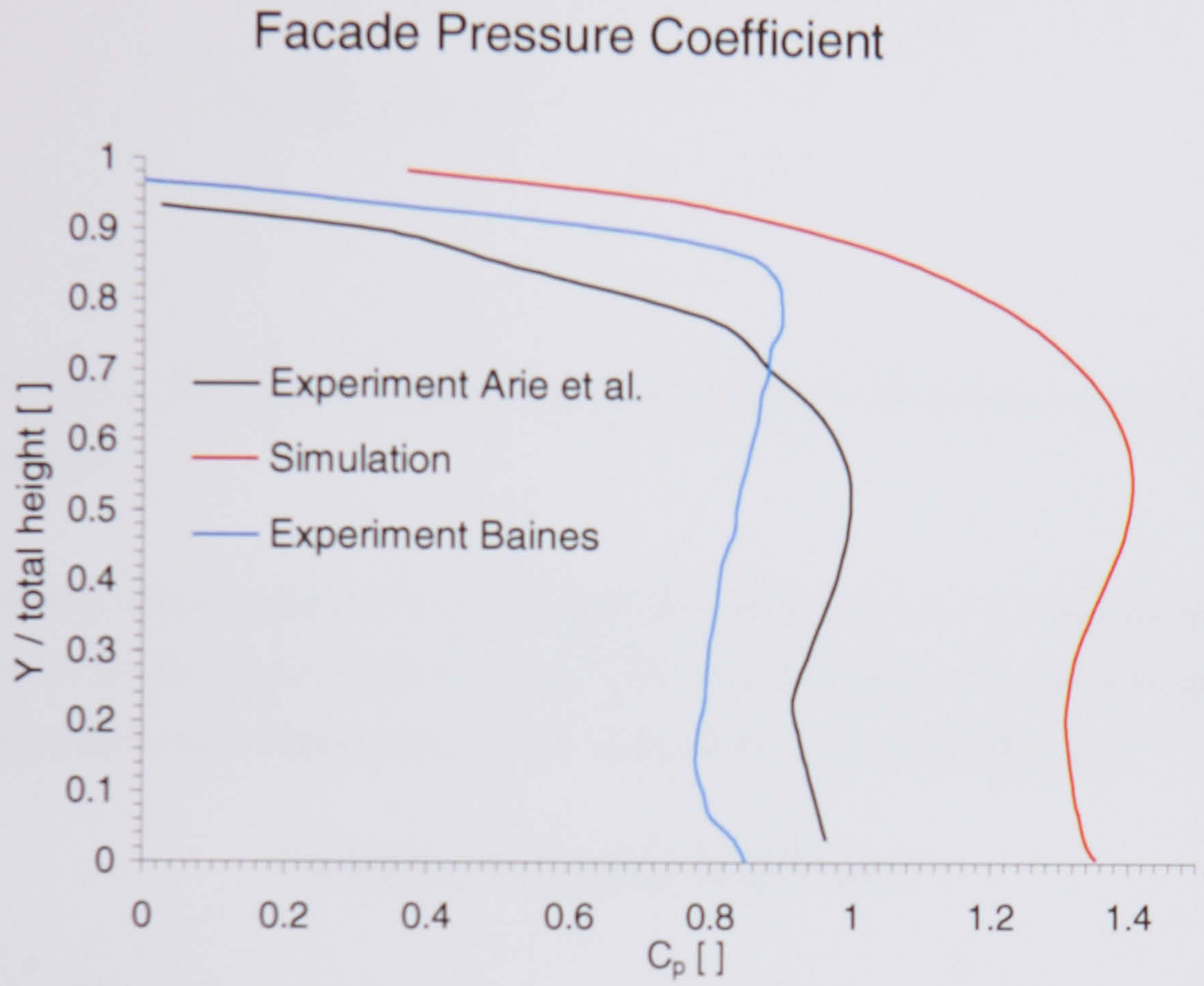

Figure 6.3.2.1.1: Comparison of the pressure coefficient distribution for two dimensional flow on the front façade of a surface mounted cuboid, experimental and simulated values

Comparison with the ESDU standards is difficult, as the ESDU defines the two dimensional flow over an obstacle in a physically different situation (ESDU 1993). The flow passes over and below the isolated infinitely long rectangular beam between endplates (see Figure 6.3.2.1.2), while the presented two dimensional simulation assumes the obstacle as surface mounted. If we only look at the upper part of the two dimensional simulated model, the flow situation might be similar to the flow over the isolated cuboid as defined in ESDU. For the latter, the stagnation point on the front is of course in the middle. As the stagnation point for the surface mounted obstacle is towards the upper part, it might well be that the upper part of the obstacle is surrounded by a similar flow field to an isolated cuboid with an aspect ratio height/depth < 1.

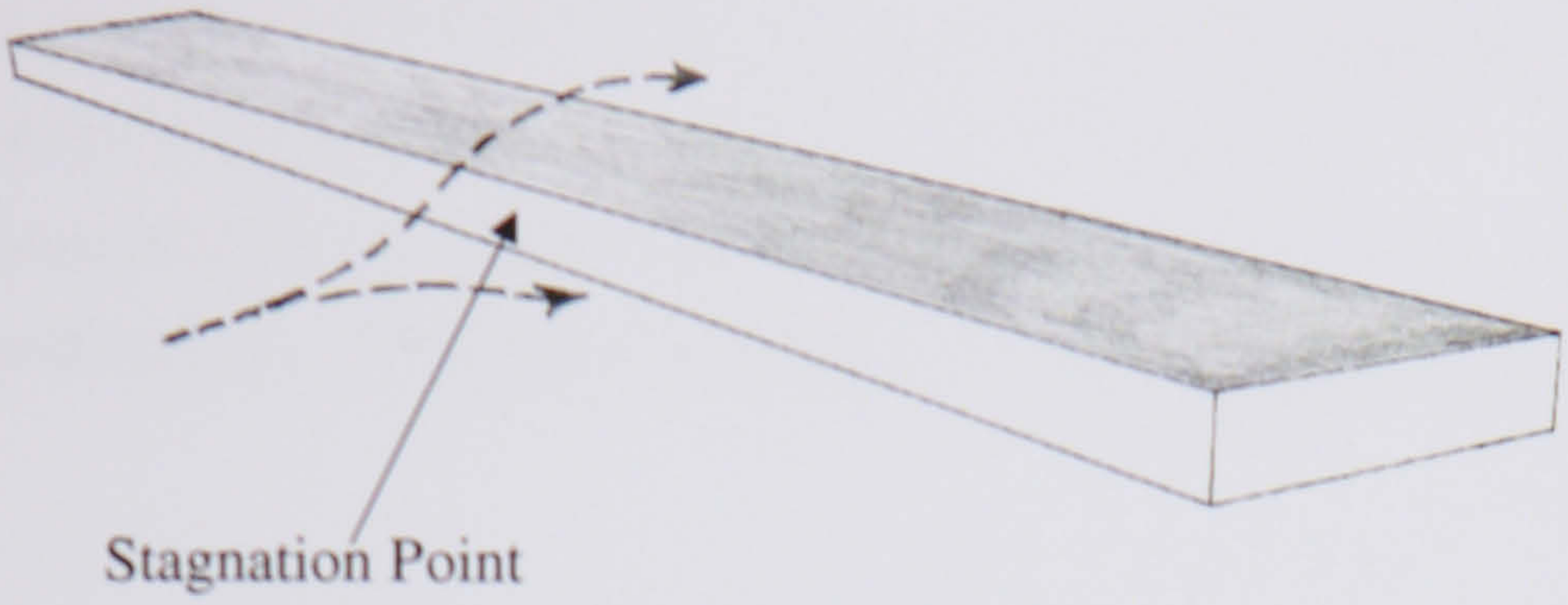

Figure 6.3.2.1.2: Two dimensional flow around infinitely long isolated rectangular beam with end plates

The following Figure attempt such a comparison: Figure 6.3.2.1.3 compares the pressure coefficient of the simulated model with the ESDU standard for a rectangular isolated infinite beam (with aspect ratio depth/height = 3/2) on the upper part of the front face.

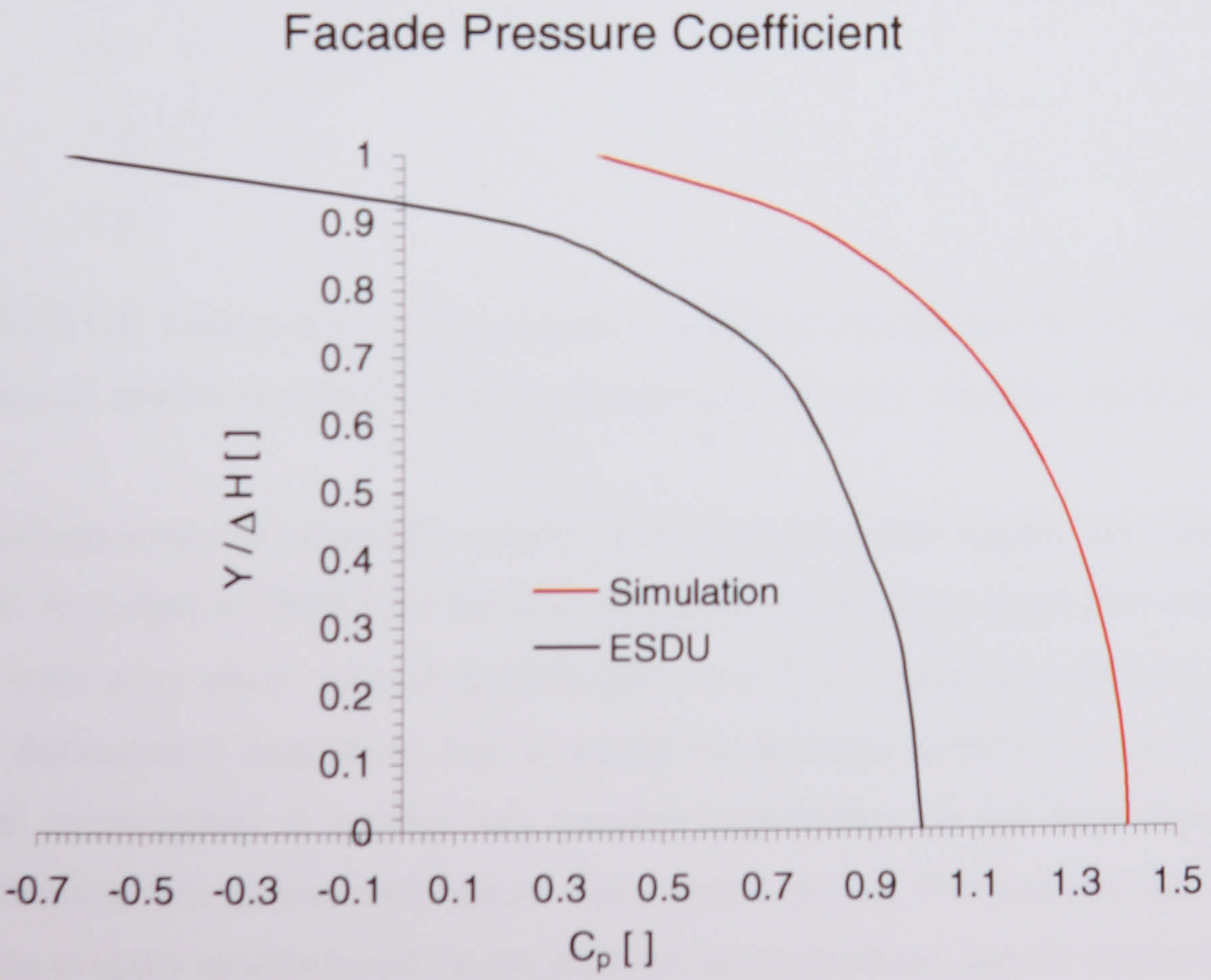

Figure 6.3.2.1.3: Comparison of simulated values and ESDU standard values on the upper part of the front façade

The vertical scale is nondimensionalised with the distance Δ H between the stagnation height and the top. The now familiar shift of the simulated values beyond the margin of one disqualifies the values. But the shape of the distribution is very similar.

Striking is the comparison of simulated values with ESDU standard values on the flat roof, where both the distribution of the pressure coefficient and its magnitude corresponds (Figure 6.3.2.1.4).

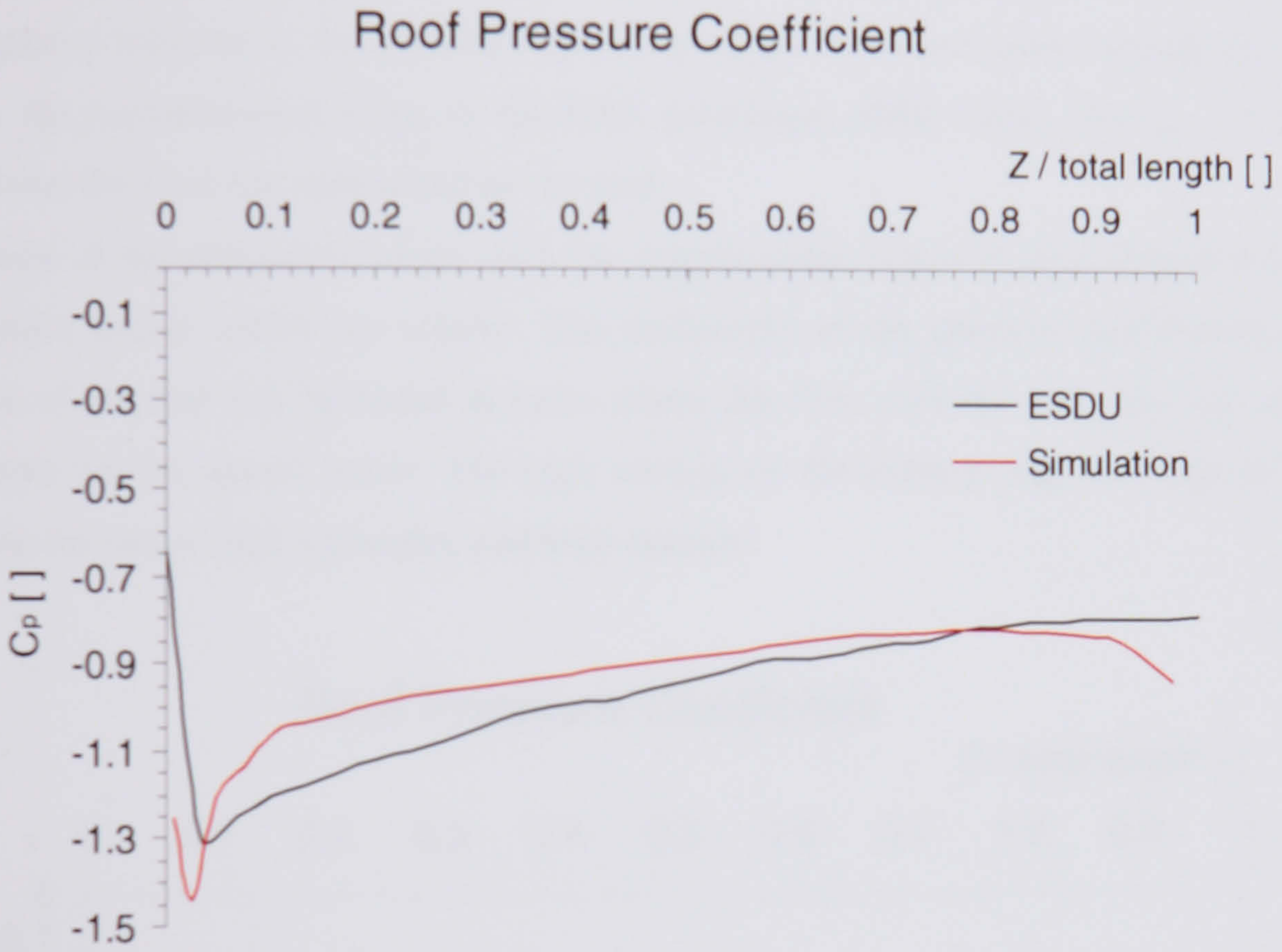

Figure 6.3.2.1.4: Comparison of the pressure coefficient distribution for two dimensional flow on top of surface mounted obstacle and standard values for isolated obstacle

This good agreement is especially surprising as the equivalent aspect ratio can only be estimated. According to ESDU, for the isolated block the two dimensional flow reattaches to the side walls at an aspect ratio of depth/height ≥ 2.8. This comparison does not 'validate' the two dimensional simulation, but it would be probably worthwhile to undertake a systematic investigation to explore any possible equivalence in the flow situation over surface mounted two dimensional objects and isolated objects. For potential fields it is not uncommon to apply models based on the principle of equivalence, but for recirculating flow it may not necessarily work.

Unfortunately, the aspect ratios in the experiments of Arie do not correspond to the one used for the presented simulation (Figure 6.3.2.1.5). The pressure distribution over the front as presented above is measured for square-section beams as well as for various steps, but the pressure distribution on the upper surface varies. For the flow over the square surface mounted section, Arie reports a nearly uniform negative pressure distribution of $C_p \sim -0.7$. For the flow over various steps with aspect ratios depth/height = 2/1 to 6/1, a certain pattern becomes obvious. With deeper steps the pressure at the leading edge becomes more and more negative, whereas at the trailing edge it converges more and more towards $C_p \sim -0.2$, which is the recommended value in the BRE guidelines (BRE 1989). For $C_p \sim -0.2$, it is assumed that the flow has reattached on the roof.

Comparison of the simulated values with the experimental values of Arie (Figure 6.3.2.1.5) show certain trends which are similar. The uniformity of the pressure distribution over a large area of the roof can be found in cases where the flow over the roof does not reattach, for example for the square beam. The high suction on the leading edge is a sign of strong streamline curvature, high velocities and high stresses.

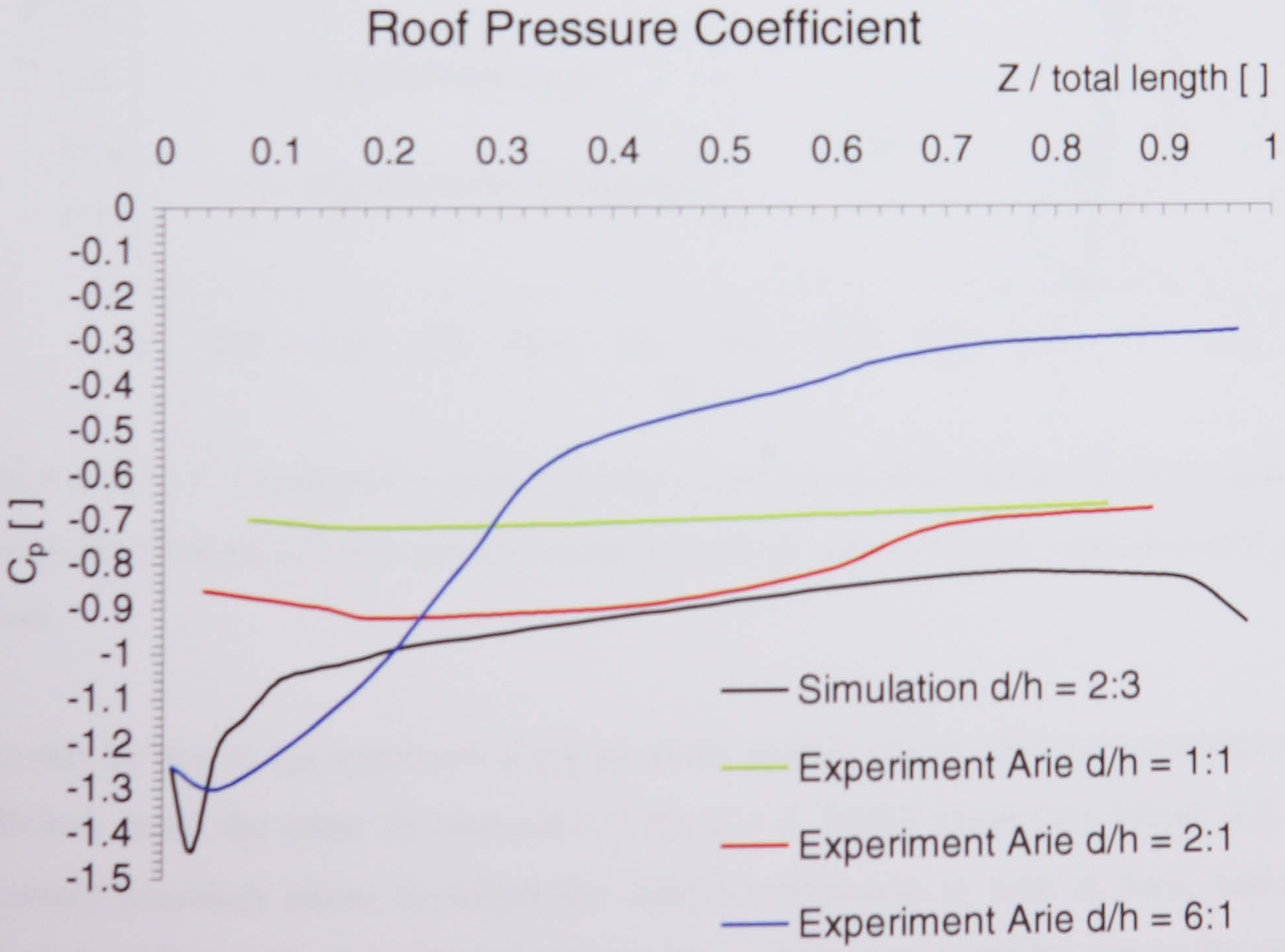

Figure 6.3.2.1.5: Comparison of the pressure coefficient distribution for two dimensional flow on top of a surface mounted infinitely long beam

6.3.2.2. Comparison for Three Dimensional Flow

The standards for flow around three dimensional rectangular surface mounted obstacles show that for different height / width aspect ratios, the pressure coefficient distribution at the front façade corresponds to the one on the face of a cube (ESDU 1993). The isobars on the cube's front face are stretched vertically or horizontally, according to the different aspect ratios. Comparison on the front façade shows that the simulated values in the plane of symmetry are slightly overpredicted.

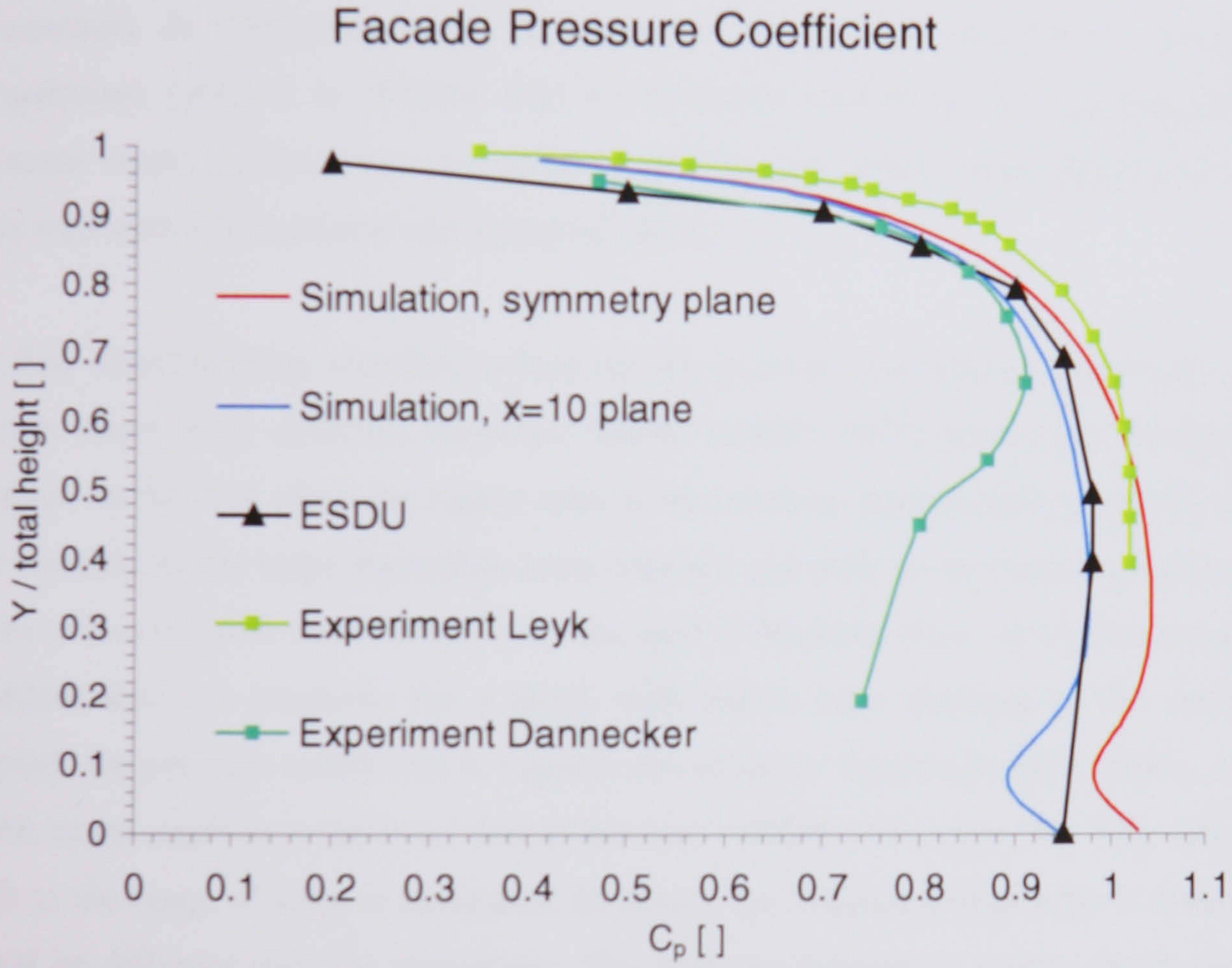

Figure 6.3.2.2.1: Comparison of the pressure coefficient distribution for three dimensional flow on the front façade of a surface mounted cuboid: experimental, simulated and standard values

This may be due to the symmetrical set up of the model, where only one symmetrical half is modelled. Here, the plane of symmetry is the x = 1 WEST plane (see Figure 6.1.1.2), the symmetry boundary plane in which the lateral component is kept at zero, which might disturb the balance of momentum and stagnation pressure in a similar way to the systematic error which occurs in the two dimensional simulation. If we look at a cross-sectional plane away from the symmetry plane, the simulated values agree well with the standard values

(ESDU 1993). The simplified real scale standard for the construction industry recommends a single value of $C_p = 0.89$ vertically along the whole height of the façade (BRE 1989). Also, for a thin boundary layer compared to the obstacle height, the non-dimensionalised pressure coefficient distribution on the front façade seems to be not sensitive to changes in height. Previous experimental work (Leyk 1997) recorded the pressure coefficient on the front façade for a block twice as high as simulated. Its distribution is slightly shifted towards greater values compared with the ESDU standard. Figure 6.3.2.2.1 shows as the last curve the pressure coefficient distribution for the 30 cm high model on its front façade (Experiment Dannecker). In comparison with the previous experiments with the 60 cm high model (Experiment Leyk) it is obvious that the boundary layer over the turntable affected the pressure values for the lower part of the model, but the values on the upper part correspond very well with the simulated and standard values.

To find corresponding standard values for the pressure coefficient distribution on the flat roof is much more difficult. However, ESDU (ESDU 1993) states that the flow does not reattach on the roof when the aspect ratio of the obstacle depth/height is smaller than 2.5. In the simulation, the large separation zone over the top with its recirculating flow generates a more or less uniform suction field over the roof. Difficulties arise, as no detailed distribution standard data are available for a block with aspect ratio identical to the simulated one. Instead, the pressure coefficient is vaguely described as 'approximately uniform, around $C_p = -0.68$, more negative at the front than at the rear' (ESDU 1993, page 39). This value fits quite well in the range of what is simulated. In detail, the compared distributions from ESDU are based on different obstacle geometries. The first one belongs to a cube, the second one to a tall parellellepiped, with an aspect ratio close to the tall model used in the previous experimental work of Leyk (60 x 35 x 20). Unfortunately, unlike the pressure distribution on the front façade, the pressure coefficient distribution on the flat roof can not simply be derived from data measured on a cube. But obviously, the experimental distribution of the recessed model corresponds very well with the standard values over the cube.

However, it is possible to produce some plausible arguments. As the aspect ratio of the front façade of the experimental model is nearly a square, it is very likely that the flow corresponds closely to that at the cube's front, and carries a similar amount of momentum over the roof. This may cause a similar value of the mean pressure coefficient on the roof. However, as the roof is shorter than in case of the cube, the pressure coefficient will not recover downstream with the largest suction in the middle. Rather it is expected to be similar to the case of the 'tall block', because it is based on the same depth / width ratio. In this sense, the simulated values seem to be plausible. Probably, the steep increase in suction at the rear does not correspond to values found in experiments and overestimates the impact of the recirculating wake behind the building. But this possible shortcoming is not relevant for the pressure and flow field in the area of interest at the front of the roof.

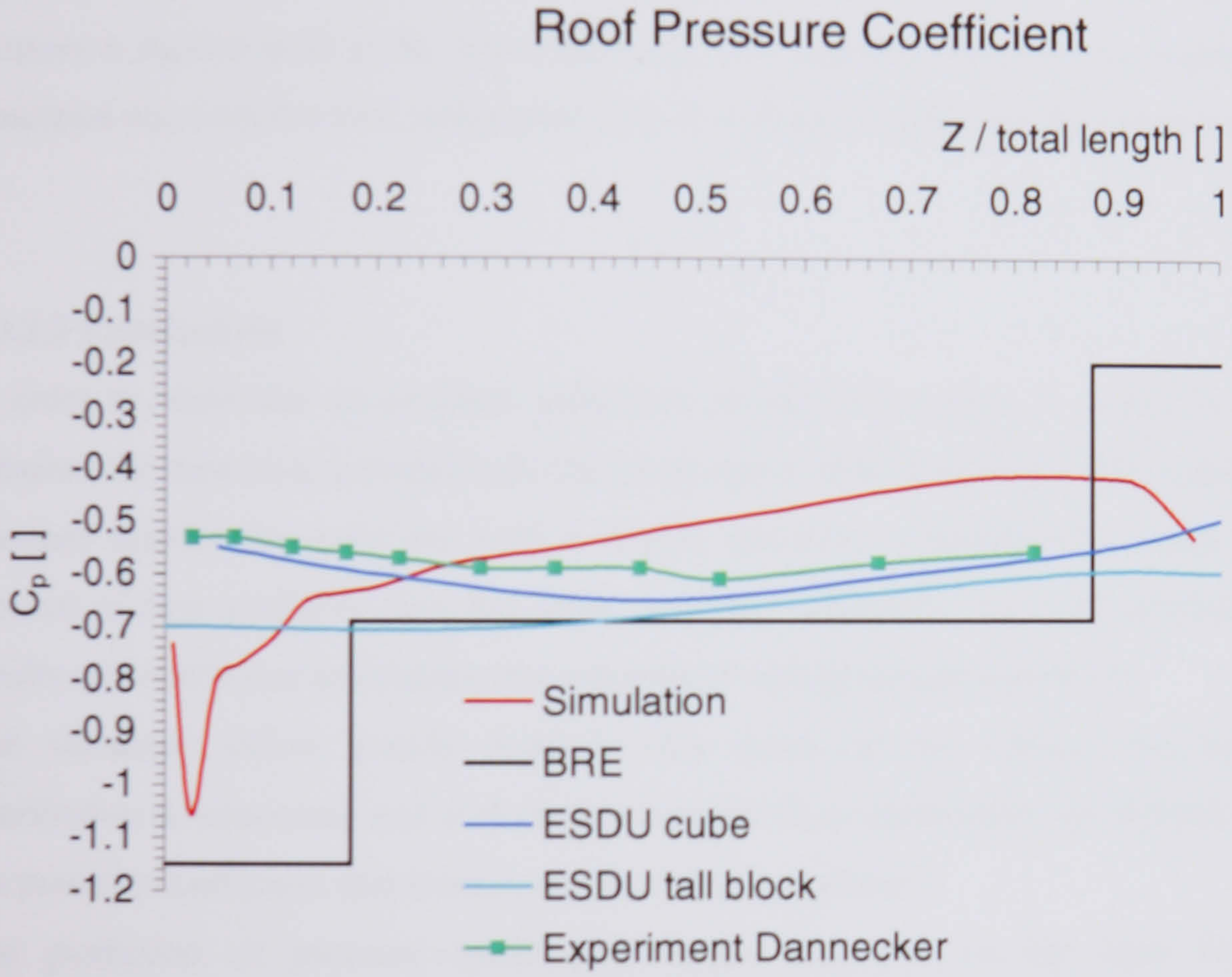

Figure 6.3.2.2.2: Comparison of the pressure coefficient distribution for three dimensional flow on the roof of a surface mounted cuboid: experimental, simulated and standard values

Very important for the purpose of integrating a ducted wind turbine is the increased suction arising at the front edge of the roof, where the flow separates. The absolute value of suction in this region depends on how the flow separates, which itself depends on the nature of the approaching flow. In ESDU datum conditions of a uniform inflow profile, the separating flow seems not to generate a strong suction, at least not when the flow approaches normal to the façade. Small deviations from these conditions, in particular the development of a boundary layer in the approaching flow, may result in increased suction at the leading edge. Such a case is measured for a cube, quoting a value of $C_p = -0.91$ at the very front part of the roof (Robins and Castro 1977). Even with uniform inflow conditions, the numerical model generates a boundary layer profile due to applied wall functions at the solid ground in front of the obstacle.

When compared with the real scale recommendations for the construction industry (BRE 1989), it is obvious that the increased suction at the leading edge is significant. Apart from the very rear part, the BRE standard envelops the simulated distribution.

The main experiments in the wind tunnel were conducted with a model height lower than the simulated case. But many alternative heights were tested, and it was never possible to measure a suction peak at the front. Basically, the experimental pressure coefficient and the simulated one over the roof correspond only as average. Locally the distribution differs.

6.3.2.3 Conclusions

In order to undertake an accurate validation of the CFD model, it would be necessary to compare the data from a model with the same aspect ratio in the same flow conditions, as the pressure distribution over the roof is highly sensitive to changes in either. The limited amount of data available does not allow accurate validation. But it is possible to compare results and conditions to evaluate the simulation with plausible arguments.

The simulated inflow profile depends very much on the vertical and horizontal cell distribution downstream, and it changes when the flow approaches the obstacle. This affects the pressure coefficient distribution on the obstacle surfaces.

The prediction of pressure coefficients larger than one on the front façade in two dimensional flow simulation is a serious limitation. Therefore, the two dimensional approach can only be used to compare different duct design options qualitatively with each other, when subject to the same boundary conditions at inlet and outlet. As the momentum is carried away only in two dimensions, it is very likely that the flow shows a higher tendency towards separation. Therefore, the qualitative evaluation of the two dimensional flow field can not directly predict three dimensional behaviour.

Three dimensional modelled flow around the cube creates a pressure coefficient distribution at the walls which basically agrees well with expected values. Therefore it allows qualitative and quantitative evaluation of the flow through any integrated duct. In particular the peak suction at the leading edge of the roof corresponds with reported values and the standards for the construction industry.

Still, comparison of experimental and simulated values is not straightforward. The experiment does not show the high peak suction at the leading edge as on a real scale roof. In the experiment, the model was either 15 or 30 cm high, so the cross-section was in the latter case nearly a square. The pressure coefficient distributions remained basically unchanged (apart from the lower part on the front façade) for both heights, and are close to the ESDU standard values for the small scale model cube. The experimental flow conditions with the low amount of turbulence in the free stream is despite the generated boundary layer relatively close to the ESDU conditions and produces similar suction at the leading edge to ESDU standards. At full size a turbulence scale effect could play a role. Perhaps at the leading edge, it might be important to monitor the root mean square of the fluctuating surface pressure coefficient. Therefore it would have been necessary to record the lateral, vertical and longitudinal turbulence intensities and their cross-correlations. The fluctuating surface pressure coefficient can be calculated as function of the turbulent intensities and the mean pressure coefficient (Robertson et al. 1977/78).

Because of the discrepancy between the simulated and the measured pressure differentials across the inlet and the outlet area of the duct, it might well be that simulated and measured wind speeds in the duct turn out to be not the same. As the simulated pressure differential reflects more the real scale situation, it might well be that the simulation generates more realistic values for the induced wind speed in the duct. The measured wind speed in the model duct reflects the wind tunnel model situation, with different flow conditions.

References

Engineering Science Data Unit ESDU. Wind Engineering - Mean Loads on Structures, Volume 2b - Fluid Forces, Pressures and moments on Rectangular Blocks; Item No. 71016, 1993; ESDU International, London.

BRE Digest 346; The Assessment of Wind Loads, Part 6: Loading Coefficients for Typical Buildings, November 1989; British Department of the Environment, Building Research Establishment BRE, Garston, Watford

Rahnema M., Yaghoubi M. and Sabzervari A.; Turbulent Wind Flow Patterns and Pressure Fields across a Tall Building; Wind Engineering, Vol. 20, No. 4, pp. 241-257, 1996

Sam R.G. et al.; An Experimental Study of Flow over a Rectangular Body; Transactions of the American Society of Mechanical Engineering ASME, Journal of Fluids Engineering, Vol. 101, pp. 443-448, 1979

Sakamoto H., Moriya M., Taniguchi S. and Arie M.; The Form Drag of Three-Dimensional Bluff Bodies Immersed in Turbulent Boundary Layers; Transactions of the American Society of Mechanical Engineering ASME, Journal of Fluids Engineering, Vol. 104, pp. 326-334, September 1982

Arie M., Kiya M., Tamura H., Kosugi M. and Takaoka K.; Flow over Rectangular Cylinders Immersed in a Turbulent Boundary Layer (Part 2, Flow Patterns and Pressure Distributions); Bulletin of the JSME, Vol. 18, No. 125, pp. 1269-1276, 1975

Baines W.D.; Effects of Velocity Distribution on Wind Loads and Flow Patterns on Buildings; Proceedings of the Conference "Wind Effects on Buildings and Structures", Department of Scientific & Industrial Research, Symposium No. 16, held at the National Physical Laboratory, Teddington, Middlesex, England, 26th to 28th June 1963, pp. 198-225

Leyk M.; Aerodynamical Investigation of a Ducted Wind Turbine; externe Studienarbeit, Fachgebiet Energietechnik und Reaktoranlagen, Fakultät für Maschinenbau, Technische Universität Darmstadt, Germany / Student Research Project, Energy Systems Division, Department of Mechanical Engineering, University of Strathclyde, Glasgow, Scotland; October 1997

Robertson J.M., Wedding J.B., Peterka J.A. and Cermak J.E.; Wall Pressures on Separation-Reattachment Flow on a Square Prism in Uniform Flow; Journal of Wind Engineering and Industrial Aerodynamics, Vol. 2, pp. 345-359, 1977/78

7. Computational Fluid Dynamics Simulation of Building Integrated Duct Flow

As described earlier, the idea to integrate a Ducted Wind Turbine in the leading roof edge is based on the assumption that the local pressure differential over the edge will induce higher wind speeds in the duct, which will enhance massflow and power production. A very simplified model with basic fluid mechanics predicts induced wind speed proportional to $(\Delta C_p)^{1/2}$ taken on the front part of the roof and the upper face of the wall (see Chapter 2.6). This simplified model requires modification, as the flow patterns are complex and the entrainment behaviour of the flow through the duct into the outer flow is difficult to predict. Additionally, flow separation in the duct plays a significant role and restricts the massflow. Therefore the design of an optimal duct is not straightforward, and the presented work should be seen as only an initial step in this direction.

7.1. Two Dimensional Simulation

The aim of the two dimensional simulation is to compare the performance of different duct designs qualitatively. A quantitative assessment does not make sense because of the shortcomings described in Chapter 6.

7.1.1. Geometry and Grid

Only six configurations were modelled to compare certain features while keeping other geometrical parameters constant.

In order to achieve sufficient resolution, the whole grid has a Body-Fitted coordinate system and is decomposed into sub domains which are linked together.

Configuration 1 (see Figure 7.1.1.1) consists of a 90° curved tapering duct with an inlet opening at around 11°. In three dimensional extension, the inlet would be a square, but the duct itself would have a round cross-section. The area ratio of inlet to outlet would then be around 3. Based on the same duct, configuration 2 (see Figure 7.1.1.2) is fitted with a smooth curved bell mouth inlet, which increases the diameter ratio by more then a factor of 2. Further, a small spoiler above the inlet extends forward by about a quarter of the inlet diameter.

Configuration 3 (see Figure 7.1.1.3) has a basic quarter circle shape with a straight inlet. The duct has no taper. Configuration 4 (see Figure 7.1.1.4) is a combination of configuration 3 with the spoiler from configuration 2. Configurations based on the quarter circle do not require the non-natural grid link approach, which otherwise applies at the outlet, where the z-direction of the duct aligns with the vertical (y-direction) of the flow environment.

Configurations 5 and 6 (Figures 7.1.1.5 and 7.1.1.6) are both based on a straight duct, the first one tapering as a concentrator, the second opening as a diffuser. Configuration 5 has the inlet of configuration 1, but the upper wall of the duct is straight and inclines at 45°. It has the same diameter ratio as configuration 1. Configuration 6 expands towards the roof as a diffuser and its diameter opening ratio approximates to the inverse of the ratio of configuration 5.

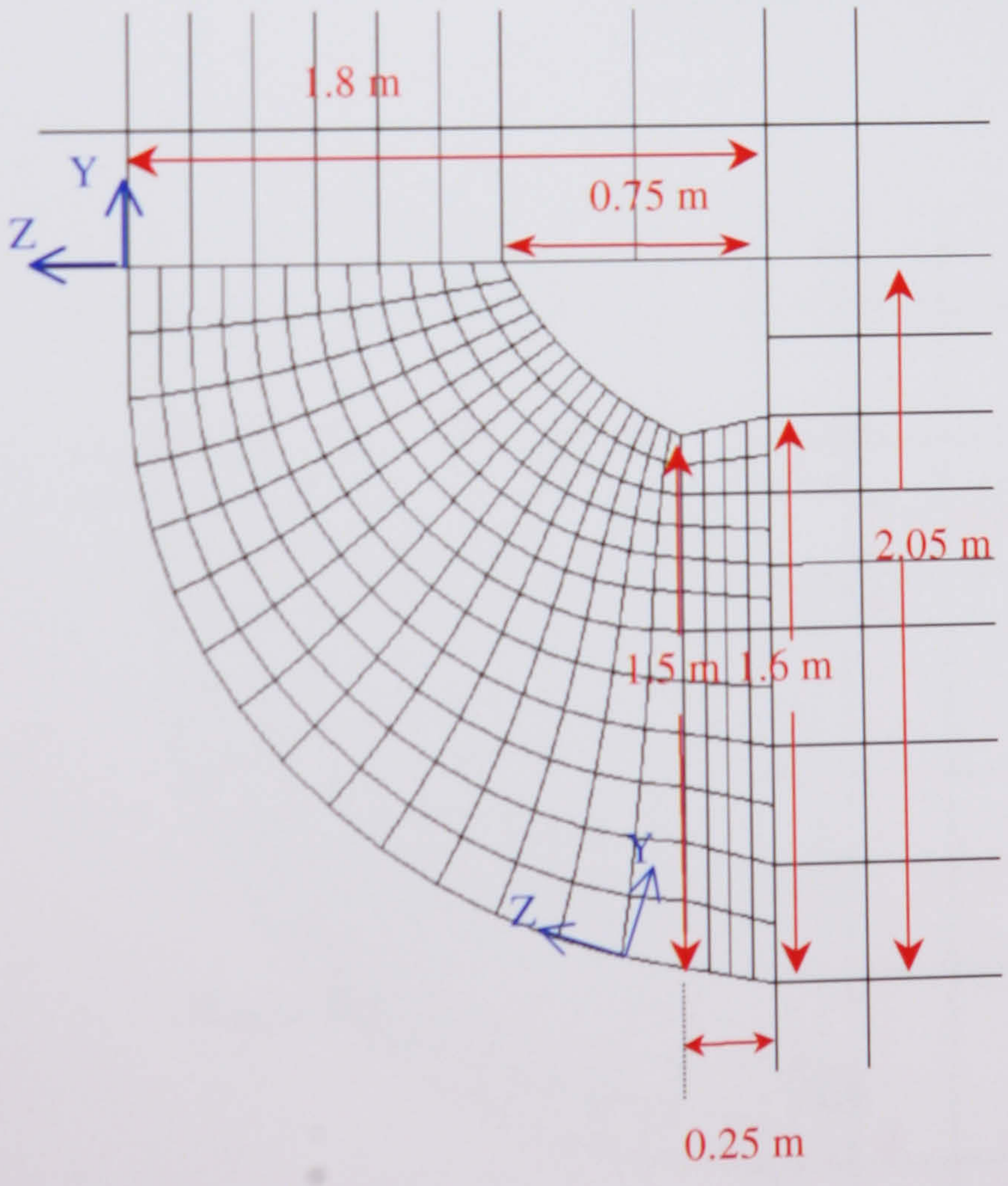

Figure 7.1.1.1:
Configuration 1

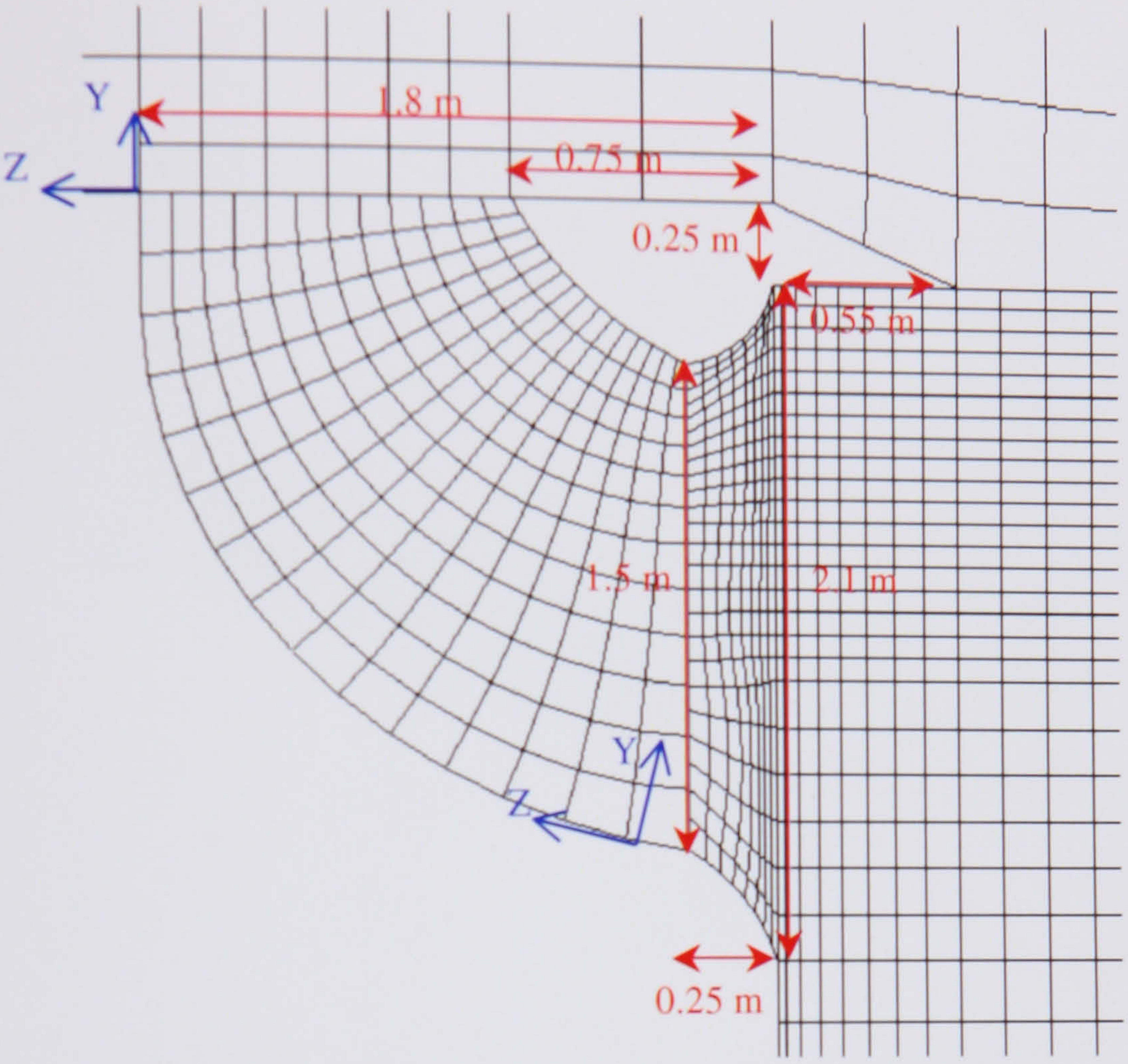

Figure 7.1.1.2:

Configuration 2

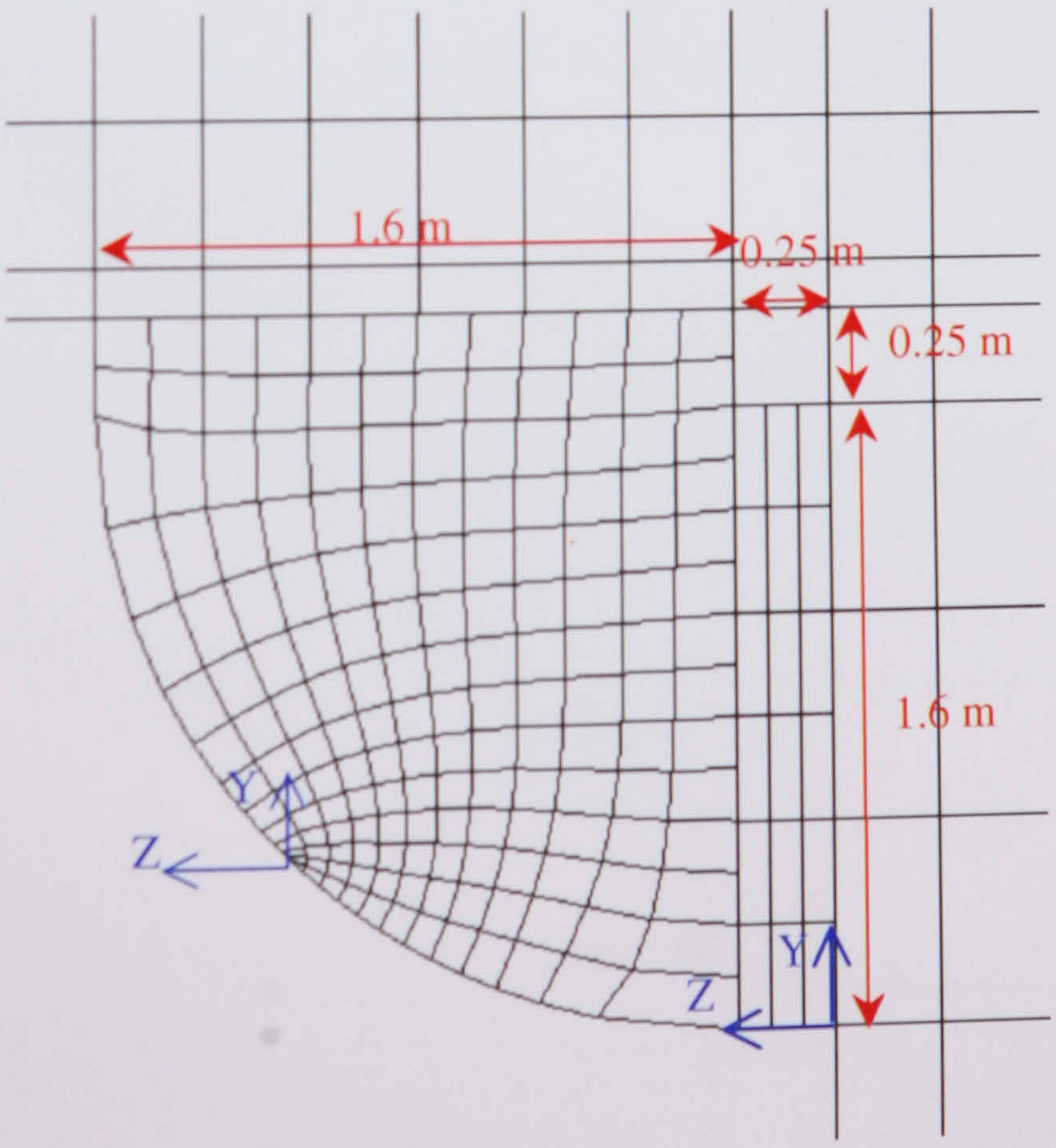

Figure 7.1.1.3:

Configuration 3

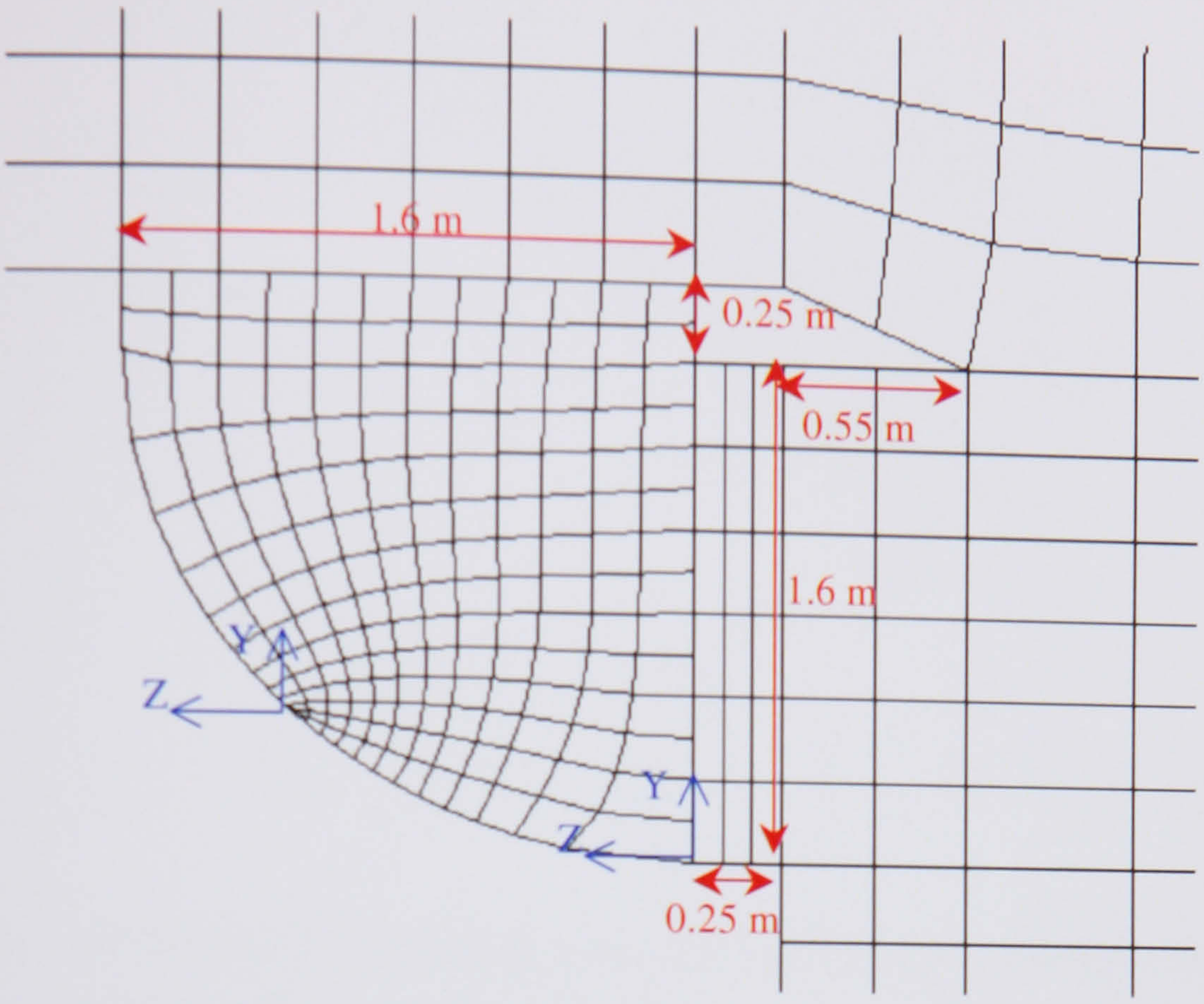

Figure 7.1.1.4:
Configuration 4

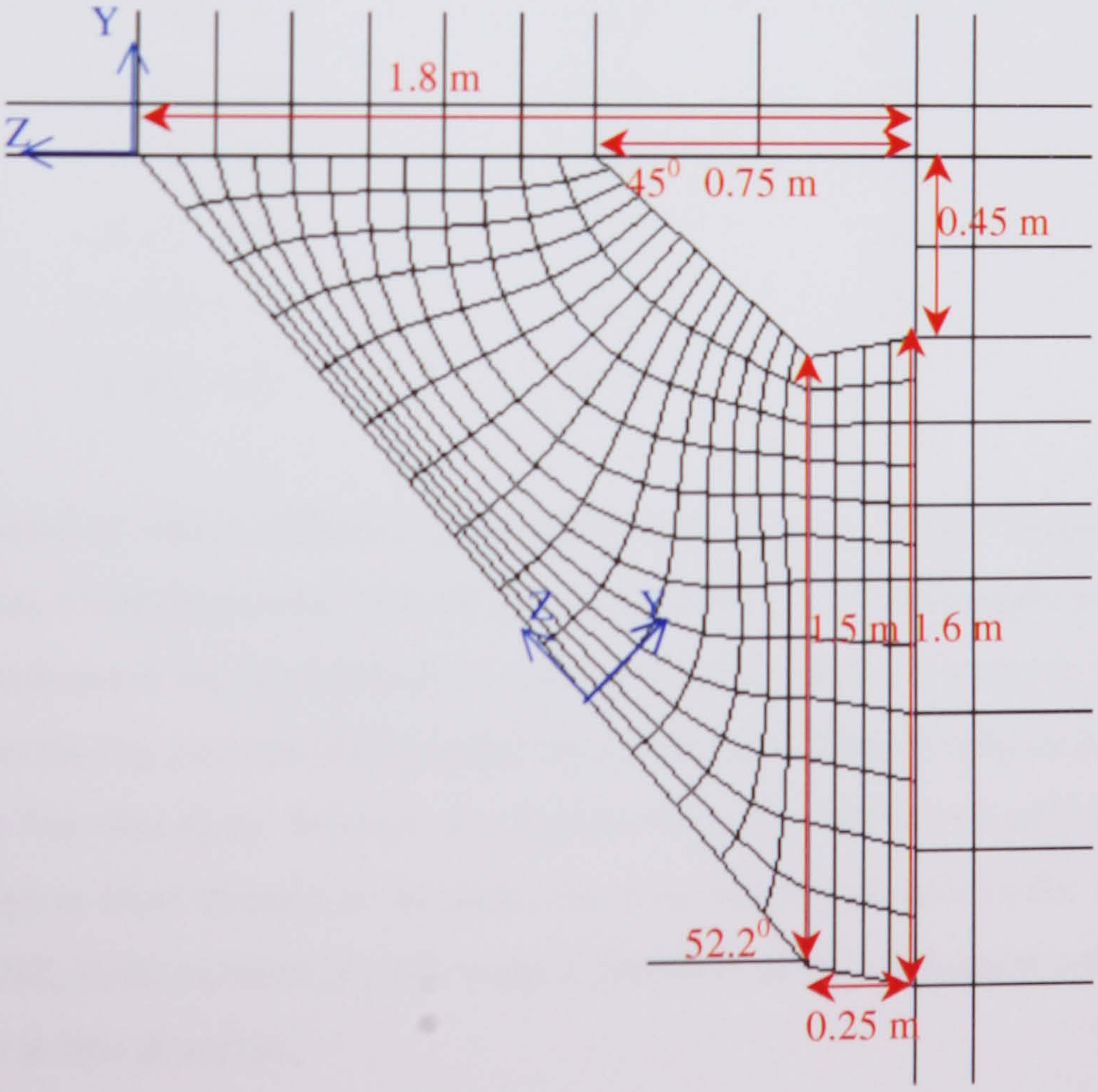

Figure 7.1.1.5:
Configuration 5

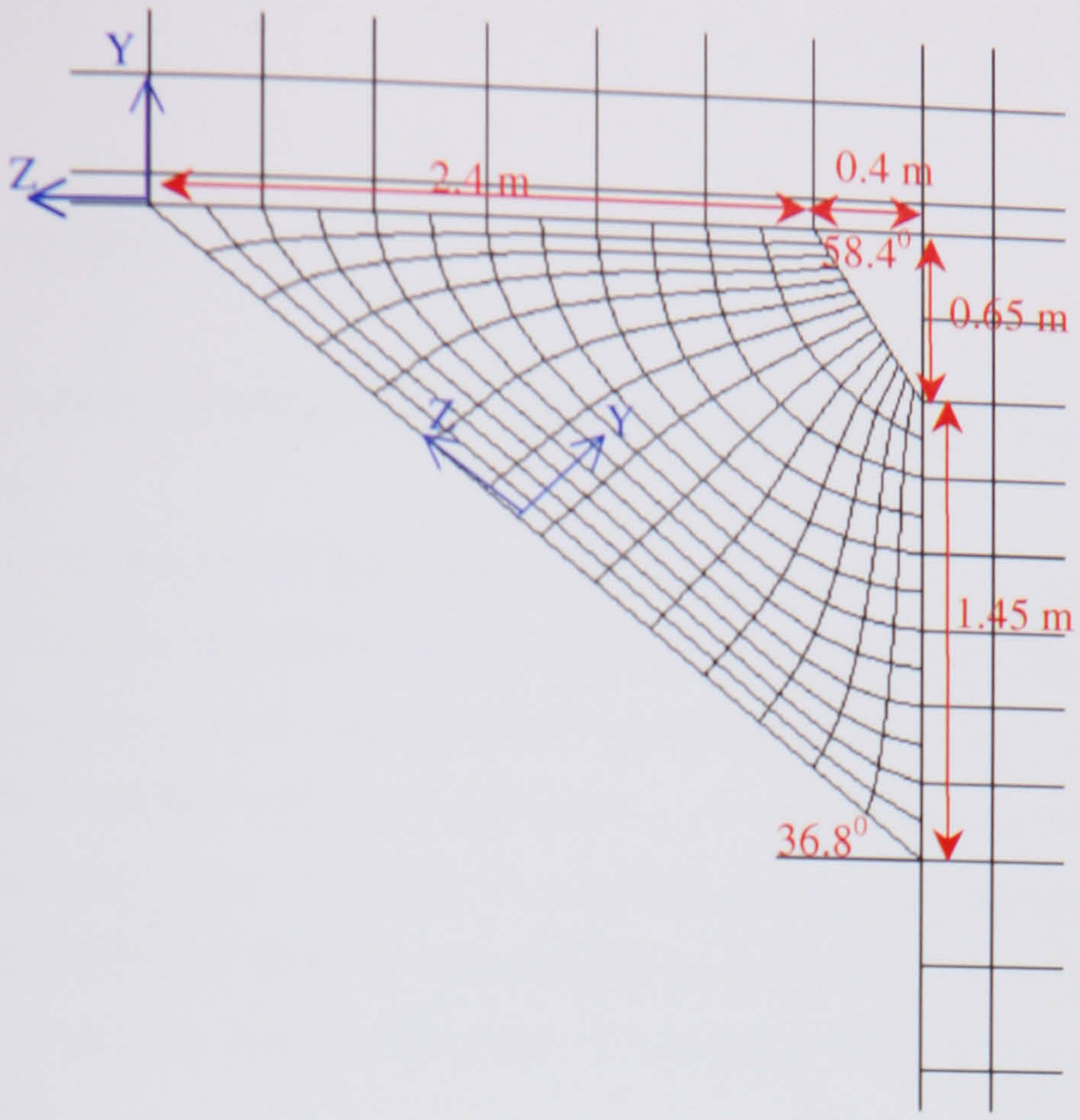

Figure 7.1.1.6:
Configuration 6

The non-dimensional wall distance Y^+ was taken at the bottom of the inlet opening, at the cell where the flow separation initialised. The values are in a range which support the accurate application of the wall boundary functions (see Chapter 5.6).

Configuration	Total number of cells	Y^+	Number of subdomains
1	1 x 326 x 52	234.9	22
2	1 x 307 x 60	136.5	20
3	1 x 311 x 45	155.9	18
4	1 x 327 x 46	82.3	18
5	1 x 300 x 53	37.1	20
6	1 x 242 x 42	256.2	16

The whole grid is composed of many different subdomains (see Chapter 5 and Chapter 6.1.2.). Each subdomain has a certain number of cells in each direction. The subdomains are stacked in the computational space via the y-direction, and each subdomain cell receives y-direction indices. Therefore the big number NY does not represent the number of cells in the y-direction, it points to the fact that many domains are stacked via y. The number of cells in the z-direction is also different from domain to domain. The total number of cells in the z-direction of the assemble, NZ, is the number of cells in the z-direction of the subdomain with the highest number of cells in this direction.

7.1.2. The Flow through the Duct

The figures in this section show vectorplots of the flow pattern and the graphs of the wind speed ratio at the duct outlet.

The wind speed ratio at the outlet is calculated as the resultant speed at the outlet divided by the mean free wind speed, here the modelled uniform inflow velocity (16.5 m/s). The values at the outlet were taken from the very last row of cells of the duct which connect to the open flow field over the roof. The resultant velocity was chosen, as it would be the one measured with the single hot wire pointing inside the outlet, as performed in the experimental part of the presented work and described in Chapter 4. By comparison of the resultant of different design options it may be feasible to indicate the induced momentum. It is not intended to calculate figures of massflow.

The geometrical location is non-dimensionalised with the total length of the roof (20 m). The duct outlet is intended to be located in the first 10 % of the roof.

The vectorplots show direction and absolute value of the velocity vectors, through length and color.

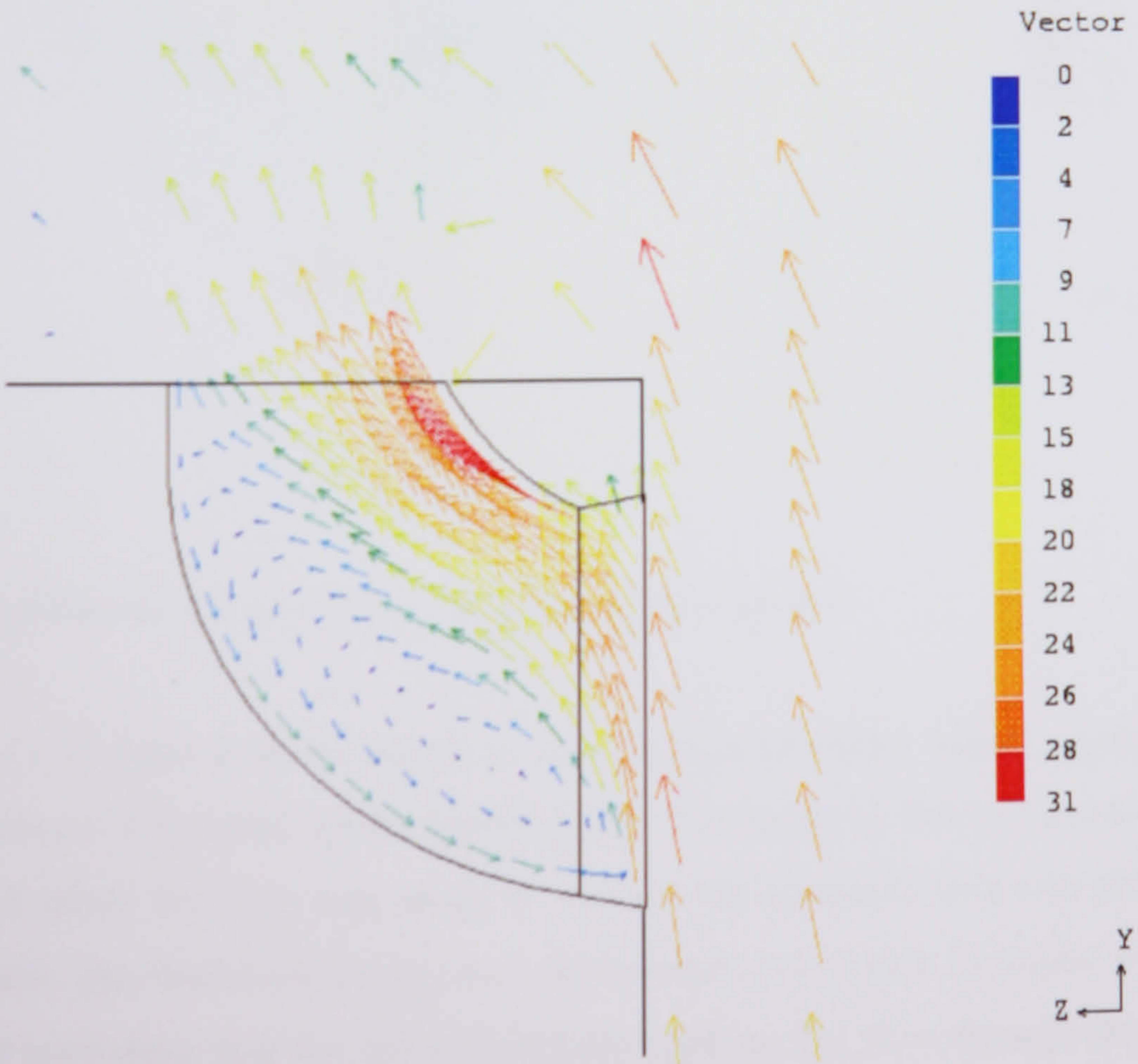

Figure 7.1.2.1: Two dimensional vector flow pattern, configuration 1

Figure 7.1.2.1 shows that the upstreaming air in front of the duct has already a higher speed than the modelled inflow velocity. Entering the duct, the flow separates at the inlet and generates a separation bubble which occupies about half the space. Accelerated flow can be found in the upper part of the duct, which results in a non-uniform distribution of air speed at the outlet (Figure 7.1.2.3). It is likely that the velocities at the duct outlet may be made more uniform by restriction of the separation bubble. The stream through the outlet enters the separated flow field over the building (see Figure 7.1.2.1).

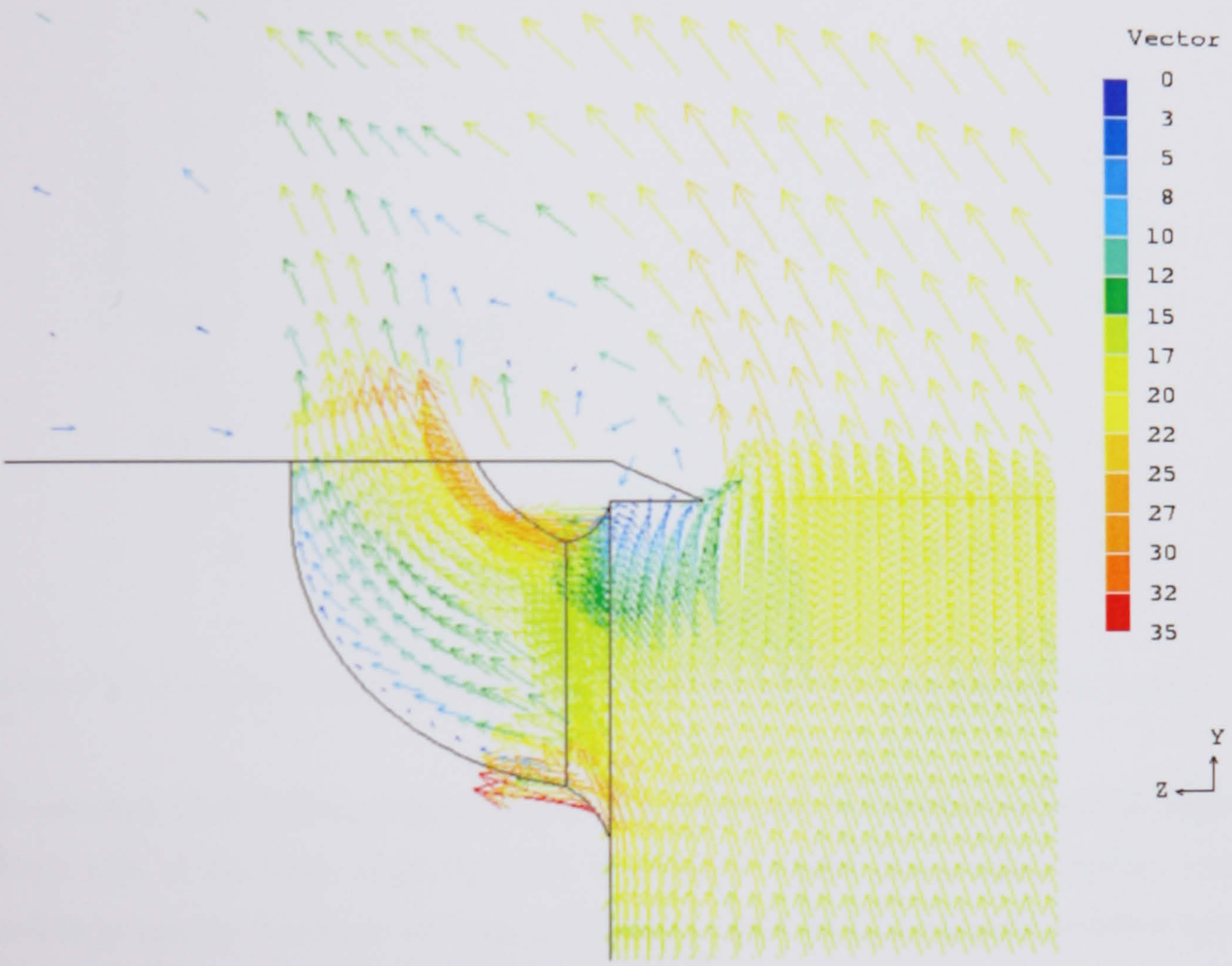

Figure 7.1.2.2: Two dimensional vector flow pattern, configuration 2

Configuration 2 has two main features added to the previous geometry which appeared to enhance the performance of the duct system significantly. The spoiler at the roof captures the upflow and guides it inside the duct, and seems to increase the separated zone over the front part of the roof. Here, the limitation of the two dimensional simulation becomes evident, even if a higher grid resolution over the spoiler had been applied. The flow through the outlet entrains nearly vertically into the separated recirculation bubble over the roof. It may well be that here the two dimensional simulation underestimates the turbulent mixing with the outer flow field. But in comparison with Figure 7.1.2.1, the positive effect of the spoiler is clear. Very important seems to be the smooth bell mouth inlet, which avoids the generation of a large separation bubble inside the duct.

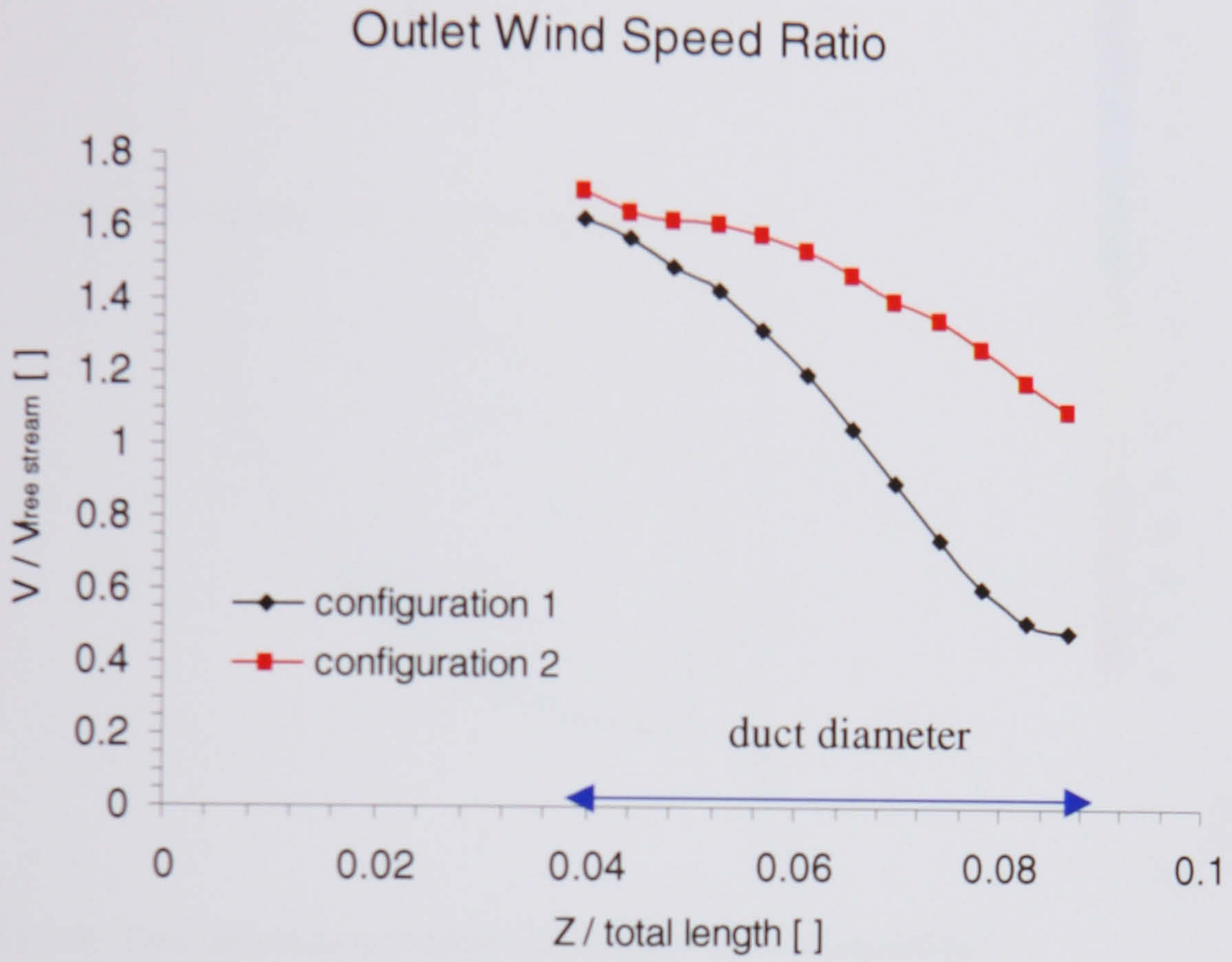

Figure 7.1.2.3: Comparison of wind speed ratio at the outlet for configurations 1 and 2

The accuracy of modelling shapes like the bell mouth inlet is limited, because the shape of certain cells is far from ideal. An error may occur which causes high velocity vectors pointing across the boundary (as seen in Figure 7.1.2.2). But the accelerated inflow around the curved inlet wall seems realistic and will carry momentum smoothly to a region which would be otherwise dominated by separated flow. This positive impact becomes obvious if we compare the wind speed ratios at the outlet. The wind speed exceeds the free flow velocity significantly, over the whole outlet (see Figure 7.1.2.3).

The basic shape of the next configurations (Figures 7.1.2.4 and 7.1.2.5) represents the experimental model (Chapter 4) and one of the first prototypes of the free standing ducted wind turbine (Chapter 2.8). Even without the tapering effect of the previous configurations, it is obvious that a high wind speed is induced in the upper part of the duct (see Figure 7.1.2.6), whereas a large separation bubble again occupies the lower part. The influence of the spoiler mainly increases the value of speed at the outlet, without changing the direction of the velocity vectors or significantly changing the flow pattern (compare Figures 7.1.2.4 and 7.1.2.5).

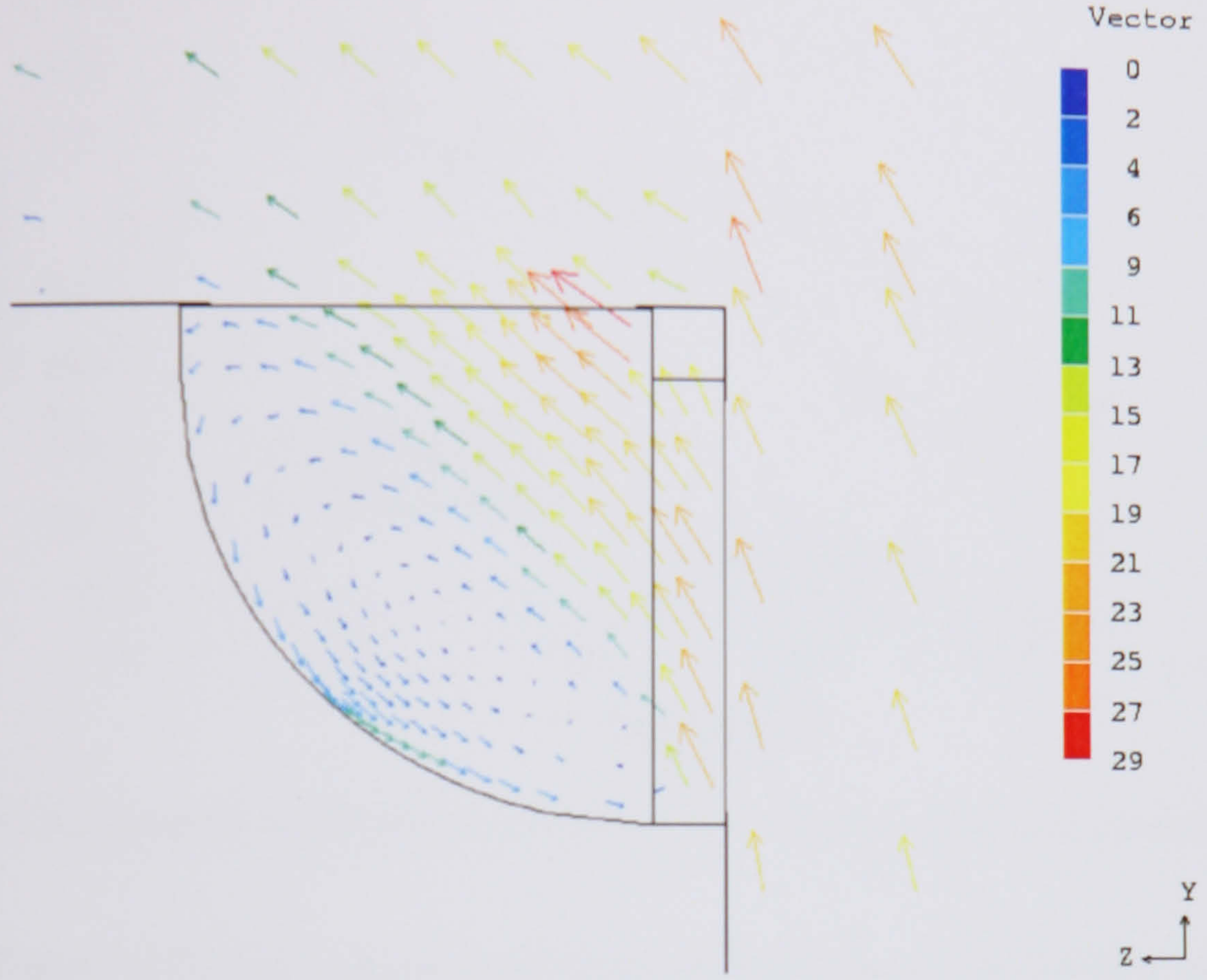

Figure 7.1.2.4: Two dimensional vector flow pattern, configuration 3

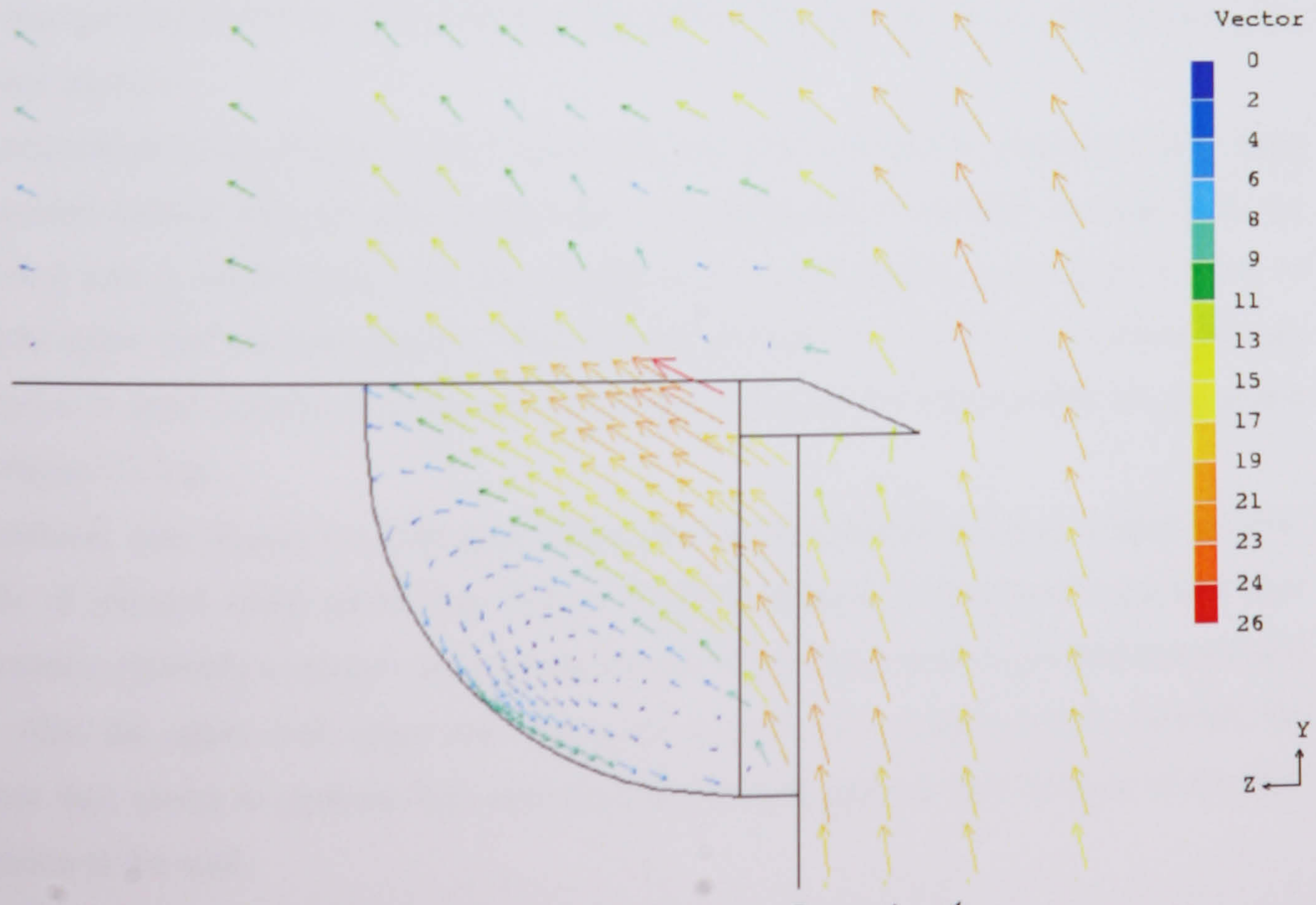

Figure 7.1.2.5: Two dimensional vector flow pattern, configuration 4

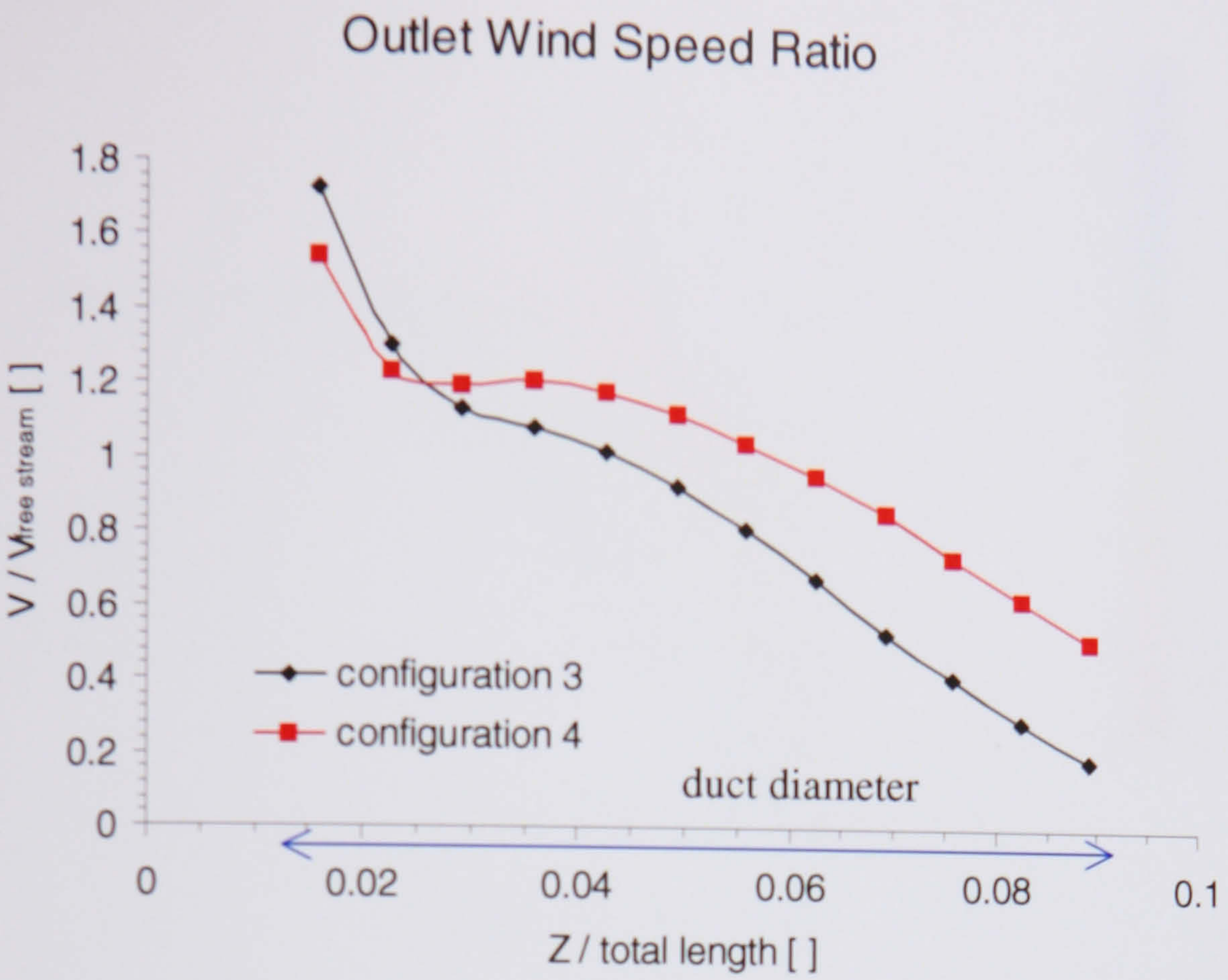

Figure 7.1.2.6: Comparison of wind speed ratio at the outlet for configurations 3 and 4

Common feature of the last four duct configurations is that the penetrating flow mainly has the tendency to pass straight through the upper part of the duct. The main stream direction may approximate to 45° or more from the horizontal. The next two duct configurations take this into account.

The concentrator type (Figure 7.1.2.7) generates less flow separation, which probably could be avoided entirely with the bell mouth inlet of configuration 2. Overall, it seems to be the case that with a streamlined inlet, the straight duct would perform quite well in terms of induced speed and uniform profile. Without such an inlet, the loss of momentum through separation is quite significant at the rear part of the outlet and the speed profile has a gradient (see Figure 7.1.2.9).

The diffuser type (Figure 7.1.2.8) generates in the upwind half of the duct a fairly uniform profile of induced wind speed (see Figure 7.1.2.9), whereas downstream separated flow recirculates. Probably a steeper angle of inclination of the lower wall to the horizontal could help. Also the upper wall edge does not work so well as a stream splitter. Overall, the diffuser duct seems to perform less well than the straight tapered duct because of the flow separation at the wall.

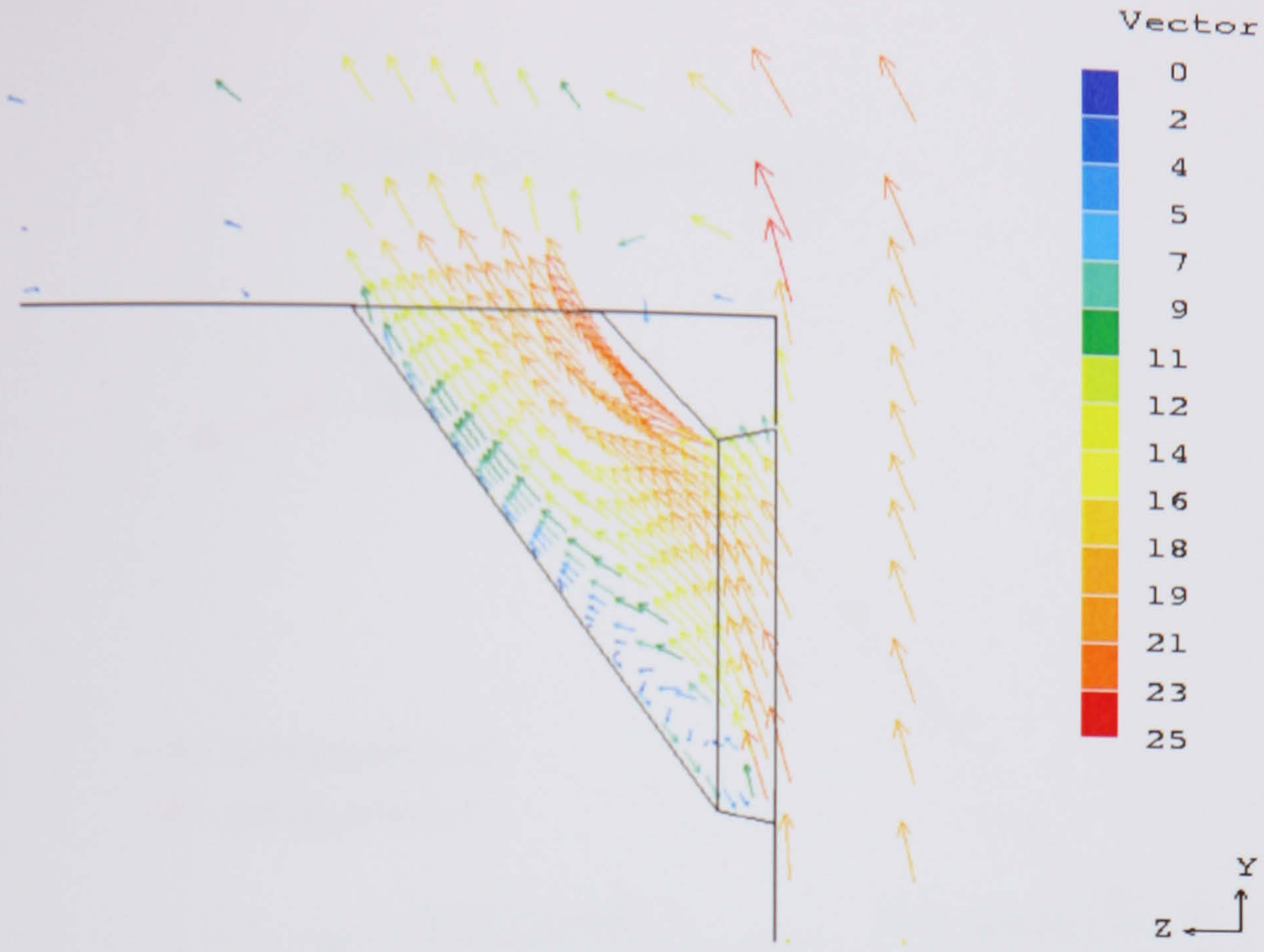

Figure 7.1.2.7: Two dimensional vector flow pattern, configuration 5

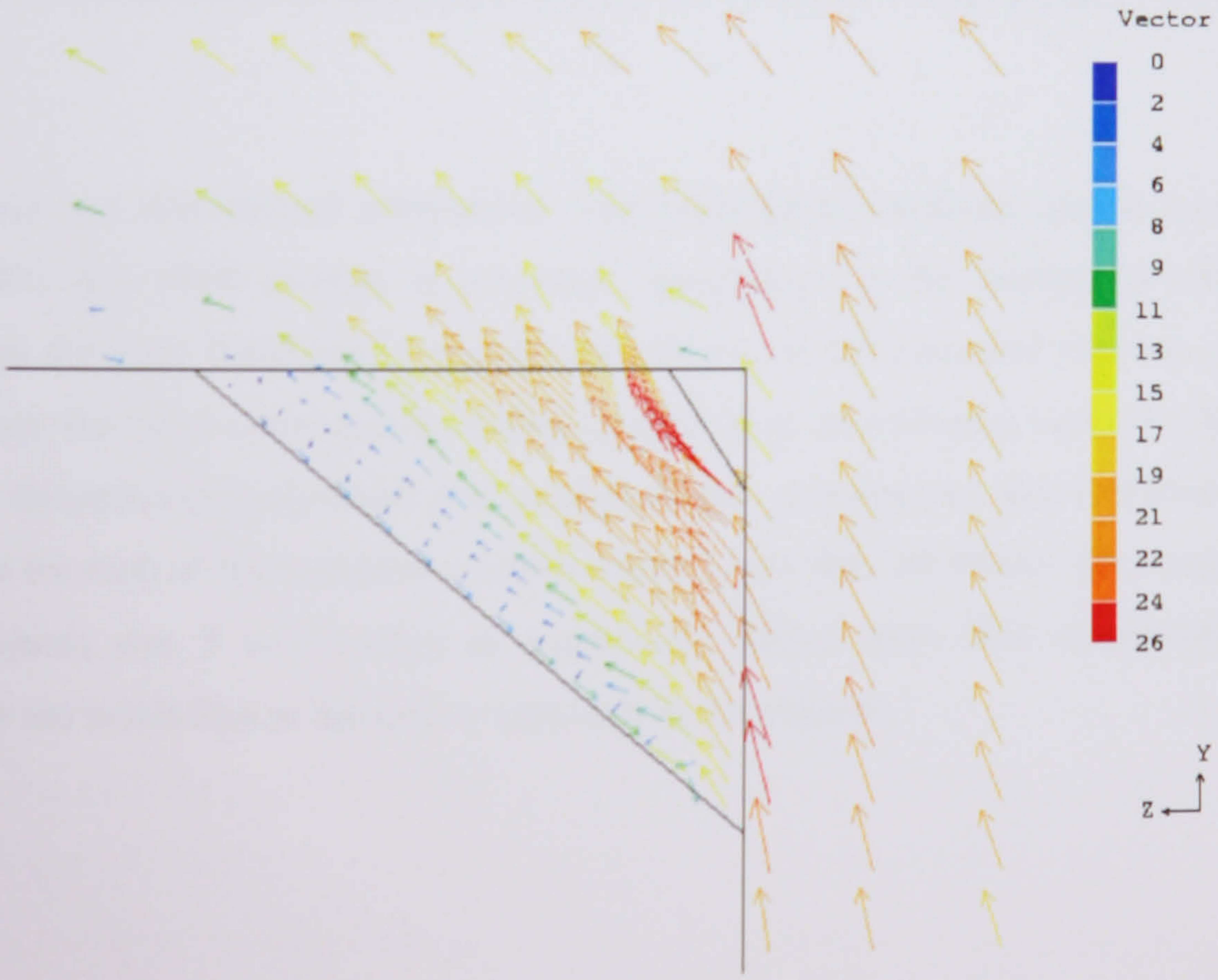

Figure 7.1.2.8: Two dimensional vector flow pattern, configuration 6

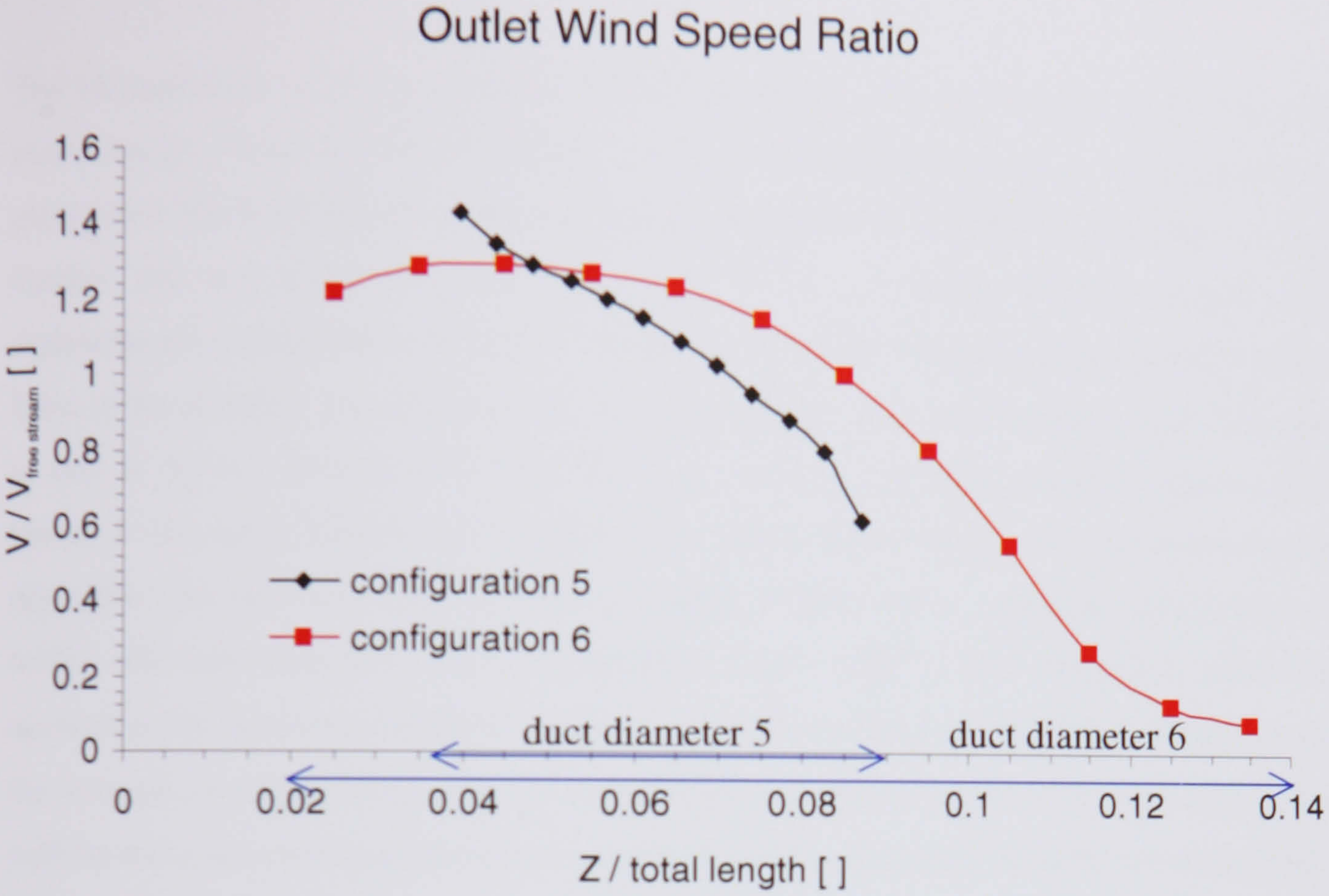

Figure 7.1.2.9: Comparison of wind speed ratio at the outlet for configurations 5 and 6

Accuracy:

The presented two dimensional simulations with body-fitted coordinate system required in between 4000 and 9000 sweeps to converge, dependent on the number of cells. The calculation in the body fitted grid is significantly slowed down compared with the cartesian grid. However, the same convergence criteria applied as in the cartesian cases of Chapter 6. For all two dimensional body-fitted grid configurations, convergence was confirmed when the residuals for each of the variables reached values lower than 20. Hence, the average drop for the residuals was 5 to 6 orders of magnitude. Global mass flow conservation was confirmed in the result files at the inflow and outflow boundaries.

7.1.3. Conclusions

The interpretation of the two dimensional flow through the duct has to deal with some shortcomings, which are directly linked to the two dimensional approach. Overprediction of pressure on the front façade may cause an overprediction of induced speed inside the duct. Further, the two dimensional solution seems to have a higher tendency towards flow separation and recirculation. In reality, momentum is always transported in three dimensions. Even in the classical two dimensional case, turbulence itself is three dimensional. The flow is said to be two dimensional when the flow pattern in different parallel cross-sectional planes is the same (ESDU 1993). The lateral mean flow velocity is then assumed to be negligible, but this definition would also apply if there were a constant lateral flow. In reality, the third direction carries momentum away, which is not sufficiently taken into account in the two dimensional k-ε turbulence model. So the amount of flow separation and the strength of recirculation may be overpredicted compared with reality. In reality it may well be that a duct configuration shows only little flow separation, while the two dimensional model predicts a significant recirculation bubble. In this sense, the two dimensional simulation gives a pessimistic view. With respect to the experimental values (as presented in Chapter 4), the two dimensional simulation indeed overpredicts the peak induced wind speed (see Figures 7.1.2.3, 7.1.2.6 and 7.1.2.9) and suggests a steep gradient of the wind speed ratio towards the downstream side of the duct, caused by separation inside the duct. In particular the large flow separations of configurations 3 and 4 were much reduced in the test model (see Chapter 4).

Completely missing in the simulation is local gustiness of the wind. Locally generated turbulence of short length scale in the incoming wind may interact with the casing of a Ducted Wind Turbine.

Difficulties arise also at the duct outlet, where the released stream of fast air entrains in the recirculating flow over the roof which separates around the leading edge. This entrained flow rises and reattaches somewhere behind the building. The outer flowfield upstream deviates only in the vertical direction, as the lateral component does not exist. In reality, one would expect more turbulent mixing and dissipation when the duct stream entraines the roof recirculation. One might even expect the entrained flow to reattach on the roof. It may well be that at the leading edge of the roof a horizontal vortex occurs. Flow entrainment into this horizontal vortex seems to be quite complex (see Chapter 4). Here, the two dimensional model certainly has a shortcoming. However, it accurately predicts that the entraining flow reduces the suction over the whole roof and the high pressure on the upper part of the front façade.

Comparing the flow through each duct configuration qualitatively, it is possible to draw some basic conclusions:

The wind speed loss inside the duct caused by flow separation might be very significant. Therefore, great attention must be paid to avoiding flow separation inside the duct on a large scale. A very important step in this direction is a streamlined inlet. A simple spoiler above the inlet can capture the upflow and guide it into the duct, without changing significantly the stream pattern inside. Further, it may increase the flow separation at the leading edge of the roof, which generates the suction at duct outlet.

Concerning the geometrical design of the duct, it seems to be the case that a straight tapered tube at a certain angle of inclination seems to be simple and efficient. The optimal angle depends on the angle of flow over the leading edge. This angle might be different for different building geometries, and the streamline pattern changes with wind direction. A reasonable universal approach would be around 45°.

Any long duct device is seen as a disadvantage, but it is important that the profile of the flow can develop to become more uniform. This has to happen inside the duct, but the proper inlet will play here a crucial role.

In the duct, the highest induced wind speed seems to occur at the turning point of the bend duct or more half way at the straight duct, not in the outlet plane.

The optimum diameter of the duct depends on the application and on the suction pattern on the flat roof. But it is realistic to assume that over the first 10 % upwind area of the roof the suction will be high, and this is also the zone of vortex generation in oblique wind directions. The duct outlet for a single installed turbine should not lay outside this region.

The impact of many turbines in a row on the suction field in this zone could be very serious, but this was not part of the presented two dimensional investigation.

7.2. Three Dimensional Simulation

In order to compare with experimental results, the experimental model with the 90° duct in the windtunnel (Experiment 5) was almost identically modelled. The main difference was that the geometry of the computer model is 1:100 upscaled. As mentioned earlier, a test simulation had shown no difference in the surrounding flow and pressure field around two blocks, one at model scale, the other at full scale. However, the value of the non-dimensionalised wall parameter Y^+ changes. But we could not find evidence from the two simulations that the duct flow is affected by changes in the function of the wall boundary. Hence, of particular interest was the comparison of experimental and simulated wind speed ratios in the duct. Upscaling makes it possible to compare all simulated models at similar scale. As described in Chapter 6, the difference in quoted standard cases of pressure distribution on the envelope of models and real scale buildings gives reasons to doubt that the wind tunnel values are confirmed in real scale. The same might prove to be the case for velocities and profiles in the duct.

In terms of geometrical details, the only difference between the experimental model and generated three dimensional CFD model is that the smoothly curved shape of the inlet could not modelled perfectly because of limitation of the cell number. The best possible approximation was a wide straight opening (see Figure 7.2.1.3). Also, it was assumed that the flow field is symmetrical. This assumption may be valid as the spinning turbine itself is not modelled.

The boundary conditions of the numerical model are identical to those described in Chapter 6, apart from the turbulence intensity. The assumed 40 % were replaced by the typical value of 1 % for wind tunnel flow.

7.2.1. Geometry and Grid

Hence, the dimensions of the obstacle are 15.5 m high, 20 m deep and 35 m wide (projecting in the symmetrical half 17.5 m). The flow domain is limited to 120 m height, 200 m downstream, 100 m upstream and 60 m to each side (see Figure 7.2.1.1). The geometry of the duct is described in Figures 7.2.1.3 and 7.2.1.4.

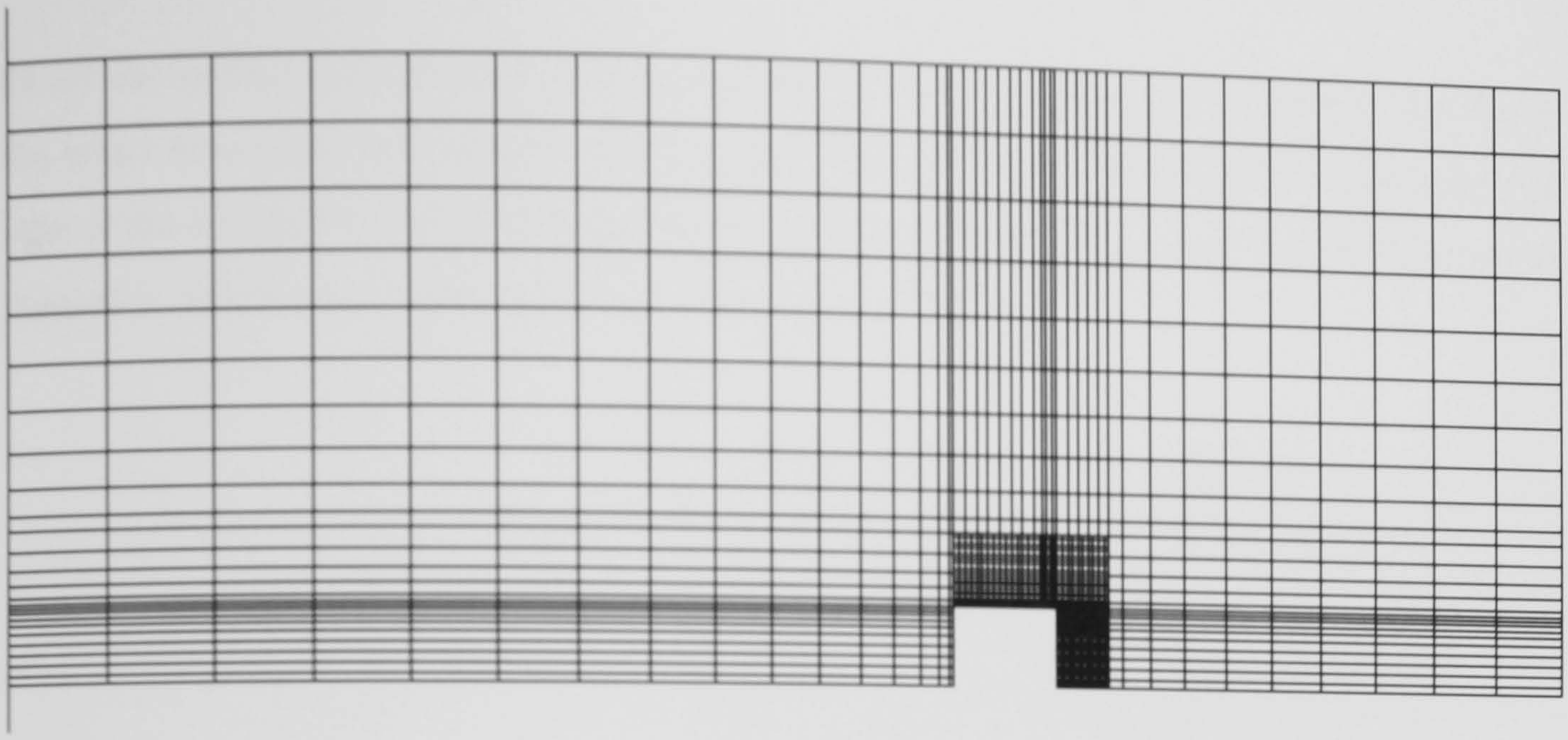

Figure 7.2.1.1: Cross-section in symmetry plane

The total number of cells NX x NY x NZ = 20 x 291 x 32 reaches close to the limits of the software package capacity (PHOENICS version 2.2.1 on a Pentium 3 processor). Sufficient convergence was achieved after around 15000 sweeps, which took around six weeks. The whole grid is composed of 27 subdomains with body fitted coordinate system, and extensive use of grid refinement and one-to-many cell links in each direction had to be made. Power law spacing for the single subdomains was applied wherever feasible. In order to achieve a grid resolution at the obstacle which is fine enough to resolve pressure gradients and the complex flow field in the duct region, it was necessary to create most of the cells in the vicinity of the façade and the roof.

Figure 7.2.1.2: Grid refinement in the symmetry plane

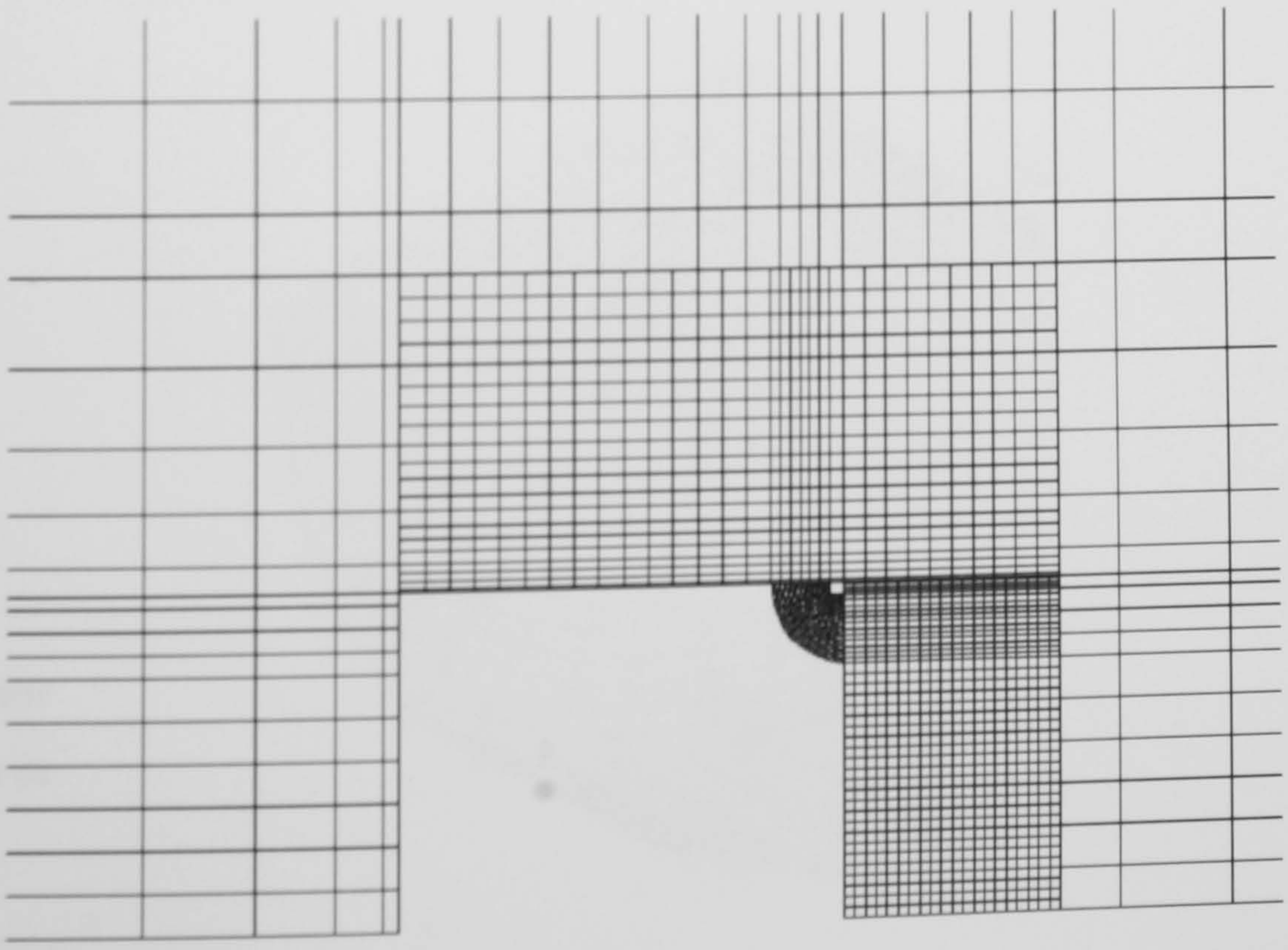

Given the limited total number of cells, it was necessary to diminish the number of cells in the wider flow area significantly. For example, the vertical distance from the ground to the inlet of the model is in the zone immediately in front of the model covered by 24 cells, which reduces to only 6 cells further upstream (see Figure 7.2.1.2).

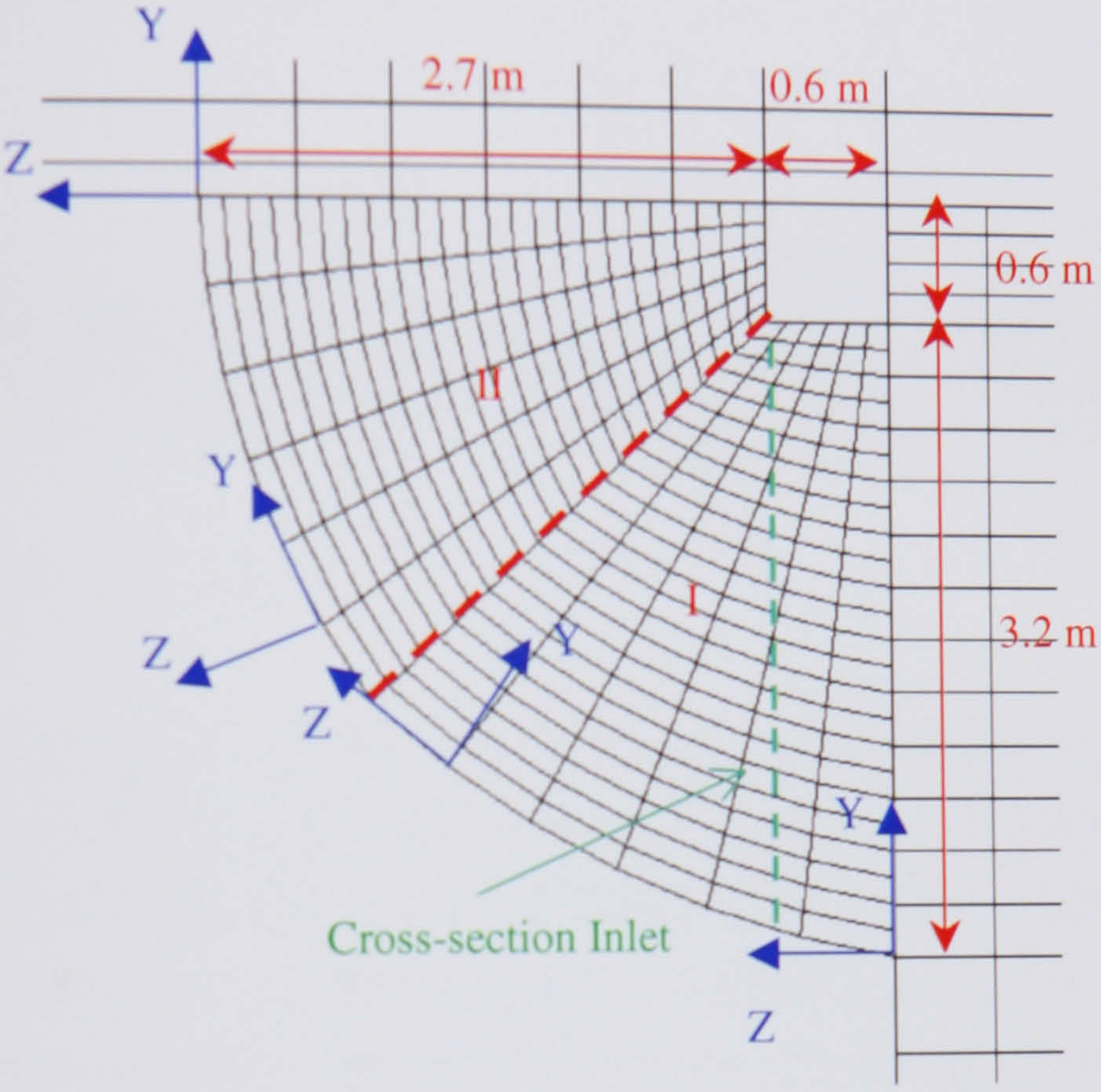

Figure 7.2.1.3: Geometry of duct in the symmetry plane. Non-natural link for domains of different coordinate axis directions.

The duct itself consisted of two domains (I and II), non natural linked at the diagonal. Each domain consists of 8 x 24 x 6 cells (Figure 7.2.1.4).

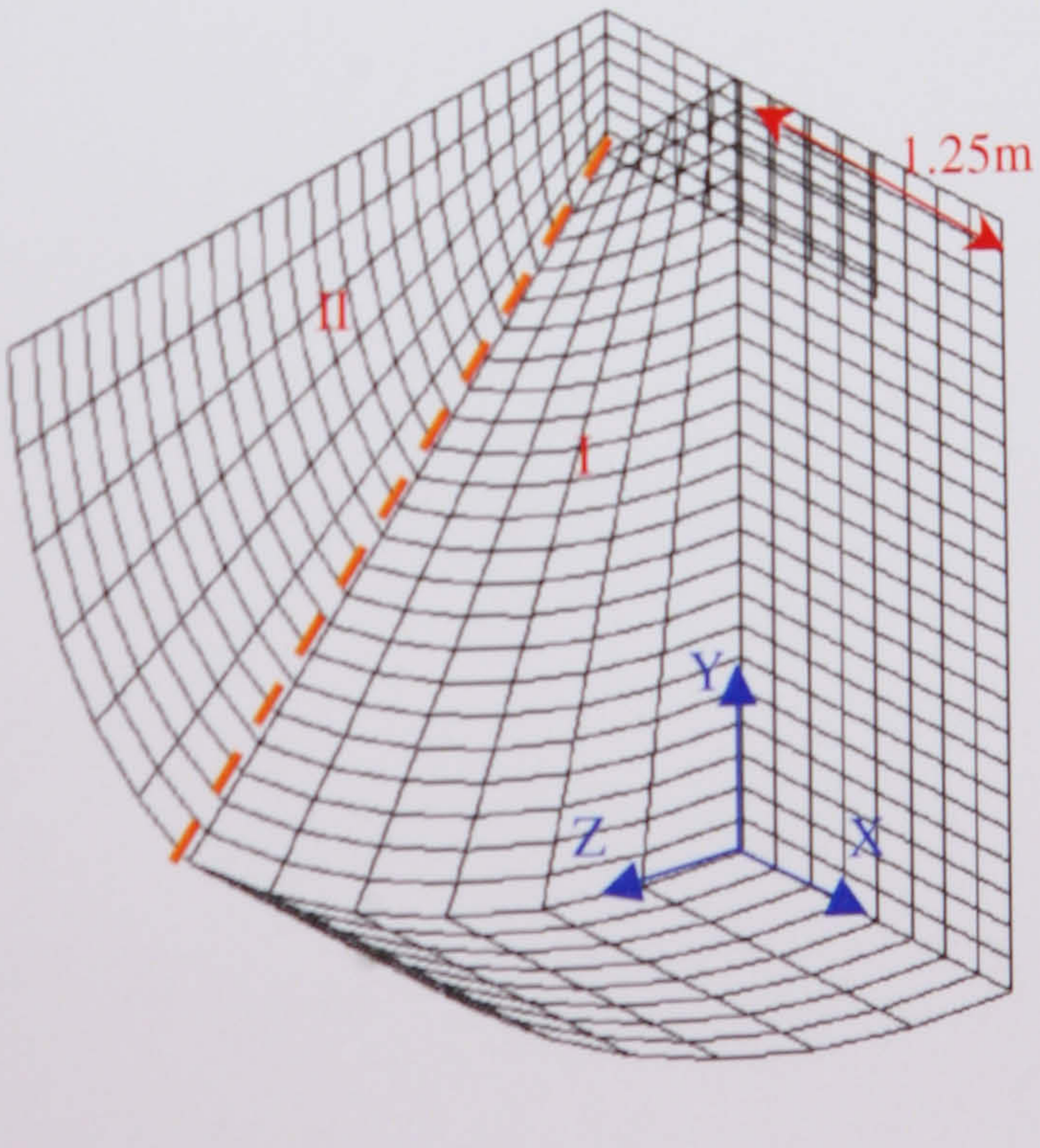

Figure 7.2.1.4: Three dimensional view of duct, cross-section in the symmetry plane.

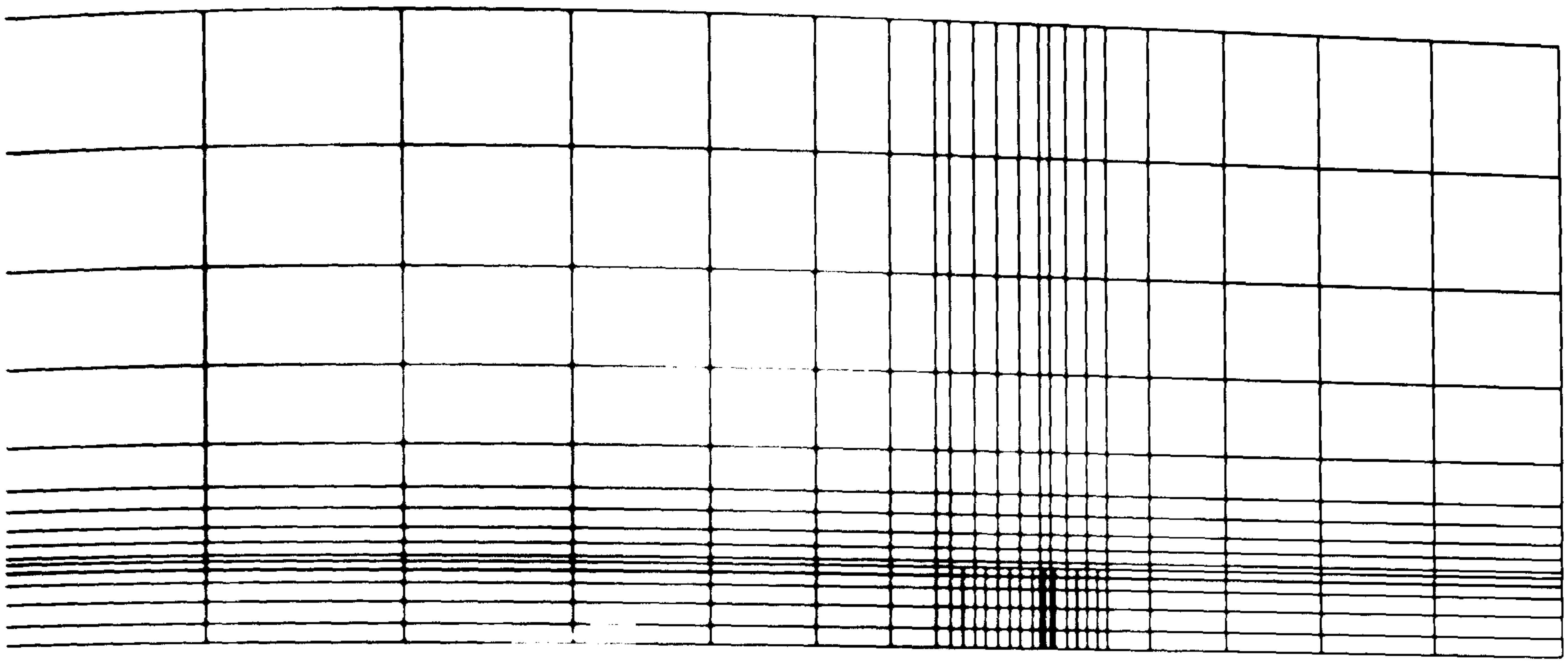

Figure 7.2.1.5: Open boundary coarse grid

The open EAST side (see Figure 6.1.1.2) of the flow domain is composed with a much coarser grid (Figure 7.2.1.5). Generally, the whole flow domain is decomposed with three layers in the x-direction, with gradually decreasing grid density. The first layer comprises NX = 10 cells, with the symmetry plane as WEST-boundary (see Figure 7.2.1.1). This layer contains the duct with its high grid density. The second layer covers the building to the side of the duct, with decreasing grid density (cell number ratio 2:1) in each direction. Finally, the third layer presents the open outflow with its coarse grid (Figure 7.2.1.5). The outer coarse grid has an impact on the flow conditions approaching the obstacle, as well as on its wake. This will be shown later in this chapter.

7.2.2. The Flow and Pressure Field

As the flow approaches the obstacle, the coarse grid towards the ground upstream from the obstacle causes the generation of a significant boundary layer but does not resolve the steep gradient in momentum. Hence, the approaching flow at building height has slowed down from 16.5 m/s (inflow condition) to 14.7 m/s. In this plane upstream, no significant vertical or lateral flow component exists. Therefore it was decided that 14.7 m/s be used as the reference velocity for the calculation of pressure coefficients and wind speed ratios.

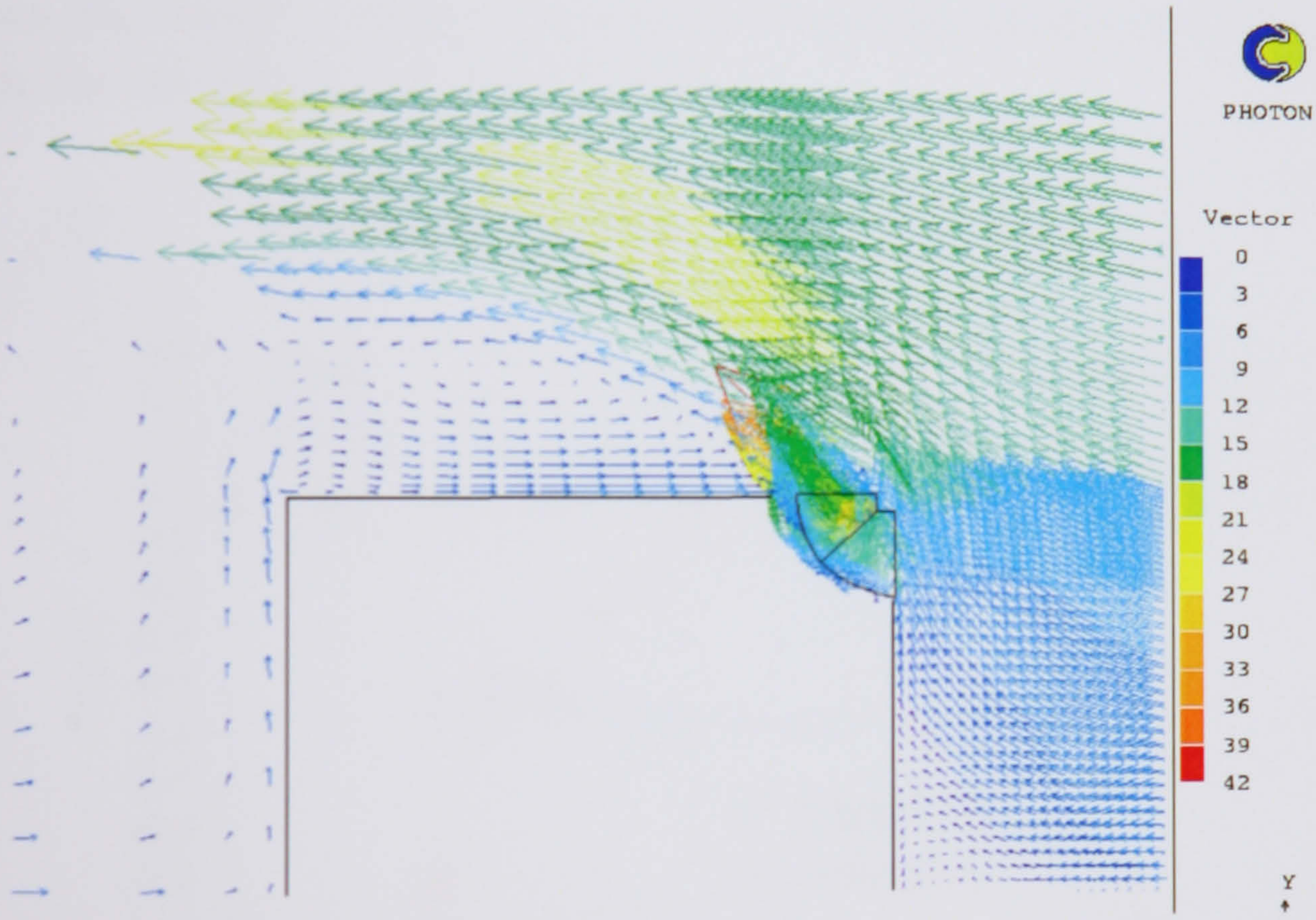

Figure 7.2.2.1: Recirculation in the roof zone with duct flow entrainment, plane of symmetry

The recirculation in the wake behind the obstacle is very similar to that what was found in the refined grid approach for the flow around the plain block as described in Chapter 6. The length of the recirculation zone behind the obstacle is around 3.8 H. The flow separates at the leading edge and generates a large recirculating wake over the roof, where even the upstream flow at the rear side of the obstacle is entrained (Figure 7.2.2.1). This leads to a second flow separation at the trailing edge of the roof. This flow pattern can not be confirmed in previous simulations or with experiments. Above the rear part of the roof, the height of the recirculation is about 0.4 H. Generally, the size and momentum in the recirculation zone is overestimated, but the flow patterns are apart from the second separation at the trailing edge similar to the refined grid approach in Chapter 6. Unfortunately, this is not true for the distribution of the pressure coefficient on the flat roof (see Figure 7.2.2.2). The simulated pressure coefficient indicates the separation at both leading and trailing edges, and the reattachment at the rear part of the roof.

As can be seen in the vectorflow pattern (Figure 7.2.2.1), the recirculating flow from the rear reattaches, and not the jet stream from the duct. Here the simulation certainly fails. Also, the simulation gave the value $C_p = -2.12$ for the leading edge in close vicinity upstream from the outlet. In the experimental model, it was impossible to place a pressure tapping at this location. But referring to values of suction observed at large scale for wind normal to the facade, this value might be a factor of 2 too high.

Figure 7.2.2.2: Comparison of simulated and experimental values of the pressure coefficient downstream of the duct outlet on the flat roof in the symmetry plane.

A finer and more uniform grid spacing in the wake region combined with a finer grid in the outer region would alter this overestimated result quite significantly. Unfortunately, given the limited number of cells and the lengthy runtime of the simulation as described in the previous section, the presented cell distribution has not much room for improvement. In particular, it was not possible to apply a grid along the lines described in Chapter 6. Therefore, the simulation focuses on the flow situation in and around the duct. The following diagram (Figure 7.2.2.3) compares the simulated pressure coefficients on the roof to the right of the duct opening with the experimental values (see Figure 4.2.8 pressure tappings P5, P7 and P9).

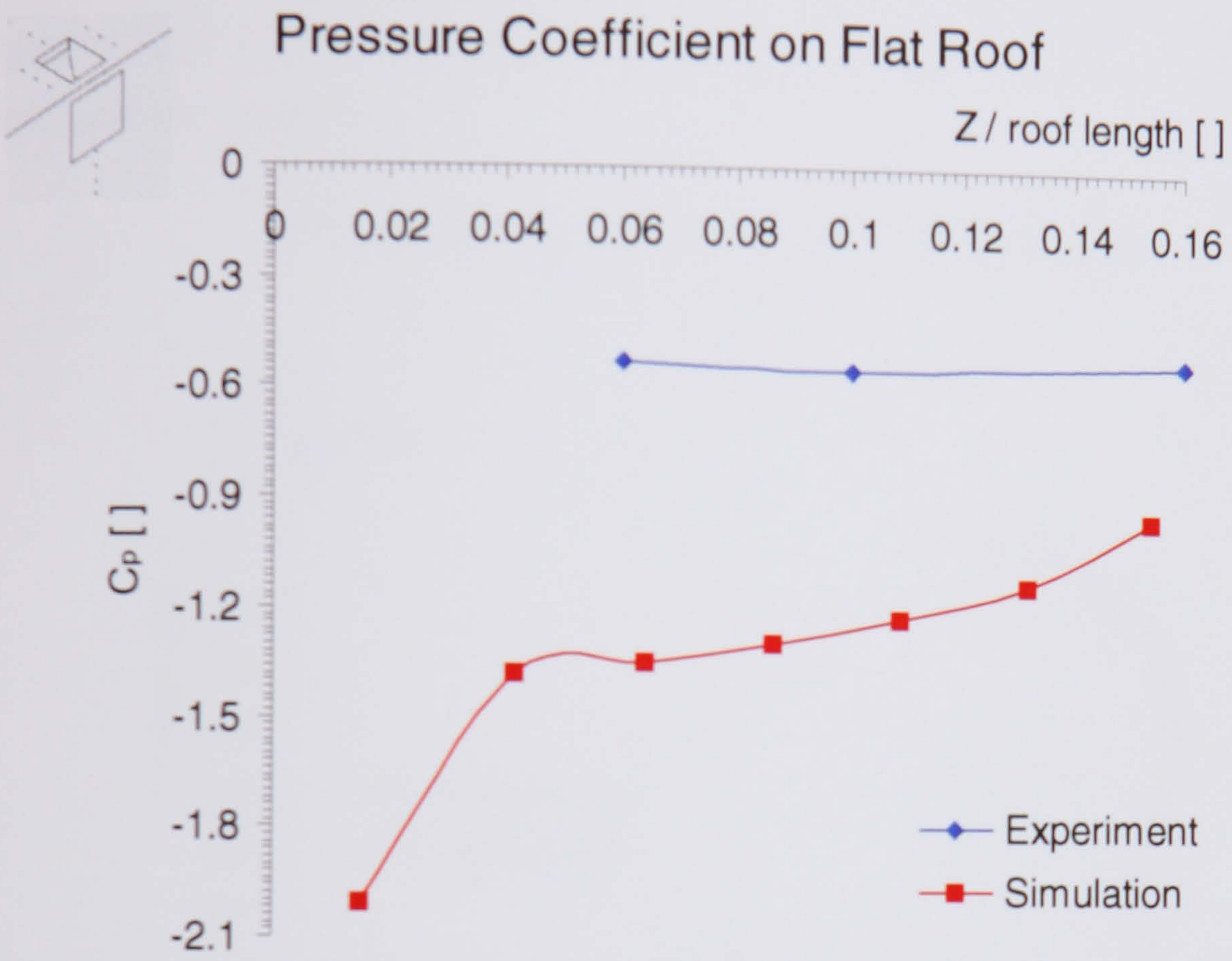

Figure 7.2.2.3: Comparison of simulated and experimental values of the pressure coefficient to the right of the outlet

The experimental values follow the uniform distribution measured downstream from the outlet (see Figure 7.2.2.2) and compare well with the pressure distribution measured on the model without duct (see Figures 4.7.1.2 and 4.7.2.2). In other words, for inflow normal to the front façade there is no experimental evidence that the uniform distribution of suction on the roof is altered in the vicinity of the outlet. The simulated values indicate the separation at the leading edge. We still have the discrepancy of the experimental values from the wind tunnel model and the standard values of suction for the full scale building, which state in this region of the roof a pressure coefficient of around –1.1 (compare Figure 6.3.2.2.2). As mentioned earlier, this can not be simply a Reynolds number effect (Chapter 6.3.2). Cell size and distribution plays a major role.

The comparison of the simulated and measured values at the front façade shows more coherence (Figure 7.2.2.4). Below the duct inlet, the pressure values correspond quite well.

Further down, the experimental model seems to experience a more significant boundary layer above the wind tunnel table. Immediately above the inlet, the simulation shows a pressure coefficient larger than one, because of local flow acceleration at the duct inlet. In the experiment without the duct (Chapter 4.7.), it was not possible to install pressure tappings above Y/H = 0.96 because of the wall thickness. At Y/H = 0.96 the pressure coefficient was around 0.6.

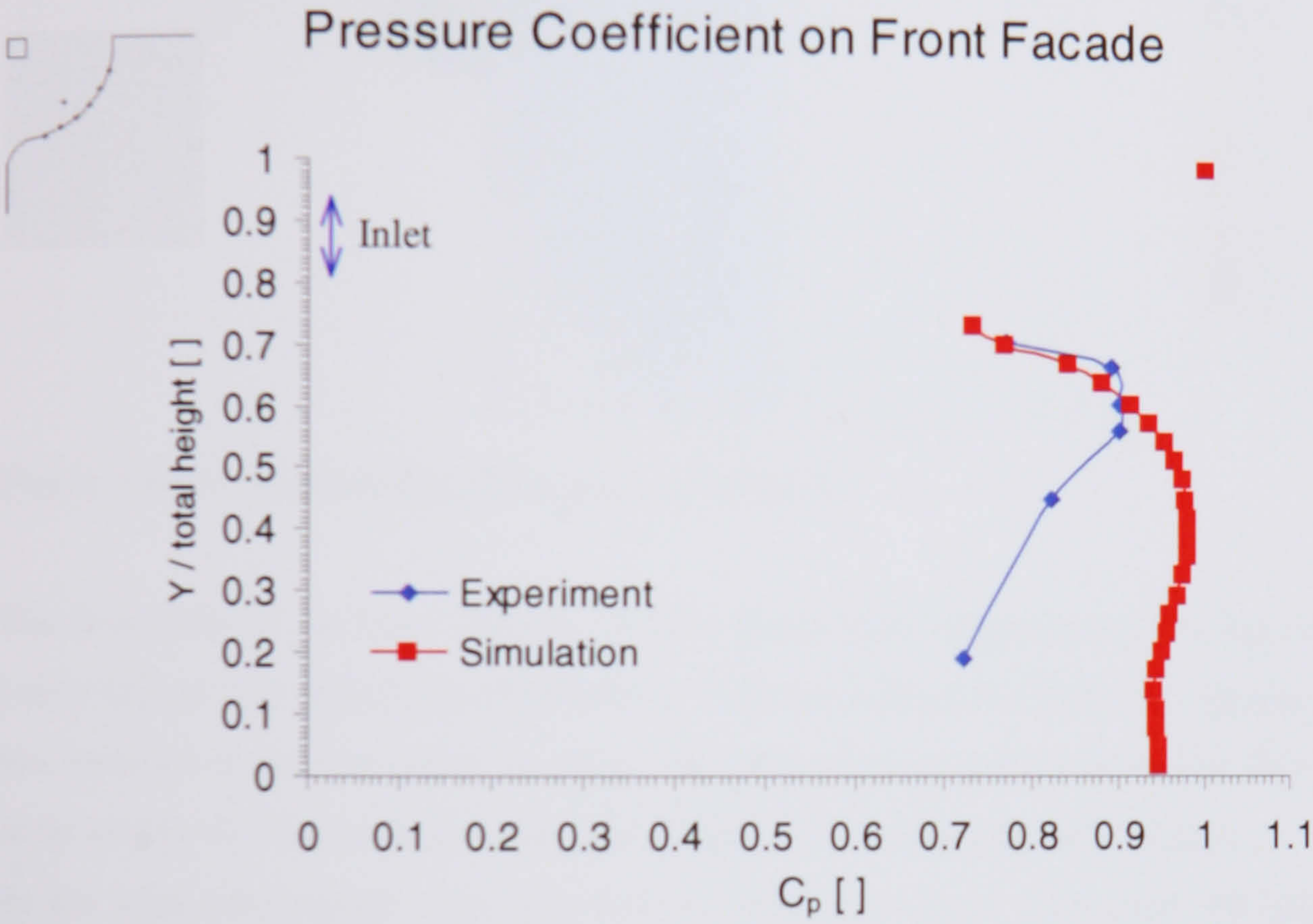

Figure 7.2.2.4: Comparison of simulated and experimental values of the pressure coefficient on the front façade.

The fine grid zone in front of the obstacle shows how the approaching flow decelerates (Figure 7.2.2.5). It already slows down in the outer region of the coarse grid. At the base of the obstacle, it generates the attached horizontal vortex as expected. Stagnation height is around 0.4 H, which is due to the inflow profile and the existence of the duct.

Very important for our purpose is the flow acceleration through the duct, which is influenced by the acceleration in the flow field around the leading edge. As the pressure coefficient in immediate vicinity of inlet and outlet do not correspond with measured values, it might well be that the flow through the duct is not modelled well. Due to the edge, further above the roof the flow speeds up by about 25 % compared with the approach conditions, and probably around 10 to 15 % compared with the undisturbed flow speed at building roof height.

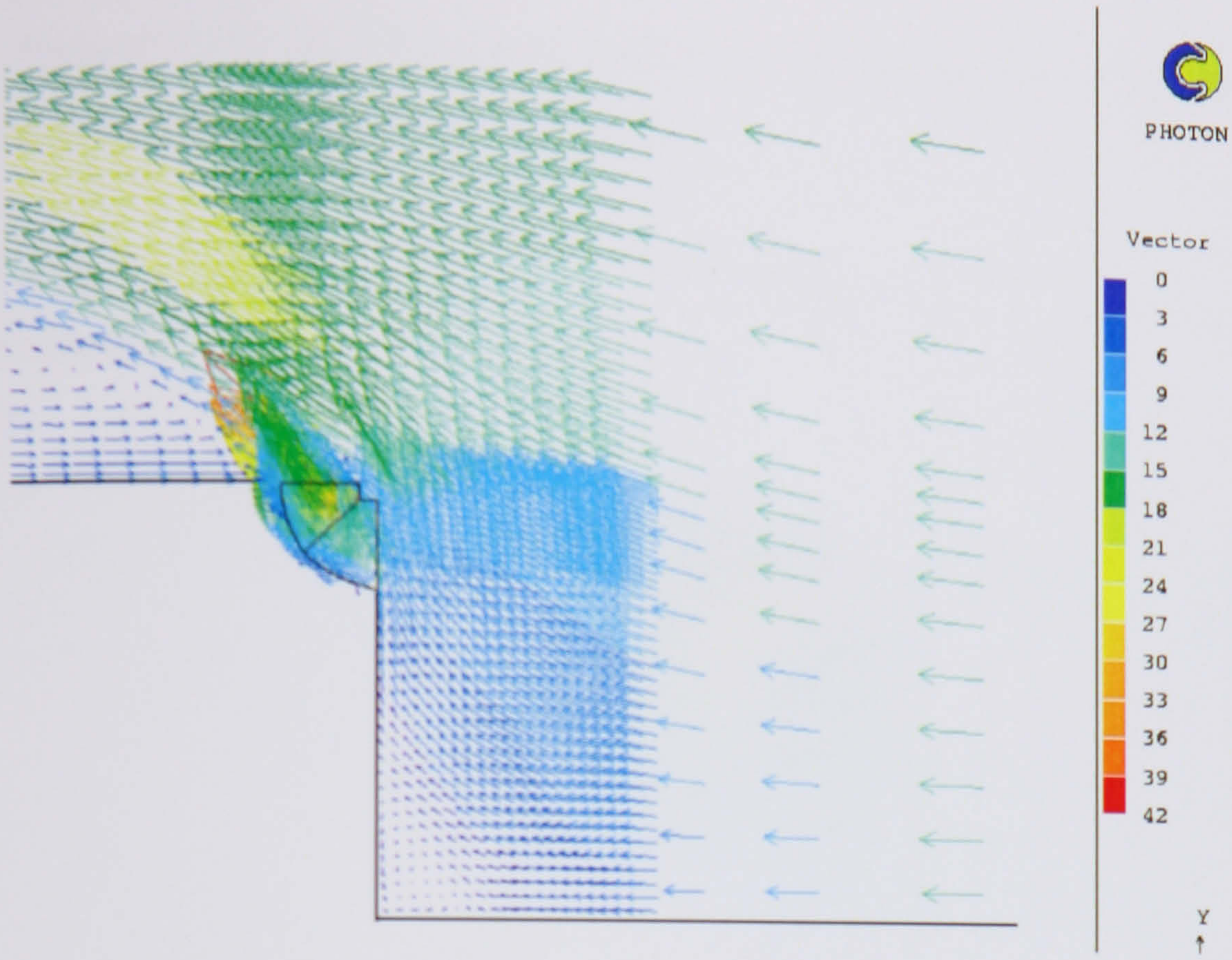

Figure 7.2.2.5: Approaching flow, plane of symmetry

The flow field in the duct (Figure 7.2.2.6) shows flow separation at the inlet, but to less extent than in two dimensional modelling. The non-dimensionalised wall distance $Y^+ = 247$ was recorded at the first cell at the inlet wall, where the separation initialised. This value lays in the middle of the accepted range (see Chapter 5.6) to apply the wall function.

At the inner rectangular edge, the flow accelerates to more than twice the inlet velocity (Figure 7.2.2.6). This seems to be a sharp edge effect. It is very difficult to confirm this value experimentally (for comparison Figure 7.2.2.7). Measurement of the speed near this location produced very unsteady values. Also, with the need for a safety clearance between probe and wall it was not possible to measure velocities in exactly the right place.

The flow entrainment at the outlet into the surrounding flowfield is influenced by the separation of the external flow at the leading edge of the building (Figure 7.2.2.6). Immediately between leading edge and duct outlet, there is a region of decelerated flow, in the wake of the separation at the edge.

Comparing the measured and the simulated profiles of the wind speed ratio in the duct (Figures 7.2.2.7 and 7.2.2.9), there is good agreement. One has to remember that the model duct in the wind tunnel was equipped with a smoothly curved inlet (see Figures 4.2.8 and 4.2.9). This is the reason for the smaller recirculation zone at the bottom of the duct compared with the simulation, and explains the deviation of the values in the lower 20 % of the duct (Figure 7.2.2.7). Also, because of the limited number of cells, it was not possible to model exactly the inflow of the experimental case.

Figure 7.2.2.6: Duct flow, plane of symmetry.

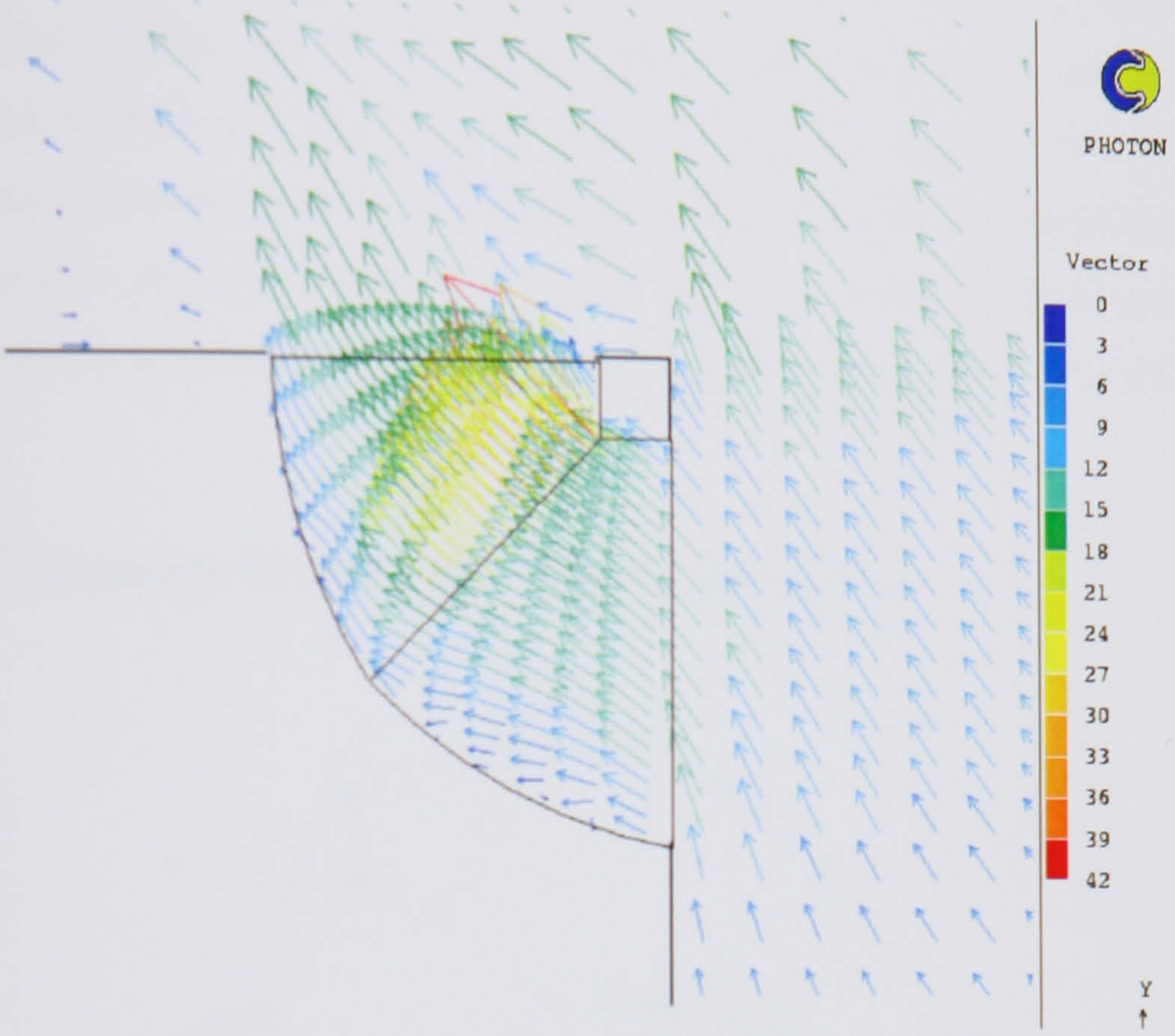

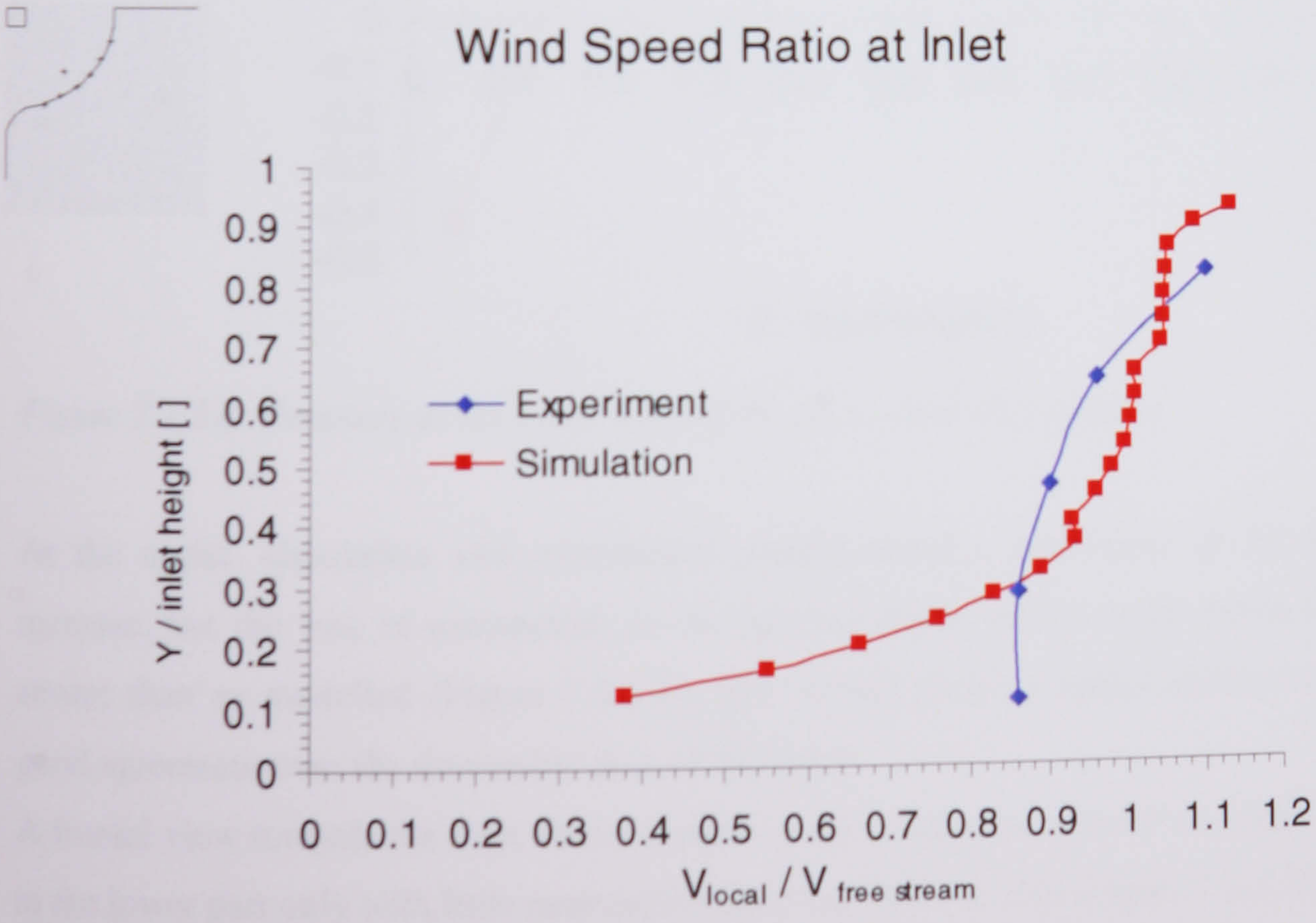

Figure 7.2.2.7: Vertical profile inside the duct (at plane shown in Figure 7.2.1.3), plane of symmetry

Both profiles in Figure 7.2.2.7 show accelerated flow towards the inner upper edge of the duct and values of similar magnitude.

The simulated flow separation at the inlet is accompanied by a pressure drop (Figure 7.2.2.8). Because of the curved inlet, the first pressure tapping is deeper inside the model duct (see Figure 4.2.9), and the pressure directly at the inlet could not be measured. But the experimental values suggest a smoother inflow. Half way through the duct, the simulated and the measured pressure value is about the same. In a curved duct it is generally difficult to estimate the flow field from the pressure field on the wall, as the flow might deflect into the tapping.

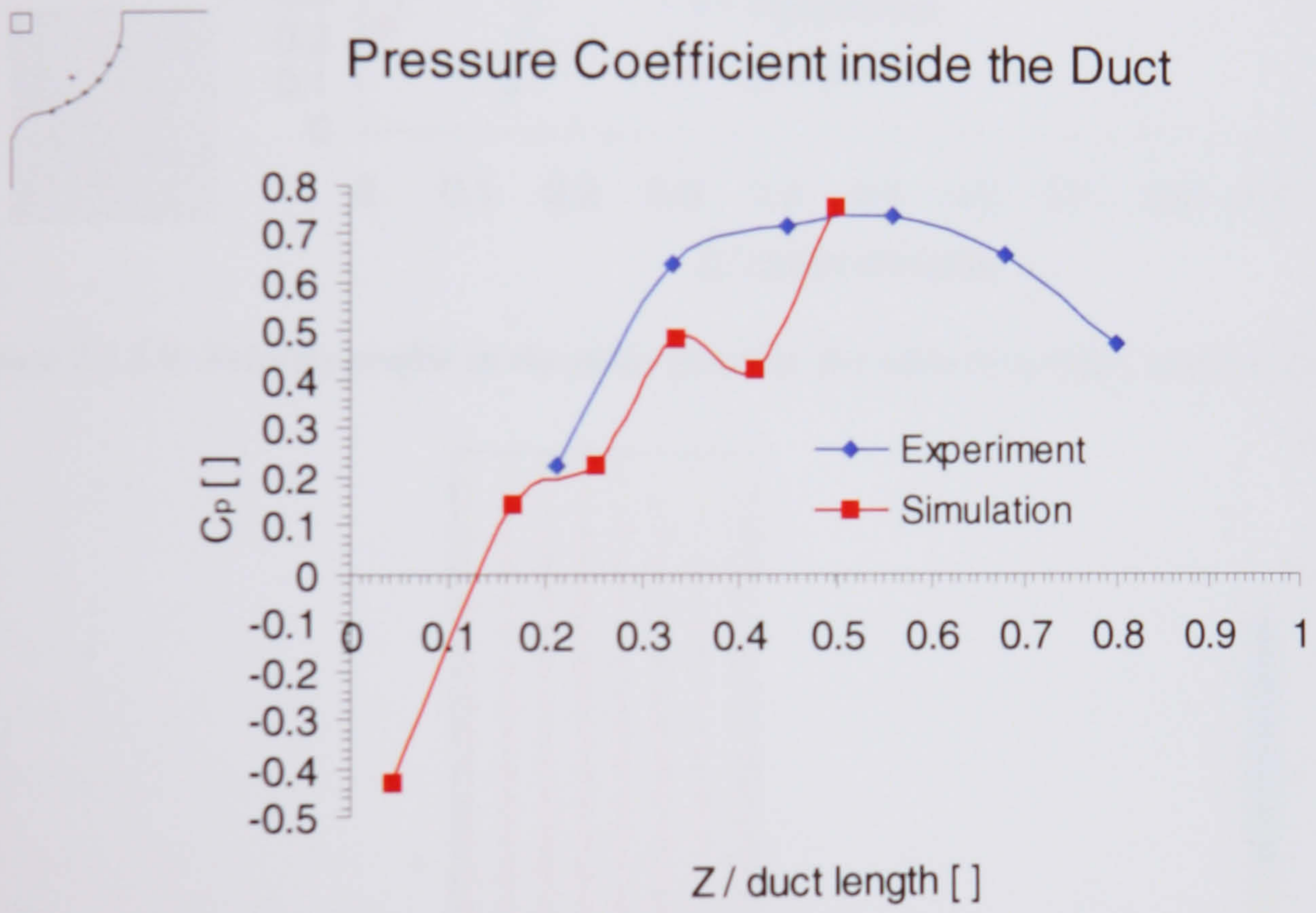

Figure 7.2.2.8: Pressure at the outer wall of the duct, plane of symmetry

At the outlet, simulation and experiment predict about a maximum 15 % wind speed increase, but the loss of momentum in the upwind region of the outlet seems to be more severe than as modelled (Figure 7.2.2.9). But overall there is sound agreement, and very good agreement over the downwind part of the outlet.

A frontal view towards the inlet shows a small swirl component towards the symmetry plane, in the lower part only with little momentum entering from the side (Figure 7.2.2.10).

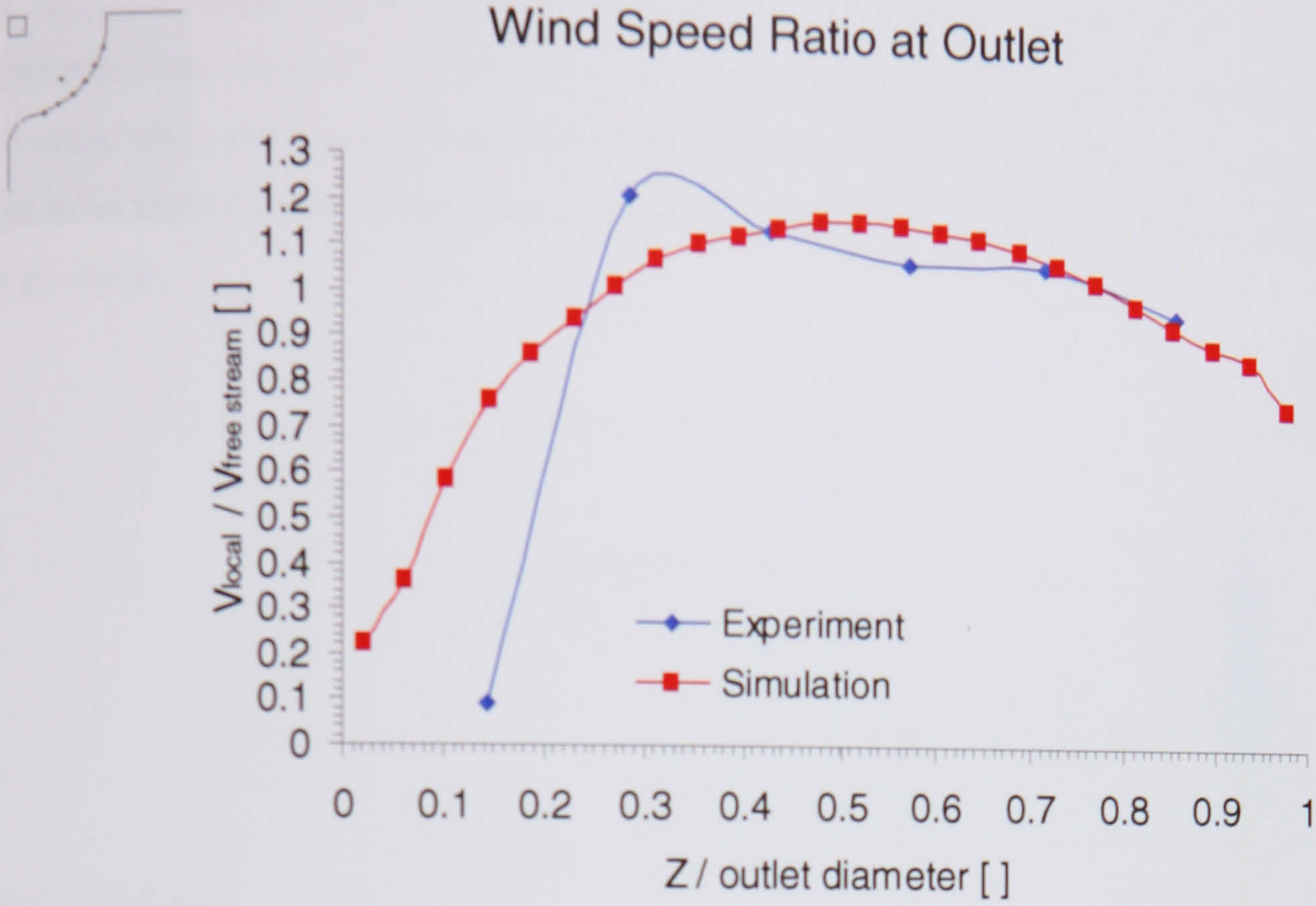

Figure 7.2.2.9: Velocity profile in the outlet opening (location of turbine), plane of symmetry

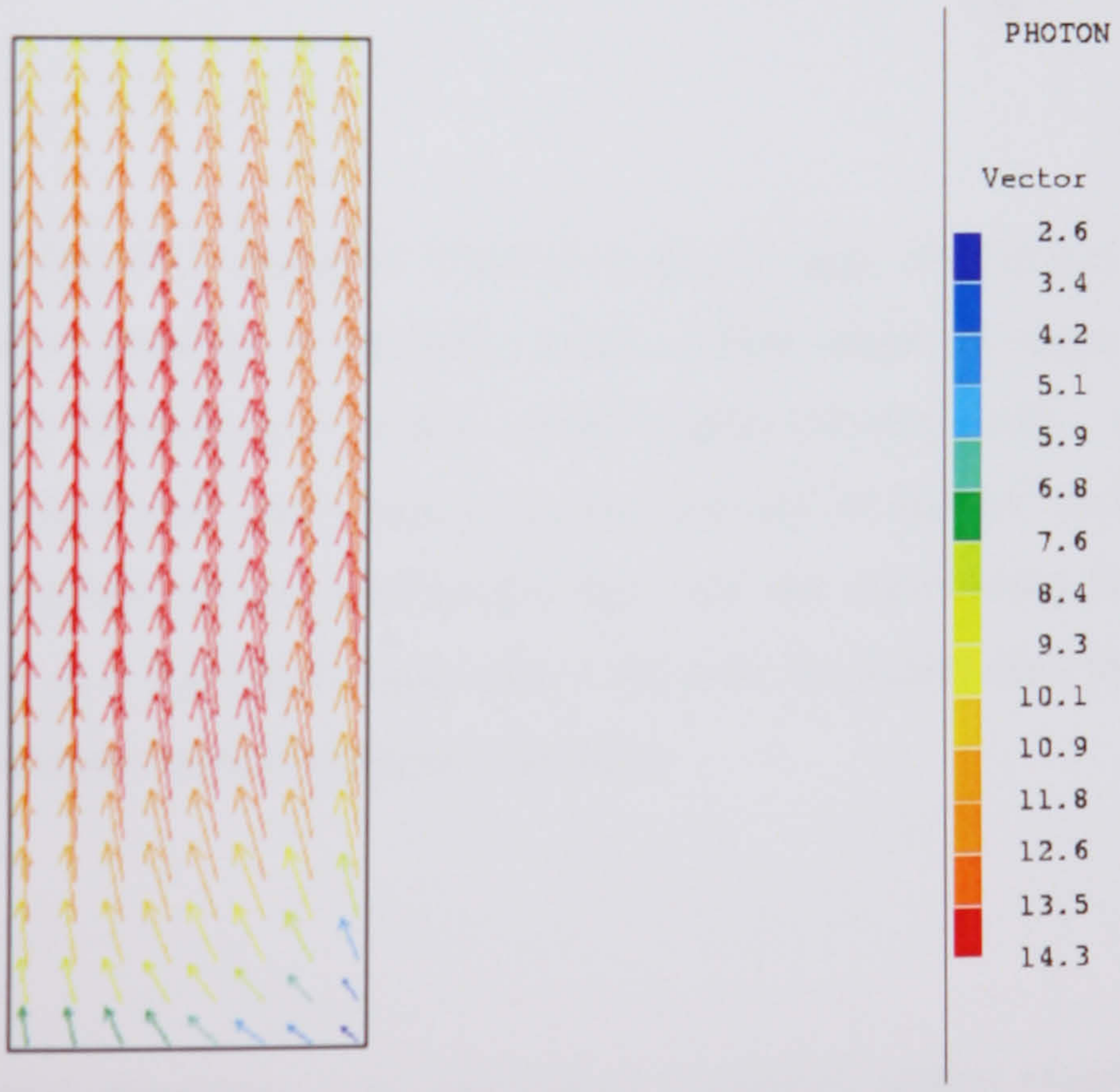

Figure 7.2.2.10: Frontal view of flow field entering the duct (symmetrical half)

This swirl seems to be carried downstream and supports recirculation left (and right) of the symmetry plane over the outlet at the flat roof (Figure 7.2.2.11). The view above (see Figure 7.2.2.1) shows that the entraining flow mainly interacts with the reverse flow over the roof, caused by flow separation at the leading edge. As previously mentioned, the recirculation over the roof might be overpredicted. Here, the entrainment breaks down the main recirculation over the roof only locally. There is no impact on the far neighbourhood of the duct outlet along the leading edge for wind normal to the façade. Closely spaced outlets might be in the influence of the generated swirl in the horizontal plane starting immediately over the outlet.

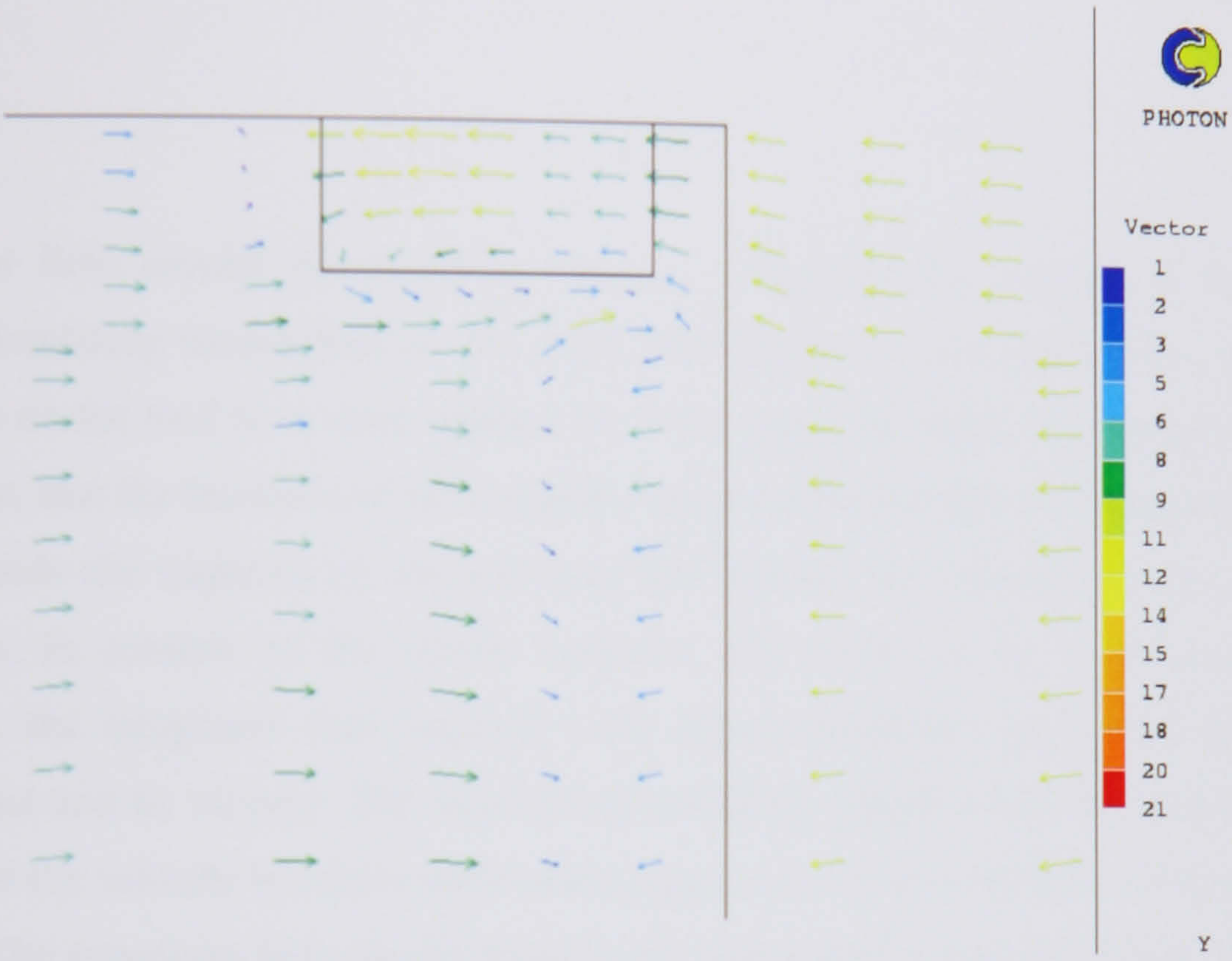

Figure 7.2.2.11: View from the top on the roof corner with outlet

It might be interesting to speculate on a situation of inflow under an angle of incidence of perhaps 45°. (As the simulation assumes a symmetry plane, inflow under an angle of incidence can not be simulated. Modelling the whole would require too many cells - see Chapter 6). In this situation, a horizontal vortex runs along the front part of the roof. As the simulation shows that the interaction of the entrainment flow and the recirculating flow generates swirl around the duct in a horizontal plane above the roof, the exiting duct flow may feed into the vortex and maintain suction along the roof edge.

Accuracy:

The presented three dimensional simulation with body-fitted coordinate system required around 15000 sweeps to converge, which took around 6 weeks on a Pentium 3 processor. Similar convergence criteria applied as in the cartesian cases of Chapter 6. Convergence was confirmed when the residuals for each of the variables reached values of around 20. Hence, the average drop for the residuals was 5 to 6 orders of magnitude. Global mass flow conservation was confirmed in the result files at the inflow and outflow boundaries.

7.2.3. Conclusions

The simulated flow field around the building seems to overpredict the strength of flow separation, the recirculating momentum in the wake and the size of the wake. Also, the pressure coefficient on the roof is in most regions out of the expected range. The reason for this failure is simple, that the numbers of cells required to model the building with integrated duct in detail exceeds the capacity of the software and extends the required runtime to unacceptable limits. In contrast to the simple cartesian grid model of the wind around rectangular shapes, the integrated duct requires body fitted coordinates and a fine grid resolution in the duct and its vicinity. The body fitted coordinate system solves not only the three components of the velocity but three additional components of the co-located velocities (see Chapter 5.3). The transition from the fine grid to the coarse grid is here too abrupt, and the far field is modelled too coarsely.

Around the leading edge in vicinity of the duct, pressure coefficients on the roof and on the façade wall do not agree with experimental values, however the internal flow field through the building integrated duct agrees well with the experimental measurements. Hence, under the given limitations this simulation does not confirm the relation between the differential pressure and the induced wind speed. However, the vectorflow patterns show the impact of different geometrical zones on the flow field. It seems that the flow inside the duct is accelerated by a similar magnitude as the flow around the roof edge. Compared with the free stream wind speed at building height, this is around 15 %. However, the wind acceleration around the leading edge of a building may exceed this magnitude (see Chapter 2).

The three dimensional simulation shows the importance of a smoothly curved inlet to the duct, although without it the flow separation predicted inside the duct is less severe than in the two dimensional simulation.

The duct flow entrains into the separated flow around the roof edge and joins the main stream over the roof without reattaching. It seems that the more or less vertical jet stream out of the duct even deviates the flow around the roof edge further upwards. As the flow is modelled as incompressible, this deviation does not cause a loss in momentum.

Closer views at inlet and outlet show the lateral flow. The simulation shows at the bottom of the duct some inflow from the side, and over the outlet a recirculation where reversing flow from the roof wake meets with the entraining flow, which deviates laterally.

There is no evidence that the interaction of the ductflow with the surrounding flow might restrict the induced speed or massflow through the duct. However, there is no simple relation between the pressure difference across the ends of the duct and the massflow. The pressure boundary conditions of the duct flow are quite complex, in particular as the zones of inflow and outflow are not really isolated. In the two dimensional simulation it was observed that, for each configuration, the overall positive pressure on the front façade and the overall suction on the whole roof declined markedly compared with the simulation with 'closed' duct (solid wall functions at inlet and outlet, see Chapter 6.2.2). In the three dimensional simulation, this effect was not so severe.

Certainly, a significant amount of kinetic energy is dissipated in turbulence, inside and outside the duct. But it can be concluded that a well designed duct might induce air speeds at the outlet up to 20 % higher than the undisturbed free stream velocity at roof height, for wind approaching normal to the facade. A spoiler over the inlet might have a positive effect to guide the upflow into the inlet and widen the zone of flow separation at the leading edge over the roof.

So it might be that a streamline shaped duct induces speeds which correspond to the average pressure difference in the wider flow field between the connecting zones according to basic fluid mechanics. For example, for stagnation pressure at the duct entrance on the front façade and a suction over the roof corresponding to $C_p = -0.5$ (see experimental values in Chapter 4 and comparison in Figures 7.2.2.2 and 7.2.2.3), the induced speed would be 22 % higher. This corresponds roughly with the experimental results in Chapter 4 and the findings of this simulation.

The simulated results of the duct flow are encouraging, but they have limitations for performance speculation and power output prediction (see Chapter 8). In particular for the latter, no flow resistance in the duct representing a turbine was modelled. This would have changed the flow pattern and pressure fields. Similarly, the experiments were performed without any inserted grid in the duct to mimic the effect of a turbine.

7.3. Flow Field Mapping as a Coupled Two and Three Dimensional Simulation

Modelling of the flow field over the roof for the building with an integrated duct faces the constraint of the limited number of cells permissible in the flow domain. In three dimensions, the grid refinement in and around the duct requires a vast amount of cells, which prevents good resolution in other parts of the flow field. The presented approach was born out of the situation 1998/1999 (Dannecker 1999), when no facility was available at the Department to solve the three dimensional model with integrated duct in sufficient detail.

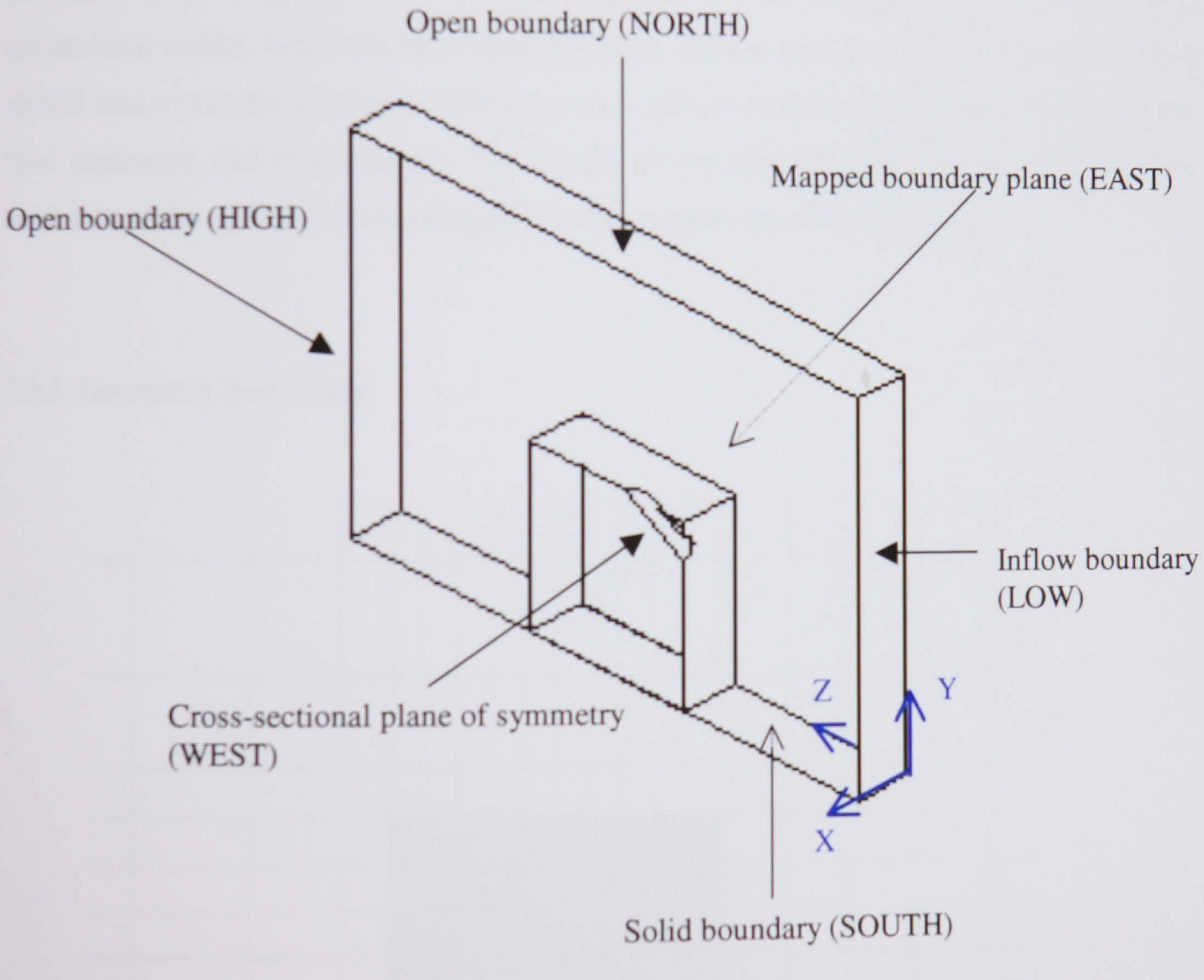

Figure 7.3.1: Convention of coordinates and planes, schematic drawing

Hence, this attempt deals with the solution in two steps:

1. The flow field around the building without integrated duct is solved in a coarse cartesian grid in three dimensions. The boundaries of the flow domain are (apart from solid walls) either the symmetry plane or the open flow condition. From this solution, the field at a cross-sectional plane a few meters to one side of the suggested duct is stored.

2. A second body fitted grid is generated, with the integrated duct and necessary grid refinement and linked domains. This model is basically a thick slice at the symmetry plane, just wide enough to include the integrated duct at the plane of symmetry plus a few meters to one side of the integrated duct. The boundaries right and left are either the symmetry plane (WEST-plane) or on the opposite side (EAST-plane) the stored cross-sectional plane from the first simulation (see convention Figure 7.3.1).

The aim of this procedure is to provide a distribution of momentum in the flow field around the house with integrated duct, which corresponds to the momentum field in the three dimensional model, where the flow actually passes around the house. This adapted flow field should lead to similar pressure coefficients as in the three dimensional model, and to similar flow separation and reattachment. The impact of the integrated duct in this adapting flow field around the duct will be investigated in the second step of the simulation.

7.3.1. Geometry and Grids

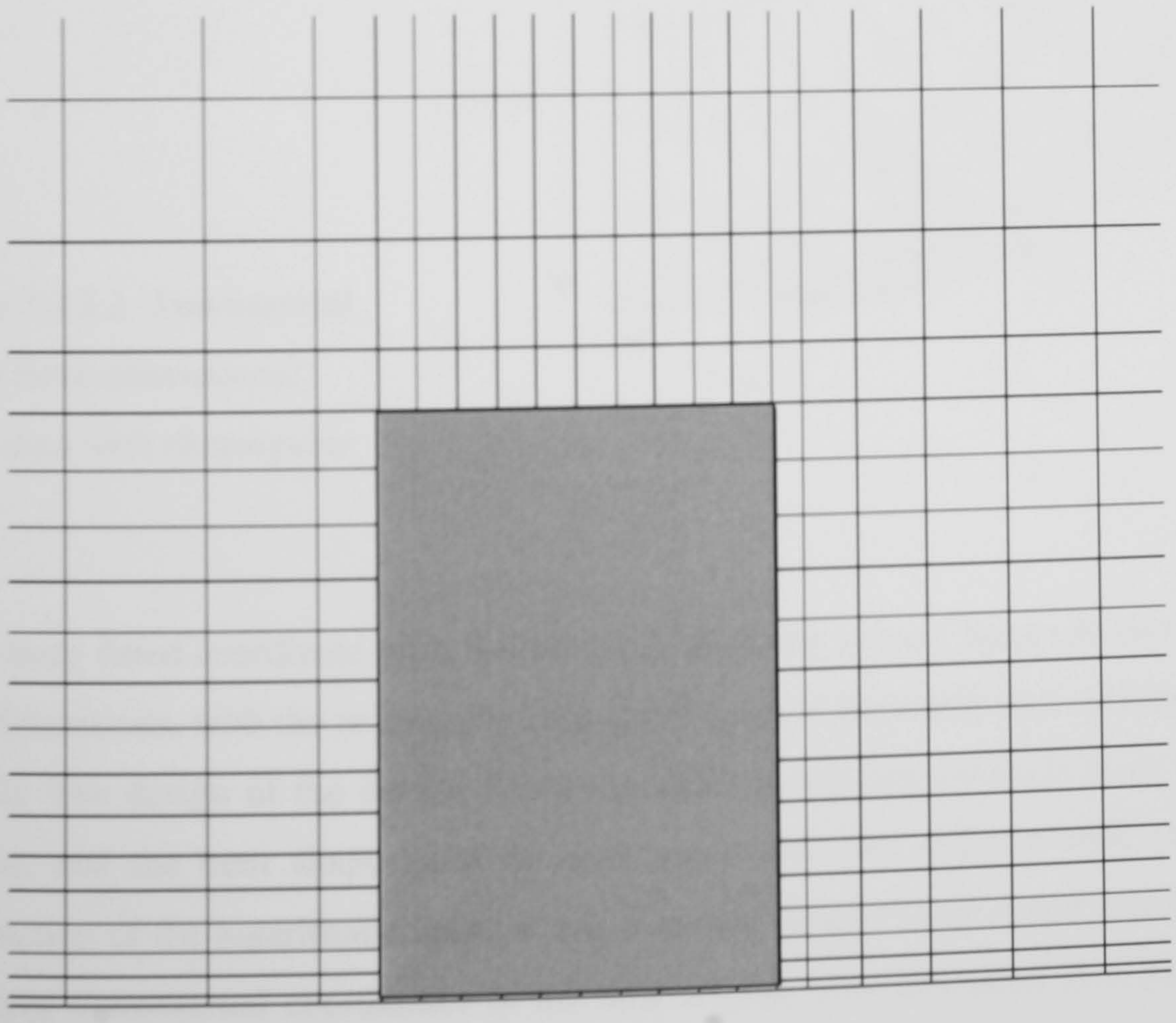

Figure 7.3.1.1: Coarse cartesian grid around the building

In a cartesian grid, the building block was modelled as 30 m high, 20 m deep and 20 m wide overall. Only one symmetrical half was modelled. Upstream and to the sides there is 160 m free flow domain, downstream from the obstacle 500 m, and above 320 m. It is basically the same block model with the coarse grid approach, as described in Chapter 6. The only difference is, that the width of the block is only 20 m instead of 35 m, and therefore there are 5 cells missing in the x-direction compared to the previous model. The number of cells is 32 x 37 x 62, and the solution reaches convergence with 5000 sweeps after around 12 hours.

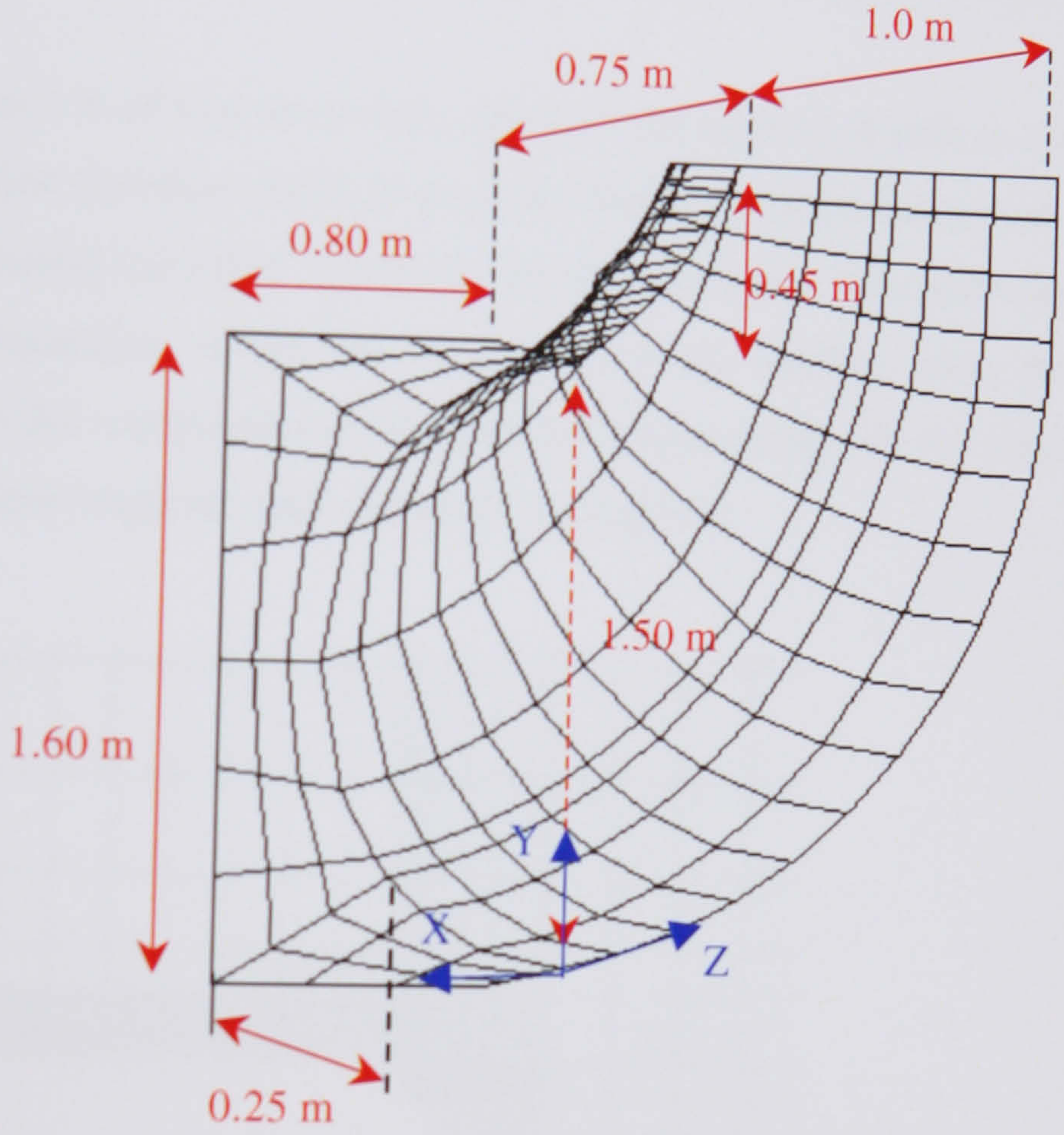

Figure 7.3.1.2: Symmetrical half of three dimensional round duct with rectangular inlet

In the body fitted coordinate grid, the duct configuration 1 (see Chapter 6) was modelled in three dimensions, with the rectangular inlet converging to the round duct opening (see Figure 7.3.1.2). The design of the duct is based on ratios of tapering common in air conditioning systems, and the bent shape itself is constructed with two different radii similar to the construction of the logarithmic spiral of the inlet to a turbine blade runner (see Chapter 2.8). The three dimensional coordinates of the duct section were generated by a small program, which calculated the coordinates with the help of trigonometry from input parameters (like opening size, degree of bending and taper for the sections).

The whole flow domain is linked together with 16 domains of different grid density, to resolve the flowfield in the duct, at the inlet and at the entrainment above the roof. Overall, the model has 9 x 240 x 40 cells. As explained in Chapter 6.1.2, the large number of cells in the y-direction arises because of stacking of the domains in the y-direction in the computational space (F-array). But the model consists of only 9 cells in the x-direction, and it is only 5.80 m wide. It is basically a thick slice next to the plane of symmetry, comprising the symmetrical half of the 1.60 m wide duct plus 5 m width of the building (see Figure 7.3.1).

The runtime to reach convergence is around one week, although the number of cells is not significantly larger than in the first cartesian stage. In the body fitted coordinate system with many linked domains, the collocated velocities are solved for each direction. This increases the number of variables and equations, which has its impact on the runtime. Also, the mapping procedure slows down the computational time for one single sweep. On the other hand, it might be that the flow field mapping leads to earlier convergence.

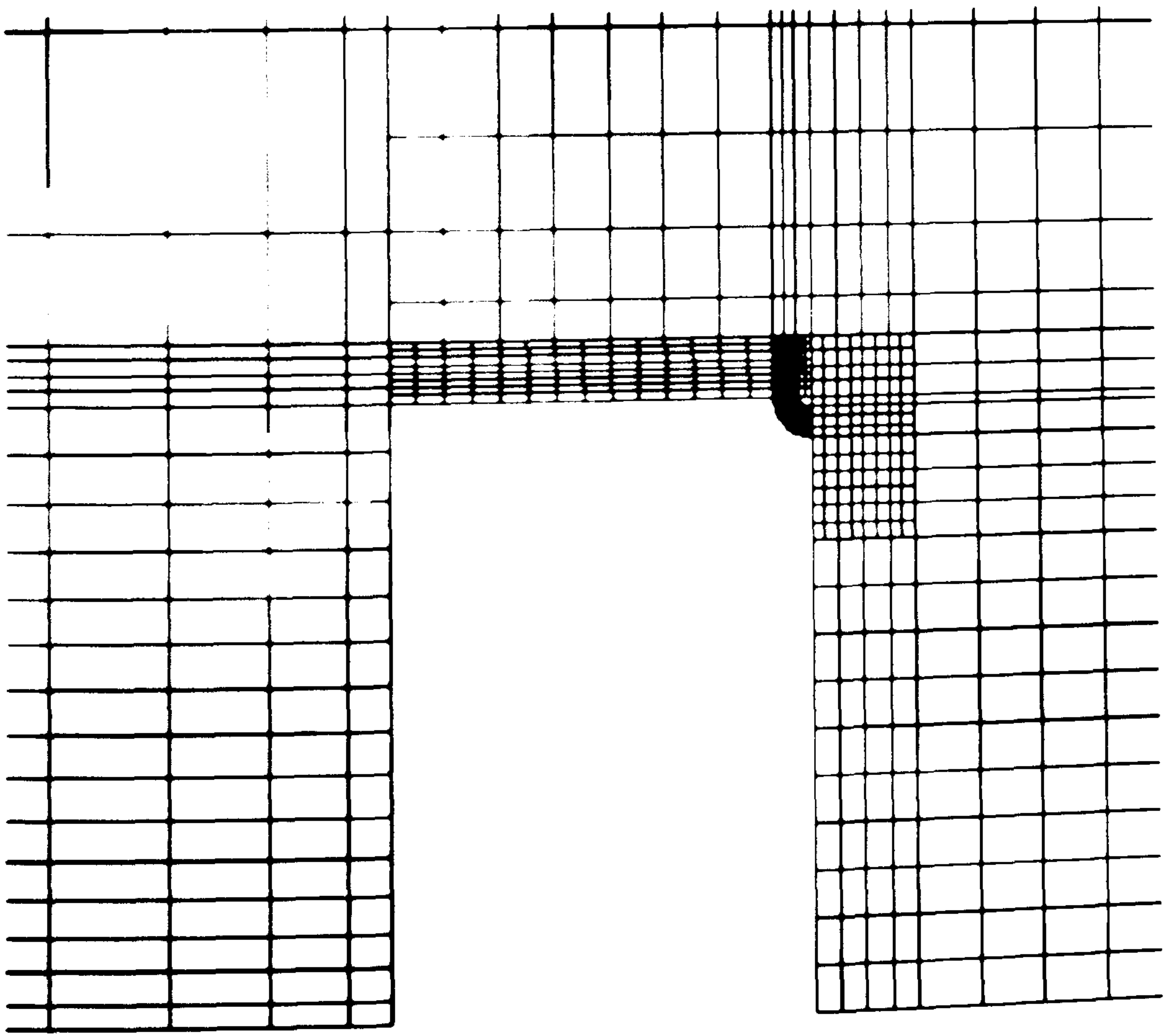

Figure 7.3.1.3: Grid refinement by linked domains in the body fitted coordinate system.

7.3.2. The Computational Procedure

The software package PHOENICS 2.2.1 comprises the common GROUND file, which is specially designed to enable the user to apply features to the solver. The file is divided into sections, which are addressed according to the sequence of the solver. Here, it is possible to intervene (PHOENICS 2.2.1). As described in Chapter 6.1.2, all variables and parameters attached to the single cell are stored in the one dimensional F-array. In order to gain access to a specific value, the zero location index number is required, which is the entry number in the one dimensional array for this specific value for the very first cell. To address the corresponding value of the other cells, an addressing function is used to calculate the change in the entries in the one dimensional F-array. This addressing function depends solely on the index numbers of the cell in question.

As mentioned above, the procedure consists of two stages:

First stage in GROUND file of coarse cartesian grid simulation:

Gaining the solution in the specific cross-sectional plane IX = k of the three dimensional coarse simulation:

At the end of the last sweep

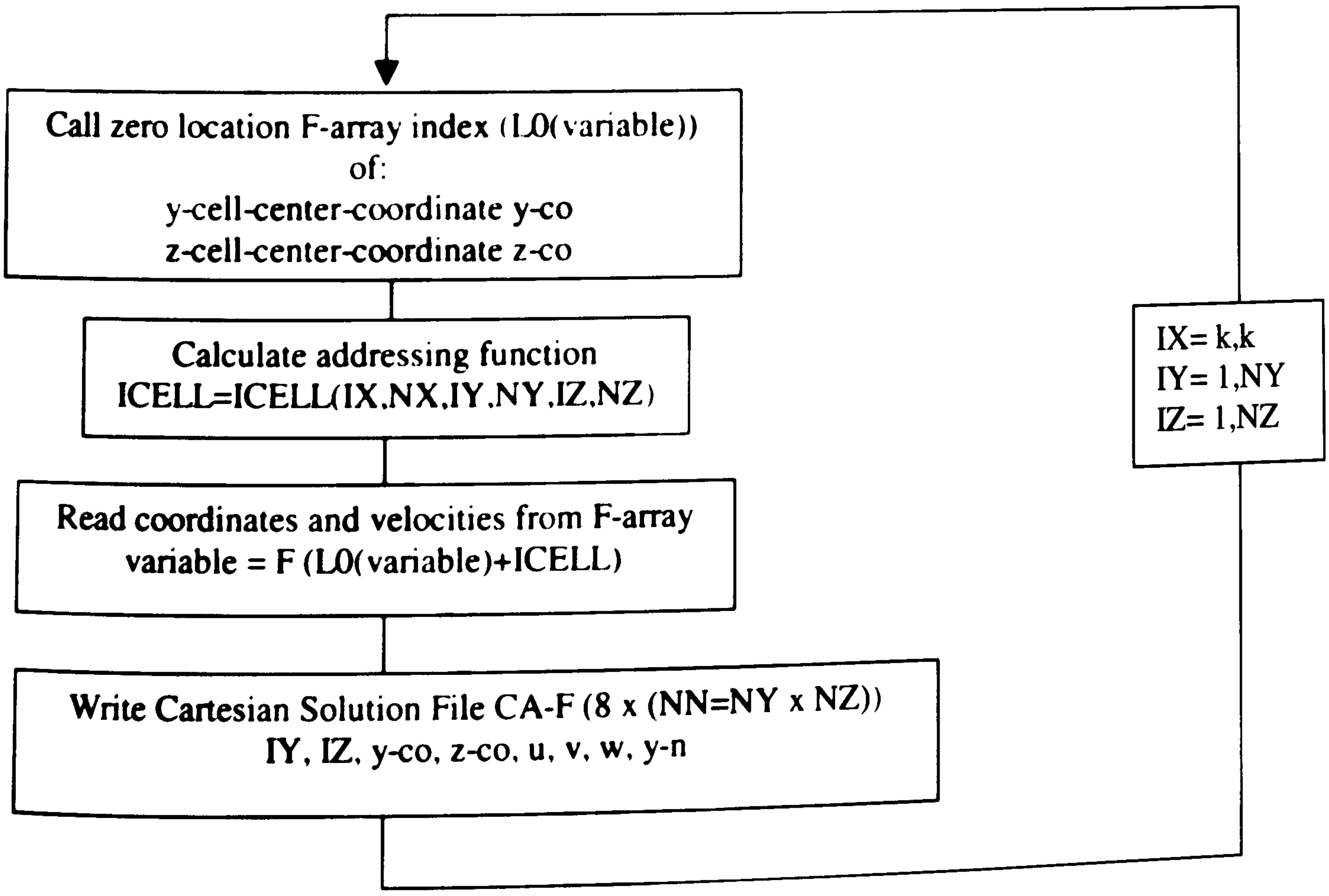

Second stage in GROUND file of refined body fitted coordinate grid simulation:

Mapping the coarse grid cartesian solution as a boundary to the refined grid simulation. In order to achieve this, the geometrical coordinates and the corresponding cell indices of the EAST boundary cells of the body fitted grid have to be accessed. The refined grid simulation comprises 16 linked domains, stacked in the y-direction. Each domain is scaled to its own body fitted coordinate system. The following flowchart describes the procedure, and how to access the cell corner coordinates of the EAST boundary of each specific domain. In sequence this procedure has to follow on for all domains which have the EAST boundary and are therefore subject to the mapping procedure. For example, the duct itself, the inlet of the duct and the fine grid zones over the building do not comprise the EAST boundary and are therefore not subject to this routine. The aim of this procedure is to populate a two dimensional array FIELD (N,4), which comprises for each of the N EAST-boundary layer cells their geometrical y,z cell-center coordinates and their corresponding cell indices IY,IZ.

At the start of the first sweep:
for all domains ii in sequence:

Indices:

IX : 1 always (EAST boundary)

IY : IY-first, IY-last of current domain ii

IZ : 1, IZ-last of current domain ii

J : Number of cells in the EAST boundary plane of current domain ii

J_D : Total number of cells in the boundary layer of the previous domains in the sequence of this routine, 1+.....+ii-1

N: Total number of cells of the EAST-boundary of the whole flow domain, N=NY x NZ

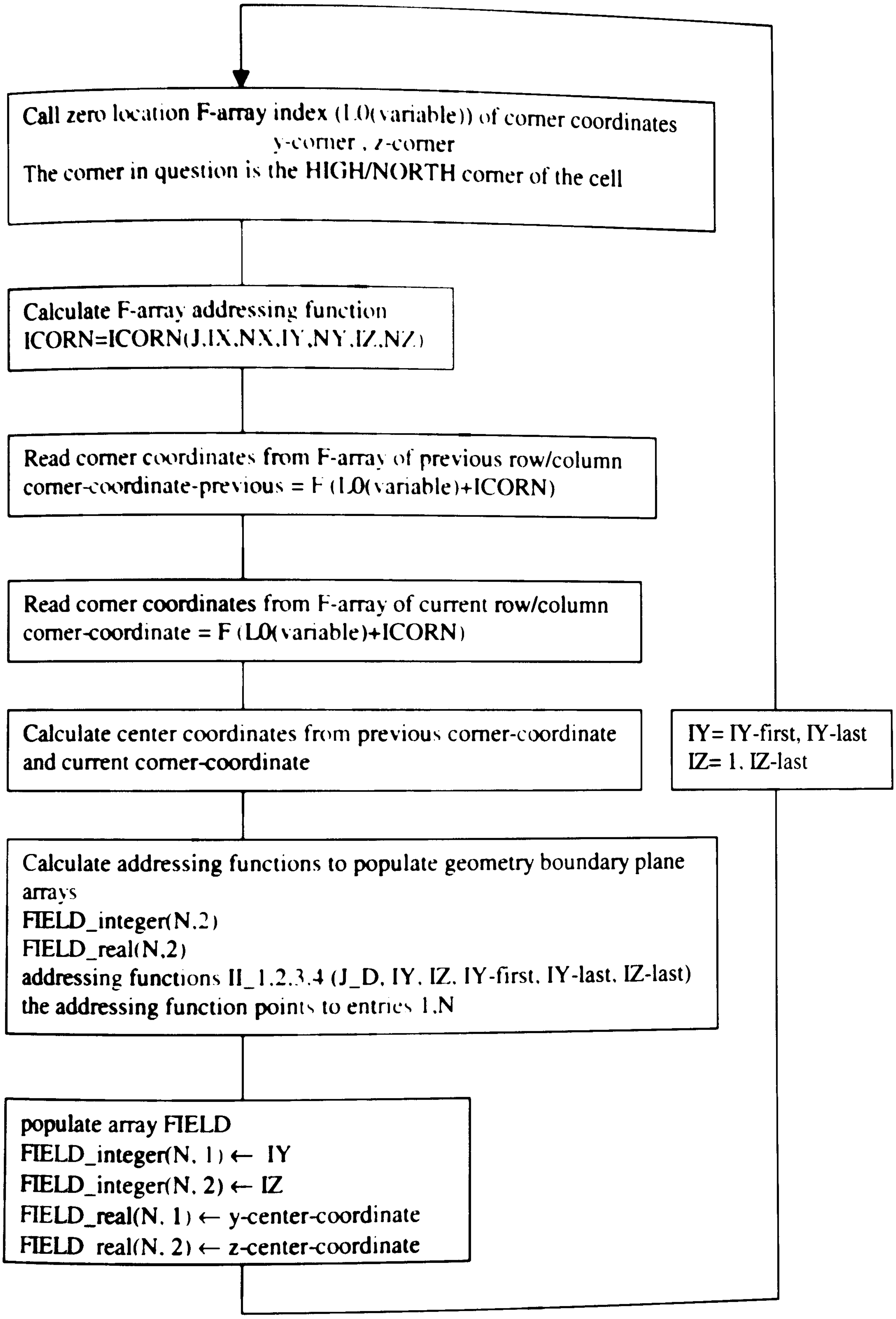

Call zero location F-array index (L0(variable)) of corner coordinates
y-corner , z-corner
The corner in question is the HIGH/NORTH corner of the cell

Calculate F-array addressing function
ICORN=ICORN(J,IX,NX,IY,NY,IZ,NZ)

Read corner coordinates from F-array of previous row/column
corner-coordinate-previous = F (L0(variable)+ICORN)

Read corner coordinates from F-array of current row/column
corner-coordinate = F (L0(variable)+ICORN)

Calculate center coordinates from previous corner-coordinate and current corner-coordinate

IY= IY-first, IY-last
IZ= 1, IZ-last

Calculate addressing functions to populate geometry boundary plane arrays
FIELD_integer(N,2)
FIELD_real(N,2)
addressing functions II_1,2,3,4 (J_D, IY, IZ, IY-first, IY-last, IZ-last)
the addressing function points to entries 1,N

populate array FIELD
FIELD_integer(N, 1) ← IY
FIELD_integer(N, 2) ← IZ
FIELD_real(N, 1) ← y-center-coordinate
FIELD_real(N, 2) ← z-center-coordinate

A corresponding two dimensional array CA_FIELD is populated with the stored values of the cartesian solution file CA-F, which was generated previously as first stage in the cartesian coarse grid simulation:

CA_FIELD_integer(NN,1) ← IY

CA_FIELD_integer(NN,2) ← IZ

CA_FIELD_real(NN,1) ← y-cell-center-coordinate

CA_FIELD_real(NN,2) ← z-cell-center-coordinate

CA_FIELD_real(NN,3) ← u

CA_FIELD_real(NN,4) ← v

CA_FIELD_real(NN,5) ← w

CA_FIELD_real(NN,6) ← y-cell-north-wall-coordinate

The next step is a sorting routine, which incorporates both arrays FIELD and CA_FIELD.
Scanning procedure:

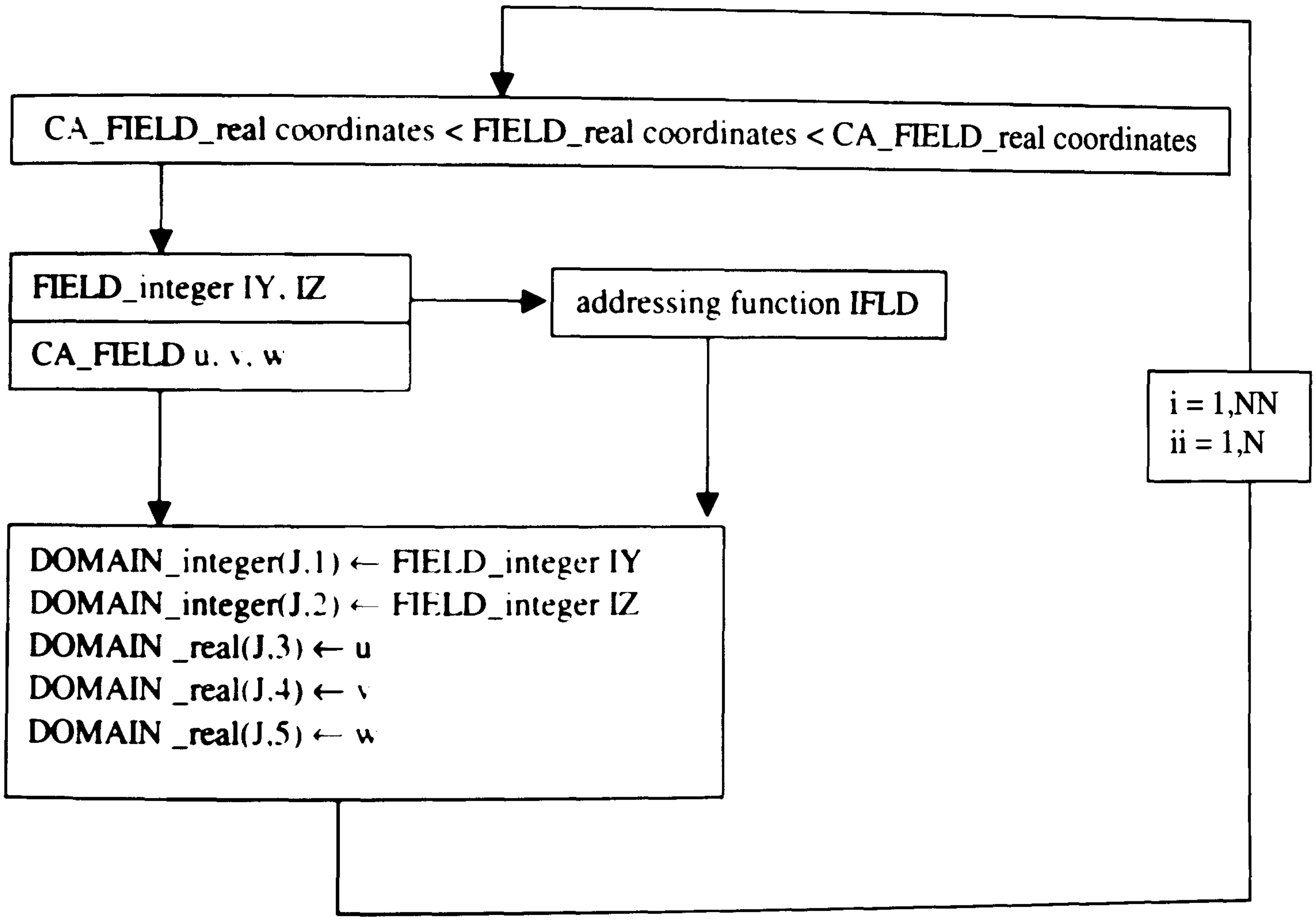

The y-center-coordinate and the z-center-coordinate of the array FIELD are compared with the coordinates of CA_FIELD. It is a scanning process of the geometrical coordinates of both different grids in order to sort out the best match (see following flowchart). If the bfc (body-fitted-coordinate) cell matches to a cartesian cell, the corresponding bfc-cell index IY,IZ from the FIELD_integer array and the corresponding velocity values u, v, w from

CA_FIELD_real array are used to populate a set of new two dimensional arrays, the DOMAIN_arrays. In order to populate the new arrays, an addressing function is calculated : IFLD(IY,IZ,IZ-last,IY-last, IY-first). The addressing function points to the entries 1 to J, where J is the number of cells at its EAST boundary of the current domain in question. For each domain which comprises an EAST-boundary, a DOMAIN_array is populated.
Hence, each DOMAIN_array comprises the complete information to provide the domain in question with boundary conditions. The DOMAIN_arrays are populated at the start of the first sweep. For the following sweeps, they are addressed in sequence.

The mapping itself actually takes place in another section of the GROUND file, which is dedicated to provide boundaries and special sources. Here, the EAST boundary of each domain is provided with velocity values according to the corresponding DOMAIN_array.
As described in Chapter 5, the boundary condition is modelled as a fixed flux. As an alternative it would be possible to fix the values in the cells. The latter approach causes difficulties of convergence, in particular the residual error does not decline. But in both approaches, the boundary conditions are fixed with a certain stiffness coefficient (see Chapter 5), which provides some flexibility.
The use of the arrays facilitates the structure of the coding. It makes it possible to store the values which are accessed and sorted just once in the whole routine, at the beginning of the first sweep. The mapping itself takes place sweep by sweep.

Mapping routine:

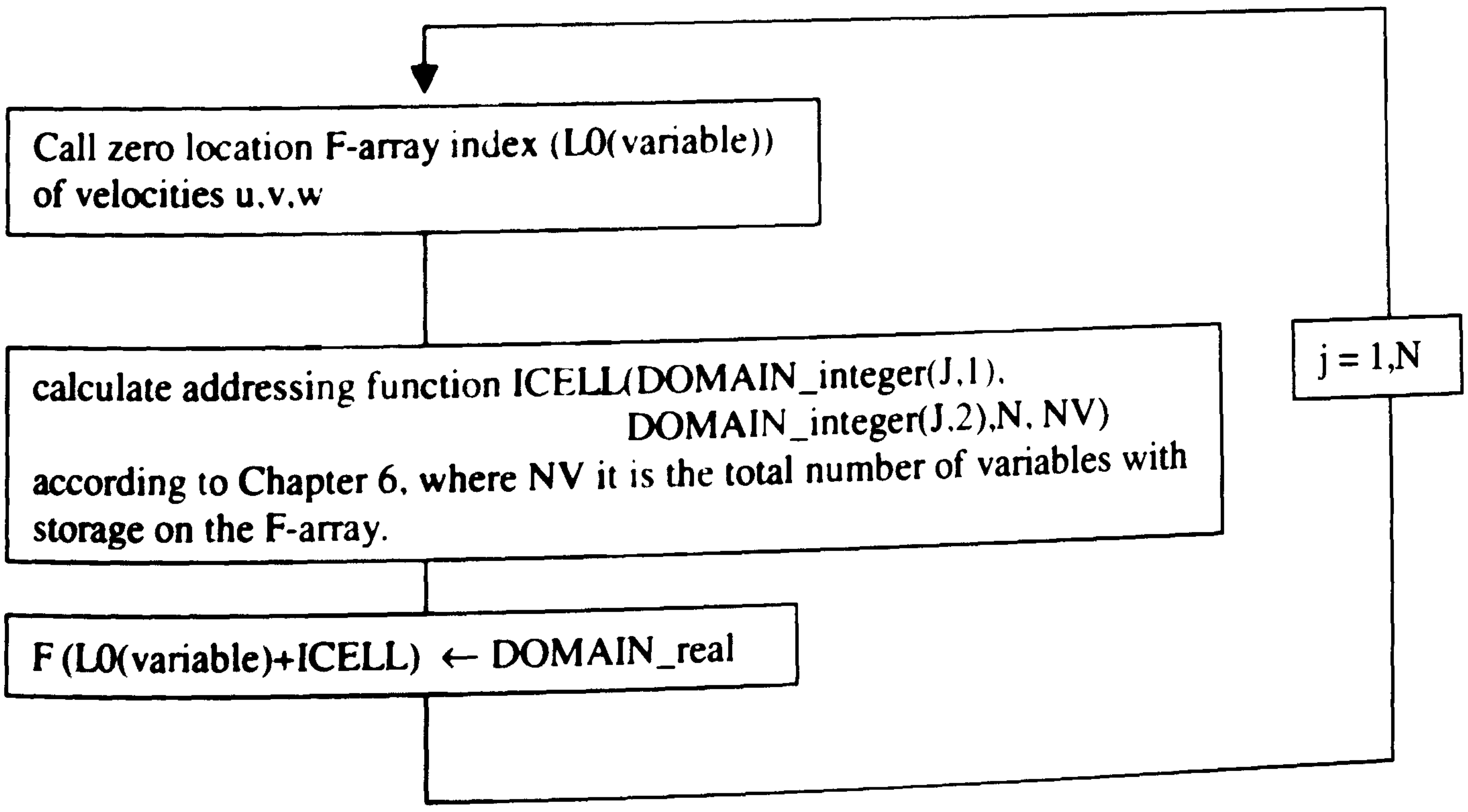

7.3.3. The Resulting Flow Field

For both simulations, the inflow profile was kept uniform, with a wind speed of 20 m/s and a homogeneous air density of 1.2255 kg/m^3. The inflow values of k and ε were calculated according to a turbulence intensity of 37 % at 10 m height and a variable turbulence length, with inner city parameters referring to ESDU (ESDU 1993).

The flow field solution for the cross-sectional plane of the coarse grid was mapped on the EAST boundary of the multi-domain refined grid with its body fitted coordinate system. A stable numerical solution was achieved by fixing the flux of the longitudinal velocity component w and the vertical component v. The flux of the lateral component u was set to zero. It was found in the flow field solution of the cross-sectional coarse grid plane, that the u-component was always so small, that its effect could be neglected. The u-component is the missing third component in the purely two dimensional simulation, but two and three dimensional solutions differ significantly. The cross-section of the three dimensional solution with neglected u-component approximates to the three dimensional solution in all three components. Therefore, this condition is seen as a simplification. The boundary conditions of the scalar variables pressure p, turbulence k and dissipation ε were set as 'open boundary' condition (see Chapters 5.7 and 6.1.1).

At the first stage, the simulation from the cartesian coarse grid shows that on approaching the obstacle, the uniform inflow profile changed and generated a shear layer. Hence, the reference velocity (22.3 m/s) to calculate the pressure coefficients was taken in the flow field upstream from the building at roof height. In this section, a shear layer is developed but the vertical and the lateral velocity component is still negligible small. Hence, it was suggested that 22.3 m/s is the reference velocity at building height in the undisturbed mean flow

The vector flow pattern over the roof in the cross-sectional plane, which is intended to provide the boundary for the mapping procedure, shows flow separation at the leading edge of the roof, but rapid reattachment and thereafter a smooth flow (Figure 7.3.3.1). Comparison with the coarse grid result from Chapter 6 (Figure 6.2.3.4) shows that the wider building does not generate such a smooth flow over the roof, having a higher tendency to separate and not to reattach. The two simulations differ solely in the width of the building.

Behind the building, there is no uprising flow as in the fine grid approach (Figure 6.2.3.3) or in the three dimensional model of the building with integrated duct (Figure 7.2.2.1). The recirculation length is only around 1.3 H. The flow accelerates around the leading edge, and slows down at the front façade.

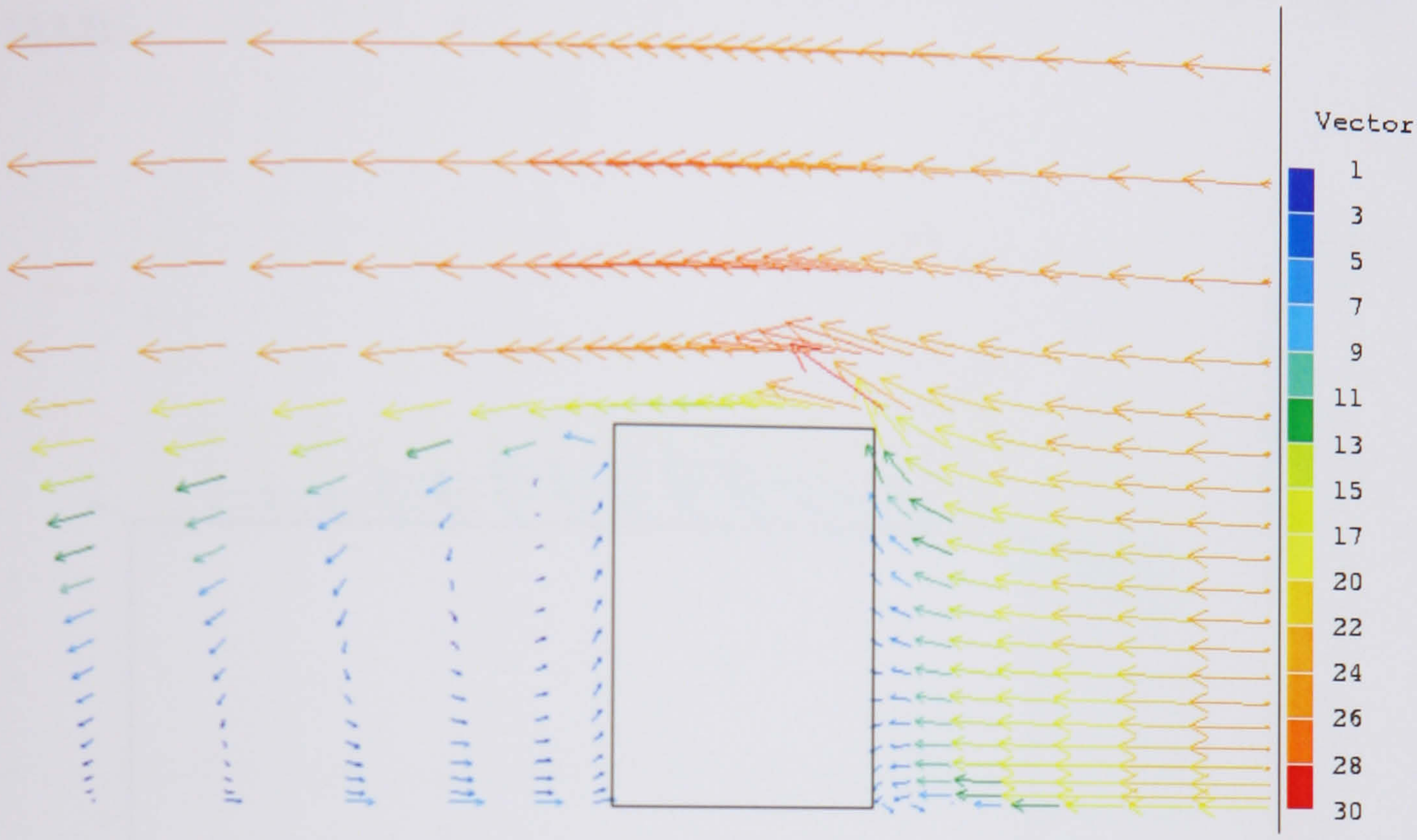

Figure 7.3.3.1: Cross-section of coarse cartesian grid simulation

All of the previous simulated results with the fine grid showed flow separation at the leading edge of the roof, without reattachment. The recirculating wake behind the building exceeded the building height and reattached in the far distance downstream. Also, the recirculation over the roof was very significant. In the previous three dimensional simulation with integrated duct, it became obvious that a constraint in the distribution of cells predicted recirculation behaviour over the roof, which is not compatible with the observed flow pattern in such a case.

Separation and recirculation at the leading edge become stronger with the width of the building. The two dimensional simulation (where the building width is infinite) led to results where separation and recirculation greatly exceeded any three dimensional results. The mapping of this three dimensional calculated field (Figure 7.3.3.1), with its very modest recirculation pattern, is intended to avoid the overpredicted recirculation of the model with integrated duct.

The refined grid in Figure 7.3.1.3 of the second stage, the simulation in the body fitted coordinate system, corresponds more to the refined grid in Chapter 6, which resulted in flow separation at the leading roof edge without reattachment. When the mapping procedure is applied, there is indeed a reduction of the separating flow field over the flat roof (Figure 7.3.3.2).

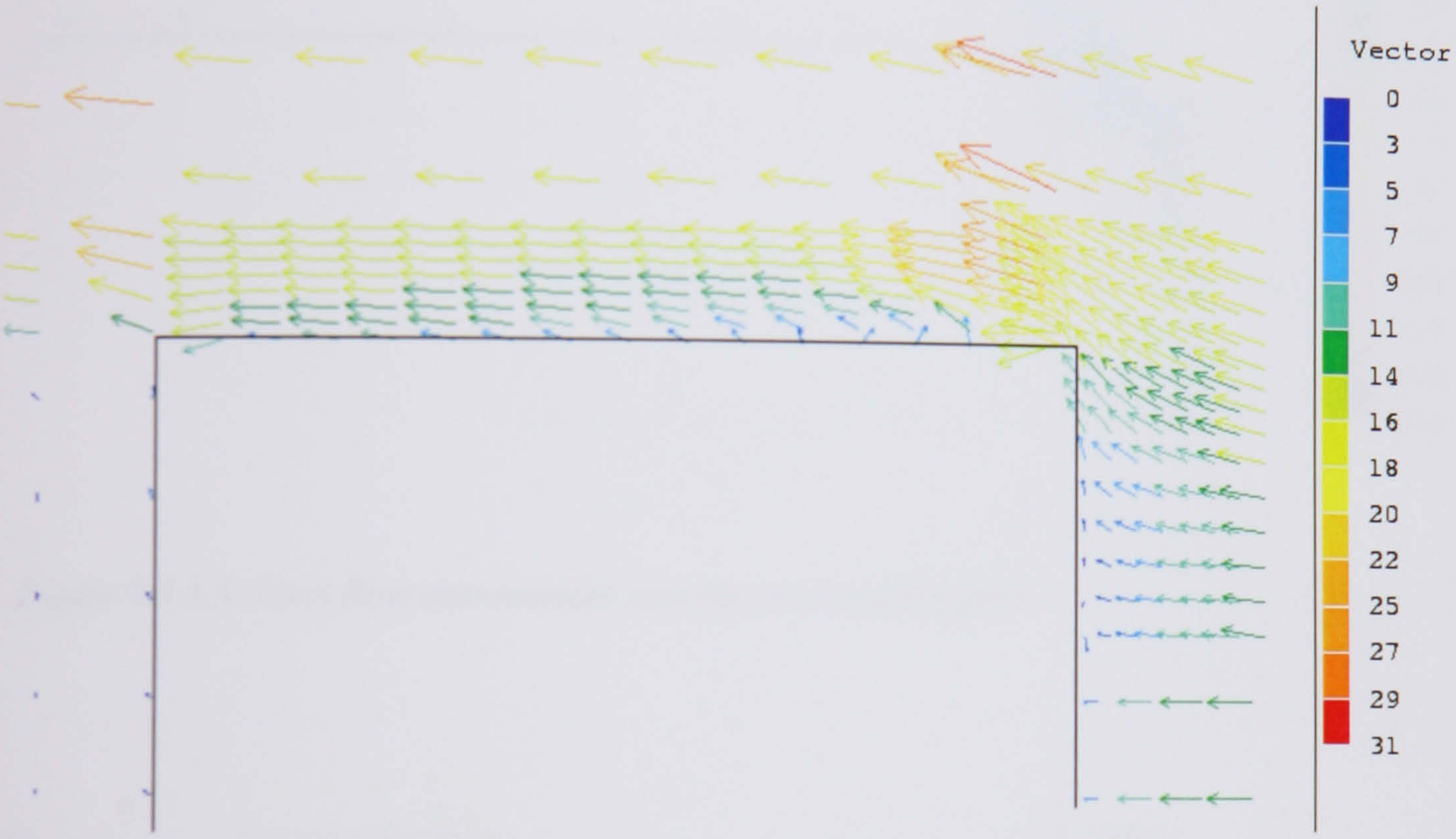

Figure 7.3.3.2: Flow over the roof and around the leading edge

It is interesting to observe the entrainment of the duct flow in the surrounding flow field (Figure 7.3.3.3). There is only a very localised high velocity region in and immediately above the outlet. The outflow generates downstream a small separation zone over the roof, but the flow reattaches after the first third of the roof and then remains smooth and slow moving. Further, the flow decelerates more uniformly upstream from the roof, corresponding to the mapped boundary field. In the surrounding flow, the vast vertical acceleration immediately above the duct is very likely a false prediction (Figure 7.3.3.3) in a few cells. However, the general flow pattern of the surrounding flowfield is encouraging.

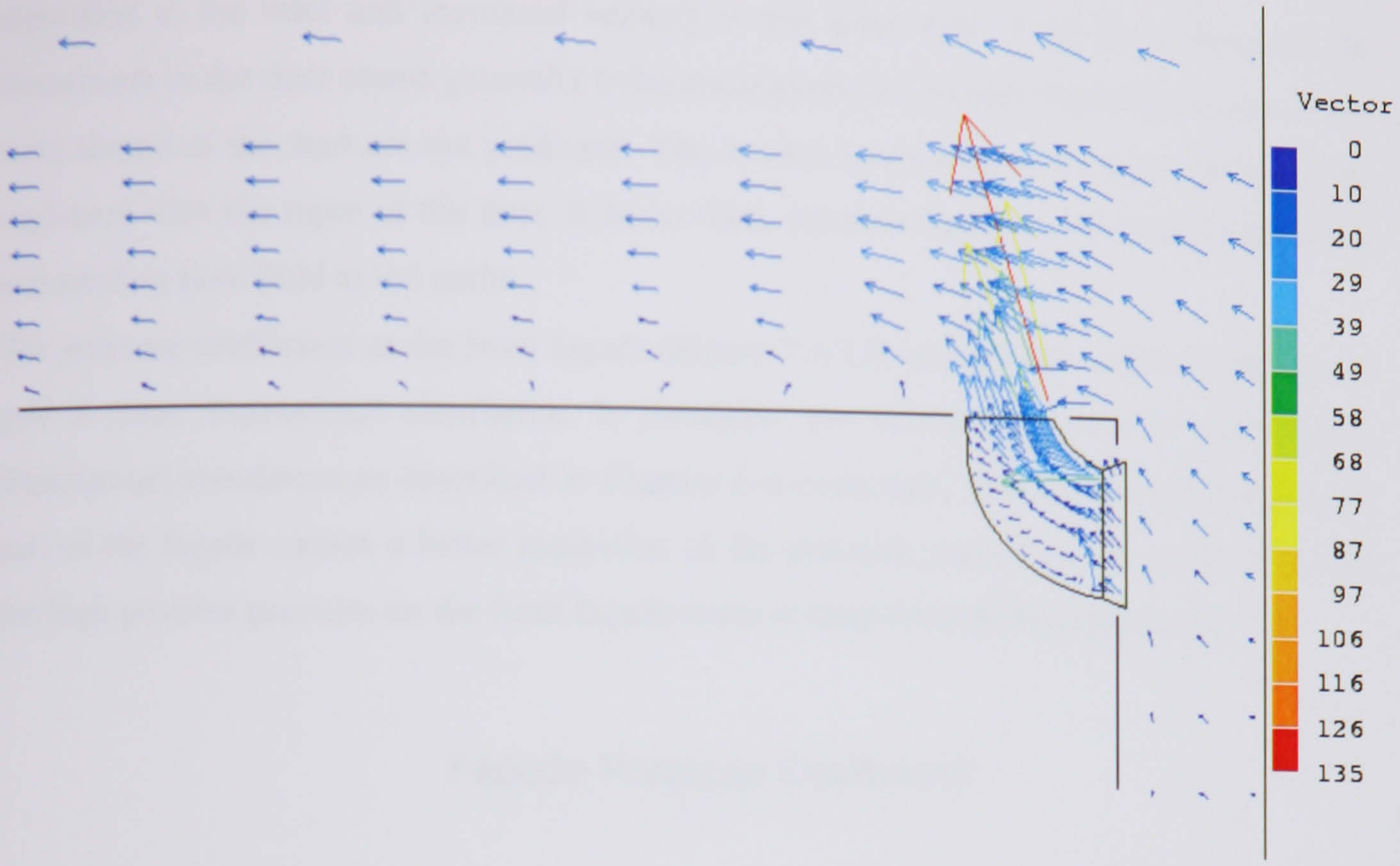

Figure 7.3.3.3: Duct flow entrainment into the surrounding flow

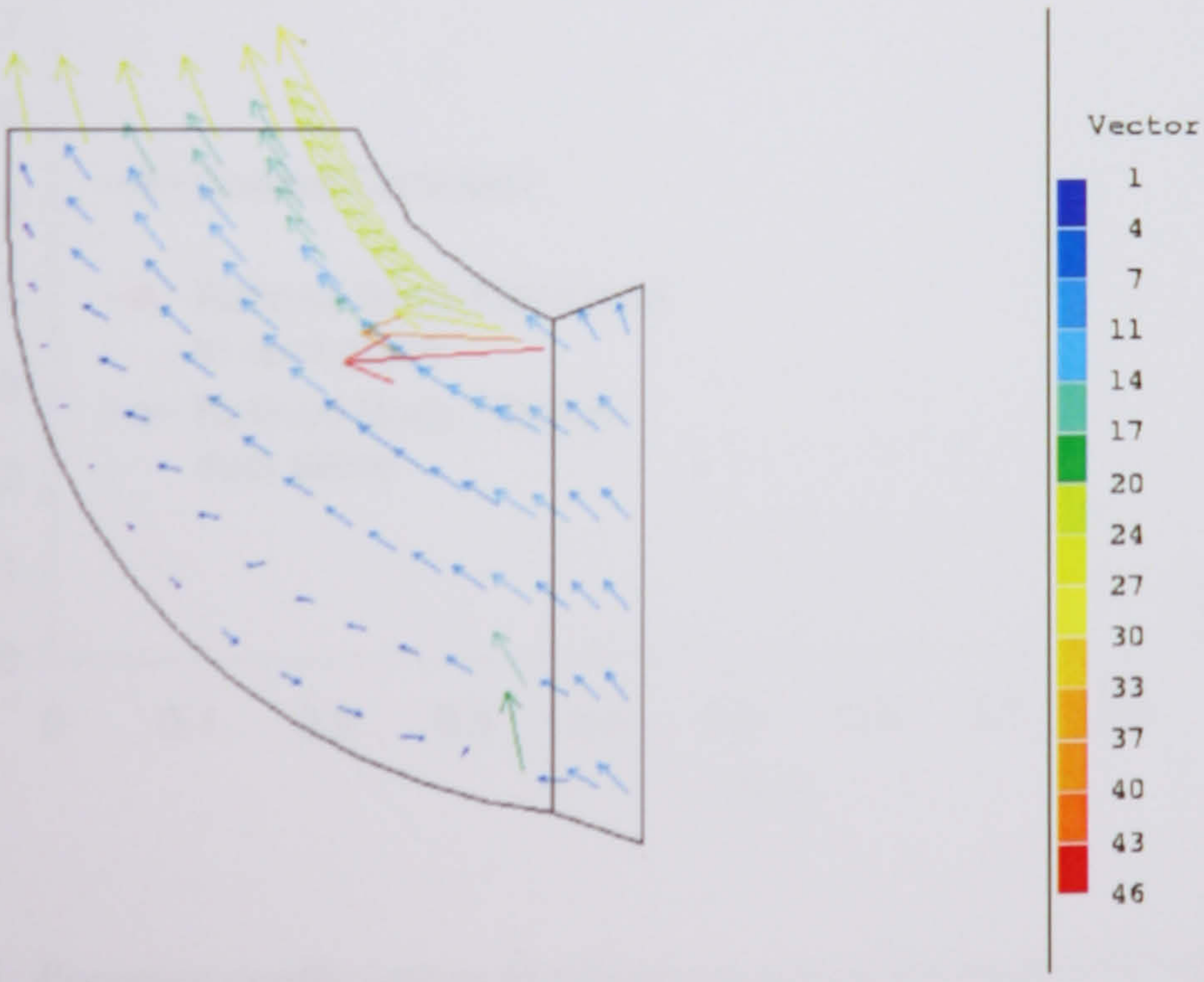

Figure 7.3.3.4: Flowfield in the duct in symmetry plane.

Overall, the flowfield in the duct (Figure 7.3.3.4) follows the expected pattern, with separation at the inlet and increased velocity at the inner wall of the duct. However, the momentum in the duct seems generally to be underpredicted. Induced higher velocities in the main stream of the duct are not predicted. The sudden increase in speed at the outlet can be explained with the taper of the duct. It is not sure, whether there is a localised effect of the surrounding flow field at the outlet.

The pressure coefficient at the front façade (Figure 7.3.3.5) corresponds well with the coarse grid in three dimensional simulation. In particular, the systematical error of a purely two dimensional simulation as described in Chapter 6 is overcome. The refined grid in the upper part of the façade causes a better resolution of the pressure gradient at the upper edge, and the high positive pressure on the front façade starts to drop towards the upper edge.

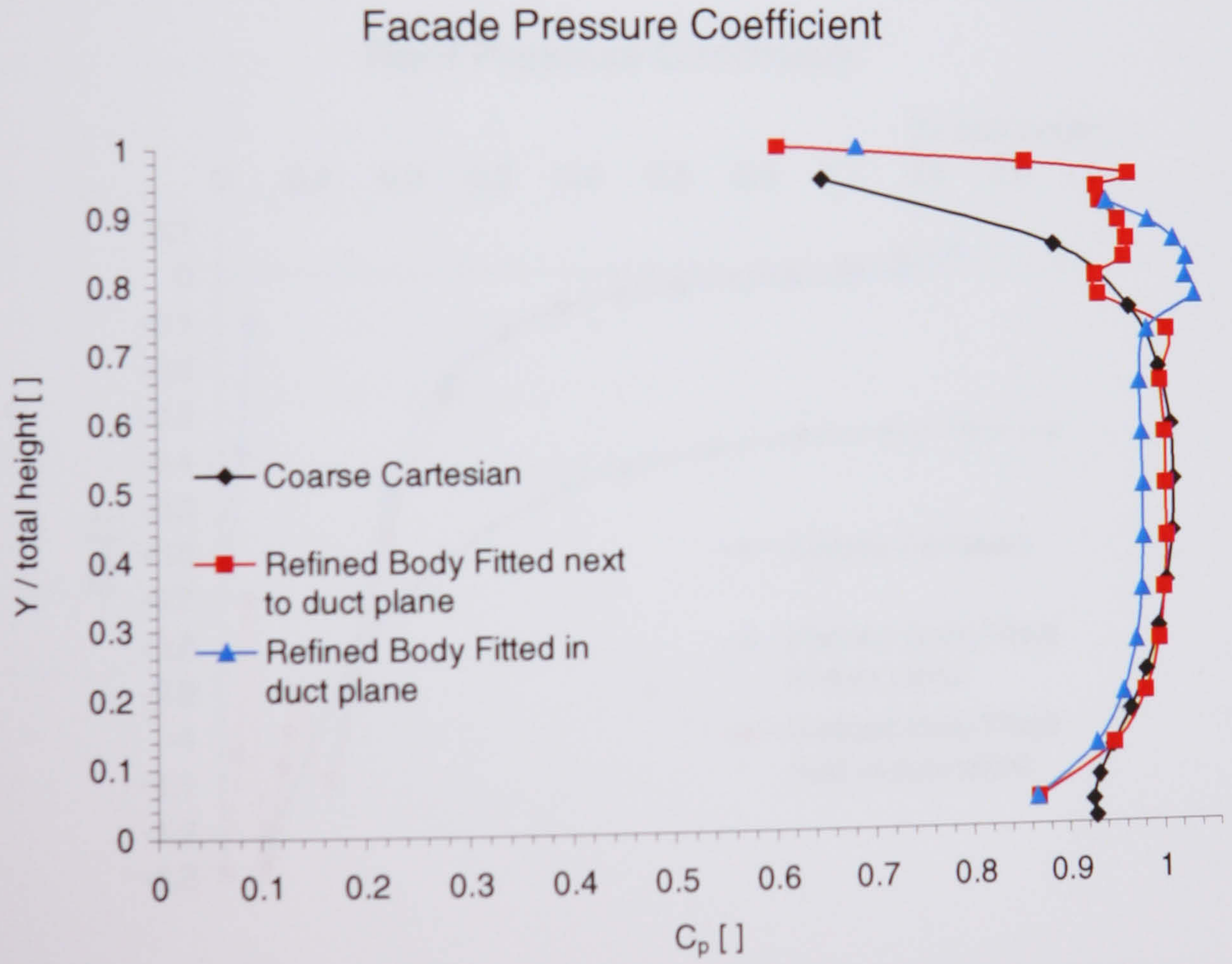

Figure 7.3.3.5: Pressure coefficient at the front façade in the mapped flowfield simulation

The irregularity in the slope might well be due to the mapping.

The pressure coefficient in the plane of the duct (symmetry plane) is in the lower part with its coarser grid slightly diminished, but in the area of grid refinement in the upper part of the façade, the pressure coefficient suddenly rises. This might be connected with the underpredicted momentum in the duct itself and is therefore more a sequential error following what might have gone wrong in the outlet region of the duct. This will be examined later in the 'discussion' section.

The pressure coefficient on the flat roof (Figure 7.3.3.6) of the refined grid simulation shows the reattachment of the separated flow from the leading edge. The vector flow pattern from the coarse grid simulation shows also reattachment (Figure 7.3.3.1). However, the pressure coefficient converges towards a negative value (C_p ~ -0.3). The convergence towards a uniform negative pressure coefficient was hitherto connected with the flow remaining separated over the flat roof. This shows that in computational fluid dynamics, it is potentially dangerous to estimate vector flow pattern from the pressure distribution and vice versa.

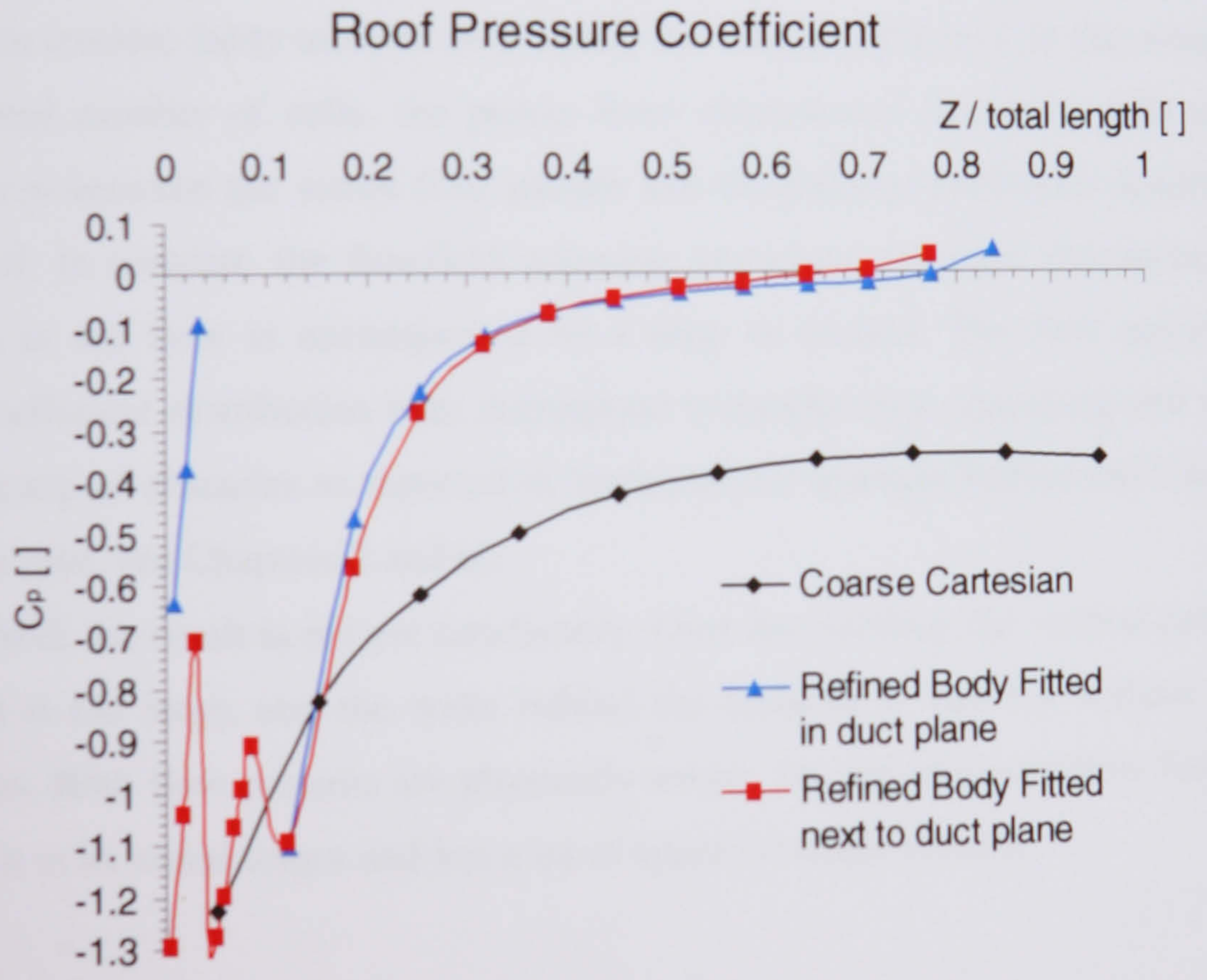

Figure 7.3.3.6: Pressure coefficient at the roof in the mapped flowfield simulation

In the coarse grid the applied ten cells in the z-direction seem insufficient to resolve the leading edge pressure gradient. With the refined grid resolution, the reattachment seems to occur after a stronger curvature of the flow over the leading edge. In the presence of the duct, the suction at the leading edge drops significantly, but rises again immediately downstream of the duct. There, the outflow separates at the outlet edge and the duct flow entrains into the surrounding flow. At the rear part of the roof, the simulation generates positive pressure coefficients. In the vector flow pattern (Figure 7.3.3.2, compare 7.3.3.1) there is no sign of recirculating upstream flow behind the building, which could cause a positive pressure from reattachment in a similar way as in the previous result of the purely three dimensional simulation (Figure 7.2.2.1). It might well be, that this error is caused by the constraint of the flow field mapping procedure at the trailing edge of the building.

Comparing the pressure coefficient on the roof of the flow field mapping (Figure 7.3.3.6) with the purely three dimensional simulation (Figure 7.2.2.2), we see a significant difference in particular for the suction downstream the duct and it's drop. But in the purely three dimensional simulation, the vector flow pattern show a vast separation with recirculation over the duct (Figures 7.2.2.1 and 7.2.2.5). All previous results in this work have shown, that for such flow pattern the pressure coefficient over the flat roof converges towards a negative value, which remains fairly uniform over nearly the whole of the roof. In this sense, because of the limited number of cells, the purely three dimensional simulation fails to generate consistency in between the vector flow pattern and the pressure coefficient distribution over the flat roof. In contrast, the flowfield mapping procedure generates consistency, and the attachment in the flow is accompanied by a drop in suction. The flow pattern and the pressure coefficient distribution both correspond to results from separating and reattaching flow on the top of obstacles as reported in literature (for example Robins and Castro for the flow over a cube, see Chapters 2 and 6).

In the far field, the result is not yet satisfactory. Over the building, the vertical component of momentum is too large, and the wake behind the building is vast but without significant recirculation. Both flow patterns are physically wrong, but the presented flow field mapping procedure is in its initial stages and has a lot of space for improvement.

Accuracy:

The first stage three dimensional simulation with coarse cartesian grid required around 5000 sweeps to converge. The same convergence criteria applied as in the cartesian cases of Chapter 6. Convergence was confirmed when the residuals for each of the variables reached values lower than 20. Hence, the average drop for the residuals was 5 to 6 orders of magnitude. Global mass flow conservation was confirmed in the result files at the inflow and outflow boundaries. The second stage simulation in the body fitted grid with the mapping procedure is slower and took around one week to complete. Convergence was confirmed when the residuals for the scalar variables reached values lower than 20 and those for the velocity components were below 40. Again, the average drop for the residuals was 5 to 6 orders of magnitude. A small error of around 0.3 % appeared in the global mass flow balance. However, local imbalances are more severe in particular in zones with refined grid.

7.3.4. Discussion and Conclusions

The flowfield mapping procedure is a by-product of the presented investigation. The results of the procedure are encouraging, but the development of this method is at an early stage. The basic procedure is now laid down, and requires fine and detailed development and numerical testing.

Currently, the mapping takes place as an inflow condition at the EAST-boundary, fixing the flux of momentum (related to the variables u, v, w) while the massflow condition for the pressure boundary remained 'open' (see Chapter 5.7). The setting of conditions means either fixing the value of the variable in the cell or fixing the related flux property in the cell. This corresponds to Dirichlet or Neumann boundary conditions. In contrast to analytical calculation, the numerical method provides the boundary conditions with a stiffness coefficient CO (see Chapter 5.7).

This is where the first numerical experiments should start in order to change the flow pattern in the far field. In particular, the never ending wake behind the obstacle and the overprediction of the vertical component of momentum over the obstacle are wrong. Probably, stiffening the factor for the domain behind the obstacle and relaxing the factor towards the upper domain boundary might have a positive impact.

Also, the pressure boundary condition behind the obstacle could be extended with an additional lateral inflow component of mass, as an additional source.

There might be various reasons for underpredicting momentum in the duct. One simple reason might be that the applied minimum number of three cells in the x-direction is not enough (see Figure 7.3.1.2). But it is more likely that relaxing of the stiffness factor for the boundary of the domains at inlet and outlet is required. The zone of entrainment of the outflow into the surrounding flow seems not to be perfectly balanced yet (Figure 7.3.3.3), whereas the surrounding flow itself independent from the entrainment seems to be well predicted (Figure 7.3.3.2). A localised imbalance could probably be tackled locally.

Apart from fixing the flux, it is possible to fix the values of the variables in the cells at the boundary. When stiffening them completely, it was observed that the spot values of the variables converged soon towards certain values, but the percentage of the residual error did not decrease. Whenever the calculation was interrupted, the display of the solution of the EAST-boundary showed that the mapping of the flow field was working (even the wake). Basically, in this way the coding was checked. Fixing the variables in the cells with various stiffness coefficients might be worthwhile to try.

Also, a boundary with a mixture of Dirichlets and Neumann conditions could be tested.

Further improvements could be achieved in the geometrical part of the procedure. The initial two grids could even now be designed with regard to better matching. Additionally, the sorting procedure could be extended with an averaging scheme in providing the body fitted cells with the values from the coarse precalculated solution – in a similar way, as is already done for the fine grid embedding feature and the linkage from one to many cells. This would have a positive impact on the balance of these values.

The thickness and the number of cells in the x-direction of the modelled slice is not optimised. The longitudinal and vertical components of momentum as provided at the boundary plane have an impact on the values at the symmetry plane, which is affected by the numbers of cells in the x-direction, in between the EAST-boundary and the symmetry plane. This is consistent with earlier experience: The generation of a shear flow depends on the grid resolution towards the solid wall, the pressure coefficient over the roof depends on the grid distribution towards the leading edge. In the presented simulation, there are only four cells in the x-direction for the far field, but nine cells for the refined grid zone.

The mapping itself is not restricted to the EAST-boundary plane. The provided coding can be used to map any cartesian precalculated field to any plane in the assembly of domains of the body fitted grid. Hence, a few planes or even the whole surrounding flow domain could be mapped.

Perhaps it is possible to apply the procedure to a purely two dimensional simulation, and to map the presolved flowfield on the two dimensional layer. A first attempt at fixing the variables (in two dimensions) in the cells was not stable, but variation of the stiffness coefficients was not tested. It might be, that the missing third component in the set of solved equations will always cause imbalance while coupling the purely two dimensional simulation to the three dimensional solution.

The driving idea behind the procedure is to adapt the surrounding flowfield to the momentum distribution, which is found in a full three dimensional simulation of the surrounding flowfield. The aim is to achieve surrounding boundaries for refined additional geometrical features, in this case the duct. Here, the pressure coefficient distribution on the façade and the roof plays a major role. It is surprising that the wrong prediction of the wake seems to go along with a sound pressure coefficient distribution on the surface of the obstacle. This is a numerical effect, in nature wake and drag are strictly related. However, the encouraging results achieved at the front and the top, in flow pattern and related pressure distribution, seems to indicate that the procedure is promising.

The presented approach could open the field for flow field simulations of very complex structures, where the surrounding flow field plays a significant role. This two step approach enables solutions, which are still difficult to achieve even with further progress in computer technology. It might be worthwhile to include such a method as a feature in CFD software.

References

PHOENICS 2.2.1, online help 'POLIS', see following entries:
Special Ground, Gxmake ,F-array

Dannecker R.: Computational Fluid Dynamics of the Wind Flow around a Building and its Influence on Design and Performance of the Integrated Ducted Wind Turbine Module; Proc. of the 4th European 'Marie Curie' Workshop Conference; Commission of the European Communities, DG XII, Directorate-General for Science, Research and Development, JOULE-Non Nuclear Energy Research; hold at the Department of Mechanical Engineering, University of Leeds, England, April 1999

Engineering Science Data Unit ESDU, Wind Engineering – Wind speed and turbulence 1a – Characteristics of atmospheric turbulence near the ground. Item No 85020, April 1993. ESDU International, London. ISBN 0 85679 526-7

8. A Power Prediction Model for the Building Integrated Ducted Wind Turbine Module

In general, wind power prediction is based on the characteristics of the wind turbine and the statistical distributed wind speed of the site in question (Eggleston and Stoddard 1987). The average power output $\langle P \rangle$ is

$$\langle P \rangle = \int_{V_{in}}^{V_{out}} P(V) f(V) dV \tag{8.1}$$

V_{in} = cut in wind speed

V_{out} = cut out wind speed

f(V) = wind speed probability distribution function

P(V) = electric power output as a function of wind speed

V_{in} and V_{out} determine the operating range of wind speeds. The power output curve is the turbine's characteristic. It depends on the aerodynamic characteristics of the rotor, the generator characteristics and the turbine's method of regulation. Therefore, the power coefficient c_p, which is the ratio of electric power output and aerodynamic power in the approaching wind, is an empirical value which has to be measured for the whole machine. Often, the plant factor c_f is used to describe the utilization as the ratio of $\langle P \rangle$ and the rated power output P_{rated} for regulated turbines. Hence, the amount of electrical energy produced during a certain period Δt is

$$\langle E \rangle = \Delta t \cdot \langle P \rangle = \Delta t \cdot c_f \cdot P_{rated} \tag{8.2}$$

In our case, any power prediction model of a Building Integrated Ducted Wind Turbine Module has the basic limitation, that these devices are still at an experimental stage. Therefore, the power curve P(V), which is crucial for the predictive model, is uncertain. Nevertheless, in the following section an attempt is made to generate a sound model, which is based on the experimental data available at this stage.

8.1. The Model Climate Data File

In contrast to the general approach, the statistical wind speed distribution does not directly play a role in the presented model. Instead, the prediction is based on a standard hourly climate data file for Glasgow, which has been generated from many data sets in a statistical manner and is used in the building energy simulation package ESP_r of the research group at Strathclyde University (Clarke 1985). The 'typical' annual wind speed distribution follows a Weibull distribution (Figure 8.1.1).

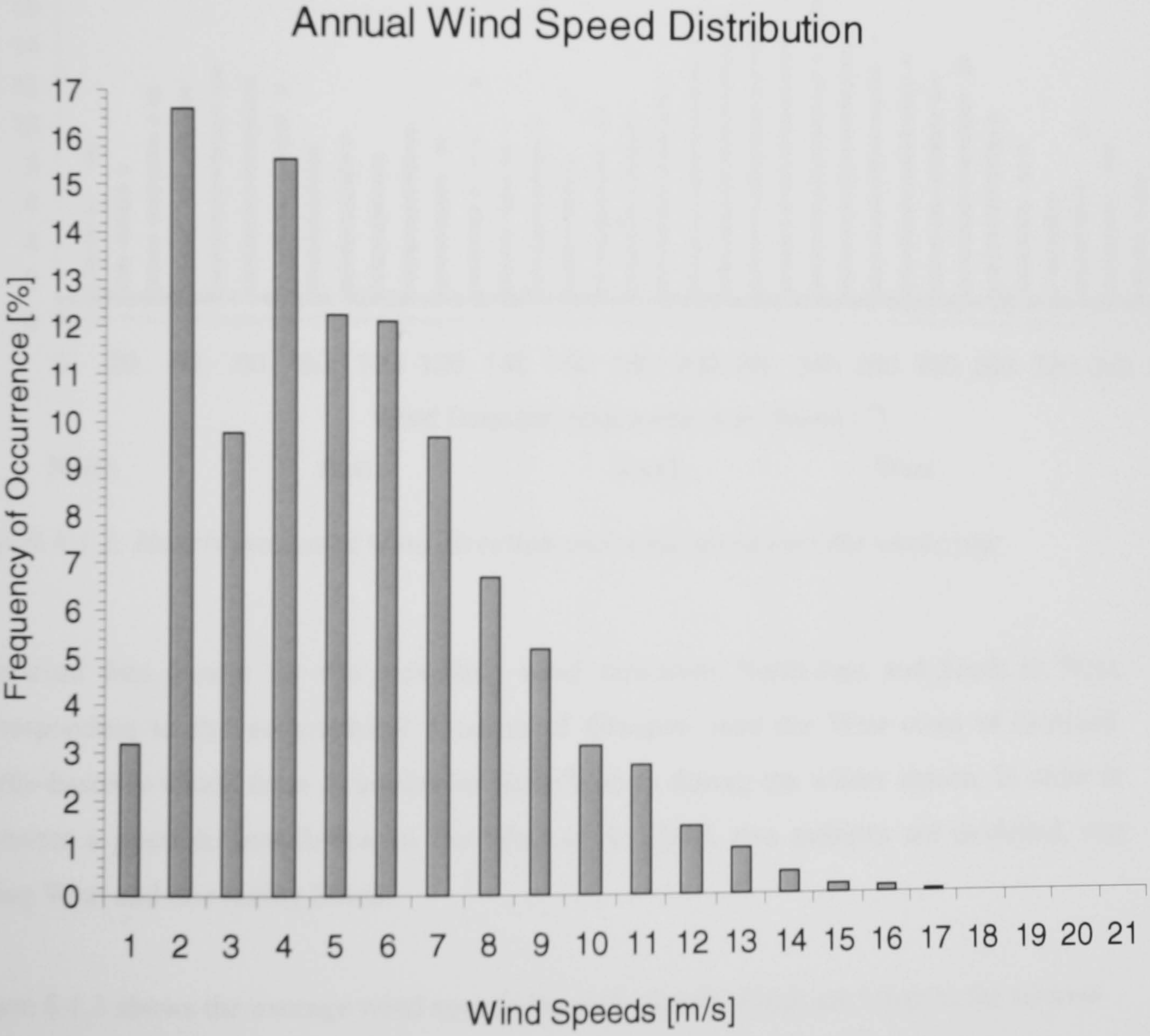

Figure 8.1.1:Annual wind speed distribution of climate model file

Most of the time, the wind is at low and medium speed. Therefore it is important to deploy a turbine with relatively good starting characteristics. However, the low wind speeds contribute little to the energy yield.

The prevailing wind direction is South-West. Figure 8.1.2 displays the hourly averaged wind data in the same manner as the windrose normally does. The angle of incidence is measured clockwise starting from the North, which is at 0^0.

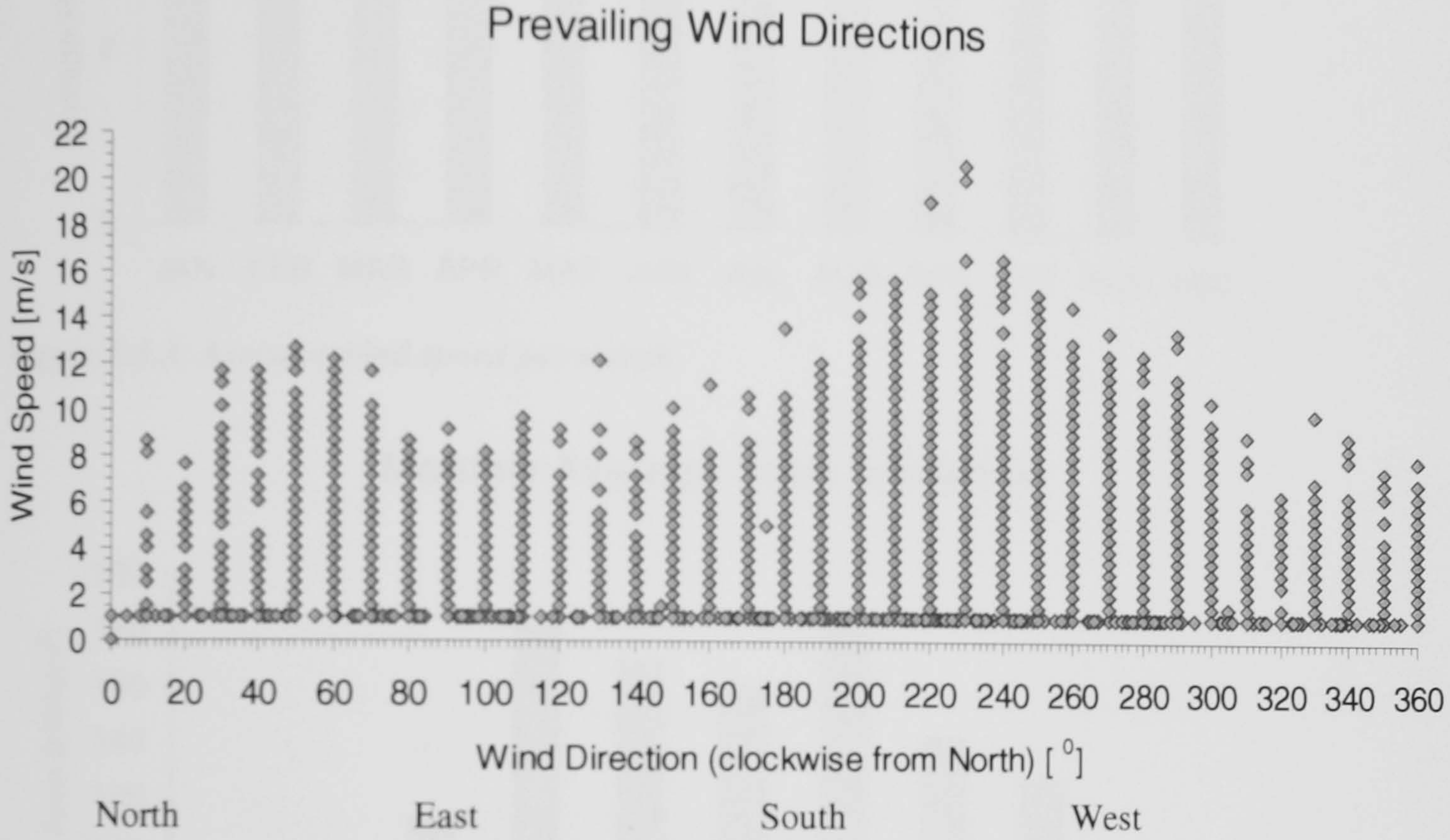

Figure 8.1.2: Hourly measured wind direction and wind speed over the whole year

The wind data cluster for the prevailing wind directions North-East and South to West, corresponding to the geographical location of Glasgow near the West coast of Scotland. North–Easterly winds from Scandinavia occur mainly during the winter season. In order to represent a possible installation in the West of Scotland, two turbines are modelled, one facing West and one facing South.

Figure 8.1.3 shows the average wind speeds for each month, which are lower in the summer season than at other times. Figure 8.1.4 displays the monthly incidence of solar energy per unit area on a flat roof, which was measured as the sum of direct and diffuse solar radiation.

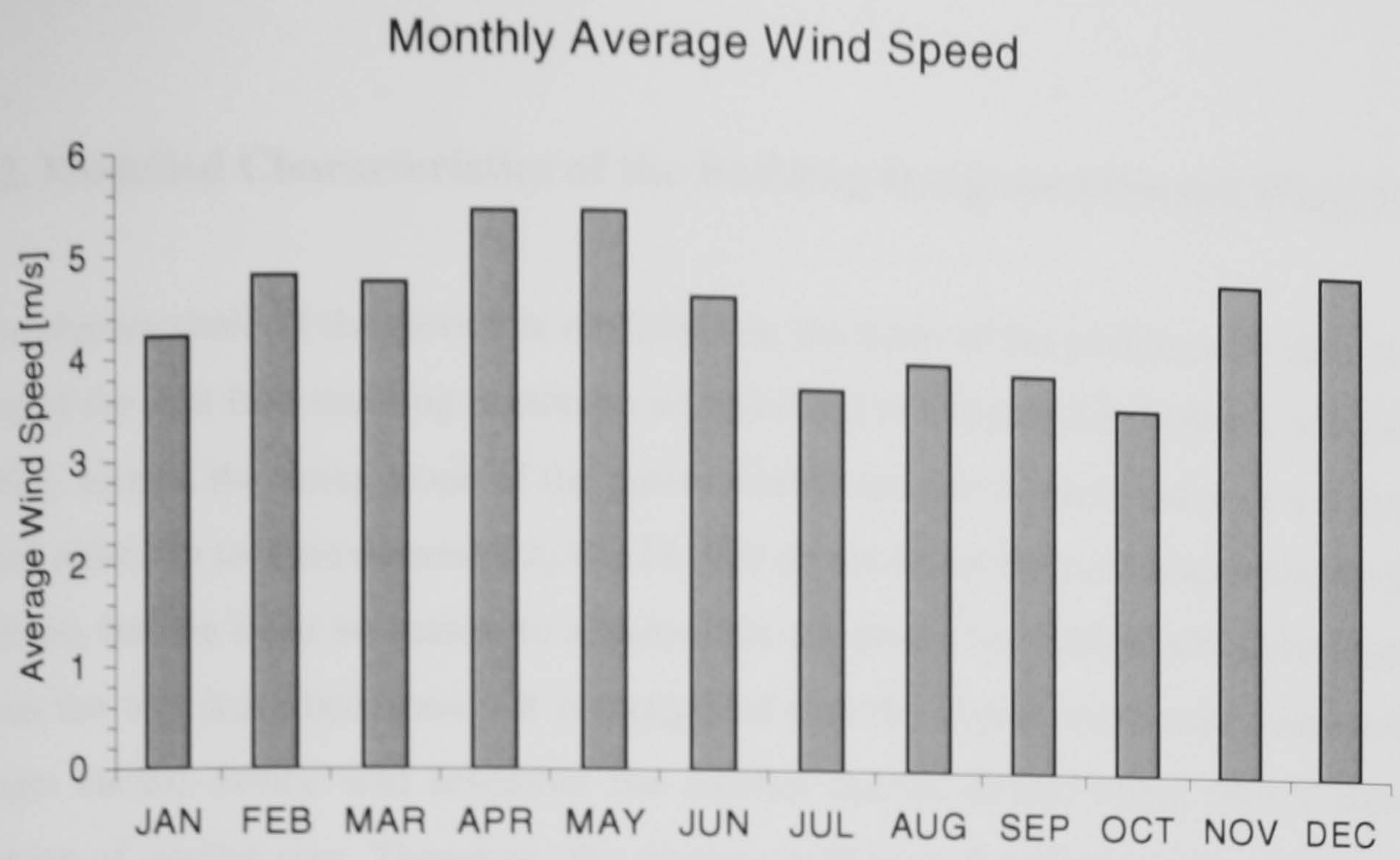

Figure 8.1.3: Average wind speed per month

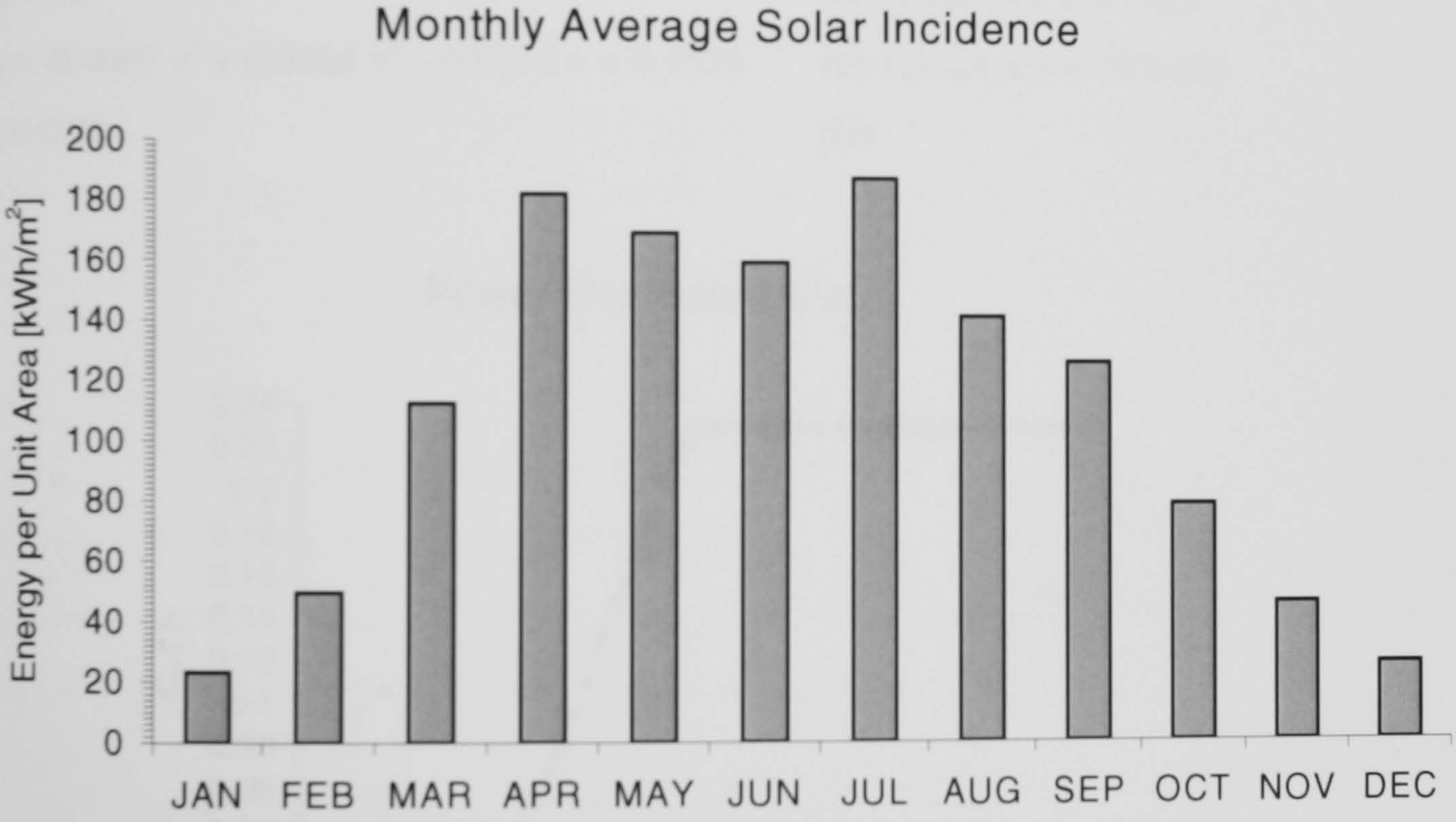

Figure 8.1.4: Incident solar energy per unit square meter on the flat roof - summation of direct and diffuse solar radiation for each month

The distribution of solar incidence over the year (Figure 8.1.4) is typical for the northern latitude of Scotland.

Those data were not further analysed in a statistical manner. Hence, the predicted power output is calculated on an hourly averaged basis. The energy yield is the summation of the hourly energy production over the specific period of time.

8.2. Modelled Characteristics of the Building Integrated Ducted Wind Turbine

The characteristic of the device is modelled on the basis of the performance data of the field trial of the first free standing prototype as described in Chapter 2.8, Figure 2.8.2 (Grant et al. 1994). Hence, the rising slope of the power coefficient curve was fitted with a polynomial of third order, up to a maximum of $c_p = 0.23$. We do not know the c_p characteristic for the larger turbine, but we have no reason to assume that the power coefficient will differ significantly from the one described above. It is suggested that the power coefficient characteristic of a larger ducted device will resemble the smaller ducted device rather than a conventional turbine of similar size. Therefore, the power coefficient distribution was approximated as a function of the wind speed v

$c_p = 0.0$ for $0.0 \text{ m/s} \le v \le 4.3 \text{ m/s}$

$c_p = -0.0007 v^3 + 0.0164 v^2 - 0.0812 v + 0.1036$ for $4.3 \text{ m/s} < v < 10.0 \text{ m/s}$

$c_p = 0.23$ else

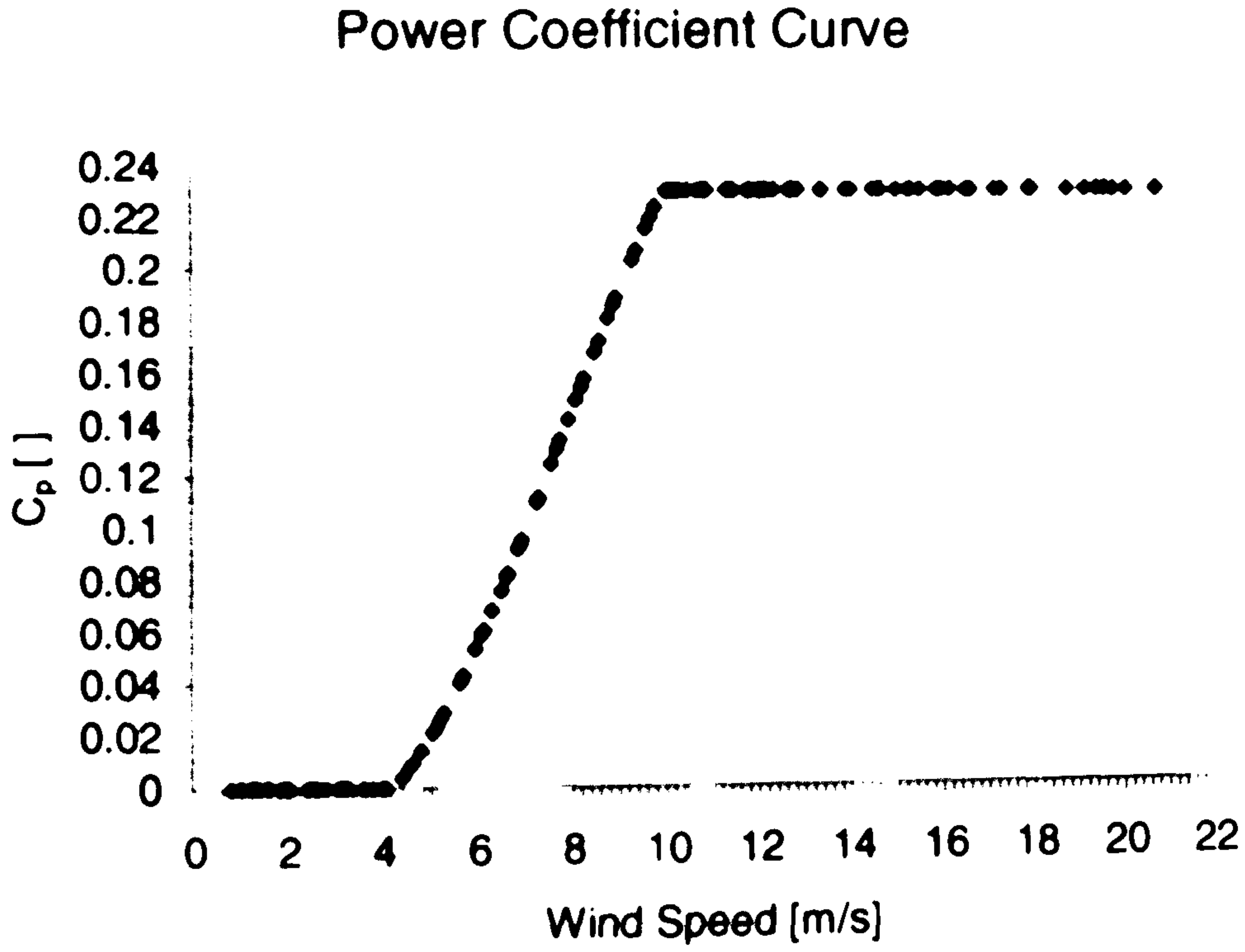

Figure 8.2.1: Modelled power coefficient characteristic for the turbine

In this field trial (Grant et al. 1994), in order to calculate the power coefficient, the current and the voltage across a fixed load resistor of 50 Ω was measured. It might be that this load resistor was not optimal. On the other hand, a power coefficient of $c_p = 0.23$ is a good value given the low efficiency of the permanent magnet alternator used.

For the first prototype, the wind speed was measured next to the turbine at the same height in the free flow. It was a free standing machine, mounted on the roof of the data logging shelter on an open site. Here, the wind had possibilities to deviate in all directions (apart from flowing underneath the machine). However, we don't know the wind speed at the rotor in the duct of the free standing machine. Experimental and simulated values for the flow in the normal direction through an integrated 90^0 duct without spoiler show, that the increase in speed in rotor area is only marginal (see Chapter 4 and Chapter 7, in particular Figure 7.2.2.9). However, this was observed for the duct without modelling the rotor. We assume in our model, that the integrated turbine follows the characteristics of the free standing prototype but experiences higher wind speeds due to the duct.

According to the wind tunnel tests described in Chapter 4, the wind speed in the duct at the rotor plane increases by a certain ratio, dependent on the angle of incident wind. Here, two configurations were taken into account: the 30^0 duct with spoiler II (Figure 4.2.6) and the 90^0 duct with spoiler II (Figure 4.2.10). Both of them show an increased wind speed in the duct for a wide range of angles of incidence (see 'with spoiler II' in Figure 4.10.1 and 'with spoiler II' in Figure 4.10.2). In the calculation, these wind speed ratios were used. The performance is predicted for every 10^0, as the standardised climate file holds the wind speed data in steps of 10^0 wind direction. It was assumed that the performance is completely symmetrical for clockwise and anti-clockwise angles of incidence.

Experiment 4: 30^0 duct with spoiler II

incident angle from normal to the facade	wind speed ratio
$\alpha = 0^0$	1.26
$\alpha = \pm 10^0$	1.32
$\alpha = \pm 20^0$	1.26
$\alpha = \pm 30^0$	1.32
$\alpha = \pm 40^0$	1.02
$\alpha = \pm 50^0$	0.80

Experiment 6: 90° duct with spoiler II

incident angle from normal to the facade	wind speed ratio
$\alpha = 0^0$	1.05
$\alpha = \pm 10^0$	1.18
$\alpha = \pm 20^0$	1.19
$\alpha = \pm 30^0$	1.25
$\alpha = \pm 40^0$	1.22
$\alpha = \pm 50^0$	1.21
$\alpha = \pm 60^0$	0.95
$\alpha = \pm 70^0$	0.85

Hence, the power of the building integrated ducted wind turbine was calculated as

$P(v) = 0.5 \cdot \rho \cdot A \cdot c_p(v) \cdot v^3$ and $v = v(\alpha)$ = free wind speed · wind speed ratio (α)

$\rho = 1.2255\ kg/m^3$ (constant air density)

$A = \pi \cdot (0.5\ m)^2$ (rotor swept area)

As the power output is related to the free wind speed, each configuration is characterised with a parametric set of power curves, according to the angle of incidence (see Figures 8.2.2 and 8.2.3).

The model incorporates two types of regulating schemes: first, the power coefficient c_p is kept constant for higher wind speeds, once it reached its maximum (see Figure 8.2.1). This is similar to pitch regulated machines. Secondly, the resulting power is restricted (in Figure 8.2.3 1000 W cut-off power). Indeed, when the power restriction applies, the power coefficient will drop. In this sense, the models can not be consistent. But this inconsistency does not significantly affect the calculation of the power curve (Figures 8.2.2 and 8.2.3) nor the estimated monthly energy yield (see Figures 8.4.1 to 8.4.4).

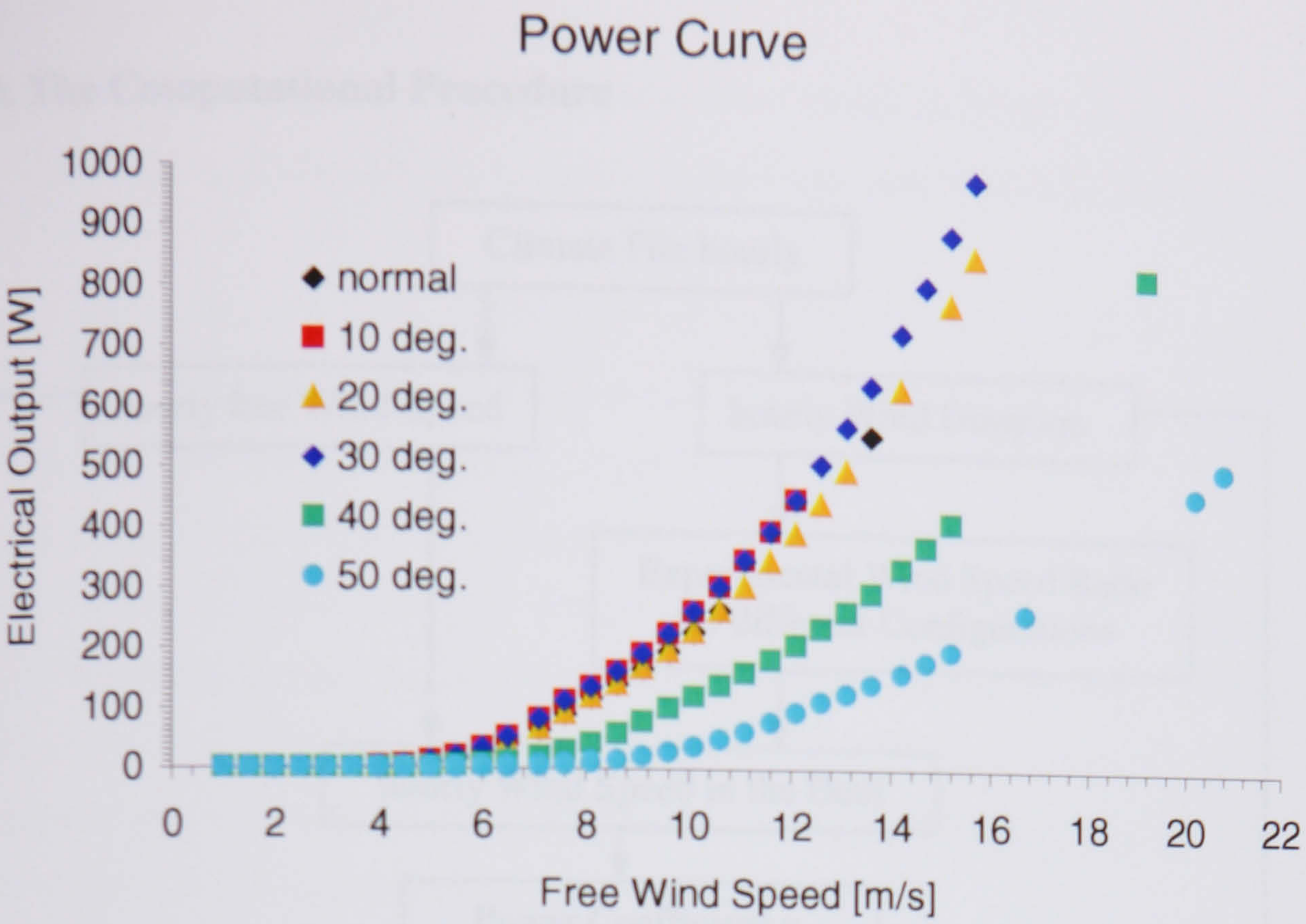

Figure 8.2.2: Modelled power curve for the configuration of experiment 4 (30° duct, spoiler II). Parametric set for various angles of incidence

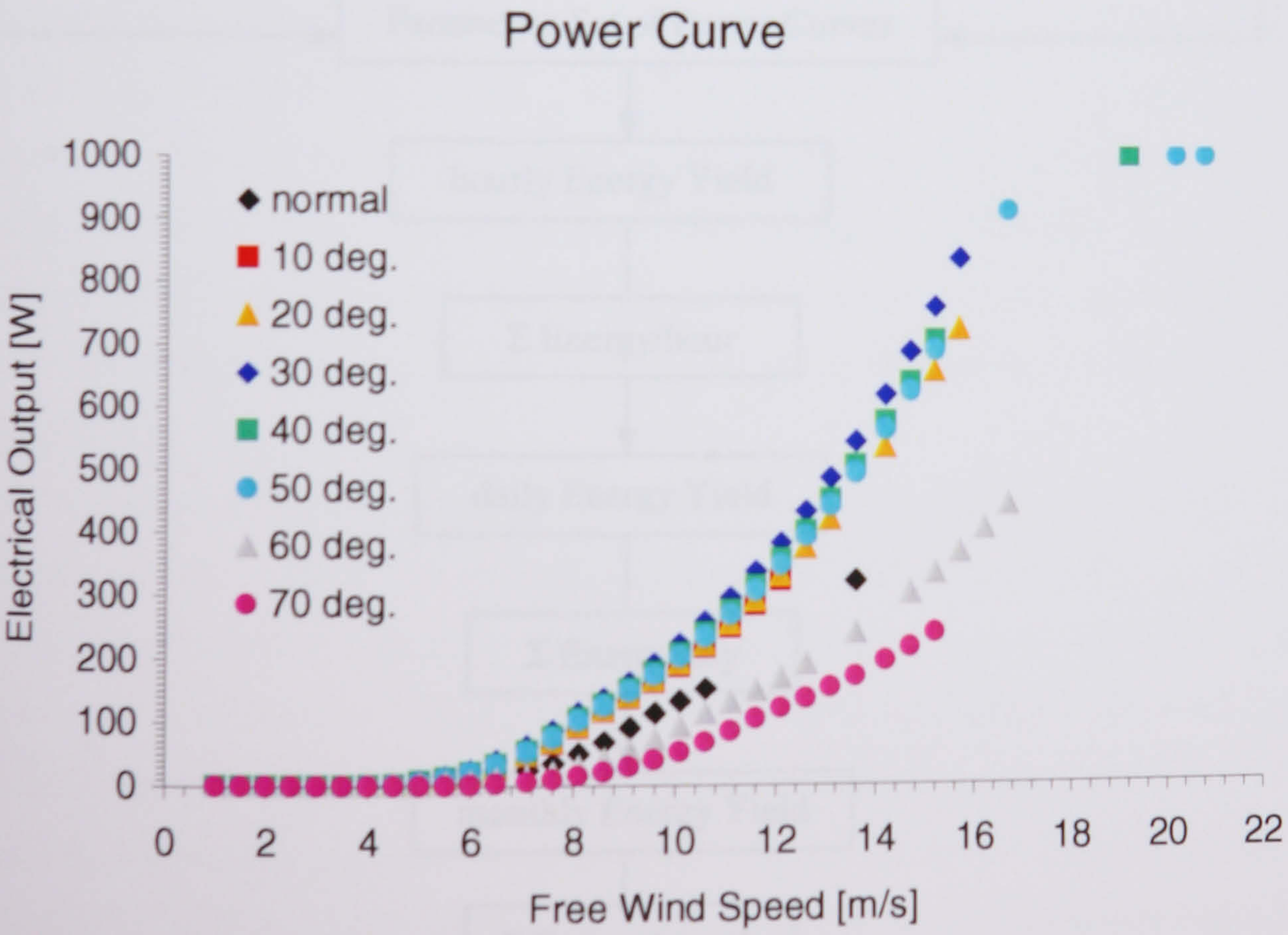

Figure 8.2.3: Modelled power curve for the configuration of experiment 6 (90° duct, spoiler II). Parametric set for various angles of incidence

8.3. The Computational Procedure

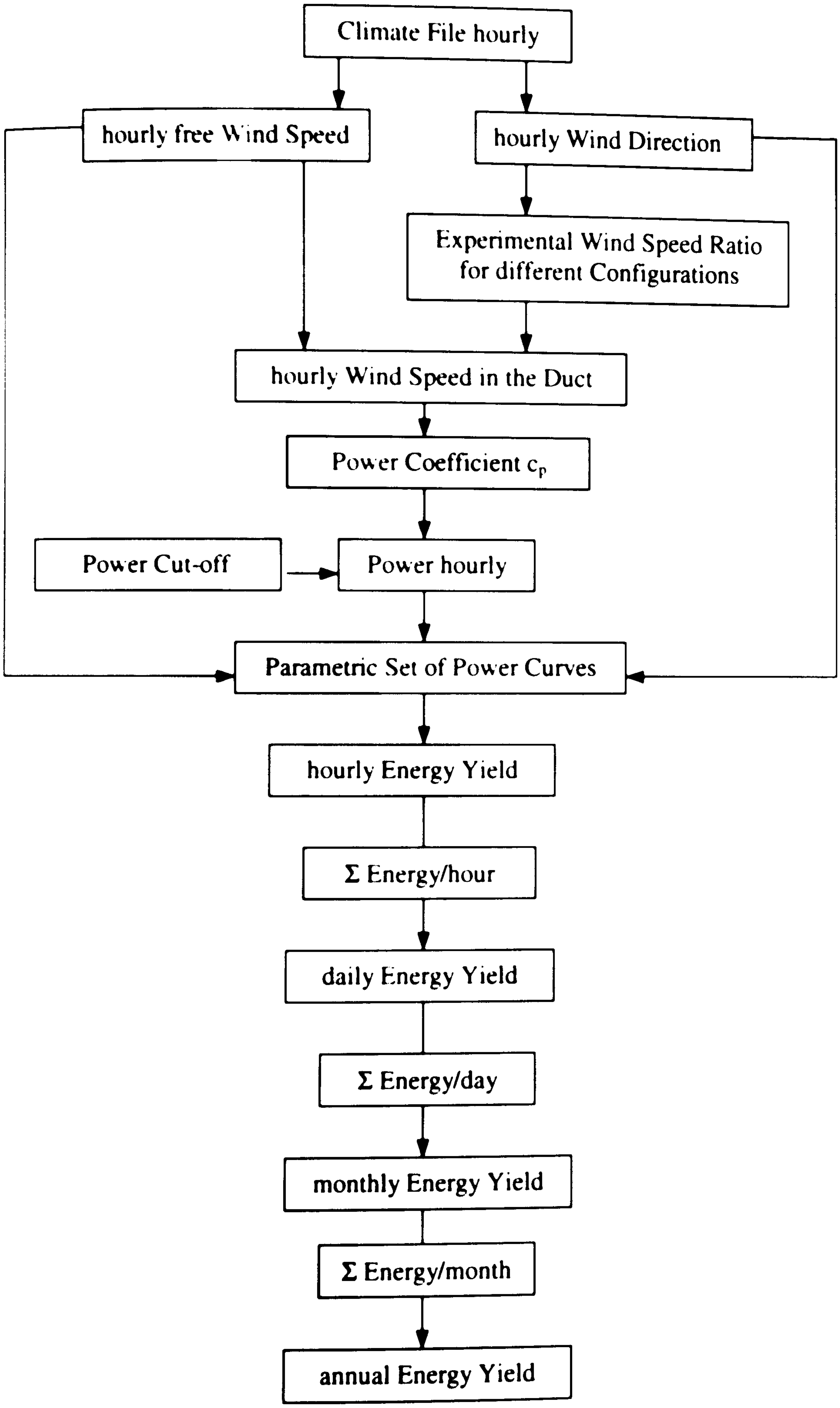

8.4. Monthly Energy Yield of the Integrated Ducted Wind Turbine in Comparison with Photovoltaics and a Conventional Wind Turbine

The modelled hourly averaged power output (Figures 8.2.2 and 8.2.3) of the two configurations, facing South and West, are the basis for estimating the monthly energy yield. In particular, the impact of different power restrictions (1000 W, 500 W, 250 W and 100 W in Figures 8.4.1 to 8.4.4) was investigated.

Those values are compared with the performance of two different competitive forms of renewable energy generation for small scale application: the free standing wind turbine type Rutland WG 910 'Standard' from the British Manufacturer Marlec Engineering Co., and the crystalline silicon solar panel type 585 'Saturn' from BP Solar. Characteristics and technical data are provided in Appendix I and II accordingly.

The monthly energy yield for the conventional turbine was calculated on the basis of the power curve from the manufacturer. This turbine has a smaller rotor diameter of 0.91 m, compared to the suggested ducted rotor of 1 m diameter. It is important to mention that the manufacturer's characteristic is based on charging a 12 V battery. Here, the power slope was measured for constant voltage and not for a constant load resistor, as is the case with the Ducted Wind Turbine in Figure 2.8.2. It is assumed that the manufacturer's data are optimised. The load resistor for recording the Ducted Wind Turbine might not have been optimised, but the determined power coefficient is seen as a reasonable value. Until now, the Ducted Wind Turbine has not been deployed for battery charging. It is assumed, that the measured power coefficient for the small prototype turbine applies for higher rated turbines as simulated.

The photovoltaic performance was modelled with the regenerative energy simulation program MERIT, which was recently developed in the research group at the Strathclyde University (Born 2001). In order to allow comparison, the energy yield of the photovoltaic panel (with area 0.525 m x 1.183 m) was scaled up to correspond to the swept area of the ducted rotor ($\pi \cdot (0.5\ m)^2$). As modelled, the optimal angle for the installation of the solar panel for a Glasgow site would be around 36^0 from the horizontal. Photovoltaic modelling is based on an equivalence circuit, comprising a diode and a shunt resistance (Köthe 1982). An important feature is the drop of efficiency due to increased panel temperature. The prediction code was developed in the research group in the context of Building Energy Simulation (Kelly 1998).

Even in the summer months (apart from July), the conventional wind turbine with its small rotor swept area and low power coefficient, which is characteristic for such a small machine, compares favourably with the solar panel. The prediction of the annual energy yield from the conventional wind turbine is around a factor of two larger than the solar energy production (see Figure 8.4.5).

The performance of the Ducted Wind Turbine depends very much on the wind direction. However, in general the effect of power augmentation overcompensates the losses due to unfavourable wind direction. In the presented case, the duct should ideally be orientated towards the West.

Energy estimations for the Ducted Wind Turbine are related to the power restriction applied in the model (see Figures 8.2.1 to 8.2.4). As the high wind speeds contribute disproportionately to the generated power, modelling of different cut-off ratings is most significantly reflected in the energy yield for the windy months (compare Figure 8.1.3). Obviously, at lower windspeeds, the generator does not produce the rated power.

A realistic power cut-off rating may be in the range from 250 to 500 W (see Figures 8.4.2 and 8.4.3), which is suitable for higher wind speeds. Here, the electrical configuration plays an important role. For direct battery charging, a higher rated generator will generate a higher current and therefore requires more torque at the shaft, which has to be provided from an optimally designed rotor in the duct. For constant load resistance, for example an electric heater, it depends on the load. A higher load resistance requires a lower shaft torque at the generator, which will improve the starting characteristics of the turbine. Whatever the case, for this range of rating the Ducted Wind Turbine facing to the West compares favourably with the conventional turbine.

For the low power cut-off of 100 W (Figure 8.4.4), the conventional wind turbine produces in many months a higher amount of energy than the Ducted Turbine. This is not surprising, as the Ducted Wind Turbine has a higher cut-in speed, and can not compensate this loss of energy capture with larger power production at higher wind speeds.

Figure 8.4.5 shows the impact of the rated power cut-off on the annual energy yield. A power cut-off at 500 W reduces the energy yield only marginally, and for 250 W power cut-off the annual energy yield drops only by around 12 to 15 %. A significant decrease of 40 to 45 % in energy production is predicted for low rated 100 W. As the duct serves the power augmentation with induced higher wind speeds, it is obvious that the generator should be higher rated than for a conventional turbine of the same size.

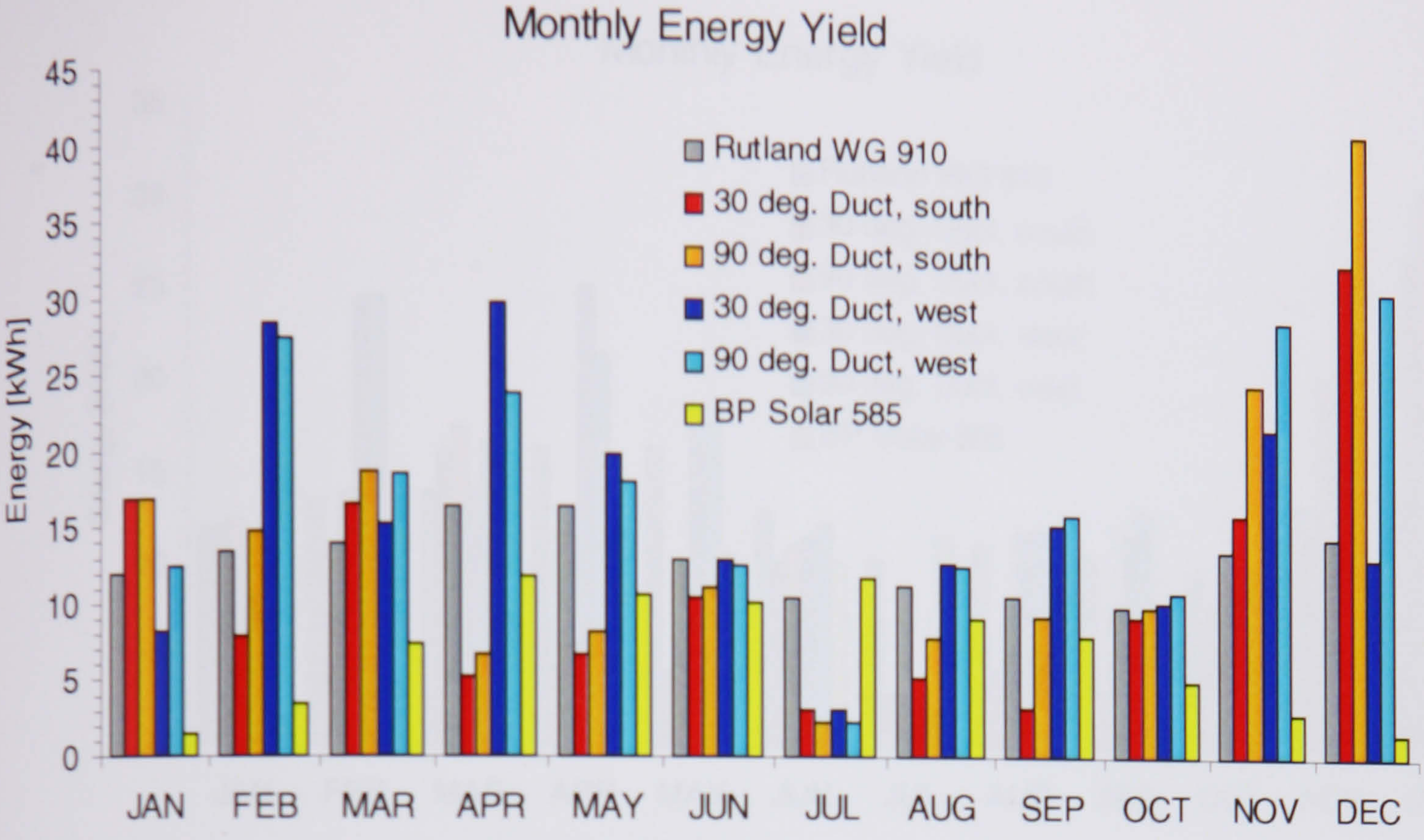

Figure 8.4.1: Monthly energy yield, 1000 W power cut-off

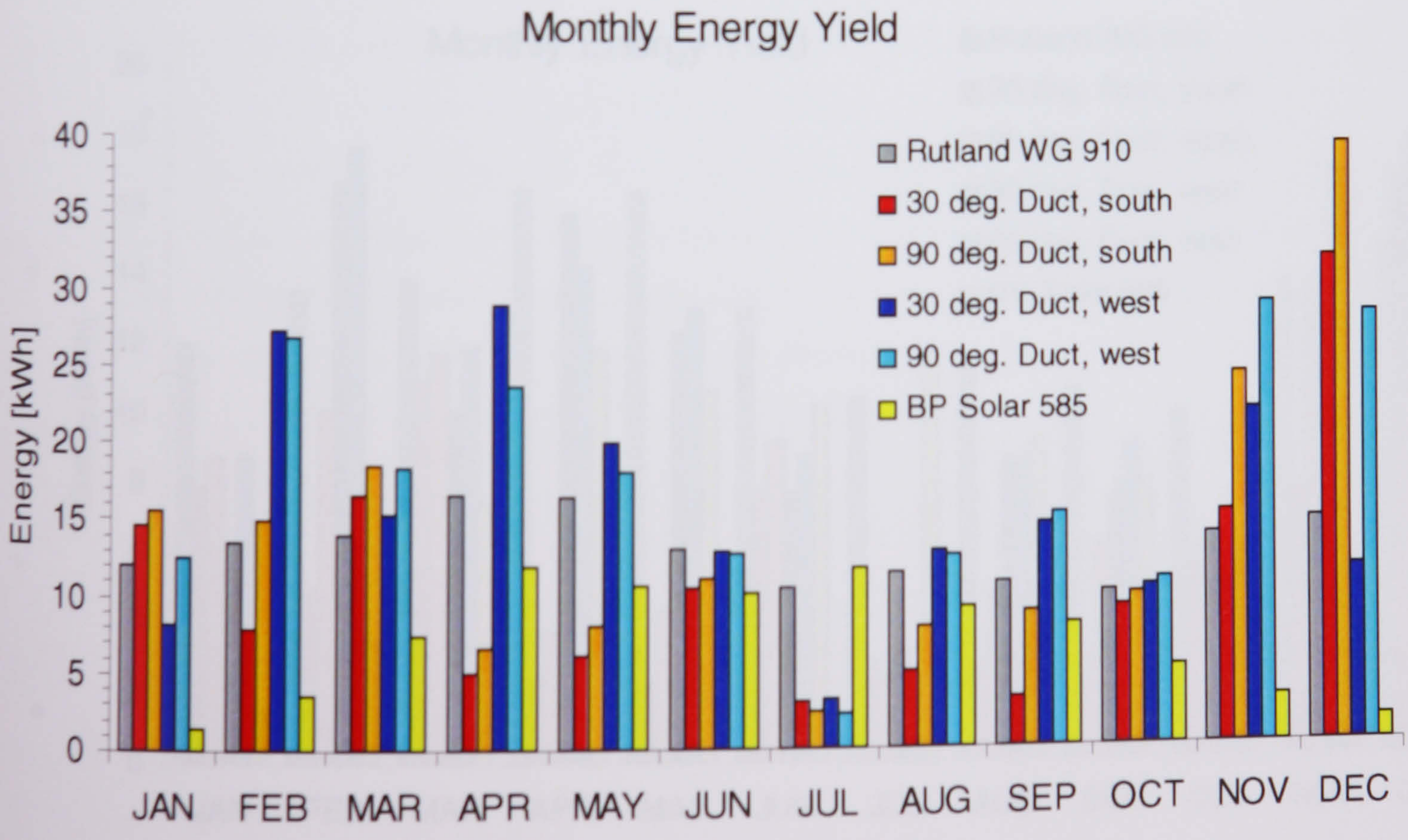

Figure 8.4.2: Monthly energy yield, 500 W power cut-off

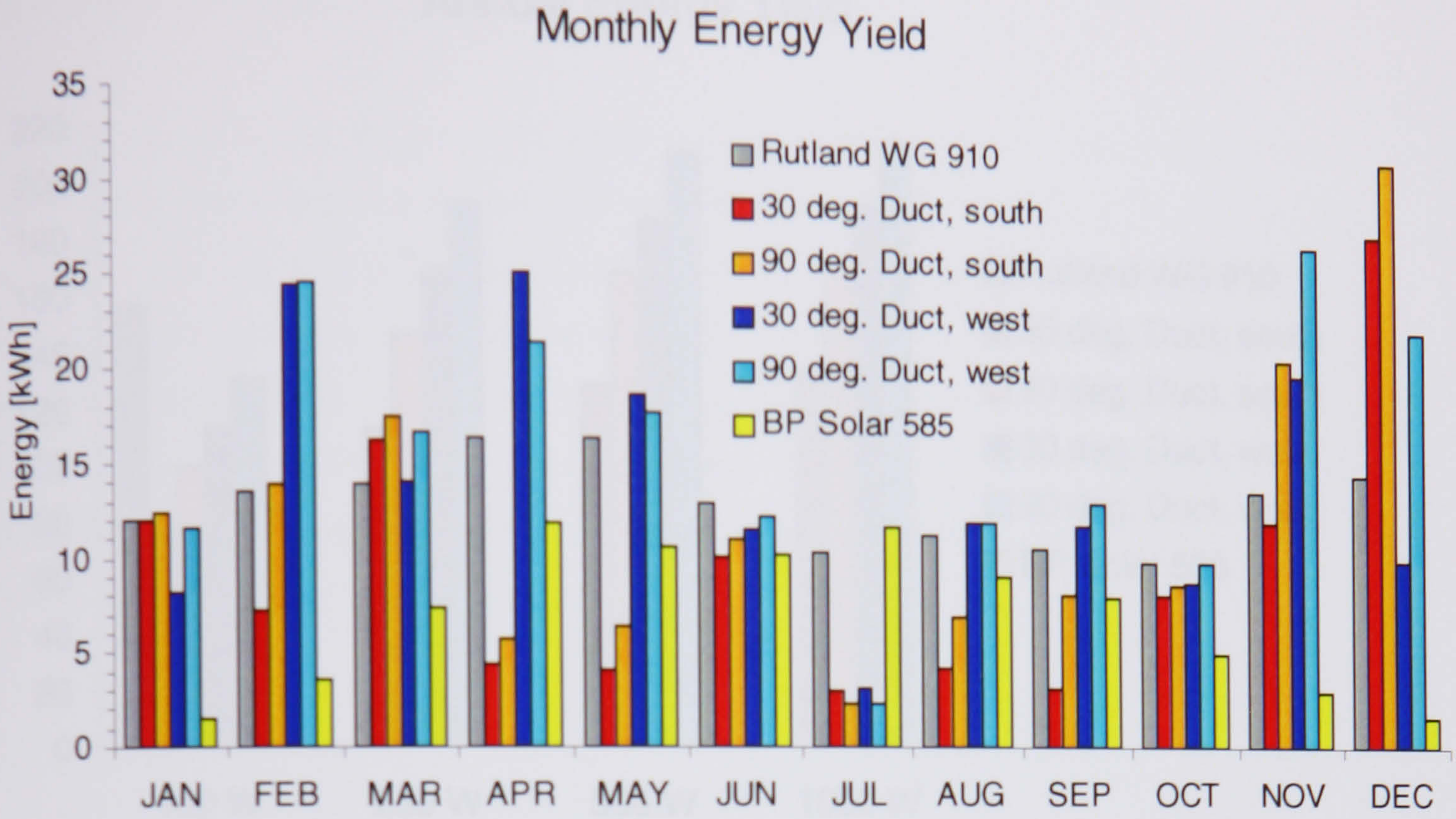

Figure 8.4.3: Monthly energy yield, 250 W power cut-off

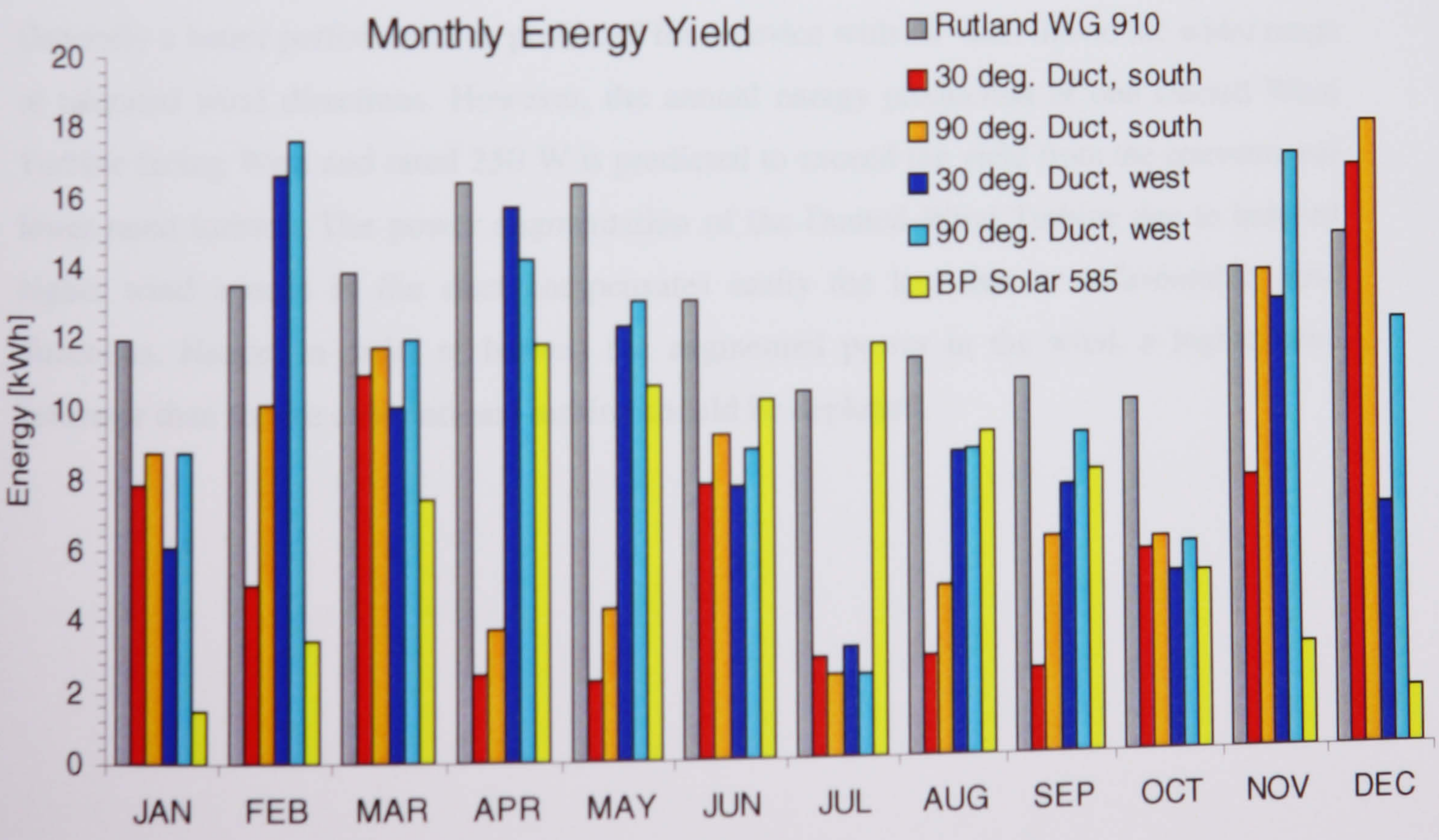

Figure 8.4.4: Monthly energy yield, 100 W power cut-off

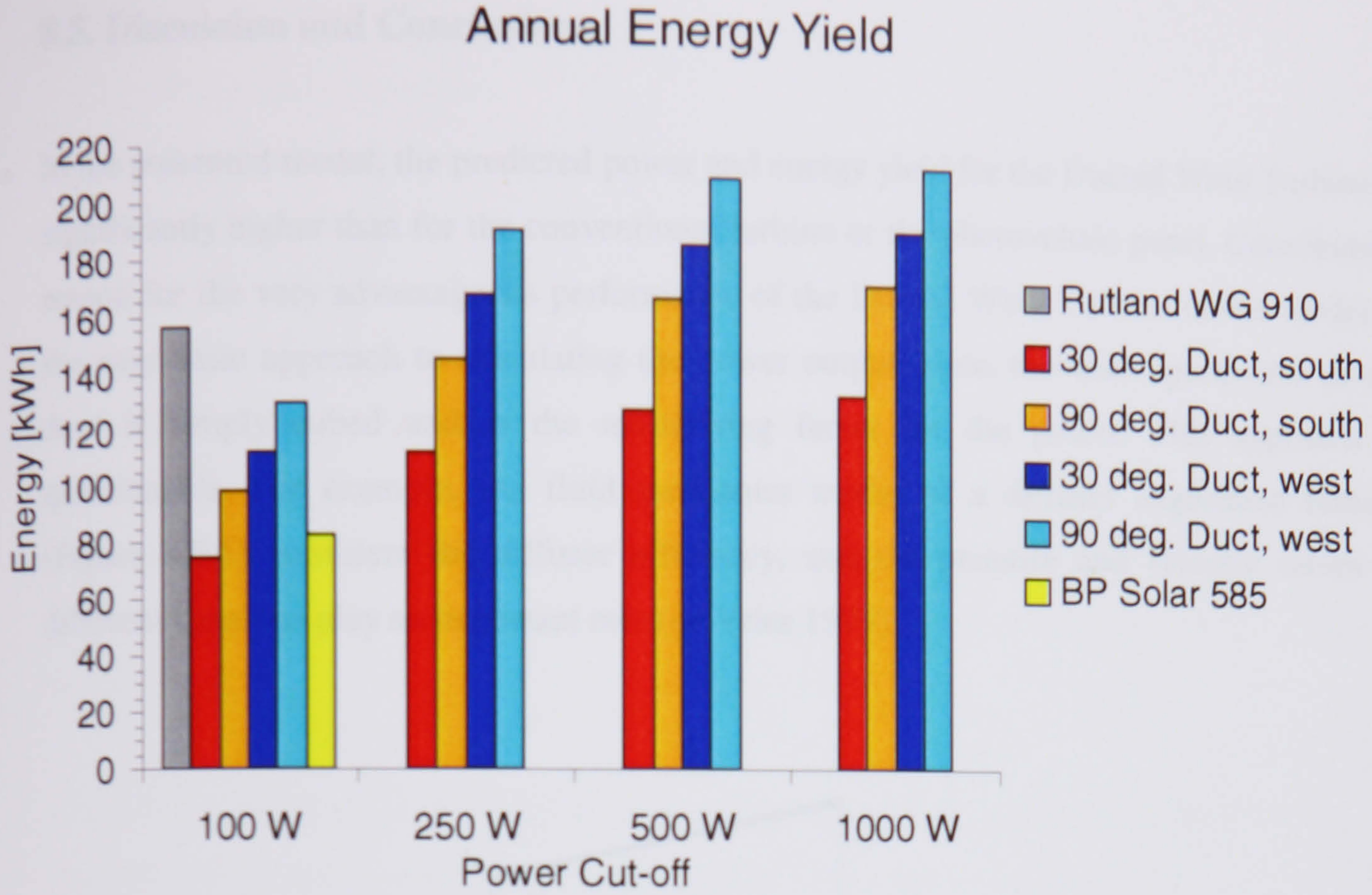

Figure 8.4.5: Annual energy yield

Generally a better performance is predicted for a device with 90° duct due to the wider range of tolerated wind directions. However, the annual energy production of one Ducted Wind Turbine facing West and rated 250 W is predicted to exceed the yield from the conventional lower rated turbine. The power augmentation of the Ducted Wind Turbine due to induced higher wind speeds in the duct compensates easily the loss due to unfavourable wind directions. Hence, in order to harvest the augmented power in the wind, a higher rated generator than for the conventional turbine should be deployed.

8.5. Discussion and Conclusions

In the presented model, the predicted power and energy yield for the Ducted Wind Turbine is significantly higher than for the conventional turbine or the photovoltaic panel. Contributory reason for the very advantageous performance of the Ducted Wind Turbine in this model is the very basic approach to calculating the power output. Here, the wind speed ratio in the duct is simply cubed and is the multiplying factor for the power. This approach is questionable. For example, the fluid mechanics model of a diffuser augmented turbine (Figure 8.5.1) considers the diffuser efficiency, and the pressure and velocity values at different locations play an important role (de Vries 1979).

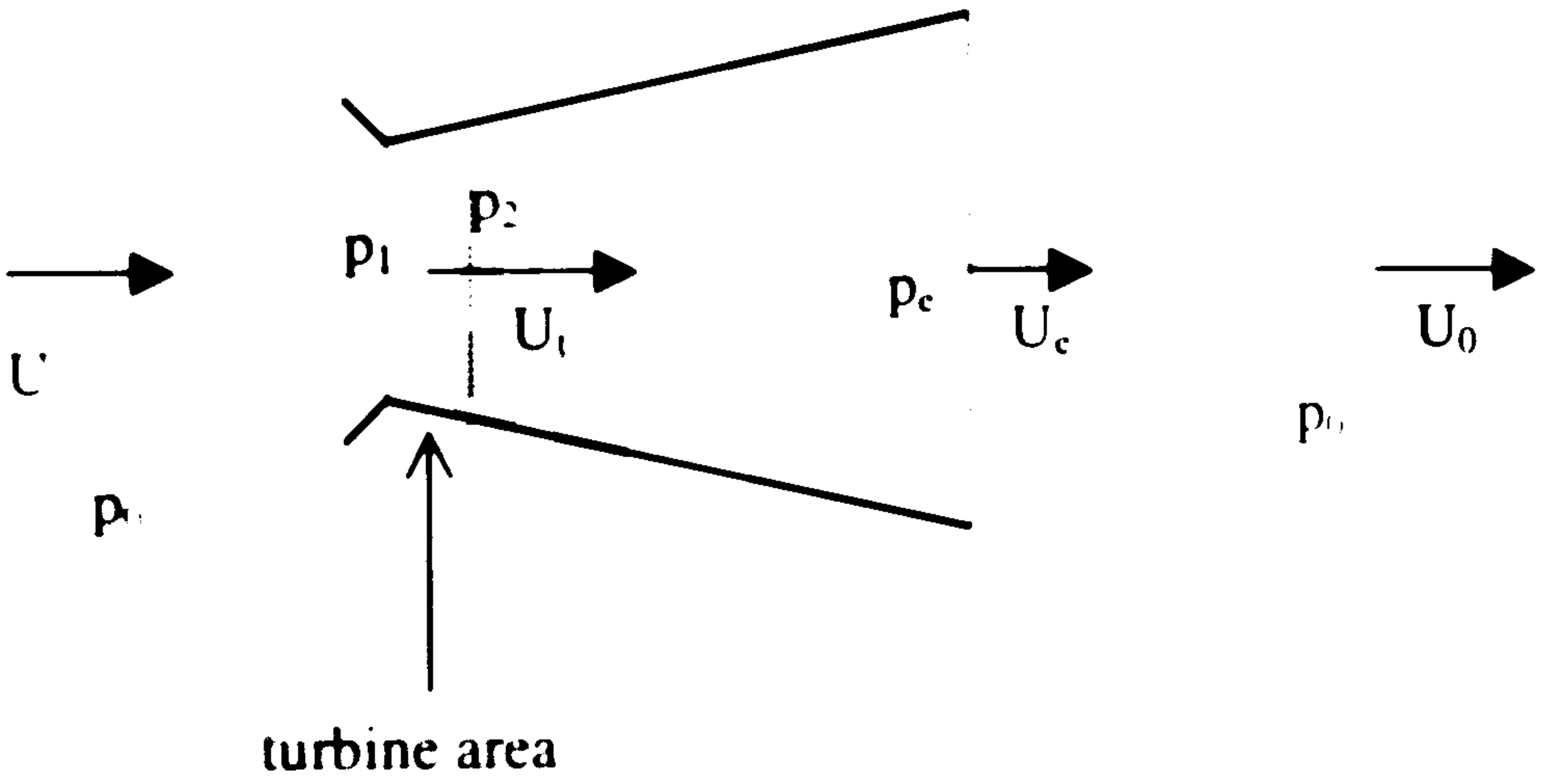

Figure 8.5.1: Schematic diagram for the diffuser augmented wind turbine

The power adsorbed by the turbine is

$$P = U_t \cdot A \cdot (p_1 - p_2) = 0.5 \cdot \rho \cdot U_0^2 \cdot U_t \cdot A \cdot (1 - B \cdot (U_t / U_0)^2) \text{ with } B = 1 - \eta_d \cdot (1 - 1/a^2)$$

The power coefficient depends on the difference in static pressure at the diffuser exit (p_0 - p_e).

$$c_p = (U_t / U_0) \cdot (1 + [(p_0 - p_e) / 0.5 \cdot \rho \cdot U_0^2] - B \cdot (U_t / U_0)^2)$$

where

A = turbine swept are

a = diffuser area ratio

(p_1 - p_2) = pressure drop across the turbine

U_t = velocity in turbine plane

U_0, p_0 = free stream conditions

U_e, p_e = exit conditions

η_d = diffuser efficiency

It is difficult to apply this fluid mechanics model to the situation of the duct in the wall roof edge. The low pressure behind the turbine at the outlet is caused by the free air stream over the obstacle, and it is very speculative to suppose an equivalence to the diffuser in this situation. The regions which establish a pressure differential do not have exact boundaries, and the flow is highly turbulent. Also, any change of wind direction has a large impact on conditions.

However, it is possible to model a turbine. Experimentally, the power absorption is often simulated by a wire screen, and the pressure drop over a screen at the rotor is

$$(p_1 - p_2) = 0.5 \cdot \rho \cdot k \cdot U_t^2$$

with

k = resistance factor of the screen.

In Computational Fluid Dynamics, the pressure drop can be modelled by blocking the cells in the intended turbine plane with a porosity factor (CHAM PHOENICS). Both methods require information about the turbine characteristics. But in order to choose a turbine, one needs information about the flow situation in the duct. The presented work will hopefully contribute to the latter.

In a two dimensional computational fluid dynamic simulation of a diffuser augmented turbine, the rotor disc was simulated by specifying volume forces in the cells (Hansen et al. 1999). In this way, it is possible to simulate a turbine with constant thrust. Comparing the velocity profiles at the rotor plane, Hansen derives that the power coefficient c_p for the augmented turbine is proportional to the ratio between the mass flows through the turbines with and without duct. That is to say, according to Hansen, the speed up ratio in the diffuser duct does not contribute cubed to the power output, only as a simple factor

$$\frac{c_{p,ducted}}{c_{p,bare}} = \frac{V_{ducted}}{V_{bare}}$$

Again, it is difficult to transfer these results to the flow situation under investigation.

The presented power prediction should be interpreted with common sense as a potential. It represents the offered power of the wind flow through the duct. Without modelling the turbine itself, it is not possible to model absorbed power. The actual generated power may be smaller than the offered power, even if the power coefficient in this prediction model is based on the measured coefficient of a prototype. Here, generator losses are included. Any induced higher wind speed would result in a better power coefficient. The power output however, might deviate from the one calculated in this power prediction model.

The crucial point of power prediction modelling is that the model tries to predict the performance of a machine, which does not exist yet in this form. A more accurate model requires information, which is only available when the machine is built and tested at large scale. For example, the pressure drop across the turbine, with different pressure conditions at duct entry and exit. Or, the outlet velocity for the jet entrainment into the roof edge vortex. However, if we reach this stage, power prediction modelling might be replaced with measurement series of actual generated power. Then the power coefficient of the whole device will measured as the fraction of the generated electrical power and the aerodynamic power available in the free stream.

The directional performance is modelled according to the wind tunnel experiments. So far, no work has been done to confirm these results either at large scale or through Computational Fluid Dynamics (as explained in Chapter 7). The directional performance is one of the most important features which contributes to power augmentation and to the energy yield. The integration of a Ducted Wind Turbine is particularly suitable for a site with a very significant prevailing wind direction.

Compared with the source of errors related to the cubed speed up factor and uncertainty over directional performance, the effect of the different electrical loading regimes seems to be rather minor.

The presented power prediction model may overestimate the actual power generation, but it describes other features of the turbine well. For example, the turbine will have a parametric band of power curves according to its directional sensitivity. And the generated power will be significantly higher than for a conventional small turbine. In this sense, the result of this model gives convincing evidence of the value and the necessity for a prototype development.

References

Eggleston D.M. and Stoddard F.S.; Wind Turbine Engineering Design; Van Nostrand Reinhold Company, New York, USA, 1987

Clarke J.A.; Energy Simulation in Building Design; Adam Hilger Ltd., Bristol and Boston, England, 1985

Grant A.D., Nasr el-Din S.A. and Kilpatrick J.; Development of a Ducted Wind Energy Converter; Wind Engineering, Vol.18, No.6, 1994

Born F.J.; Aiding Renewable Energy Integration through Complimentary Demand-Supply Matching; PhD thesis, Energy Systems Research Unit, Department of Mechanical Engineering, University of Strathclyde in Glasgow, Scotland, March 2001

Köthe H.K.; Praxis solar- und windelektrischer Energieversorgung; Verlag des Vereins Deutscher Ingenieure VDI, Düsseldorf, Germany, 1982

Kelly N.J.; Towards a Design Environment for Building-Integrated Energy Systems: The Integration of Electrical Power Flow Modelling with Building Simulation; PhD thesis, Energy Systems Research Unit, Department of Mechanical Engineering, University of Strathclyde in Glasgow, Scotland, October 1998

de Vries O.; Fluid Dynamic Aspects of Wind Energy Conversion; NATO, Advisory Group for Aerospace Research and Development AGARD, AGARDograph No. 243, July 1979, ISBN 92-835-1326-6.

CHAM; PHOENICS, version 2.2.1, POLIS online help encyclopaedia, see for porosity: -Conpor statement

Hansen M.O.L., Sørensen N.N. and Flay R.G.J.; Effect of placing a Diffuser around a Wind Turbine; Proc. of the 1999 European Wind Energy Conference, 1st-5th March 1999, Nice, France, pp. 322-324

9. General Conclusions, Perspective and Future Work

The contribution of 'renewable energy' generation in the built environment has gained in significance in the past years. So far, the large resource of wind energy has been neglected in this context.

The Department undertook pioneering steps with the work on its free standing Ducted Wind Turbine, which is being further developed and tested.

The objective of the presented work is to provide proof of concept for such a building integrated Ducted Wind Turbine module to be situated in the upper edge of the façade of a tall building with flat roof, with the outlet to the roof. The pressure differential arising from the wind flow over the building and locally accelerated flow should induce a high mass flow through the turbine.

This concept was explored by means of experimental and numerical methods.

A building model with different integrated duct configurations and a series of attached spoilers has been tested in the Department's open section wind tunnel. The experimental investigation comprised pressure measurements in combination with localised wind speed recordings with hot wire anemometry. The results of these tests are in many ways encouraging. There is evidence, that for some combinations of duct and spoiler, windspeeds more than 30 % higher than the velocity of the approaching free stream are induced in the duct. Also, the duct tolerates a large angle of incident wind, in some cases ± 60^0. In this context, the increased suction over the roof due to vortex development with rising angles of incidence seems to play an important role. The induced wind speed in the duct peaks at a certain angle of incidence, not at normal incidence. Of particular interest is the assessment of the impact of the duct flow entrainment into this suction zone over the roof. As the high suction goes along with recirculating flow, disturbance of this pattern might cause significant changes in the pressure. To shed more light on this complex situation, the pressure distribution upwind and downwind of the jet entrainment has been measured. But no clear pattern emerges, and different combinations of duct and spoiler lead to contrary results. However, in the worst case, the suction on the roof downwind of the entrainment drops significantly compared to the situation upwind, but still approximates to the value measured for inflow normal to the facade. Hence, there is evidence that the installation of several turbines in a row along the wall roof edge is feasible, but a future detailed investigation of multiple ducts is necessary for a final evaluation.

Additionally, there is a wide range of duct and spoiler combinations which have not yet been considered. The basic wind tunnel model in its modular form is suitable for all kinds of modifications, and numerous experiments can be conducted. The flow pattern through the duct, its speeding up and the tolerated angle of incidence all depend very much on the geometry of the duct. For each duct, careful design of the inlet is very important, in order to enable a smooth inflow and to prevent separation. The general effect of a spoiler above the inlet seems to be to increase the mass flow, but it may also have the effect of widening the range of tolerated angles of incidence. Here, the characteristics of each combination of duct and spoiler differ.

Different design options may be evaluated with the help of Computational Fluid Dynamics. However, the actual size of the flow domain and the fine grid necessary to resolve turbulent flow around corners require a vast amount of cells. In this work, the necessary requirements for the cell distribution of wind flow simulations around buildings are explored. In particular the distribution of suction over the flat roof and the generation of a realistic recirculation pattern over the roof and in the wake depend highly on the cell distribution in each direction. Some of the important findings concern the pressure distribution at the solid boundary and the flow pattern in its vicinity. For the flow over the roof, it became obvious that it is not reliable to predict flow pattern from measured pressure distributions.

Also, the influence of the cell distribution in the far field is significant. The cell distribution towards the solid ground determines the developed inflow profile. Hence, a specific implemented atmospheric boundary layer profile at the inflow boundary of the modelled flow domain has, for most applications, been drastically modified by the time the inflow reaches the building. A uniform inflow profile generates a boundary layer profile, and the shape of this profile depends on the grid distribution upstream of the building. Because of the limited number off cells, one is tempted to implement a very coarse grid in the far field of the building. This results in a generated boundary layer thickness which could easily exceed the building height.

Comparison of the simulation with reported and own experimental work shows that there is a discrepancy in the pressure coefficient standards for the full scale approach and for small scale wind tunnel models. For full scale, there is a much higher suction observed at the leading roof edge than at model scale. This is not simply a Reynolds number effect. Small variations in the flow caused by turbulence and gusts may alter the pressure distribution in particular on the roof, because of flow separation, possible reattachment and vortex generation. The flow at datum conditions in the wind tunnel has not much in common with the real wind flow around buildings. On the other hand, predictions with Computational Fluid Dynamics of wind flow in the close vicinity of buildings are very much affected by the cell size and distribution, but the limited number of cells and the required runtime is a serious constraint to model accurately pressure and velocity fields. Due to higher suction on the leading roof edge in full scale, it might well be that a prototype of a building integrated Ducted Wind Turbine performs better than predicted by experimental and numerical modelling.

Important to note is the systematic difference between two dimensional and three dimensional simulation. A two dimensional simulation does not accurately reflect the flow situation in the cross-sectional symmetry plane of a three dimensional flow domain. For the flow towards a simple rectangular block, two dimensional simulation causes overprediction of positive pressure on the front façade and suction over the roof. Further, the flow seems to separate more and generates a larger pattern of recirculation.

In the progressed simulation work with a multi domain grid based on the body fitted coordinate system for modelling aerodynamical shapes, it turned out that the requirements for modelling the whole flow domain including the integrated duct exceeded hardware and software limitations. Still, a qualitative comparison of different design options is possible on the base of two dimensional flow simulations.

A three dimensional simulation could confirm the measured induced wind speed in the duct, in spite of its failure to predict the pressure field over the roof properly (due to the limited amount of cells). This might suggest that in the simulation the pressure field on the roof has less effect on the induced wind flow through the duct, than the flow velocity pattern around the roof edge.

In the frame of this work, a new approach has been developed and tested to couple the two dimensional simulation to a precalculated three dimensional solution in a cross-sectional plane. Here, the mapping of the three dimensional cartesian grid solution as a boundary to the rather two dimensional grid in body fitted coordinate system resulted in a coherent prediction of flow pattern at the front façade and over the roof. However, in particular the wake of the building is not yet solved in a satisfying way. The flow field mapping procedure is at an early stage of development and was devised in an attempt to overcome difficulties in the presented work. Various ways of extending and improving the method are suggested. Eventually, this method might facilitate the generation of flow field solutions for two dimensional models with complex geometry, which accurately represent the cross-sectional solution of a three dimensional flowfield.

The standard form of the k-ε turbulence model, widely used in wind engineering, has been applied. However, as this model assumes isotropic turbulence, it may be that it was not entirely appropriate for the flow field with its streamline curvature, swirl in the duct, separation and reattachment. Another turbulence model would be required to account for any local anisotropy, for example the Algebraic Stress Model. This would be a suggestion for future work.

A simplified power prediction model has been presented, which predicts a much higher monthly energy yield than for other competitive deployments of renewable energy generation in the built environment. However, the fluid dynamics of the integrated duct is much more complex than for a conventional augmented wind turbine. Also, the optimum rotor characteristics have yet to be established. Therefore, at this stage it is impossible to develop a more sophisticated model.

What is possible at this stage is to suggest the construction and installation of a real scale prototype of the building integrated Ducted Wind Turbine module. Basic design outlines can be derived from the presented work.

Appendix I:

Technical Specification of the Wind Turbine Rutland WG 910 'Standard'

The Rutland Windcharger is specially designed to maintain the charge in 12 or 24 V batteries and incorporates among others the following design features:

- Permanent magnet disc type ironless generator which also acts as flywheel
- Charging commences at very low wind speeds (1.8 m/s)
- Thermostat and choke protect windings in prolonged gale force winds
- 6 bladed rotor, 0.91 m diameter

The power curve was determined from the characteristics for the electric current output charging into a 12 V battery, as provided by the manufacturer (Marlec).
For the power prediction model, the slope was approximated with a linear function.

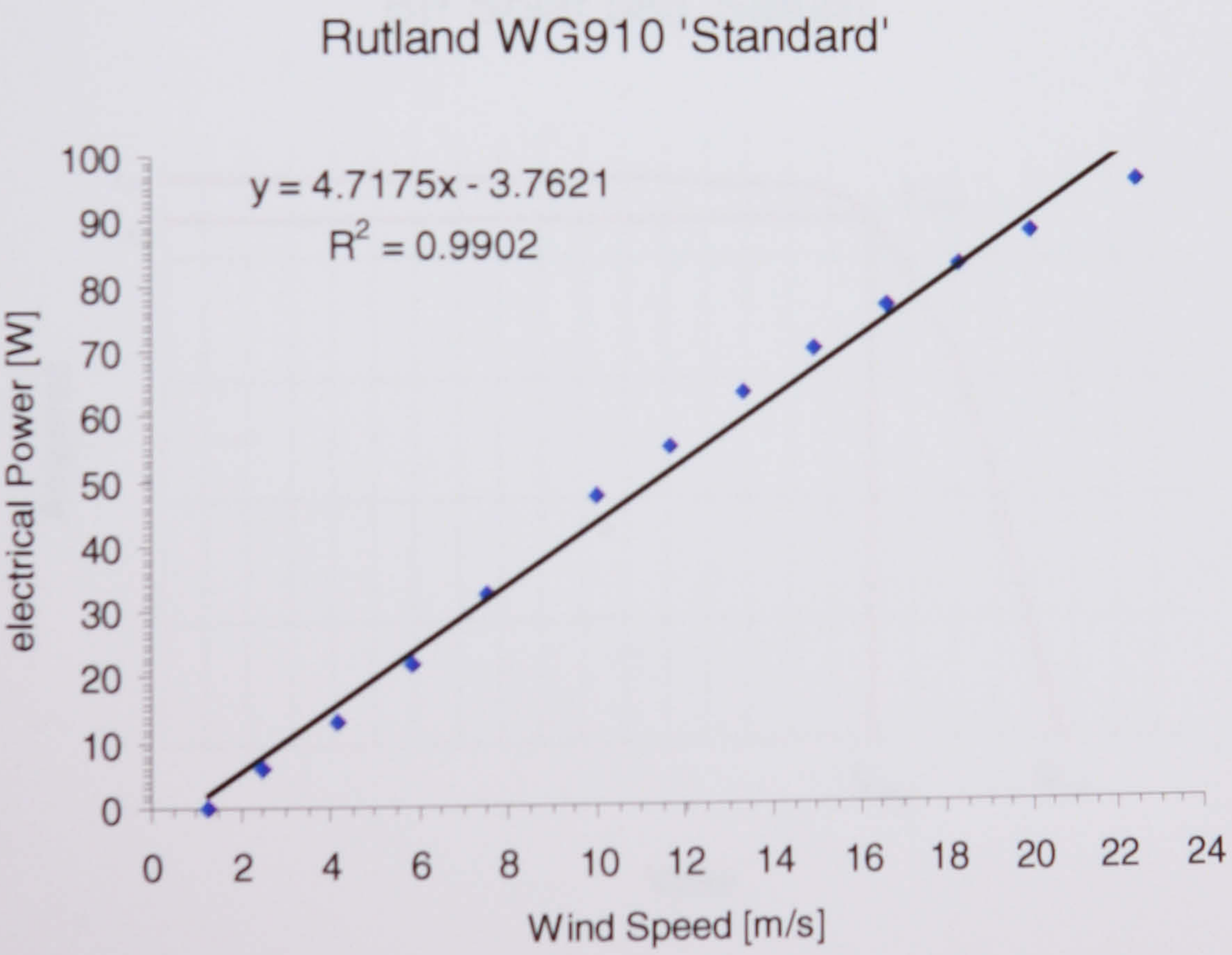

Reference:

The Rutland Windcharger, Technical Specification sheet WG910 'Standard'
Marlec Engineering Co. Ltd., Rutland House, Corby Northants NN17 5XY, UK

Appendix II:

Technical Specification of the Solar Module BP Solar 585 'Saturn'

All performance specifications are as measured at standard test conditions (Insolation of 1000 / Wm^2, AM 1.5, 25^0 C cell temperature).

- 36 silicon solar cells connected in series
- Peak power voltage: V_{mp} ~ 17 to 19 V
- Nominal peak power: $P_{max} = 85$ W
- Peak power current: $I_{mp} = 4.72$ A
- Short circuit current: $I_{sc} = 5.0$ A
- Open circuit voltage: $V_{oc} = 22.03$ V
- Minimum Power: 80 W
- Size: 525 mm x 1183 mm

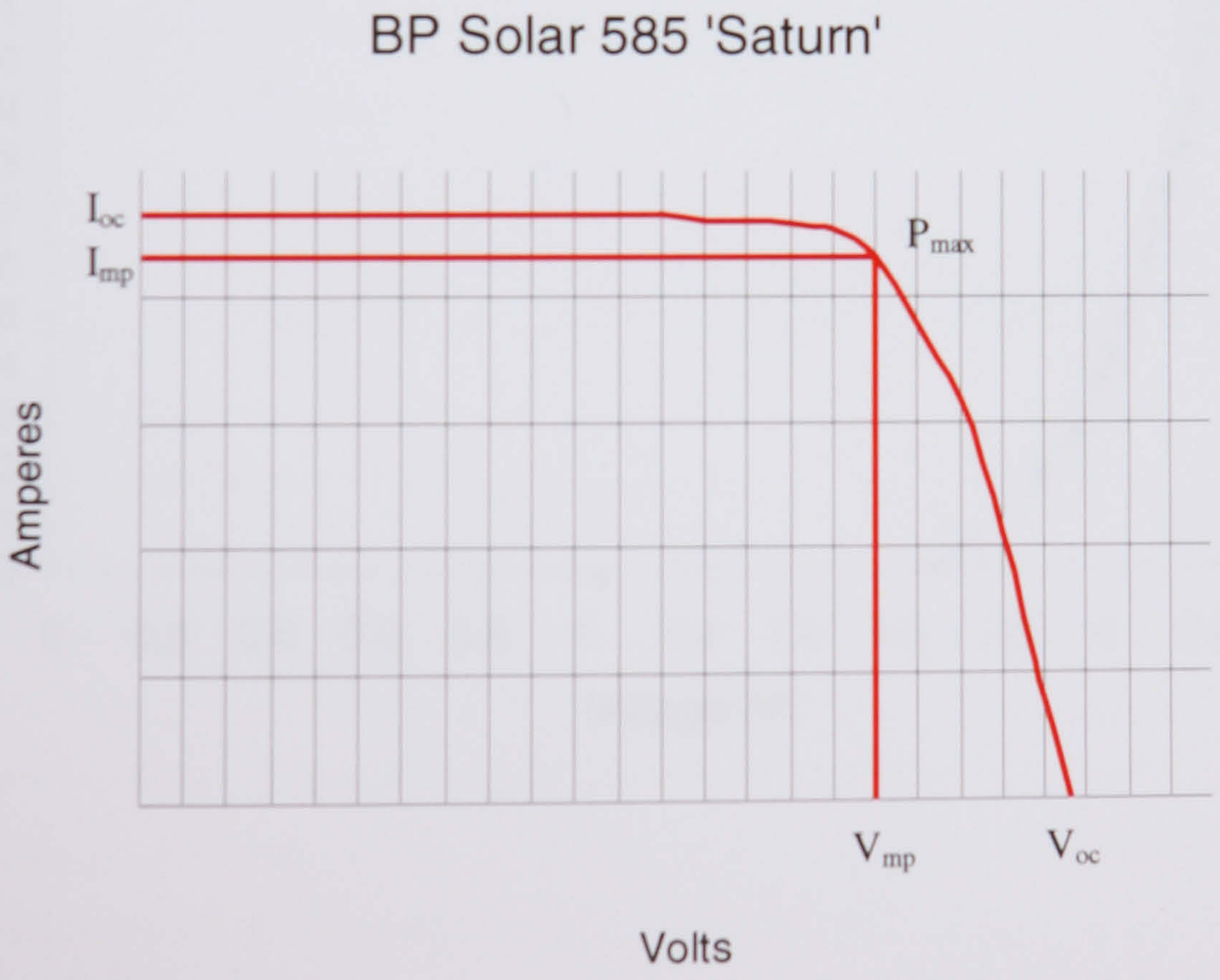

Reference:

Solar Modules, Technical Specification Sheet BP Solar 585 'Saturn'

BP Solar, Sunbury-on-Thames, Middlesex TW16 7XA, UK

Appendix III:

Technical Specification of the Hot Wire Probe DANTEC (probe type 55)

Sensor resistance at 20° C	$R_{20} = 3.51\ \Omega$
Leads resistance at 20° C	$R_l = 0.5\ \Omega$
Sensor TCR	$\alpha_{20} = 0.36\ \%\ /\ C$

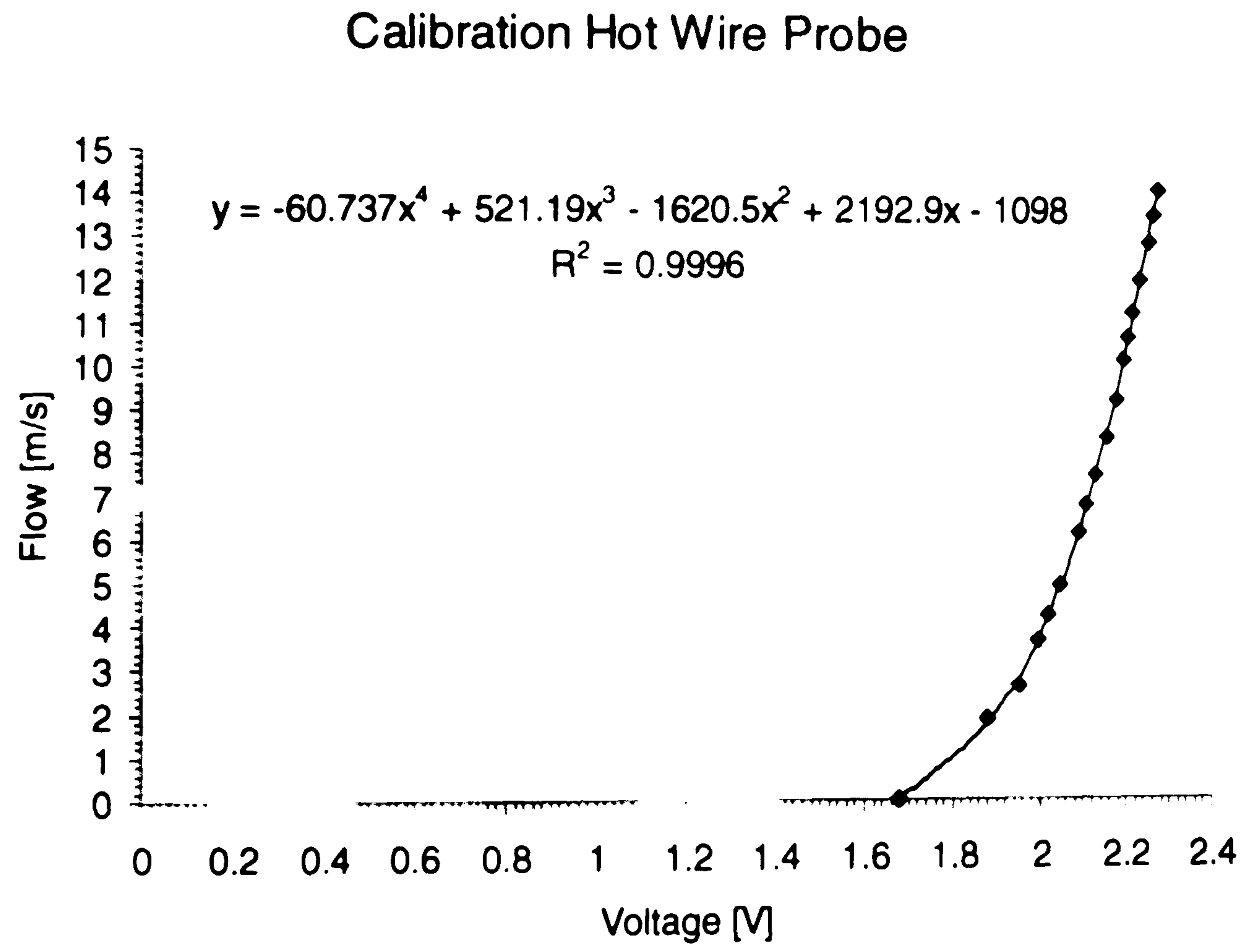

Reference:

Dantec 56C 17 CTA (Constant Temperature Anemometer) probe type 55, DISA Electronik, Denmark

Acknowledgements

First of all, I wish to thank Prof. Dr. J. Clarke, Director of the Energy Systems Research Unit at the University of Strathclyde in Glasgow, and all associated colleagues for receiving me kindly in the international research unit. I appreciate very much the interest of the Unit in the presented work and experienced plenty of support. I express my gratitude in particular to Dr. A. Grant, Deputy Director of the Energy Systems Research Unit, for his competent supervision, guidance and advice through all stages of the work. The pleasant atmosphere of our co-operation contributed much to the success of the work.

In the same way I am grateful to Dr. T. Scanlon, Lecturer in the Division of Thermofluids, who provided most competent advice and assistance in the field of Computational Fluid Dynamics. Here, fruitful discussions with several scientists in the University were of great help.

For the experimental part of the presented work in the Aerodynamics Laboratory, Dr. M. Stickland and A. Oldroyd M.Sc. of the Division of Thermofluids gave valuable guidance.

I would like also to extend my appreciation to all craftsmen and technicians at the Department, without them not much would actually have been realised. Special thanks to E. Duncan, Superintendent of the Mechanical Engineering Laboratory, and to the late T. Craigie, former Senior Technician in charge of the Wind Tunnel. Similarly, thanks are due to P. McGuiness, Electronic Superintendent and to his assistant R. Galbraith, Junior Electronic Technician.

The help of my friend and colleague Ing. G. Quinonez Varela was inestimable throughout all those years.

Further, I would like to show recognition to all those who contributed to the presented work with their student projects: above all Dipl.-Ing. M. Leyk, who designed, built and tested the wind tunnel model; A. Docherty B.Eng. who investigated the flow conditions in the wind tunnel working section; M. Aris M.Sc. and Ing. I. Andina Pendas M.Sc. who focused on the free standing model; A. Parkinson who considered the integration of the Ducted Wind Turbine in an architectural study.

Very special thanks to my wife Ing. M. Tamayo Cantón M.Sc. for her assistance in generating all the AutoCAD drawings in the presented thesis.

I like to extend my recognition to Prof. Dr. R. McD. Galbraith, Shoda Chair, Head of the Department of Aerospace Engineering at the University of Glasgow, for taking on the external examination. Thanks again to Dr. T. Scanlon for the internal examination and to Prof. Dr. D. Gorman, Division of System Dynamics and Control, who acted as Chairman during the doctoral viva.

I am grateful to my parents, to my sister and brother in Germany for their unconditional support and solidarity. Above all I appreciate very much the love and energy of my wife Mayra which accompanied the progress of my work.

Finally, I would like to thank Dr. B. Robertson, Commission of the European Communities, DG XII, Directorate-General for Science, Research and Development, for providing the framework and the supportive environment during the European Marie Curie Workshop Conferences throughout the duration of the project.

The presented work was carried out within the Marie Curie Research Fellowship, Commission of the European Communities, DG XII, Directorate-General for Science, Research and Development, under the 4th framework, JOULE – Non Nuclear Energy Research: Project: Wind Energy in the Built Environment, Project No. JOR3-CT97-5008 (DG12-DEMA).